

Durham E-Theses

Seismic investigation of crustal accretion at the slow spreading Mid-Atlantic Ridge-The Reykjanes Ridge at 57 45'N

D.A. Navin

How to cite:

Navin, D.A. (1996) Seismic investigation of crustal accretion at the slow spreading Mid-Atlantic Ridge-The Reykjanes Ridge at 57 45'N. Doctoral thesis, Durham University.

Use policy

The full-text may be used and/or reproduced, and given to third parties in any format or medium, without prior permission or charge, for personal research or study, educational, or not-for-profit purposes provided that:

- a full bibliographic reference is made to the original source
- a <https://etheses.durham.ac.uk/id/eprint/5387/> is made to the metadata record in Durham E-Theses
- the full-text is not changed in any way

The full-text must not be sold in any format or medium without the formal permission of the copyright holders.

Please consult the [full Durham E-Theses policy](#) for further details.

**Seismic investigation of crustal accretion
at the slow spreading Mid-Atlantic Ridge –
The Reykjanes Ridge at 57° 45'N**

**by
D.A. Navin**

The copyright of this thesis rests with the author.
No quotation from it should be published without
his prior written consent and information derived
from it should be acknowledged.

**A thesis submitted for the degree of
Doctor of Philosophy
at the University of Durham**

10 MAR 1997



Department of Geological Sciences

December 1996

Declaration

This dissertation describes my own work, except where acknowledgement is made in the text, and is not substantially the same as any work that has been or is being submitted to this and any other university for any degree, diploma or other qualification.

D.A. Navin

December 1996

A journey of a thousand miles must begin with a single step.

Lao Zi (c. 604 - c. 531 B.C.)

**Seismic investigation of crustal accretion at the slow spreading
Mid-Atlantic Ridge – The Reykjanes Ridge at 57° 45'N
D.A. Navin**

Abstract

Studies of mid-ocean ridges have provided evidence of magma chambers beneath both fast and intermediate spreading ridges. However no such features have been observed to date beneath slow spreading ridges. These contradictory observations are in direct conflict with seismic studies which reveal that the resulting crustal structures are similar and hence crustal structure is independent of the spreading rate. These latter observations in turn lead to the implication that the accretionary processes operating at all ridge types must also be similar. The aim of this study is to attempt to resolve between this discrepancy in geophysical observations of magma chambers at fast, intermediate and slow spreading ridges and investigate the nature of accretionary processes operating such that the same crustal structure is achieved. Therefore an apparently currently magmatically active section of the slow spreading Mid-Atlantic Ridge at 57° 45'N on the Reykjanes Ridge, was selected as the target of a multidisciplinary geophysical experiment to be conducted aboard the *RRS Charles Darwin* in 1993.

Wide-angle seismic data recorded using 10 digital ocean bottom seismometers were used to generate models of the crustal structure along and across-axis. These models were confirmed and further constrained by modelling of normal incidence seismic and gravity data and by comparison with the results of modelling controlled source electromagnetic data.

The resultant models indicate that a magma chamber exists beneath the axial volcanic ridge studied, providing the first geophysical observation of such a feature at any slow spreading ridge. This magma chamber is similar in dimensions to those observed beneath fast and intermediate spreading ridges and consists of a thin, narrow sill-like body which appears to be continuous along-axis, and which is underlain by a region of partial melt extending almost to the Moho. This latter feature also appears to be both longer-lived and more extensive than the magma chamber. The 2.5 km depth to the top of the magma chamber is only slightly greater than that observed at fast spreading ridges, which indicates that magma chamber depth does not vary significantly with spreading rate. However, there are insufficient data available to fully constrain and develop this relationship to its fullest.

Therefore the results of this study indicate that the processes of crustal accretion occurring at all spreading ridges are similar, with the lack of observations of magma chambers being due to the fact that the periods of magmatic activity at slow spreading ridges are considerably more widely separated in both space and time than for fast and intermediate spreading ridges. The main difference however, appears to occur in the process of emplacement of layer 2A, which is observed to thicken off-axis at fast spreading ridges due to the less viscous lavas produced at these ridges being able to flow further off-axis. The results of this study, and of two other studies at slow spreading ridges, show that layer 2A is completely formed on-axis and thins off-axis due to extensional faulting. The remainder of the crust is completely emplaced, and the Moho formed, on-axis at all spreading rates.

Acknowledgements

Studying for a Ph.D. inevitably requires the support, both technical and moral, of a large group of people who all deserve thanks for making my 3½ years in Durham (and the Mid-Atlantic and Lau Basin) memorable, interesting and fun.

Probably the most important of these is my supervisor, Chris Peirce, who has bravely tackled the inadequacies in my knowledge of wide-angle seismics, computing and the English language and has also grappled with numerous drafts of this thesis. Chris has also given me the opportunity to participate in two unforgettable research cruises and showed me just how marine wide-angle seismic data **should** be collected and processed and provided invaluable advice on forward modelling. Thanks.

The Cambridge DOBS were an integral part of this experiment and were kindly provided by Martin Sinha, who also helped guide me through the intricacies of CDOBS data processing and volunteered valuable advice on seismic and gravity models and the use of seasickness bands.

This study was part of a multidisciplinary investigation and therefore thanks go to everyone involved in this project including: Dave, Mike and John (seismics); Steve, Pravin and Lucy (CSEM); Anthony and Graham (MT); the RVS personnel – most importantly the shot firers Kev, Mike and Tony – essential to any seismic experiment; and the officers and crew of the *RRS Charles Darwin* who were also somewhat indispensable.

Thanks to Lucy MacGregor for her CSEM models and explaining to me just what they mean (before long I may even come to understand the relative importance of E_p and E_ψ) and for joining me on a somewhat indirect route to the Lau Basin.

Mike Inglis deserves a mention for the work he undertook for his M.Sc. dissertation on the normal incidence data.

Ian Turner kindly read sections of this thesis for me and alternately drove me up the wall and provided light relief over the last year with his incessant questions.

Guidance in the use of computers and computer programs came from Chris, Martin, Dave, Roger, Abby, John, George, Ziad, Simon, Michelle, Matt and special thanks to Rupert for helping to resolve the complexities of 2-D marine geometry!

I have been financed by NERC throughout my Ph.D. and the research cruise on which this dataset was collected was also NERC funded.

Overlapping the bounds of "technical and moral" support, thanks to "Team DOBS" – Tufty, Chalkie and Skippy.

..... and into purely moral support thanks to all friends and past house mates: Alison, Andy, Casey, Emma, Jon, Kate, Meg, Michelle, Simon M., Simon W., Toby, Zoe, etc..

And last but not least to my parents – thanks for everything.

Contents

1 Introduction

1.1	Mid-ocean ridges	1
1.1.1	Fast spreading ridges	1
1.1.2	Intermediate spreading ridges	5
1.1.3	Slow spreading ridges	6
1.1.4	Segmentation of mid-ocean ridges	8
1.2	Oceanic crust	13
1.3	Magma chambers at mid-ocean ridges	14
1.4	Investigations of slow spreading ridges to date	18
1.5	The Reykjanes Ridge	20
1.6	Previous geophysical and geochemical surveys of the Reykjanes Ridge	21
1.7	Aims of this study	29
1.8	Summary and structure of this dissertation	30

2 Experimental configuration, acquisition and data processing

2.1	Introduction	32
2.2	Experimental configuration	33
2.3	Wide-angle data acquisition	37
2.3.1	Instrumentation	37
2.3.2	Seismic energy sources	44
2.4	The wide-angle seismic dataset	49
2.5	Data replay	53
2.5.1	Determination of explosive shot instants and detonation depths	53
2.5.2	SEG-Y _i	54
2.5.3	Replay of DDOBS data into SEG-Y _i files	55
2.5.4	Replay of CDOBS data into SEG-Y _i files	58
2.6	Wide-angle data processing to final record sections	64
2.6.1	Corrections applied to wide-angle seismic data	64
2.6.2	Generation of interpretable sections	70
2.7	Errors associated with the wide-angle seismic data	71
2.7.1	DDOBS	71
2.7.2	CDOBS	72
2.8	Normal incidence data acquisition	73
2.8.1	Instrumentation	75
2.8.2	Source	75

2.8.3	Acquisition problems	76
2.9	The normal incidence seismic dataset	76
2.9.1	Data collected	76
2.9.2	Replay of SAQ multichannel seismic reflection data tapes	77
2.9.3	Normal incidence data processing	78
2.10	Additional datasets	80
2.11	Summary	84
3 The Reykjanes Ridge wide-angle seismic dataset		
3.1	Introduction	85
3.2	Source signatures and frequency content	85
3.3	Frequency analysis, filtering and phase identification	92
3.4	Wide-angle data	103
3.4.1	Prominent features of across-axis data sections	109
3.4.2	Prominent features of along-axis data sections	112
3.5	Summary	114
4 Modelling of the Reykjanes Ridge wide-angle seismic data		
4.1	Introduction	115
4.2	Along and across-axis initial models	115
4.2.1	Across-axis initial model	118
4.2.2	Along-axis initial model	120
4.2.3	Ray-trace modelling	122
4.3	Final velocity–depth models	126
4.3.1	Modelling strategy	126
4.3.2	Best-fitting across-axis velocity model	132
4.3.3	Best-fitting along-axis velocity model	139
4.4	Modelling resolution	145
4.5	Modelling techniques applied to the dataset	146
4.5.1	<i>Maslov</i>	147
4.5.2	<i>Beam87</i>	149
4.5.3	<i>Rayinvr</i>	150
4.6	Comparison of the results obtained with the individual techniques	151
4.7	Summary	158
5 Interpretation of the Reykjanes Ridge wide-angle seismic models		
5.1	Introduction	159
5.2	Gravity	159

5.2.1	2-D gravity modelling	160
5.2.2	Residual mantle Bouguer anomaly	172
5.3	The Reykjanes Ridge normal incidence seismic data	188
5.4	Comparison with the results of modelling the controlled source electromagnetic data	195
5.5	Relationship to previous studies of mid-ocean ridges	199
5.5.1	Seismic models	199
5.5.2	Gravity data	211
5.6	Summary	212
6 Conclusions and further work		
6.1	Introduction	215
6.2	Processes of crustal accretion at mid-ocean ridges	215
6.3	Results and conclusions from this study	217
6.4	Further work	223
6.4.1	Further work on the existing CD81/93 dataset	224
6.4.2	Collection of additional data	224
6.5	Conclusions	232
References		234
Appendix A		246
Appendix B		251
Appendix C		256
Appendix D		260
Appendix E		266

Glossary of terms and abbreviations

The following terms and abbreviations are used throughout this dissertation:-

DOBS	Digital Ocean Bottom Seismometer
DDOBS	Durham Digital Ocean Bottom Seismometer
CDOBS	Cambridge Digital Ocean Bottom Seismometer
NERC	Natural Environment Research Council
RVS	Research Vessel Services
P_g	Crustal diving ray
P_n	Mantle diving ray
P_mP	P-wave reflecting from the Moho
P_mS	P-wave converting to an S-wave on reflection at the Moho
first order boundary	boundary across which there is a distinct change in velocity
second order boundary	boundary across which only the velocity gradient changes
CDP	Common Depth Point
TWTT	Two-way travel time
SEG-Y	Multichannel seismic recording standard (see Barry <i>et al.</i> , 1975)
SEG-Y _{WA}	Variation on SEG-Y for wide-angle seismic data
SEG-Y _i	Version of SEG-Y used for in-house processing at Durham (consists of SEG-Y _{WA} files divided into their constituent parts)
PDAS	Portable Data Acquisition System
PC	IBM-compatible Personal Computer
SIMM	Static In-line Memory Module
RAM	Random Access Memory
SCSI	Small Computer Serial Interface
AVR	Axial Volcanic Ridge
MAR	Mid-Atlantic Ridge
EPR	East Pacific Rise
MBA	Mantle Bouguer anomaly
RMBA	Residual Mantle Bouguer anomaly
CSEM	Controlled source electromagnetic
GPS	Global Positioning System
GMT	Generic Mapping Tool (version 3.1, see Wessel and Smith, 1995)

Chapter 1

Introduction

1.1 Mid-ocean ridges

Since Hess (1962) first proposed seafloor spreading as a mechanism of explaining the volcanism and high heat flow observed at mid-ocean ridges, further studies of the ocean floor and crust have provided evidence to support this hypothesis, e.g. the mapping of linear magnetic anomalies which were found by Vine and Matthews (1963) to be symmetrical about the ridge axis. The process of seafloor spreading fits neatly into the framework of plate tectonics and mid-ocean ridges (see figure 1.1) are now widely recognised as the sites of crustal accretion (Vine, 1966; Keen and Tramontini, 1970; Fowler, 1976; Macdonald, 1982; Orcutt *et al.*, 1984; Detrick *et al.*, 1987; Vera *et al.*, 1990; Purdy *et al.*, 1992; Sinton and Detrick, 1992; Solomon and Toomey, 1992; Kent *et al.*, 1993). However due to their relative inaccessibility, lying beneath 3 km of water on average, the processes of crustal accretion across the broad range of spreading rates observed are not fully understood, despite having been the target of numerous studies (e.g. Detrick *et al.*, 1990; Vera *et al.*, 1990; Christenson *et al.*, 1993; Harding *et al.*, 1993).

The morphology of mid-ocean ridges has been observed to vary with spreading rate (Macdonald *et al.*, 1988; and see figures 1.2 and 1.3). The three main categories of mid-ocean ridge are described below together with the four scales of segmentation also recognised.

1.1.1 Fast spreading ridges

Fast spreading ridges such as the East Pacific Rise (EPR), are generally defined as having a half spreading rate of greater than 45 mm yr⁻¹ and the main characteristics of these ridges are listed below.



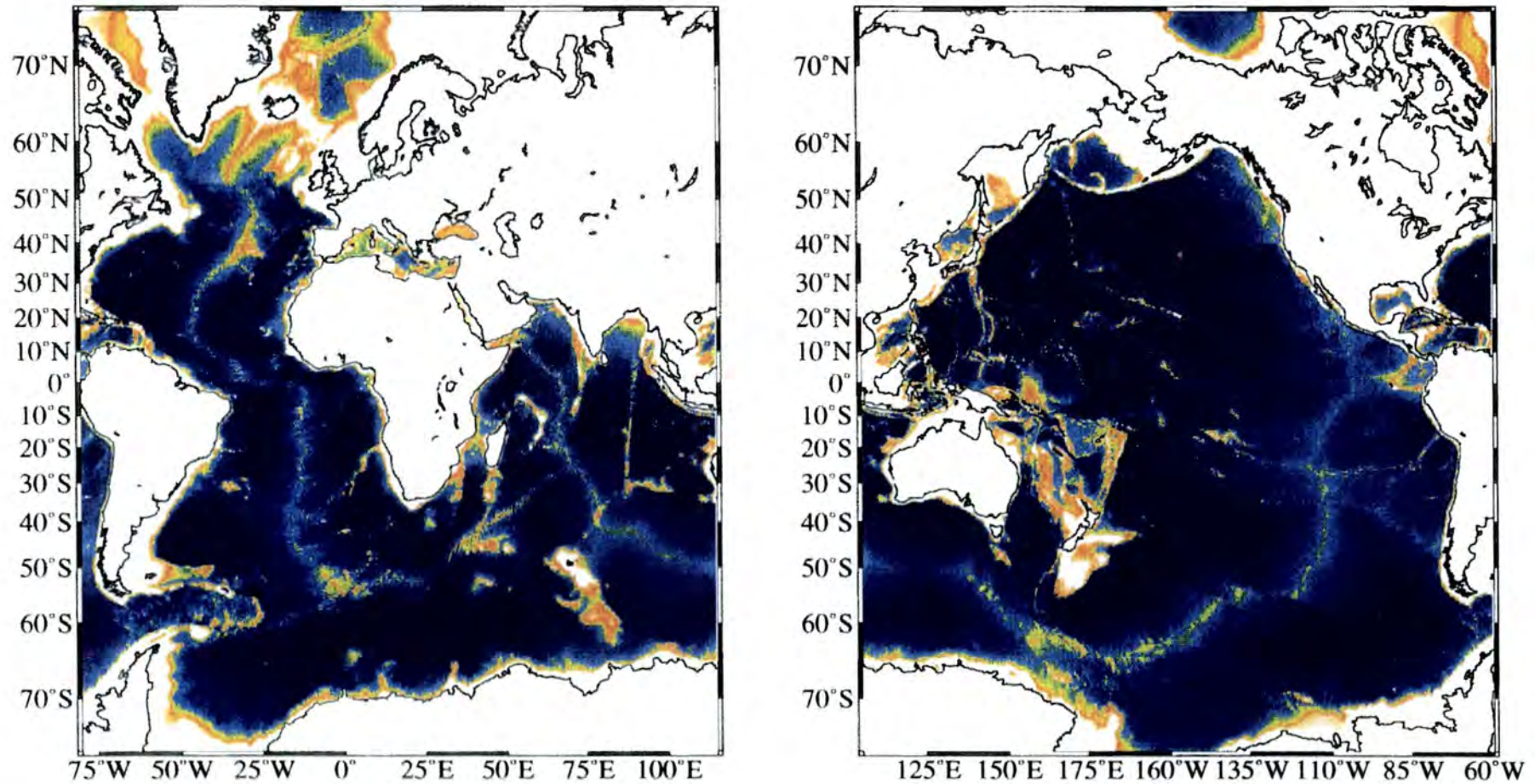


Figure 1.1: Distribution of mid-ocean ridges in the Atlantic and Indian Oceans (left) and the Pacific Ocean (right). Ocean depths* between 800 and 10 000 m are colour shaded from red (800 m) to blue (10 000 m). Note the broader, smoother bathymetric signature of the East Pacific Rise compared to that of the Mid-Atlantic Ridge, which is disrupted by numerous fracture zones.

* from the National Geophysical Data Centre's ETOPO5 bathymetry dataset.

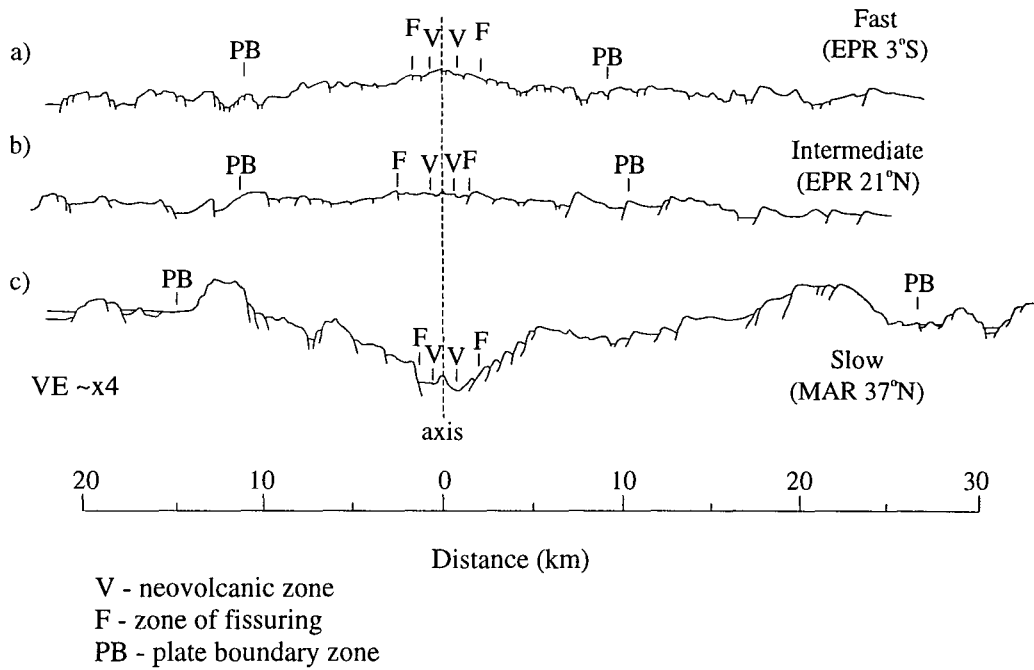


Figure 1.2: Across-axis bathymetric profiles of fast, intermediate and slow spreading ridges (after Macdonald, 1982). Note the transition from axial high to median valley topography and the increase in fault throw with decreasing spreading rate.

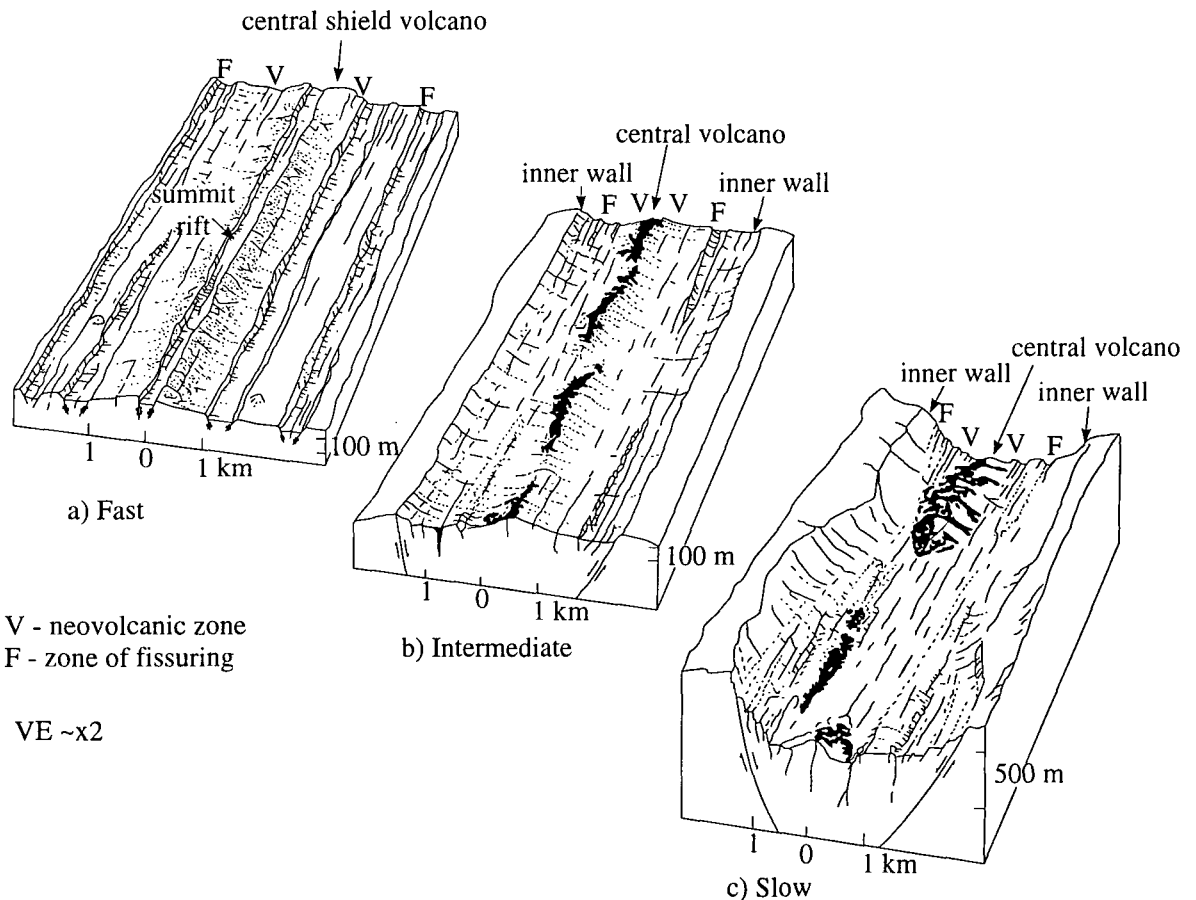


Figure 1.3: Sketches illustrating the axial morphology of fast, intermediate and slow spreading ridges (after Macdonald, 1982). The continuity of the central volcano decreases and the height of the faulted inner wall increases as spreading rate decreases.

- The average depth to the seafloor tends to increase with age away from mid-ocean ridges (Parsons and Sclater, 1977). However at fast spreading ridges an axial rise is observed between 200 and 300 m above the regional trend of the seafloor (Carbotte and Macdonald, 1994a; and see figure 1.2a). This rise has the form of an elongate shield volcano which is continuous between major offsets (see figure 1.3a).
- From the volume of lavas erupted and the spreading rate of the ridge, the interval between periods of magmatic activity has been estimated to be approximately 50 years (Lonsdale, 1977). Therefore the axial zone of weakness persists between eruptions, with the process of plate separation tending to spilt pre-existing volcanoes, transporting volcano segments off-axis on either plate. This persistent zone of crustal weakness results in a stable neovolcanic zone, 1-2 km in width, although some lava flows extend up to 4 km off-axis (Macdonald, 1982).
- The higher thermal regime at fast spreading ridges through which magma ascends to the surface, results in less viscous lavas and a higher proportion of eruptions occurring in the form of flows rather than pillow lavas.
- Tectonic faulting occurs at the axis, with inward facing fault scarps developing between 1 and 4 km offset from the ridge axis, and the faulting taking place along elongate fault planes (Macdonald, 1982). The elevated thermal regime at the axis results in the throws on these faults being less than 50 m (Carbotte and Macdonald, 1994a and b). Within 10 km of the axis outward dipping faults develop which, together with the back tilting of fault blocks, prevents the development of a deep rift valley and creates a relatively smooth flanking topography, with off-axis horsts and grabens forming abyssal hills.
- The amount of extension due to faulting at fast spreading ridges is estimated at ~5% (Macdonald, 1982).
- The axial highs observed at fast spreading ridges are also associated with free-air gravity highs which do not vary in amplitude as the spreading rate increases from the lower limit of 45 mm yr^{-1} half rate (Small and Sandwell, 1994).

1.1.2 Intermediate spreading ridges

Intermediate spreading ridges, e.g. the Juan de Fuca Ridge, are generally defined as having a half spreading rate of between 25 mm yr⁻¹ and 45 mm yr⁻¹. Most of their features are transitional between those of fast and slow spreading ridges.

- Intermediate spreading ridges are observed to have a broad axial high associated with a shallow median valley, 50 to 200 m deep (Macdonald, 1982; and see figure 1.2b). Within this median valley lies a series of elongate axial volcanic ridges (AVRs), arranged en echelon (Macdonald, 1982; and see figure 1.3b).
- Using the thickness of the extrusive section and the areal extent of AVRs combined with the spreading rate of the ridge, the interval between periods of magmatic activity is estimated to be between 300 and 600 years at intermediate spreading ridges (Macdonald, 1982). Layers of pillow lavas show magnetic continuity across a large vertical extent implying that these eruptions are fairly rapid and last of the order of 100 years (Hall, 1976). Therefore again, like fast spreading ridges, the zone of weakness persists between eruptions and tends to concentrate recent magmatic activity into a neovolcanic zone some 1-2 km in width and causes splitting of pre-existing volcanoes.
- In contrast to the bathymetric highs observed at fast spreading ridges which are supported by buoyancy forces and therefore not preserved off-axis, highs at intermediate spreading ridges tend to be caused by volcanic construction and are preserved off-axis as abyssal hills (Carbotte and Macdonald, 1994a).
- The *crustal temperature* at intermediate spreading ridges is not as high as at fast spreading ridges, therefore the erupting lavas travelling through this regime have a higher viscosity, which results in less extensive basaltic sheet flows and more extensive pillow lavas being observed than at fast spreading ridges (Macdonald, 1982).
- Although an anomalous thermal regime in the mantle has little effect at fast spreading ridges, it can profoundly influence the morphology of slow and intermediate spreading ridges. For example, the Juan de Fuca and Gorda Ridges are both spreading at 30-35 mm yr⁻¹ (half rate). The former is located proximal to

the Cobb hot spot, which increases the mantle thermal gradient, and is observed to have an axial high whereas the latter, located distal from any thermal anomaly, has a median valley (Hooft and Detrick, 1995).

- Like fast spreading ridges, inward facing normal faults develop within 1-4 km of the ridge axis and these have throws of 50 m or less. These faults lead to the development of a shallow rift valley which has gentle relief due to the back tilting of fault blocks and the outward facing faults which also develop within 4 km of the axis (Macdonald, 1982). As the crust at this class of spreading ridge is cooler and stronger, faulting produces rougher topography than observed at fast spreading ridges.
- The gravity anomaly observed at these ridges varies with morphology. Free-air gravity highs are associated with ridges where axial highs dominate and gravity lows are observed over median valley topography (Small and Sandwell, 1994).

1.1.3 Slow spreading ridges

Slow spreading ridges, such as the Mid-Atlantic Ridge (MAR), are generally defined as having a half spreading rate of less than 25 mm yr⁻¹. The main characteristics of this type of ridge are described below.

- Slow spreading ridges are generally marked by a median valley 1-3 km deep which has an inner floor varying between 5 km and 15 km in width (Macdonald, 1982; and see figure 1.2c). Within this median valley is a discontinuous chain of AVRs, slightly elongate parallel to the ridge axis (Macdonald, 1982; and see figure 1.3c).
- The interval between eruptions at slow spreading ridges is estimated, from the thickness of the extrusive section and the extent of volcanoes combined with the spreading rate, at between 5 000 and 10 000 years (Bryan and Moore, 1977). This relatively long period allows the crust to completely cool between each eruption which individually last of the order of 100 years (Hall, 1976; and see section 1.1.2). Permanent zones of weakness are not observed at slow spreading ridges

which implies that eruptions are unlikely to remain in the same location. Consequently wider, less stable neovolcanic zones are observed.

- The colder thermal regime also results in the extrusive layer being composed predominantly of pillow basalts rather than sheet flows.
- Inward facing faults develop at between 1 and 4 km offset from the ridge axis. These faults develop large throws which are supported by the colder, stronger crust present at this kind of ridge. These normal faults combine to form the tilted blocks of the median valley walls (Laughton and Searle, 1979; and see figures 1.2c and 1.3c). The median valley bounding faults are not laterally extensive parallel to the ridge axis, being ~1-2 km in length with several faults combining to produce the appearance of a median valley wall which is, in turn, apparently continuous between offsets. This pattern of faulting produces either a U-shaped valley with two main lines of faults or a V-shaped valley made up of several terraced faults (Macdonald, 1982). Outward facing faults develop at ~30 km offset from the axis and are less common than at fast spreading ridges as the thick brittle layer hinders their development.
- This thicker brittle layer, which is able to support severe topography, combined with the extensive faulting results in the much rougher seabed topography observed at slow spreading ridges (Macdonald, 1982).
- The amount of extension due to faulting at slow spreading ridges is estimated at ~15% (Macdonald, 1982).
- In regions with elevated mantle temperatures such as hot spots, the typical median valley topography is not observed. Instead an axial high-type topography predominates, more akin to that observed at faster spreading ridges (e.g. the Reykjanes Ridge north of 59°N). This characteristic is believed to be due to the existence of a thicker crust, generated by a higher degree of partial melting in the mantle at depth due to the increased thermal gradient. The thick crust extends to a greater depth and is therefore hotter and weaker and unable to support topography (Bell and Buck, 1992).

- The median valley at slow spreading ridges is marked by a free-air gravity anomaly low which has an amplitude that decreases as the spreading rate increases (Small and Sandwell, 1994).

1.1.4 Segmentation of mid-ocean ridges

Segmentation of mid-ocean ridges is evident from their morphology, geochemistry and associated gravity anomaly. This segmentation occurs on a variety of scales (see figure 1.4):-

- *First order segments* are bounded by transforms, the surface expression of which is a fracture zone. Propagating rift segments have a wavelength of ~200-400 km at slow spreading ridges and ~600-1000 km at fast and intermediate spreading ridges (Sandwell, 1986). These discontinuities offset the ridge axis by more than 30 km (Macdonald *et al.*, 1991), which is equivalent to an age offset of 0.5 to 1 million years, and hence active ridges terminate against cold, rigid lithosphere on the opposing side of the fracture zone (Macdonald *et al.*, 1988). The bathymetry of ridges generally increases towards transform offsets by as much as 500-3000 m and seismic evidence indicates that crustal thinning occurs at the fracture zones themselves (Minshull *et al.*, 1991). The boundaries of these first order segments are often marked by pronounced geochemical anomalies with rare earth element enrichment observed towards the ends of segments (Langmuir *et al.*, 1986). These boundaries also offset the linear magnetic anomalies associated with ridge axes and their influence can be traced for many kilometres off-axis, indicating that these features persist for over several millions of years. Where magma chamber reflectors are imaged at fast and intermediate spreading ridges they are seen to be disrupted at first order boundaries.
- *Second order segments* have a wavelength of approximately 50-300 km at fast and intermediate spreading ridges and their ends are marked by increases in axial depth of the order of 100-1000 m (Macdonald *et al.*, 1991). Their boundaries are marked by large overlapping spreading centres (OSCs), which offset the ridge axis by up to 3-5 km, or small non-transform offsets of less than 20 km in width

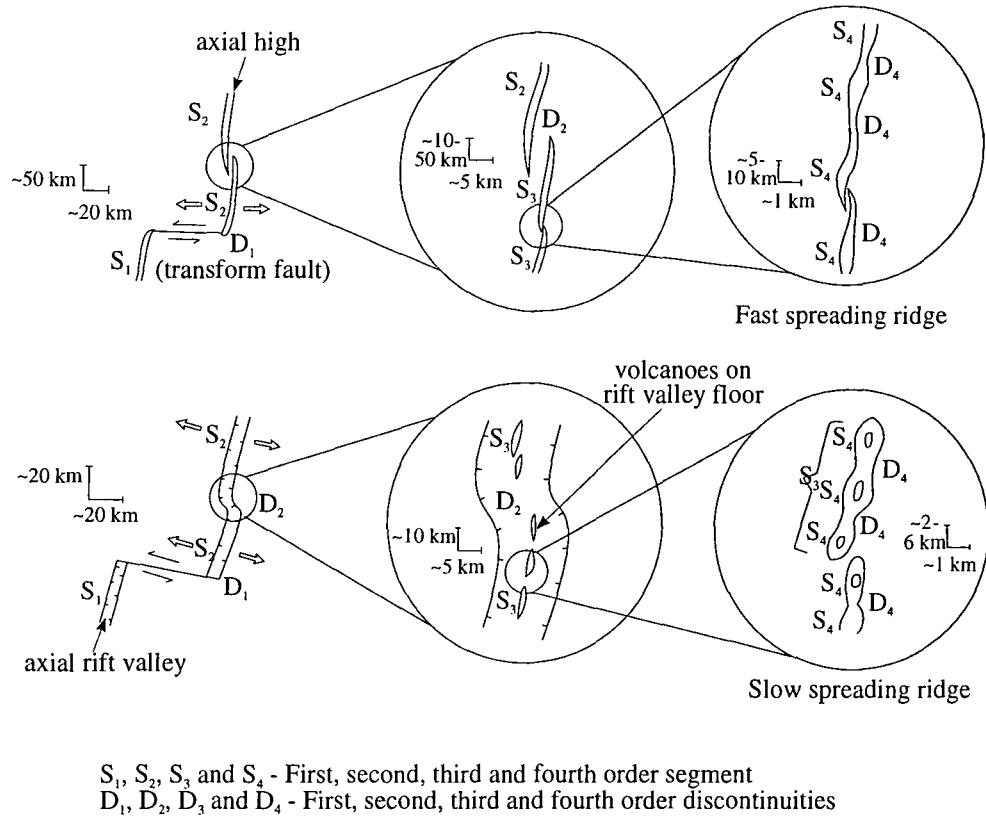


Figure 1.4: Scales of segmentation at fast and slow spreading ridges (after Macdonald *et al.*, 1991). First order discontinuities are marked by transform faults at all spreading rates; second order discontinuities consist of overlapping spreading centres (OSCs) at fast spreading ridges and non-transform offsets at slow spreading ridges; third order discontinuities consist of small OSCs at fast and intervolcano gaps at slow spreading ridges; and fourth order discontinuities are marked by devals at fast and intervolcano gaps at slow spreading ridges.

(Macdonald *et al.*, 1988). The influence of these boundaries persists off-axis, indicating that they exist for 0.5 to 3 million years. However, off-axis they tend to be observed as V-shaped bathymetric anomalies which indicates that second order discontinuities migrate along the ridge axis with time. These second order segments are similar to first order segments in that they are also marked geochemically and axial magma chambers are observed to be truncated at their boundaries. At slow spreading ridges these segment boundaries coincide with gaps in the discrete volcanic centres within the neovolcanic zone.

- *Third order segments* have a wavelength of ~30-100 km and their boundaries are small overlapping spreading centres with offsets of ~0.5-3.5 km at fast and intermediate spreading ridges (Macdonald *et al.*, 1988). The associated

bathymetric anomaly is of the order of 30-300 m (Macdonald *et al.*, 1991). The off-axis trace of these small discontinuities persists for only a few kilometres implying that they are short-lived features, lasting less than 10^4 years (Macdonald *et al.*, 1988). Again where magma chamber reflectors are observed they are truncated at the ends of these third order segments, and at slow spreading ridges the boundaries coincide with gaps between AVR's.

- *Fourth order segments* have a wavelength of ~10-50 km and offsets of less than 0.5 km. They have little or no measurable bathymetric signature and segmentation on this scale is usually observed geochemically. Alternatively these segments may be defined by a deviation in the linearity of the axis by up to 1-5°. Hence the boundaries are known as devals (deviations in axial linearity – Macdonald *et al.*, 1988). This segmentation is the shortest-lived of the four and has no off-axis signature.

As crustal thinning occurs at both transform and non-transform offsets, this indicates that segmentation is generated by individual cells of upwelling material rather than cold edge effects which could be caused if ridges truncate against significantly colder crust (Lawson, 1996). The distribution of partial melt therefore defines the segmentation at first, second and third order boundaries and the wavelength of fourth order segmentation is controlled by circulation cells within the axial magma chamber itself (Macdonald *et al.*, 1988; and see figure 1.5).

Ridge segmentation is also observed in the mantle Bouguer gravity anomaly (Kuo and Forsyth, 1988; Lin *et al.*, 1990; and see figure 1.6) with "bull's-eye" gravity lows observed at slow spreading ridge segment centres and both the gravity anomaly and seafloor depth decreasing towards segment ends. This kind of ridge segmentation is believed to be caused by mantle upwelling, or melt production, that is focused towards the centre of segments and which results in lower magma supply towards segment ends (Tolstoy *et al.*, 1993; and see figure 1.5).

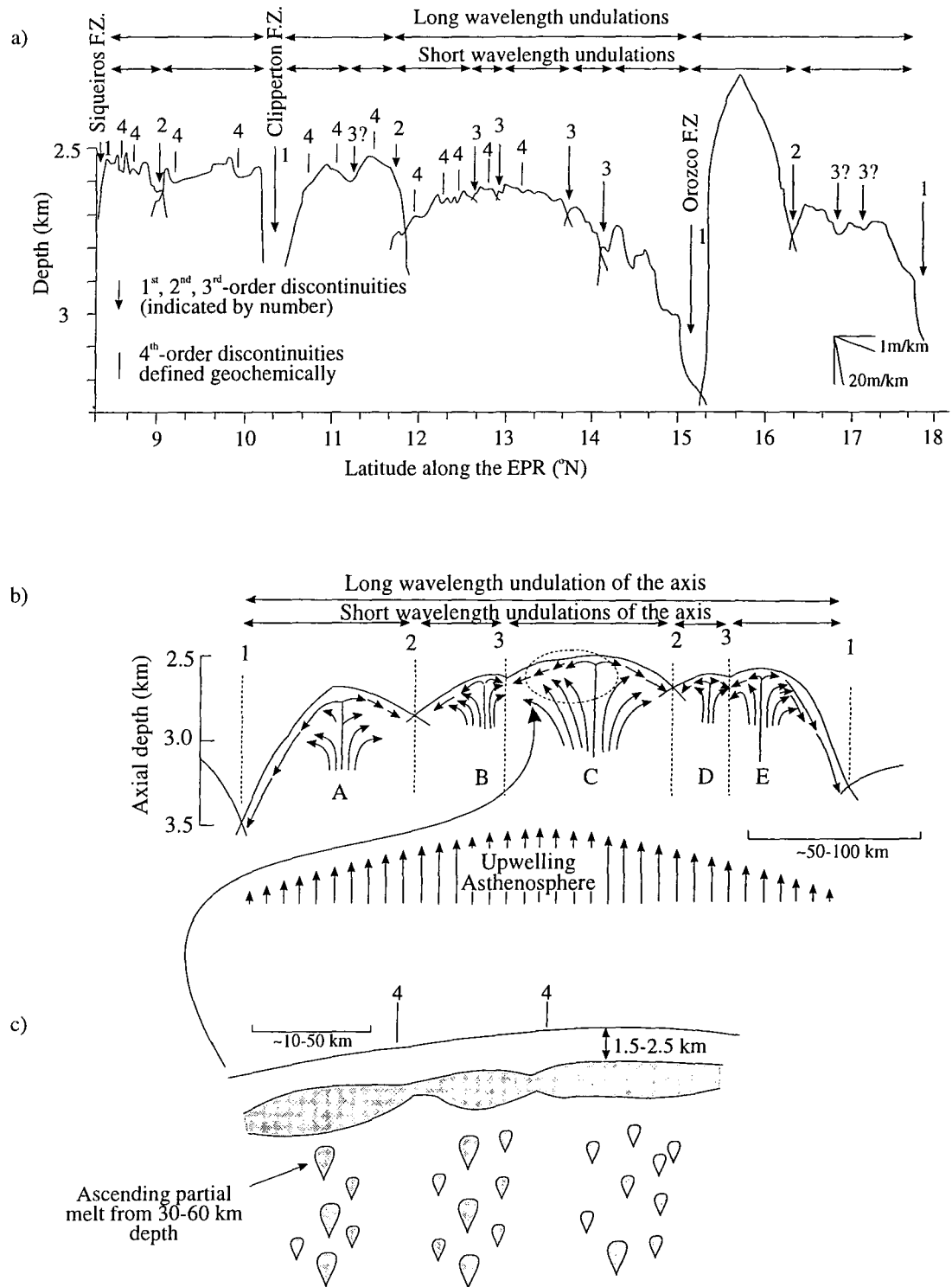


Figure 1.5: Bathymetric segmentation and its possible causes (after Macdonald *et al.*, 1988).

- Along-axis profile of the EPR with the various scales of segmentation labelled.
- Possible cause of segmentation – individual pulses of magma upwell beneath first, second and third order segments.
- Fourth order segmentation – possibly caused by circulation cells within individual magma chambers.

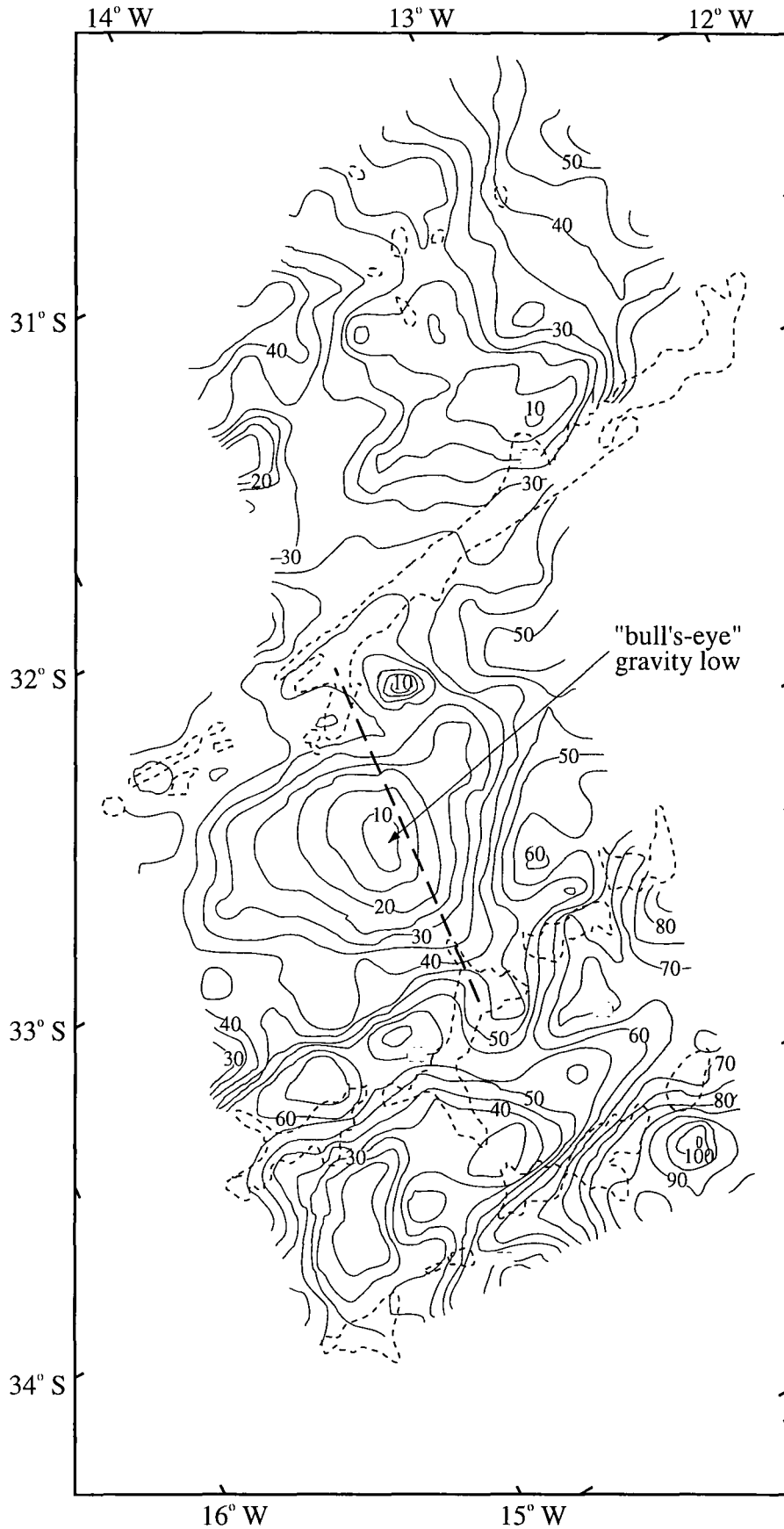


Figure 1.6: "Bull's-eye" mantle Bouguer gravity anomaly low centred over a MAR segment (after Kuo and Forsyth, 1988). The 3600 m contour is shown as a dotted line and outlines segment bounding fracture zones and the long dashed line marks an individual spreading segment.

1.2 Oceanic crust

Mature oceanic crustal structure is surprisingly uniform and apparently independent of the spreading rate at which it was produced. Early investigations of the oceanic crust based on earthquake seismology and refraction seismic studies indicated that the oceanic crust comprised of three main layers (Raitt, 1963). An upper layer of sediments (oceanic layer 1) overlies an extrusive volcanic section (layer 2) which in turn overlies a layer of gabbroic composition (layer 3). The underlying mantle is defined as layer 4. Improvements in seismic data acquisition and processing methods have led to the subdivision of these three main layers (e.g. Bratt and Purdy, 1984; Fowler, 1990; and see figure 1.7). Layer 2 has been subdivided into:-

- Layer 2A which has a low P-wave velocity ranging from 2.5 km s^{-1} to 4.5 km s^{-1} and a high velocity gradient. This layer is believed to consist mainly of highly fractured basalts in the form of sheet flows and pillow lavas (Christenson *et al.*, 1994).

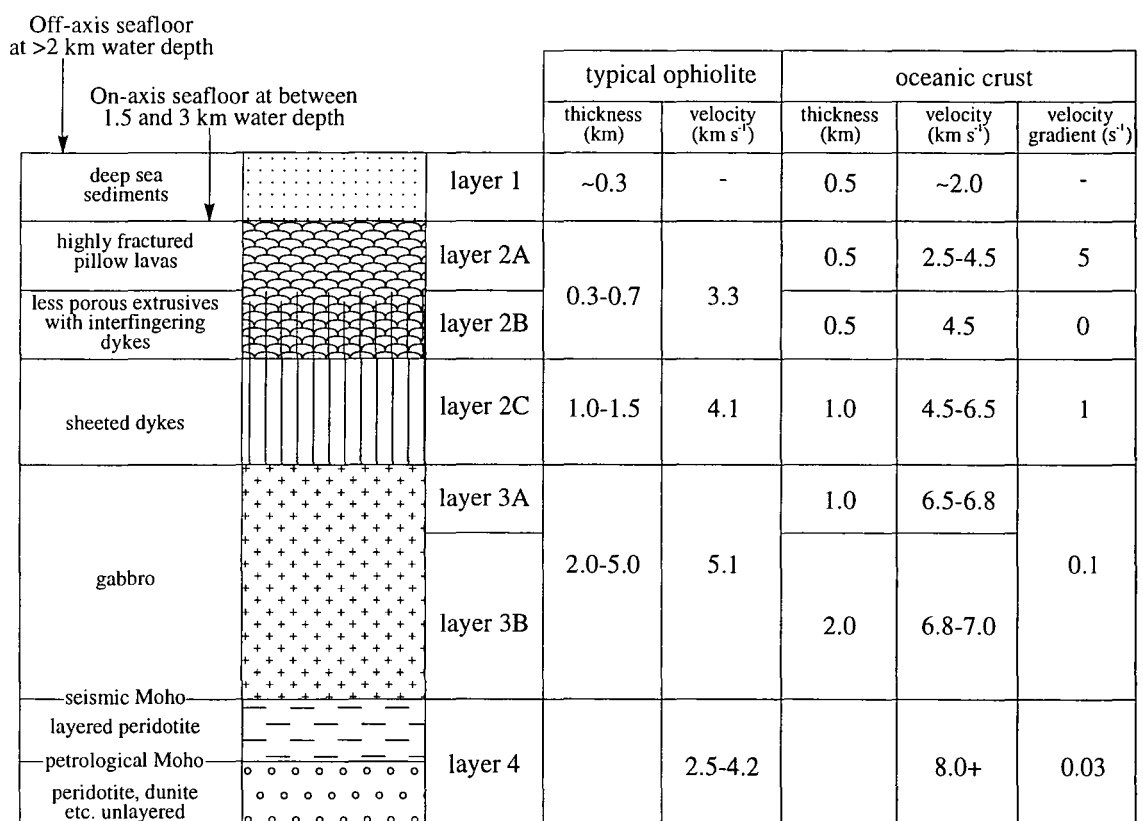


Figure 1.7: Schematic diagram showing the composition and physical properties of the oceanic crust based on ophiolite studies and seismic investigations of the oceanic crust (after Brown and Musset, 1981; Bratt and Purdy, 1984). Note the different positions of the petrological and seismic Mohos.

- Layer 2B which has an almost zero velocity gradient and a velocity of 4.5 km s^{-1} and appears to consist mainly of less porous extrusives with some interfingering dykes (Bratt and Purdy, 1984).
- Layer 2C which has a low velocity gradient and a velocity of 4.5 km s^{-1} at the top of the layer increasing to 6.5 km s^{-1} at the base. This layer is thought to consist of sheeted dykes (Bratt and Purdy, 1984).

Some studies have also suggested subdivisions of layer 3 with the transition from sheeted dykes to gabbros in the top of this layer (Bratt and Purdy, 1984) and more cumulate rich gabbros at the base (Fowler, 1990).

The Moho, as defined petrologically, lies between layered and massive peridotites (Brown and Musset, 1981). However this transition is not marked by a change in seismic velocity and is therefore not detectable with seismic techniques. Therefore the seismic Moho is defined by the transition from gabbros to peridotites which is marked by a seismic P-wave velocity contrast, generally from 7 km s^{-1} to 8 km s^{-1} , and this boundary lies above the petrological Moho (Brown and Musset, 1981).

1.3 Magma chambers at mid-ocean ridges

Models of crustal accretion based on ophiolite studies require the presence of a large steady-state magma chamber to explain the geological observations (Cann, 1974; Pallister and Hopson, 1981; and see figures 1.8a and b), with eruptions from the top of the chamber forming the sheeted dykes and extrusive pillow basalts of oceanic layer 2, and the solidifying sides forming the gabbros of layer 3. Hence in these "infinite onion" models (Cann, 1974), with layer 3 formed by cooled magma peeling off the sides of the magma chamber, the chamber extends the full thickness of layer 3. Thermal modelling studies of magma chambers indicate that at slow spreading rates of less than 10 mm yr^{-1} (full rate) a large steady-state magma chamber cannot exist (Sleep, 1975; Kusznir and Bott, 1976). As an alternative Sleep (1975) suggested that magma chambers may consist of a narrow molten sill at the top of layer 3, with the remainder of layer 3 below this sill consisting of partially crystalline material (see figure 1.8c). However, the interpretation of geophysical and petrological data from the MAR has led to the development of the

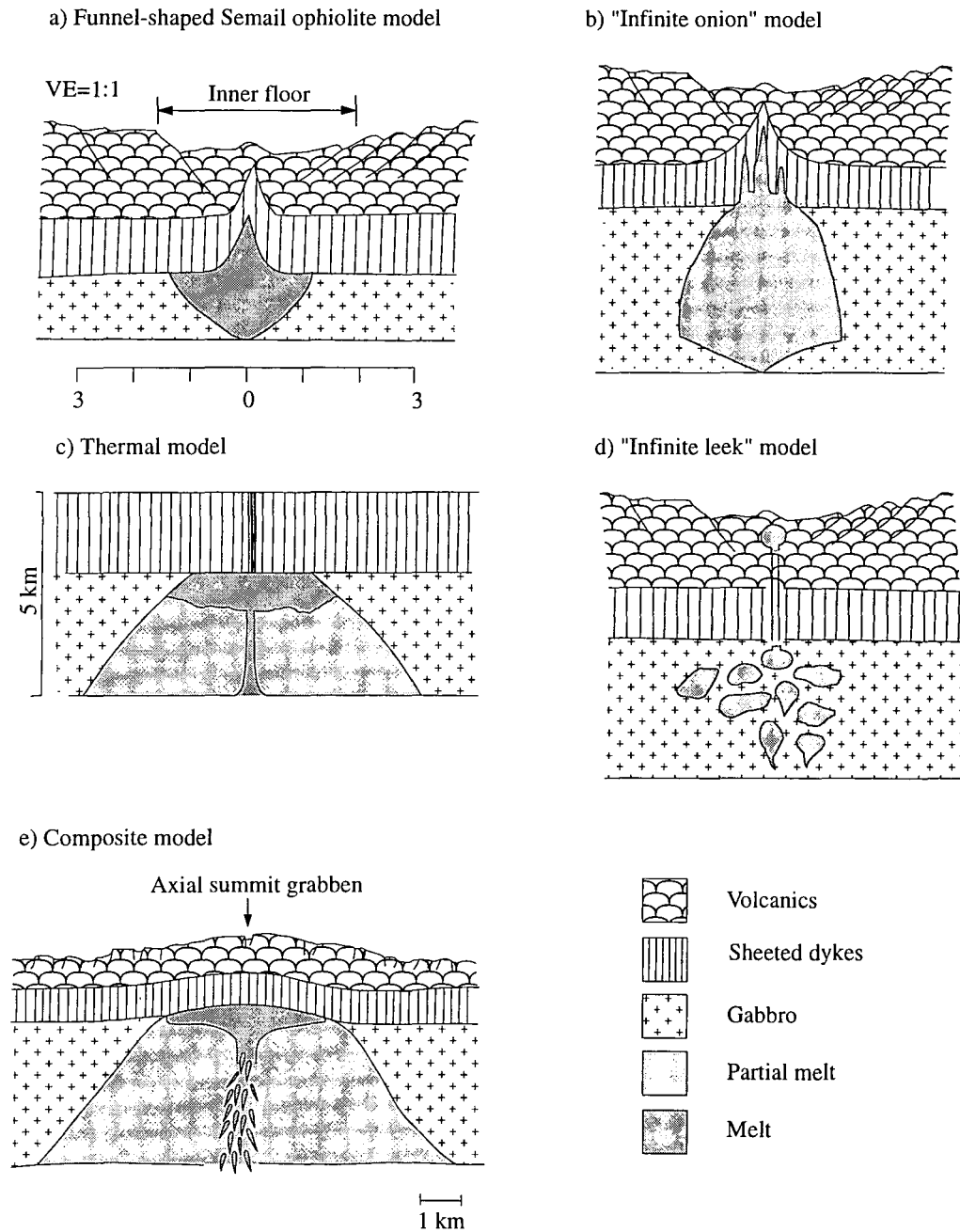


Figure 1.8: Magma chamber models.

a) Model based on the Semail ophiolite (after Pallister and Hopson, 1981) with a narrow magma chamber extending the full thickness of layer 3.

b) "Infinite onion" model (after Cann, 1974) based on petrological studies. The magma chamber extends the full thickness of layer 3, eruptions occur from the top of this chamber and the sides solidify and move away from the axis as the plates separate to form layer 3.

c) Thermal model (after Sleep, 1975). This consists of a thin magma chamber which erupts to form layer 2 surrounded by a partially molten region which solidifies to form layer 3.

d) "Infinite leek" model (after Nisbet and Fowler, 1978) developed for the slow spreading MAR based on petrologic evidence which require the presence of a magma chamber, and geophysical studies which indicate that no sizeable magma chamber exists beneath this ridge. Small pockets of melt form in layer 3 which either solidify in place or erupt to form layer 2.

e) Composite model based on seismic and gravity data (after Macdonald, 1989). This model consists of a thin magma chamber surrounded by a region of partial melt and is similar to c).

"infinite leak" model (Nisbet and Fowler, 1978; and see figure 1.8d). This model indicates that non-steady-state pockets of melt exist in layer 3 which occasionally erupt to form layer 2. This model is also consistent with the results of thermal modelling studies which indicate that a steady-state magma chamber cannot exist at this location (Sleep, 1975; Kuszniir and Bott, 1976).

Early geophysical evidence for the existence of mid-ocean ridge magma chambers was obtained from ocean bottom seismometer studies at 9°N on the EPR where a shadow zone (a rapid attenuation of signal amplitudes associated with travel time delays) suggested the presence of an axial low velocity zone (Orcutt *et al.*, 1975). Many recent detailed studies of the East Pacific Rise using conventional refraction, expanding spread, tomographic, wide aperture and normal incidence seismic techniques have provided information on the position and extent of numerous low velocity zones observed beneath this fast spreading ridge (e.g. McClain and Lewis, 1980; Detrick *et al.*, 1987; Harding *et al.*, 1989; Vera *et al.*, 1990; Caress *et al.*, 1992; Kent *et al.*, 1993; Toomey *et al.*, 1994; Mutter *et al.*, 1995). These studies indicate that a significant proportion of melt only exists in thin (10-100 m), narrow (1-2 km) lenses located ~1 km beneath the seafloor. These melt bodies overlie a broad zone of partial melt of up to 10 km in width, with P-wave velocities 0.5-1.0 km s⁻¹ below normal which, in turn, persists almost to the Moho (see figure 1.8e). The narrow neovolcanic zone (Ballard *et al.*, 1981) and short wavelength gravity anomaly (Speiss *et al.*, 1980) at the EPR also implies that a magma chamber ~1 km deep and 1 km wide exists.

Between 9°N and 13°N at the EPR Detrick *et al.* (1993) have identified a magma chamber reflector beneath more than 60% of this section of the ridge. This continuity suggests that, at fast spreading ridges, the magma chamber is a fairly continuous feature beneath segments. However, at offsets in the ridge the reflector depth either increases or the reflector disappears completely (Mutter *et al.*, 1995).

Seismic studies of intermediate spreading ridges have also shown evidence of low velocity zones and magma chamber reflectors on-axis at ~3 km depth (Collier and Sinha, 1992; Christenson *et al.*, 1993). Depths to the top of magma chamber reflectors at fast and intermediate spreading ridges, and depths to low velocity zones at

intermediate and slow spreading ridges have been used as evidence to suggest that the depth to the top of magma chambers increases as spreading rate decreases (Purdy *et al.*, 1992). Numerous failed attempts to identify magma chambers at slow spreading ridges have resulted in the conclusion that *no significant* body of partial melt exists, as the results of most wide-angle seismic experiments conducted to date have shown that both P and S-waves are observed which have travelled beneath the axis with little effect on their travel time or attenuation of their amplitude (e.g. Fowler, 1978). There is also little evidence for a magma chamber reflector (cf. Detrick *et al.*, 1990 and Calvert, 1995). Detrick *et al.* (1990)'s dataset has since been reprocessed to remove seafloor diffractions and it has been suggested by Calvert (1995) that an indistinct reflector located some 1.2 km beneath the seafloor, represents a magma chamber at equivalent depths to those imaged at the EPR. Calvert (1995) also suggests that the low apparent amplitude of this reflector (i.e. why it was not observed as a result of the original processing of this dataset by Detrick *et al.*, 1990) is caused by a low percentage of partial melt in the chamber, which only slightly reduces the velocity from that of the surrounding crust and produces a lower reflection coefficient than would be expected for a completely molten body. This study is the *only* study to date to report the somewhat inconclusive observation of a magma chamber beneath *any* slow spreading ridge.

Therefore, although the structure of mature oceanic crust produced at all spreading rates is similar there remains the contradiction that there is still little, or no, evidence for a steady-state body of melt beneath slow spreading ridges. To account for this apparent contradiction hypotheses have been formulated that require there to be a different accretionary process operating at slow spreading ridges than at fast and intermediate spreading ridges, with both processes yielding the same crustal structure. A further complication exists in that magma chambers observed at fast and intermediate ridges are much smaller than those predicted from ophiolite studies (Macdonald, 1982). This observation implies that rather than there being a large molten body beneath the ridge axis there must be a small melt lens surrounded by a zone of partial melt.

1.4 Investigations of slow spreading ridges to date

Petrological studies of the rocks which comprise mid-ocean ridges indicate that a magma chamber should exist at slow spreading ridges. To account for the lack of observations of such a feature it has been suggested that the periodicity of magmatism at all ridges varies with spreading rate (see section 1.1), such that long periods of magmatic quiescence at slow spreading ridges reduce the chance of observing a robust magma chamber.

Seismic studies are the main method of locating magma chambers at mid-ocean ridges. Unfortunately, the effectiveness of the various seismic techniques at slow spreading ridges is reduced by the inevitable scattering of energy incident at the rough seabed associated with these ridges. Hence the reason magma chambers have not been observed may simply be a function of the inadequacies of the seismic method itself.

Conflicting evidence for and against the existence of magma chambers on the slow spreading MAR exists:-

- Centroid depths of earthquakes observed at slow spreading ridges generally indicate that faulting occurs to a depth of 8 km (Huang and Solomon, 1988), implying that the axial crust is brittle to this depth. However a study by Kong *et al.* (1992) at 26°N on the MAR and located on a segment centre, indicates that earthquakes beneath the ridge axis originate on fault planes that lie at depths of less than 4 km and that the attenuation of observed P-waves indicates a low velocity ($\sim 5.0 \text{ km s}^{-1}$) zone exists 3 km beneath the axis. A similar study located at an axial deep at 23° 35'N found no evidence of a low velocity zone (Kong *et al.*, 1992).
- At 45°N on the MAR a refraction seismic experiment conducted by Keen and Tramontini (1970) found no evidence for a low velocity zone. A nearby study, also at 45°N and conducted by Fowler (1978), found a high attenuation zone ~ 6 km deep. However S-waves were observed to propagate beneath the ridge, indicating that even if lower velocities existed there was no significant body of partial melt.

- A study by Whitmarsh (1975) on the MAR at 37°N, indicated that arrivals passing beneath the axis expressed a delay in their travel times. These delays were interpreted as resulting from propagation through a low velocity (3.2 km s^{-1}) zone, 2.5 km in width and centred on the ridge axis. This zone in layer 2 was interpreted as a magma conduit. However the low velocities in layer 2 may also have been caused by a high percentage of fracture porosity in the young crust. A nearby study, also at 37°N, indicated that both P and S-waves propagated beneath the axis without significant attenuation, implying that no sizeable magma chamber could be present (Fowler, 1976).
- A high fold normal incidence seismic dataset was collected at 23° 20'N on the MAR and was used to finally prove that a magma chamber did not exist at this location and hence, that magma chambers did not exist beneath slow spreading ridges at all (Detrick *et al.*, 1990). However, as previously mentioned, part of this dataset was reprocessed by Calvert (1995) and used as evidence for a magma chamber reflector on-axis at the MAR – the first observation of such a feature at *any* slow spreading ridge.
- Refraction seismic data collected at 59° 30'N on the Reykjanes Ridge (a section of the MAR southwest of Iceland) by Bunch and Kennett (1980) indicated only a slight velocity inversion of 0.2 km s^{-1} on-axis in layer 3, which was not observed in crust of 3 Ma age (Bunch and Kennett, 1980) at the same latitude.

Therefore, to date there is no conclusive geophysical evidence for a significant body of melt beneath the axis of the slow spreading MAR. However petrological, geochemical and thermal studies indicate that magma chambers must exist although they may be, and probably are ephemeral features (Macdonald, 1982). The aim of the study described in this dissertation is to attempt to resolve this discrepancy in our knowledge of the processes of crustal accretion at slow spreading ridges, and resolve the apparent contradiction that magma chambers do not exist beneath these kinds of ridges, even though the models of the different accretionary process required, generate an identical crustal structure to fast spreading ridges.

1.5 The Reykjanes Ridge

The Reykjanes Ridge is a section of the slow spreading MAR south of Iceland which is located between the Reykjanes Peninsula ($63^{\circ} 30'N$) and the Bight transform ($56^{\circ} 50'N$) (Applegate and Shor, 1994; and see figures 1.9 and 1.10). The ridge also has no transform offsets along its entire 900 km length (Murton and Parson, 1993; Searle *et al.*, 1994). The overall trend of the Reykjanes Ridge is 036° , which is oblique to the spreading direction. Therefore the en echelon AVR's, into which the ridge is consequently segmented, are oriented orthogonal to the spreading direction and are all separated by right-stepping offsets. Segmentation occurs on three scales (Murton and Parson, 1993; and see figure 1.9):-

- A long wavelength swell caused by the Icelandic hot spot, with the depth to the ridge increasing from sea level at the Reykjanes Peninsula to 2 600 m below sea level at the Bight transform (Searle *et al.*, 1994). A break in the slope of this swell occurs at $59^{\circ}N$ which is coincident with the transition from median valley topography to the south and an axial rise to the north of this point (Ritzert and Jacoby, 1985).
- Intermediate wavelength troughs and swells on the scale of ~40-120 km, with geochemical segmentation showing that more fractionated basalts are produced in the thickened crust associated with the swells and less fractionated basalts in the thin crust associated with the troughs (Taylor *et al.*, 1995).
- A short wavelength volcanic segmentation on an ~5-30 km scale which represents the individual AVR's (Murton and Parson, 1993). These are subdivided into young AVR's showing fresh, untectonised volcanic construction, with aspect ratios (length:width) of 8-12; mature AVR's showing fresh volcanic material, with aspect ratios of 5-8; and AVR's with a low aspect ratio (<5) which are being broken down by tectonism (Murton *et al.*, 1995).

The only major ridge offset lies at $57^{\circ} 55'N$ (Searle *et al.*, 1994). This offset is seen as a basin in the topography and a corresponding high in the residual mantle Bouguer gravity anomaly. Searle *et al.* (1994) have interpreted the latter as reflecting thin crust resulting from a restricted magma supply in the offset region.

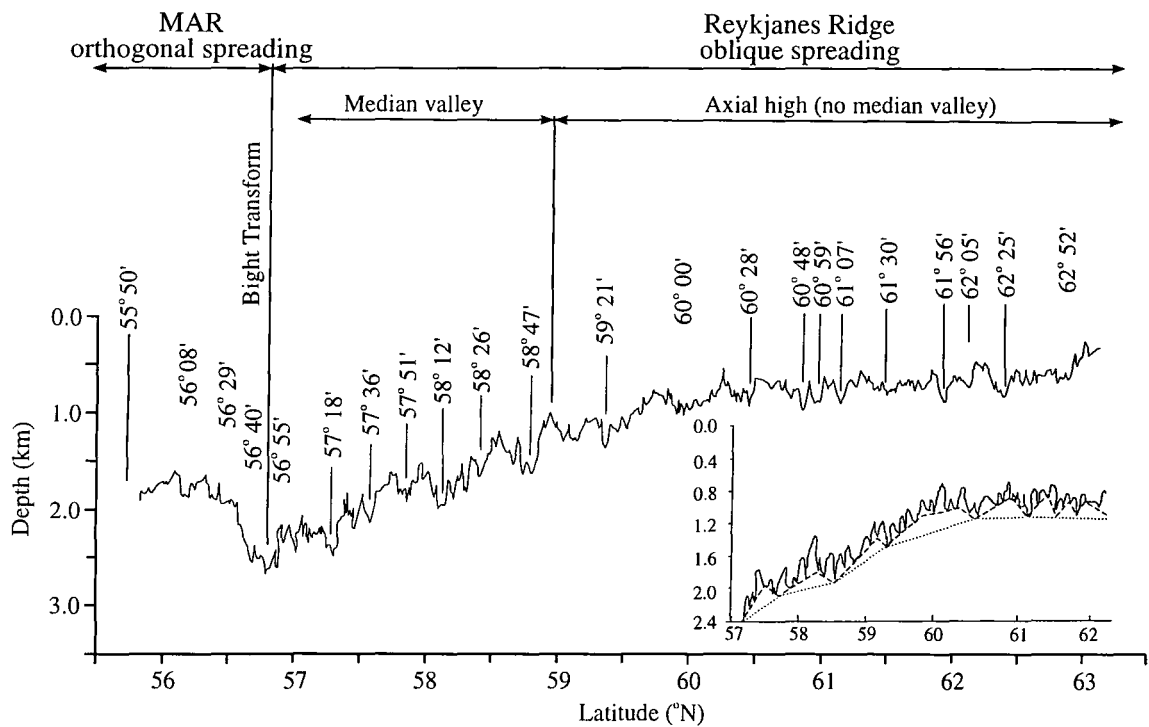


Figure 1.9: Along-axis bathymetric profile of the MAR and Reykjanes Ridge north of $55^{\circ} 50'N$ (after Applegate and Shor, 1994) showing the transition from orthogonal to oblique spreading at the Bight transform, where the bathymetry also begins to shallow towards the Iceland hot spot. Also shown is the transition from median valley to axial high morphology at $59^{\circ}N$ which coincides with the break in slope of the swell towards Iceland. Inset (after Murton and Parson, 1993) shows the same profile divided into the three scales of segmentation recognised. Dotted line – long wavelength swell towards Iceland. Dashed line – intermediate wavelength variations in the bathymetry which coincide with geochemical variations. Solid line – short wavelength bathymetric variations marking individual AVRs.

1.6 Previous geophysical and geochemical surveys of the Reykjanes Ridge

The higher mantle temperature beneath the Reykjanes Ridge due to the influence of the Iceland hot spot, potentially produces an increased magma budget which should result in a thicker crust (7-10 km – White *et al.*, 1995). The thick crust and higher mantle temperatures combine to create a weaker brittle layer which is unable to support tectonically created topography such as the median valley walls (Bell and Buck, 1992). Hence the northerly section of the Reykjanes Ridge close to Iceland expresses a smoother topography and a fast spreading ridge style axial high. The break in slope of the long wavelength swell and the transition from median valley to axial high morphology coincide with a decrease in seismicity north of $59^{\circ}N$ (Francis, 1973; and

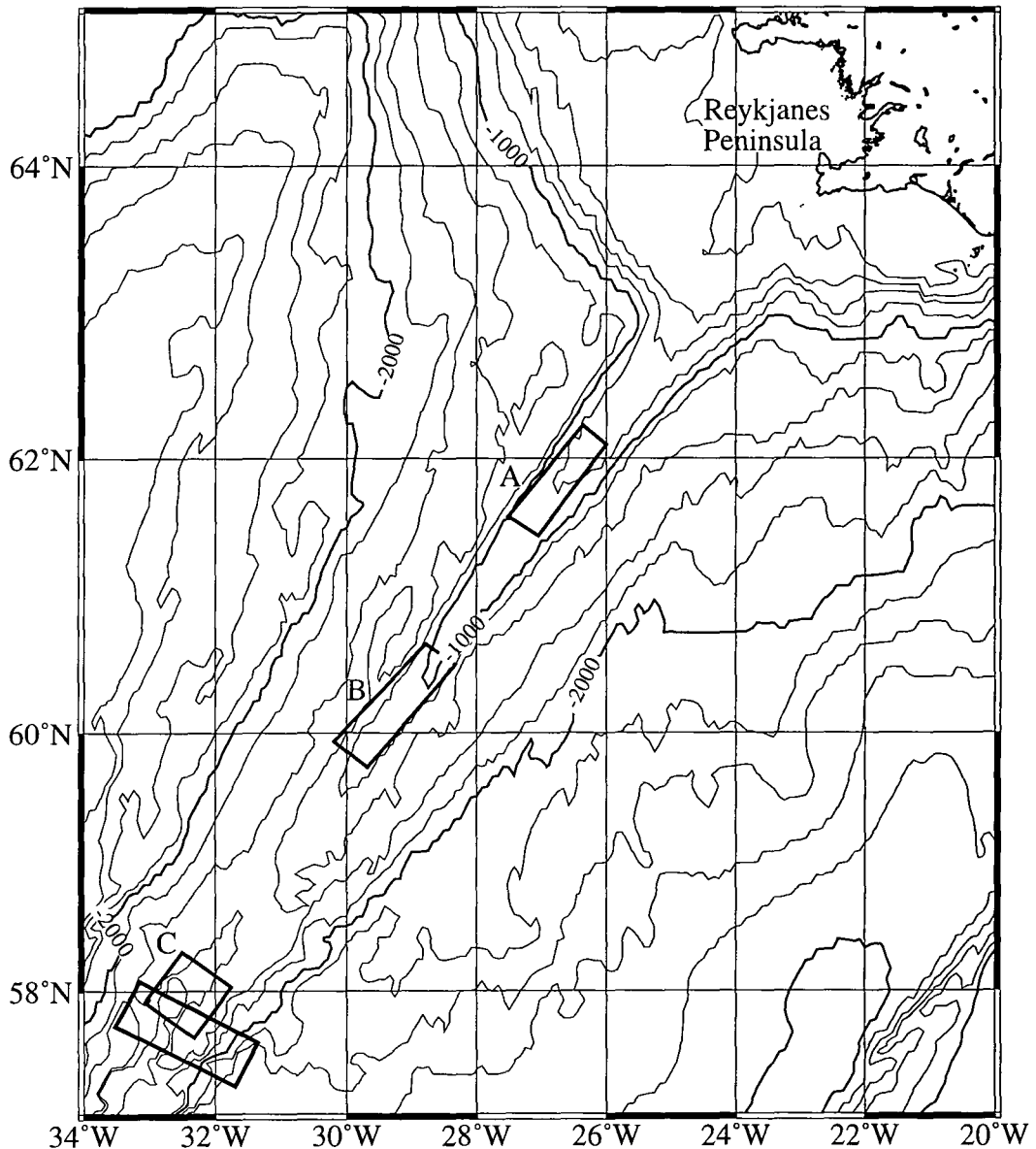


Figure 1.10: The Reykjanes Ridge trending southwest from the Reykjanes Peninsula on Iceland. Areas A, B and C of Parson *et al.* (1993) are labelled and the southernmost rectangle marks the location of this study.

see figure 1.11). This evidence also indicates hotter, less brittle crust northwards towards Iceland than south of this point.

A detailed survey of hydrothermal activity along 750 km of the Reykjanes Ridge crest, from 58°N to 63° 09'N, identified only one vent site, Steinahóll, located at 63° 06'N (German *et al.*, 1994a). This lack of observations indicates that the hydrothermal activity on the Reykjanes Ridge is more widely spaced than elsewhere on

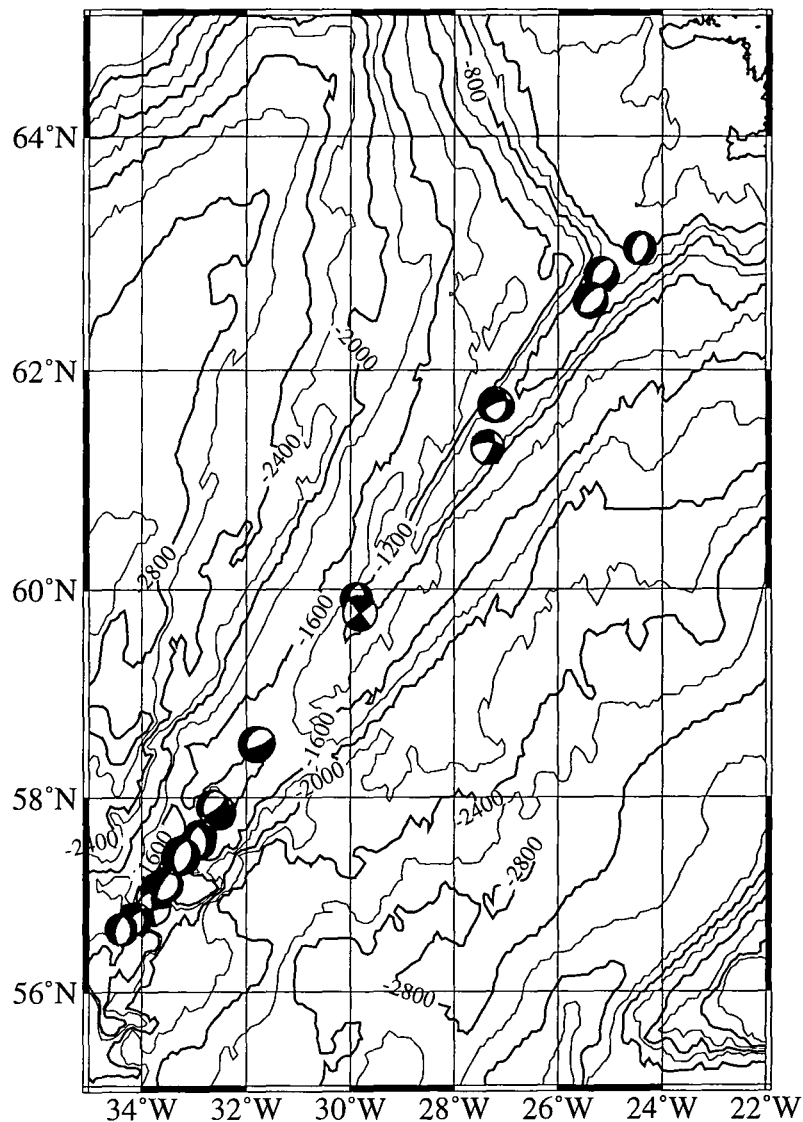


Figure 1.11: Distribution of earthquakes at the Reykjanes Ridge occurring between 1977 and 1995 from the Harvard centroid-moment tensor catalogue (Dziewonski and Woodhouse, 1983). Note the increased density of earthquakes to the south of 59°N.

the MAR where vent fields are encountered at a frequency of one every 150 km (German *et al.*, 1994a). From the morphology versus spreading rate characteristics of mid-ocean ridges, Phipps Morgan and Chen (1993) suggested that if magma chambers exist at the Reykjanes Ridge they should occur at 6-8 km depth. German *et al.* (1994a) therefore attribute this lack of observed hydrothermal activity as being caused by inhibited hydrothermal circulation in the resulting thick extrusive section. Heat flow measurements conducted on the flanks of the Reykjanes Ridge do not show any distinct variation in heat flow with age away from the ridge. However heat flow is greater to the east of the axis than to the west (Bram, 1980).

Linear magnetic anomalies are observed on the Reykjanes Ridge as elsewhere on mid-ocean ridges (Fleischer, 1974) – the peak anomaly on the youngest oceanic crust (the Brunhes-Matuyama anomaly) occurring either on the topographic highs or just to the east (Johnson and Jakobsson, 1985).

Fleischer (1974) collated the results of geophysical surveys on the Reykjanes Ridge to that date. However all the seismic studies included were based purely on 1-D travel time inversions of refraction profiles collected pre-1970, rather than 2-D or synthetic seismogram based modelling interpretations. These 1-D inversions provide much less accurate estimates of velocity and depth than 2-D or synthetic seismogram modelling (Chen, 1992; White *et al.*, 1992) as oceanic crust is far from one-dimensional. Later seismic surveys of crustal structure which will now be described, all used synthetic seismogram modelling of travel times and amplitudes. A seismic survey conducted as part of RRISP (Reykjanes Ridge Iceland Seismic Project; Goldflam *et al.*, 1980) on 9 Ma crust on the eastern flank of the Reykjanes Ridge, found two main crustal layers of 4.6 km s⁻¹ and 6.6 km s⁻¹ respectively, and an anomalously low mantle velocity of 7.7 km s⁻¹ just below the Moho which increased to ~8.2 km s⁻¹ at 16 km depth (Goldflam *et al.*, 1980). A more detailed seismic experiment located at 59° 30'N consisted of three, 120 km long ridge-parallel profiles located on crust of 0, 3 and 9 Ma (Bunch, 1980; Bunch and Kennett, 1980). The results of this experiment are as follows (and see figure 1.12):-

- Layer 2A at 0 Ma has a velocity of ~2.2 km s⁻¹. This P-wave velocity increases to 3.8 km s⁻¹ at 9 Ma. This layer was interpreted as being 0.4 km in thickness and representing highly fractured basalt with the increase in velocity with age caused by infilling of void spaces.
- Oceanic layer 2B, with a velocity of 4.6 km s⁻¹ [equivalent to the upper layer of Goldflam *et al.* (1980)], thins with age from 1.3 km at 0 Ma to 0.8 km at 9 Ma, and consists of basalts with approximately 11% porosity.
- The gradual closing of pore space with depth results in the higher velocities of 5.4-6.2 km s⁻¹ for oceanic layer 2C. This layer is approximately 1 km in thickness and consists of a series of constant velocity layers representing a velocity gradient.

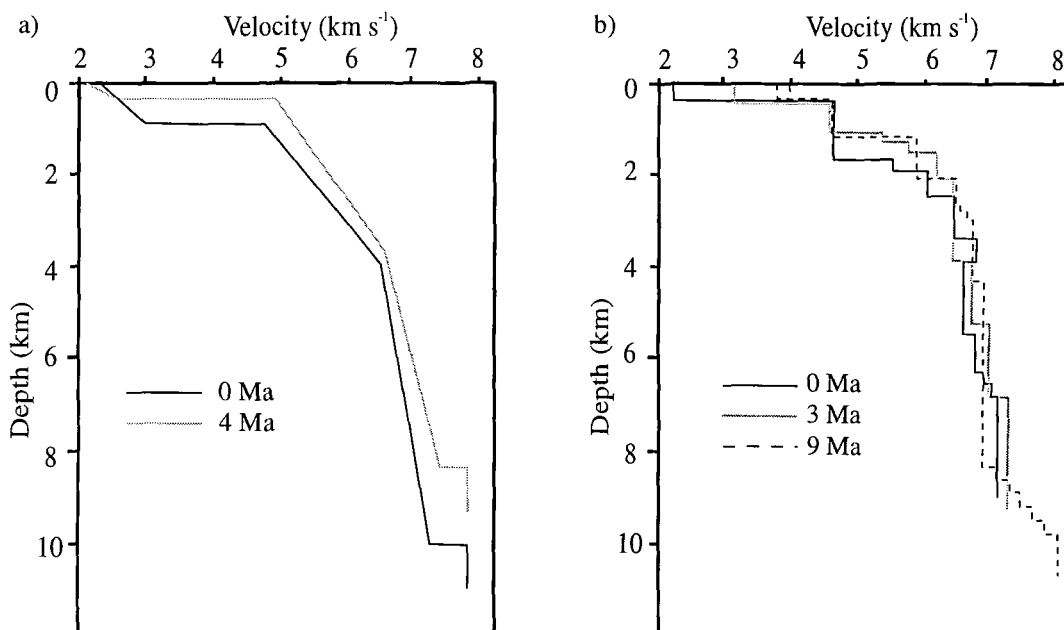


Figure 1.12: Crustal structure of the Reykjanes Ridge from previous geophysical surveys. Depths are measured from the seabed.

a) Study at $61^{\circ} 40'N$ conducted by Smallwood *et al.* (1995). Profiles show the average crustal structure at 0 Ma and 4 Ma, indicating that the upper crust thins with age as does the overall crustal thickness.

b) Study at $59^{\circ} 30'N$ conducted by Bunch and Kennett (1980) along axis-parallel profiles at 0 Ma, 3 Ma and 9 Ma. These profiles also show thinning of the upper crust with age but with the overall crustal thickness increasing with age.

- Oceanic layer 3 consists of gabbros, metagabbros and metabasalts and is divided into two layers. The upper layer has a thickness of ~ 0.8 km and a velocity of ~ 6.4 – 6.6 km s^{-1} and the lower layer has a velocity of 6.6 km s^{-1} to 7.2 km s^{-1} . Again several layers are included to represent a velocity gradient. The thickness and mean velocity of this lower layer increase with age. Within layer 3 on-axis a velocity inversion is required to model data amplitudes, with velocities decreasing from 6.8 km s^{-1} to 6.6 km s^{-1} , which suggests the presence of a high temperature body. At 9 Ma this velocity inversion is replaced with a positive velocity gradient.
- The Moho was modelled as a series of constant velocity layers to represent a velocity gradient.
- The velocity in the mantle also increases with age from 7.1 km s^{-1} on-axis to 8.2 km s^{-1} at 9 Ma.

A survey conducted at $61^{\circ} 40'N$ (Smallwood *et al.*, 1995; and see figure 1.12a), which was modelled using a series of velocity gradients, revealed average velocities

similar to those of Bunch and Kennett (1980) with layer 2A thinning off-axis. Velocities observed in 4 Ma crust were found to be slightly higher than on-axis, however this increase was within the error bounds of the data and was therefore inconclusive (Smallwood *et al.*, 1995). Crustal thickness estimates from this experiment, based on sparse observations of mantle diving rays and Moho reflections, indicated that the crust was 8 to 10 km in thickness and that the Moho was present beneath the ridge axis.

These seismic experiments indicate that, in general at the Reykjanes Ridge, the upper subdivisions of layer 2 thin off-axis, probably reflecting a decrease in porosity and increase in layer velocity with age (Bunch, 1980; Bunch and Kennett, 1980; Smallwood *et al.*, 1995) or faulting as the newly formed crust moves off-axis. There is also evidence for layer 2 thickening towards Iceland (Ritzert and Jacoby, 1985) possibly supporting the hypothesis that the influence of the Iceland hot spot should increase the thermal regime and hence the magma budget, which in turn leads to the generation of thicker crust. None of these seismic experiments conducted on the Reykjanes Ridge show any evidence for a significant body of molten material within the crust.

The free-air gravity anomaly associated with the Reykjanes Ridge reveals distinctive V-shaped ridges (figure 1.13) that can also be recognised in the seabed topography. These V-shaped ridges are interpreted as changes in crustal thickness due to pulses of melt from the Iceland hot spot. These crustal thickness variations correspond to an increase in temperature of $\sim 30^{\circ}\text{C}$ on a 5 to 10 million year time scale, migrating along the ridge from Iceland (Hwang and Parsons, 1995; White *et al.*, 1995; and see figure 1.14). The residual mantle Bouguer anomaly of the Reykjanes Ridge shows a low located over the axial region. As the thermal effects of passive upwelling have been removed in calculating this residual anomaly, the low must relate to density or thickness variations in the upper crust (Field, 1993).

TOBI and hydrosweep side-scan sonar data were collected during a cruise aboard the *R/V Maurice Ewing* in 1990 (EW9008) (Parson *et al.*, 1993; Murton and Parson, 1993; Searle *et al.*, 1994) at three locations on the Reykjanes Ridge (see figure 1.10). This study has revealed an axial zone 6-10 km wide with high acoustic backscatter. As previously mentioned these AVRs are subdivided by Murton and Parson

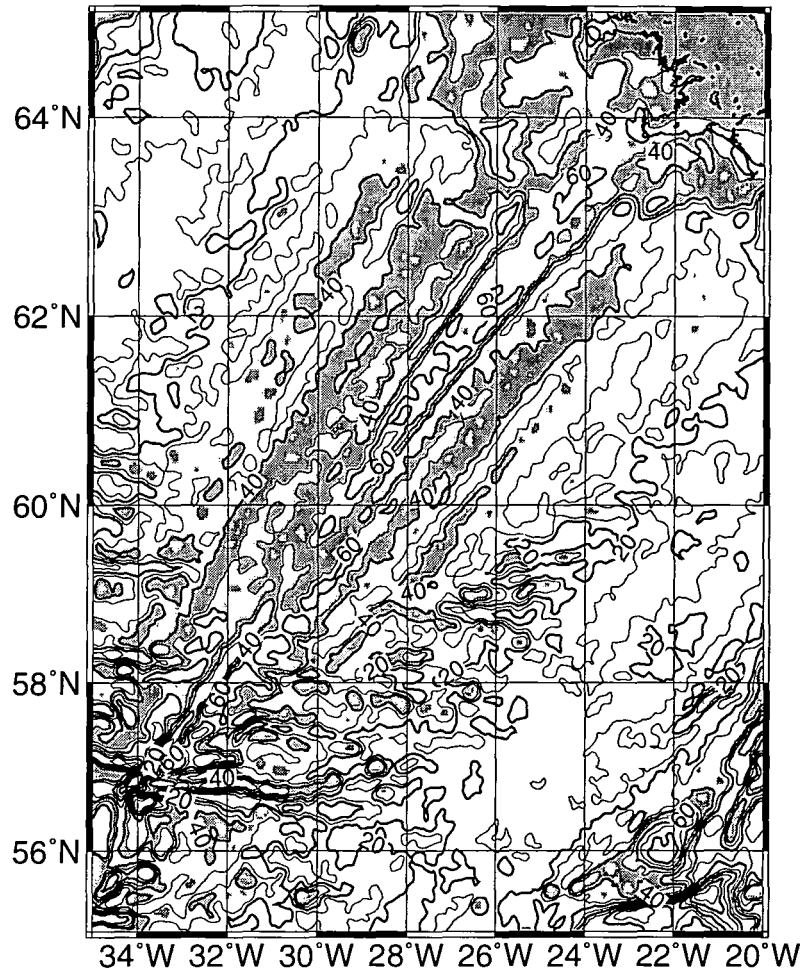


Figure 1.13: Free-air gravity anomaly over the Reykjanes Ridge from the Sandwell and Smith (1986) $2' \times 2'$ grid. Contours are plotted every 10 mGal and values between 40 and 50 mGal are shaded grey to highlight the V-shaped ridges in the gravity anomaly.

(1993) in terms of their aspect ratio and morphological features, as observed with side-scan data, into:-

- AVRs with high aspect ratios showing high backscatter, hummocky topography, linear seamounts, no evidence of sedimentation or faulting and some sheet flows onlapping onto old sedimented regions (Murton and Parson, 1993).
- AVRs with moderate aspect ratios which are large volcanic constructions with little sedimentation and tectonism, hummocky topography and circular seamounts.
- Low aspect ratio AVRs which often have low backscatter due to sedimentation which smoothes the neovolcanic terrain and which are marked by intense fracturing and faulting.

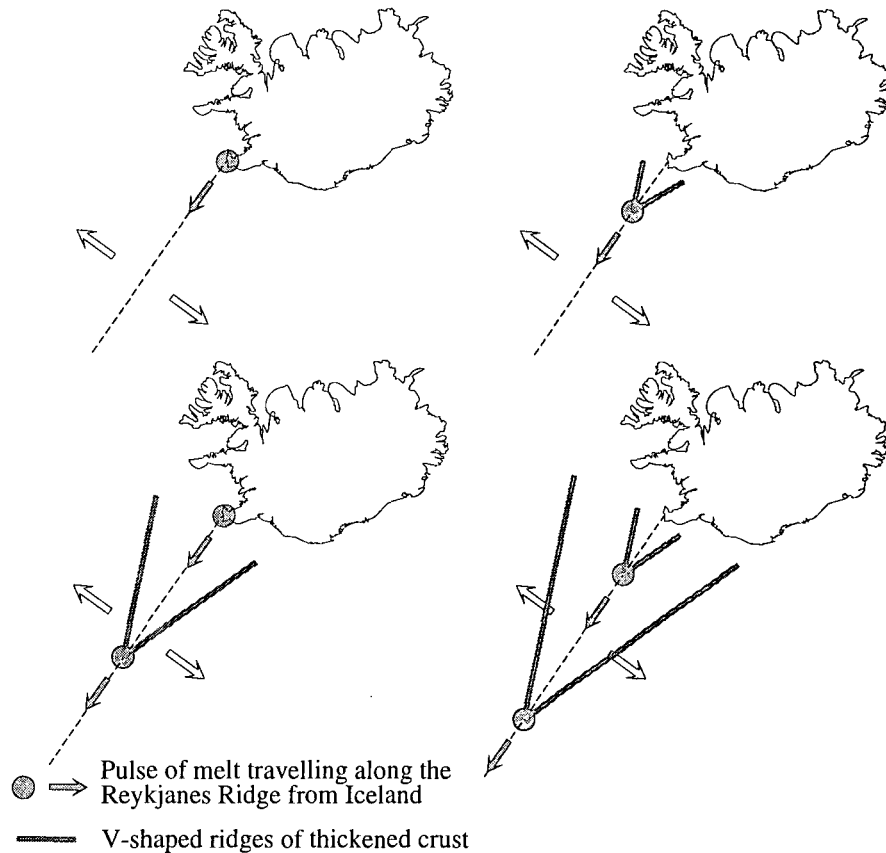


Figure 1.14: Formation of V-shaped ridges on the Reykjanes Ridge by pulses of melt migrating along the ridge from Iceland.

These characteristic features are interpreted by Murton and Parson (1993) as indicating an evolutionary cycle of AVR development and destruction, with narrow AVRs developing from fissure eruptions onto old sedimented seafloor at the early stages of magmatism. From this early stage, point sources of magmatism generate circular seamounts and faulting begins to develop on broader more robust AVRs. This faulting begins to breakdown the AVR when magmatism ends and the topography on these low aspect ratio AVRs is smoothed by sedimentation (Murton and Parson, 1993).

Although previous studies of the Reykjanes Ridge have shown no greater evidence for a magma chamber of significant size than elsewhere on slow spreading ridges, it was selected as the target area for a NERC-funded, multidisciplinary geophysical experiment in October 1993 aboard the *RRS Charles Darwin* for the following reasons:-

- The rough seafloor usually associated with slow spreading ridges and which causes significant scattering of seismic energy, has been moderated by the influence of the Iceland hot spot, hence allowing potentially improved quality seismic data to be collected.
- The southern end of the Reykjanes Ridge lies beneath over 1 000 m of water, which is greater than the skin depth of atmospheric electromagnetic signals. Therefore these signals would be minimised and no longer swamp sub-seabed data recorded during the controlled source electromagnetic (CSEM) component of the experiment.
- The Reykjanes Ridge was also designated as a target area for BRIDGE (British Mid-Ocean Ridge Initiative), which meant that an extensive bathymetric, gravity and magnetic dataset was already being accumulated for this region and use of this data would help to constrain any models generated from the seismic and CSEM data.
- Its proximity to the UK made it a logistically viable region to study.

1.7 Aims of this study

The aim of this study is to address the apparent discrepancy between geophysical observations at fast, intermediate and slow spreading ridges, by investigating an apparently magmatically active slow spreading ridge (see section 2.1) using seismic techniques, and integrating the resulting models with those obtained from a coincident controlled source electromagnetic survey. In particular the following points will be addressed:-

- The crustal structure at this survey location will be compared to that imaged elsewhere on the mid-ocean ridge system and any implications for variations in the process of crustal accretion associated with different spreading rates will be considered.
- The position of the Moho, in terms of its continuity beneath the ridge axis, will be investigated to identify when the Moho is formed.
- The crustal structure will be examined to identify when full crustal thickness is

achieved and this crustal thickness compared to that found elsewhere on the mid-ocean ridge system with respect to spreading rate.

- The presence, or absence, of evidence for a body of partial melt and, should one exist, definition of its shape, along-axis continuity and depth.

The remaining question which will be addressed is the applicability of the results obtained from studying a particular location on the mid-ocean ridge system to slow spreading ridges in general. The section of the Reykjanes Ridge to the south of 59°N was targeted as this area is not profoundly influenced by the Iceland mantle plume and can therefore be assumed to be representative of slow spreading ridges. This assumption is supported by the median valley topography, a break in the slope of the long wavelength swell, an increase in the seismicity and geochemical anomalies all of which indicate that to the south of 59°N, the Iceland hot spot has little influence on ridge processes and hence this location is suitable, if not ideal, for a study of this kind.

1.8 Summary and structure of this dissertation

Mid-ocean ridges are the sites of oceanic crustal accretion. The morphology and gravity field vary with spreading rate but mature oceanic crust is relatively simple and uniform in structure, whether it was produced at fast, intermediate or slow spreading ridges. Although magma chambers capable of generating the structure and geochemistry of the oceanic crust have been observed at fast and intermediate spreading ridges, there is no conclusive evidence for similar features at slow spreading ridges. Therefore the aim of this study is to investigate the processes of crustal accretion occurring at a slow spreading ridge. A study area on the Reykjanes Ridge, located to the south of the southernmost influence of the Iceland hot spot, was selected for this study as there was evidence of recent volcanic construction and the location was favourable for the geophysical techniques applied during the investigation.

In this chapter the morphology and structure of the three categories of mid-ocean ridge have been described with emphasis placed upon the Reykjanes Ridge. The reasons for selecting this area and the aims of this study have also been discussed.

Chapter 2 outlines the seismic experimental configuration, the datasets

collected and the instrumentation used to collect each dataset. The processing required to generate interpretable wide-angle and normal incidence seismic record sections is described.

In Chapter 3 the final wide-angle seismic dataset is described and interpreted in terms of the main features observed and their significance.

In Chapter 4 the generation of the initial wide-angle seismic models, and the process of ray-trace modelling these to generate final best-fitting models are discussed. The initial and final wide-angle seismic models are described and interpreted. The three different ray-tracing techniques employed are explained and their advantages and disadvantages in terms of the wide-angle seismic models generated are considered.

In Chapter 5 the 2-D modelling of the gravity and normal incidence seismic data collected coincident with the wide-angle seismic lines is described together with the generation of a residual mantle Bouguer anomaly map for the study area. The 2-D gravity, normal incidence seismic and CSEM models are compared to the wide-angle seismic models and the resulting models of the crustal structure at the Reykjanes Ridge compared with those from previous studies of mid-ocean ridges, and interpreted in terms of the processes of crustal accretion occurring.

The main conclusions which are drawn from this investigation are detailed in Chapter 6 and possible further studies which could be employed to resolve some of the remaining uncertainties in the models suggested.

Appendix A contains listings of the shot and instrument positions for the wide-angle and normal incidence seismic experiments. Sound velocity profile data used in processing and modelling the wide-angle seismic dataset are included in Appendix B. The specifications of the in-house seismic data formats used at Cambridge and Durham, and the differences between these, are summarised in Appendix C. The seismic processing programs used in processing digital ocean bottom seismometer data from both Durham and Cambridge instruments with their functions and authorship are outlined in Appendix D. Finally, Appendix E contains a complete set of wide-angle seismic data sections together with ray-traced models and calculated synthetic and observed seismograms for each instrument.

Chapter 2

Experimental configuration, acquisition and data processing

2.1 Introduction

The dataset described in this dissertation was collected on an axial volcanic ridge (AVR) located at 57° 45'N on the Reykjanes Ridge to investigate the processes of crustal accretion at a slow spreading ridge. We intended to investigate these processes at the ridge axis using seismic techniques and integrate these results with those obtained from a coincident controlled source electromagnetic study which was used to study the conductivity and porosity of the crust.

The choice of a target area for this study was governed by: 1) an area likely to show evidence of accretion processes; 2) the limitations of the survey techniques used; and 3) the applicability of observations in the study area to other slow spreading ridges. Therefore the AVR centred on 57° 45'N was selected for the following reasons:-

- The influence of the Iceland hot spot results in smoother topography on the Reykjanes Ridge compared to other slow spreading ridges which in turn causes less scattering of seismic energy incident on the seafloor and hence allows greater transmission, in turn allowing more detailed investigation of crustal structure.
- Although the northern Reykjanes Ridge has a morphology more typical of a fast spreading ridge (with an axial high and no evidence of a median valley) due to the influence of the Iceland hot spot, south of 58°N true median valley topography is developed. There is also increased earthquake activity to the south of 59°N (Francis, 1973; see figure 1.11). These factors suggest that the area is beyond the profound influence of the hot spot and that processes of accretion are similar to those operating elsewhere on slow spreading ridges.
- TOBI side-scan sonar data collected during a cruise aboard the *R/V Maurice Ewing* in 1990 (EW9008 – Parson *et al.*, 1993; Searle *et al.*, 1994; and see figure

2.1) shows that the northern half of the AVR centred on $57^{\circ} 45'N$ exhibits bright backscatter, hummocky topography and little evidence of post-magmatic faulting and fissuring implying that this area consists of fresh young basalts. The AVR centred on $57^{\circ} 45'N$ also has a small volume compared to AVRs further north which, combined with the young appearance of the seafloor, suggests it is currently magmatically active and has not yet completed its constructional phase.

- To conduct a CSEM experiment it is necessary to minimise atmospheric electromagnetic (EM) signals (which swamp expected sub-seabed data amplitudes) by surveying in an area where the water column is thicker than the skin depth of atmospheric EM signals in water, i.e. greater than 1000 m.

Hence the AVR centred on $57^{\circ} 45'N$ was the most apparently magmatically active (from the TOBI data), was beyond the profound influence of the Iceland hot spot as its median valley topography shows (figure 1.10), lay under 1000 m of water and was smooth enough to provide good transmission of seismic energy into the crust.

For the seismic component of the experiment, which is the subject of this dissertation, we planned to collect two wide-angle seismic lines fired with explosives and airgun shots and recorded by 11 digital ocean bottom seismometers (DOBS) plus one along-axis and six across-axis normal incidence seismic lines designed to constrain the upper crustal velocity structure and layer geometry, and identify the location and depth of any off-axis sediment ponds.

This chapter contains a description of the methodology and instrumentation used for seismic data collection, plus details of the data replay and processing schemes applied to the recorded data. Additional datasets collected throughout the *RRS Charles Darwin* cruise CD81/93 will also be described.

2.2 Experimental configuration

The CD81/93 seismic experiment, centred on the AVR at $57^{\circ} 45'N$, comprised of two perpendicular lines (figure 2.2). The across-axis line (Line 1) ran perpendicular to the overall trend of the Reykjanes Ridge and intersected the AVR at its highest bathymetric point, running from $57^{\circ} 52.5'N$ $33^{\circ} 09'W$ (30 km off-axis to the northwest)

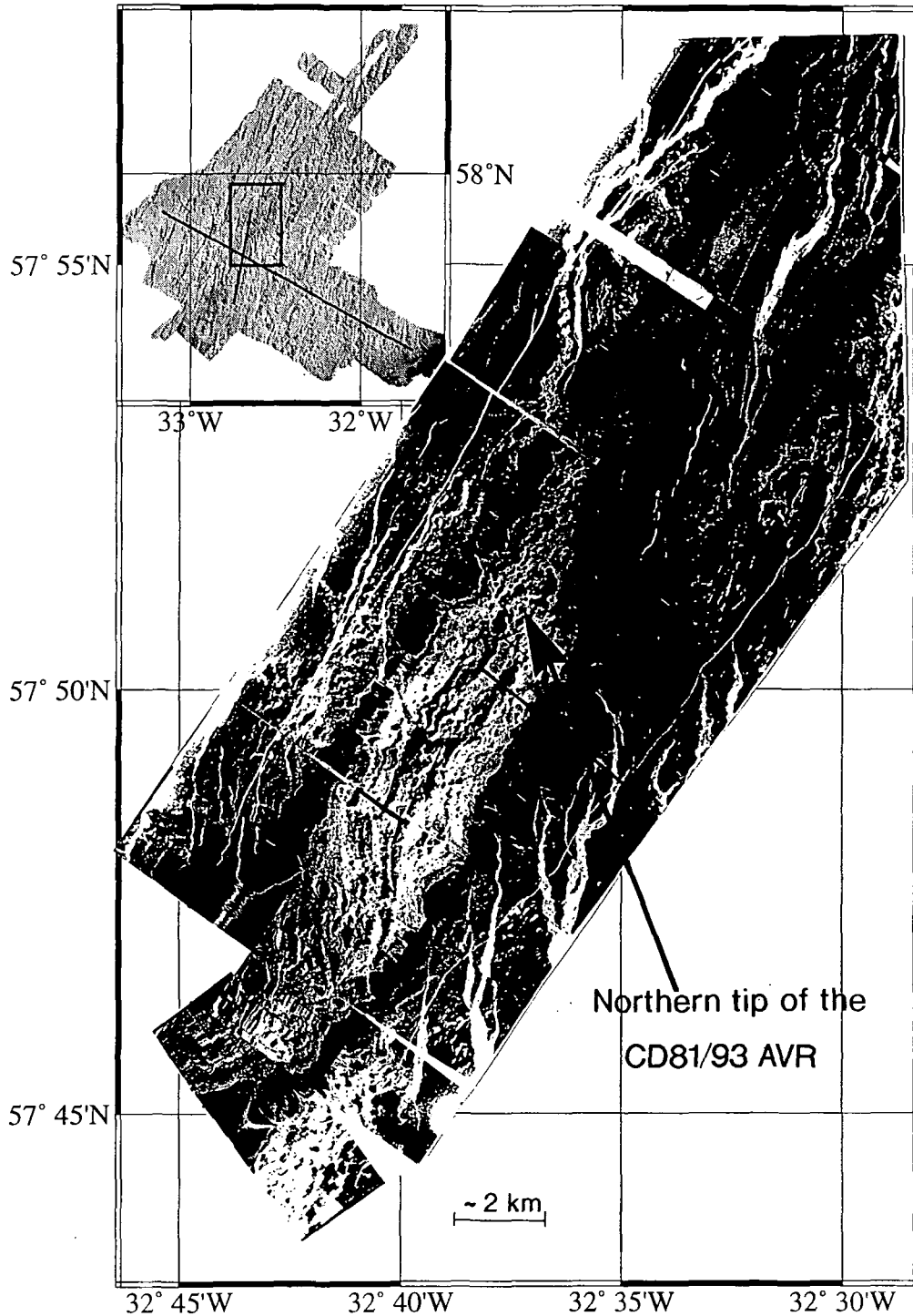


Figure 2.1: TOBI side-scan sonogram of the northerly tip of the AVR centred on 57° 45'N, collected during *R/V Maurice Ewing* cruise EW9008 (Parson *et al.*, 1993). The inset shows the location of the sonogram (solid box) in relation to the wide-angle seismic lines. Note the bright backscatter and hummocky topography along the AVR indicating fresh lava flows.

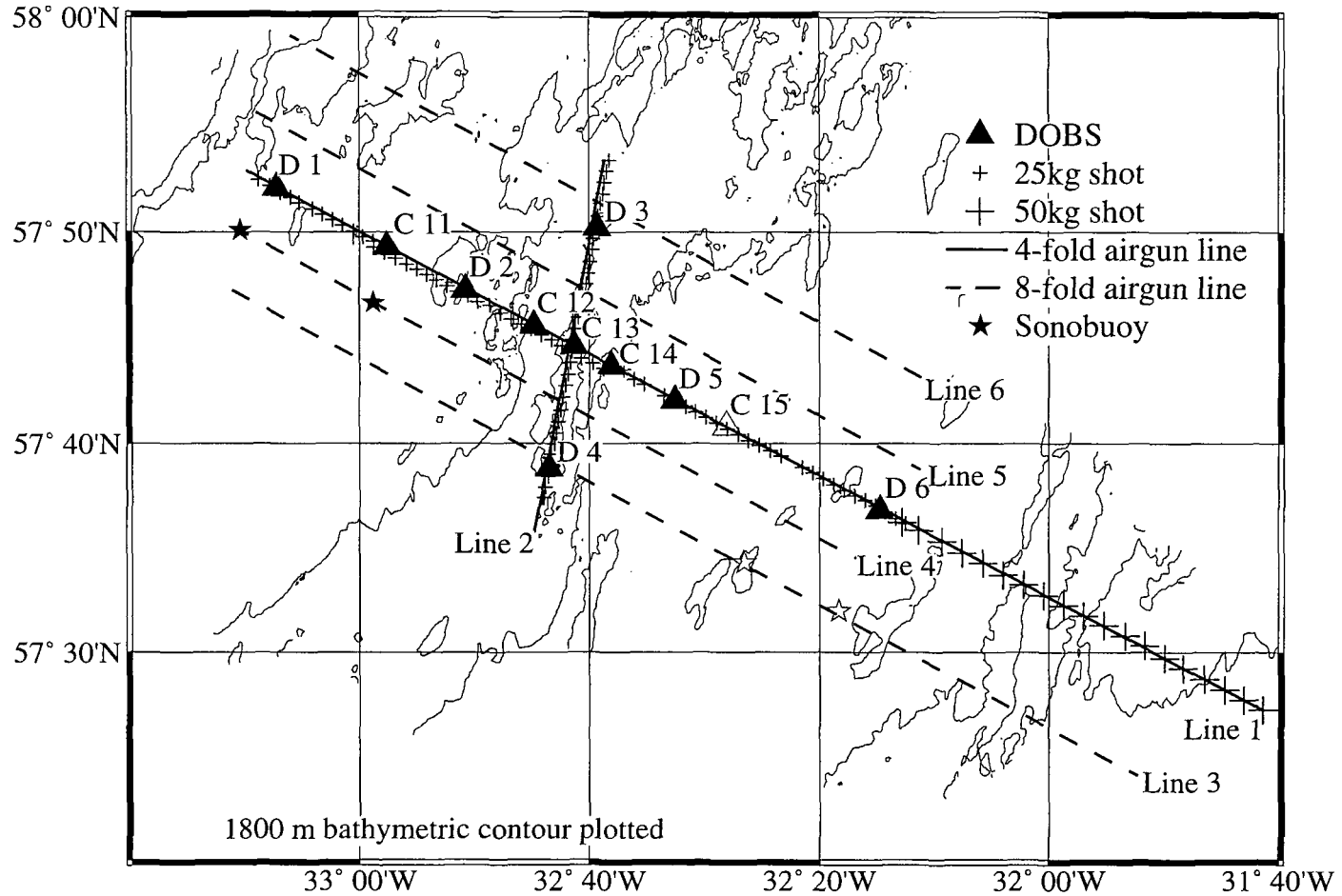


Figure 2.2: The CD81/93 seismic experimental configuration overlain by the 1 800m bathymetry contour which outlines the AVR studied. DOBS locations are marked by triangles with D denoting a Durham and C a Cambridge instrument. Airgun reflection profiles are shown as solid and dashed lines while explosive shot locations are marked by crosses (see key). Open symbols indicate an instrument which failed to work correctly or was lost (see text). Sonobuoy deployment positions are marked by stars. See Appendix A for line, instrument and explosive shot locations.

continuing for some 100 km and terminating at $57^{\circ} 27'N$ $31^{\circ} 42'W$ (70 km off-axis to the southeast). The along-axis line (Line 2) extended along the entire 35 km length of the AVR, from $57^{\circ} 53'N$ $32^{\circ} 39'W$ to $57^{\circ} 37'N$ $32^{\circ} 45'W$ (see figure 2.2).

In total 11 DOBSs were deployed along Lines 1 and 2, six four-component University of Durham' DOBSs (DDOBSs) and five single-component University of Cambridge' (CDOBSs) instruments. Deployment positions were chosen from existing Hydrosweep swath bathymetry data (Parson *et al.*, 1993; Keeton *et al.*, in press) to ensure that each instrument was located on a relatively flat section of seabed to maximise instrument stability, seabed coupling and the chances of retrieval by avoiding overhangs and seabed crevasses. Instrument spacings were designed so that in the case of instrument failure (either to record or return) the DOBSs on either side provided full data coverage over the resulting data gap. The Durham and Cambridge DOBSs were deployed alternately so that in the unlikely event that one set of instruments failed to record completely, or were lost, a spatially complete dataset was still collected. Instrument deployment locations and depths are given in Appendix A.

The wide-angle lines were shot twice, once with 111 explosive charges varying in size between 25 and 50 kg and a second time using a 4 566 in³ (74.9 litre), 12 airgun array. A complete listing of shot locations and airgun lines is given in Appendix A. For the explosive lines, the northwesternmost 60 km of Line 1 was shot using sixty-one 25 kg charges, detonated every 4 minutes which resulted in a shot spacing of 1 km. Two of these charges misfired. The remaining 40 km of the across-axis line, located towards the southeast (figure 2.2) was shot using nineteen 50 kg charges detonated every 8 minutes, resulting in a shot spacing of 2 km. Again two of these misfired. The longer detonation interval between 50 kg charges was influenced by RVS safety limits on the magnitude of shock waves permissible on the stern plates of the NERC' research fleet, and our ability to construct the 50 kg charges rapidly. The along-axis line (Line 2) consisted of thirty-one 25 kg charges, fired every 4 minutes.

Initially six seismic reflection profiles were planned. Two of these profiles were coincident with the wide-angle seismic lines and were shot using the full 4 566 in³ (74.9 litre) airgun array fired at 40 s intervals, giving a shot spacing of 100 m. These

shots were recorded by an 8-channel streamer giving rise to 4-fold normal incidence data and also by each DOBS to provide two further wide-angle seismic profiles coincident with the explosive lines but with a closer trace spacing. Lines 3, 4, 5 and 6 (see figure 2.2) were located across-axis either side of Line 1. It was planned to shoot these later lines with a reduced volume airgun array fired every 20 s (50 m) to generate 8-fold normal incidence data. The airgun array volume was to be reduced to provide a higher frequency source, more suitable for normal incidence data acquisition, by turning off the lower frequency, large volume airguns. Four disposable sonobuoys were also deployed along the normal incidence lines to provide details of sedimentary and upper crustal layer geometry and velocity.

2.3 Wide-angle data acquisition

The wide-angle data were collected using instrumentation from Durham and Cambridge Universities to record both the explosive and airgun shots. These instruments and the accompanying seismic energy sources are described below. A sound velocity dip was taken at $57^{\circ} 47.2'N$ $32^{\circ} 50.45'W$, using an AML sound velocity profiler, to provide details of the water column velocity and temperature structure (see Appendix B) which are used in the calculation of explosive shot instants and during the wide-angle seismic data modelling process (see Chapter 4).

2.3.1 Instrumentation

DDOBS

The six DDOBS can record up to 540 Mbytes of four-component data (for a more detailed description of these instruments see Peirce and Kirk, in prep.). Inside each spherical pressure vessel (figure 2.3) is mounted a three-component, gimballed geophone package comprising of three Mark L-15B geophones with a frequency range of 4.5 to 10 Hz; the two horizontal components enabling the recording of S-waves. The fourth component of the dataset is provided by a Benthos hydrophone (AQ-11) mounted externally, with a frequency range of 1 Hz to 12 kHz, accompanied by a 26 dB gain Benthos pre-amplifier (AQ-202).

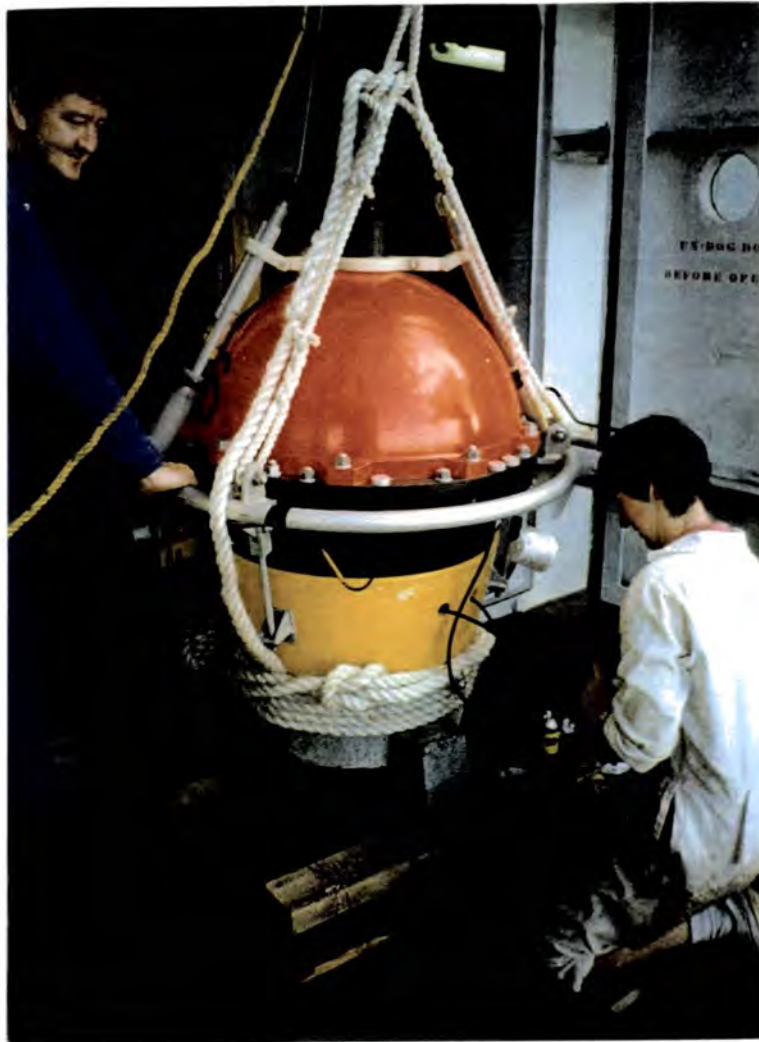
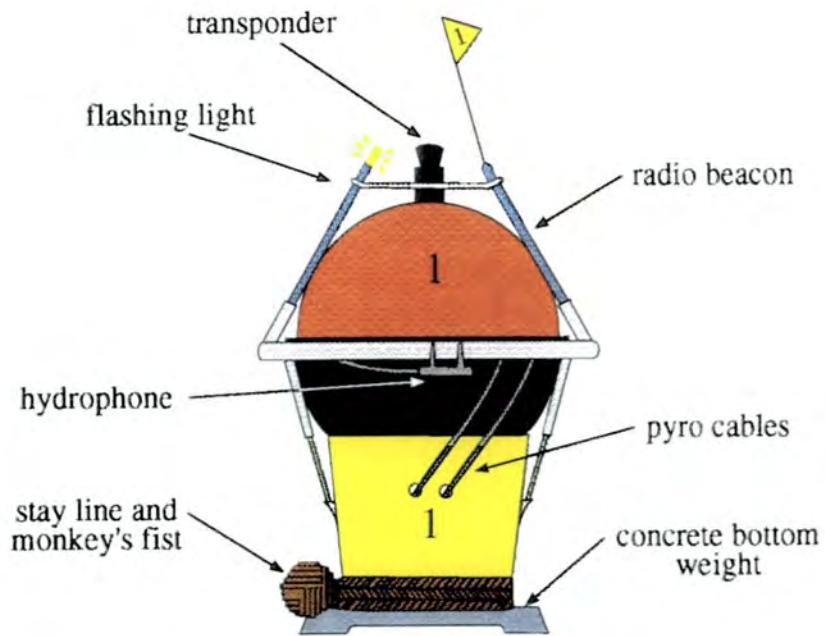


Figure 2.3: Schematic diagram of a Durham digital ocean bottom seismometer (original drawing by Peirce) (top) and a photograph of a DDOBS being prepared for deployment (bottom).

The analogue sensor outputs are digitised and recorded using a Teledyne Geotech PDAS-100 (Portable Data Acquisition System) datalogger, designed originally for land use. The PDAS can record digital data from six input channels at up to 1 000 samples s^{-1} . During this experiment a primary sample rate of 200 samples s^{-1} was used for recording the explosive shots and a secondary rate of 100 samples s^{-1} for the airgun data. Channels 1, 2, 3 and 6 were used to record Z, Y, X and H respectively. Channel 6 is used to record the hydrophone component to allow the connecting wire to be easily attached to the datalogger within the confines of the DDOBS. As signals from different sensors often vary in amplitude by several orders of magnitude it is possible to record signals with different gains on each channel of the PDAS logger, hence the horizontal geophone and hydrophone data were recorded with a gain of 10 and the vertical geophone with a gain of 100.

The digitally compensated internal clock of the PDAS can be synchronised to a one pulse per second phase locked reference clock signal; in this case the Cambridge 'Lucky 7' clock was used. The datalogger clocks are also temperature compensated and have a maximum drift rate of 6 ms a day. In practice the drift rate of the datalogger's clock was less than one sample a day and therefore was not significant over the entire duration of the seismic experiment.

The PDAS has several possible modes of recording; event triggered, scheduled window and continuous (see Teledyne Geotech, 1988). For this wide-angle experiment the scheduled window mode was used. The dataloggers are programmed by downloading a configuration file through the parallel interface of a PC. Data files are written in DOS format binary with an ASCII header to an external 127 (in this instance the full 540 Mbyte capacity was not necessary) Mbyte hard disk as (optionally) gain-ranged data with 14 data bits and 2 bits of gain information to optimise memory usage.

The aluminium alloy pressure vessel consists of two 711 mm diameter hemispheres which have a depth rating of 10 000 m. The geophone package is directly mounted onto the lower hemisphere and the remaining space is used to house the PDAS datalogger and batteries, the electronics for the acoustic release and a back-up clock for the release mechanism should the former fail or be unusable in certain water column

conditions (i.e. very shallow water or if there is a wide thermocline). The 10 kHz acoustic release transponder mounted on top of the upper hemisphere has a 45° arc of "view". This transponder has a depth rating of 6 000 m which is sufficient for the majority of experimental situations. The two hemispheres are joined by an equatorial ring and sealed with O-rings, holes bored through the equatorial ring allow electrical links between the internal electronics and external hardware through SeaCom underwater connectors. The lower hemisphere sits in a fibreglass egg cup with a grab ring attached for lifting purposes.

The DDOBS is inherently buoyant, therefore to make it sink to the seabed on deployment at a rate of 60 m minute⁻¹, a concrete ballast weight is bolted to the release mechanism mounted on the outside of the lower hemisphere and protected by the egg cup. The bolt is locked in place by a spring loaded arm fastened by two pyro charges which, when fired, part and release the arm and hence the concrete weight is dropped. To release the DDOBS a 9 V DC current is applied to each pyro charge, the ballast weight is jettisoned and the DDOBS ascends at approximately 45 m minute⁻¹. Under normal circumstances the acoustic release system operates at low power only listening, until it receives a 10 kHz acoustic signal, frequency modulated at 320 Hz, to which it responds with a double ping at 10 kHz allowing the instrument to be accurately located. The release signal from the ship is also a 10 kHz signal, frequency modulated at unique values for each DDOBS, after receiving the correct signal the short 9 V pulse is switched across the pyro charges firing them. Should this acoustic release fail, for example due to the thermocline preventing the release signal of a shipboard static or dunking transducer from reaching the transponder, the back-up clock is set for a time after the expected release time and also switches a constant 9 V signal across the pyros and fire them. Only one pyro is required to fire to release the DDOBS, the second acts only as a back-up.

Due to the value of daylight for explosive shot firing and other shipboard operations, instruments are often deployed and recovered at night. To facilitate recoveries in darkness the DDOBSs are equipped with flashing lights and radio beacons. The flashing light is a Novatech xenon flasher (ST400A) with a pressure sensitive

switch that turns the power on when the instrument is in less than 8 m of water, there is also a photoelectric cell which turns the light off in daylight. The light has a maximum life-span of 15 days and can be seen for up to 3 nautical miles. The Novatech VHF (RF700A-1) radio beacon has a similar pressure sensitive switch and operates at 170-180 MHz. The radio can be detected for up to 8 nautical miles in calm sea conditions with a maximum duration of 8 days; this varies however with the cycle, or pattern, of transmissions selected.

A buoyant strayline is attached to the grab ring, on deployment this is wound around the base of the egg cup and held in place by a metal strip wedged between the egg cup and concrete weight. This arrangement of the strayline prevents it from being caught under the concrete weight on landing on the seabed which would anchor the instrument to the seafloor, or from moving and creating noise while the instrument is on the seabed and recording. When the weight is jettisoned, the instrument ascends and the strayline unravels and floats freely. The DDOBS design is fairly low and smooth to minimise noise created by the flow of water currents, and rigid to prevent resonance in the seismic wavelength (Kirk *et al.*, 1982). As the buoyancy is located at the top of the system, it always remains within 30° of upright; its tripod-shaped ballast weight enables deployment on the roughest of seabeds (for example mid-ocean ridges).

CDOBS

The five CDOBSs (figure 2.4) only record gain-ranged hydrophone data on C90 audio cassettes using four 'Sony Walkmans'. These instruments can be used with a deployed geophone package to record four-component data, but the data storage limitations of this system make it impractical to record significant amounts of four-component data at useful sample rates. The 8-bit analogue-to-digital converter can sample the input data at 128 or 256 samples s⁻¹ only (Owen and Barton, 1990). For this experiment a sample rate of 256 samples s⁻¹ was used. The instrument has a temperature controlled crystal oscillator clock which was checked against the "Lucky 7" clock standard to measure the offset both pre and post-deployment, the drift on this clock should be less than 20 ms day⁻¹. However on some instruments the drift was actually

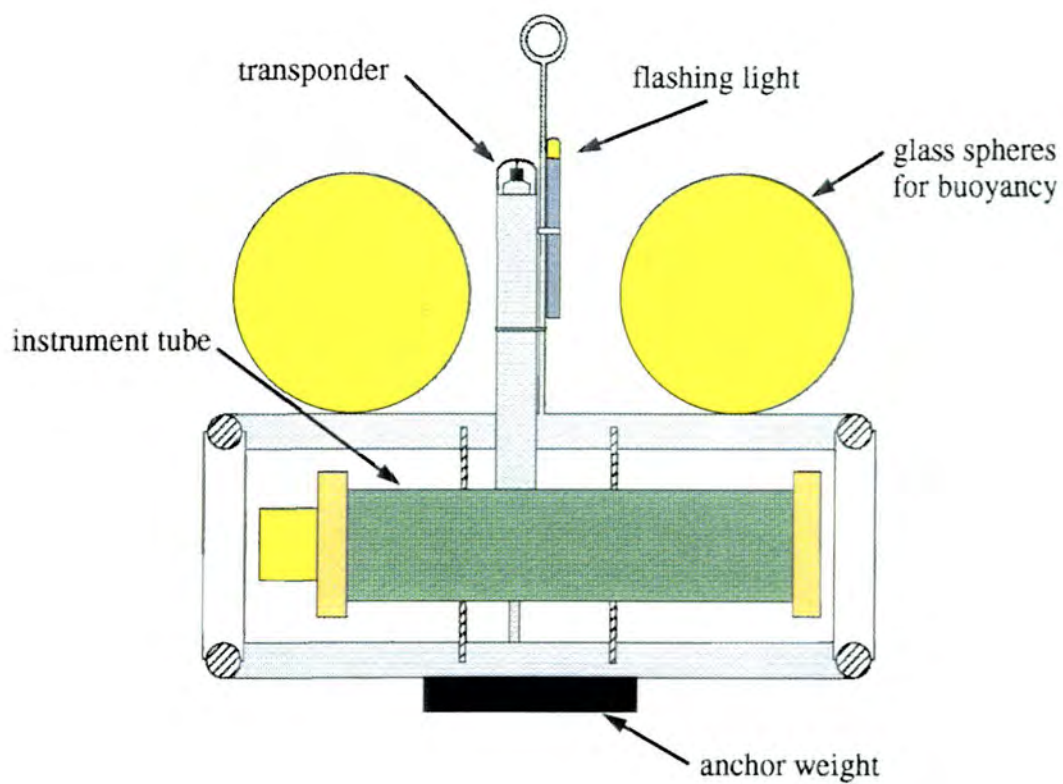


Figure 2.4: Schematic diagram of a Cambridge digital ocean bottom seismometer (top) and a photograph of a CDOBS being deployed (bottom).

measured at greater than 100 ms day^{-1} which proved significant over the duration of the seismic experiment. It is possible to use the CDOBS electronics to record in three different modes; pre-programmed, conditional save and triggered (Owen and Barton, 1990). For recording both the explosive and airgun data the instruments were used in pre-programmed mode. Like the DDOBSs the tables of recording windows are downloaded to each instrument from a PC.

The CDOBS electronics are custom built in Cambridge and are housed in a cylindrical pressure vessel. The end caps of this pressure vessel contain Glenair connectors which connect the electronics within the pressure vessel to the external hydrophone. The hydrophone is wrapped in foam and mounted on a large aluminium frame on which is also mounted the pressure vessel. The CDOBSs use an Oceano acoustic release mechanism which is a separate unit of electronics housed in its own pressure vessel and mounted on the CDOBS frame. This CDOBS assembly does not independently float and therefore it has four 19" Benthos glass spheres bolted onto the frame to create sufficient buoyancy to return it to the sea surface. On deployment two cylindrical steel tubes are attached to the Oceano release mechanism as ballast weights making the CDOBS descend at approximately 30 m minute^{-1} . The release mechanism can only be operated acoustically, and when the release signal is received it responds by rotating and so unhooking the link with the ballast weight; the CDOBS then ascends at 55 m minute^{-1} .

The instruments have flashing lights and flags to aid recovery. The strayline attached to the frame floats freely from deployment with buoyancy provided by a 10" Benthos glass sphere. Motion of the strayline and water currents passing through the irregular shape of the CDOBS create an extra source of noise on any external sensor, such that if geophone packages are used they must be detached from the main instrument housing and deployed on the seabed separately in their own pressure vessel.

Instrument recovery

It was intended to leave the instruments on the seafloor until airgun shot firing of the normal incidence lines was complete to prevent having to deploy and recover the airgun array twice. However, weather reports indicated a deep depression approaching the work area making it essential to recover the instruments with back-up clocks before the weather front arrived. Therefore shooting of the normal incidence lines was abandoned prematurely (see section 2.4.3) and the DOBS were recovered earlier than intended.

All six DDOBS and four of the CDOBS released acoustically as planned and were recovered successfully. Unfortunately, although the Oceano release on CDOBS 15 acknowledged receiving its release signal and indicated that the release mechanism had functioned, the instrument failed to return, implying the ballast weight had failed to release or that the instrument was jammed in a crevasse in the seafloor.

2.3.2 Seismic energy sources

Explosive

There were two main reasons for using explosive charges as a seismic source in the wide-angle seismic experiment. Firstly, although the Reykjanes Ridge has a smoother than average seafloor for the Mid-Atlantic Ridge it has sufficient roughness to dramatically reduce the penetration of seismic waves by scattering. Explosives were therefore used to provide a suitably large energy source and produce phases penetrating the lower crust and upper mantle with a good signal-to-noise ratio at long offsets. The direct water waves of explosive shots were over three times the amplitude of the equivalent phase from an airgun shot. Secondly it was intended to investigate the S-wave structure of the crust. Although S-waves cannot travel through water they are produced at any boundary at which there is a large change in velocity over a distance of less than half a wavelength of the incident seismic energy (White and Stephen, 1980; Fertig, 1984). However, the attenuation of S-waves is substantially larger than that of P-waves (White and Sengbush, 1963), therefore an explosive source was used to produce S-waves of a measurable amplitude.

Individual charges were constructed from 5 kg sticks of ICI E-700 Powergel (UN0241 class 1.1D) which has a density of 1.1 g cm^{-3} . For the eighty-one 25 kg charges, a detonator assembly was placed in a cardboard box with five sticks of Powergel. Two house bricks were added as ballast (figure 2.5) to make the charge sink at approximately 1 m s^{-1} . The detonator assembly consisted of a 275 g multiprimer (UN0042 class 1.1D) with 2 m of Cordtex (UN 0065 class 1.1D) through the centre, this was double detonated with two No. 6 plain detonators (UN 0030) each crimped to 4 m of Yellow Clover safety fuse (UN0105). The safety fuses are no longer manufactured by ICI therefore they were obtained from their stock pile in Canada and crimped to the detonators by RVS shot firers using tools borrowed from ICI. The nineteen 50 kg charges were constructed from one 25 kg box as described above, strapped to another 25 kg box containing five sticks of ICI Powergel only. In total 3 250 kg of explosives were used, at a cost of ~£7900.

The average ship's speed during explosive shot firing was chosen as 15 km hour^{-1} (8.1 knots) to achieve a 1 and 2 km shot interval (see section 2.2). Fuse lengths were calculated prior to the cruise to ensure that shock waves from each charge would comply with NERC safety limits and not damage the ship's stern plates and also to ensure the charge would sink to a great enough depth before detonation to prevent blow out. Although the safety fuse has an even burn rate of 2 minutes 30 s for a 3 m fuse in air, the burn rate in water is uneven and generally unpredictable (figure 2.6). This variable burn rate is believed to be due to the increase in pressure as the charge sinks and water entering the yellow tubing behind the burning fuse. Hence fuse lengths were adjusted during shot firing to keep the shot instant within the DOBS recording windows while still maintaining the safety limits.

NERC regulations require that explosive shot firing is limited to 4 hour periods during daylight hours, with a maximum of 8 hours a day. Therefore the first sixty-one 25 kg charges of Line 1 were shot in a 4 hour period on the morning of Julian day 283 with the remaining nineteen 50 kg shots on this line fired in the afternoon. All of the Line 2 explosive shots were fired the following morning.

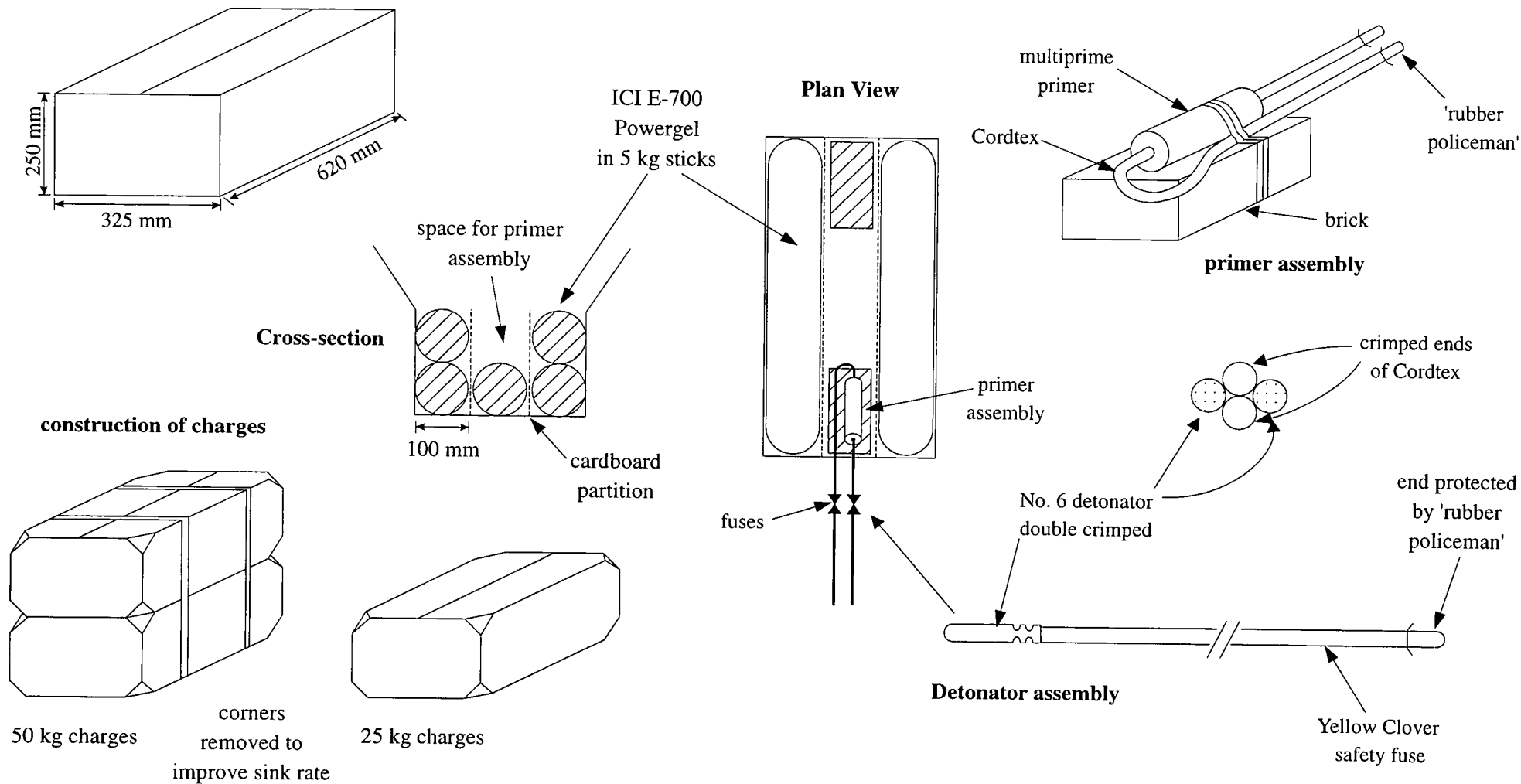


Figure 2.5: Construction of the 25 and 50 kg explosive charges detonated during CD81/93 (after Peirce in Sinha *et al.*, 1994).

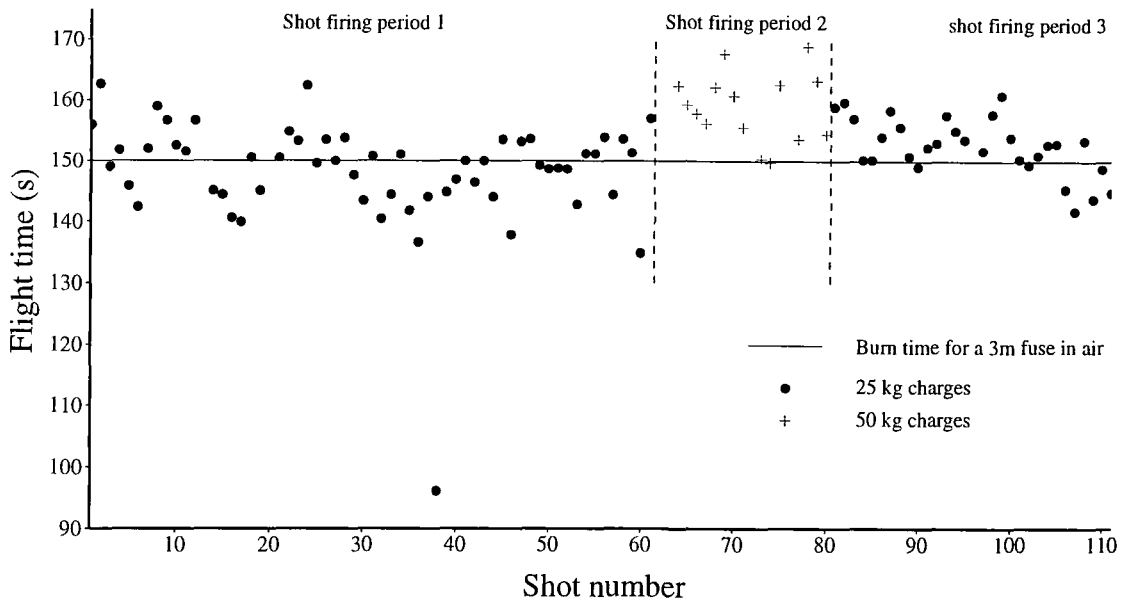


Figure 2.6: Variable burn rate of the Yellow Clover safety fuse in water. Note the greater flight times of the 50 kg charges, although these charges had shorter fuses they sank more rapidly and the increased pressure increased the burn rate of the fuse. Note also the early detonation of shot 38, it is not known why this fuse burnt so rapidly.

Shot instants were determined using the Cambridge 'Lucky 7' clock as master and were detected by a hull-mounted geophone and a towed hydrophone. The signals from these receivers were recorded, together with the clock pulse, on a spare PDAS-100 (see section 2.3.1) and a paper back-up was made on a six-channel Siemens jet pen. These data were used to calculate the shot depth and instant (see section 2.6.1). The source signatures recorded by the datalogger are discussed further in Chapter 3 and shown in figure 3.1. The range of frequencies produced by each explosive charge is fairly broad with a dominant frequency of ~11 Hz.

Airgun source

The maximum volume of airgun array available from NERC provided a smaller energy source than the explosives. The array was tuned to have a dominantly low frequency (similar to that of the explosives at ~11 Hz see Chapter 3) as required for maintaining signal energy over the long path lengths associated with wide-angle seismic data acquisition. The main advantage of using airguns (apart from cost and safety) is the rapidity of firing. The spacing of explosive shots is limited by the NERC safety requirements, however the only limitation to firing the airguns is the recovery rate, to

peak pressure of the air compressors. The closer shot spacing obtainable with airguns provides better trace-to-trace coherence and improved horizontal resolution for detailed travel time and amplitude modelling of the P-wave velocity structure.

The airgun array used for CD81/93 consisted of four beams, each with three Bolt 1 500C airguns, towed at a depth of 13 to 15 m below the mean sea surface and with the centre of the array 70.5 m from the stern of the ship (figure 2.7). The full array was used for the two lines shot coincident with the wide-angle profiles and had a total capacity of 4 566 in³ (74.9 litres). Array firing and gun synchronisation was controlled by a Reftek seismic source controller triggered with a 40 s pulse generated by the shipboard DMW master clock. The Reftek incorporated a 50 ms delay to allow synchronisation of the array before firing.

To investigate the nature of the source signature, the signal recorded by the near-offset trace of the 8-channel streamer was utilised. This signal, which had a peak frequency of 11.5 Hz, is discussed further in Chapter 3 and shown in figure 3.2. This low dominant frequency was due to the contribution of the large volume guns in the array which had been used to tune the source to the low frequencies required for wide-angle seismic investigations of the lower crust and upper mantle.

Initial problems were experienced with the airgun compressors; the two containerised compressors failed to start and a gasket blew in one of the fixed compressors. Once the fixed compressor was repaired it was able to provide a sufficient volume of air at the required pressure to fire the full airgun array every 40 s (100 m). Once we were able to fire the array we then experienced further problems in synchronising the shots with the DDOBS recording windows. These firing problems meant that the first 55 of the 190 along-axis DDOBS recording windows and 110 of the 380 CDOBS recording windows were missed, losing the northernmost 11 km of closely spaced wide-angle seismic data. Problems were also experienced with some of the guns throughout shot firing (Sinha *et al.*, 1994). On the port inner beam, the 400 in³ (6.56 litre) gun appeared not to fire at all and was probably flooded. The port outer beam 1 000 in³ (16.39 litre) gun had a short bubble pulse, implying that it was partially flooded, and the near-field hydrophone on the 120 in³ (1.97 litre) gun failed to work

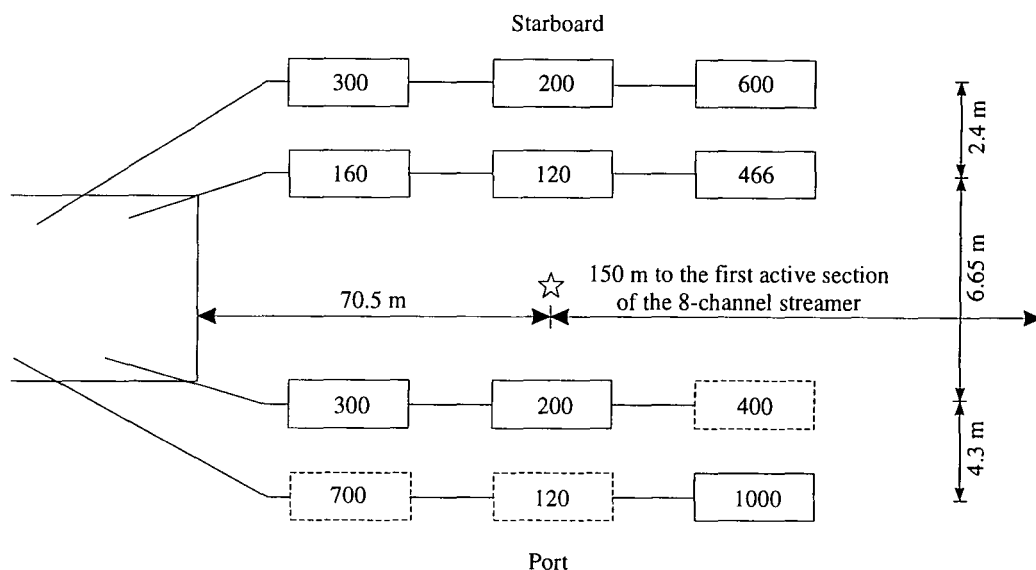


Figure 2.7: Schematic diagram showing the construction of the full airgun array used during shooting of the along and across-axis wide-angle seismic profiles. The airguns which were turned off for normal incidence profiling are shown with dashed outlines. Gun sizes are in cubic inches and the star represents the centre of the airgun array. (modified from Peirce in Sinha *et al.*, 1994)

entirely, therefore the timing of this latter gun had to be manually set and adjusted.

2.4 The wide-angle seismic dataset

During explosive shot firing, the Durham' and Cambridge' DOBSs were programmed to record all of the shots in individual windows (table 2.1). Due to restrictions in data bus speed when acquiring four channels of data at 200 s.p.s. while at the same time transferring data from the instruments RAM to its hard disk, the DDOBS were programmed to record alternate shots during airgun shot firing. The CDOBSs were programmed to record all of the airgun shots in 60 s windows repeated every 80 s, i.e. with two shots in each window.

The DDOBSs performed well, with five of the six instruments recording 100% of the programmed windows (table 2.2). The remaining instrument, DDOBS 3, only recorded the explosive shots. This failure was believed to have been caused by the magnitude of the shock waves generated by explosive charge detonations in the vicinity of this instrument. This shock wave tripped the solid state relays in the power supply on-off switch located within the PDAS, thus effectively switching the instrument off. All of the explosive shots fired up until "switch off" were recorded and provide a useful

dataset. However the airgun shots were never recorded.

	sample rate (samples ⁻¹)	window length (s)	window repeat time (s)		total bytes programmed
Explosives			25 kg	50 kg	
DDOBS	200	150	240	480	53 280 000 †
CDOBS	256	30	240	480	1 704 960 †
Airguns					
DDOBS	100	19	80		20 976 000
CDOBS	256	60*	80		21 657 600

Table 2.1: DOBS recording windows. * allows collection of two shots per window with 20 s trace lengths, † DDOBS record 4 byte integers compressed to 2 bytes while CDOBS only record 2 byte integers.

When the CDOBSs were programmed, a timing block had been time-tabled immediately prior to the first window of the along-axis airgun line, without taking into account the 20 s switching time between switching one tape recorder off and the next on. Hence, none of the CDOBSs switched on to record this line due to operator failure. During deployment CDOBS 11 began to write corrupted headers, preventing the replay program (see section 2.6.4) from locating the start of a data block. This problem got progressively worse during deployment, affecting one in 80 blocks during the first line (explosive shot firing on the across-axis line). By the end of shot firing (across-axis airgun line) less than 10% of data blocks were recoverable from CDOBS 11. The remaining three instruments recorded approximately 75% of programmed shots (table 2.2).

The loss of airgun shots at the start of the across-axis line, due to problems synchronising the triggering of the array with the DDOBS recording windows was discussed in section 2.3.2.

In addition to collecting the planned 2-D dataset along Lines 1 and 2 a 3-D dataset was fortuitously collected (see table 2.2 and figure 2.8). This consists of the across-axis airgun and explosive shots recorded by the along-axis instruments and the along-axis shots recorded by the across-axis instruments, combined with the airgun shots recorded by the CDOBS as the *Darwin* turned from Line 1 towards Line 3. This

3-D dataset has not been considered in this dissertation.

DOBS	Planned shots		Actual shots		Total no. seismograms	% shots	% actual shots	No. Mbytes
	Explosive	Airgun	Explosive	Airgun				
Line 1 (in-line)								
D 1	80	500	76	500	2304	99	100	51.1
D 2	80	500	76	500	2304	99	100	51.1
D 5	80	500	76	500	2304	99	100	51.1
D 6	80	500	76	500	1992	99	100	51.1
Line 1 (off-line)								
D 3	80	0	76	0	304	13	13	8.7
D 4	80	500	76	500	2304	99	100	51.1
D ideal	80	500	76	500	2304	100	100	51.1
C ideal	80	1030	76	1030	1106	100	100	16.2
Line 2 (in-line)								
D 3	31	0	31	0	124	14	19	14.2
D 4	31	190	31	135	664	75	100	19.7
C 13	31	0	31	0	31	7	10	0.5
Line 2 (off-line)								
D 1	31	190	31	135	664	75	100	19.7
D 2	31	190	31	135	664	75	100	19.7
D 5	31	190	31	135	664	75	100	19.7
D 6	31	190	31	135	664	75	100	19.7
C 11	27	0	27	0	27	6	8	0.5
C 12	31	0	31	0	31	7	9	0.5
C 14	31	0	31	0	31	7	9	0.5
C 15	0	0	0	0	0	0	0	0
D ideal	31	190	31	135	664	100	100	19.8
C ideal	31	380	31	270	301	100	100	6.1

Table 2.2: Wide-angle seismic dataset recorded by each of the Durham (D) and Cambridge (C) instruments compared with their ideal programs. The in-line instruments represent the 2-D dataset described in this dissertation. The off-line instruments refer to the 3-D dataset which was also collected but is beyond the scope of this dissertation.

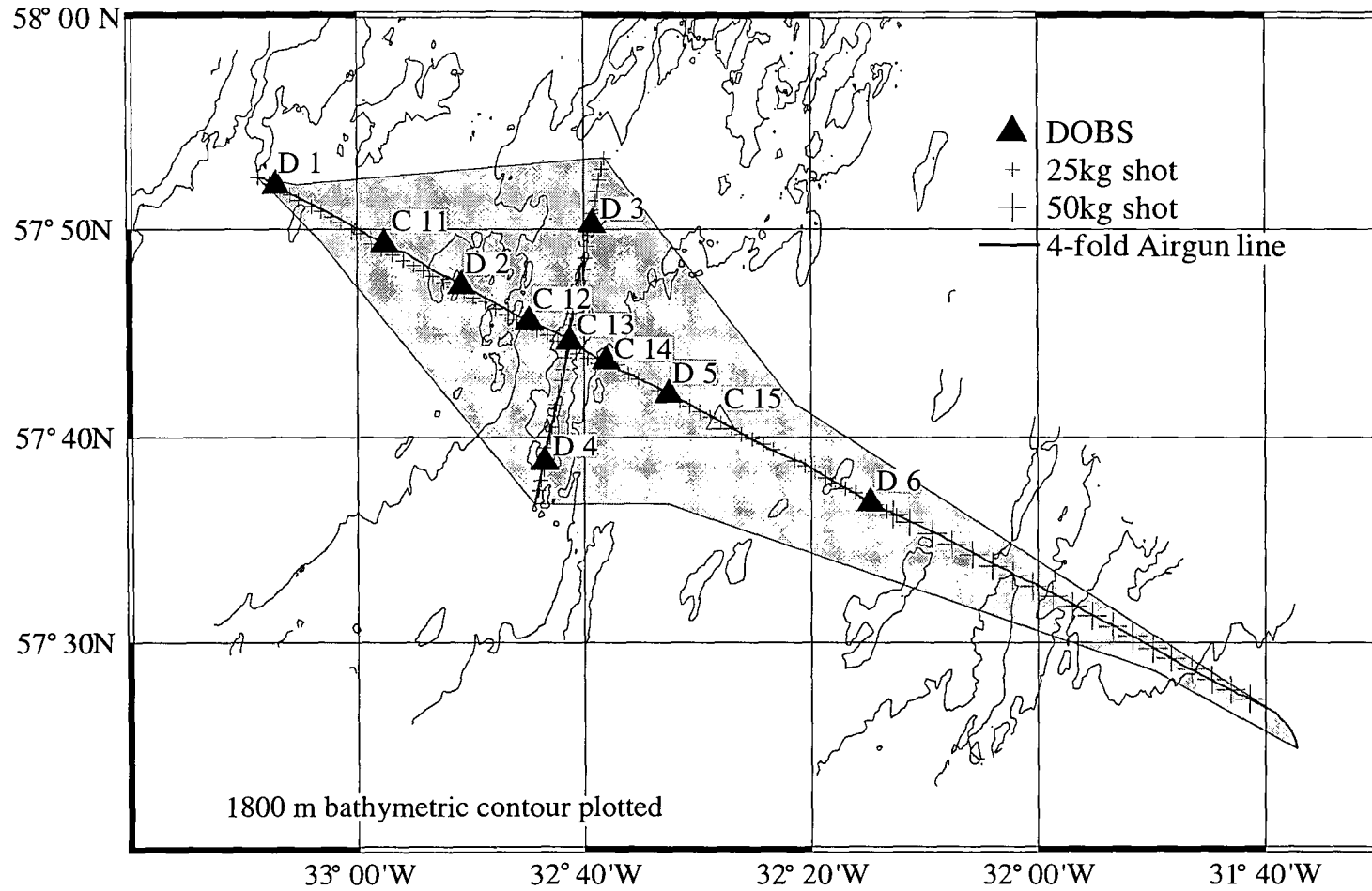


Figure 2.8: The CD81/93 wide-angle seismic experimental configuration (see also figure 2.2). The shaded area shows the three dimensional wide-angle seismic data coverage.

2.5 Data replay

The main stages in producing wide-angle seismic data in the Durham in-house format from both the DDOBS and CDOBS datasets are described below. Calculation of explosive shot instants and detonation depths is described together with the replay of the raw multichannel tapes recorded aboard the *Darwin*. The Durham in-house variation on the standard format for seismic data storage (SEG-Y) and the conversion of data recorded by both sets of instruments to this in-house format are also described. The programs used in all of the above procedures are listed in Appendix D.

2.5.1 Determination of explosive shot instants and detonation depths

The paper jet pen records of the explosive shot instants recorded by the hull geophone and towed hydrophone (see section 2.3.2; and figure 2.9), were used to pick the arrival times of the direct water waves, the seabed reflections and the first and second bubble pulse periods. These times, together with the water velocity structure, ship's speed, an estimate of sink rate for a given shot size, the relative position of the hydrophone and geophone and the shot flight times were input into the program *shotinst* (originated by A. Bunch in 1978 and subsequently modified by several Cambridge Ph.D. students) and the detonation depths and shot instants were calculated by an iterative process. From the first run of the program, the direct and reflected waves were used to calculate the shot instant, detonation depth and sink rate. This calculation is based on a method of ray-tracing through the water column (White and Bunch, 1976). The second, and subsequent runs use the improved estimation of sink rate to calculate the shot instant and detonation depth from the bubble pulse (Spudich and Orcutt, 1980a). This calculation gave average sink rates of $1.45 \pm 0.2 \text{ ms}^{-1}$ for the 25 kg charges and $1.32 \pm 0.3 \text{ ms}^{-1}$ for the 50 kg charges (figure 2.10). The calculated shot instants and detonation depths are tabulated in Appendix A for reference, and the errors involved in this process are described in section 2.7.

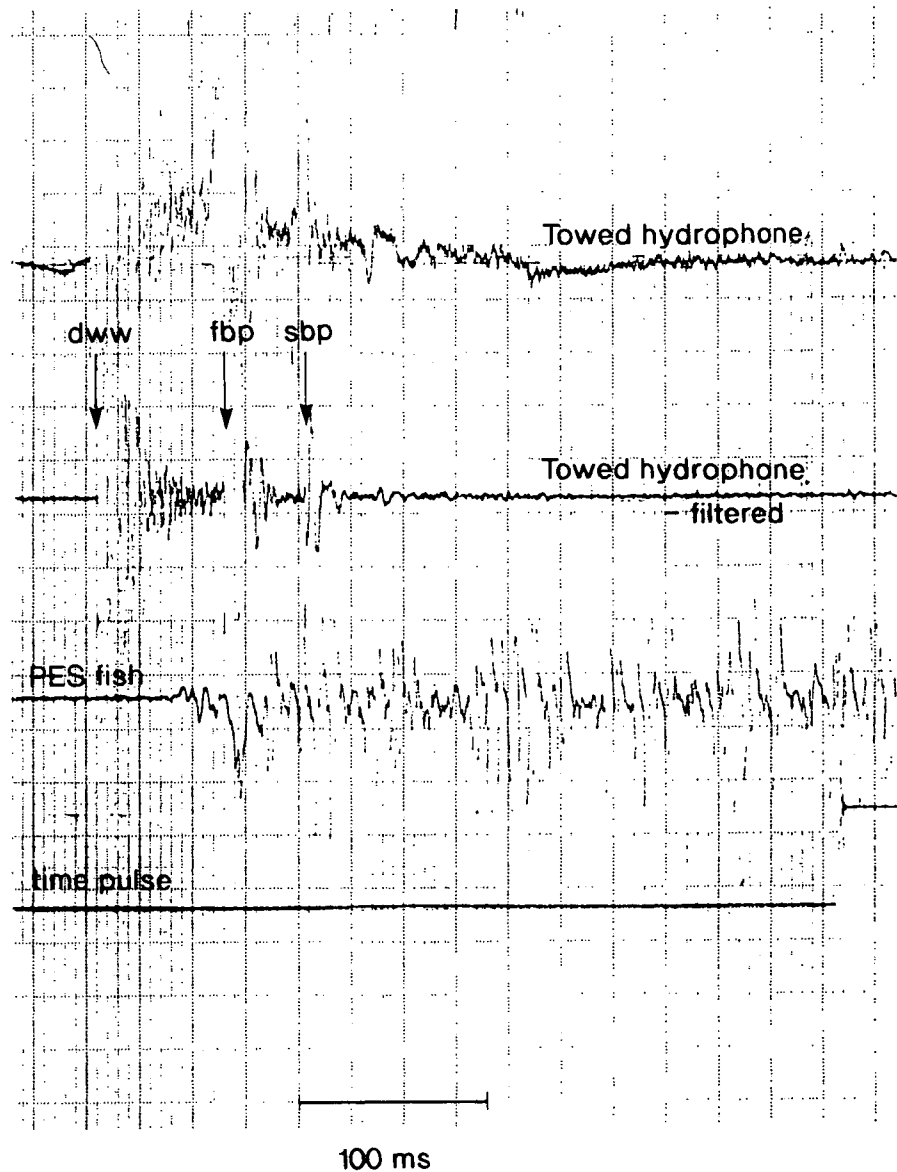


Figure 2.9: An example of a jet pen record showing the first arrival and two bubble pulses generated by an explosive shot and recorded by the towed hydrophone (upper two plots). These recorded shot instants are measured against a phase locked time code (lower plot). dww – direct water wave. fbp – first bubble pulse. sbp – second bubble pulse. PES – precision echo sounder.

2.5.2 SEG-Y_i

The standard format for recording seismic reflection data is SEG-Y (Barry *et al.*, 1975). Data are normally recorded on a 9-track, ½" magnetic tape with a 3 200 byte EBCDIC and 400 byte binary reel header followed by an inter-block gap, then a series of blocks including a 240 byte binary data header followed by the trace data itself (length of record = number of samples × 4) separated by inter-block gaps. The final

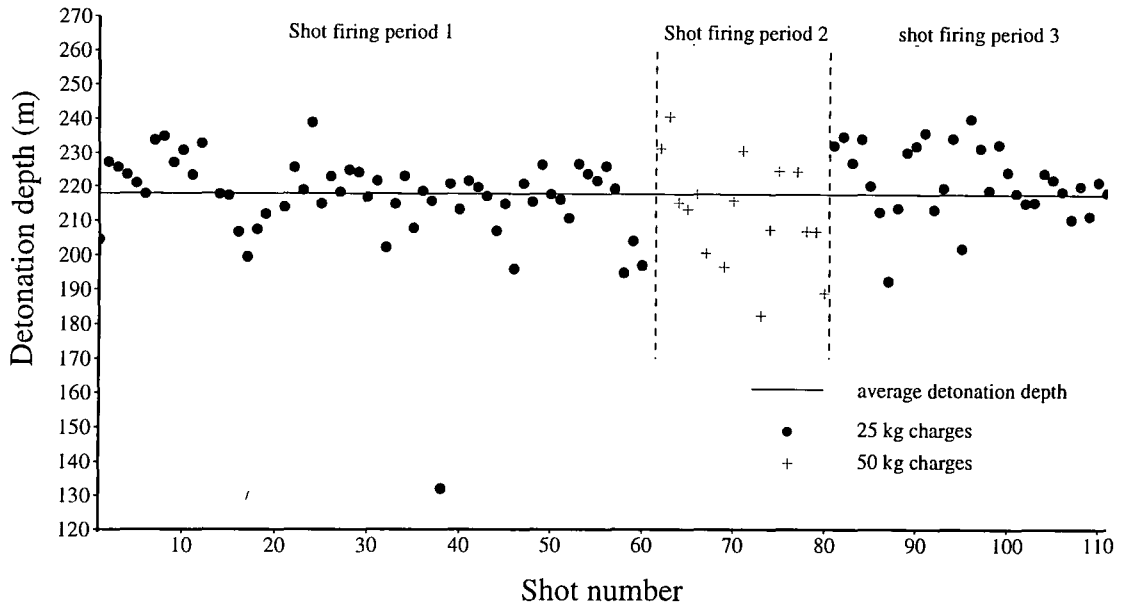


Figure 2.10: Graph showing the variation in detonation depths (hence sink rates) of explosive charges. Note the greater variability for the 50 kg charges and the shallow detonation depth of shot 38 due to an unexpectedly rapid fuse burn rate.

block is terminated by an end of file mark.

This format is modified for wide-angle seismic data (SEG- Y_{WA}) with blank header values used to define wide-angle parameters (for a full description see Peirce, 1990b; Matthews, 1993 and the summary in Appendix C). In Durham, to minimise data storage requirements and for ease of data manipulation, the files are split into their four constituent parts on disk to form the SEG- Y_i format. This format has been used for all data processing.

<u>file suffix</u>	<u>contents</u>
~.hdr	3 200 byte ASCII header
~.bfh	400 byte binary file header
~.bth	240 byte binary trace header data for each trace
~.btd	IBM real*4 binary trace data

2.5.3 Replay of DDOBS data into SEG- Y_i files

A schematic diagram showing the main processing stages is presented in figure 2.11. These processes are described in detail below.

The PDAS datalogger stores data as DOS binary files which are given unique names in the form:-

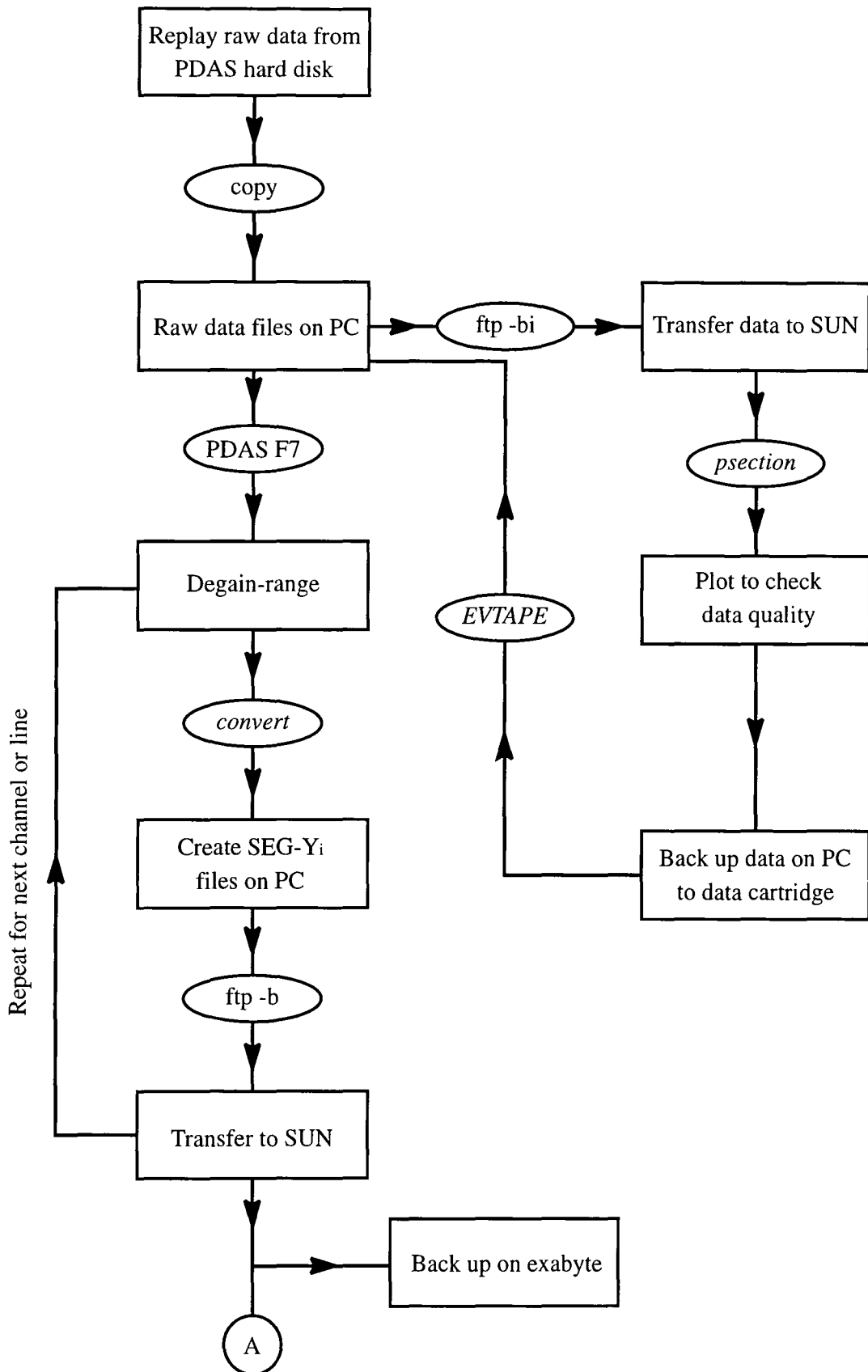


Figure 2.11: Flow diagram showing the main processing stages required to create SEG-Y_i files from the raw DDOBS data. Processes are described in detail in the text and are surrounded by rectangles while *programs* or system commands are surrounded by ellipses. A – the continuation point for further data processing (see figure 2.14). Refer to figure 2.12 for a comparison with CDOBS data processing.

P2105316.285

- P – primary recording window (explosive source),
or S– secondary (airgun) window
- 2 – channel number
- 105 – PDAS datalogger number
- 316 – sequential window number
- 285 – Julian day

After the instrument is recovered and the internal clock checked, the PDAS is turned off and its disk removed. The disk is then connected to a power supply and the replay PC via a SCSI cable before powering the disk up and then switching the PC on. When the PC boots, the external disk partitions are mounted as DOS partitions D, G, H, I, J, K and L on the PC. This letter sequence is due to the nature of primary and extended disk partitions under the DOS operating system. The raw data files can then be directly copied from each external hard disk partition to one or more (depending on volume) large PC disk partitions using a series of batch files (written by C. Peirce). The transfer of 70.8 Mbytes of data took approximately 4 minutes. Once these data files are on the PC it is turned off and the external disk disconnected before rebooting the PC in a local area networked (LAN) mode. To check all data has been transferred from the PDAS disk, and as a means of quality control, the raw PDAS format data files are copied to a networked SUN using *ftp* in binary mode and plotted using *psection* (written by C. Peirce) to view the raw data as seismic sections. The data on the PC are then backed up using a QIC-02, ¼" data cartridge and the tape control program *EVTAPE*.

The PDAS recorded gain-ranged data as 2 byte integers 2 bits of which contain gain information (see section 2.3.1). These data were degain-ranged to 4 byte integers using the PDAS software option F7. The next stage in the conversion process to SEG-Y_i involved extracting the appropriate sections of data after each shot instant from the raw data files to form each individual trace on the resulting record sections. Three files containing the experimental parameters are used in this process (see Appendix D for examples of these files):-

- event file - containing the shot number, shot instant, shot size, detonation depth, shot location (for explosive shots this was the position the charge was deployed and for airgun shots this was left as zero) and the water depth
- station file - containing the logger number, instrument location and depth and any clock drift, negligible for DDOBSs
- options file - containing header information and the trace length required

The experiment files and the degain-ranged data files were input into *convert* (written by P.A. Matthews and modified for marine DDOBS data by C. Peirce) which created the appropriate SEG-Y_i headers, selected the required trace data (specified by the shot instant and trace length) from the raw data file and wrote the required section of data as IBM real*4 integers. The four SEG-Y_i files created on the PC hard disk were transferred to a networked SUN, again using *ftp*, ready for plotting and further processing.

2.5.4 Replay of CDOBS data into SEG-Y_i files

The main processing stages are shown schematically in figure 2.12 and are described in detail below. Unless otherwise stated the CDOBS processing programs were written by T.R.E. Owen (University of Cambridge).

The program *332COMM* was used to replay the C90 data cassettes from a replay unit onto a PC. The raw data quality was checked using *DB_SHOW* which identified any unexpected data streams in the binary file and estimated the number of errors in the replayed file. The majority of these errors were caused by poor tape head alignment between the recording 'Sony Walkman' and the replay unit. If necessary the replay process was repeated to reduce the number of errors in the raw data before backing it up onto 9-track, ½" magnetic tape using *DEPOT*. Two files containing the experimental parameters were created (example files are in Appendix D):-

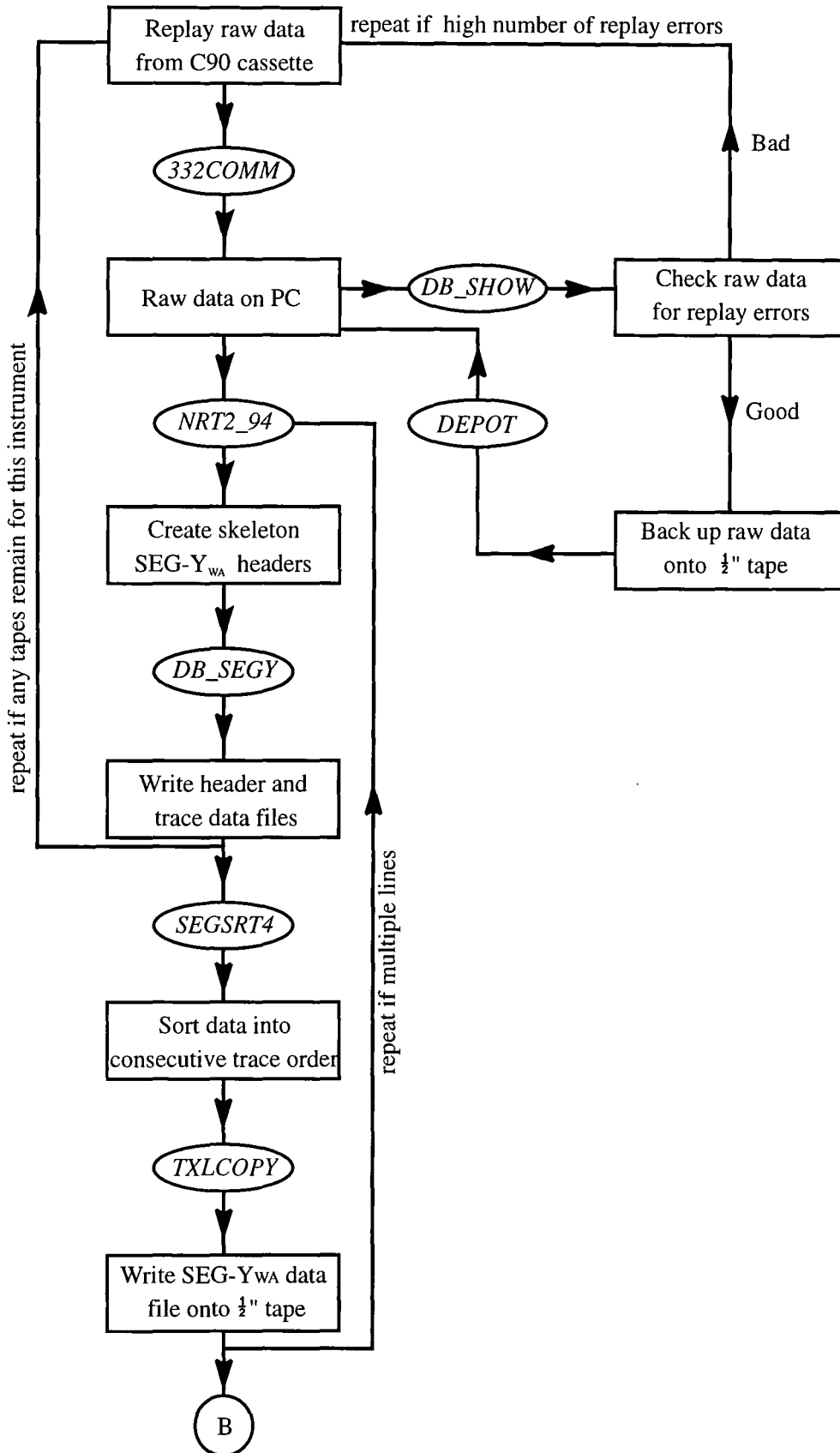


Figure 2.12: Flow diagram showing the main processing stages required to create SEG-Y_i files from the raw CDOBS data. Processes are described in detail in the text and are surrounded by rectangles while *programs* or system commands are surrounded by ellipses. B – the continuation point overleaf. Refer to figure 2.11 for a comparison with DDOBS data processing.

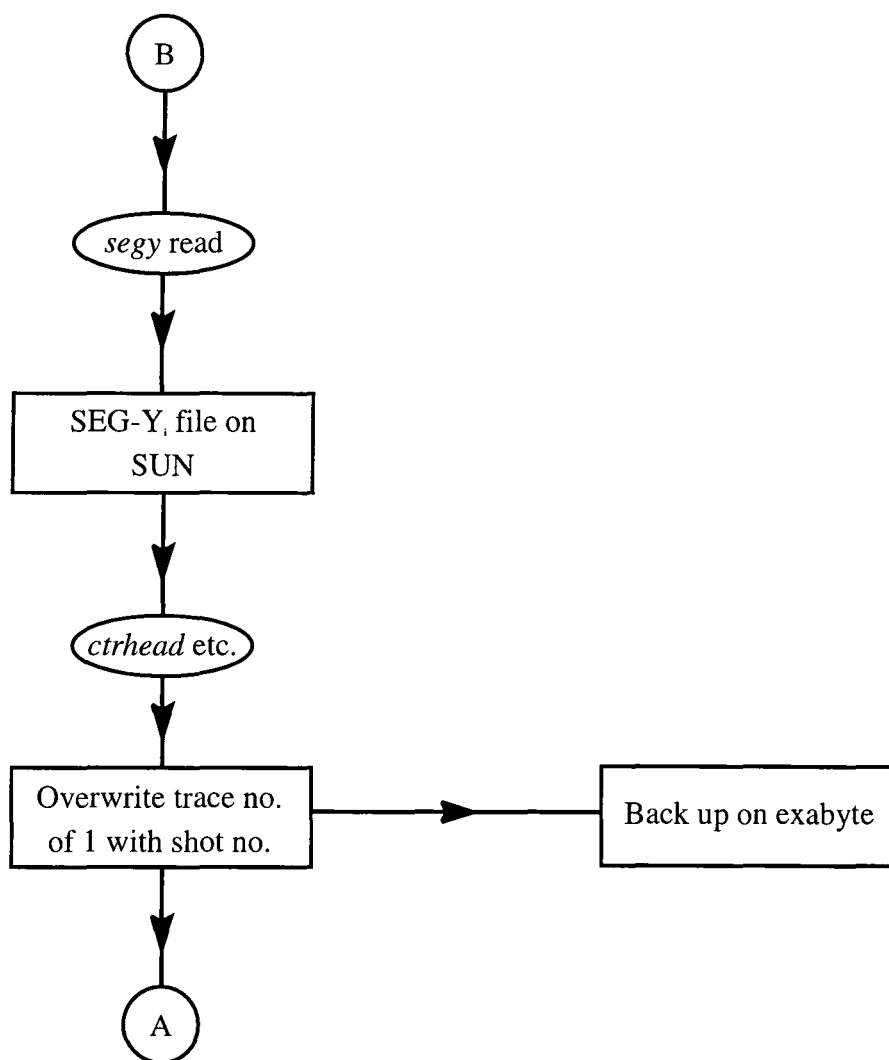


Figure 2.12: cont.. Flow diagram showing the main processing stages required to create SEG-Y_i files from the raw CDOBS data. Processes are described in detail in the text and are surrounded by rectangles while *programs* or system commands are surrounded by ellipses. B – the continuation point from the previous page. A – the continuation point for further data processing (see figure 2.14). Refer to figure 2.11 for a comparison with DDOBS data processing.

- event file - containing the shot number, shot instant, shot size, shot location and water depth
- instrument file - containing the instrument name, location and depth and the time and offsets of pre and post-deployment clock checks against the Cambridge 'Lucky 7' clock

These experiment files and the required output trace length were input into the program *NTR2_94* (originally written by P.J. Barton and since modified by several Ph.D. students), which corrected the shot instants for clock drift calculated from the pre

and post-deployment clock checks (between 19 and 900 ms drift over the deployment period of the CDOBS), and produced skeleton SEG-Y_{WA} headers with the corrected shot instant and trace length. Where the shots were less than 60 s apart multiple header files were created by *NTR2_94*. The skeleton headers produced by *NTR2_94*, the raw replayed data files, the sample rate of the data and the output data format (IBM real*4) were then input into the program *DB_SEGY* which wrote SEG-Y_{WA} reel header and trace header files and selected the required traces from the raw data file (specified by the clock drift corrected shot instants and trace length) and wrote them to disk in IBM real*4 format. These files were then sorted into consecutive trace order using *SEGSRT4* and written to 9-track, ½" tape in SEG-Y_{WA} format using *TXLCOPY*.

The ½" tapes were replayed at Durham using *seg*y (written by D.L. Stevenson) to produce a SEG-Y_i file on disk. As this program is capable of reading non-standard SEG-Y files and tapes it routinely checks the format identification value in the input binary header file. However, the minimal header information produced by the processing system in Cambridge does not include a header value identifying the data format. Therefore, to be able to read CDOBS data in from tape, a disk file containing the switch for IBM real*4 format was incorporated into the SEG-Y_i disk file header as data were read from tape to overcome this problem. The allocation of storage locations of SEG-Y_{WA} header values for wide-angle seismic data differs between Cambridge and Durham (see Appendix C). The trace number in the Cambridge definition refers to the trace number within a gather of traces which is the definition used in standard SEG-Y for multichannel reflection data. This trace number is always one for wide-angle data, therefore at Durham this value is defined as the shot number to ease further data manipulation. Therefore, to enable processing and plotting of the Cambridge data at Durham, the series of programs *thead*, *trtodis* and *dishead* (written by C. Peirce and detailed in Appendix D) were adapted to equate the trace number to the shot number.

Initially once plotted, the Cambridge data sections did not appear as expected. The cause of this disparity was believed to be the program *NTR2_94*, which appeared to have a sample rate of 8 ms hard coded into it. Therefore, although when running *DB_SEGY* the data sample rate is given as a required input parameter and the correct

rate of 4 ms was input, the header files were written with the 8 ms value from *NTR2_94*. This was amended by modifying *NTR2_94* and repeating the processing stage.

When the reprocessed data were plotted it could be seen that the degain-ranging had been ineffective, also only every sixth trace had the direct water wave at approximately the correct travel time; the five intervening traces were delayed by approximately 1 s. As the gain-ranging constant had been recorded on a different channel to that expected by *332COMM*, it had not been read in from the C90 data cassette and therefore an incorrect gain had been applied to the data. To read in the correct gain all the cassettes were replayed *again*, using a modified version of *332COMM*. A land replay unit was used at this stage as it was based on a 'Sony Walkman' similar to those on which the data had been recorded. This adaptation reduced the number of replay errors caused by poor tape head alignment between the recording 'Walkman' and the marine relay tape deck and significantly improved the replay process.

When selecting the start of a trace from a stream of raw data *DB_SEGY* counts samples from the nearest minute time mark. The method of instrument programming used in this experiment, which resulted in two shots occurring within one recording window (figure 2.13) led to unexpected problems when counting the number of samples after a time mark with *DB_SEGY*, hence causing the time delays seen on the direct water waves. The first attempt to overcome this consisted of producing two sets of skeleton *SEG-Y_{WA}* headers from *NTR2_94*, one to extract the shot at the start of a window and the second to extract the shot at the end of a window. These two headers were input into *DB_SEGY* and the output files combined to form one *SEG-Y_{WA}* file. When this file was plotted the resulting record section showed that a third of the traces were still delayed. When the delayed traces were compared to the timing diagram of the shot instant, window length and the position of the minute mark (figure 2.13), the effected shots were seen to have occurred immediately before a minute mark where the trace also overlapped the end of a block. This delay was measured at 1 second and 12 samples. The delay was removed by using the previous technique of extracting both shots from a window separately, combined with taking 18 s traces which no longer

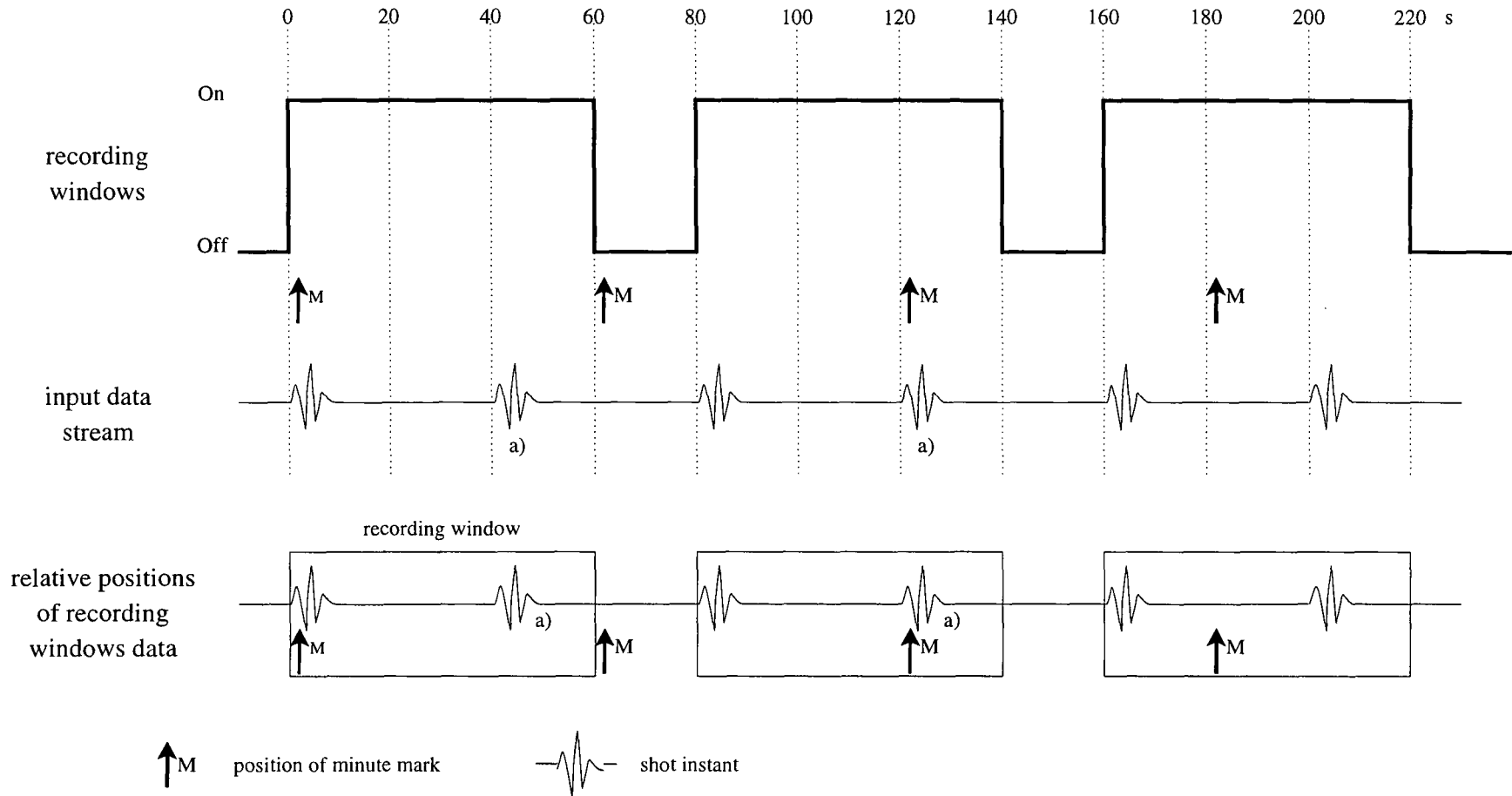


Figure 2.13: Timing diagram for the recording of airgun shots by the CDOBS. Shots were recorded every 40 s in 60 s windows which were repeated every 80 s. The shots marked a) are those which were delayed at the end of the block immediately before a minute mark (see text).

overlapped the end of a block. Once the replay process was completed satisfactorily the data were transferred into the SEG-Y_i format at Durham using the method described above.

2.6 Wide-angle data processing to final record sections

The final processing stages to produce interpretable wide-angle record sections from data collected by both sets of instruments are described below and summarised in figure 2.14.

2.6.1 Corrections applied to wide-angle seismic data

Shot to receiver ranges

The *Darwin's* GPS receiver takes a satellite fix every 2 minutes resulting in ship positions accurate to within 100 m. As the DOBSs were recovered within 200 m of their deployment position, this indicated that the instruments did not drift significantly during the 1 300 to 2 000 m descent to and ascent from the seabed and gave a total accuracy in receiver position on the seabed of ± 200 m. The DOBSs deployment positions were used initially as the instrument position when ray-tracing the direct water waves (section 2.6.1 – statics). These positions were then adjusted within the ± 200 m error bounds until a consistent water wave travel time fit was achieved for all instruments and data sections.

To calculate shot–receiver ranges for the explosive shots the direct water wave arrival times were used. The approximate ranges were calculated during the creation of SEG-Y_i files as previously described, using the instrument location and the position at which the shots were deployed. The hydrophone data sections were plotted unfiltered using these approximate ranges and the program *dazzle* (written by C. Peirce), and the arrival times of the direct water waves and water wave multiples were picked. The program *range* (written by C. Peirce) took the shot depth, time and position, water wave arrival times, water velocity structure from the sound velocity profile and instrument position and depth and calculated possible ray paths through the water column, resulting in a list of possible ranges for the shot. The appropriate new shot-receiver range was

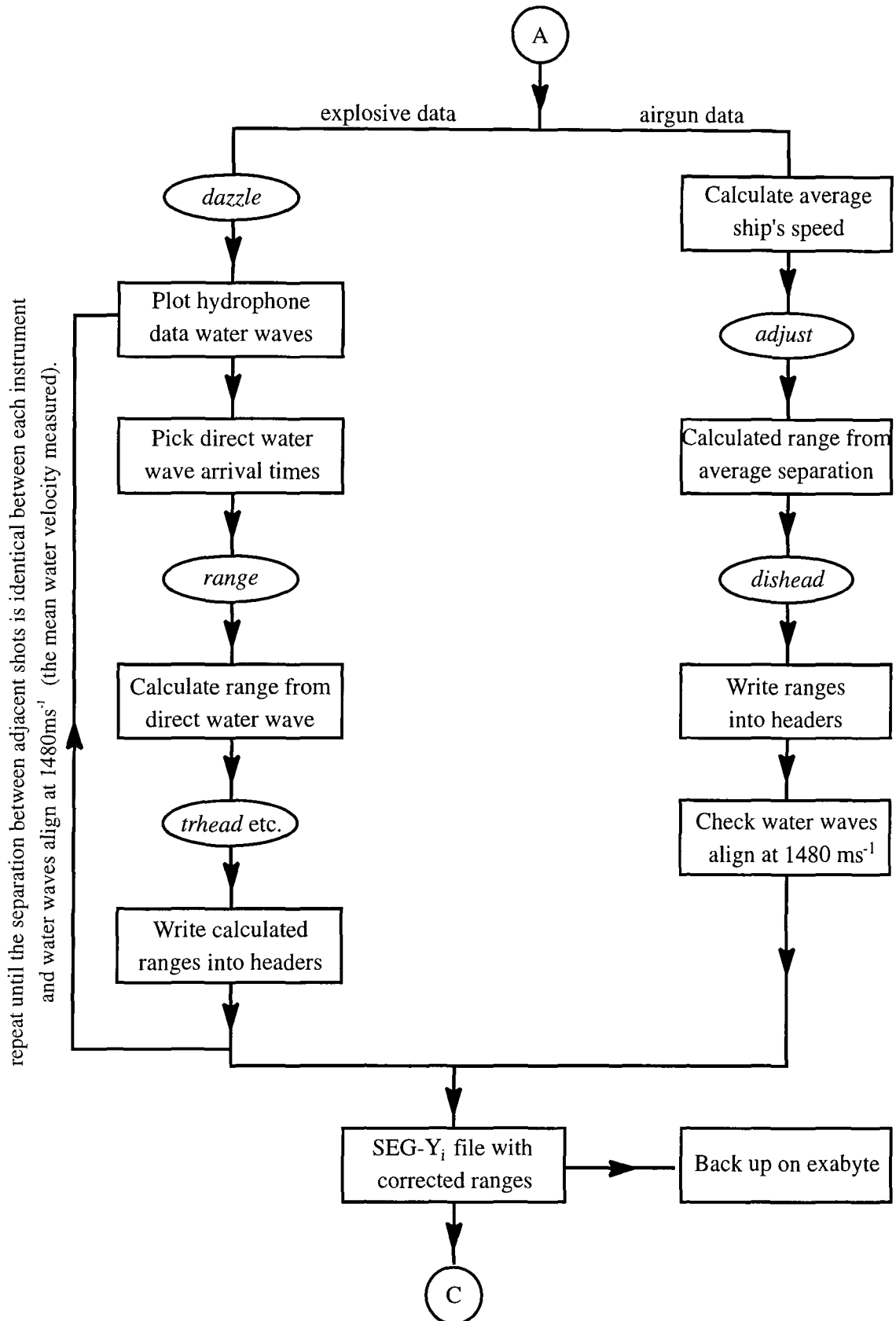


Figure 2.14: Flow diagram showing the processing stages for the SEG- Y_i files used to create final record sections. Processes, outlined by rectangles, are described further in the text while *program* names are enclosed by ellipses. A – the end points of the initial stages of data processing for both kinds of instruments (cf. figures 2.11 and 2.12). C – continuation point overleaf.

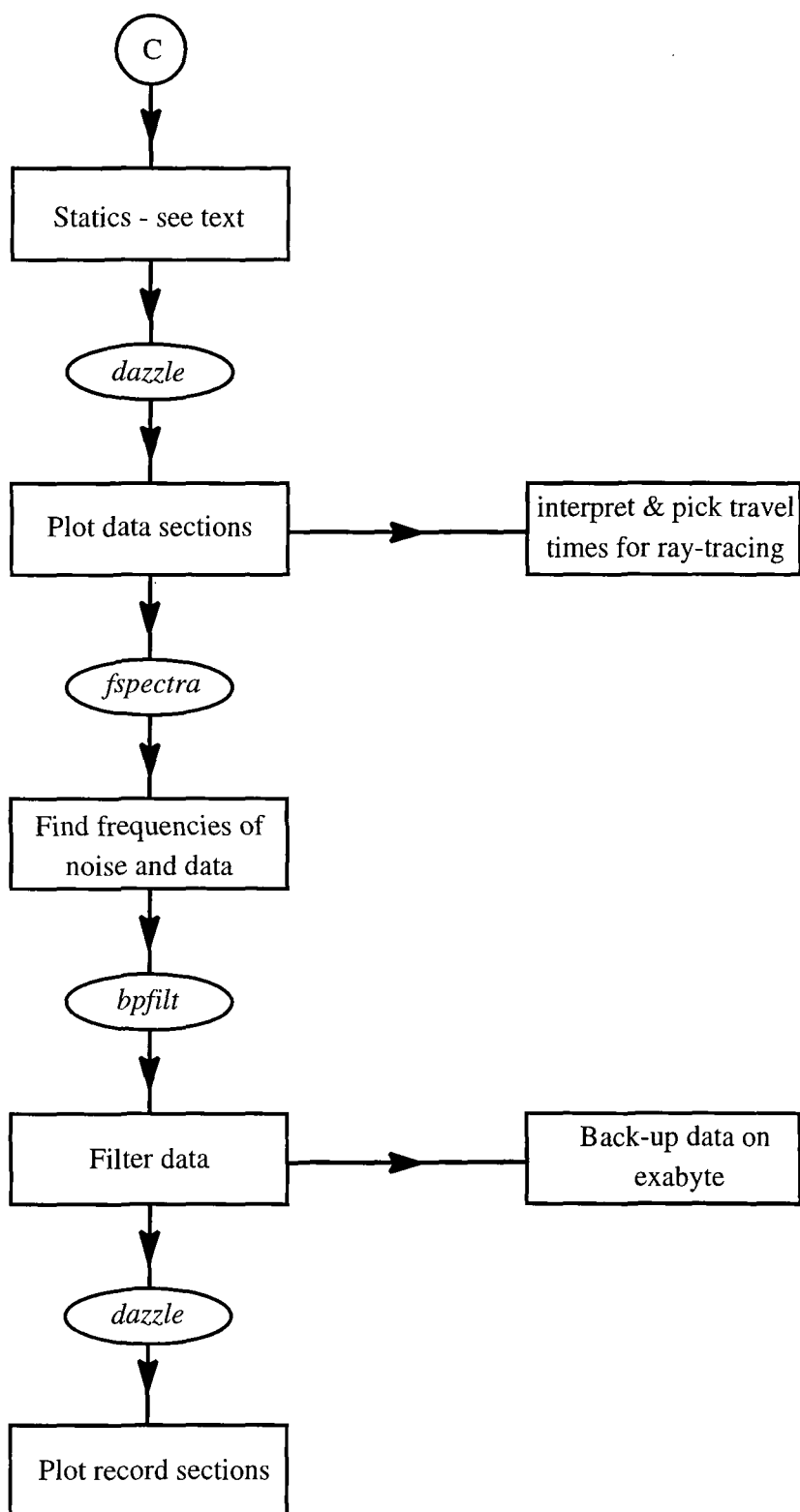


Figure 2.14: cont.. Flow diagram showing the processing stages for the SEG-Y_i files used to create final record sections. Processes, outlined by rectangles, are described further in the text while *program* names are enclosed by ellipses. C – continuation point for the previous page.

then input into the header using the series of programs *trhead*, *trtodis* and *dishead*. The sections were re-plotted and the process repeated until the water waves aligned along the 1480 m s^{-1} hodochron – the mean water velocity obtained from the sound velocity profile.

As the shots were only fired once they have the same separation no matter which seabed instrument records them. Therefore once the best-fit ranges had been calculated for each instrument, the shot separation was compared between instruments and, where necessary, the DOBS positions adjusted within their error bounds to achieve a consistent shot separation for all instruments.

Airgun shot–receiver ranges were calculated assuming a constant ship's speed. Throughout surveying the ship's speed was logged every 30 s and from this dataset the average speed during airgun shot firing was calculated:-

$$\text{Line 1 average speed} = (2.5 \pm 0.2) \times 10^{-3} \text{ ms}^{-1}$$

$$\text{Line 2 average speed} = (2.5 \pm 0.4) \times 10^{-3} \text{ ms}^{-1}$$

Shots were recorded every 40 and 80 s by the CDOBSs and DDOBSs respectively. From the shot interval and ship's speed the average shot separation was calculated. For this calculation it was assumed that the instrument was located on line and hence the point of closest approach would occur at zero lateral range. From a hydrophone data section for each instrument, the shot number at closest approach, i.e. zero range, was picked. Given the shot separation and the zero range shot number the shot range could then be calculated for every other shot:-

$$\text{range} = \text{number of shots from closest approach} \times \text{shot separation}$$

The program *adjust* (written by C. Peirce) calculated these ranges and output the shot number–range pairs in the format required by *dishead* which was then used to write the new range values into the SEG-Y_i headers. The datasets were then plotted to check that the direct water waves aligned with the 1480 m s^{-1} hodochron.

Statics

Initially the intention was to fire the airgun array using the Cambridge "Lucky 7" clock as a master clock, hence all the DOBSs were synchronised to this clock. However in practice, after the DOBSs had been deployed, it was found the pulse output from the "Lucky 7" clock was too short to trigger the Reftek gun synchronisation system. Therefore the shipboard DMW clock had to be used. This resulted in numerous clock checks over the deployment period, directly comparing the outputs from the two clocks. The "Lucky 7" clock, and therefore also the DOBSs, were delayed by 76 ms behind the DMW clock. In firing the guns an additional 50 ms delay behind the DMW clock was incorporated by the Reftek before firing, due to the gun synchronisation process. These two offsets were not taken into account when producing a listing of shot instants for processing the raw data to SEG-Y_i files and therefore had to be incorporated as static corrections at this stage. The two offsets combined to a -26 ms static (see figure 2.15) which was written to the SEG-Y_i header files using adapted versions of the programs *thead*, *trtodis* and *dishead* (see Appendix D).

If water waves (both direct and multiples) are ray-traced, using water velocities from the sound velocity profile and the seafloor depth from along track bathymetry measurements, and the instrument is positioned on the seafloor in the deployment location, then the calculated travel times should agree with the observed, provided all positional information, water depths and shot instants are correct. When this ray-tracing was performed a good match was obtained for the DDOBS data but the CDOBS data appeared to require a further static shift (see figure 2.16). As the observed and calculated direct water waves and multiples for the DDOBSs matched to within the lowest error bounds of the data (see section 2.7) this suggested that the position information, water depth and shot instants (which were the same for both sets of instruments) were correct. In some cases the CDOBS data required shorter water wave ray paths, implying that the static shift could not be caused by the instrument being off-line and as the instruments were not floating in the water column, these "short ray paths" implied the static shift was caused by an instrumental timing or processing problem that could not be readily identified. Also there was no evidence of a gradational static that

could be caused by an erroneous clock drift correction. Therefore, in an attempt to retrieve usable data, direct water waves and multiples were ray-traced through the water column and the time difference between the calculated and observed arrivals was used as a static correction to move the observed water waves to agree with those calculated (see table 2.3 and figure 2.16). Although with these statics the direct water wave arrivals agreed well with the bathymetry and the DDOBS data, there still appeared to be a shift between the CDOBS airgun and explosive data and between these and the DDOBS data. This shift was not consistent between CDOBSs nor on either side of an instrument and proved extremely problematic to resolve with any degree of rigor or confidence in the resulting dataset.

The cause of this mismatch still remains somewhat of an enigma and its consequences will be discussed later in context of the reliability of the data (see section 2.7.2).

Instrument	Static required (ms)	
	Airgun data	Explosive data
CDOBS 11	-	+550
CDOBS 12	-440	-388
CDOBS 13	+130	+ 82
CDOBS 14	+220	+272

Table 2.3: Static corrections required by CDOBS data.

2.6.2 Generation of interpretable sections

Once corrected ranges had been incorporated into SEG-Y_i file headers, the data were plotted with *dazzle*. For the DDOBS vertical geophone data, this was generally sufficient to produce an interpretable section. However the signal-to-noise ratio was lower for horizontal geophone and hydrophone data therefore these benefited from filtering. The causes of these lower signal-to-noise ratios are:-

- Horizontal geophone – signals of lower amplitude
- DDOBS hydrophone – more sensitive than the geophone and detected the spin of the storage disk within the pressure vessel
- CDOBS hydrophone – higher background noise levels due to an overly sensitive hydrophone

The program *fspectra* (written by D. Graham and modified by C. Peirce) was used to identify the dominant frequencies of the signal and noise, and the program *bpfilt* was then used to apply a Hanning band-pass filter to the data (the data sections and corner frequencies used for filtering are discussed in the next chapter). The band-pass filtered record sections were then plotted with *dazzle* for interpretation. As filtering can affect wavelet shape and onset time; travel times for use in the modelling process were picked from large-scale unfiltered sections.

2.7 Errors associated with the wide-angle seismic data

2.7.1 DDOBS

Explosive data

The calculation of the shot instant and detonation depth from records of the towed hydrophone and hull geophone, relied on an accurate knowledge of the water velocity structure and correctly picking arrivals from the jet pen records (figure 2.9). The errors involved in the shot instant and detonation depth calculations were estimated to be ± 20 ms and approximately ± 30 m (± 20 ms) respectively. The clock drift over the length of deployment of the DDOBSs was less than one sample, giving an error over the entire explosive shot firing period of ± 5 ms (the sample rate).

The error in picking travel times from large-scale unfiltered data sections was estimated at ± 10 -80 ms, the lower bound was estimated assuming the arrival can be picked to within two samples and the upper depends on the data quality and range, i.e. at a greater range the signal-to-noise ratio is lower, hence travel time picks are less accurate. The calculation of range by modelling of the direct water wave was estimated to be accurate to ± 100 m (± 67 ms).

The shot instant, detonation depth and clock drift error are related and when combined with the picking and range errors give a total error of approximately ± 100 ms (see table 2.4).

Airgun data

The airgun shot instants could be controlled to within ± 4 ms and the depth of the airgun array to within ± 1 m (± 1 ms). The clock drift for the DDOBS was also minimal hence the errors in the shot instant and depth and clock drift are less than one sample. However the travel time could only be picked as accurately as the sample rate of the recording instrument, which for the DDOBSs during airgun shot firing was 10 ms.

The travel time picking error is the same as for the explosive data. The range was calculated from the ship's velocity, which was 2.5 ± 0.4 km s⁻¹ in the worst case, giving an error in range of ± 30 m (± 20 ms).

When these errors were combined they gave a total error for the DDOBSs of ± 50 ms (table 2.4).

2.7.2 CDOBS

Explosive data

The calculation of shot instant and detonation depth of the explosive shots for the DDOBSs and CDOBSs was identical, therefore the errors involved are again ± 20 ms and ± 30 m (± 20 ms) respectively. The CDOBS had clock drifts averaging 200 ms over the entire deployment and 90 ms over explosive shot firing which increases the error in the shot instant for the CDOBS.

The travel time picking error is unchanged for this dataset at ± 10 -80 ms and the range error is the same as for the DDOBS explosives data at ± 100 m (± 67 ms).

When the shot instant, detonation depth, clock drift, picking and range errors are combined the total error is approximately ± 120 ms, however the static corrections involved with this dataset reduces the level of confidence in the associated travel time picks.

Airgun data

Again the airgun shot instants and depths lie within the sample rate of the data, which for the CDOBS was 4 ms, hence the errors in these values are ± 4 ms. The CDOBS clock drift was approximately ± 150 ms over the duration of airgun shot firing.

The travel time picking error and the range error are the same as for the DDOBS airgun data at ± 10 -80 ms and ± 20 ms respectively. However when these errors are combined, due to the larger clock drift and the static corrections solely related to the CDOBS data, a value of ± 200 ms seemed to be a reasonable accuracy within which to model this latter dataset.

Source of error	Explosive errors (ms)		Airgun errors (ms)	
	DDOBS	CDOBS	DDOBS	CDOBS
Shot instant	± 20	± 20	± 4	± 10
Shot depth	± 20	± 20	± 4	± 10
Clock drift	± 5	± 90	± 10	± 150
Picking error	± 10 -80	± 10 -80	± 10 -80	± 10 -80
Range	± 67	± 67	± 20	± 20
Total error	± 100	± 120	± 50	± 200

Table 2.4: Errors in the travel time picks obtained from the processed wide-angle seismic data.

2.8 Normal incidence data acquisition

In the initial plan for CD81/93 it was not intended to collect normal incidence seismic reflection data, however as the *Darwin* had an 8-channel streamer aboard this dataset was collected with the aim of imaging off-axis sediments and hence, provide a constraint on the detailed upper crustal structure of the wide-angle model and hopefully also to image any prominent upper crustal reflectors. The experimental configuration is described in section 2.2 and shown in figure 2.17 and in figure 2.2 in relation to the wide-angle seismic experiment.

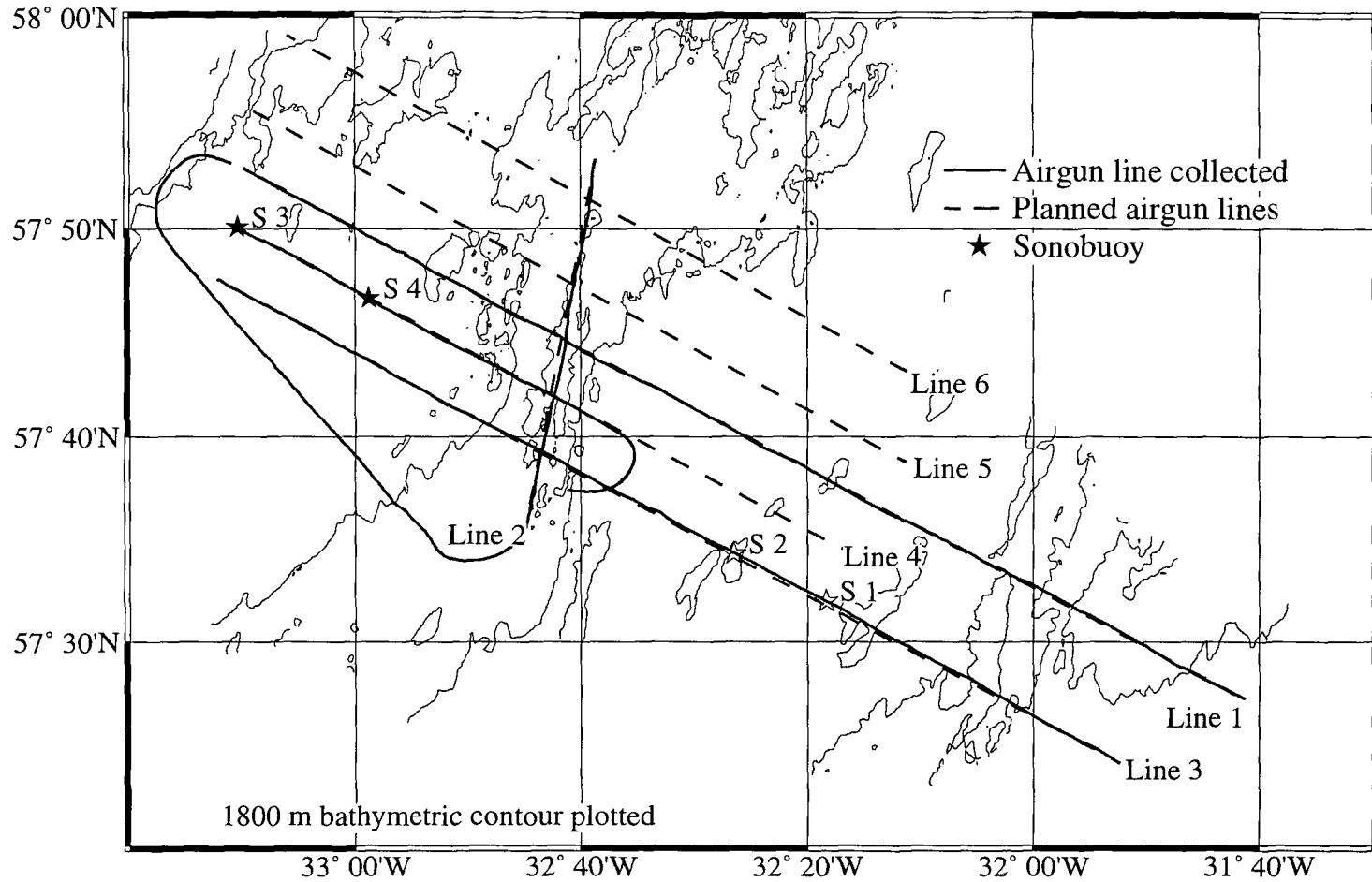


Figure 2.17: The CD81/93 normal incidence seismic experimental configuration overlain by the 1800m bathymetry contour which outlines the AVR studied. The planned airgun reflection profiles are shown dashed lines and those actually collected are solid. Sonobuoy deployment locations are shown by stars, with open symbols indicating instruments which failed on deployment.

2.8.1 Instrumentation

The normal incidence data were collected with an 8-channel Geoméchanique hydrophone streamer consisting of alternating 50 m active and passive sections (figure 2.18) and five Ashbrook depth controller birds which maintained the streamer depth at 11 m below mean sea level. The output from this streamer was recorded using the SAQ seismic data acquisition system (Owen and Sinha, 1990). This system records seismic data on 9-track, ½" tape in SEG-Y format (Barry *et al.*, 1975) with a 4 ms sample rate and 125 Hz anti-alias filter. This recording system has only one front loading tape drive that writes at low density (1 600 b.p.i.). This low recording density means that at a sample rate of 4 ms, a tape only lasts 4.5 hours when recording an 8 s trace every 20 s, for CD81/93 this corresponded to 40 km of 8-fold data and was insufficient to fit a complete line on a single tape. Hence data was lost during tape changes while each tape was rewound and the next loaded.

Four disposable sonobuoys were deployed along Lines 3 and 4 with the data from each being used to constrain the upper crustal velocity structure and as an aid in interpretation of the normal incidence lines. Two sonobuoys were Dowty Marine SSQ 906A (D) and two were of an older type. One of each type was deployed on Line 3 (figure 2.17) and both failed to work, probably being damaged by the airgun array as it towed past. The remaining two were deployed on Line 4 and transmitted data (see section 2.9.1). The transmissions were received by an aerial located on the main mast and amplified using a broad band RF pre-amplifier located close to the aerial, before reception by a ICOM radio receiver (ISR 7 000) located in the main laboratory. These signals were recorded using a spare PDAS-100 datalogger.

2.8.2 Source

The wide-angle airgun array, discussed in section 2.3.2 and shown in figure 2.7, was used for Lines 1 and 2 of the normal incidence survey. The low peak frequency at 11.5 Hz and the wide shot spacing on these lines were designed primarily for wide-angle data acquisition with the DOBSs as opposed to the higher frequencies and shot repetition rates necessary for the acquisition of good quality normal incidence seismic

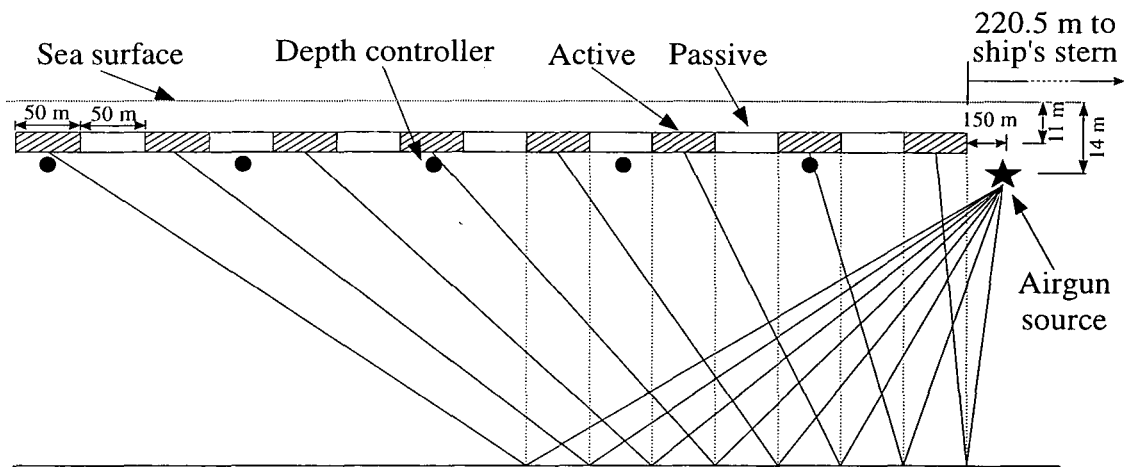


Figure 2.18: Schematic diagram showing the construction of the 8-channel Geoméchanique streamer.

data. The shot spacing of 100 m generated 4-fold data coverage on Lines 1 and 2. It was planned to shoot the remaining four lines (Lines 3, 4, 5 and 6) with a closer shot spacing, achieved by redesigning the array (by turning the large capacity, low frequency guns off, the dominant frequency of the array could be increased) and firing more rapidly. However, as some of the guns had already failed (section 2.3.2) these were turned off and the large capacity guns retained in the array to maintain signal energy. Unfortunately, the peak frequency was only increased from 11.5 Hz to 12.5 Hz which is not ideal for reflection work (see figure 3.2). However, the compressors were able to provide enough air pressure at 2 000 p.s.i. to fire the reduced array every 20 s (50 m) giving 8-fold data coverage along these lines. The reduced array proved to have a more repeatable source signal than the full array, which was possibly due to the removal of the airgun with the failed near-field hydrophone. Signal repeatability is vital for normal incidence data processing techniques such as stacking and deconvolution and it is therefore more important to achieve a stable array of lower dominant frequency and high energy than a high frequency signal with a highly variable signature.

2.8.3 Acquisition problems

Although six airgun lines were planned, shot firing was abandoned after 3.5 lines were completed (see figure 2.17) as weather reports indicated a deep depression

with winds in excess of 40 knots entering the area within the next 24 hours. Therefore the airgun array and streamer were recovered so that we could return to pick up the DOBSs before weather conditions made operations impossible and the DDOBSs, which would otherwise release on their back-up clocks and be lost.

2.9 The normal incidence seismic dataset

2.9.1 Data collected

Initially it was planned to collect six normal incidence lines comprising of 130 km of 4-fold data coincident with the wide-angle seismic lines and 274 km of 8-fold normal incidence data. The loss of data at the start of Line 2, due to problems with the airgun compressors, reduced the coverage along Lines 1 and 2 to 122 km at a 100 m shot point spacing. In total 74.5 Mbytes of 4-fold data were collected along these two lines on four 9-track, ½" magnetic tapes. The first 8-fold line and part of a second (Lines 3 and 4) were collected before this seismic survey was abandoned (see section 2.4.3), 140 km of data (2 800 shots) were recorded on four ½" tapes, totalling 170.9 Mbytes. The processing of these data will be described in section 2.9.3.

Of the four sonobuoys deployed, the two on Line 3 failed to work at all (see section 2.8.1). The first sonobuoy deployed at the northwestern end of Line 4 transmitted for 1 hour 23 minutes and the second for only 48 minutes. This sonobuoy data was recorded by a spare PDAS-100 datalogger in continuous mode (see section 2.3.1) at 500 samples^s⁻¹, producing 10.9 Mbytes of data. However, this dataset was very noisy due to rough sea conditions and is unfortunately of little use.

2.9.2 Replay of SAQ multichannel seismic reflection data tapes

The normal incidence seismic data tapes were copied at Cambridge by a direct tape-to-tape copy with the new copy recorded at a higher density (6 250 b.p.i.). Recording at a higher density meant more than one SEG-Y file could be stored on a single 9-track, ½" tape. These copies were replayed at Durham using the UNIX *mt* command to position the tape at the beginning of each SEG-Y file and *tget* (written by D.L. Stevenson) to read the block size of the first and second blocks (3 200 byte

EBCDIC and 400 byte binary reel headers) and extract these from the tape. The third block size is then read (240 byte trace header + 4 × number of samples per trace) and this block length extracted from tape repeatedly until an end of file mark is reached. The program progressively writes these data blocks to disk as a disk image of a SEG-Y file.

2.9.3 Normal incidence data processing

The disk image SEG-Y normal incidence data files (section 2.6.3) were read into Advance Geophysical Corporation's ProMAX (version 6.0) installed on a SUN Sparc 10. Before any processing was possible a geometry database was created using *2-D Marine Geometry Database* and *In Line Geometry Installation*. On inspection of the shot gathers traces 1, 2, 5, 6, 7 and 8 were found to be reversed, assuming the first break at the seabed should result in a positive peak. These were corrected and noisy traces and misfired shots were removed using *trace kill / reverse*. A 3 dB s^{-1} amplitude correction was applied to each trace to correct for the effects of geometrical spreading and absorption. The traces were then sorted into common depth point (CDP) gathers and plotted as brute stacked sections (stacked using the water velocity for normal moveout correction) to identify any obvious reflectors and check the data quality.

The further processing of this normal incidence dataset was based on the processing undertaken by M.A. Inglis for his M.Sc. dissertation research conducted in Durham (Inglis, 1995) using ProMAX version 4.0.

The main processing stages were as follows:-

Process	Purpose
data input	described above
geometry creation	described above
trace editing	described above
trace muting	described above
true amplitude recovery	a 3 dB s ⁻¹ ramp was applied to 5 s TWTT to correct for the effect of spherical divergence and attenuation, beyond 5 s this process artificially enhanced the seabed multiple
band-pass filter	corner frequencies 1 - 3 - 40 - 50 Hz used to filter out background noise
pre-stack predictive deconvolution	to collapse the signal and reduce ringing in the section, operator length 80 ms, prediction distance 22 ms, white noise level 0.1%
band-pass filter	corner frequencies 1 - 3 - 40 - 50 Hz
normal moveout correction	using a 1-D velocity profile picked from a series of constant velocity stacks
stack	this resulted in little multiple attenuation due to the short streamer length
phase shift migration	this migration technique was used as it had the best effect at the sub-seafloor depths of interest
band-pass filter	corner frequencies 1 - 3 - 40 - 50 Hz
trace mute	to mute out ringing at the seabed caused by the migration

The main problems with the data were the high levels of background noise due to severe scattering of seismic energy at the rough seafloor, wavelet ringing, shallow diffraction hyperbola and the strong seabed multiple. The relationship between this dataset and the wide-angle seismic data and model will be discussed in Chapter 5.

2.10 Additional datasets

Swath bathymetry and side-scan sonar

The *RRS Charles Darwin* is equipped with a Simrad EM12-S echo sounder. This is a hull mounted system with 81 beams over a 90° angle giving a swath width of twice the water depth (Simrad product specification, 1992; Blondel and Parson, 1994). The data is logged using Simrad software which is also used to merge the swath data with the navigation data. The bathymetry data is corrected for the ship's roll and pitch and for changes in the water column velocity that cause ray bending. The sound velocity profile and XBT temperature probe data were used to correct for this ray bending. This merged dataset is edited to remove bad pings and is then gridded ready for plotting. The EM 12-S can optionally produce side-scan sonar images giving a geometrically corrected image, undistorted by seafloor topography and with a grey scale related to the backscatter strength.

This echo sounder was used to extend previous surveys of the Reykjanes Ridge (Parson *et al.*, 1993; Keeton *et al.*, in press) and to acquire detailed bathymetry and side-scan sonar coverage of the AVR centred on 57° 45'N. During transit to the work area swath data were collected parallel to and half a swath width away from a previous along-axis swath profile (Parson *op. cit.*) doubling the width of the axial coverage to enable study of the AVR-parallel faults located within the neovolcanic zone. In the work area over 12 000 km² of swath data were collected (figure 2.19), the track spacing was set at half the water depth to provide overlapping swath tracks and complete coverage of the seabed. RVS personnel logged, processed and gridded the swath data during the cruise using the techniques mentioned above. For the analysis presented in this dissertation the grid of xyz data points were merged with the Area C (Parson *et al.*, 1993) bathymetry values and re-gridded.

The bathymetry data were used during the cruise to identify areas of seafloor suitable for the location of the seabed instruments (see section 2.2). These data were also used together with the side-scan sonar data to locate sediment ponds for the interpretation and modelling of the seismic and gravity data. Chapter 4 on the modelling of the wide-angle dataset describes in detail how the bathymetry data were used.

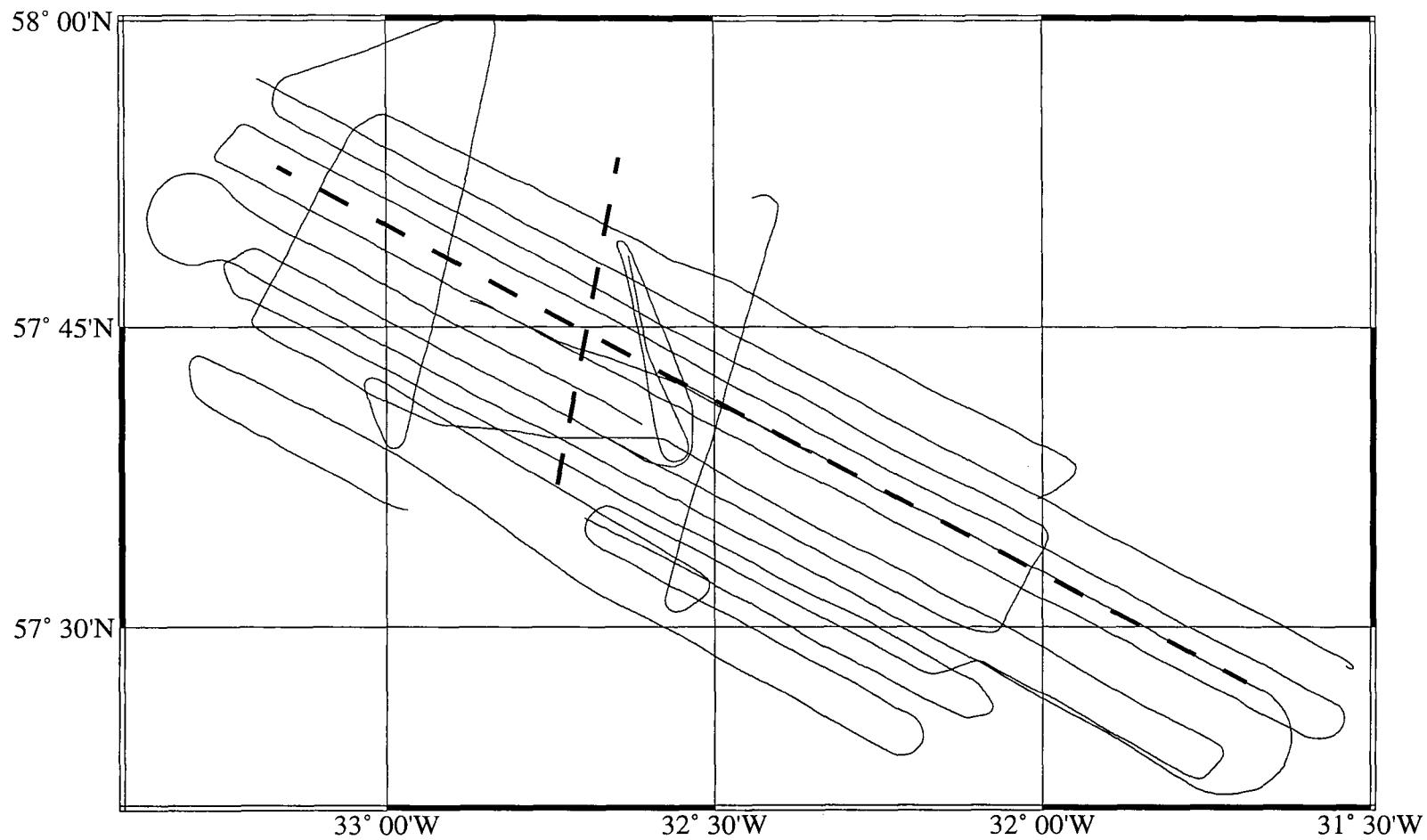


Figure 2.19: Swath bathymetry survey track chart, showing the data coverage obtained during CD81/93. The dashed lines show the location of the wide-angle seismic profiles for reference.

Gravity

Gravity data were collected throughout the cruise (figure 2.20) using the shipboard LaCoste-Romberg gravimeter. A base station tie in was conducted in Reykjavik Harbour immediately prior to the cruise. The raw gravity data were logged against GPS navigation and the shipboard DMW clock every 10 s. These data were then processed by RVS personnel applying the Eötvös and latitude corrections to give the free-air gravity anomaly every 30 s. This dataset was collected to further constrain the seismic models and to allow the calculation of a mantle Bouguer anomaly in this area.

Magnetics

Magnetics data were collected while airgun and swath bathymetry profiling (figure 2.21). These data were logged every 30 s and corrected using the International Geomagnetic Reference Field 90 (Langel, 1992). This dataset has not been used as it is beyond the scope of this dissertation.

2.11 Summary

In this chapter the experimental configuration and the datasets collected have been described. The main processing involved in producing interpretable wide-angle and normal incidence seismic datasets are detailed. A consideration of the errors involved with the wide-angle dataset indicates the DDOBS dataset is reliable, however the statics required by the CDOBS data reduces confidence in the CDOBS explosive data and these statics, combined with the offset seen on either side of an instrument for the CDOBS airgun data, indicates that this latter dataset is considerably less reliable.

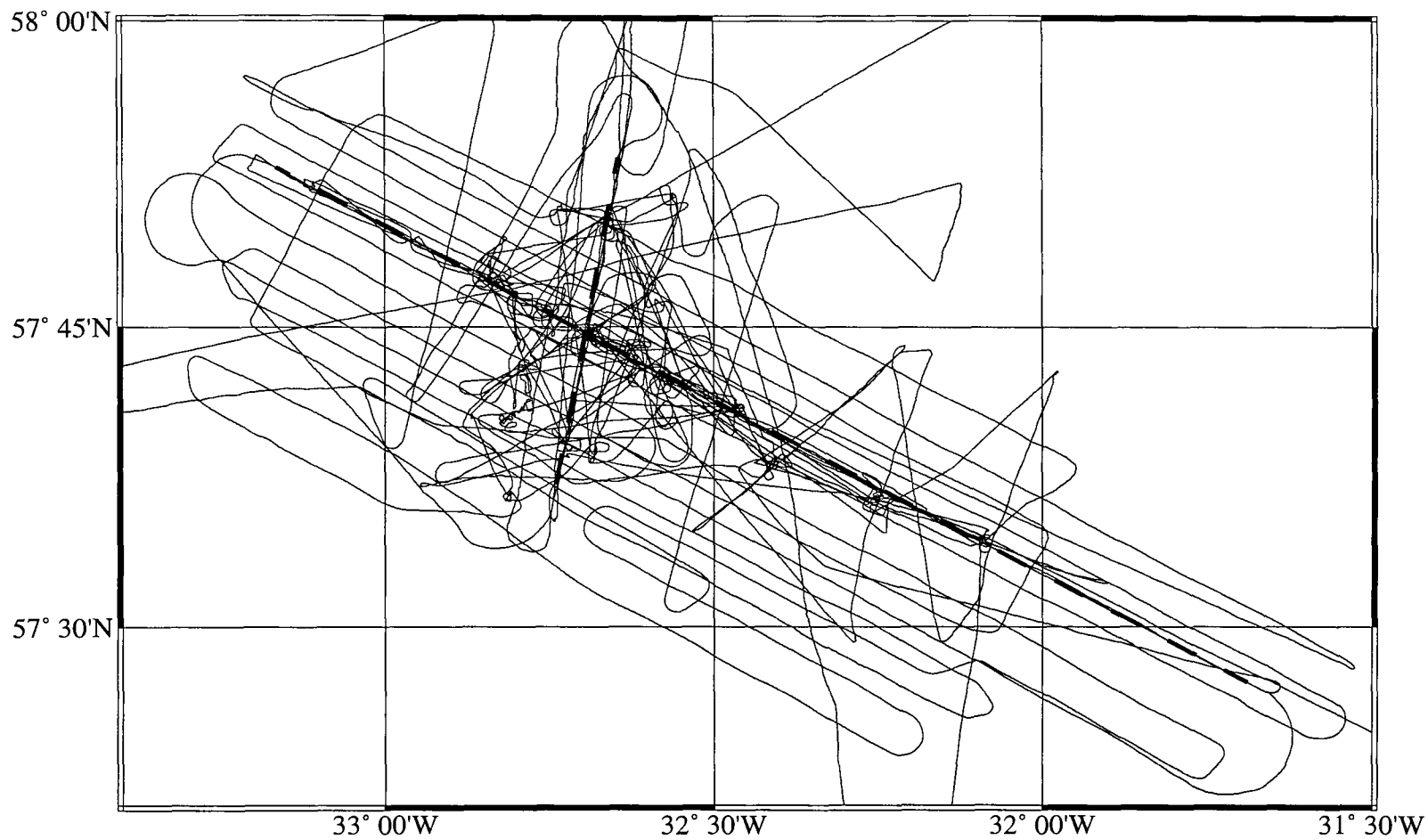


Figure 2.20: Gravity survey track chart, showing the data coverage obtained during CD81/93. The dashed lines show the location of the wide-angle seismic profiles for reference.

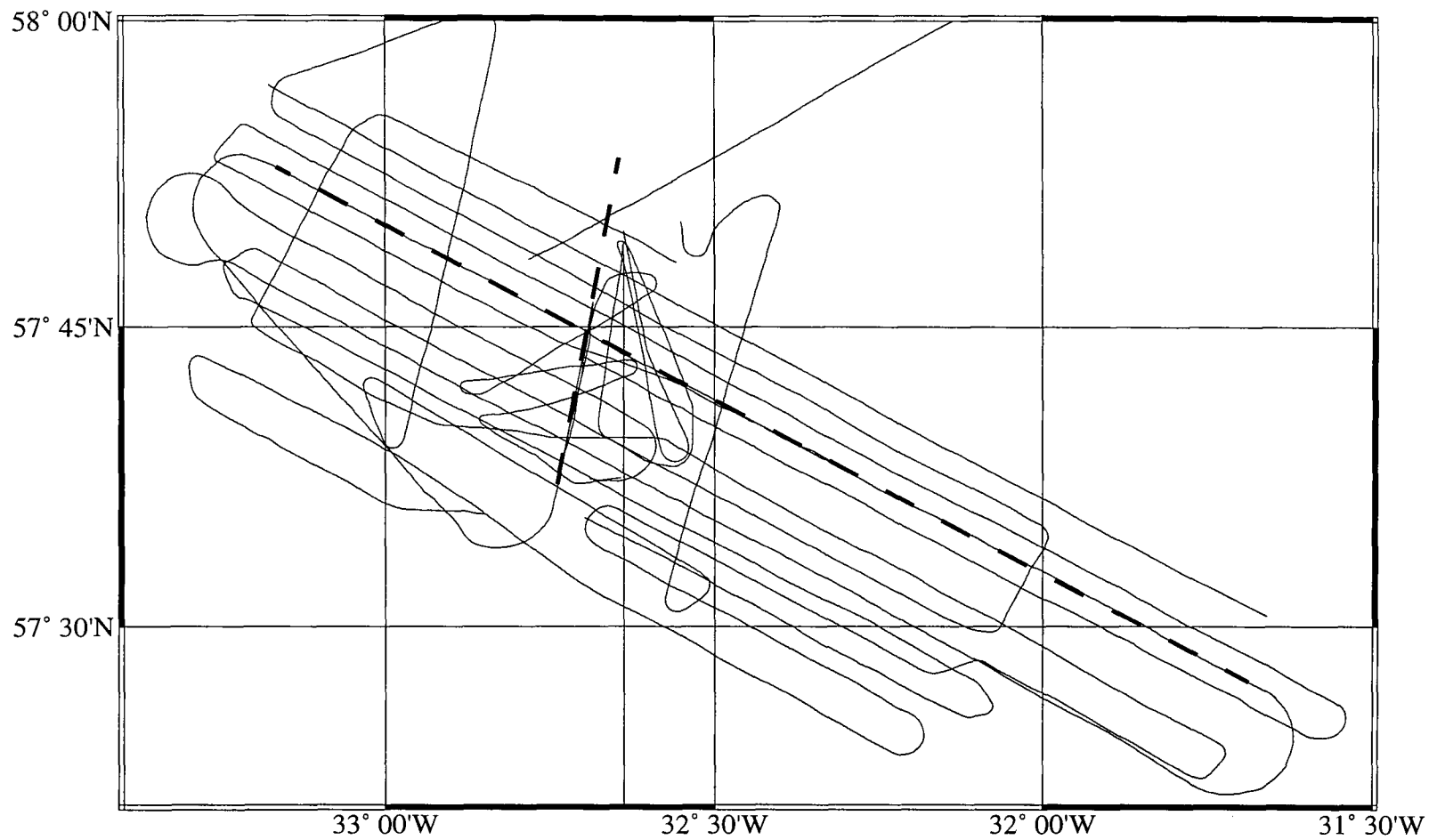


Figure 2.21: Magnetic data track chart, showing the data coverage obtained during CD81/93. The dashed lines show the location of the wide-angle seismic profiles for reference.

Chapter 3

The Reykjanes Ridge wide-angle seismic dataset

3.1 Introduction

In this chapter the main features of the processed wide-angle seismic sections are described, together with the method of phase identification and associated frequency analysis of the data. Application of the results of frequency analysis to filtering the dataset for display, interpretation and modelling is also discussed.

3.2 Source signatures and frequency content

The explosive source signatures were detected by both a towed hydrophone and a hull mounted geophone (see section 2.3.2). The airgun source was detected by the near offset hydrophone group of the 8-channel streamer. Ideally these signals would be compared using the hydrophone components but unfortunately the towed hydrophone produced a noisy signal in which it was difficult to isolate the source signal. Therefore the near offset signature of the explosive and airgun sources, detected by the hull geophone and near offset hydrophone group respectively were compared.

Each explosive shot produced a large amplitude primary pulse associated with several secondary bubble pulses and the combination of these resulted in a reverberative signal (see figure 3.1). The principle of design of an airgun source is based on the effect of combining several individual primary source pulses of differing sizes and bubble pulse periods, depending on the airgun chamber size. Destructive interference of the variously delayed bubble pulses results in a sharper primary signal with less secondary ringing (compare figure 3.2 to figure 3.1).

The dominant frequencies of the individual sources in the near-field are as follows (see section 2.3.2 and table 3.1):-

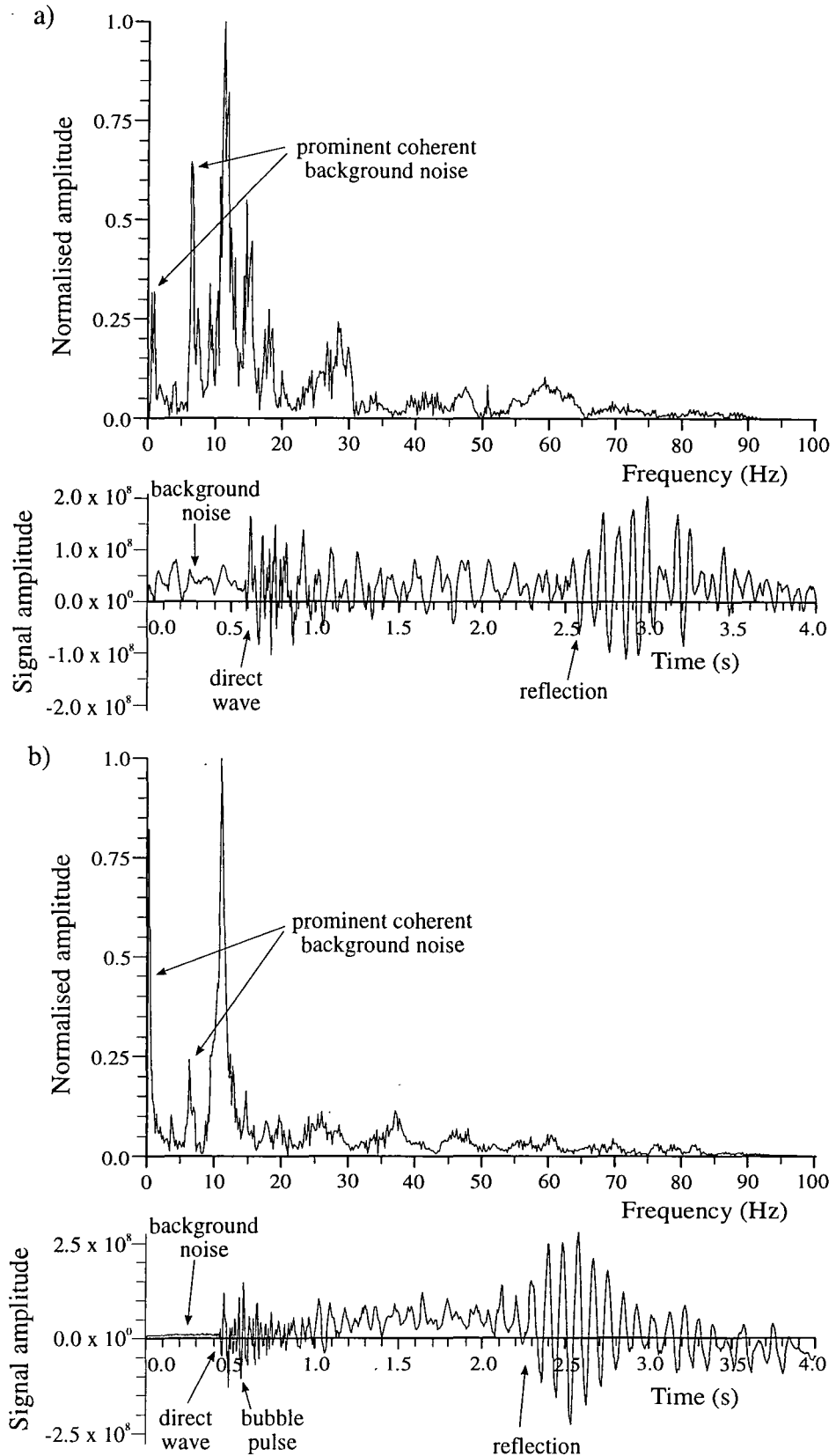


Figure 3.1: Explosive source signatures detected by the hull geophone: a) 25 kg charge; and b) 50 kg charge. The peaks at 1 and 7 Hz represent coherent ship noise common to most marine seismic datasets.

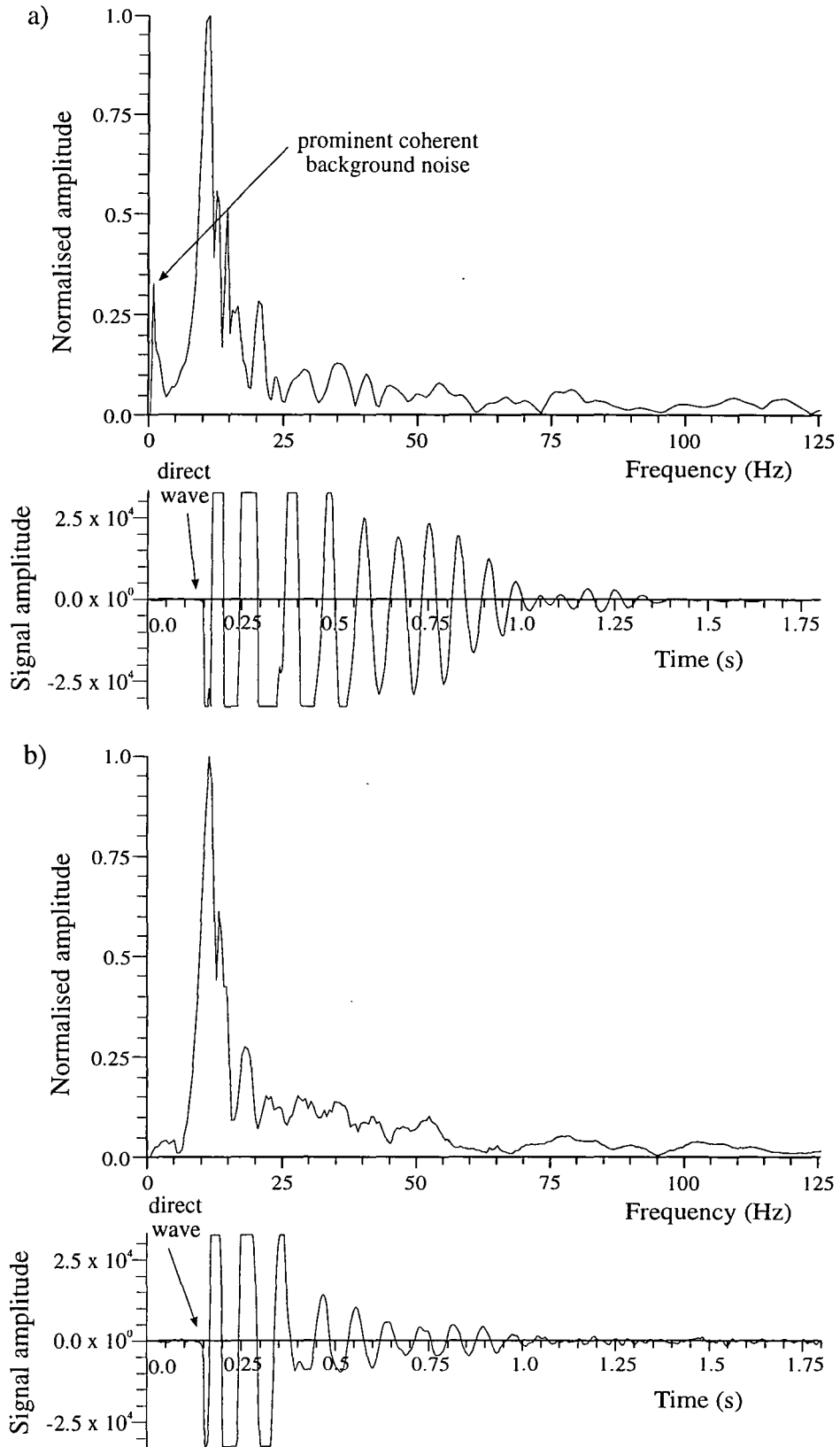


Figure 3.2: Airgun source signatures recorded by the near-field hydrophone of the 8-channel streamer: a) signal of the full airgun array used during wide-angle seismic surveying; and b) reduced array used for the normal incidence profiles. The clipping of the direct water wave is due to saturation of the recording hydrophone.

- The 25 kg explosive source had a peak frequency of approximately 11.5 Hz and a bandwidth of 6.6 Hz (see figure 3.1a).
- The 50 kg explosive source also had a peak frequency of approximately 11.5 Hz and a bandwidth of 2.9 Hz (figure 3.1b).
- The full airgun array has a peak frequency of 11.2 Hz and a bandwidth of 8.8 Hz (see figure 3.2a – figure 3.2b shows the signature of the reduced array used for the normal incidence seismic survey and discussed in section 2.8.2).

Signals detected at near offsets are significantly affected by ghost effects and source array directionality compared with the far-field source waveforms. Therefore the direct water waves detected by the vertical geophone of the DDOBSs are also considered by comparing the signal at similar horizontal offsets from an instrument for each source.

source	near offset signal		direct water wave signal	
	dominant frequency (Hz)	bandwidth (Hz)	dominant frequency (Hz)	bandwidth* (Hz)
25 kg	11.5	6.6	10.8	5.9
50 kg	11.5	2.9	10.8	5.9
airgun	11.2	8.8	10.3	2.8

Table 3.1: Comparison of the near and far offset source signatures for the individual sources used in collection of the wide-angle seismic data. * The term bandwidth as used here is defined as the width of the dominant frequency peak where the amplitude drops to ~25%.

The amplitudes of the direct water waves from the explosive sources near zero horizontal offset saturate the geophone and the frequency spectra of these clipped records are not fully representative of the signal. Therefore the signals from adjacent 25 and 50 kg explosive sources at 22.6 and 22.8 km range respectively, and from a 25 kg explosive and an airgun source at 7.2 km range (separated by ~50 m which is of the order of the errors) are compared, with the ranges selected so that the direct water wave is not clipped (see figure 3.3).

The main features of the source signatures at the seabed are as follows (see also table 3.1):-

- The 25 kg explosive source has a dominant frequency of 10.8 Hz and a bandwidth of 5.9 Hz (see figure 3.3a and 3.3c).
- The 50 kg explosive source also has a dominant frequency of 10.8 Hz and a bandwidth of 5.9 Hz at the seafloor (see figure 3.3b).
- The airgun source at the seafloor has a dominant frequency of 10.3 Hz and a bandwidth of 2.8 Hz (see figure 3.3d), which is a much sharper spectrum than the explosive sources.

The 50 kg explosive source's peak-to-peak amplitude was 1.6 times that of the 25 kg source and the 25 kg explosive source had a peak-to-peak amplitude 3 times that of the airgun source.

The main effect on the source signal of travelling through the water column is to reduce the low frequency coherent noise peaks suggesting that these were mainly ship generated.

A reverberative source can cause problems when picking arrival times, particularly in shallow water or where secondary arrivals (e.g. P_mP) arrive close behind the first arrivals. This is not the case in the Reykjanes Ridge dataset. Also the phases of most interest are the first arrivals, particularly the travel times and amplitude of the first peak which is not affected by the reverberative nature of the source. Hence the reverberations have little effect on the data being modelled and therefore these data have not been deconvolved to reduce the signal to a single pulse.

The source wavelet used for generating synthetic wide-angle sections in the modelling process was derived from the direct water wave of an explosive source as this was representative of the signal penetrating the seabed. The same wavelet was used for modelling both the airgun and explosive data as there proved to be little difference

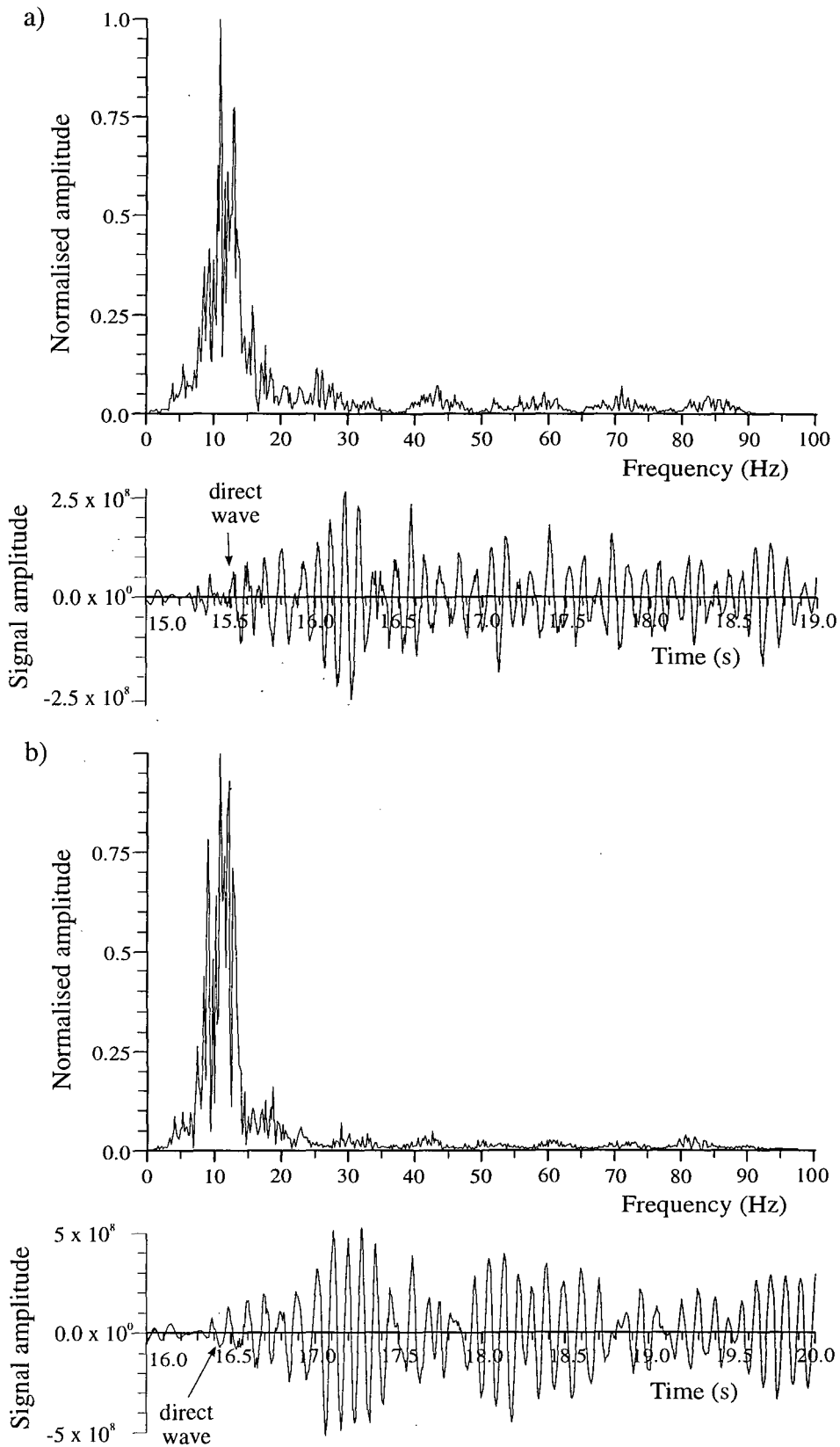


Figure 3.3: Direct water waves recorded by the vertical geophone component of DDOBS 5: a) 25 kg explosive charge; and b) 50 kg explosive charge. Note the similar dominant frequency and bandwidth for both explosive charges and that the amplitude of the direct water wave produced by the 50 kg charge is approximately 1.6 times that from the 25 kg charge, also the 50 kg charge has a slightly lower dominant frequency (0.1 Hz).

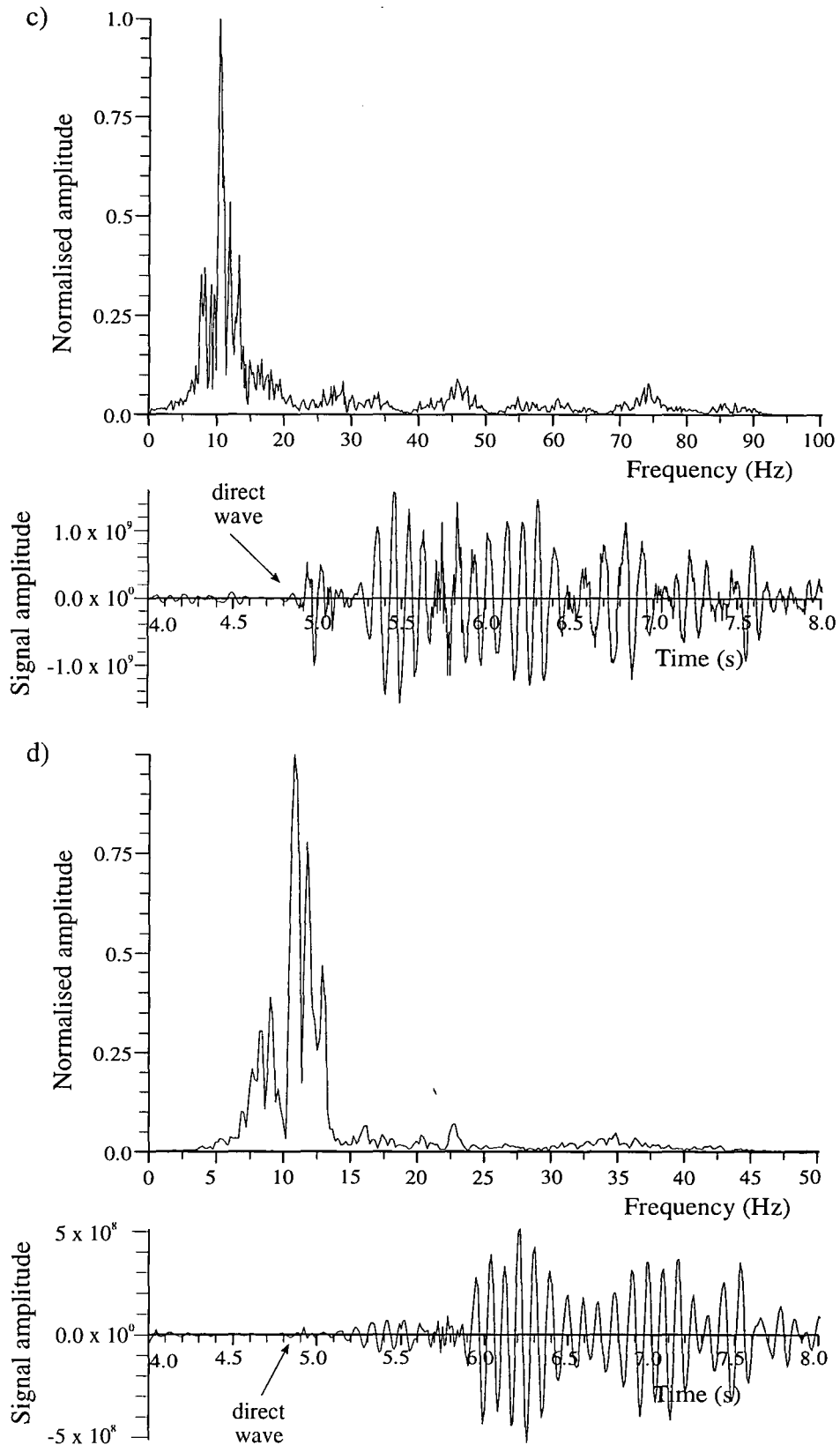


Figure 3.3: cont.. Direct water waves recorded by the vertical geophone component of DDOBS 5: c) 25 kg explosive charge; and d) full airgun array. Note the similar dominant frequency for both explosive and airgun sources, the narrower bandwidth of the airgun source and that the amplitude of water waves produced by the 25 kg explosive charge is approximately three times that of the airgun source. The prominent background noise peaks seen on the near *offset* source signatures (cf. figures 3.1 and 3.2) are no longer evident, suggesting that they are either ship generated or attenuated within the water column.

between the direct water wave waveforms on arrival at a DOBS located on the seabed after propagation through the water column.

3.3 Frequency analysis, filtering and phase identification

Before the dataset could be interpreted, i.e. individual phases identified and one-dimensional velocity–depth profiles calculated, the instrumental and background "ambient" noise were analysed by calculating frequency spectra of these features in the data. This noise was then removed by means of band-pass filtering. The program *fspectra* was used to calculate the frequency spectra of entire seismic traces. These were then analysed to reveal dominant phase frequencies, the frequency band of the background noise and the fixed frequencies of any coherent internal instrument noise (see table 3.2 and figure 3.4).

As the seabed is generally sediment free along almost the entire length of both seismic lines, the first arriving phases (apart from the direct water waves arriving at the instrument location which will be discussed later) are crustal diving rays (P_g). Specific frequency analysis of these phases revealed that they generally have peak frequencies in the range of 10 to 14 Hz (figures 3.5a and b) for all instruments. The lower peak frequency of between 5 and 7 Hz (figures 3.5c and d) observed on the horizontal components is believed to be an instrument resonance. The only other significant first arrivals (when observed on the data sections) were identified as upper mantle diving rays (P_n), with a peak frequency of approximately 7 Hz (figure 3.6a) on the vertical geophone sections and 9 Hz on the hydrophone sections (see figure 3.6b).

Prominent features of any marine wide-angle seismic section are the water waves and their multiples. Although these signals are vital for instrument and shot location and ranging (see section 2.7.1) they are generally of little interest throughout the modelling process (see section 4.3.1). Unfortunately the direct water waves in the Reykjanes Ridge dataset have a dominant frequency within the crustal diving ray band (i.e. ~12 Hz – see figure 3.4) and could not be filtered out, hence some masking of second arriving phases occurred at close instrument offset distances. However, as most of these secondary phases at less than 10 km offset were multiples of the primaries this

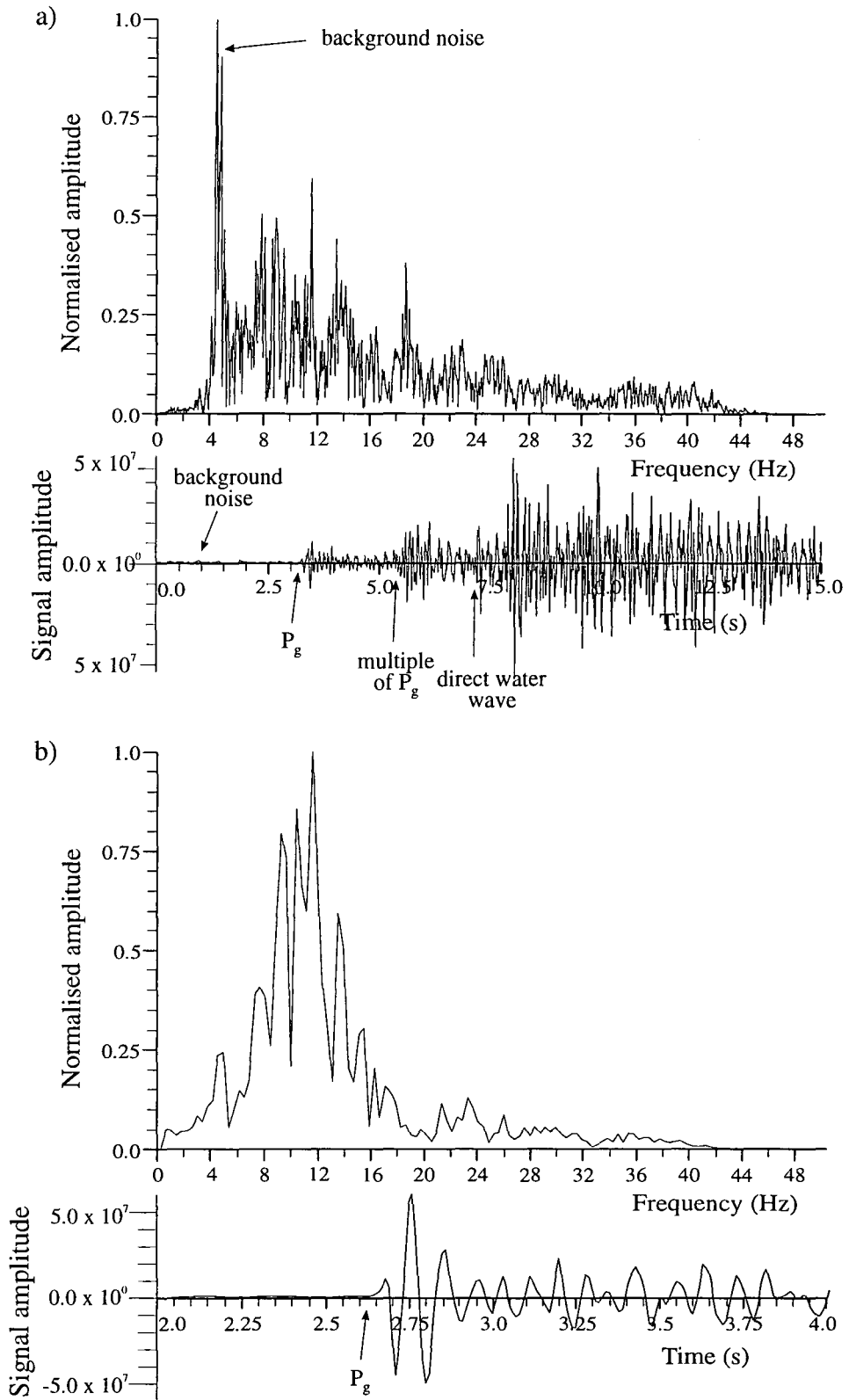


Figure 3.4: Frequency spectra of the main phases recorded by DDOBS 1. a), b), c) and d) were recorded during airgun shot firing by the vertical geophone, while e) was recorded by the external hydrophone. a) Full trace showing the main phases. b) Crustal diving ray (P_g) with a peak centred on ~ 12 Hz.

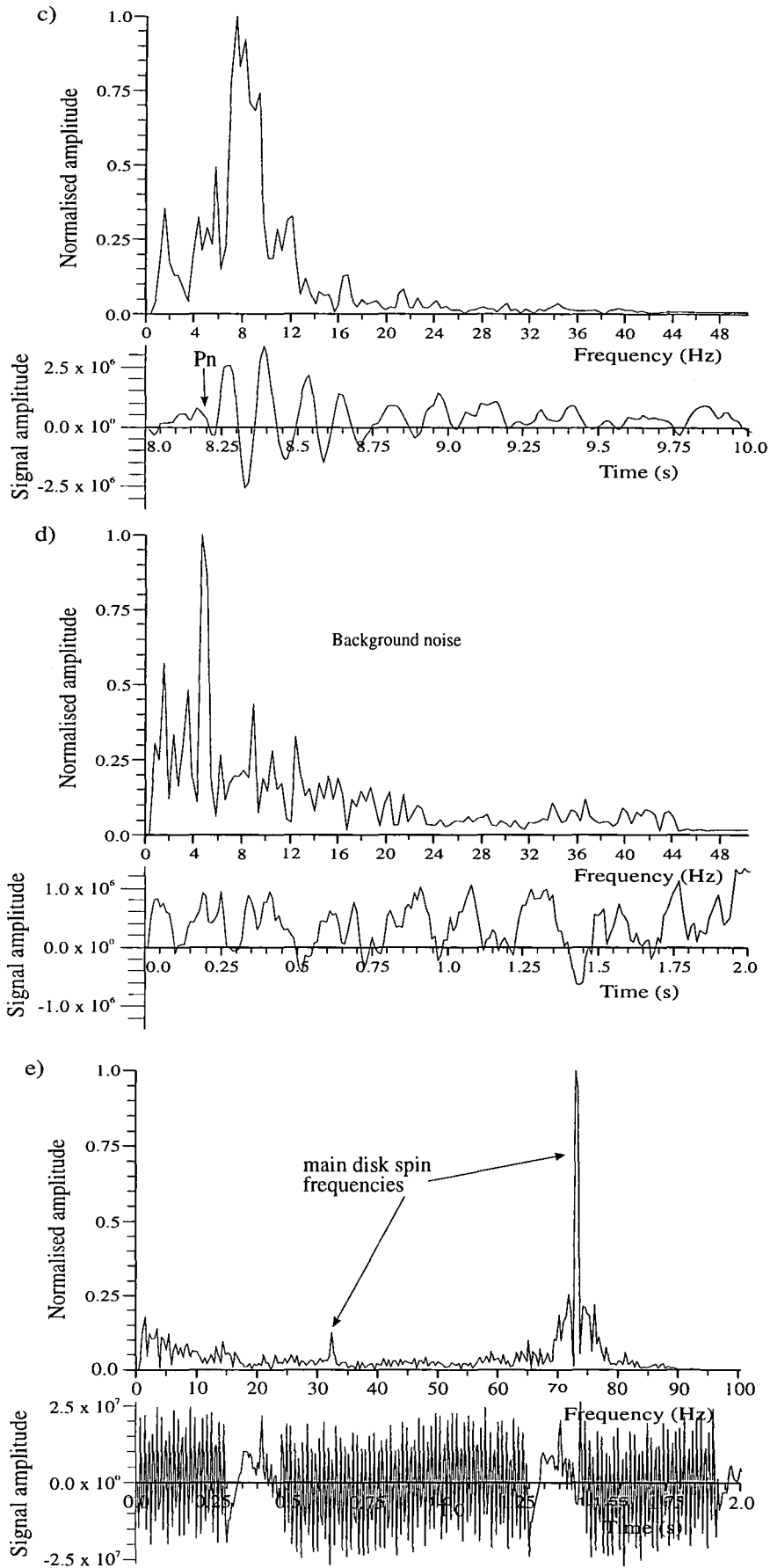


Figure 3.4: cont.. Frequency spectra of the main phases recorded by DDOBS 1. a), b), c) and d) were recorded during airgun shot firing by the vertical geophone, while e) was recorded by the external hydrophone. c) Mantle diving ray (P_n) with a peak frequency centred on ~ 8 Hz. d) Background noise. e) Disk spin frequencies.

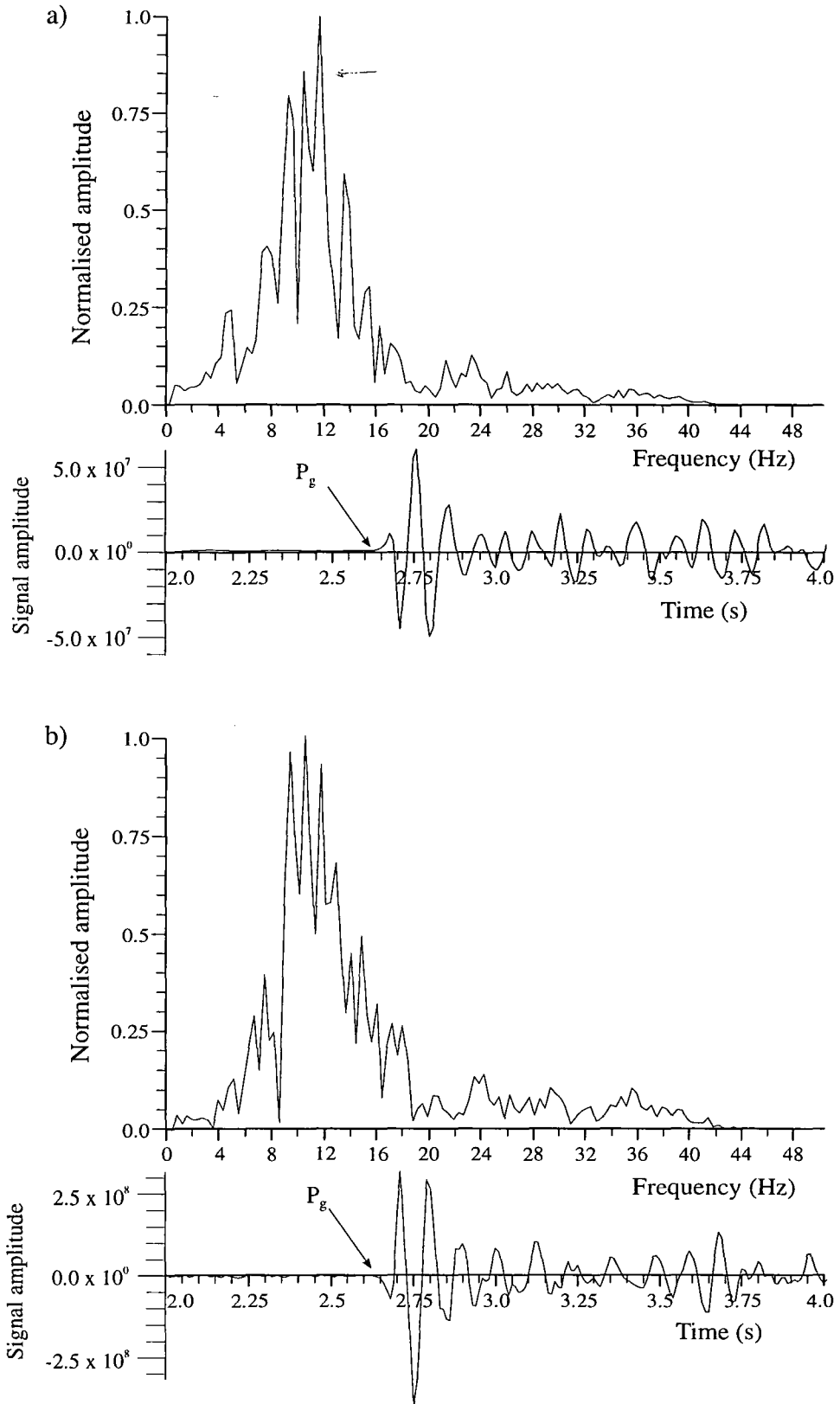


Figure 3.5: Frequency spectra of crustal diving rays recorded by DDOBS 1 during airgun shot firing. a) Vertical geophone component. b) Hydrophone. Note the similarity in frequency spectra between the hydrophone and vertical geophone components and the lower dominant frequency observed on the horizontal components. Note also the reversed polarity of phase due to DDOBS internal wiring conventions.

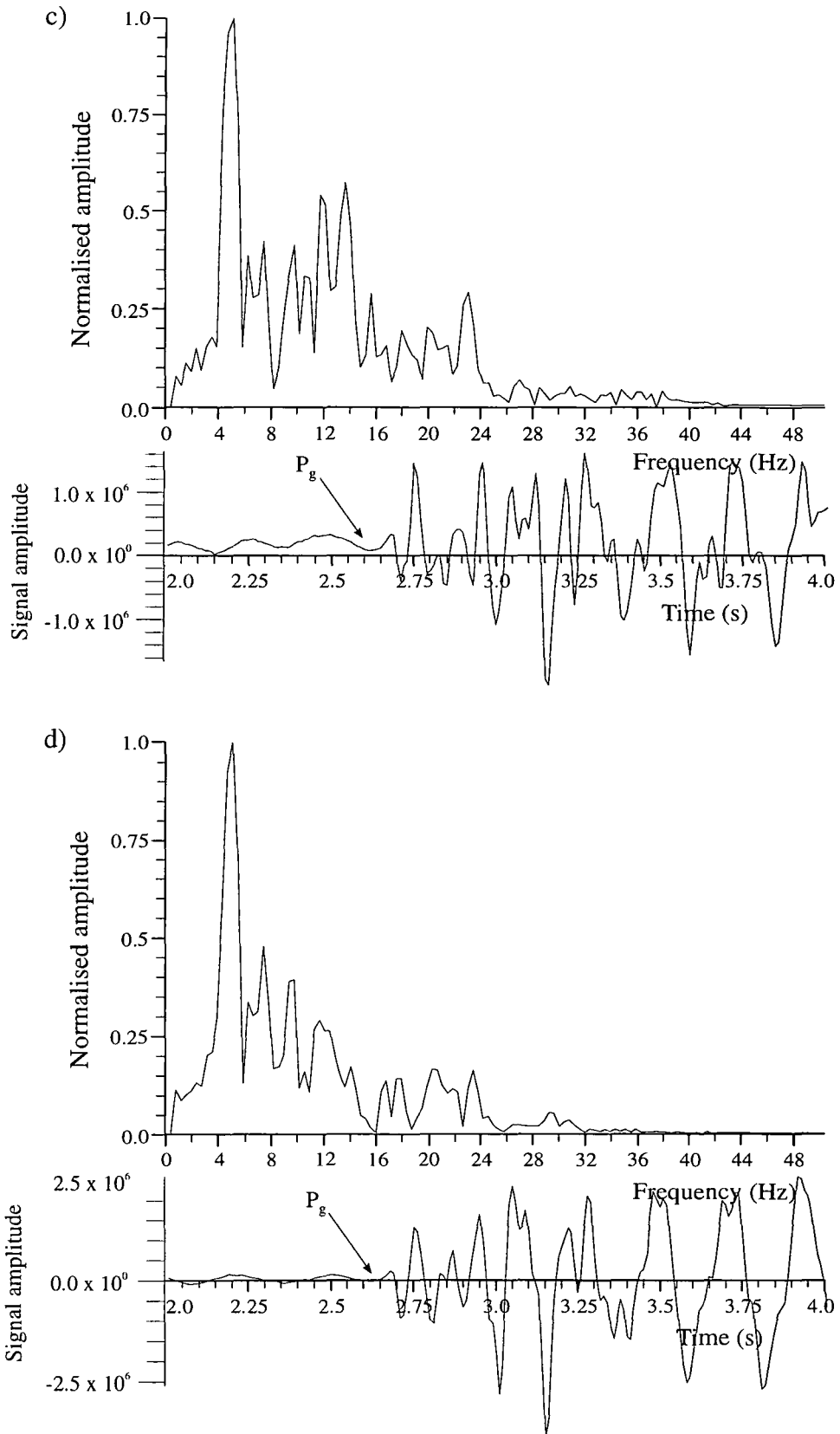


Figure 3.5: cont.. Frequency spectra of crustal diving rays recorded by DDOBS 1 during airgun shot firing. c) Horizontal X-component. d) Horizontal Y-component.

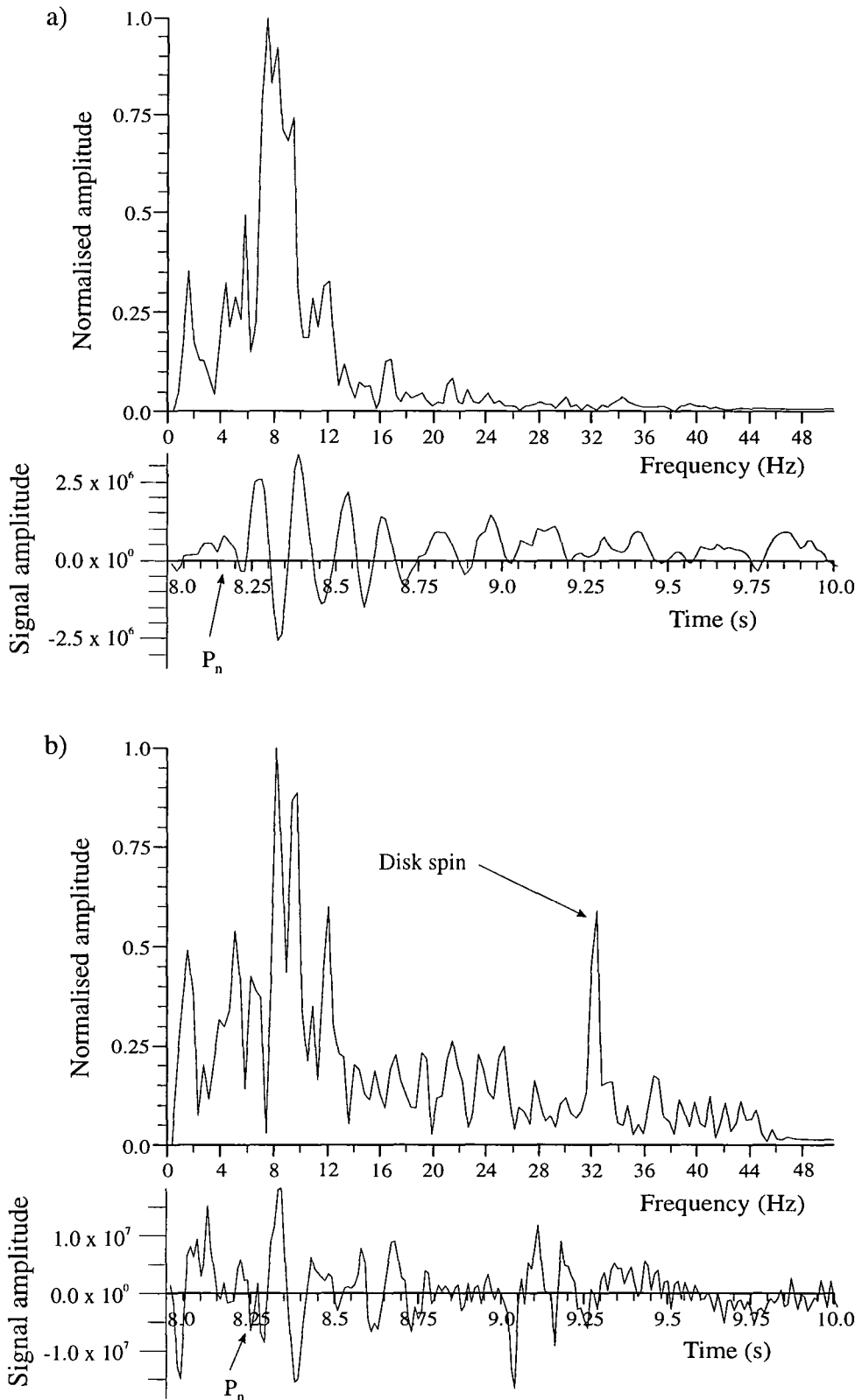


Figure 3.6: Mantle diving rays (P_n) recorded by DDOBS 1 during airgun shot firing. a) Vertical geophone component. b) Hydrophone component. Note the lower dominant frequency of the mantle diving rays compared to the crustal diving rays (figure 3.5) and the greater noise associated with the hydrophone data.

masking did not impair the dataset nor hinder modelling.

The majority of the background noise is of a low frequency with dominant peaks at between 2 and 5 Hz, varying with the receiver type (figure 3.7). These signals fall well below the frequency band of the modelled data and were easily filtered out (see table 3.2). Unfortunately, in the axial region the rough seabed topography caused significant scattering of energy within the signal frequency band of interest, increasing incoherent background noise levels (figure 3.8). It did not prove possible to reduce this "noise" significantly by filtering. Hence the data sections from the near and on-axis DOBSs are noisier and consequently travel time picks cannot be made with the same degree of accuracy as from the off-axis instrument data sections.

A third, and potentially more irritating, source of noise observed particularly on the hydrophone sections is associated with the construction of the DDOBSs and their mode of data storage. The DDOBSs record data into 3 Mbytes of SIMM chips located on two internal datalogger RAM cards. Once this storage area is full (to a user pre-set level) an external SCSI hard disk, ranging in size from 127 to 540 Mbytes (254 to 1 080 Mbytes of uncompressed data), is automatically spun up and the data transferred until the RAM area is at a lower user specified level. The disk is then spun down. While data are transferred from RAM to disk "incoming" data continue to be recorded to the RAM so that no data gaps are produced. There are two reasons why data storage operations are conducted in this manner. Firstly the spinning disks are a significant drain on battery power and if they were kept spinning for 100% of the time, deployment duration would be significantly reduced. Also the chance of significantly damaging the disk during deployment, landing on the seabed and recovery from the water surface onto the ship's deck such that it would be impossible to read or write to, are significantly enhanced if the disk is spinning when it experiences any of the jolts unavoidably associated with the deployment and recovery process.

Secondly, and more importantly, each instrument's hard disk is mounted in a horizontal plane on top of the logger, which in turn sits on top of the internal geophone package. Despite sitting in a cradle of shock absorbent foam, vibrations associated with the spin of the hard disk drive and movement of the writing heads are easily detectable

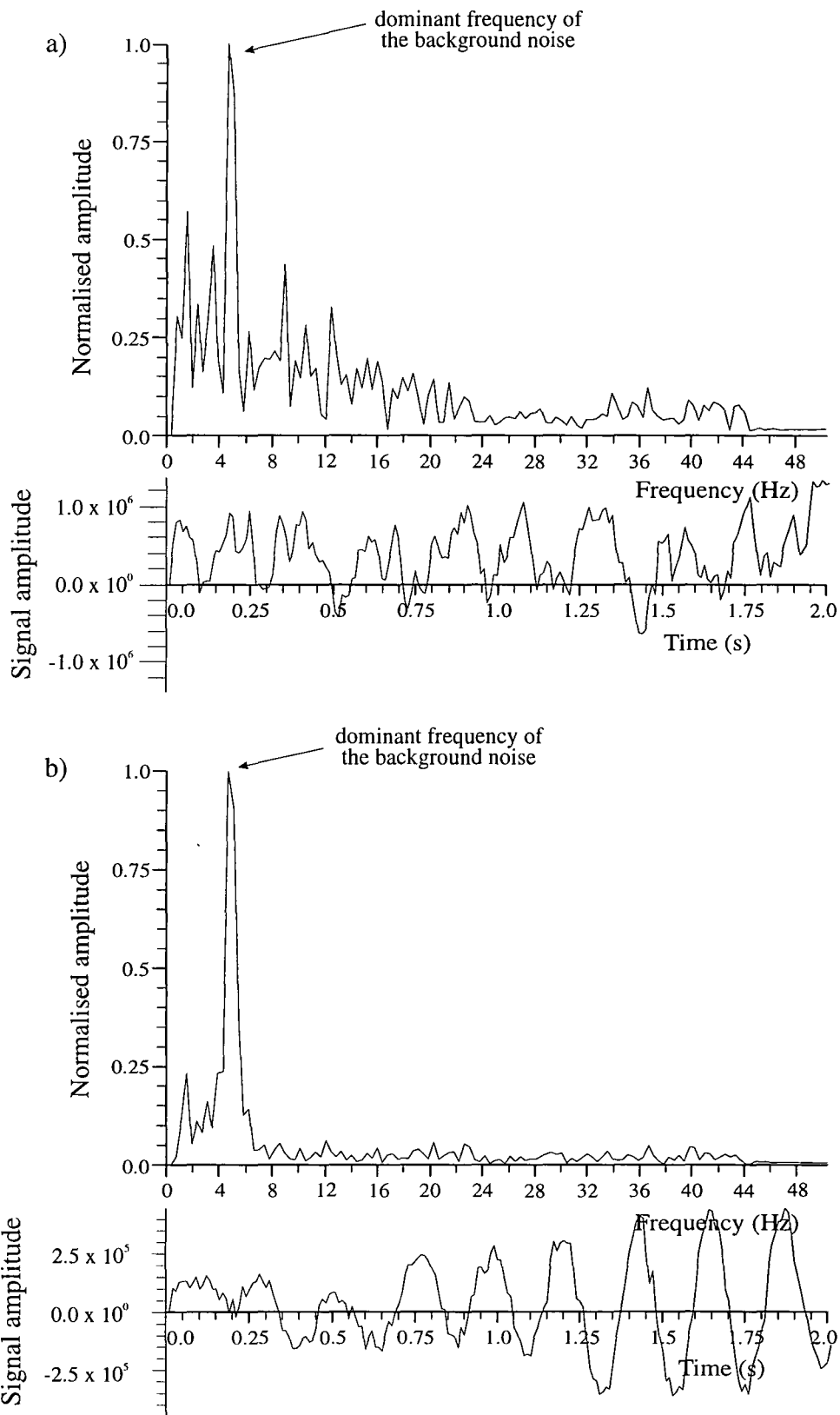


Figure 3.7: Background noise recorded by DDOBS 1. a) Vertical geophone component. b) Horizontal geophone component. Note the dominant frequencies of the main phases of interest are higher than this noise.

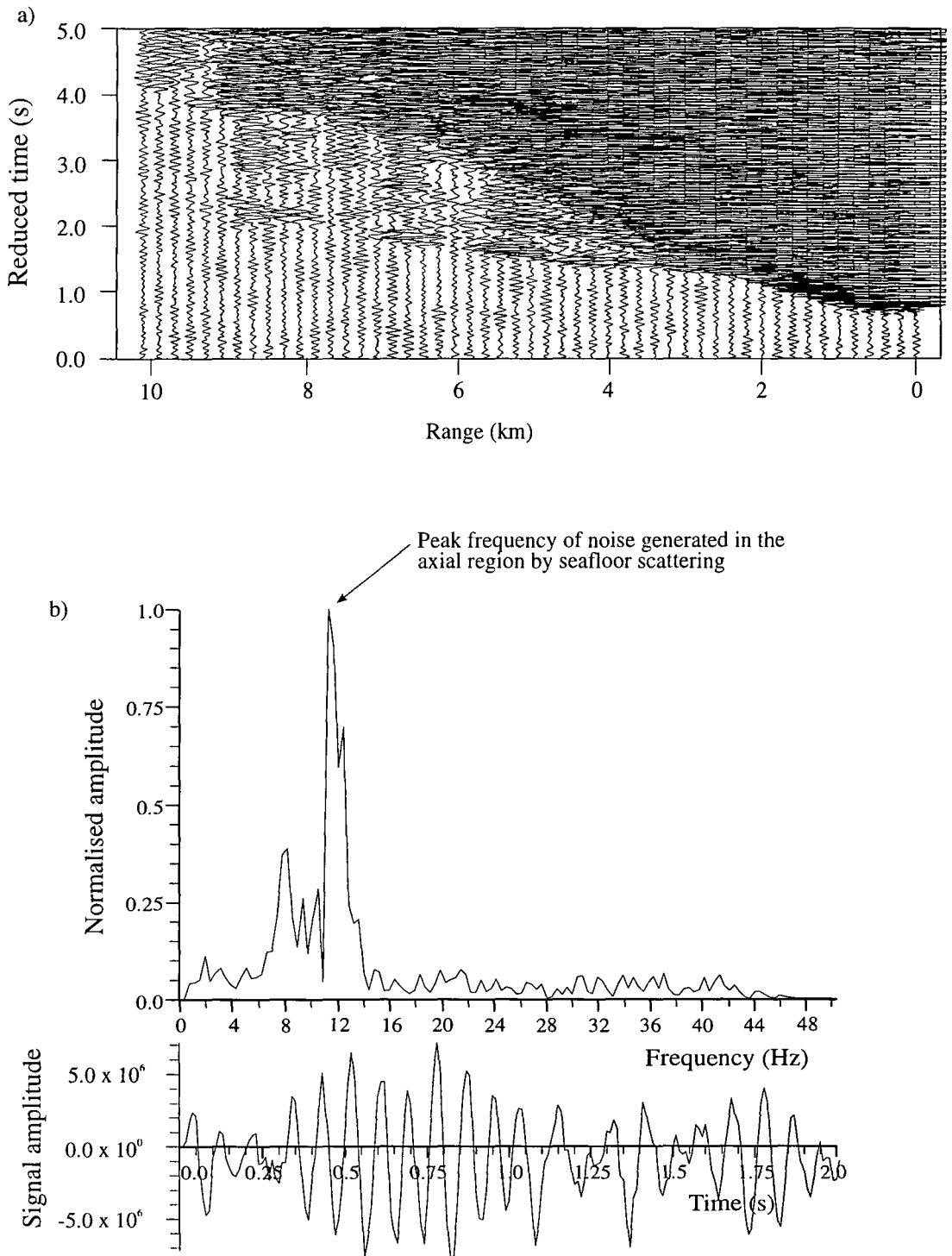


Figure 3.8: Greater scattering of energy by the rough axial seabed causes higher noise levels within the frequency range of the data. a) Example vertical geophone record section recorded by an instrument located adjacent to the ridge axis. The section is plotted unfiltered with a reduction velocity of 6 km s^{-1} . b) Frequency spectra of the background noise. Note that the background noise in this area has a dominant frequency close to that of the crustal diving rays.

by the DDOBS sensors. Hence, if allowed to spin for the entire shot firing period, the data copying process would incorporate significant noise into the data sections. Hence the data transfer is done at specific periods, defined by the shot data window length and the shot firing rate. Generally, a RAM full of data takes approximately 6 minutes to copy and this process is repeated every 30 minutes. Hence the raw unfiltered data sections sometimes appear striped by noise as data recorded during data transfer to the external SCSI hard disk (figure 3.9). Two main "spin" frequencies are detected – 32 Hz and 74 Hz – and as these occur well above the signal frequency band they can easily be filtered out (see figure 3.10).

instrument	P_g peak (range) (Hz)	P_n peak (range) (Hz)	dww peak (range) (Hz)	noise peak (range) (Hz)	filter (Hz)
DA vert	12 (7-15)	7 (4-12)	12 (7-15)	5 (1-12)	6-9-20-30
DX vert	14 (7-18)	7,14 (6-17)	11.5 (2-34)	2 (1-5)	6-8-20-30
DA hor	5 (4-14)	— —	12 (6-38)	5 (1-7)	4-6-20-30
DX hor	7 (4-20)	7 (1-12)	15 (2-85)	5 (1-7)	4-6-20-30
DA hydr	11 (6-18)	9	12 (8-35)	(32-42)	6-8-16-20
DX hydr	10,15 (7-20)	14 (7-20)	25 (1-90)	5,32 (1-42)	6-8-16-20
CA hydr	12 (6-25)	11 (2-17)	9 (1-50)	14 (1-25)	6-8-20-30
CX hydr	14 (1-27)	14 (1-28)	16,20 (2-50)	3 (1-4)	3-5-20-30

Table 3.2: The peak frequencies of the dominant phases and noise observed on all instruments. D – DDOBS, C – CDOBS, vert – vertical geophone component, hor – horizontal component, hydr – hydrophone component, A – airgun source, X – explosive source, P_g – crustal diving ray, P_n – mantle diving ray, dww – direct water wave. The frequency ranges are specified at the level at which the peak drops to 25% amplitude. The corner frequencies specified correspond to those of the Hanning band-pass filters applied to each component of the dataset.

Once the frequency analysis of all observed phases on all components was complete band-pass filtering was conducted using the corner frequencies shown in table 3.2 and the program *bpfilt*. As can be seen from the data shown in table 3.2, corner frequencies of 6-8-20-30 Hz were appropriate for most of the data sections, eliminating



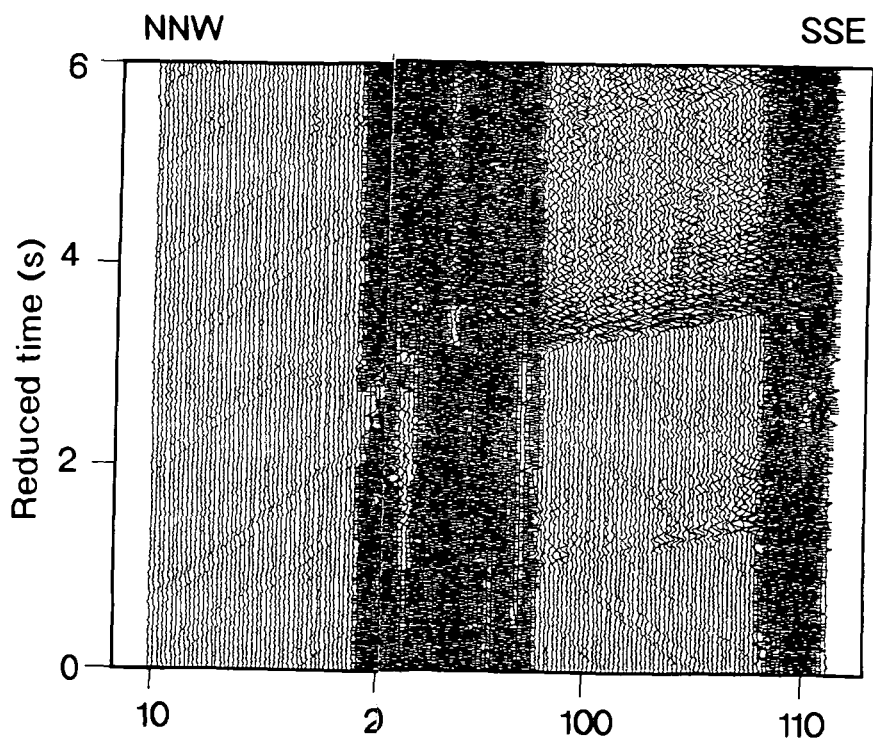
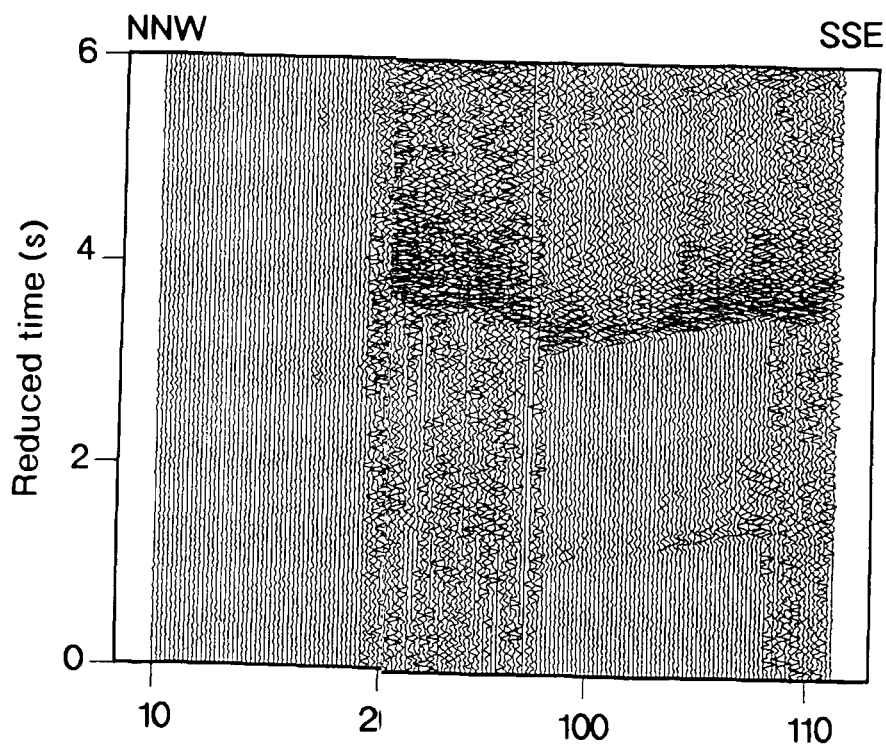


Fig section is plotted at true amp its hard disk (disk spin).



Figplitude and reduced at 6 km

most of the background and instrumental noise (for example see figure 3.11). For the DDOBS hydrophone data the high frequency cut-off corner frequencies were reduced to 16-20 Hz from 20-30 Hz to remove the more prominent "disk spin" noise on these sections. In addition, as the DDOBS horizontal component data is of a generally lower frequency, the low frequency cut-offs were lowered to 4-6 Hz. Examples of filtered and raw datasets are shown in figures 3.11-15, the record sections from the entire seismic dataset are shown in Appendix E. These sections highlight the majority of the "noise" problems associated with the wide-angle seismic dataset and how effectively they have been minimised by selective and careful band-pass filtering alone. All further data sections shown in this dissertation have these filters applied except the airgun data recorded by the vertical geophone of the DDOBSs which, due to the already high signal-to-noise ratio did not benefit significantly from filtering.

3.4 Wide-angle data

The hydrophone and three-component geophone data recorded by the ten DOBSs were replayed and processed as described in Chapter 2 and section 3.3. The record sections shown throughout this section are plotted at true amplitude. However the across-axis explosive sections have been charge weight balanced* for amplitude modelling to account for the variation in charge size at the southeast end of the line. No range corrections have been applied. For the DDOBS data the hydrophone record sections generally show the same features as the vertical geophone sections, but tend to be noisier and of a slightly higher frequency content. All across-axis lines have been oriented with the northwestern end of the line plotted towards the left, while all along-axis sections have been oriented with the northern end of the line plotted towards the left. All record sections exhibit large amplitude water wave arrivals, which have been clipped for plotting at scales suitable for crustal and upper mantle phase identification. The complete wide-angle seismic dataset is included in Appendix E.

* The explosive sections were charge weight balanced using the formula

$$\left(\frac{\text{normalizing charge weight (kg)}}{\text{charge weight (kg)}} \right)^{\frac{2}{3}} \quad \text{normalizing charge weight} = 25 \text{ kg}$$

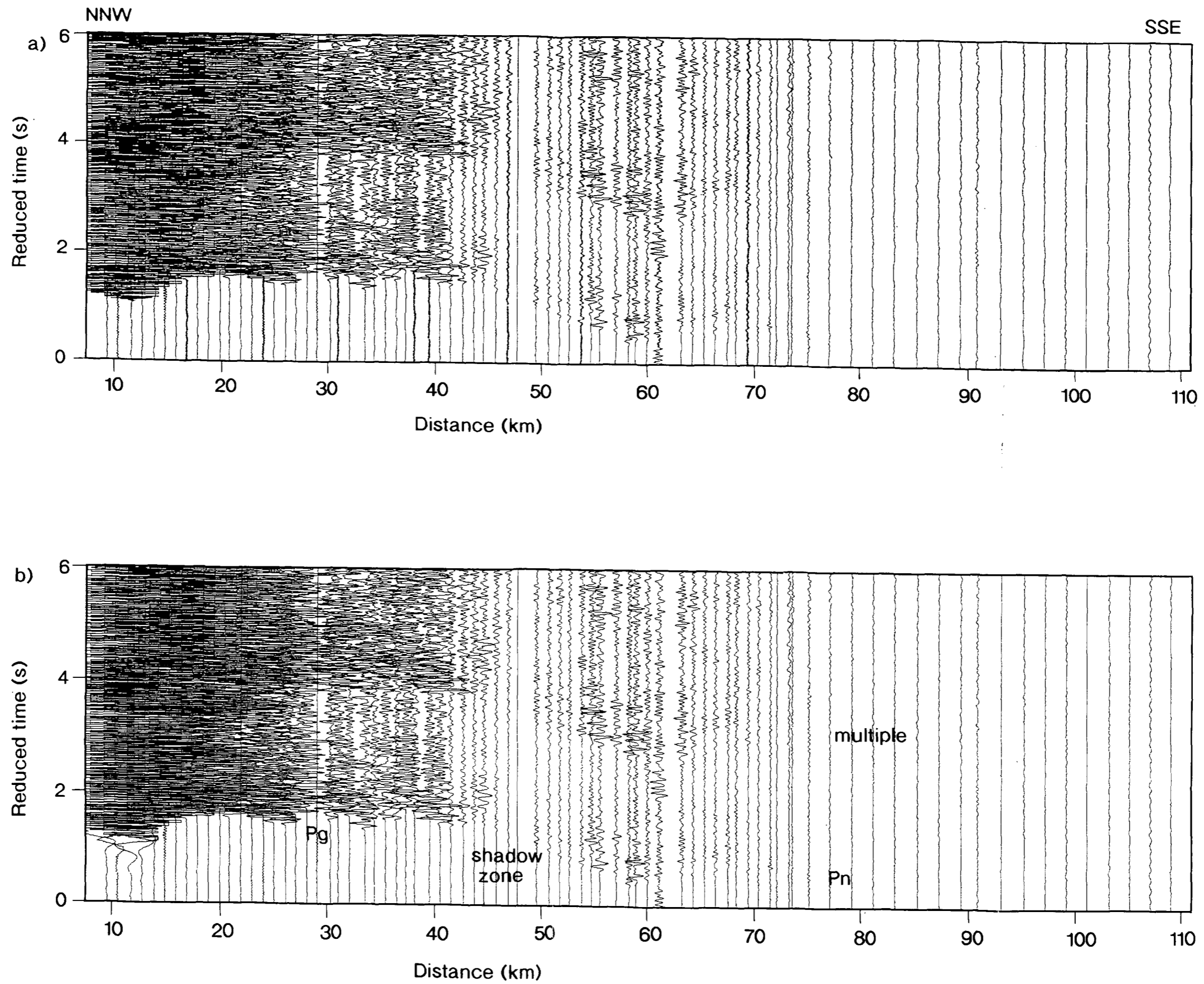


Figure 3.11: Data from DDOBS 1 recorded by the vertical geophone component during explosive shot firing along the across-axis line. Both sections are plotted at true amplitude and reduced at 6 km s^{-1} : a) unfiltered; and b) band-pass filtered at 6-8-20-30 Hz. Prominent features of this section have been annotated.

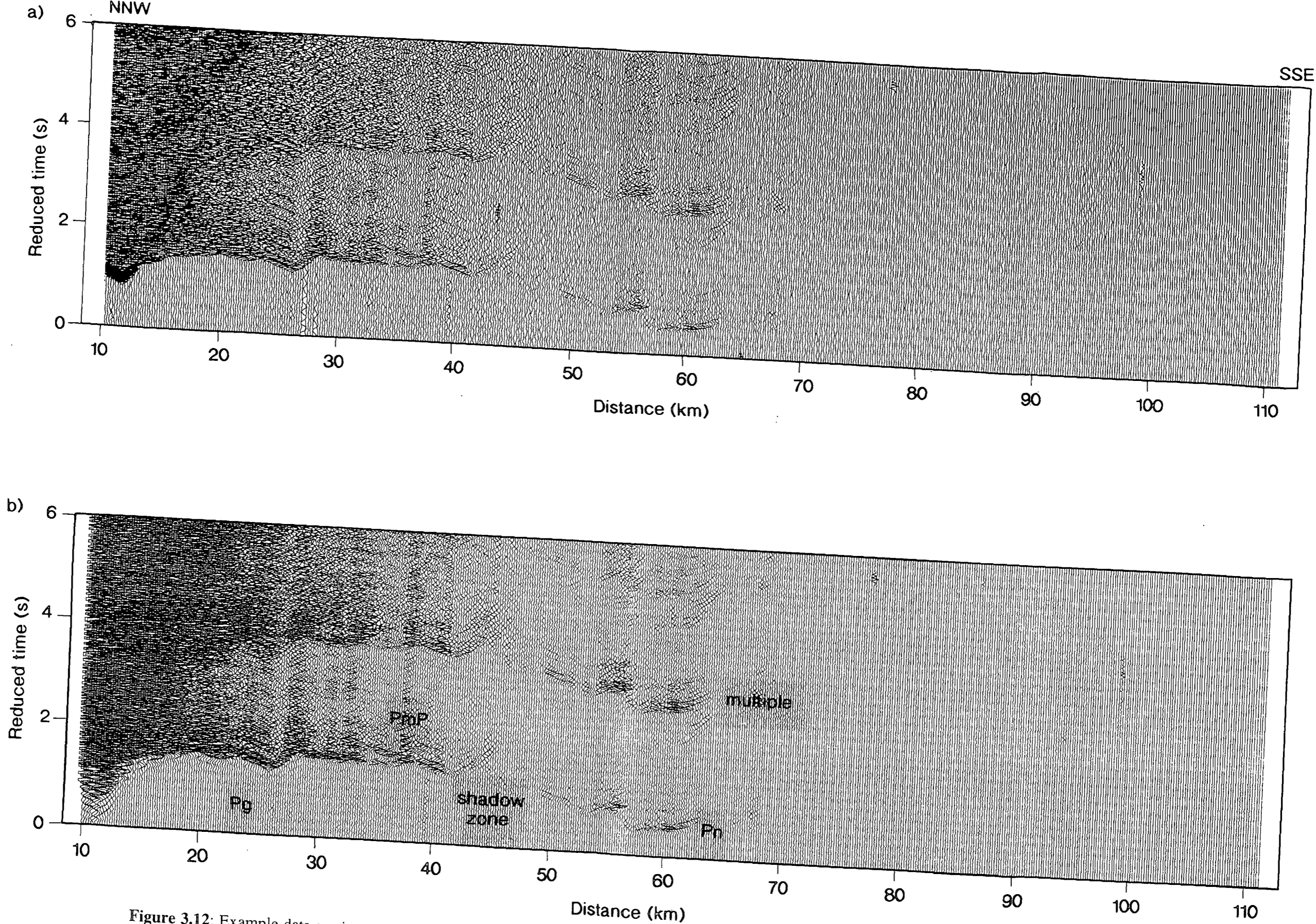


Figure 3.12

Figure 3.12: Example data sections recorded by DDOBS 1 showing the main phases of interest. Note that filtering does not significantly improve this data section. Both sections are plotted at true amplitude and reduced at 6 km s^{-1} .
 a) Data from airgun shot firing along the across-axis line recorded by the vertical geophone component of DDOBS 1 plotted unfiltered.
 b) Same as a) but band-pass filtered between 6-9-20-30 Hz. Prominent features of this section have been annotated.

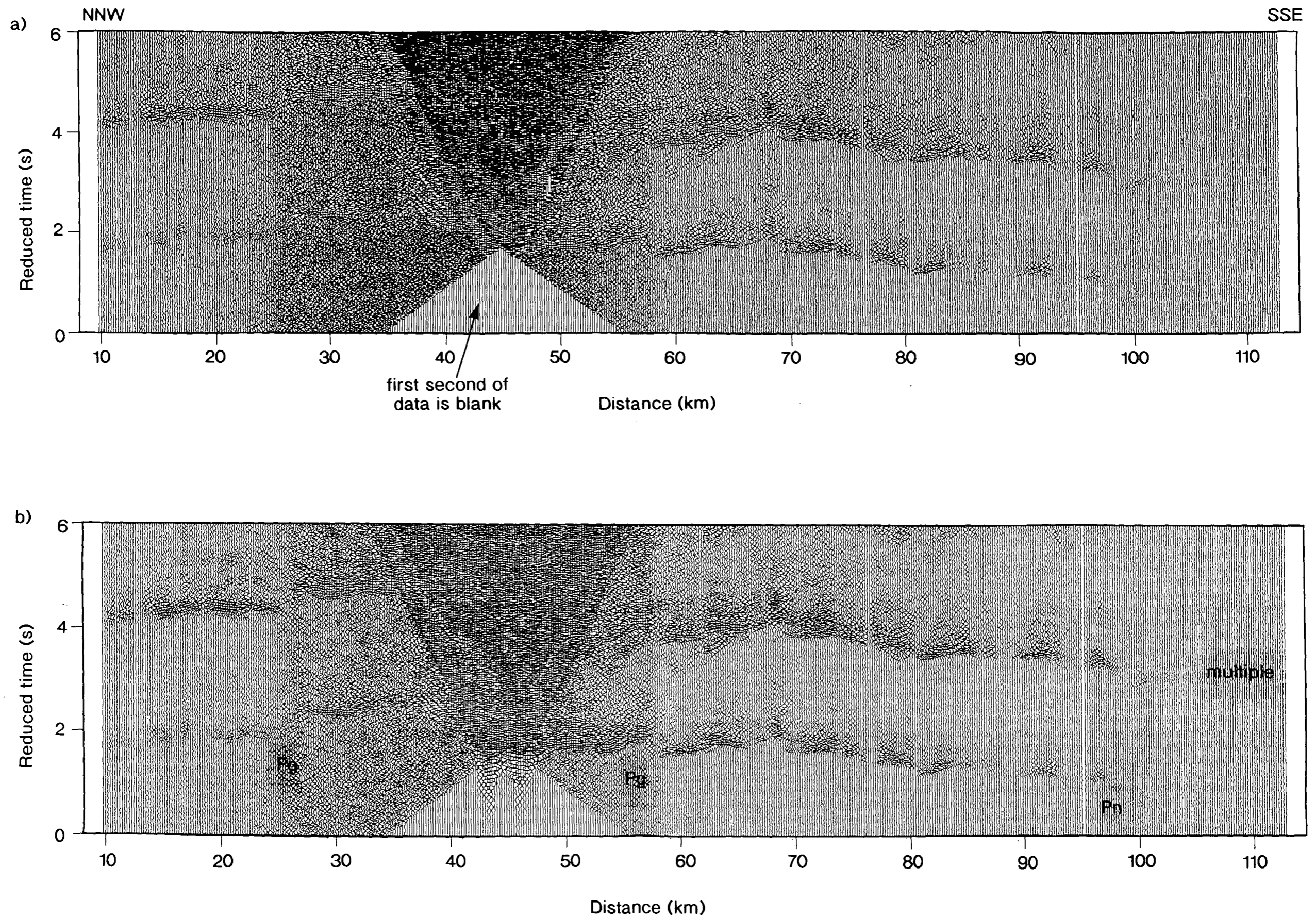


Figure 3.13

Figure 3.13: Example data sections recorded by CDOBS 14 showing the main phases of interest and the improvement seen in the data after filtering. Both sections are plotted at true amplitude and reduced at 6 km s^{-1} . Only alternate shots are plotted for clarity.
 a) Data from airgun shot firing along the across-axis line plotted unfiltered.
 b) Same as a) but band-pass filtered between 6-8-20-30 Hz. Prominent features of this section have been annotated.

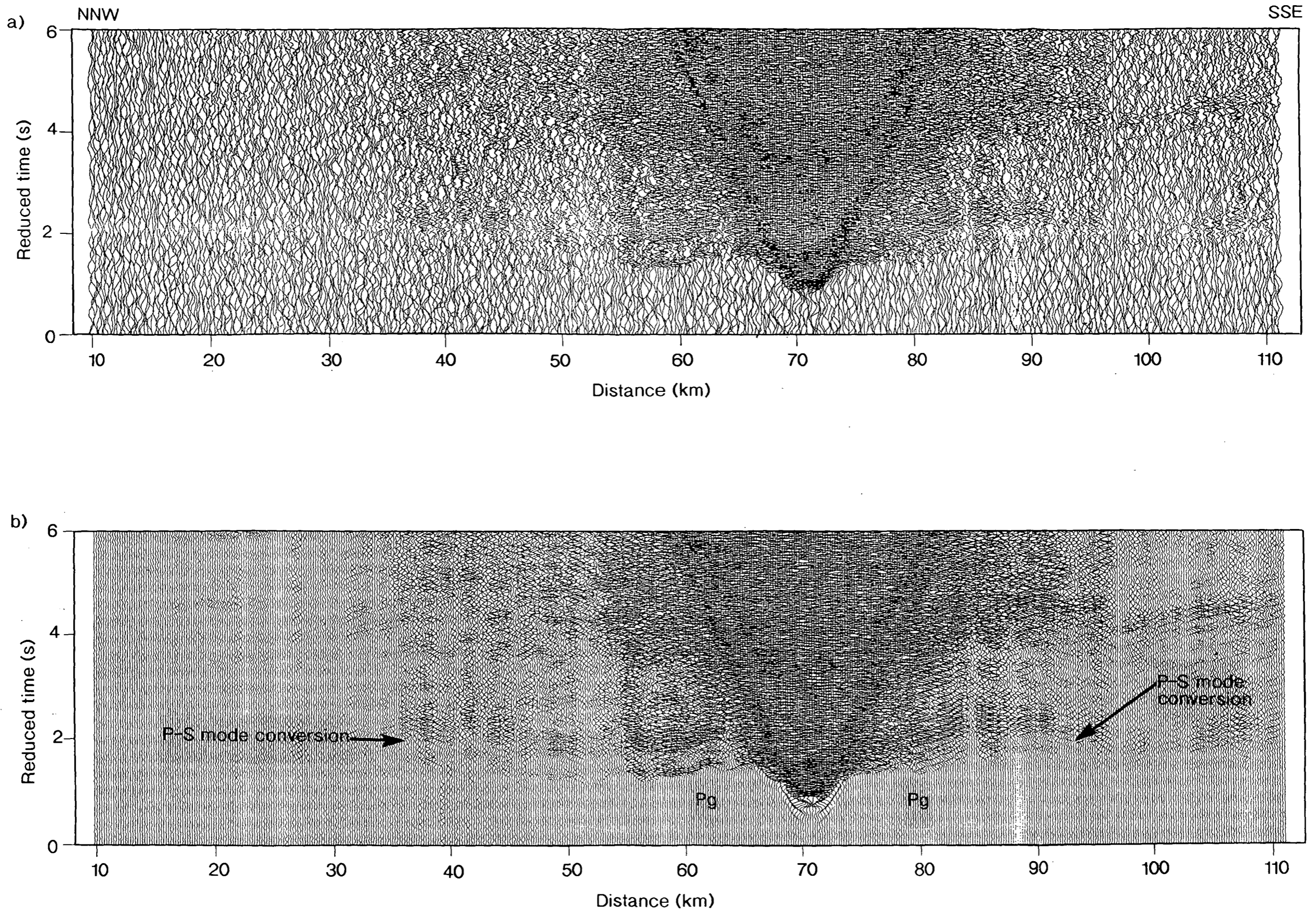


Figure 3.14

Figure 3.14: Example data sections recorded by DDOBS 6 showing the main phases of interest and the improvement seen in the data after filtering. Both sections are plotted at true amplitude and reduced at 6 km s^{-1} .
 a) Data from airgun shot firing along the across-axis line recorded by the horizontal geophone Y-component of DDOBS 6 plotted unfiltered.
 b) Same as a) but band-pass filtered between 4-6-20-30 Hz. Prominent features of this section have been annotated.

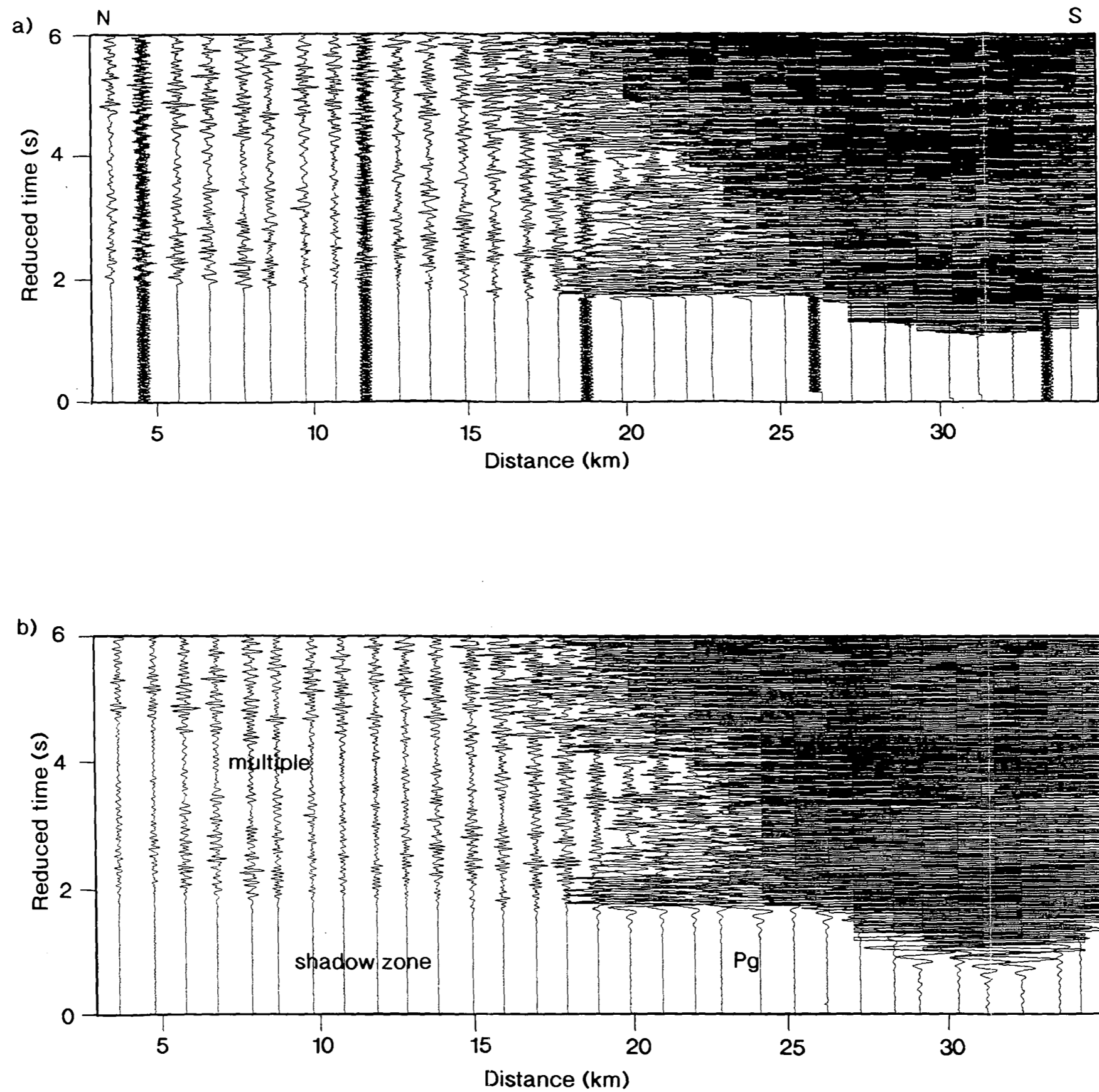


Figure 3.15: Example data sections recorded by DDOBS 4 showing the main phases of interest and the improvement seen in the data after filtering. Both sections are plotted at true amplitude and reduced at 6 km s^{-1} .
 a) Data from explosive shot firing on the along-axis line recorded by the vertical geophone component of DDOBS 4 plotted unfiltered.
 b) Same as a) but band-pass filtered between 6-8-20-30 Hz. Prominent features of this section have been annotated.

3.4.1 Prominent features of across-axis data sections

The main features of the across-axis data sections are as follows:-

- 1) Both crustal and upper mantle diving rays (P_g and P_n respectively) are observed as first arrivals on the across-axis record sections. The P_n phases have a much lower amplitude than the P_g phases and hence are not easily observed on the airgun record sections at the greater offset ranges associated with this phase. However, the explosive data were shot with the primary aim of constraining Moho depth and geometry with P_n and Moho reflected (P_mP) phases and due to greater source energy (see sections 2.3.2 and 3.2) P_n phases are clearly observable on these later sections.
- 2) First arrivals are observed out to ranges of ~50 km for the airgun, and ~60 km for the explosive data from each instrument.
- 3) The first arrivals on all across-axis sections show significant variation in amplitude with offset. These amplitude variations are caused by a number of factors. Firstly increased attenuation in the mid to lower crust sub-axis causes marked amplitude loss for arrivals travelling to off-axis instruments at greater offsets (see figure 3.13). Secondly many of the low amplitude zones can be associated directly with areas of severe seabed topography which also accounts for the wide variation in first arrival travel time with offset. Finally, some of these low amplitude zones are unrelated to the seabed topography and are spatially related to the ridge axis position with phase amplitudes returning ~5 km after crossing the axis. These low amplitudes are seen on all across-axis instruments and on all components. These shadow zones appear to be associated with higher levels of sub-axis attenuation and will be discussed further in relation to possible geological causes in the following two chapters.
- 4) A prominent secondary arriving phase is the multiple which occurs at a constant delay behind the first arrival. This delay is proportional to the water depth and leads to the conclusion that they are generated at the seabed/sea surface adjacent to each instrument location (see section 4.3.2). Off-axis these multiples have a very similar amplitude to the first arrivals (implying near perfect reflection at the sea

surface), while near and on-axis instruments have multiples of a lower amplitude than the first arrivals, resulting from the greater degree of scattering by the rough axial seafloor.

- 5) P-S mode conversions (figure 3.16) are also observed as secondary arrivals, particularly so on the DDOBSs horizontal component record sections. These phases arrive at approximately 1 s behind the first arrivals. On the vertical geophone record sections this phase is lower in amplitude than the first arrivals. However, on the horizontal component record sections this mode converted phase tends to be of a higher amplitude than the first arrivals, particularly so at greater ranges. Closer examination of the horizontal component DDOBS data also reveals a possible second P-S mode conversion occurring at approximately 0.5 s behind the first arrival. As the delay of both of these phases is approximately constant for a particular instrument, this implies that they are generated proximal to each DOBS by the up-going signals (see section 4.3.2).
- 6) The Moho reflections (P_mP) observed have a relatively low amplitude and as a consequence are not easily observed on the explosive data with its wider trace spacing (figure 3.12). However, these phases are more easily observed on the airgun record sections due to the greater trace-to-trace coherence provided by the ~0.2 km shot spacing even though the source signal is of a lower amplitude. An example section showing these arrivals is shown in figure 3.12.

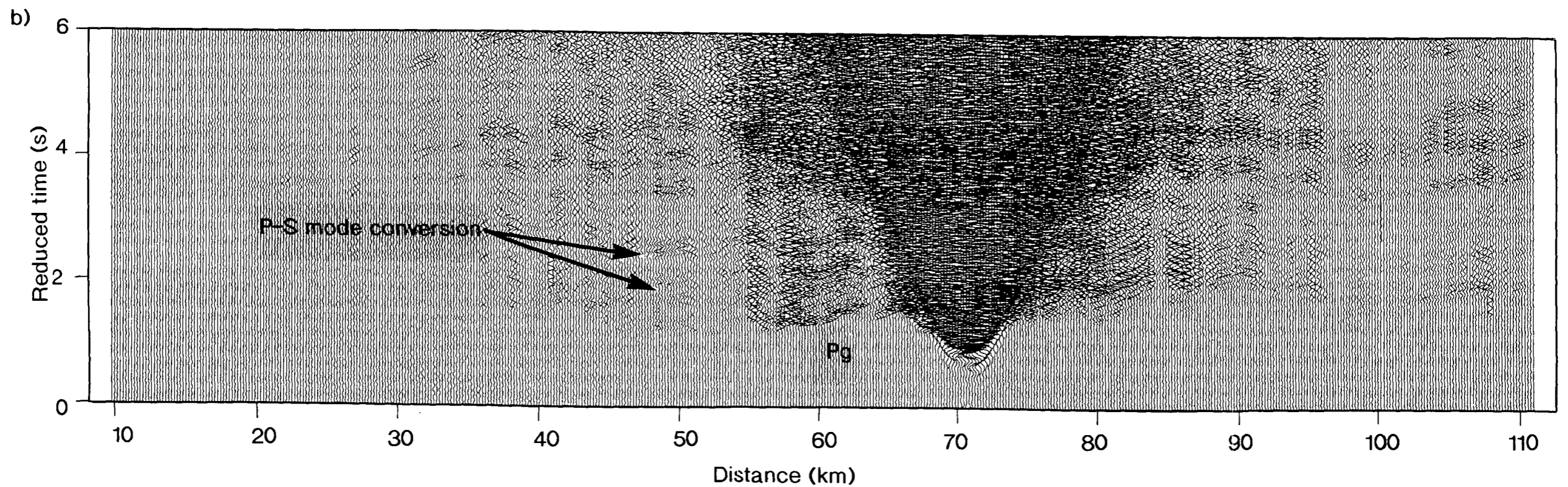
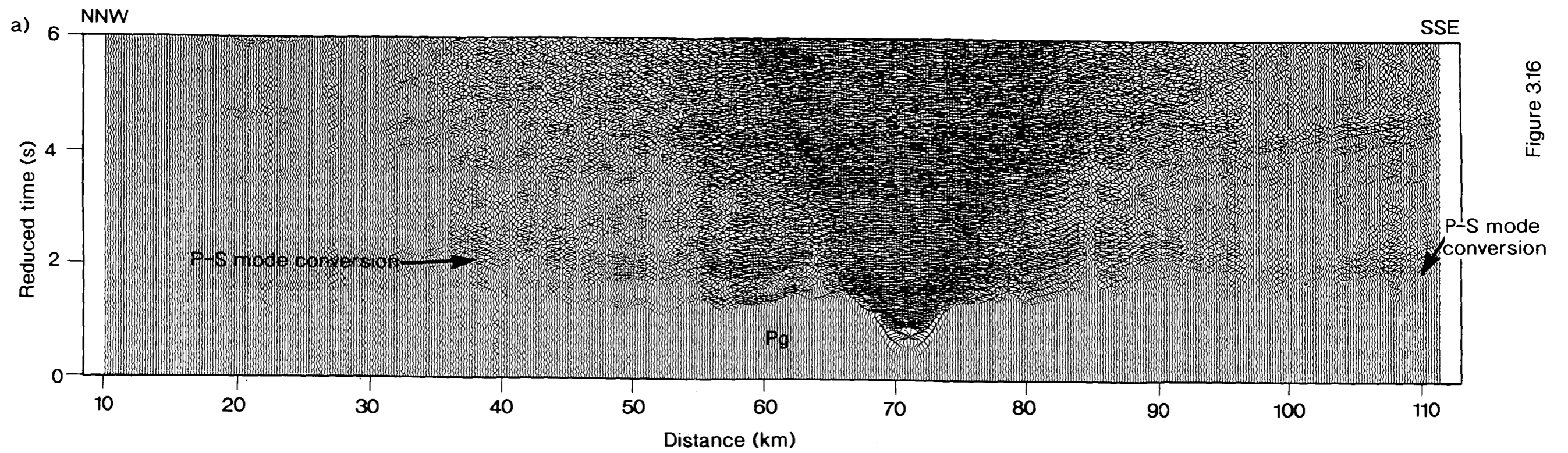


Figure 3.16

Figure 3.16: Data sections recorded by DDOBS 6 during airgun shot firing of the across-axis line showing the main phases of interest and comparing the perpendicular horizontal components. Both sections are plotted at true amplitude, reduced at 6 km s^{-1} and filtered at 4-6-20-30 Hz.
 a) Y-component.
 b) X-component.

3.4.2 Prominent features of along-axis data sections

The main features of the along-axis data sections are as follows:-

- 1) Crustal diving rays (P_g) are observed as first arrivals out to ranges of greater than 30 km (see figure 3.15), the maximum shot-receiver range on this line. Upper mantle diving rays (P_n) are not observed on any of the along-axis sections as they appear to arrive at greater offsets than the 30 km maximum, this is confirmed by modelling.
- 2) A sharp reduction in signal amplitude is again observed in the P_g phase at ~11 km offset for all arrivals travelling at mid-crustal depths. Signal amplitude increases after approximately 8 km range (see figure 3.15). This phase "shadowing", its cause and correlation with the shadow zones observed in the across-axis data will be discussed further in Chapter 4 (section 4.3.3).
- 3) Multiples arrive as secondary phases, again at an approximately constant delay proportional to the water depth, behind the first arrivals. These multiples are of a lower amplitude than the first arrivals due to scattering by the rougher seafloor along the entire length of this line (cf. across-axis line; see section 3.4.1).
- 4) The P-S mode conversions observed on these sections are of a lower amplitude than the equivalent across-axis phases, although they are still observable on the horizontal geophone component data sections (figure 3.17). These phases again occur approximately 1 s behind the first arrivals, with a possible second phase with a 0.5 s delay.
- 5) Finally, Moho reflections are again observed although the amplitude of this phase is very low and the wide trace spacing of the explosive data on this line makes identification by inspection alone difficult.

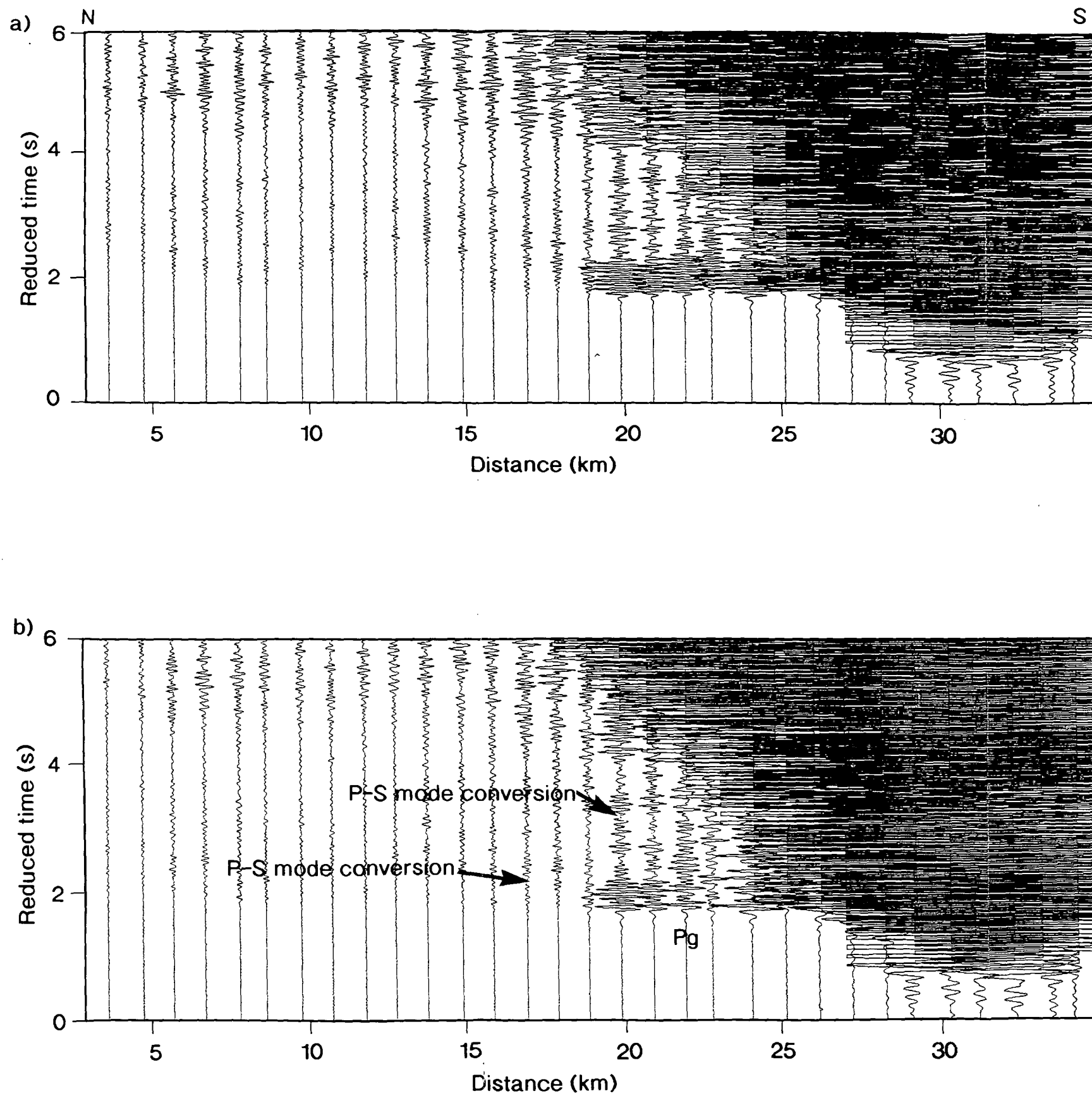


Figure 3.17: Data sections recorded by DDOBS 4 during explosive shot firing of the along-axis line showing the main phases of interest and comparing the perpendicular horizontal components. Both sections are plotted at true amplitude, reduced at 6 km s^{-1} and filtered at 4-6-20-30 Hz.
 a) Y-component.
 b) X-component.

3.5 Summary

In this chapter the main phases of interest (and those which have been modelled) are described in detail, together with all the significant features of the wide-angle seismic data sections. Frequency analysis of the dataset is described in terms of the dominant phases and the instrumental and background ("geological" or otherwise) noise. The procedures adopted to minimise the effects of this noise are also described. For modelling, travel time picks were made on non-filtered (i.e. raw) record sections plotted at a variety of scales to maximise picking accuracy. Modelling of the dataset described here will be discussed in the next chapter.

Chapter 4

Modelling of the Reykjanes Ridge wide-angle seismic data

4.1 Introduction

In this chapter the results of modelling the Reykjanes Ridge wide-angle seismic data are described. The positions of the wide-angle explosive and airgun lines are shown in figure 2.2, together with individual instrument deployment locations. Two along and across-axis velocity-depth models are presented: 1) two initial models based on one-dimensional slope-intercept inversion of observed travel times, combined with water depths obtained from the *Darwin's* echo sounding system, side-scan sonar and seismic reflection data interpretations plus sound velocity dip information regarding the water column velocity structure; and 2) two final models that fit the observed explosive and airgun DOBS data, normal incidence reflection profiles and observed underway gravity data. The modelling process is described in detail in this chapter, together with a description of the application of three different modelling techniques to the DOBS data. A consideration of the suitability and limitations of each of these techniques is also included here.

4.2 Along and across-axis initial models

Initially the six wide-angle explosive and six airgun DDOBS record sections were interpreted using a one-dimensional slope-intercept travel time inversion to provide an estimate of the velocity-depth structure adjacent to each instrument. The six resulting velocity-depth profiles were combined to form the two initial models shown in figure 4.1. The seabed geometry was incorporated into both initial models using central beam depth measurements from the *Darwin's* Simrad echo sounding system made while shooting along each line. Data obtained from a sound velocity dip conducted at 57° 47.2'N 32° 50.5'W using an AML profiler provided details of variations in vertical

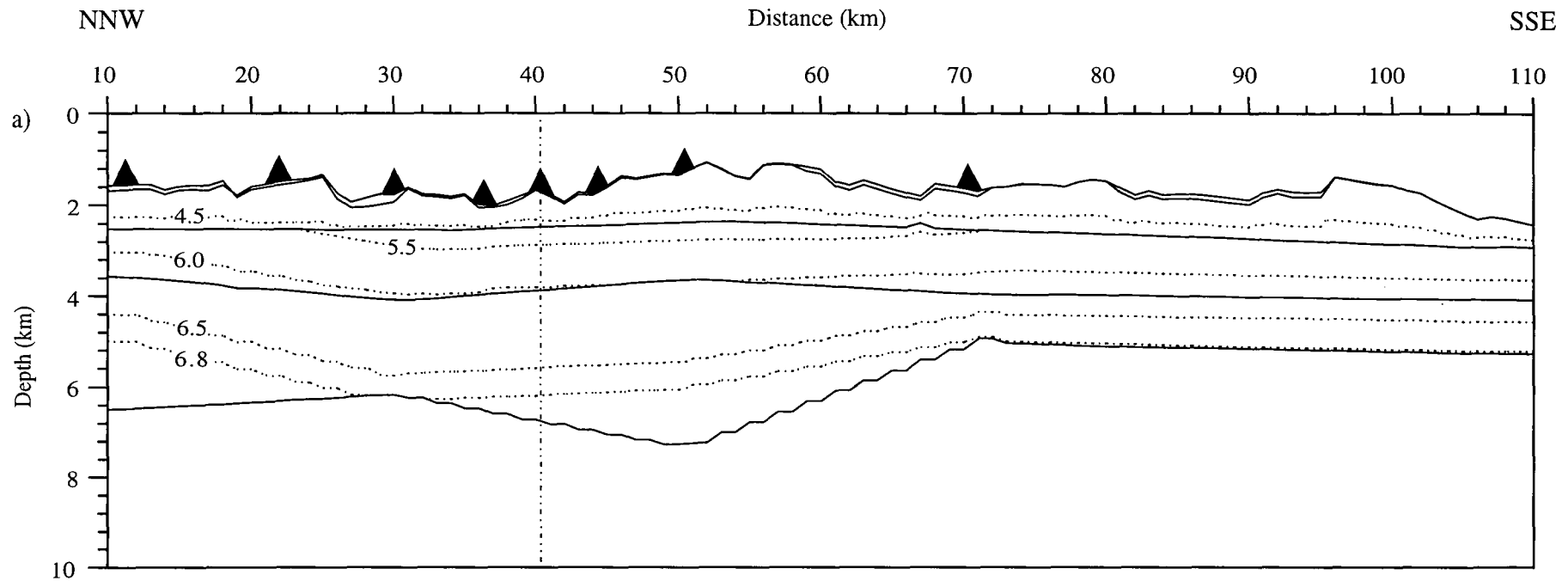


Figure 4.1: Initial wide-angle seismic models. The solid lines represent first order boundaries and the dotted lines isovelocity contours labelled in km s^{-1} . DDOBS locations are marked by triangles and the intersection point of the two lines is marked with a long-short dashed line. The upper layer of each model represents the water column and all layers extend the full width of the model. (see section 4.2.1)

a) Across-axis initial model. The first layer below the seabed is sedimentary (e.g. oceanic layer 1; Fowler, 1990) and is underlain by three layers interpreted as oceanic layers 2A, 2B and 3 (Spudich and Orcutt, 1980b; Bratt and Purdy, 1984), each separated by first order boundaries. The lowermost layer represents the upper mantle with velocities ranging from 8.0 km s^{-1} just below the Moho to 8.4 km s^{-1} at 20 km depth.

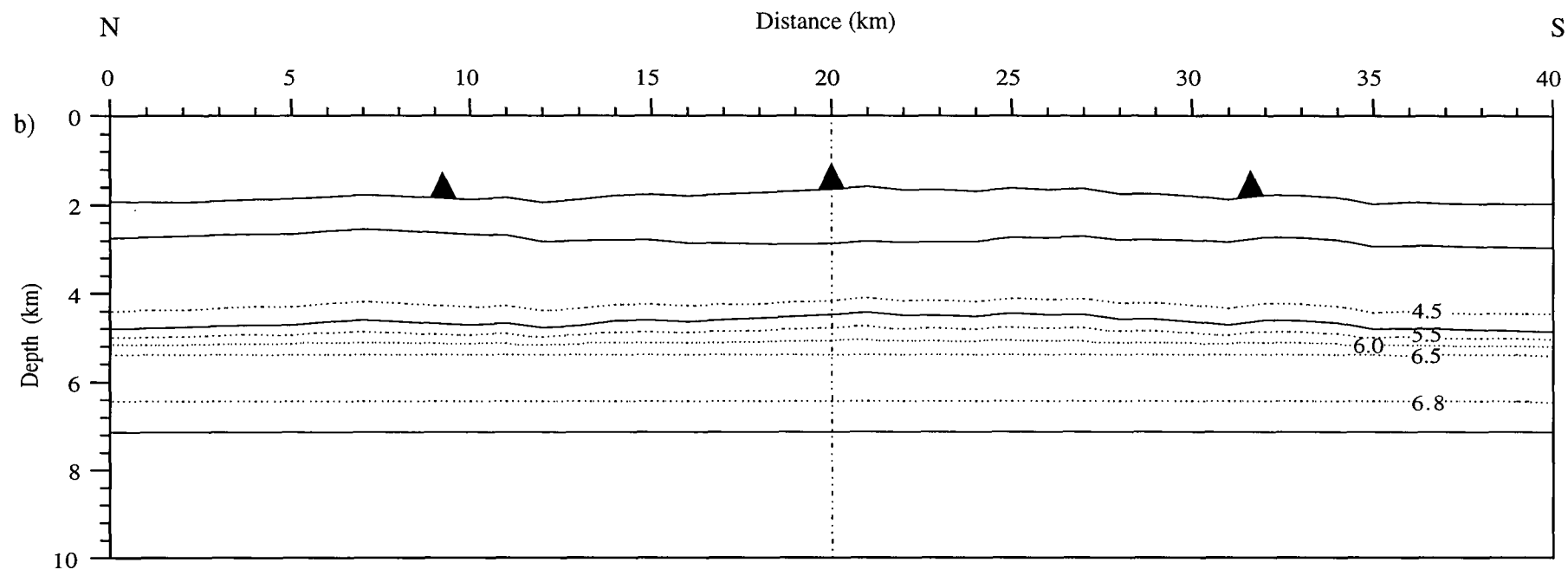


Figure 4.1: cont.. Initial wide-angle seismic models. The solid lines represent first order boundaries and the dotted lines isovelocity contours labelled in km s^{-1} . DDOBS locations are marked by triangles and the intersection point of the two lines is marked with a long-short dashed line. The upper layer of each model represents the water column and all layers extend the full width of the model. (see section 4.2.2)

b) Along-axis initial model. There was no evidence of sediments on-axis, therefore the seabed in the initial along-axis model is directly underlain by oceanic layers 2A, 2B and 3 (Spudich and Orcutt, 1980b; Bratt and Purdy, 1984) which are separated by first order boundaries. Layer 3 is subdivided by a second order boundary coincident with the 6.5 km s^{-1} isovelocity contour to provide the change in gradient required by preliminary ray-trace modelling of the across-axis line. The Moho in this model is horizontal and the velocities increase from 7.8 km s^{-1} just below the Moho to 8.4 km s^{-1} at 20 km depth.

velocity structure within the water column which were incorporated into these models. Areas of sediment cover were located using the underway side-scan sonar images collected during pre-surveying of the wide-angle seismic lines again with the *Darwin's* Simrad EM12 system. The thickness of these sediments was initially estimated at ~100 m as no other data constraining their vertical extent were available. Initial sediment layer velocities were based on Deep Sea Drilling Project results in the North Atlantic (site 115, Walker *et al.*, 1970; sites 403-406 Shipboard Scientific Party, 1979). Due to the lack of initial constraints on the sedimentary sequence, this feature of the ridge crustal structure was incorporated as a single layer in the across-axis initial model. As sediments were not observed on-axis a sedimentary layer was not incorporated into the along-axis initial model.

Due to the processing problems experienced with the CDOBS data these initial models were primarily ray-traced contemporaneously with the data processing of this latter dataset (see sections 2.5.4 and 2.6.1). Therefore one-dimensional travel time inversions of these data sections were incorporated at a later stage, before the final ray-trace modelling of both seismic lines took place.

4.2.1 Across-axis initial model

The across-axis initial model (figure 4.1a) consists of 6 blocks with varying vertical and horizontal gradients. The P-wave velocity, density and depth are specified at 111 points along each interface and at this stage first order discontinuities (with a distinct change in velocity across the boundary) were used to define individual layers. The main features of this initial model, which extends from 10 km northwest of the first shot point in a southeastwards direction for 110 km across-axis, are as follows:-

- 1) The water column was incorporated using a single layer of velocity 1.479 km s^{-1} at the surface increasing to 1.495 km s^{-1} at the base.
- 2) The base of this water column layer, representing the seabed, was constructed using actual shipboard bathymetry measurements spaced at 1 km intervals. This spacing was restricted by the modelling packages and fairly coarsely defined the severe topography associated with a slow spreading ridge.

- 3) Beneath the seabed lies a layer of variable thickness representing the sediment ponds observed off-axis on the side-scan sonar data. In areas of no observable sediment accumulation this layer was given a thickness of ~ 0.01 km, while in sedimented areas the estimated thickness of ~ 0.1 km was incorporated at this stage. This single layer of sediments was adopted initially to generate as simple a model as possible for initial ray-tracing by incorporating layers in the early stages that were continuous across the entire model length.
- 4) Oceanic layer 2A (Houtz and Ewing, 1976; Spudich and Orcutt, 1980b; Bratt and Purdy, 1984) was incorporated beneath this sedimentary layer by combining the results of the initial one-dimensional travel time inversions with the results of similar surveys located on other mid-ocean ridge systems (e.g. Purdy and Detrick, 1986; Vera *et al.*, 1990; Solomon and Toomey, 1992; Kappus *et al.*, 1995 etc.). This layer was assumed to be approximately 1 km in thickness (e.g. Bunch and Kennett, 1980). An average velocity, compatible with results obtained at other spreading ridges, of 3.5 km s^{-1} was assigned to this layer accompanied by a gradient of $\sim 1.0 \text{ s}^{-1}$ – velocity increasing as a function of depth. In the axial region travel time inversions of data from DDOBS 3 and 4 and CDOBS 13 indicated that the layer 2A velocity was lower than that at equivalent sub-seafloor depths off-axis, which was reinforced by the across-axis data interpretation. Hence beneath the axis the velocities of this layer were decreased by $\sim 0.2 \text{ km s}^{-1}$ in the model.
- 5) Beneath the above layer, oceanic layer 2B (Spudich and Orcutt, 1980b; Bratt and Purdy, 1984) was incorporated with a thickness of approximately 1 km. Layer velocities of on average, 5 km s^{-1} off-axis and 4.7 km s^{-1} on-axis accompanied by a velocity gradient of 1.0 s^{-1} , were selected based on previous ridge work (Bunch and Kennett, 1980; Purdy and Detrick, 1986) and the initial one-dimensional data inversion.
- 6) The basal crust layer was interpreted as oceanic layer 3 (Spudich and Orcutt, 1980b) and varied in thickness laterally from 3 km at the northwestern end of the model to 1 km at the southeastern end. This layer was incorporated with an average velocity of 6.5 km s^{-1} and the 0.5 s^{-1} vertical velocity gradient typical of

this region of the oceanic crust (Cudrack and Clowes, 1993; Detrick *et al.*, 1994).

- 7) The lowest layer of the initial model represents the uppermost mantle. Inversion of the DOBS travel time data indicated velocities in the broad range of 7.54 to 8.6 kms^{-1} for this layer. However, few arrivals which have travelled through the upper mantle (P_n phases) are actually observed. Those which are observed exhibit quite low amplitudes and large undulations in travel time with offset due to the severe seabed topography, making measurement of the P_n velocity quite inaccurate. Hence a more standard velocity range of 8.0 km s^{-1} at the Moho to 8.4 km s^{-1} at 20 km below sea level was incorporated (White *et al.*, 1992).
- 8) Based on measurements of the shot-to-instrument offset at which first arrivals change from P_g phases to become P_n phases, an estimated crustal thickness of ~5.5 km was made from each data section and incorporated into the initial model. Although this value seems rather thin for normal oceanic crust even at a ridge axis (cf. White, 1979; White *et al.*, 1992; White and Clowes, 1994 – average oceanic crustal thickness of 7.0 km), it has been reported that one-dimensional travel time inversions generate crustal thickness estimates that tend to be up to 20% thinner than final ray-traced crustal thicknesses (White *et al.*, 1992). The thin crustal thicknesses obtained from one-dimensional inversion were used to avoid biasing the initial model towards the crustal structure expected of normal mid-oceanic ridge oceanic crust.

4.2.2 Along-axis initial model

As this line was effectively shot along strike of the main sub-surface features, the along-axis initial model (figure 4.1b) consists of 5 layers which are almost one-dimensional in their velocity structure, i.e. there is little lateral variation in the velocity or velocity gradient. Therefore this initial model is far simpler than that for the across-axis line and hence it is potentially easier to produce a good fitting ray-traced model. The along-axis initial model was constructed using a one-dimensional travel time inversion of data from the three in-line DOBS plus velocity and layer thickness information obtained at the intersection point with the across-axis line which, by the

time of construction of this model, had already undergone significant ray-tracing. No sediment ponds exist on-axis. The initial model runs for 40 km along the AVR and the P-wave velocity, density and depth are specified at 41 points along each interface. The main features of the along-axis initial model are as follows:-

- 1) Like the across-axis model the water column was modelled with a single layer of velocity ranging from 1.479 km s^{-1} to 1.495 km s^{-1} .
- 2) Oceanic layer 2A, with an upper surface geometry constrained by underway bathymetry measurements, was incorporated below the seabed with velocities ranging from 3.5 to 4.0 km s^{-1} and an average gradient of 0.5 s^{-1} . The boundary between the base of this layer and the layer beneath is marked by a first order discontinuity.
- 3) Based on the intersection with the partially modelled across-axis line, oceanic layer 2B was modelled initially with an average thickness of about 2 km, velocities in the range of 4.0 to 4.6 km s^{-1} and gradient of 0.5 s^{-1} . The upper and lower surfaces of this layer run parallel to the seabed (figure 4.1b) and the lower boundary is of first order.
- 4) Oceanic layer 3 was again incorporated with an upper first order boundary parallel to the seabed and was on average 2 km in thickness. However, as no P_n phases were observed on the along-axis data sections no direct measurements of the base of this layer (i.e. the Moho) could be obtained from the data. Therefore the Moho depth from the across-axis model was used and this interface was input as a horizontal first order boundary along the entire model length. Preliminary ray-trace modelling of the across-axis data revealed at an early stage that this layer was divided into two layers with different velocity gradients. Hence for the along-axis initial model this layer was subdivided using a second order discontinuity (with a change in velocity gradient only across the boundary) into an upper region of velocity 5.0 km s^{-1} at the upper surface, increasing to 6.5 km s^{-1} after an increase in depth of $\sim 0.7 \text{ km}$ (i.e. a gradient of $\sim 2.14 \text{ s}^{-1}$) and a lower region with velocity increasing from 6.5 km s^{-1} to 7.0 km s^{-1} over $\sim 1.7 \text{ km}$ (i.e. a gradient of $\sim 0.3 \text{ s}^{-1}$).
- 5) Below the horizontal Moho, the upper mantle was modelled with an

approximately 13 km thick layer with a sub-Moho velocity of 7.8 km s^{-1} increasing to 8.4 km s^{-1} at 20 km depth.

4.2.3 Ray-trace modelling

Both initial models were ray-traced using a trial-and-error approach based on the Maslov method – the program *maslov* is based on the Maslov asymptotic ray theory of Chapman and Drummond (1982) (see section 4.5.1) – to examine the travel time and amplitude fit with the synthetics for both the observed airgun and explosive data. The trial-and-error approach consisted of ray-tracing a particular model, assessing phase travel time and amplitude fit, adjusting the model accordingly and re-tracing using the method outlined in Peirce (1990a). Examples of the initial ray-tracing are shown in figures 4.2-4.4 and details of the modelling strategy will be discussed in the next section.

The main features of the fit and the conclusions drawn from the initial attempts at modelling are as follows:-

- 1) The use of a continuous layer of varying thickness across the entire model to represent the observed sediment ponds proved to be problematic in areas with no sediment cover and where the layer was given a thickness of less than 0.01 km. In these regions the velocities were either given the same velocity as the sediment ponds elsewhere on the model which caused high vertical velocity gradients, or the velocity structure of the layer below was used, generating high lateral velocity gradients. The thickness and high velocity gradient of the sedimentary layer, combined with the severe seabed topography creating strong lateral velocity gradients, made it difficult to trace any rays through the model and impossible to source rays from non-sedimented areas.
- 2) When rays could be traced, most calculated phase arrival travel times misfit the observed by 0.25-0.6 s depending on the instrument location.
- 3) Modelled P_g phases were consistently of too high an amplitude, particularly so in the axial region, indicating the need for an axial low velocity zone.
- 4) No first order discontinuities could be used in the definition of the igneous crust as

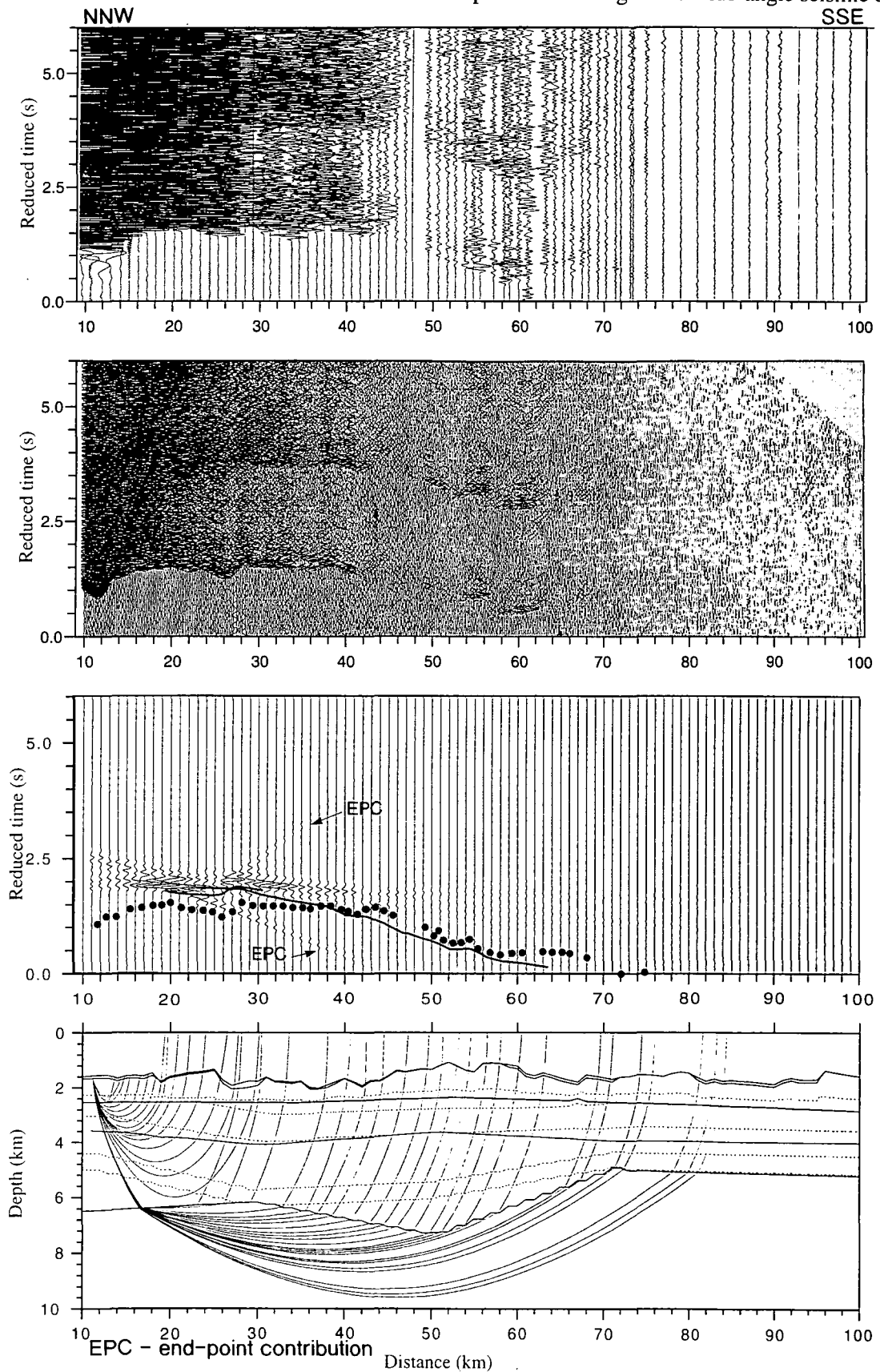


Figure 4.2: Ray-trace modelling of the Reykjanes Ridge initial across-axis wide-angle seismic model for DDOBS 1. The observed travel time picks are indicated by dots and the geometrical ray-traced solution by a solid line. Dot size gives an indication of the modelling error bounds (see section 2.7). Both the observed explosive (top) and airgun (second), vertical geophone component record sections are shown at the same scale as the calculated synthetic seismograms (third) for comparison. Seismograms are plotted at true amplitude with a reduction velocity of 6 km s^{-1} .

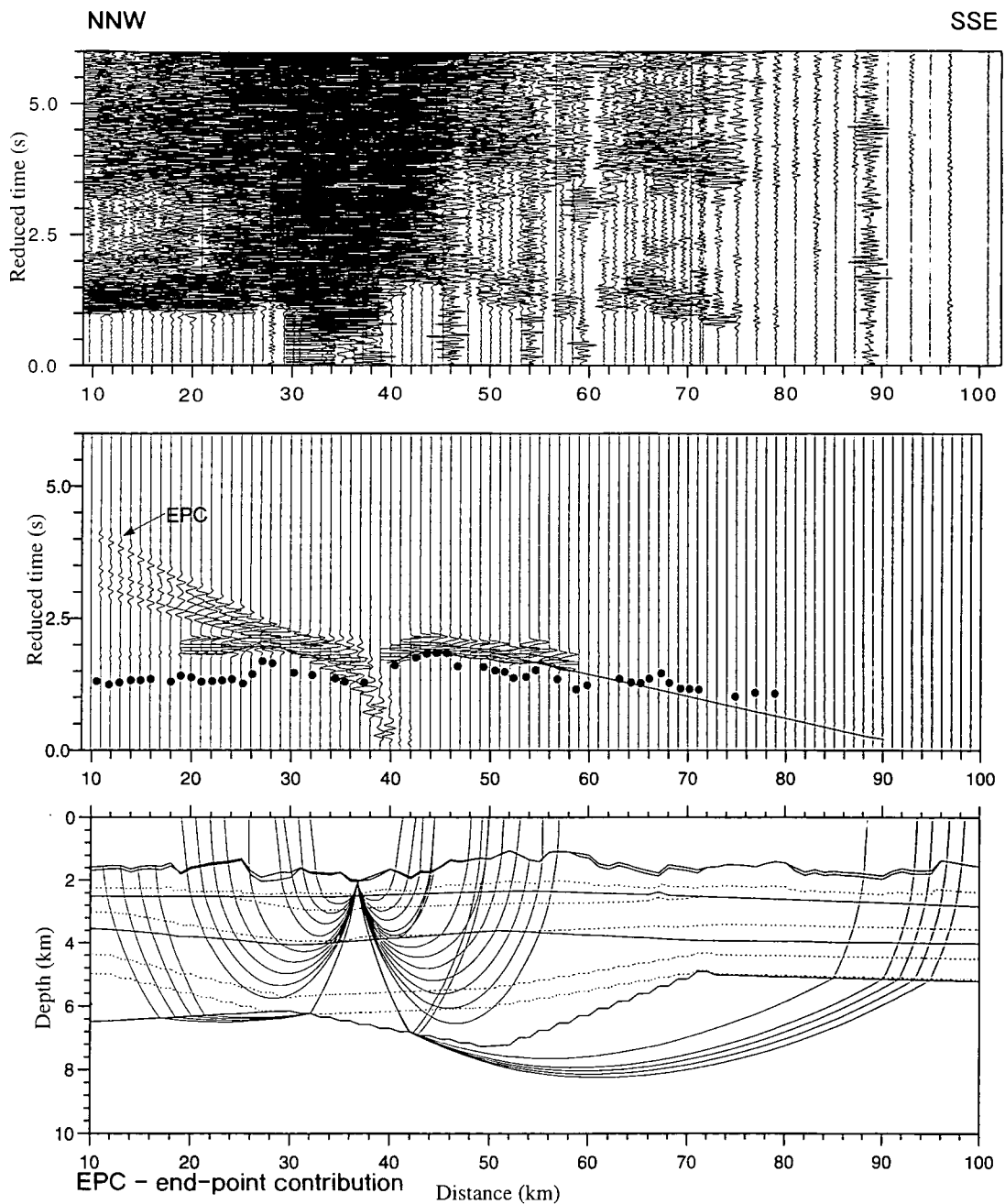


Figure 4.3: Ray-trace modelling of the Reykjanes Ridge initial across-axis wide-angle seismic model for CDOBS 12. The observed travel time picks are indicated by dots and the geometrical ray-traced solution by a solid line. Dot size gives an indication of the modelling error bounds (see section 2.7). The observed explosive, vertical geophone component record section (top) is shown at the same scale as the calculated synthetic seismograms (middle) for comparison. Seismograms are plotted at true amplitude with a reduction velocity of 6 km s^{-1} .

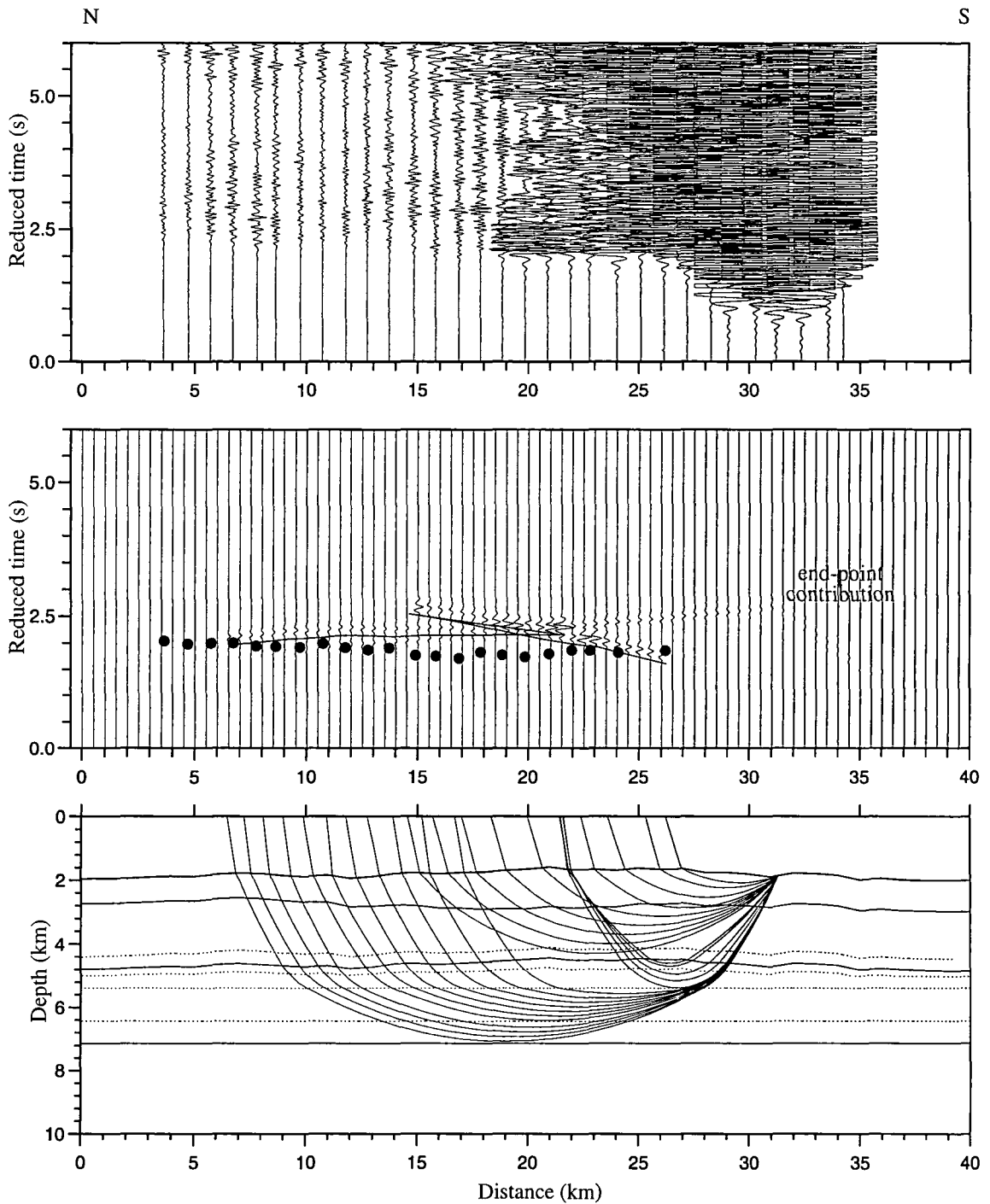


Figure 4.4: Ray-trace modelling of the Reykjanes Ridge initial along-axis wide-angle seismic model for DDOBS 4. The observed travel time picks are indicated by dots and the geometrical ray-traced solution by a solid line. Dot size gives an indication of the modelling error bounds (see section 2.7). The observed explosive, vertical geophone component record section (top) is shown at the same scale as the calculated synthetic seismograms (middle) for comparison. Seismograms are plotted at true amplitude with a reduction velocity of 6 km s^{-1} .

intra-crustal reflections were not initially identified on any DOBS record section.

- 5) The initial velocity definition of the upper mantle (an increase from 8.0-8.4 km s⁻¹ in the first 13 km) proved incorrect in that, where P_n phases could be modelled they arrived too early and at too close an offset.

4.3 Final velocity–depth models

4.3.1 Modelling strategy

The final models were obtained using a trial-and-error method based primarily on *maslov* ray-tracing each model, investigating the fit of synthetic travel times and amplitudes with the observed data, adjusting the model accordingly and re-tracing. The Reykjanes Ridge is a highly two dimensional structure in cross-section, particularly so across-axis with a variation in seafloor topography of over 1 500 m. Defining this 2-D structure proved difficult within the constraints of the forward modelling programs. Hence for the majority of modelling *maslov* was used (see section 4.5.1) and once a good-fitting model was obtained it was tested with the *beam87* and *rayinvr* methods (see section 4.5.2 and 4.5.3). Each model (see figures 4.5a and b) was defined in terms of the velocity, depth and density at numerous points along each interface. The close separation of the points defining the model in areas of irregular interface geometry (e.g. at the ridge axis) causes significant instabilities in the *maslov* program which acted as a limit to the complexity of models that could be ray-traced successfully.

The modelling procedure began using data from an instrument located towards one end of each model. Once observed first arrival travel times had been well matched for this instrument, data from an instrument located at the opposite end of each model was ray-traced and the fit assessed. Once a good fit had been obtained for data from both ends of each model data from the central instruments were incorporated into the modelling process. As each instrument's data were included the models were re-ray-traced, adjusted and the fit of all travel time data assessed. This 'cross-correlation' caused numerous difficulties in that a good fitting, stable model for one instrument was often unstable and impossible to ray-trace satisfactorily for another.

The most variable part of the oceanic crust, and hence any model of it, is the

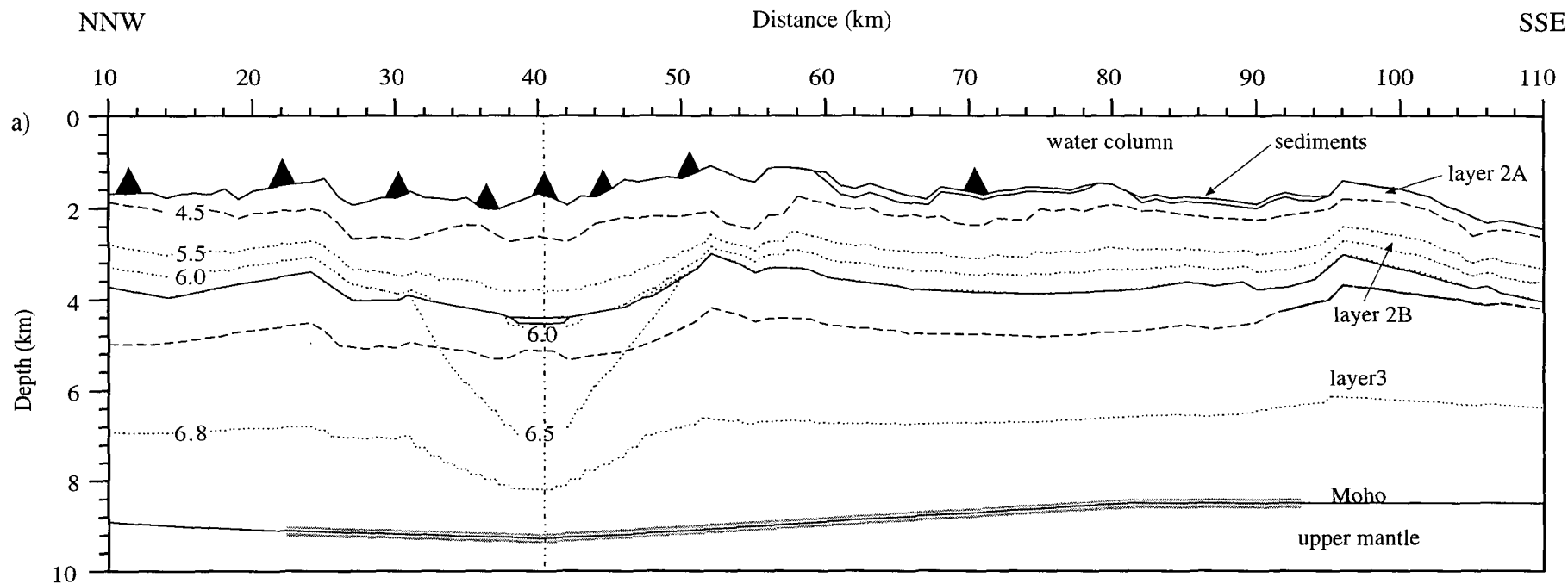


Figure 4.5: Final wide-angle seismic models. Solid lines represent first order boundaries, dashed lines are second order boundaries and dotted lines are isovelocity contours which are labelled in km s^{-1} . DDOBS positions are marked by triangles and the intersection point of the two lines is marked with a long-short dashed line. The upper layer of each model represents the water column and extends across the full width of the model.

a) Across-axis final model. On this model there are two off-axis sediment ponds underlain by two layers interpreted as oceanic layers 2A and 2B which extend across the entire width of the model. These layers are underlain by oceanic layer 3 (Spudich and Orcutt, 1980b) and separated from it by a "pseudo" second order boundary – i.e. a first order interface without a sharp change in velocity across it for most of the model length. This type of boundary is necessary to define the discrete axial block. Layer 3 is subdivided into two by a second order boundary to enable changes in velocity gradient at 93 km (see shaded line). The velocity ranges from 7.9 km s^{-1} just below the Moho to 8.2 km s^{-1} at 20 km depth. On-axis there is a thin, narrow, low velocity block with velocities of $3.0\text{-}3.01 \text{ km s}^{-1}$.

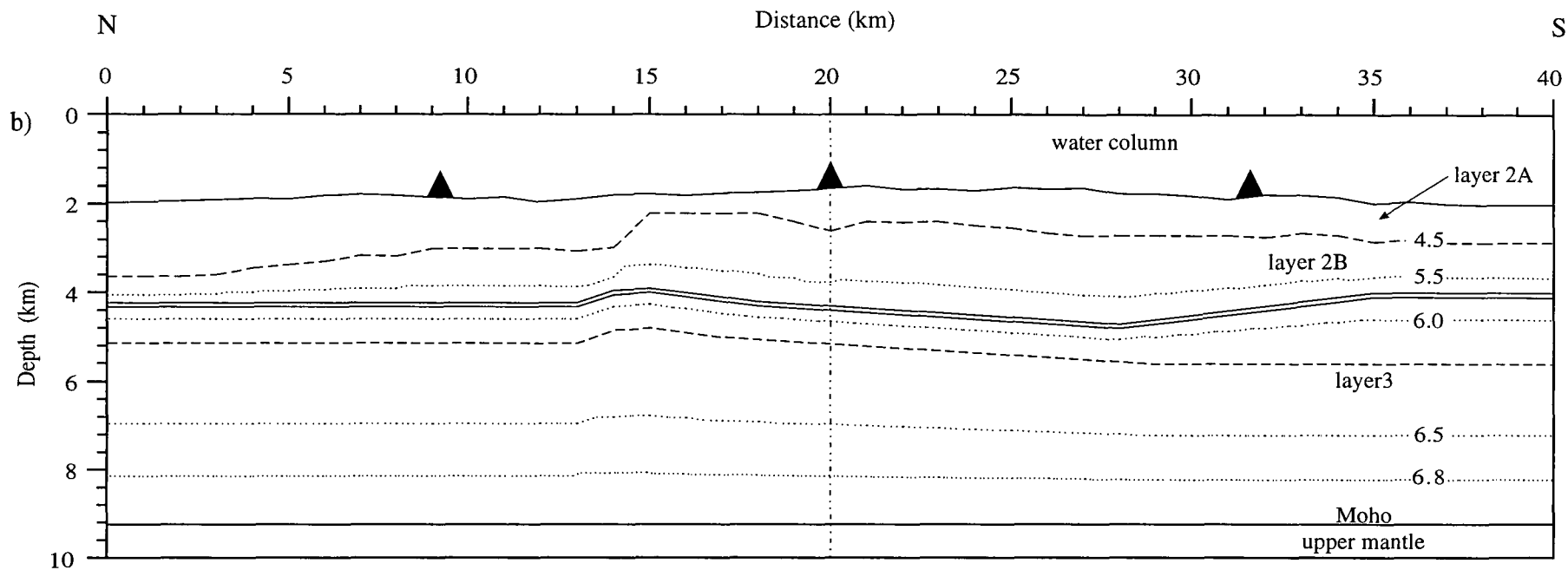


Figure 4.5: cont.. Final wide-angle seismic models. Solid lines represent first order boundaries, dashed lines are second order boundaries and dotted lines are isovelocity contours which are labelled in km s^{-1} . DDOBS positions are marked by triangles and the intersection point of the two lines is marked with a long-short dashed line. The upper layer of each model represents the water column and extends across the full width of the model.

b) Along-axis final model. The seabed on this model is directly underlain by oceanic layers 2A and 2B (Spudich and Orcutt, 1980b) which in turn are separated by a second order boundary located along the 4.5 km s^{-1} isovelocity contour. Layer 3 (Spudich and Orcutt, 1980b) is approximately 4.8 km in thickness and is subdivided by a second order boundary at the 6.1 km s^{-1} contour. The Moho is poorly constrained by observed phases along-axis, therefore it has been input at a depth obtained from the intersection point with the across-axis line. Between 2 and 3 km depth a low velocity layer extends the full length of the model. The velocity of this layer lies between $3.0\text{-}3.01 \text{ km s}^{-1}$ and the layer is at least 0.1 km in thickness. However this layer is poorly constrained and it may be discontinuous along-axis and bounded by gradient zones.

first few kilometres below the seabed. The variability of this affects not only the down-going wavefield but also the up-going. Hence it is important that this part of the model and the corresponding phases in the observed data be well matched *before* any attempt is made to model the lower crustal (P_g), upper mantle (P_n) and Moho reflected (P_mP) phases which largely define crustal thickness variations and Moho geometry. In the case of the Reykjanes Ridge dataset, the great variability in seabed topography caused a significant amount of scattering of the down-going wavefield, particularly noticeable in the explosive data which has a higher signal-to-noise ratio. At this point it should be mentioned that, particularly in the axial region, a significant number of second arrivals are observed which, by considering the out-of-plane seabed topography (see figure 4.6), can be identified as side-swipe originating from near-vertical seabed structures. Apart from acting as an aid in identifying these features on the data sections, no attempt has been made to ray-trace model them.

Throughout modelling the fit of both the synthetic phase travel times and amplitudes to the observed data were considered. The modelling method employed was as follows:-

- 1) In the first instance direct water waves and water wave multiples were modelled for all instruments to check their positions on the seabed. Only when a good fit of these phases was achieved, to within the lower bound of the systematic errors involved (see section 2.7), did modelling proceed further.
- 2) Firstly travel times and amplitudes of the close trace spacing airgun data at near offsets were modelled in order to constrain the sediment pond location, velocity structure and thickness adjacent to each DOBS. In areas with no sediment cover the top of layer 2A was modelled at this stage.
- 3) Near offset arrival times and amplitudes were then modelled for the explosive data. Any changes in sediment structure necessary to model this wide trace spaced data, were then remodelled for the airgun data. The explosives and airgun data were then combined for the DDOBS data to enable modelling of both datasets together.
- 4) Once a consistent upper crustal structure had been obtained from the two steps

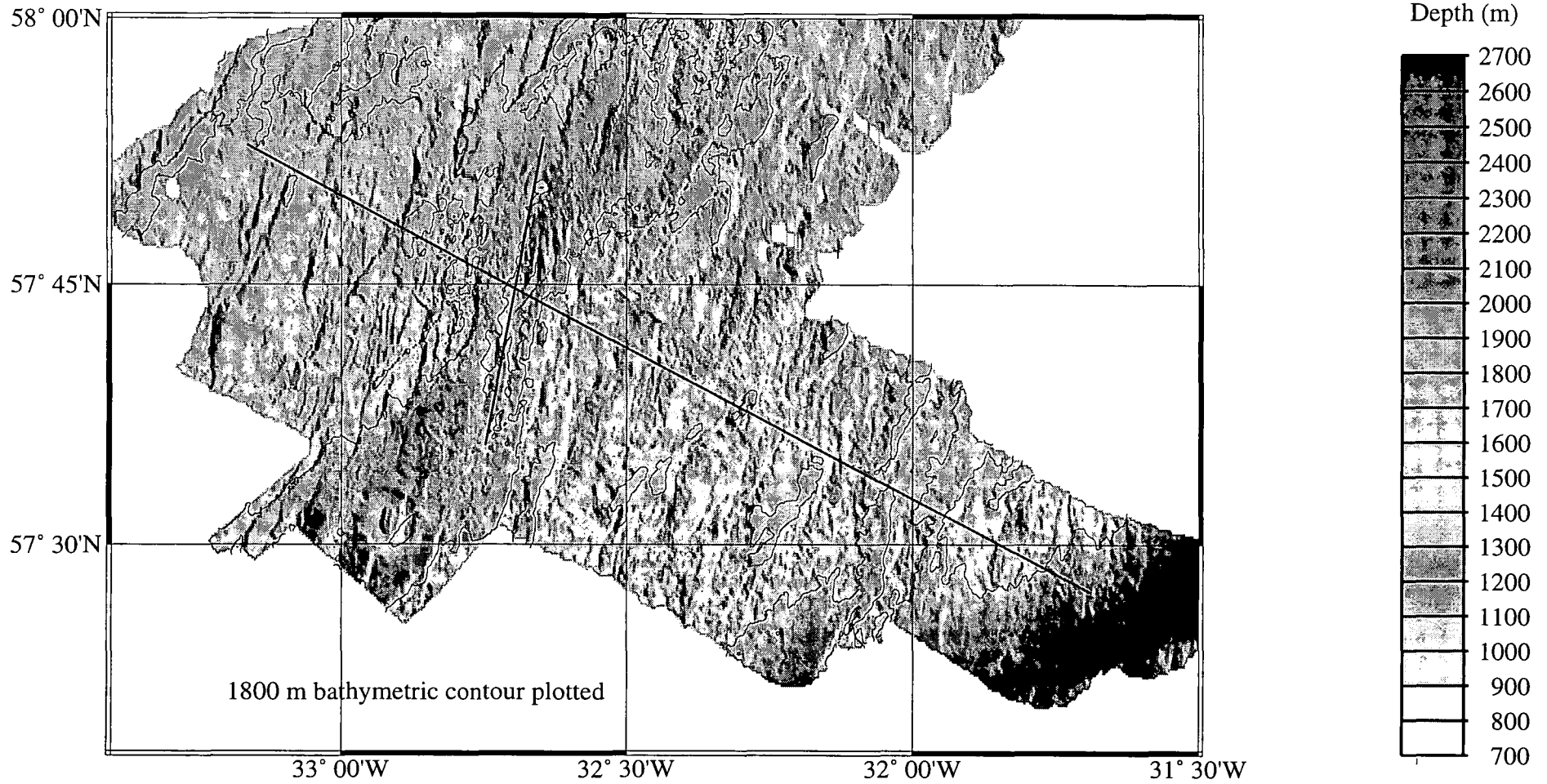


Figure 4.6: Shaded relief image of the swath bathymetry data collected during CD81/93 combined with data from Area C of Parson *et al.* (1993). The solid lines show the positions of the wide-angle seismic profiles for reference. Note the rough seabed in the area which causes significant scattering of seismic waves.

outlined above, middle to lower crustal and upper mantle arrivals were investigated by adjusting the crustal velocity structure while leaving the upper crustal structure unchanged. As mentioned in section 4.2, the crust at the Reykjanes Ridge was modelled with layers corresponding to oceanic layers 2A, 2B and 3 having the mostly "normal" velocities and velocity gradients associated with those layers as observed beneath ridge systems world-wide (Spudich and Orcutt, 1980b; Vera *et al.*, 1990; Solomon and Toomey, 1992), bound by first order interfaces. As modelling continued it became clear that the crust could not be modelled in terms of first order interfaces alone as the synthetic reflected phases these generated were not observed on the DOBS record sections. Also velocities at first order boundaries could not be defined within the constraints of the *maslov* program such that no spurious amplitude effects were produced and that only transmitted rays were permitted. Consequently layer 2 was redefined using a second order discontinuity (i.e. a change in gradient as a function of depth), which dramatically improved both the travel time and amplitude fit with the observed data. As modelling proceeded it soon became clear that an extensive low velocity zone was required beneath the axis to match not only the observed travel times, but also the amplitude variation as a function of offset. At the top of this zone, a very low velocity region at least 0.1 km in thickness and ~4 km in width, needed to be incorporated into the model to account for the shadow zones associated with the axis location and the offset at which lower crustal phases are again observed. This feature could only be incorporated under the limitations of the modelling method as an isolated body within the model, by splitting the crustal layer into two between layers 2B and 3 using a first order interface with no step in velocity across it (i.e. a "pseudo" second order discontinuity). This feature will be discussed in more detail in the next section.

- 5) Finally, the best-fitting travel time model was assessed for amplitude fit. Where necessary, velocity gradients and contrasts across interfaces were adjusted slightly and rechecked for all instruments until a good overall fit, consistent with all data sections, was obtained.

4.3.2 Best-fitting across-axis velocity model

The best-fitting across-axis model, shown in figure 4.5a, is the last in a series of about 2 500 trial models and over 10 000 runs of the *maslov* synthetic seismogram program. Example final ray-traced solutions for DDOBSs 1, 5 and 6 are shown in figures 4.7-4.9, and a complete set of ray-traced solutions for the explosive and airgun data from all instruments can be found in Appendix E.

Ray-tracing programs are sensitive to highly irregular boundary shapes as they produce singularities in the synthesised seismic wavefield (Cary, 1987 and Morgan, 1988) and hence any complex structure must be modelled with care. It proved virtually impossible to define the rugged seabed topography and the sediment and upper basement surface geometries in such a way as to model all low amplitude (shadow) zones successfully and at the same time generate stable solutions to the *maslov* program, devoid of end-point contributions (see Thomson and Chapman, 1986). The main features of the across-axis model are described below and their interpretation and relevance to ridge accretionary processes will be discussed in the following chapter.

- 1) Two off-axis sediment ponds are modelled by discrete blocks ranging in velocity from 2.5 to 2.6 km s⁻¹ and are on average 0.1 km in thickness, but exceed this thickness adjacent to DDOBS 5 and 6 at ~ 65 km model offset. The lateral extent of these ponds is consistent with those imaged on the side-scan sonar data, however the thickness and velocity of these sediment blocks are poorly constrained as sediment diving rays (P_s phases) are not observed as first arrivals. Therefore the delay in arrival times of rays travelling through these areas was used as the primary constraint.
- 2) The first sub-seabed layer to cross the entire model is interpreted as oceanic layer 2A (cf. Spudich and Orcutt, 1980b). The velocity at the top of this layer varies laterally, with P-wave velocities in the range 2.6 to 3.5 km s⁻¹ and an S-wave velocity of 0.9 km s⁻¹. Layer thickness varies between 0.5 km off-axis and 0.8 km on-axis. The lower boundary of this layer is modelled as a second order interface defined by the 4.5 km s⁻¹ P-wave (1.6 km s⁻¹ S-wave) isovelocity contour. The significance of these layer velocities and thickness variations in relation to

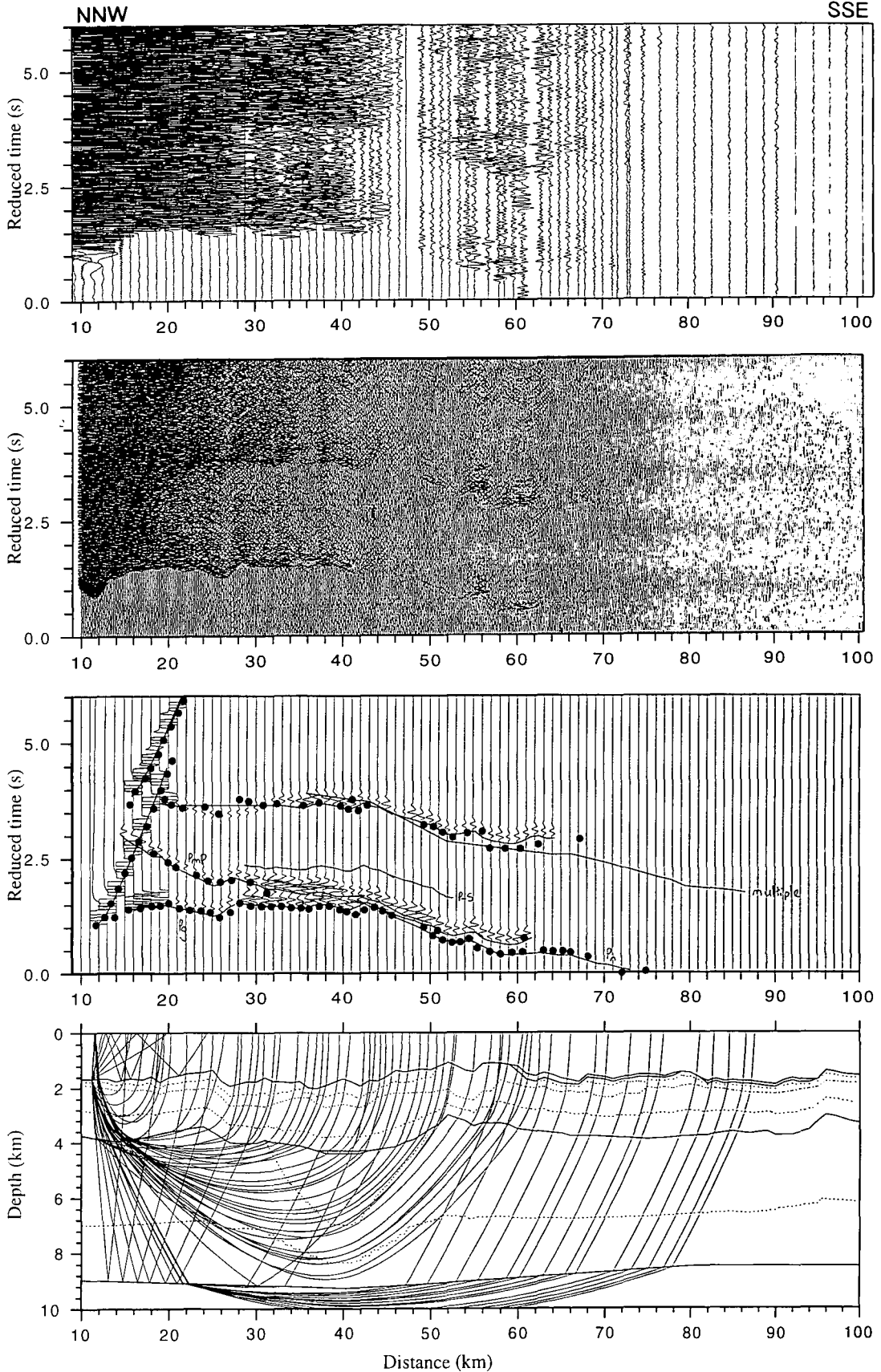


Figure 4.7: Ray-trace modelling of the Reykjanes Ridge final cross-axis wide-angle seismic model for DDOBS 1. The observed travel time picks are indicated by dots and the geometrical ray-traced solution by a solid line. Dot size gives an indication of the modelling error bounds (see section 2.7). Both the observed explosive (top) and airgun (second) vertical geophone component record sections are shown at the same scale as the calculated synthetic seismograms (third) for comparison. Seismograms are plotted at true amplitude with a reduction velocity of 6 km s^{-1} .

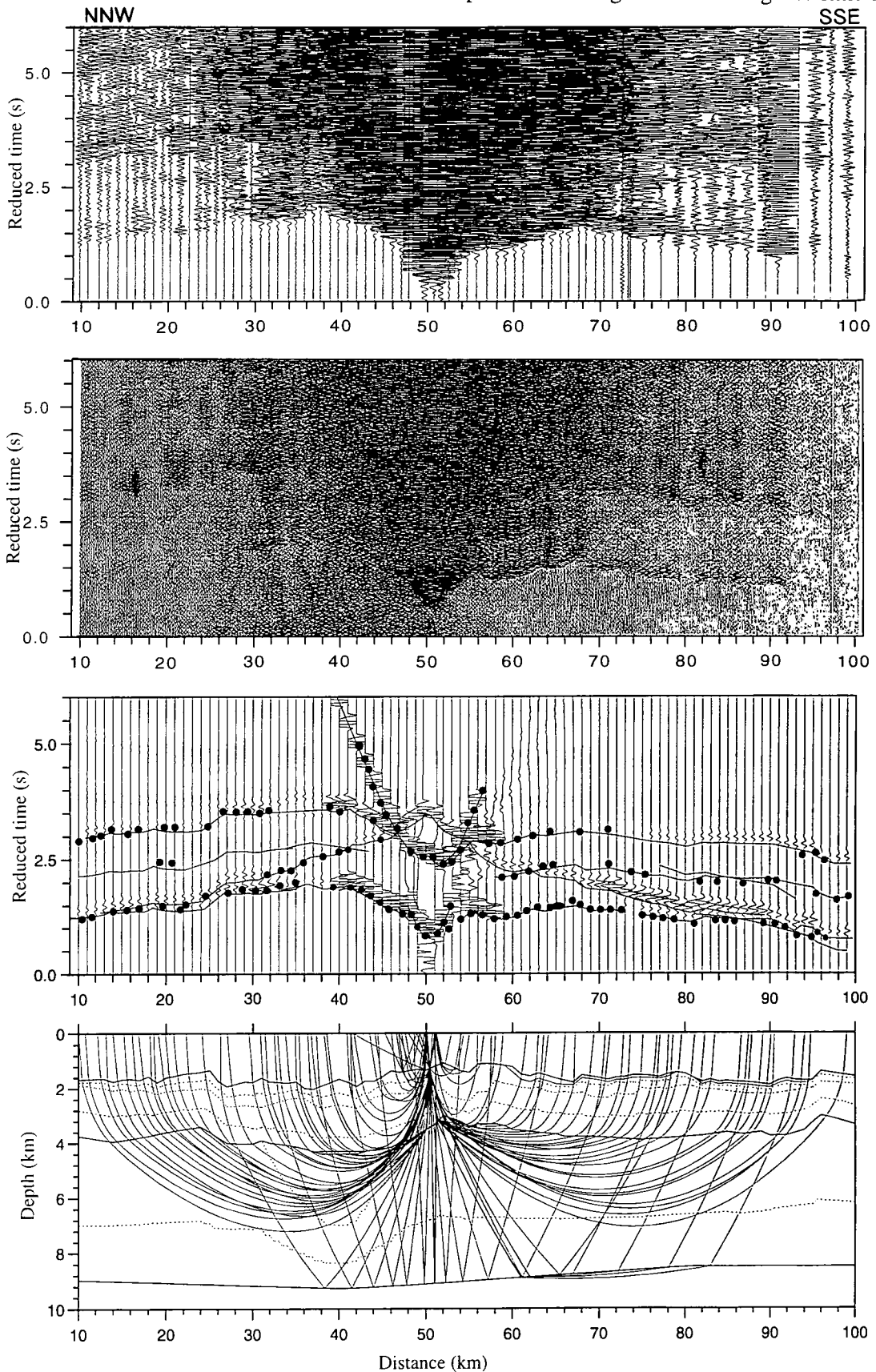


Figure 4.8: Ray-trace modelling of the Reykjanes Ridge final cross-axis wide-angle seismic model for DDOBS 5. The observed travel time picks are indicated by dots and the geometrical ray-traced solution by a solid line. Dot size gives an indication of the modelling error bounds (see section 2.7). Both the observed explosive (top) and airgun (second) vertical geophone component record sections are shown at the same scale as the calculated synthetic seismograms (third) for comparison. Seismograms are plotted at true amplitude with a reduction velocity of 6 km s^{-1} .

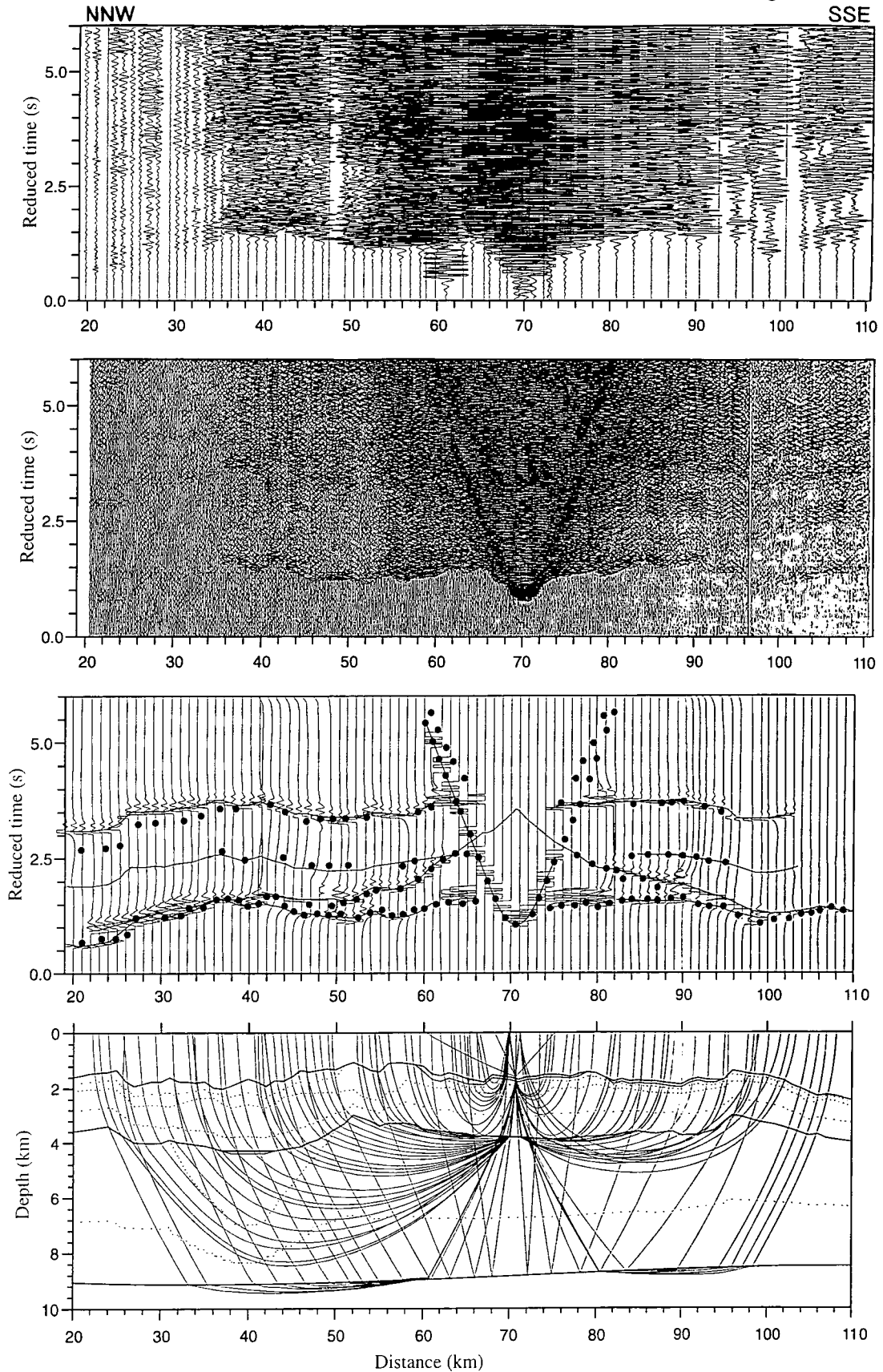


Figure 4.9: Ray-trace modelling of the Reykjanes Ridge final across-axis wide-angle seismic model for DDOBS 6. The observed travel time picks are indicated by dots and the geometrical ray-traced solution by a solid line. Dot size gives an indication of the modelling error bounds (see section 2.7). Both the observed explosive (top) and airgun (second) vertical geophone component record sections are shown at the same scale as the calculated synthetic seismograms (third) for comparison. Seismograms are plotted at true amplitude with a reduction velocity of 6 km s^{-1} .

- ridge dynamics will be described in detail in the next chapter.
- 3) Below the 4.5 km s⁻¹ second order boundary a layer approximately 1.6 km in thickness with velocities in the range 4.5 to 6.5 km s⁻¹ exists. This layer is interpreted as oceanic layer 2B (Bunch and Kennett, 1980; Solomon and Toomey, 1992; Wolfe *et al.*, 1995) and its lower boundary is defined by a first order interface although off-axis there is no distinct P-wave velocity increase specified across it. Beneath the axis P-wave velocities are generally depressed relative to normal oceanic crust by up to 0.8 km s⁻¹ (see figure 4.10), and in general this layer has a relatively low S-wave velocity of 1.6 to 2.4 km s⁻¹. The relevance of these low S-wave velocities in relation to crustal porosity will be discussed in the next chapter (sections 5.2.1 and 5.4).
 - 4) Beneath oceanic layer 2B lies oceanic layer 3 which has P-wave velocities ranging from 6.5 to 7.0 km s⁻¹. This layer is approximately 5 km thick and the velocity just above the Moho is 7.0 km s⁻¹. About 1 km below the top of this layer lies a second order discontinuity which changes the velocity gradient beneath the axis from 1.0 to 1.4 s⁻¹. Once again in the axial region the velocities are depressed by up to 1.5 km s⁻¹ and this low velocity zone extends almost all the way to the Moho.
 - 5) The igneous crustal thickness along almost the entire length of the model is approximately 7.5 km, with an increase of only 0.3 km in the axial region. However, at this depth the resolution of the model is only 0.5-1.0 km (see section 4.4), therefore the topography on this boundary is not well constrained. The upper mantle velocity varies between 7.8 km s⁻¹ on-axis and 7.9 km s⁻¹ off-axis with a gradient of 0.03 s⁻¹ for the upper 11 km of the mantle. Mantle diving rays (P_n) are mainly observed in the explosive data and constrain the Moho and upper mantle from 22 to 93 km offset along the model. The significance of the almost constant crustal thickness in relation to the evolution of oceanic crustal structure with age at ridge axes and the influence of the Iceland hot spot in relation to anomalies in the upper mantle will be discussed in the next chapter (see section 5.5).
 - 6) The most interesting and significant feature of this model is the thin, narrow, low

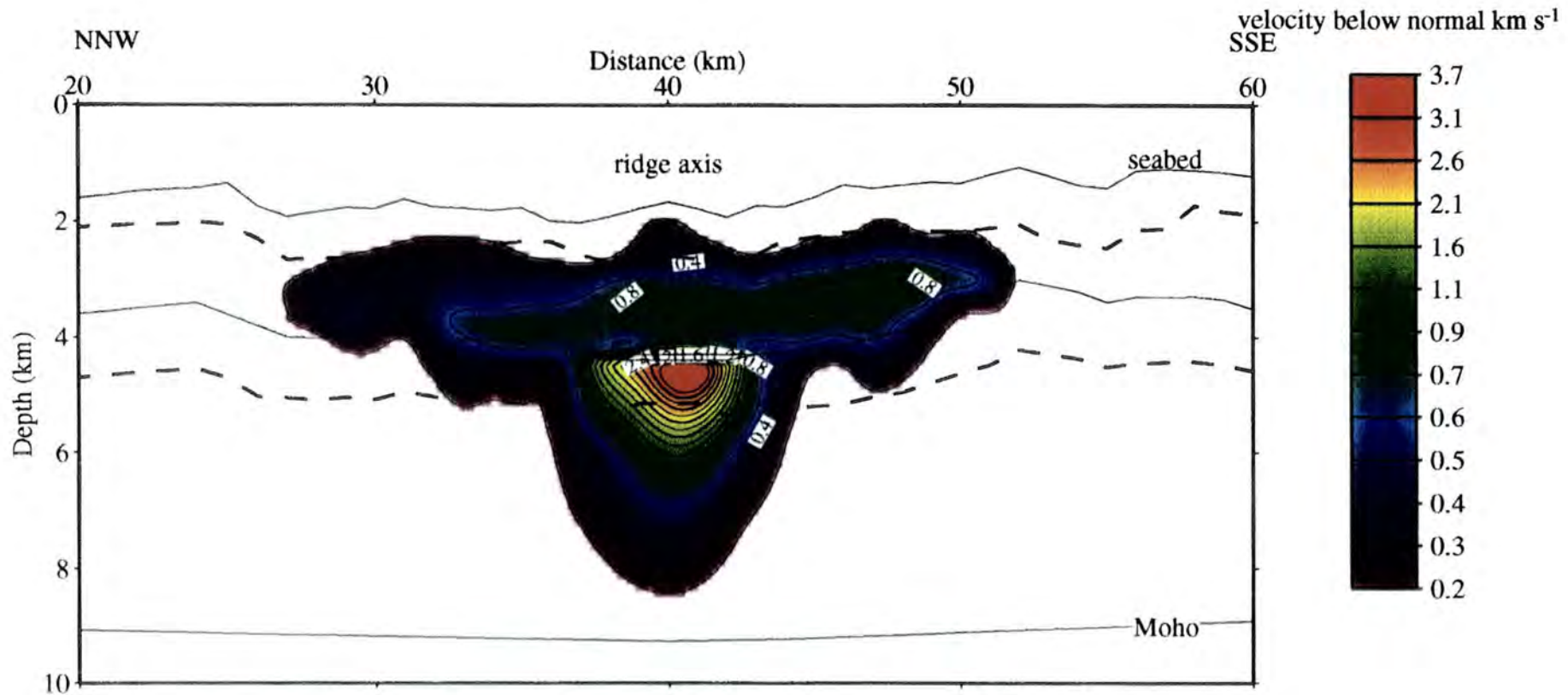


Figure 4.10: Axial velocity anomaly relative to normal oceanic crustal velocities at equivalent depths off-axis. Contours of velocity below normal are in km s^{-1} . The section of the model shown extends 20 km either side of the ridge axis located at 40 km offset. Solid lines represent first order P-wave velocity boundaries and dotted lines second order. From the top of the model the layers consist of the water column, layers 2A, 2B, 3 and the upper mantle. Within layer 2B a zone approximately 20 km wide has velocities up to 0.8 km s^{-1} below normal. This low velocity region narrows to ~8 km in layer 3, with velocities up to 1.5 km s^{-1} below normal, and extends nearly to the Moho. Between layers 2B and 3 lies a low velocity block with velocities some 3.5 km s^{-1} below normal.

velocity block located between 2 and 3 km depth sub-seabed beneath the ridge axis. This discrete block has a velocity of 3.0 to 3.01 km s⁻¹, a thickness of at least 0.1 km and a width of ~4 km. As no crustal diving rays turn within this block the exact location of its lower boundary is uncertain. However, the width and thickness of this body are constrained by the lateral extent of the low amplitude shadow zone it generates in the observed data. The significance of this body in relation to the presence of accumulated melt beneath this slow spreading ridge will be discussed in the following chapter (see section 5.5).

The across-axis final model produces synthetic seismograms which show a good travel time and amplitude fit with the observed data. The synthetic phases generally match the observed to better than 100-150 ms for the explosive and 80-100 ms for the airgun data. The variation in amplitude of seismograms either side of each instrument has also been well matched. Discrepancies in the travel time and amplitude fit occur mainly where steep seafloor boundaries create lateral inhomogeneities which are not smooth compared with the dominant wavelength of the seismic energy (see section 4.5).

Initially no obvious reflected phases were readily observable in the wide-angle record sections. However, modelling of reflections from the top of the low velocity block shows that these would arrive shortly behind the first arrivals on CDOBS 12, 13 and 14 and interfere with both the first arrival and direct water wave wavelets. Hence this interference, combined with the levels of background noise, explains why this phase is not readily observed.

Reflections modelled from the Moho have a relatively high amplitude and when the travel times of this phase were compared with the observed data they were found to match some rather indistinct, lower amplitude secondary arrivals, partially obscured by the later arriving phases. Once identified as P_mP phases, the observed travel times were modelled by adjusting the geometry of the Moho until a good fit was achieved.

Two further secondary phases which are prominently observed on all of the

wide-angle record sections, are multiples and P-S mode conversions (White and Stephen, 1980). For each of the eight instruments multiples occur at a constant time delay, specific to each instrument behind the first arrivals. This delay time is modelled as being equivalent to that obtained if sea surface reflection of up-going phases is occurring at each instrument location (see figure 4.11). Energy reflected at the sea surface undergoes near perfect reflection and hence these phases have amplitudes very similar to the first arriving phases (and in shallow water can interfere with first arrival wavelets and important secondary phases making identification difficult). The travel times of these multiple arrivals have been matched for all instruments.

P-S mode conversions occur where there is a sharp change in S-wave velocity or where the P-wave velocity in an overlying layer is similar to the S-wave velocity in the layer below (White and Stephen, 1980). By modelling the delay of these phases behind the first arrivals they can be seen to have an origin close to each instrument. The delay time of the P-S mode conversion is relatively large at approximately 1 s, and initially some were identified as P_mS arrivals, i.e. a P-wave converting to an S-wave at the Moho adjacent to an instrument. P_mS arrivals are only observed if there is a sharp change in velocity at the Moho or a transition zone that is less than a quarter of the incident P-wave wavelength in width (Télez and Córdoba, 1996) and are therefore indicative of off-axis melt ponded at the Moho (Garmany, 1989). However, modelling of these arrivals as mode conversions at the Moho revealed a mismatch in travel time and geometry (see figure 4.12). Mode conversion at the 2B–3 layer boundary, with very low S-wave velocities in both layers 2A and 2B, provided a good fit of both travel times and amplitudes. The very low S-wave velocities will be discussed further in the next chapter (see sections 5.2.1 and 5.4).

4.3.3 Best-fitting along-axis velocity model

The best-fitting along-axis model, shown in figure 4.5b, is the last in a series of over 2 000 trial models and approximately 9 000 runs of the *maslov* synthetic seismogram program. Example ray-traced solutions for the explosive data from DDOBSs 3 and 4 are shown in figures 4.13 and 4.14. The complete set of ray-traced

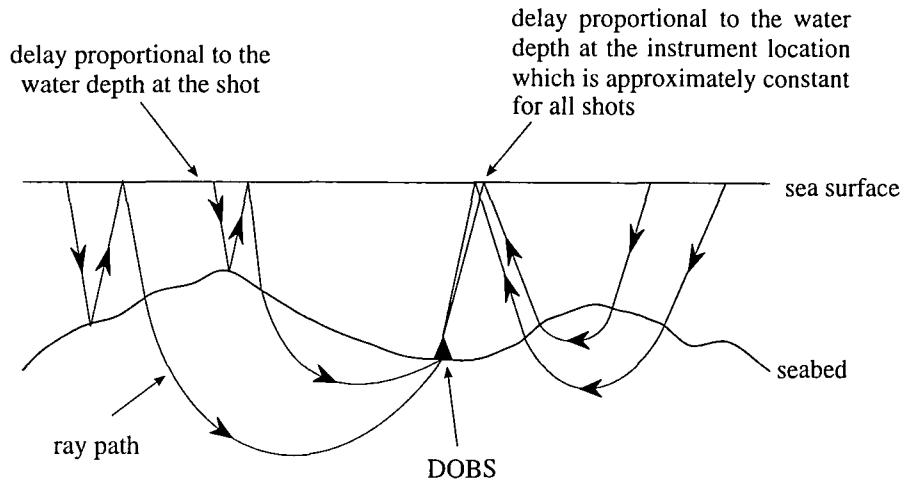


Figure 4.11: Two possible sources of water wave multiples.

The water wave from the shot can reflect from the seabed and sea surface before travelling through the crust to the DOBS. This would produce a delay behind the first arrival proportional to the water depth at the shot. If the seabed has varying depth with offset, such as at the Reykjanes Ridge, the multiple delay time behind the first arrival will vary across the seismic section.

or

The water wave travels through the crust and water column then reflects at the sea surface before arriving at the DOBS. This travel time delay would be proportional to the water depth near the instrument and would therefore be approximately constant across the seismic section for each instrument. This latter kind of multiple is of the type most commonly observed on deep-water DOBS data sections.

models for the explosive and airgun data from all instruments located along this line can be found in Appendix E.

The along-axis line parallels the main strike of ridge features and hence the final model shows a good deal of lateral homogeneity and is effectively one-dimensional in most respects. The axis is sediment free and the change in seabed topography is minor compared with the across-axis line. The main features of the best-fitting along-axis model are as follows:-

- 1) The water column velocity structure is identical to that of the across-axis line with variations in velocity of between 1.479 and 1.495 km s^{-1} .
- 2) As the axis is sediment free the first sub-seabed layer is identified as oceanic layer 2, which is subdivided by a second order discontinuity into an upper layer (layer 2A) of P-wave velocity 2.6 to 4.5 km s^{-1} and S-wave velocity 0.9 to 1.6 km s^{-1} , and a lower layer (layer 2B) of P-wave velocity 4.5 to 5.95 km s^{-1} and S-wave velocity

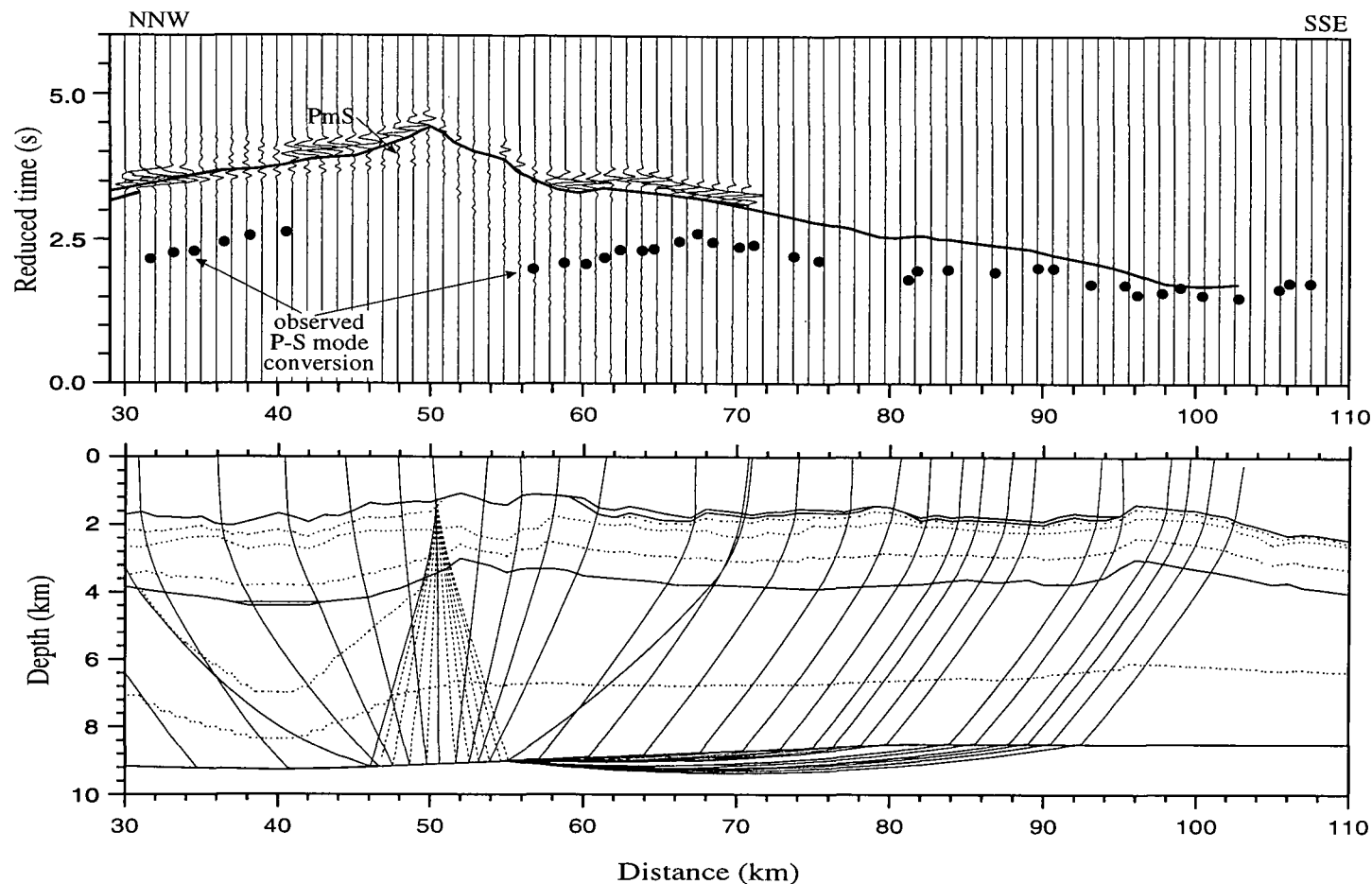


Figure 4.12: Ray-traced model and synthetics for P_mS arrivals, i.e. mode conversion at the Moho. The synthetic seismograms (upper) are plotted with a reduction velocity of 6 km s^{-1} with the solid lines representing the calculated arrival time of the P_mS phase. Dots represent observed travel times of the secondary phase seen in the data and interpreted as a mode conversion. The dashed ray paths represent travel as an S-wave and the solid ray paths are P-waves. Although the travel time match of the calculated P_mS to the observed arrival could be improved the S-wave velocities required would be unrealistically high and the geometry of the calculated arrival does not match the observed arrival.

- 1.6 to 2.4 km s⁻¹, consistent with the across-axis model. Layer 2A varies in thickness from 1.3 km at the northern end of the line to 0.9 km at the southern end and thins to 0.4 km in the centre of the AVR. In contrast, layer 2B is 0.9 km in thickness in the north, 2.0 km in the centre and 1.4 km in thickness at the southern end of the model.
- 3) Beneath the layer described above lies a layer representing oceanic layer 3 which is approximately 4.8 km in thickness. This layer is subdivided by a change in velocity gradient corresponding in depth to the 6.1 km s⁻¹ isovelocity contour. At the top of this layer the velocity is approximately 5.95 km s⁻¹ and at the base ~7.0 km s⁻¹. Velocity gradients are ~0.9 s⁻¹ and 0.2 s⁻¹ above and below the second order boundary respectively.
 - 4) Due to the short length of this line (~ 40 km) no significant P_n arrivals are observed and the Moho and the upper mantle are poorly constrained. Therefore the Moho is represented by a horizontal boundary at a depth of 9.25 km below sea level as defined by the Moho depth at the intersection point with the across-axis line. The upper mantle is defined with a velocity of 7.8 km s⁻¹ directly beneath the Moho and a gradient of 0.03 s⁻¹ down to a depth of 20 km below sea level. These values were again obtained from the across-axis model.
 - 5) The most interesting feature of this model is the layer associated with the very low velocity body modelled beneath the across-axis line. Within the resolution of the data and the constraints of the modelling package, this layer appears to be continuous beneath the entire length of the AVR, with features identical to those observed across-axis, i.e. velocities between 3.0 and 3.01 km s⁻¹ and a thickness of ~0.1 km. The continuity of this body along-axis and the modelling of its upper and lower boundaries as distinct interfaces rather than gradient zones, will be discussed in Chapter 5 in relation to the interpretation of the normal incidence reflection data.

The travel times and amplitudes of the synthetic data fit the observed data well. The variation in amplitude with range, i.e. the shadow zone and related re-arrival of lower crustal phases, constrain the velocity and thickness of the sub-axis low velocity

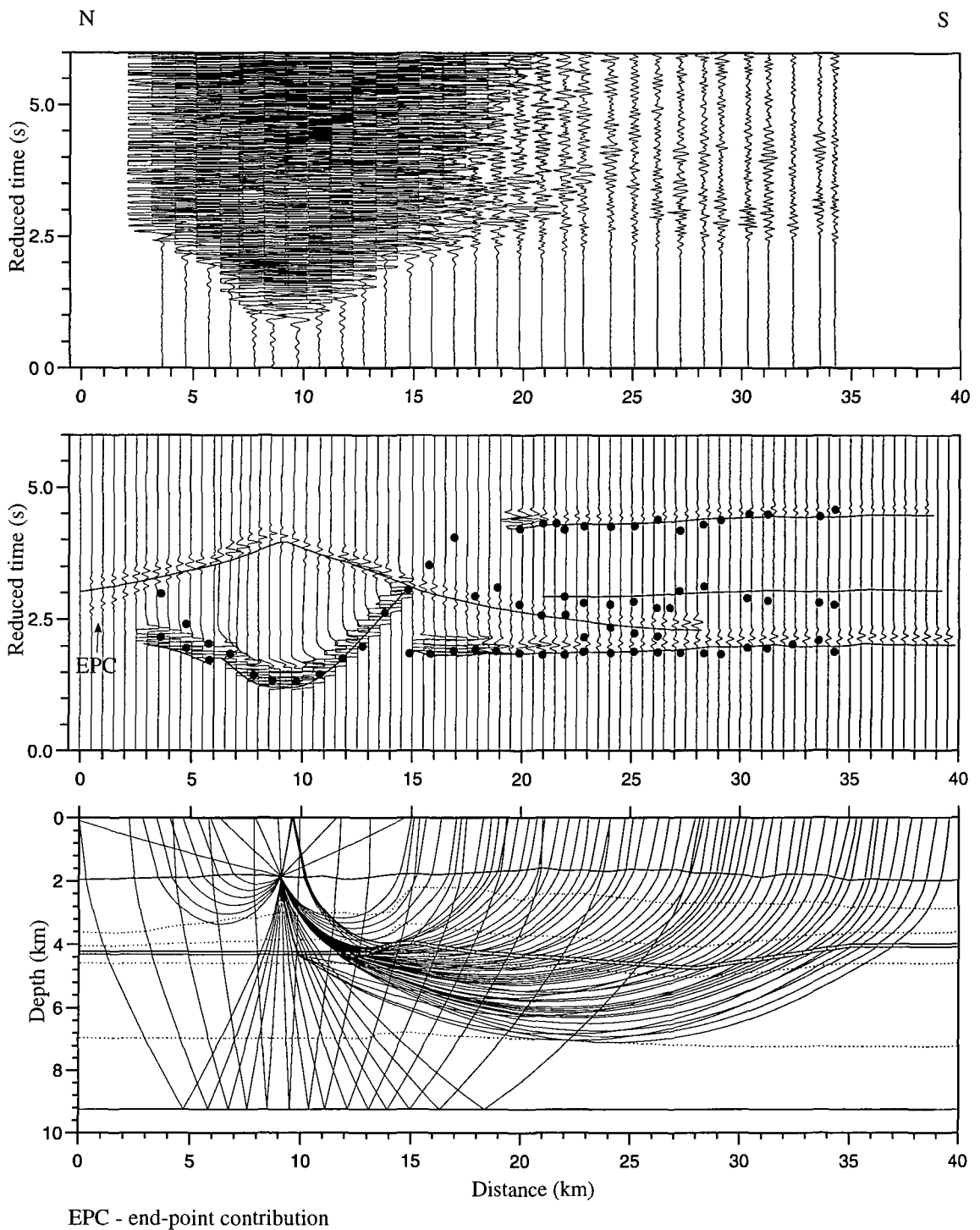


Figure 4.13: Ray-trace modelling of the Reykjanes Ridge final along-axis wide-angle seismic model for DDOBS 3. The observed travel time picks are indicated by dots and the geometrical ray-traced solution by a solid line. Dot size gives an indication of the modelling error bounds (see section 2.7). The observed explosive (top) vertical geophone component record section is shown at the same scale as the calculated synthetic (middle) seismograms for comparison. Seismograms are plotted at true amplitude with a reduction velocity of 6 km s^{-1} .

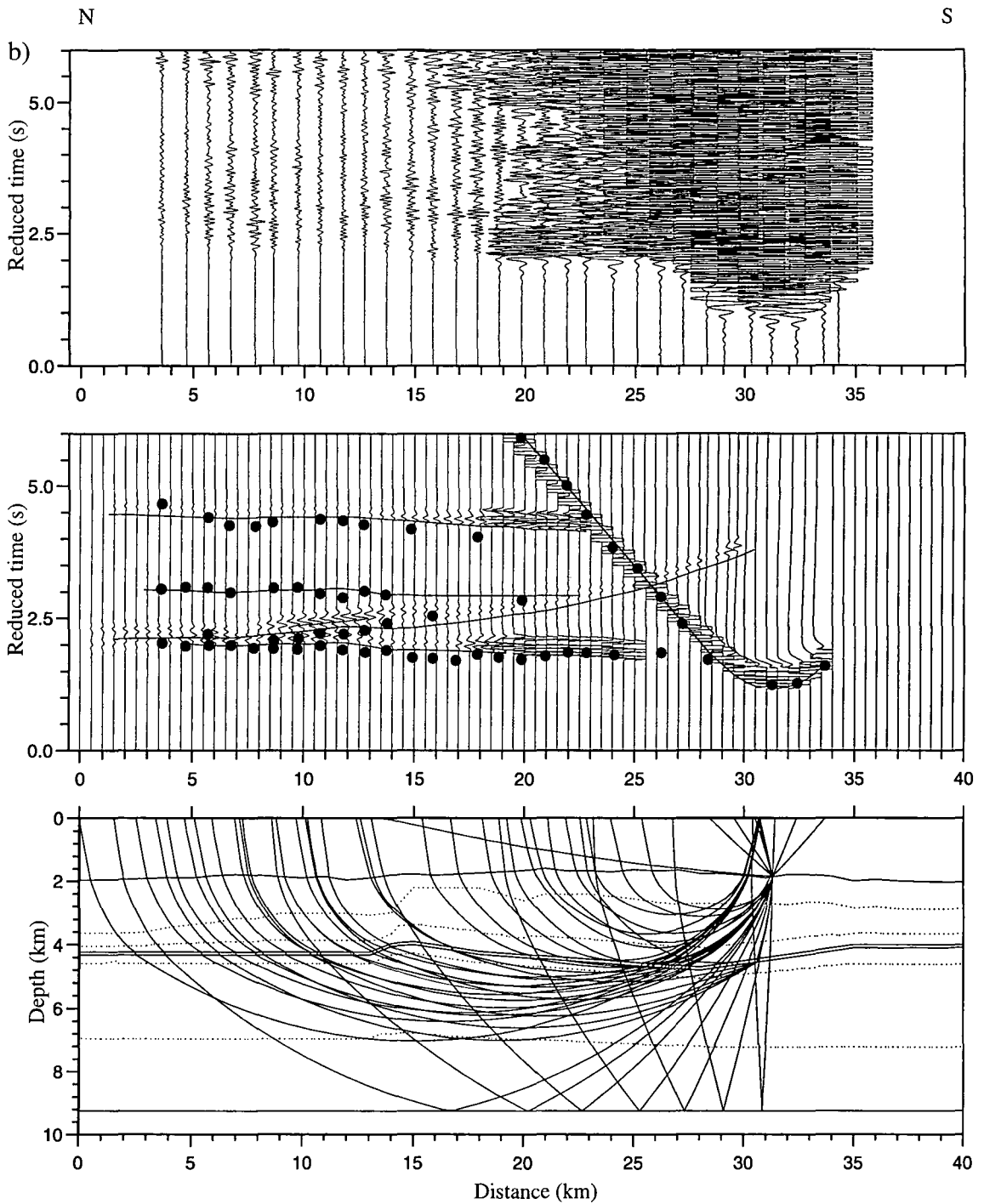


Figure 4.14: Ray-trace modelling of the Reykjanes Ridge final along-axis wide-angle seismic model for DDOBS 4. The observed travel time picks are indicated by dots and the geometrical ray-traced solution by a solid line. Dot size gives an indication of the modelling error bounds (see section 2.7). The observed explosive (top) vertical geophone component record section is shown at the same scale as the calculated synthetic seismograms (middle) for comparison. Seismograms are plotted at true amplitude with a reduction velocity of 6 km s^{-1} .

zone (see figure 4.14).

The Moho and upper mantle in this model are unconstrained due to the lack of observed P_n phases in the wide-angle data sections. However, they are constrained at the intersection point with the across-axis line and synthetic P_n and P_mP phases have been modelled and compared to the observed data in an attempt to explain why no P_n or P_mP phases were observed. Calculation of P_mP phases indicated that they are of very low amplitude compared with first arrivals due to the low axial velocities and, when compared in position and time with the observed data, they can be seen to be present even though the signal-to-noise ratio is low. P_n phases are not observed because they arrive beyond the ends of the model. Again multiples have a constant delay, specific to each instrument, behind the first arrivals. The P-S mode conversions observed are also well matched in both travel time and amplitude. S-wave splitting is also not observed in the data, hence there is no evidence of anisotropy.

4.4 Modelling resolution

The resolution of the modelling method adopted for this study, was investigated by adjusting layer velocities and depths to interfaces and examining how these changes affected the fit between synthetic and observed seismograms. A change of $\pm 0.1 \text{ km s}^{-1}$ in velocity and $\pm 0.2 \text{ km}$ on the depth of upper crustal interfaces was sufficient to generate synthetics which did not match the observed phases. The resolution on the depth to the Moho is much less, particularly so for the along-axis line, at about 0.5-1.0 km, which corresponds to approximately a wavelength of the explosive seismic source used in this survey. This resolution at Moho depths indicates that the topography modelled on the Moho (see section 4.3.2) is not well resolved. The upper mantle velocity variation with depth and offset is not well constrained.

4.5 Modelling techniques applied to the dataset

For the majority of the modelling process, the Maslov method was employed using the program *maslov*. Only when in the final stages of modelling, were the models converted into the format required by programs based on the numerical solution of asymptotic ray theory (ART) (*rayinvr* – Zelt and Smith, 1992) and the use of Gaussian beams (*beam87* – Cervený, 1985a and b) to overcome the singularities at which ART breaks down due to limitations in the ray coverage. These additional methods were applied to trace the final models in an attempt to identify and minimise tracing artefacts in the synthetic seismograms and as a check on the uniqueness of each model.

Unlike normal incidence data, wide-angle seismic data cannot be directly interpreted as knowledge of velocity and density variations along the entire ray path is required. The only exact solution is that given by the reflectivity method (Fuchs and Müller, 1971) which is limited to one-dimension (i.e. no lateral variation and ideal for truly strike lines). In two dimensions the inverse problem of solving the elastodynamic equations for travel time and amplitude is non-linear (Chapman and Drummond, 1982; Cervený, 1985a; Weber, 1988; Matthews, 1993). Solving the elastodynamic equations numerically, e.g. by using the finite difference or finite element methods, is computationally expensive and therefore forward modelling techniques are preferred and more widely used. Asymptotic ray theory is based on an approximation to the wave equation and describes body wave propagation in inhomogeneous media, in which lateral and vertical variations are smooth on the scale of a seismic wavelength. ART calculates the entire wavefield using contributions from reflected, refracted and multiple phases. However, the method fails at caustics, shadow zones and critical points where the media is not smooth (Ben-Menahem and Beydoun, 1985; Beydoun and Ben-Menahem, 1985). These special cases are often of most interest to crustal seismologists as they tend to be caused by the features of most interest (e.g. shadow zones and melt bodies), and hence ART is generally combined with a different technique valid for such aspects of a model, e.g. WKBJ, Maslov, Gaussian beams and Kirchhoff integrals.

The modelling techniques used in this dissertation are:-

- *Maslov* which combines the advantages of the ART and transform methods using WKBJ seismograms.
- *Beam87* which uses the Gaussian beam technique with a finite beam width to overcome the spatially limited ray paths associated with ART.
- *Rayinvr* which solves ART numerically and can invert the data allowing an estimate of parameter uncertainty. The inversion is linearized by beginning with a model and inverting iteratively.

In the three ray-tracing techniques used, rays are traced from one shot to several receivers. The experiment geometry was the reverse of this, with few receivers and many shots. This reversed geometry has no effect on the calculation of travel times and ray paths. However, as transmission coefficients travelling in opposite directions across a boundary differ, it does affect phase amplitudes. In general the difference in transmission coefficients and amplitudes for forward and reversed rays is small where lateral velocity gradients and boundary dips are low (Matthews, 1993). Hence it is valid to ray-trace with this reversed geometry for most of the Reykjanes Ridge, however the validity of the amplitudes may be suspect in regions where the seabed has a steep dip.

4.5.1 *Maslov*

Maslov is a ray-tracing technique that combines ART with WKBJ seismograms (Chapman and Drummond, 1982) to obtain a uniform solution. The WKBJ transform solution calculates the amplitude in the spatial domain and in the position and slowness domain. Singularities in the spatial domain are known as x-caustics and in the mixed domain of position and slowness are y-caustics. In these two domains singularities occur in different locations, hence by combining the solutions many singularities are overcome. The program *maslov* (originally written by Drummond op. cit., rewritten by D.G. Lyness, University of Cambridge, in a modular form and S. Horsefield, University of Cambridge, to run under Unix using the UNIRAS graphics package) is based on Maslov ray theory.

Model layers are defined by inhomogeneous (type 1) and homogeneous (type 2) blocks. Type 1 blocks are defined by rows of horizontal positions, depths, P-wave and

S-wave velocities, and densities for the first order boundaries at the top and bottom of the block, with equal numbers of points defining each boundary. Type 2 blocks are defined by the four corners of the region. Each block type may contain second order boundaries across which only the velocity gradient changes. Also blocks do not have to extend across the full width of the model. The shot may be placed anywhere within the model and receivers are located along a boundary, generally the upper surface of the model which may, or may not, be a free surface.

The modelling program adds semi-infinite, type 2 blocks at the left and right-hand ends of the model. To allow the modelling of complex structures, the model is divided into triangles with linear velocity gradients along each side. The linear gradients within these triangles cause the ray to follow a circular path which is computationally efficient. Elementary rays are defined by slowness bounds between which rays are traced at a user specified step interval and the boundaries at which reflections and mode conversions can occur are also user specified. These slowness bounds form the limits of integration in the calculation of synthetic seismograms and can cause arrivals associated with these end-points. Therefore the slowness bounds may have to be calculated to prevent spurious end-point contributions (Thomson and Chapman, 1986) from interfering with the "real" arrivals. The program ray-traces the model and is menu driven to allow calculation of synthetic seismograms and a variety of plots of the observed and synthetic data. The weighting between ART and WKBJ solutions is designed to test for y-caustics, where these are likely to occur and the WKBJ solution breaks down the ART solution is used. It is possible for the user to adjust the balance of the solutions and when the test value is higher than a user specified value, e.g. at y-caustics, the ART solution is used. As the WKBJ solution is more accurate the user specified value should be biased towards this solution. The WKBJ solution also breaks down at end-points therefore ART is automatically used in preference in these regions (Morgan, 1988).

The model can be output in the format required by the gravity modelling program *grav2d* as constant density blocks based on the P-wave velocity or the density input into the seismic model. A subroutine was added to the *maslov* program to down-sample the data and output the model files in the format required by *rayinvr*.

4.5.2 *Beam87*

Many of the singularities at which ART breaks down are caused by considering a limited number of rays. The Gaussian beam method overcomes this limited ray coverage by using a beam of finite width with a Gaussian profile (Cerveny, 1985a and b). However it relies on an unphysical parameter, the beam width, which is difficult to select so that it is valid for a wide range of models and types of arrival (Cary, 1987). The *beam87* programs (written by Cerveny, op. cit.) are based on this Gaussian beam method and consist of separate programs for ray-tracing, plotting ray-traced models and calculating synthetics:-

- B87_RT* calculates ray paths and travel times through the model.
- B87_RP* plots ray diagrams, travel times and observed arrivals.
- B87_GB* calculates the frequency response at specified receivers by solving the parabolic wave equation for a set of overlapping beams and summing the solutions with a Gaussian beam distribution – this may fail in regions of strong lateral inhomogeneity.
- B87_SYNT* calculates synthetic seismograms by combining the frequency response with the source signature using an inverse Fourier transform. Low frequencies are filtered out as the Gaussian beam method is a high frequency approximation.
- B87_TOR* converts the synthetic seismograms to SEG-Y_i format which can then be plotted with *dazzle*.

The model can be defined by up to 30 points on isovelocity interfaces which are used to divide the model into triangles with linear velocity gradients along the sides. Boundaries may be fictitious (i.e. do not generate reflections) and layers can pinch out to zero thickness. Receivers lie along the surface of the model and the shot may be anywhere within it. Rays may be specified by initial value ray-tracing (which does not necessarily generate a sufficient density of ray end-points in the vicinity of the receivers to produce synthetic seismograms) or by interval ray-tracing where at least one ray must end in a specified region.

4.5.3 *Rayinvr*

Rayinvr consists of a series of programs written by C.A. Zelt (Zelt and Smith, 1992) which solve the ART equations numerically. Models are defined by the depth to the top of a layer and P-wave velocities at the upper and lower boundaries, with these variables being specified at arbitrary horizontal positions. It is not possible to define a change of velocity gradient within a block (two separate blocks must be used) and all boundaries must extend the full width of the model. When ray-tracing, the model is divided into a series of trapezoids with vertical left and right boundaries and linear velocity gradients along each side. To check model input, the program *vmodel* identifies crossing boundaries, velocity inversions and extremes of velocity and gradient. This program also plots the velocity model, velocity–depth profiles and can convert the model into two-way travel time.

Rayinvr and *tramp* use initial value or two point ray-tracing with a variable, user specified step length along the rays. The step length is decreased as velocity gradients increase. Poisson's ratio within layers or individual trapezoids can be specified to enable modelling of S-waves. A smoothing option is available to smooth layer boundaries using a three point averaging filter to reduce geometrical shadow zones due to steep gradients. *Rayinvr* and *tramp* calculate travel times and can plot these for comparison with observed travel times. *Tramp* also calculates the amplitudes according to zero order ART and produces an input file for *pltsyn* which plots the calculated synthetic seismograms.

The *rayinvr* programs are designed for inversion of travel times. An initial model is formed and the layers within which the observed seismic phases turned are identified, often forward modelling is necessary to identify these phases. The model is ray-traced using *rayinvr* which calculates the travel times and partial derivatives for each receiver location by linear interpolation between the nearest two end-points. These travel times and partial derivatives are input to *dmplstsqr*, which is a damped least squares inversion program that adjusts the velocity model and calculates the standard deviation of the synthetic and observed travel times. The inversion is repeated until an acceptable standard deviation is achieved. To increase the stability of the inversion the

number of nodes must be reduced. The inversion takes no account of amplitudes, hence it has little control of velocity gradients and velocity inversions.

4.6 Comparison of the results obtained with the individual techniques

The best results were achieved using the *maslov* method which allowed close ray path spacing to be produced in areas with steep boundaries and sharp velocity variations, impossible with either of the other methods. The main disadvantage of the *maslov* method is the generation of end-point contributions (see Thompson and Chapman, 1986; Morgan, 1988; Peirce, 1990a) which often interfere with and distort synthetic waveforms and affect amplitude calculations (see figure 4.15). End-point contributions are caused by the limits of the integration used in the Maslov method, hence the solution is not evaluated for all ray parameters – i.e. it is truncated and smoothed. A further problem occurs in regions with complex boundaries where *y*-caustics are generated which in turn result in rapid amplitude variations (Cary, 1987), possibly explaining the amplitude variations observed in the synthetic data seen over severe seabed topography.

The main problems experienced with *rayinvr* are caused by the way in which the model must be defined within the constraints of the program. All boundaries must extend across the entire width of the model and interfaces are limited to being first order, although there need not be a change in actual velocity across a boundary. To define the discrete axial low velocity block within the first of these restrictions, the boundaries of the block had to be extended to the edges of the model. Away from the axis the layer had to be given zero thickness with the boundaries coinciding in depth and velocity with those of the layers above and below (see figure 4.16), causing considerable difficulty in getting rays to pass through this layer (see figure 4.17). Also with this method rays are defined by the block in which they turn and hence a separate ray packet must be defined for each block. These separate ray packets, combined with the restriction of first order boundaries, resulted in gaps in the ray coverage. It was not possible to model the multiples or P-S mode conversions observed on any record section using this method. However, synthetic travel times and amplitudes calculated using both

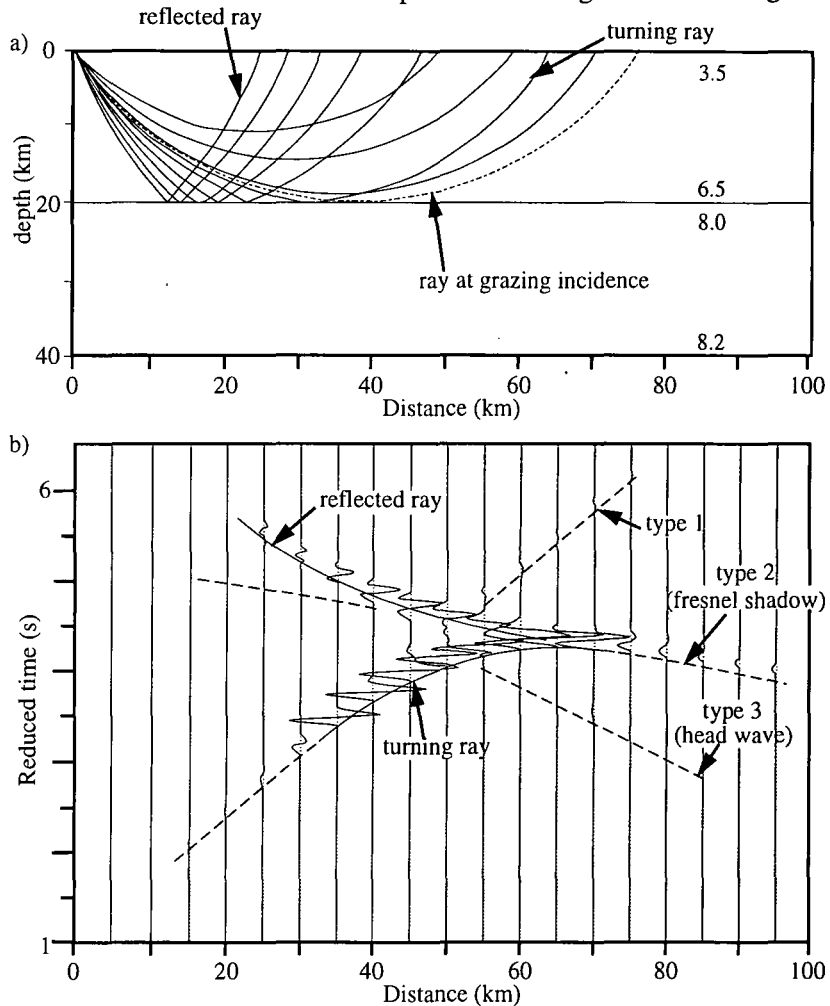


Figure 4.15: End-point contributions in synthetic data generated by *maslov* (after Morgan, 1988). a) Ray diagram for a two layer model and b) the synthetic seismograms calculated for these rays. The end-point contributions labelled are: type 1 – associated with the limits of integration; type 2 – related to the grazing ray; and type 3 – a head wave. Note the effects these can have on calculated seismogram amplitudes.

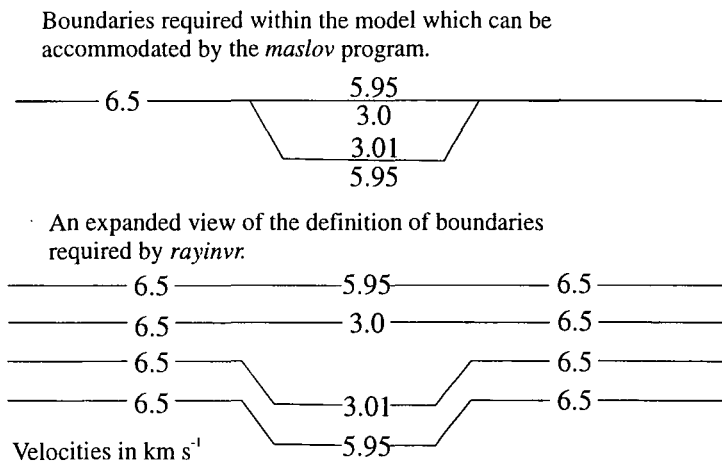


Figure 4.16: Definition of the axial low velocity block for input into the ray-tracing program *rayinvr*. As blocks must extend across the entire width of the model, to define a discrete block the thickness of the layer either side of the low velocity region must be reduced to zero and the velocities equated to those at the base of the layer above. This definition causes four first order boundaries to coincide at a point where a single second order boundary is required and can create problems when ray-tracing.

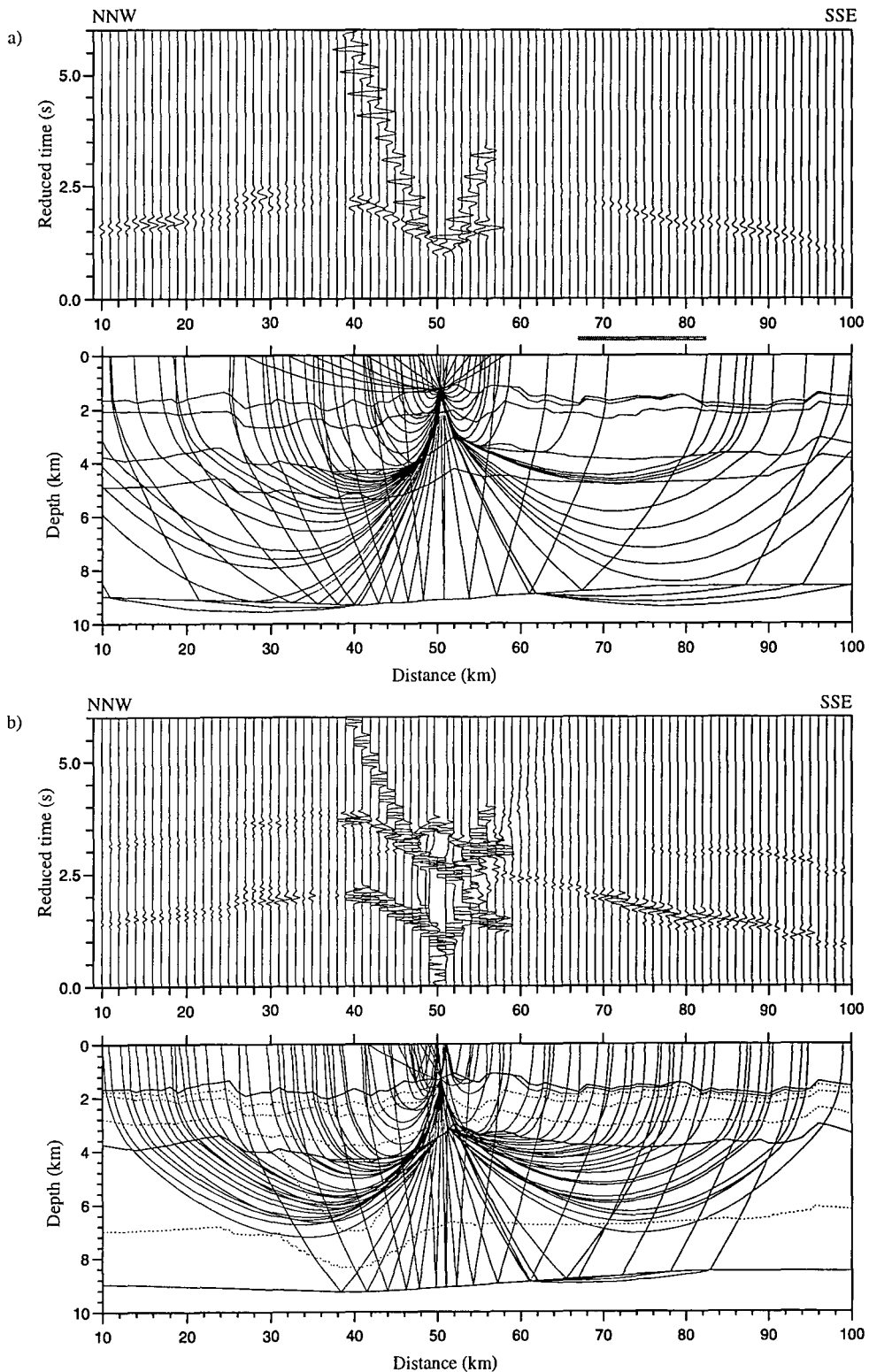


Figure 4.17: Comparison of synthetic data generated with *rayinvr* (a) and *maslov* (b) for DDOBS 5. Sections are plotted reduced at 6 km s^{-1} . Multiples and P-S mode conversions have not been calculated with *rayinvr*. Note the similarity in relative amplitudes of arrivals to the NNW of the instrument with low amplitudes occurring where arrivals have passed through the low velocity layer. To the SSE of the instrument boundary geometries create difficulties in generating arrivals with offsets of 67 to 82 km (shaded line, top diagram). In this region only reflections are seen with *rayinvr* as it is impossible to generate arrivals in this region. However with *maslov* it is possible to generate arrivals which provide a constraint on travel times although the amplitudes in this region are much lower than observed in the data (see figure 4.8).

the *rayinvr* and *maslov* programs agree well with each other (figure 4.17), giving confidence that both final models are valid solutions to the along and across-axis datasets. Unfortunately, the *rayinvr* inversion program only works efficiently with a small number of velocity and depth nodes specifying each boundary – restricting the accuracy with which complicated interface geometries (such as the seabed in ridge work) can be modelled. Finally, the *rayinvr* inversion cannot resolve velocity inversions with depth and hence performed poorly for any model which contained an axial low velocity zone.

Under the limitations of the *beam87* method it proved impossible to represent the lateral two dimensionality of the across-axis line in any way and hence no further attempts were made to model the across-axis data with this method. However, as the along-axis model is more one-dimensional in structure, it proved a fairly simple task to ray-trace this model with *beam87* until the along-axis low velocity zone was incorporated into the model, at which point no rays could be traced through the model. The *beam87* method was therefore abandoned at an early stage.

Amplitude calculations from all three modelling techniques described above are based on ray theory and therefore only accurate if lateral and vertical variations are smooth on the scale of a seismic wavelength. This is clearly not the case at the 100 m thick low velocity zone as, at the corresponding depths the seismic wavelength is of the order of hundreds of meters. Therefore to verify the amplitude calculations used in this region to model the thickness and velocity of the low velocity layer an alternative technique for calculating synthetic data was required. The *reflectivity* method (for theory see Fuchs and Müller, 1971; and a comparison with other modelling techniques see Chapman and Orcutt 1985) as previously mentioned is restricted to one-dimensional models. However the *reflectivity* method is not limited by the scale of any vertical variations and is therefore valid for a layer 100 m in thickness. The *reflectivity* program calculates the response of layers with constant P and S-wave velocities and density, so by combining numerous thin layers a velocity gradient can be simulated. The amplitude calculation includes all possible reflections, transmissions and conversions together with

attenuation and the accuracy of the technique is only limited by the number of layers used.

The final along-axis wide-angle seismic model had least horizontal variation and was therefore converted into a 1-D model (see figure 4.18) to compare the amplitudes of synthetic data generated by *maslov* and *reflectivity* methods for a model relevant to the Reykjanes Ridges wide-angle seismic dataset. In *maslov* ray-tracing the velocity–depth points specified in table 4.1 were linked by linear gradients and the following phases and their multiples were ray-traced and the synthetics calculated are shown in figure 4.18b:-

direct water wave;

P_g ;

P_mP ;

P-S mode conversion below the instrument at the base of layer 2B; and reflection from the top of the low velocity layer.

For the *reflectivity* program the model was divided into 535 homogeneous layers, each approximately 18 m in thickness in the crust and 200 m in thickness in the mantle (see figure 4.18a and table 4.1), all P-P and S-S reflections were considered to calculate the synthetics shown in figure 4.18c.

	depth (km)	V_p (kms ⁻¹)	no. layers
sea water	0	1.479	0
	1.888	1.495	90
2A	1.888	2.4	1
2B	2.706	4.5	50
	4.6	5.95	95
low velocity layer	4.6	3.0	1
	4.7	3.01	10
layer 3	4.7	5.95	1
	5.55	6.1	40
	9.25	7.0	200
mantle	9.25	7.8	1
	20	8.2	50

Table 4.1: 1-D velocity–depth points used to compare amplitudes calculated by *maslov* and *reflectivity* modelling. The "no. layers" refers to the number of homogeneous layers the model as divided into between adjacent velocity–depth points for reflectivity modelling (see also figure 4.18a).

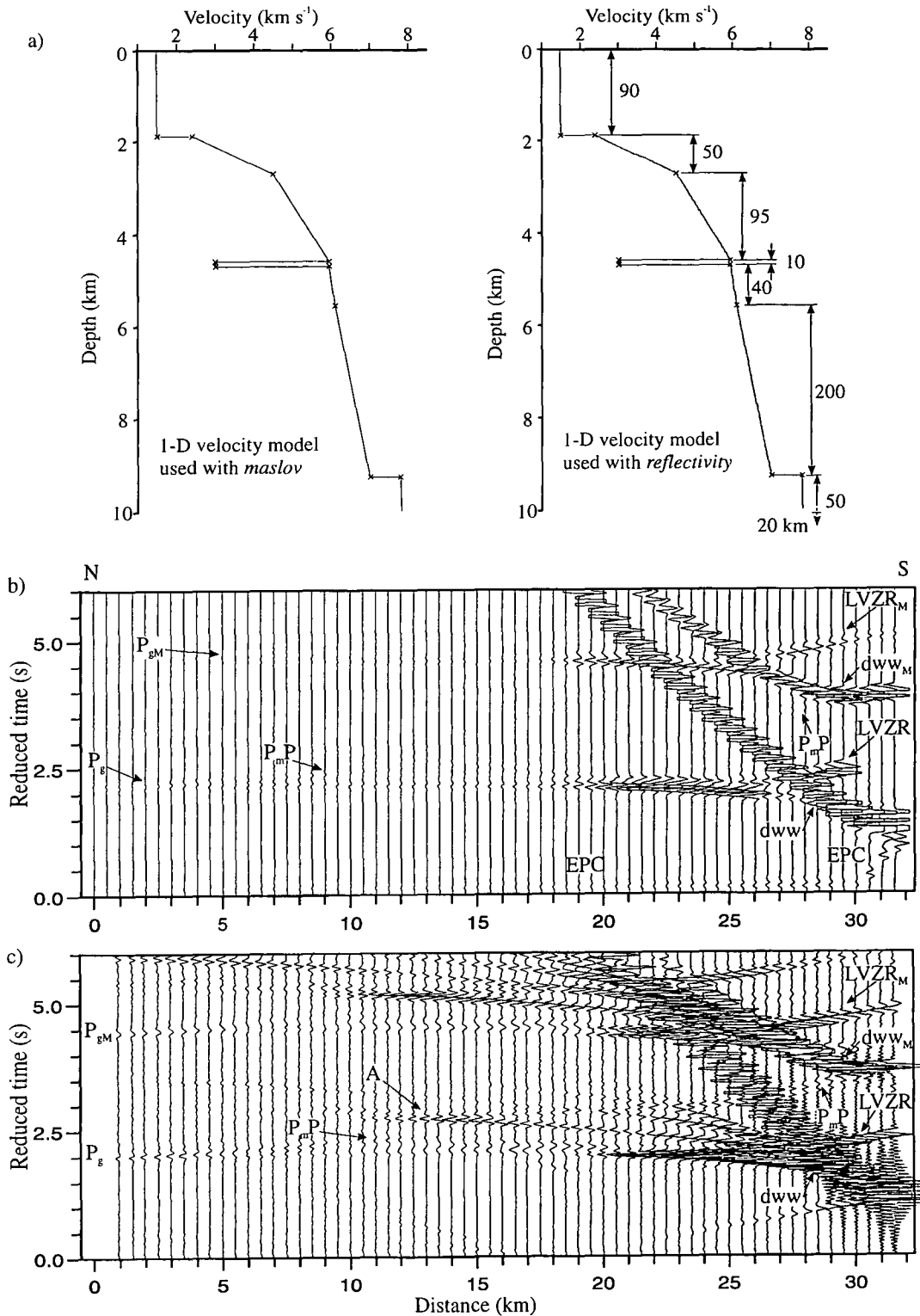


Figure 4.18: Comparison of the results of *maslov* and *reflectivity* modelling of the 1-D models shown in a). The numbers on the right of the model used for the *reflectivity* modelling indicate the number of homogeneous layers inbetween velocity–depth points.

b) Synthetic data generated by *maslov*. The low amplitudes seen from 26 to 28 km occur as rays were not traced in this region due to the associated end-point contributions.

c) Synthetic data generated by *reflectivity*. "A" indicates a phase which is doubly reflected within layer 2A (see text) which is not observed on b). Both sections are plotted reduced at 6 km s⁻¹.

The main phases labelled are:- dww – direct water wave; P_g – crustal diving ray; P_mP – Moho reflection; LVZR – reflection from the top of the low velocity layer; EPC – end-point contribution; and _M – the multiple of a phase.

As the thickness and velocity of the low velocity zone in the final along-axis wide-angle seismic model is largely constrained by the amplitude of the first arriving phase (P_g) the comparison of relative amplitudes of this phase between the two synthetic datasets indicates the applicability of using ray theory for this model. Travel times for all phases modelled with *maslov* and *reflectivity* are identical on the synthetic sections. The amplitude of the P_g phase on both synthetic sections is seen to reduce rapidly in amplitude at 21 km. On the *reflectivity* section this amplitude reduction occurs over a region ~ 1 km in width compared to ~ 2 km for the *maslov* synthetic data. This sharp change in amplitude observed with *reflectivity* is related to the style of source assumed in the calculations and is discussed in Fuchs and Müller (1971). In general however, the amplitude variations in the P_g phases are sufficiently similar to imply that the final model based on ray theory is valid.

The reflections from the top of the low velocity zone produce arrivals with equivalent amplitudes on each section. The position of these, interfering with the direct water wave and first arrival, illustrates why it would be difficult to observe any such arrival in the data. Although the P_mP arrivals near the instrument are lower in amplitude on the *maslov* synthetics, at 9 km range amplitudes from both techniques are comparable. The lower amplitudes at near offset range would not affect the ray-trace modelling of this phase as it is either of such a low amplitude in the data that only travel times are modelled or, near the instrument it interferes with the direct water wave and secondary arrivals, again preventing amplitude modelling. The remaining secondary arrival, the P-S mode conversion, is of such low amplitude that it is not observed on either synthetic section. As P-S mode conversions are seen in the data this suggests a higher proportion of energy is converted into S-waves on the Reykjanes Ridge than is suggested by modelling techniques. The multiples of the phases described above compare in much the same way as their primaries and are therefore not discussed separately.

The most obvious difference between the synthetic data sections is the arrival approximately 0.5 s behind the first arrival on the *reflectivity* synthetics (labelled A on figure 4.18c) which is not seen on the *maslov* synthetics. This arrival corresponds to

energy doubly reflected within layer 2A before reaching the instrument. Although when this phase was reproduced with *maslov* an arrival was generated at the correct travel time, as the base of layer 2A is incorporated as a second order boundary (i.e. there is no change in velocity across it) the amplitude was almost zero. The large amplitude generated by reflectivity modelling is believed to be an artefact of that particular modelling program.

Overall, the only technique that provided satisfactory results for complicated two dimensional models (including velocity inversions) was *maslov*. Although this method has the draw back of end-point contributions when very complicated models are traced, it out performs other computationally efficient forward modelling packages and successfully predicts amplitudes of arrivals passing through a low velocity layer ~100 m in thickness.

4.7 Summary

In this chapter the process of modelling all of the wide-angle seismic data is described in detail. Various techniques are compared and their individual shortfalls described in relation to complicated two dimensional models.

Final, best-fitting models for both the across and along-axis lines are presented. Interpretation of these models in relation to their significance in terms of ridge accretionary processes will be presented in the following chapter, together with the results of a test of the uniqueness of these models by independently modelling the coincident normal incidence seismic reflection and gravity data.

Chapter 5

Interpretation of the Reykjanes Ridge wide-angle seismic models

5.1 Introduction

The models described in Chapter 4 were derived from interpretation of the wide-angle seismic data only. However, several other geophysical datasets were also collected during CD81/93 and modelling and interpretation of these provides further constraint on the seismic models and some control on their uniqueness. In this chapter the final wide-angle seismic models are compared with the coincident gravity, normal incidence seismic and controlled source electromagnetic models to further constrain the physical characteristics of the crust at the Reykjanes Ridge. The resulting final models which best-fit all available datasets, are then discussed in relation to previous studies of mid-ocean ridges and interpreted in terms of the crustal structure and the process of oceanic crustal accretion at slow spreading ridges in general. Finally, the final slow spreading ridge model is compared and contrasted with those obtained at fast and intermediate spreading ridges.

5.2 Gravity

Gravity modelling comprised of two parts. Firstly gravity profiles coincident with the wide-angle seismic lines were modelled using 2-D modelling techniques (see section 5.2.1) to:- a) confirm the layer boundary positions and geometries of the seismic models; and b) obtain geologically reasonable estimates of layer density which in turn constrains the seismic velocity. These data were also combined with additional gravity data collected throughout the cruise to form an irregular network of gravity lines over the entire survey area. As the line spacing within this network was insufficient to allow regular gridding with the required resolution, additional data obtained from the Sandwell and Smith (1986) 2'x2' free-air gravity dataset were combined with the

shipboard measurements. A free-air gravity anomaly map was obtained by gridding this combined dataset using *xzy2grd*, from GMT (Generic Mapping Tool) version 3.1 (Wessel and Smith, 1995). This free-air gravity grid was used in combination with the gridded swath bathymetry data collected during CD81/93 and EW9008 (Parson *et al.*, 1993) to calculate the residual mantle Bouguer anomaly for the survey region (see section 5.2.2). The residual mantle Bouguer anomaly was then used to identify anomalous densities in the crust and mantle and any variation in crustal thickness throughout the survey area.

5.2.1 2-D gravity modelling

Gravity modelling is by nature an inverse problem with many possible valid solutions. In an attempt to minimise the number of these solutions, the initial gravity model used was derived from the final across-axis wide-angle seismic model, with P-wave velocities converted to densities as a first estimate. Modelling of the across-axis line was attempted in the first instance mainly because this line contains the most structure and hence would provide potentially more interesting results. Secondly the 2-D modelling method is based on the assumption that structures extend to infinity along strike. This is clearly only true for the across-axis line, and hence modelling of this line was likely to be more accurate than for the along-axis line. Finally, the amplitude of the along-axis gravity anomaly is low and the profile shows very few features related to variations in crustal structure other than changes in layer thickness. Hence within the resolution of the data and the errors involved in modelling in 2-D, the along-axis line was only modelled in terms of confirming layer thickness, geometries and densities and estimating the depth to the Moho, the latter being unconstrained by the along-axis wide-angle seismic data and its subsequent modelling.

There have been various attempts to relate P-wave velocity to density (Nafe and Drake, 1957 and 1962; Ludwig *et al.*, 1970; Carlson and Raskin, 1984; Barton, 1986). For this study it was decided to compare densities obtained from the mean velocity–density envelope of Nafe and Drake (1957) (see figure 5.1) with those obtained using methods 2 and 3 of Carlson and Raskin (1984) which are:-

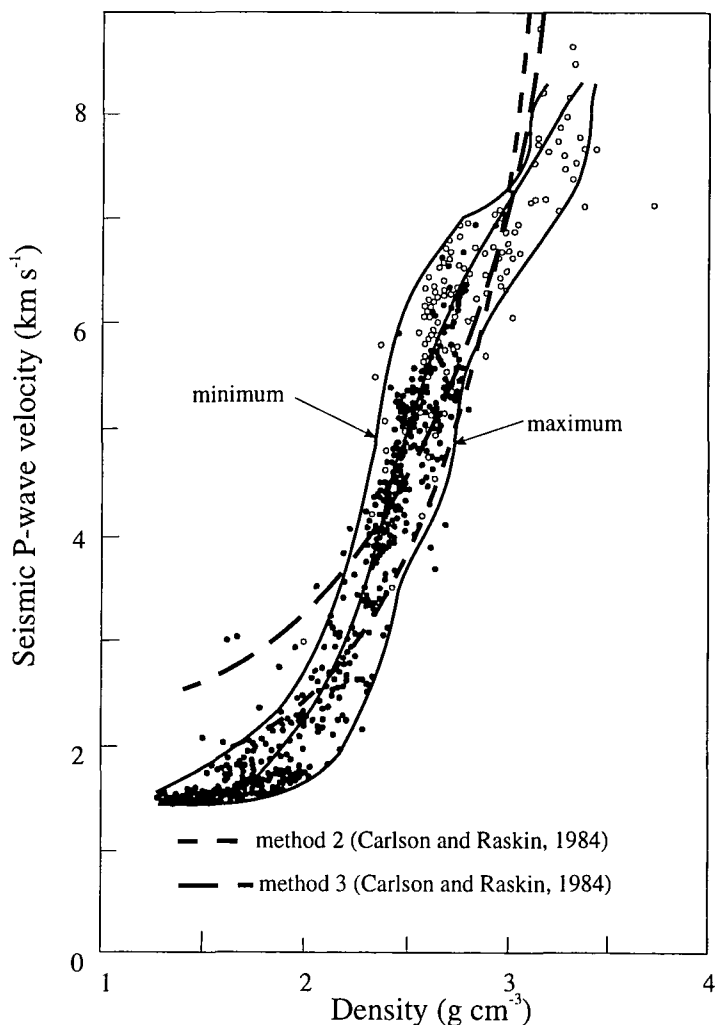


Figure 5.1: Velocity–density relationship of Nafe and Drake (1957) (after Barton, 1986 and Peirce, 1990a) which was used to estimate densities for the initial gravity model. The curves of methods 2 and 3 of Carlson and Raskin (1984) are overlain for comparison.

	V_p (kms ⁻¹)	ρ_{ND} (gcm ⁻³)	ρ_{M2} (gcm ⁻³)	ρ_{M3} (gcm ⁻³)	A_{vp} (gcm ⁻³)
sediments	2.60	2.10	1.51	2.04	1.89
2A&B	5.00	2.54	2.61	2.74	2.63
3	6.75	2.89	2.92	2.94	2.92
mantle	8.00	3.26	3.06	3.03	3.30*

Table 5.1: Calculation of model layer densities using average P-wave velocities derived from the main layers of the across-axis wide-angle seismic model. ρ_{ND} – density from the Nafe and Drake (1957) relationship. ρ_{M2} and ρ_{M3} – densities from method 2 and 3 respectively of Carlson and Raskin (1984). V_p – average P-wave velocity of the layer. A_{vp} – average density obtained from the three different calculations. * – a generally accepted value of mantle density (Kuo and Forsyth, 1988; Cormier *et al.*, 1995) which was incorporated into the initial gravity model.

$$\text{method 2} \quad \rho \text{ (g cm}^{-3}\text{)} = (3.81 \pm 0.02) - (5.99 \pm 0.11)/V_p \text{ (km s}^{-1}\text{)}$$

$$\text{method 3} \quad \rho \text{ (g cm}^{-3}\text{)} = (3.50 \pm 0.20) - (3.79 \pm 0.10)/V_p \text{ (km s}^{-1}\text{)}$$

The main difference between these two equations is that method 3 attempts to take into account the large-scale porosity encountered in oceanic layer 2A.

Initial estimates of model layer densities were obtained by averaging the results from each of the three techniques (see table 5.1), with the exception of the mantle density which was taken to be 3.3 g cm^{-3} – a value used in most gravity studies of mid-ocean ridges (Kuo and Forsyth, 1988; Cormier *et al.*, 1995). The free-air gravity anomaly along the 2-D initial model was then calculated using the program *grav2d* [written by J.H. Leutgert of the United States Geological Survey, based on the Talwani *et al.* (1959) algorithm]. Leaving interface geometries and depths unchanged, layer densities were adjusted until a good fit between the observed and calculated anomalies was achieved to within the error bounds of $\pm 2 \text{ mGal}$.

From figure 5.2 it can be seen that the amplitude of the calculated gravity anomaly on-axis from this simple model is approximately 10 mGal smaller than that observed. Therefore a number of low density blocks, corresponding to the lower velocities observed sub-axis (cf. figure 4.10) were incorporated in the axial region of the model. These low density blocks were added layer by layer, beginning at the top of the model in an attempt to match the short wavelength features observed in the data, and moving down to the lower crust to match the longer wavelength features. The axial low velocity/density block between layers 2B and 3 (centred at 40 km offset on the model shown in figure 5.3) is too thin to have a significant affect on the gravity field but has been included for completeness as it is required to satisfactorily model the wide-angle seismic refraction data. The resulting gravity model, with crustal low densities on-axis and a constant density mantle, is shown in figure 5.3 and its main features are as follows:-

- 1) The upper layer is bounded by the sea surface and seafloor and has a density of 1.03 g cm^{-3} which is the average density of sea water (Kuo and Forsyth, 1988). It can be seen that with this layer most of the short wavelength features observed in the gravity anomaly are well matched as are the general shape and amplitude of

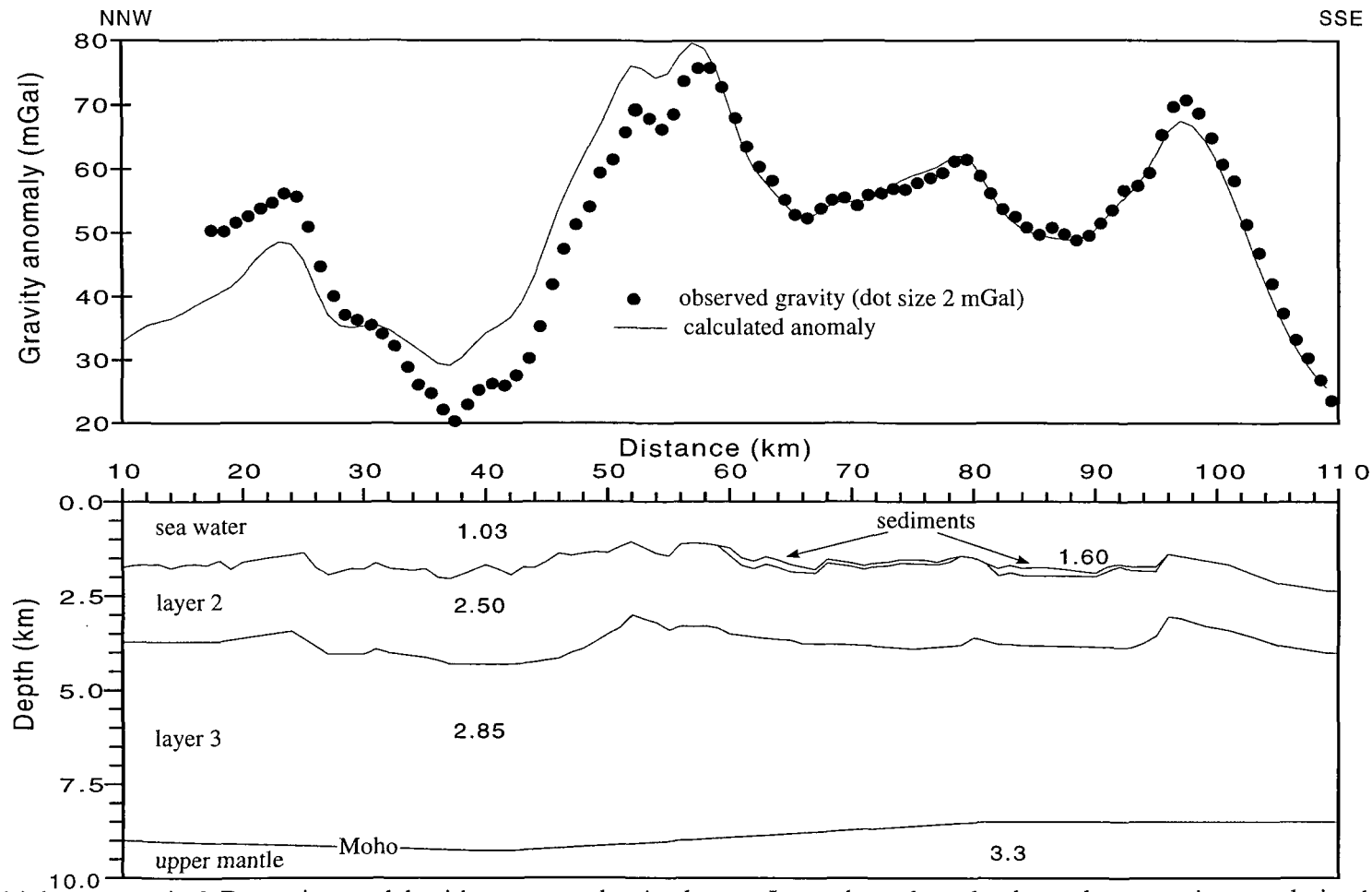


Figure 5.2: Initial across-axis 2-D gravity model with constant density layers. Layer boundary depths and geometries are derived from the coincident wide-angle seismic model. The upper diagram shows a comparison between the observed (dots) and calculated (solid line) free-air gravity anomaly. Dot size gives an indication of the error bars of ± 2 mGal. The lower diagram shows the gravity model with individual layers identified and densities in g cm^{-3} . Note that each of the gravity models extends to 20 km depth and has a semi-infinite half space at each lateral extreme. Only the section of the model directly comparable to the seismic model has been shown for clarity.

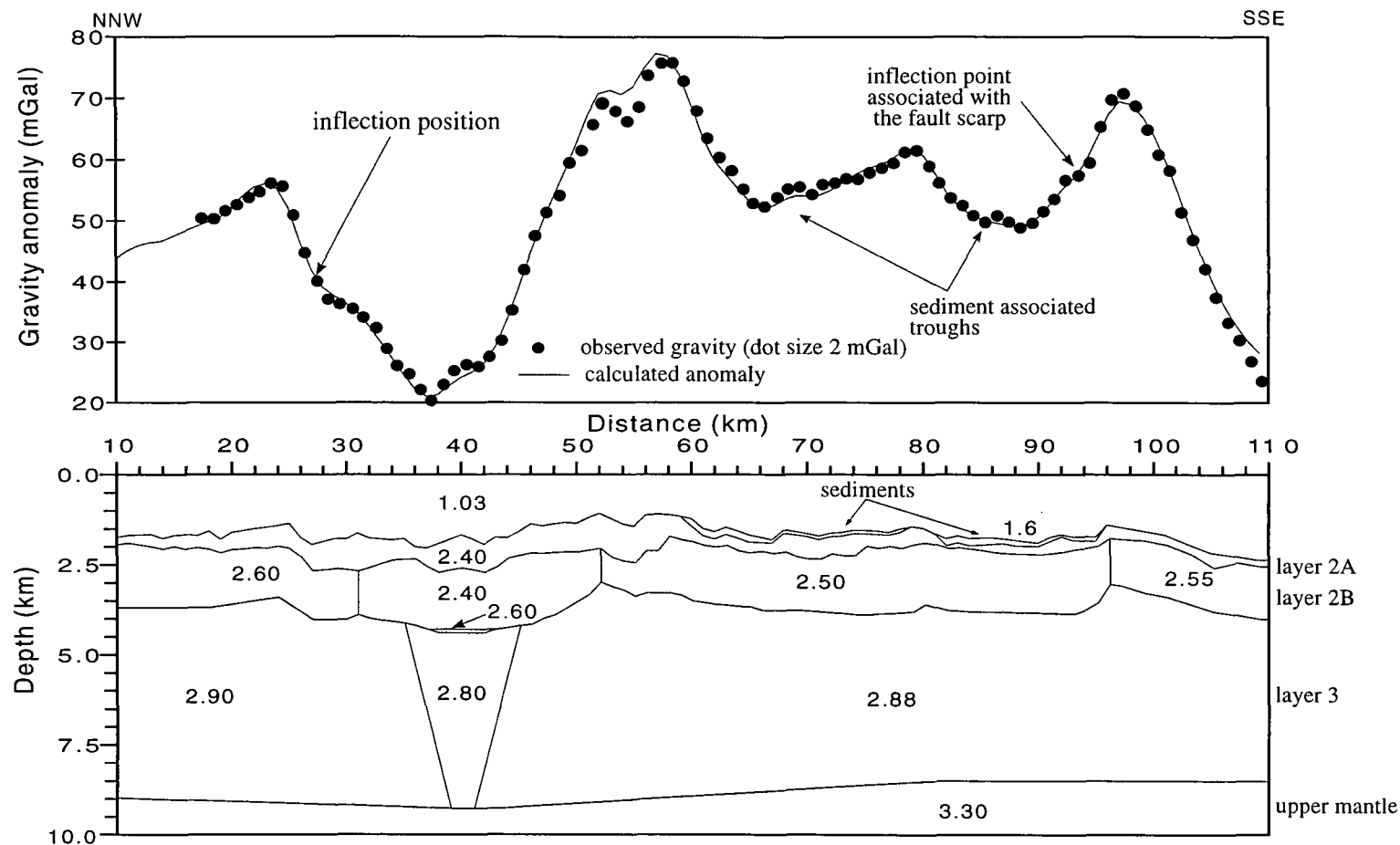


Figure 5.3: Intermediate across-axis 2-D gravity model with low axial densities in the crust corresponding to the modelled low velocities (cf. figure 4.10). The upper diagram shows a comparison between the observed (dots) and calculated (solid line) free-air gravity anomaly. Dot size gives an indication of the error bars of ± 2 mGal. The lower diagram shows the gravity model with individual layers identified and densities in g cm^{-3} . Note the two troughs in the gravity anomaly associated with the low density sediments have been well matched. Note also that each of the gravity models extends to 20 km depth and has a semi-infinite half space at each lateral extreme. Only the section of the model directly comparable to the seismic model has been shown for clarity.

the main peaks and troughs.

- 2) The off-axis sediment ponds each have a density of 1.6 g cm^{-3} – a value typical for oceanic sediments (DSDP sites 403-406 – Shipboard Scientific Party, 1979). These two sediment ponds are required to match the two troughs observed in the gravity anomaly between 60 and 90 km offset along the model.
- 3) Oceanic layer 2A was modelled as a single constant density layer extending across the entire model, as the seismically derived axial velocities were not found to be significantly lower than the average velocity within this layer (see figure 4.10). Also incorporating lower densities in the axial region of the gravity model did not improve the fit. The modelled density of 2.4 g cm^{-3} , although fairly typical of oceanic layer 2A (Vera *et al.*, 1990; Sinha, 1995), is lower than the average density obtained by sampling marine basalts and may indicate that this layer is highly fractured and porous. This high degree of porosity can also be used to explain the low S-wave velocities encountered during seismic modelling (see section 4.3.2).
- 4) Oceanic layer 2B has been divided laterally into four constant density blocks. The northwesternmost block extends from the left-hand edge of the model to 31 km offset and has a density of 2.6 g cm^{-3} ; the axial block, from 31 km to 52 km offset, has a density of 2.4 g cm^{-3} ; the central block, from 52 km to 96 km offset, has a density of 2.5 g cm^{-3} , and the southeasternmost block, with a density of 2.55 g cm^{-3} , extends from 96 km offset to the right-hand edge of the model. The density of the central block is constrained by the maximum amplitude of the gravity peak at 57 km offset to the 79 km offset peak located between the two sediment associated troughs. The densities of the remaining three blocks in this layer are constrained by their corresponding velocities and their density contrast with the central block. The lateral density contrasts within this layer play an important role in defining the shape of the inflection points on the main peaks observed. These layer 2B densities are slightly lower than the 2.7 g cm^{-3} expected both from the P-wave velocity estimate obtained in this study and densities obtained from previous studies of the oceanic crust (Christensen and Salisbury, 1973; Vera *et al.*, 1990),

indicating that this layer may also be fractured and porous. The lowest density of 2.4 g cm^{-3} occurs on-axis with density increasing with offset from the ridge axis. The general off-axis increase in density is probably caused by the closure of fractures and pore spaces with age by precipitation of minerals from circulating fluids.

- 5) Layer 3 is divided into three constant density blocks. The northwesternmost block extends from the left-hand edge of the model to 35 km offset at the top of the layer and 39 km offset at its base, with the typical oceanic layer 3 density of 2.9 g cm^{-3} (Fowler, 1990; Escartin and Lin, 1995). On-axis a block extending from 35 km to 45 km offset at the top of the layer and 39 km to 41 km offset at the base has a lower density of 2.8 g cm^{-3} , possibly reflecting higher axial temperatures. The southeasternmost block extends from this axial wedge to the right-hand edge of the model with a density of 2.88 g cm^{-3} , again within the typical range of values observed for oceanic layer 3 (Fowler, 1990).
- 6) At this stage the mantle was included as a single block of density 3.3 g cm^{-3} (Kuo and Forsyth, 1988; Cormier *et al.*, 1995; Sinha, 1995).
- 7) Between oceanic layers 2B and 3, a discrete block was included to coincide with the low velocity block in the across-axis wide-angle seismic model. The velocity of the corresponding seismic block is 3.0 km s^{-1} which, by the standard velocity–density relationships (see figure 5.1), corresponds to a density of approximately 2.0 g cm^{-3} . However at its modelled sub-seafloor depths the prevailing pressure and temperature regime prevents the existence of extensive porosity and therefore, if it is of basic igneous composition, its density cannot be less than 2.6 g cm^{-3} even if it is completely molten (Murase and McBirney, 1973).

The gravity modelling conducted thus far has shown that the layer geometries and thicknesses and density variations required to produce a good fit to the observed anomaly agree with those obtained from seismic modelling, especially so in the axial region where low densities, corresponding to the low axial velocities, are required to match the observed anomaly in any way. However as mid-ocean ridges are sites of crustal accretion (Fowler, 1990) some upwelling of mantle material must occur. This

upwelling will result in an increased thermal gradient in the mantle on-axis. Mantle upwelling is usually assumed to be passive in gravity studies (i.e. the plates separate and the resulting mass deficit is balanced by the mantle rising to fill the space – Kuo and Forsyth, 1988; and see section 5.2.2). From the resulting thermal anomaly in the axial region the variation in mantle density across-axis can be calculated and its contribution to the observed field considered (Géli *et al.*, 1994). To take passive upwelling into account and to investigate whether the observed gravity anomaly is sensitive to mantle density variations, the lowest layer of the 2-D model was divided into three blocks with an axial wedge extending from 39 km to 41 km offset at the top of the layer to 15 km to 65 km offset at the base. This wedge was modelled with a lower density of 3.28 g cm^{-3} (see figure 5.4). To accommodate the relatively lower mantle density on-axis the densities in layer 2B and 3 either side of the axis were adjusted accordingly. These changes in density altered the model in the following manner:-

- 1) The mantle was divided into 3 blocks. The northwesternmost block extends from the left-hand edge of the model to 39 km offset at the top and 15 km offset at the base of the layer (at 20 km offset) and has a standard mantle density of 3.3 g cm^{-3} (Kuo and Forsyth, 1988) as does the southeasternmost block which extends from 41 km offset at the top and 65 km offset at the base of the layer to the right-hand edge of the model. The separating axial block has a density of 3.28 g cm^{-3} .
- 2) As the mantle is now modelled with lower densities, the density contrasts in layer 3 are reduced to maintain the amplitude fit of the long wavelength ($\sim 30 \text{ km}$) observed gravity anomaly. The densities in the northwestern and southeastern blocks of layer 3 are both decreased to 2.85 g cm^{-3} . The effect of this adjustment is to make the densities of the blocks on either side of the axis equal but otherwise has little effect on the interpretation of the physical properties of the layer.
- 3) In layer 2B the density of the northwesternmost block is reduced to 2.52 g cm^{-3} to decrease the density contrast between this and the axial block, the latter retaining a density of 2.4 g cm^{-3} . As the density in the southeasternmost block of layer 3 has been reduced, the density in the central block of layer 2B is increased to 2.53 g cm^{-3} and in the southeastern block to 2.6 g cm^{-3} , in an attempt to match the short

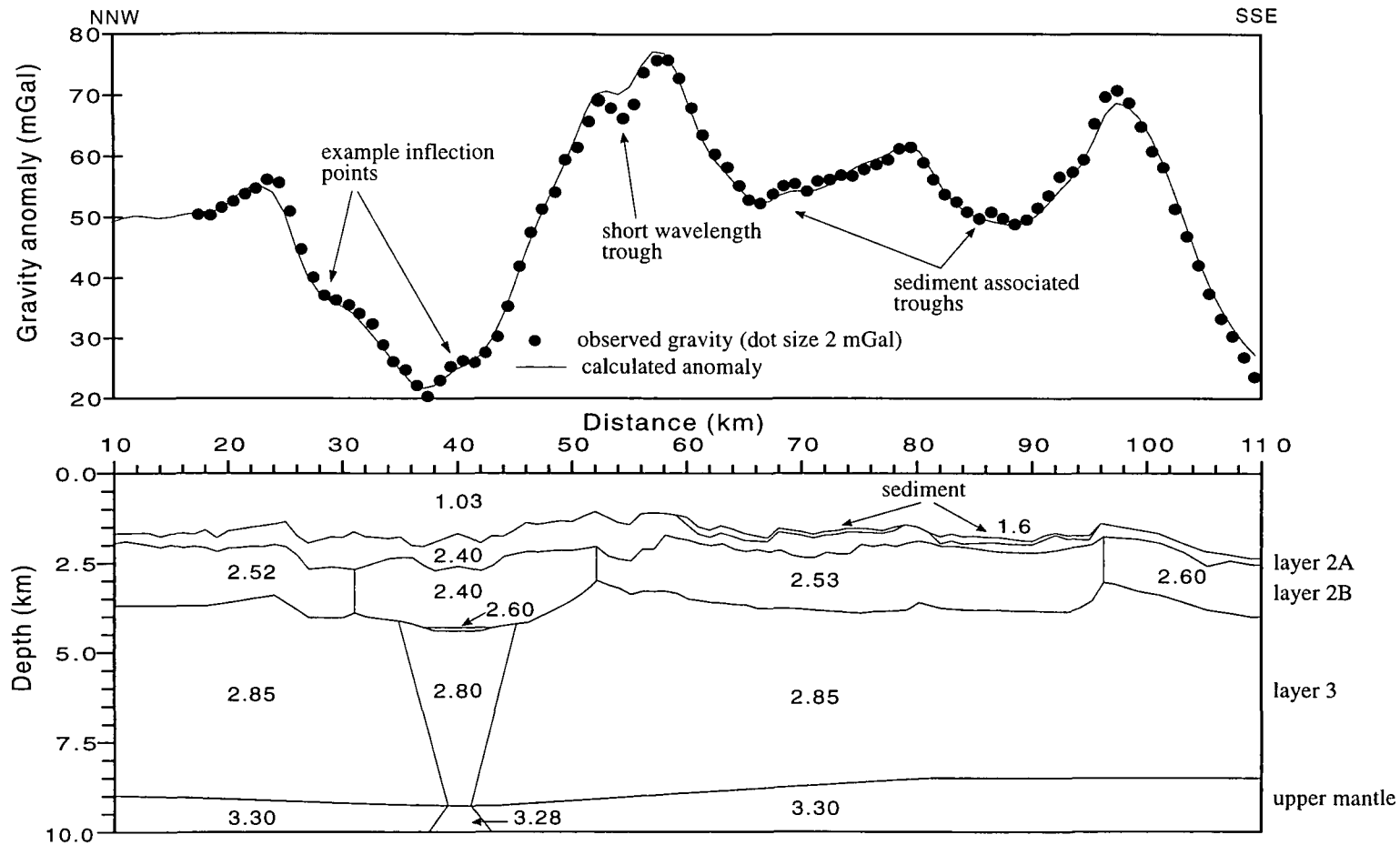


Figure 5.4: Final cross-axis 2-D gravity model with low axial densities in the crust corresponding to the modelled low velocities (cf. figure 4.10) and low axial densities in the upper mantle associated with the thermal anomaly caused by passive upwelling (see section 5.2.1). The upper diagram shows a comparison between the observed (dots) and calculated (solid line) free-air gravity anomaly. Dot size gives an indication of the error bars of ± 2 mGal. The lower diagram shows the gravity model with individual layers identified and densities in g cm^{-3} . Note the good fit of the main anomaly peaks in terms of their amplitudes, wavelengths and the associated inflection points. Note also that each of the gravity models extends to 20 km depth and has a semi-infinite half space at each lateral extreme. Only the section of the model directly comparable to the seismic model has been shown for clarity.

wavelength components of the observed gravity anomaly. These adjustments reduce the density contrast between the two blocks immediately either side of the axis, but otherwise they have not altered the densities sufficiently to affect the interpretation of the physical properties of this layer.

Both of these models fit the observed free-air anomaly to within the 2 mGal error bounds except in the 52 to 56 km offset region, where the amplitude of the short wavelength trough is not reproduced (see figure 5.4). This mismatch may be caused by an oversimplification of actual layer geometry as depth–offset data points could only specified every 1 km. This simplification is due to the limitations of the *maslov* wide-angle seismic modelling program from which the majority of the depth–offset data points are derived (see section 4.2.1). The mismatch could also result from the assumption used by the *grav2d* program that the structure is continuous along strike. This is not strictly true for the across-axis line but as variation in the third dimension is minimal compared to that along-axis, it is a reasonable assumption to make provided that these inadequacies are considered when assessing the "goodness of fit" and the geological significance of the model (see figure 4.6). In an attempt to distinguish between these two final models, both of which seem to adequately fit the observed free-air anomaly, a comparison was made between the calculated mantle Bouguer anomaly (in which a correction is made to account for the layer boundary topography assuming constant layer density and thickness) and the calculated residual mantle Bouguer anomaly (which also takes into account thermal related density changes in the mantle due to passive upwelling). If the mantle Bouguer anomaly shows no, or minor, anomalies associated with the axial region, the implication can be made that there is minimal variation in density and layer thickness across-axis and the effects of passive upwelling are negligible. If, however anomalies are observed in the mantle Bouguer anomaly which are reduced after calculation of the residual mantle Bouguer anomaly, the implication is that there are density variations in the mantle due to an increased thermal gradient. If the residual mantle Bouguer anomaly is not minimised compared to the mantle Bouguer anomaly (as is the case here), the implication is that there are density variations in both the crust and mantle (see section 5.2.2). This observation

suggests that the 2-D across-axis model with a low density in the mantle beneath the axis and laterally varying density within the crust is a more accurate representation of the structure at the Reykjanes Ridge.

The densities obtained for the axial region from the final across-axis gravity model (and also the low densities of the mantle on-axis) were incorporated into the along-axis wide-angle seismic model and the gravity anomaly calculated, again using *grav2d* (see figure 5.5). The general shape of the observed free-air gravity was reproduced by this model. However many of the short wavelength features (<3 km) are not matched accurately. This mismatch is generally less than 3 mGal, which is an acceptable error considering that the structure perpendicular to this line is clearly not continuous in the third dimension as the modelling program assumes. The largest misfit of 9 mGal occurs at the northern end of the line where the calculated anomaly slopes downwards away from the data. A similar trend is observed at the southern end although the observed gravity data do not extend the full length of the seismic line. This trend could be caused by upwelling focused into the centre of a ridge segment giving rise to higher densities at the ends of the model or by the crust thinning towards the ends of the AVR. Both the wide-angle and normal incidence (see section 5.3) seismic data indicate that a low velocity layer persists at least from the centre to the southern extremity of the 57° 45'N AVR which in turn implies that the low density layer also persists along the AVR. Also crustal thinning towards the ends of segments is often observed at transform and non-transform offsets at fast, intermediate and slow spreading ridges (e.g. Kuo and Forsyth, 1988; Minshull *et al.*, 1991). Therefore crustal thinning towards the ends of the segment appears to be the more likely cause of the mismatch between the model based on the seismic data and the free-air gravity anomaly, particularly as the depth to and geometry of the Moho is not constrained by the along-axis wide-angle seismic data and hence not constrained in the 2-D gravity model. Unfortunately neither the gravity or seismic data extend far enough from the ends of the AVR to constrain or model the implied change in crustal thickness towards the AVR tips suggested by the mismatch between the observed free-air anomaly and that calculated from the along-axis gravity model.

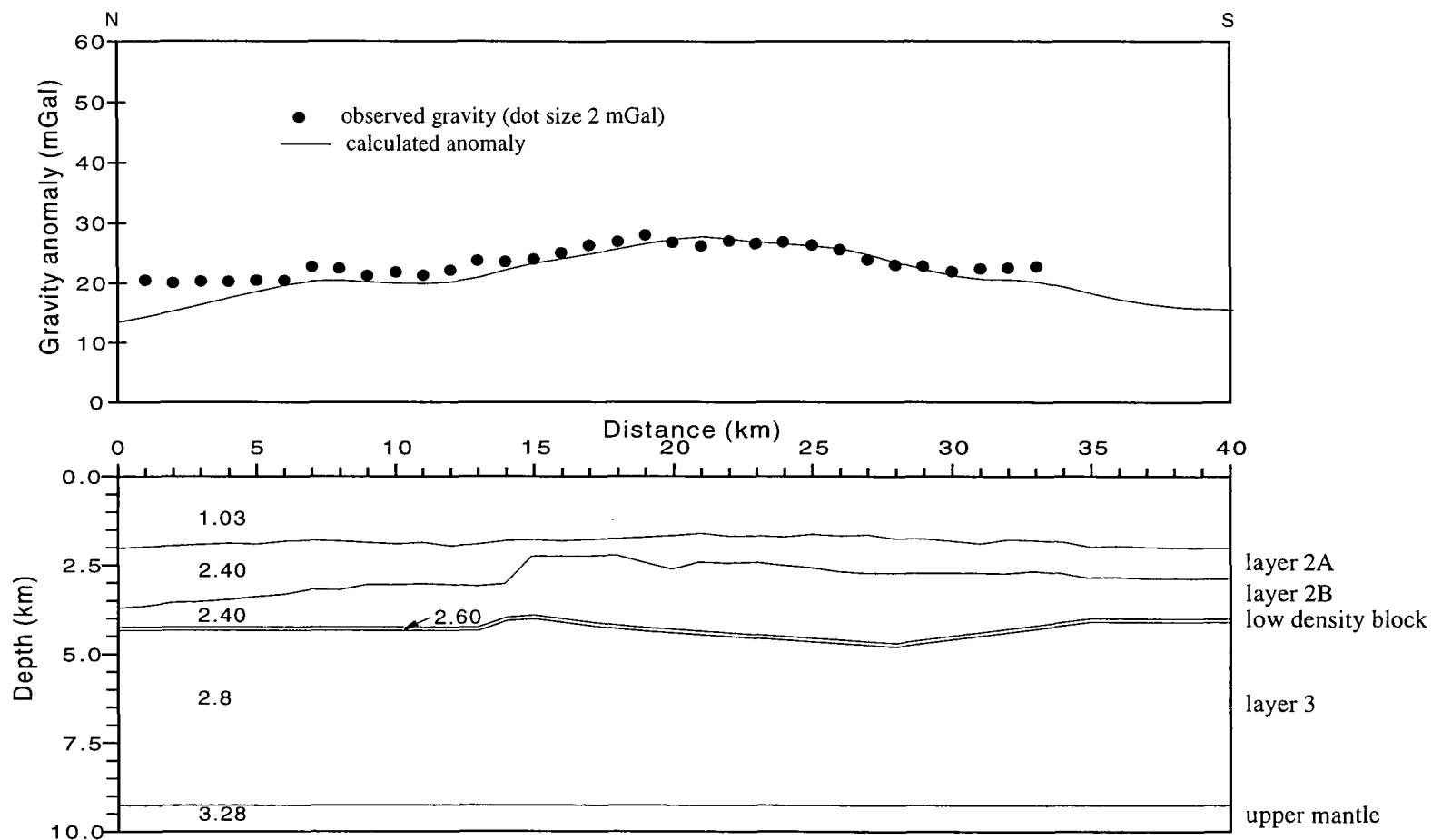


Figure 5.5: Final along-axis 2-D gravity model. Layer densities were obtained from the intersection point with the across-axis final model. The upper diagram shows a comparison between the observed (dots) and calculated (solid line) free-air gravity anomaly. Dot size gives an indication of the error bars of ± 2 mGal. The lower diagram shows the gravity model with individual layers identified and densities in g cm^{-3} . Note the reasonable fit in the region of the model that is well constrained by the along-axis seismic data (cf. figure 4.5b). Note also that each of the gravity models extends to 20 km depth and has a semi-infinite half space at each lateral extreme. Only the section of the model directly comparable to the seismic model has been shown for clarity.

5.2.2 Residual mantle Bouguer anomaly

The spacing of the tracks along which gravity data were collected during CD81/93 was not sufficiently dense (figure 2.20) to enable gridding at a reasonable node spacing without causing aliasing. Therefore the observed data were combined with the regional data derived from Sandwell and Smith (1986) 2'x2' gravity grid. The combination of these data effectively added a long wavelength component to the short wavelength observed gravity data. The Sandwell and Smith (1986) 2'x2' gridded satellite gravity data for the area of the Reykjanes Ridge studied are shown in figure 5.6. The free-air anomaly map shows lows which coincide with the axial valley of the Reykjanes Ridge and highs over off-axis seabed ridges. Before combining the shipboard gravity with the satellite data, the relative base levels of the two datasets were compared on coincident profiles from each dataset (figure 5.7). There were no obvious offsets on any of the profiles compared, therefore the satellite gravity grid was converted to xyz format and the two xyz files were combined and gridded using xyz2grd in GMT version 3.1 (Wessel and Smith, 1995) (figure 5.8). The combined gravity grid, when compared to the bathymetry grid (cf. figures 5.8 and 4.6) shows similar features to the seafloor bathymetry, i.e. the gravity anomaly is dominated by the effects of variation in seafloor topography. This regular free-air anomaly grid was then used in the calculation of the residual mantle Bouguer anomaly (RMBA). The RMBA was calculated in two stages. Firstly the mantle Bouguer anomaly (MBA) was calculated to investigate variations in density in the crust and mantle and any crustal thickness variations. Secondly the gravity anomaly associated with the thermal effects of passive upwelling were subtracted from the MBA to produce the RMBA.

Calculation of the mantle Bouguer anomaly

As can be seen from figure 5.8 the free-air anomaly is dominated by the signal from the seafloor bathymetry (cf. figure 4.6 and 5.8), with gravity lows coinciding with the median valley of the Reykjanes Ridge and highs associated with the faulted off-axis ridges. To calculate the MBA the gravitational anomaly associated with the sea water–crust interface, any sediment bodies and the entire crustal layer (assuming a

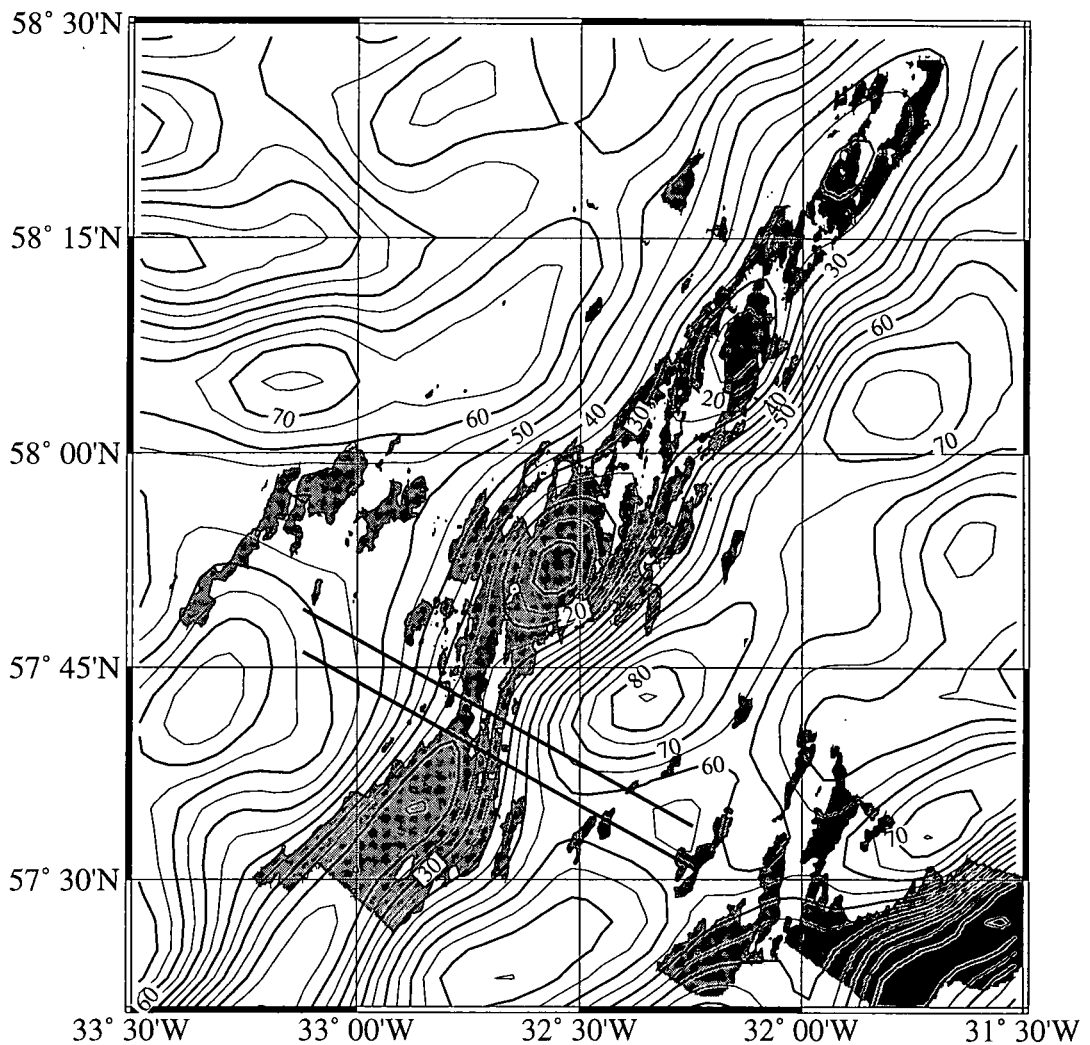


Figure 5.6: Sandwell and Smith (1986) 2'x2' free-air gravity grid overlying the seabed bathymetry. All depths greater than 1 800 m are shaded. Contour interval is 5 mGal. Note the correspondence of gravity lows with the regions of deeper bathymetry along the ridge axis. The two solid lines perpendicular to the ridge valley mark the locations of the gravity profiles shown in figure 5.7.

constant crustal thickness and density) are subtracted from the free-air gravity anomaly (Prince and Forsyth, 1988; Lin *et al.*, 1990). The remaining gravity anomaly represents any deviations from this simple model due to variations in structures within the crust and mantle. The program *grav2* [written by B.Y. Kuo and based on Parker (1972)'s method] was used to calculate the effects of the sea water–crust interface and a constant density, constant thickness crust. As the extent of sediment bodies was small on the young oceanic crust at 57° 45'N on the Reykjanes Ridge, they were considered to have a negligible effect and were thus ignored in this calculation. Parker (1972)'s method calculates the gravitational effect of topography and of a constant density contrast at a

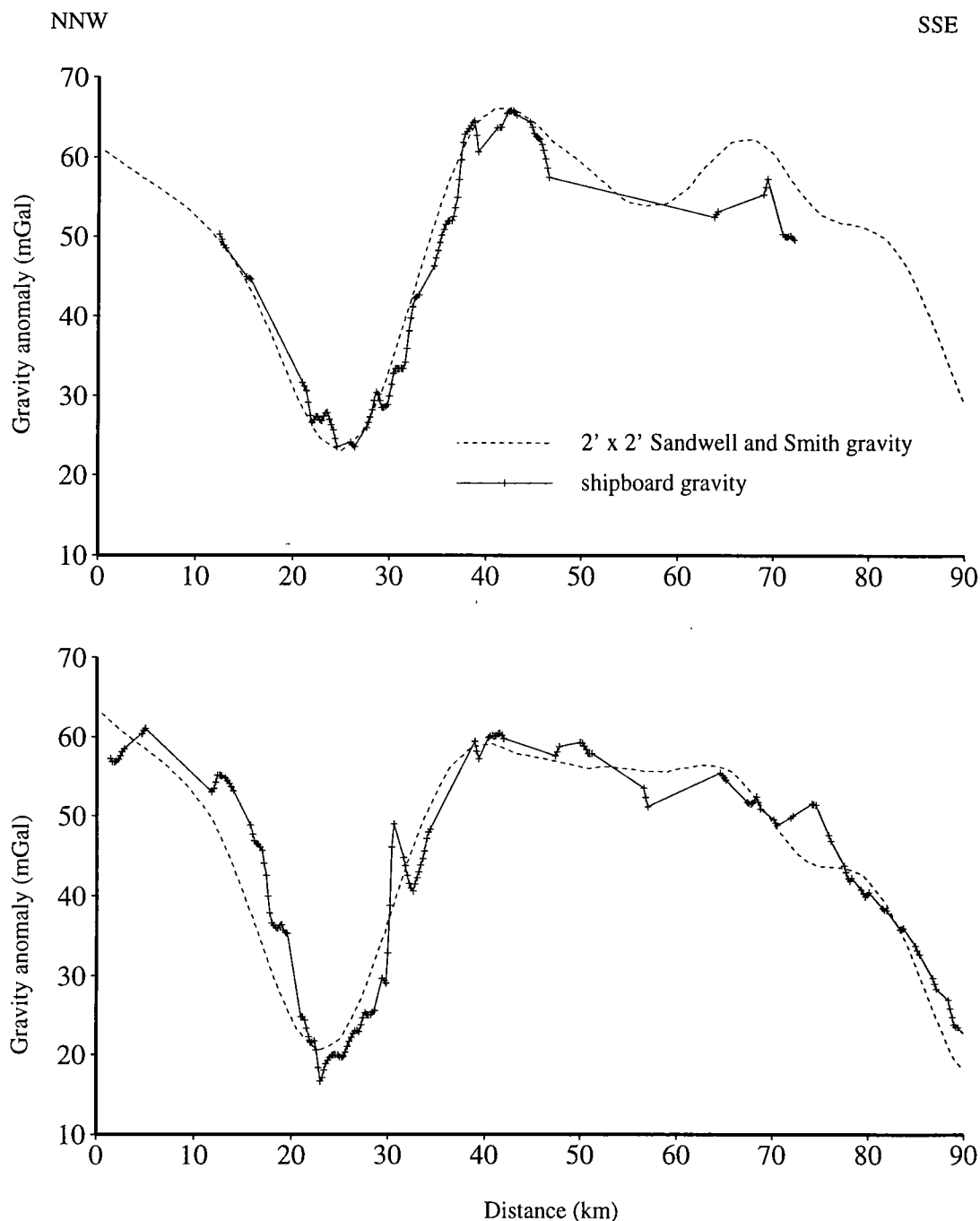


Figure 5.7: Gravity profiles from the Sandwell and Smith (1986) 2'x2' free-air gravity grid (dotted lines) and coincident shipboard gravity data (solid lines with crosses representing data points) used to compare the relative base levels of the two datasets. Note the gaps in the observed free-air gravity occurring in regions where this value could not be calculated from the shipboard raw gravity (e.g. due to changes in the ship's direction or velocity).

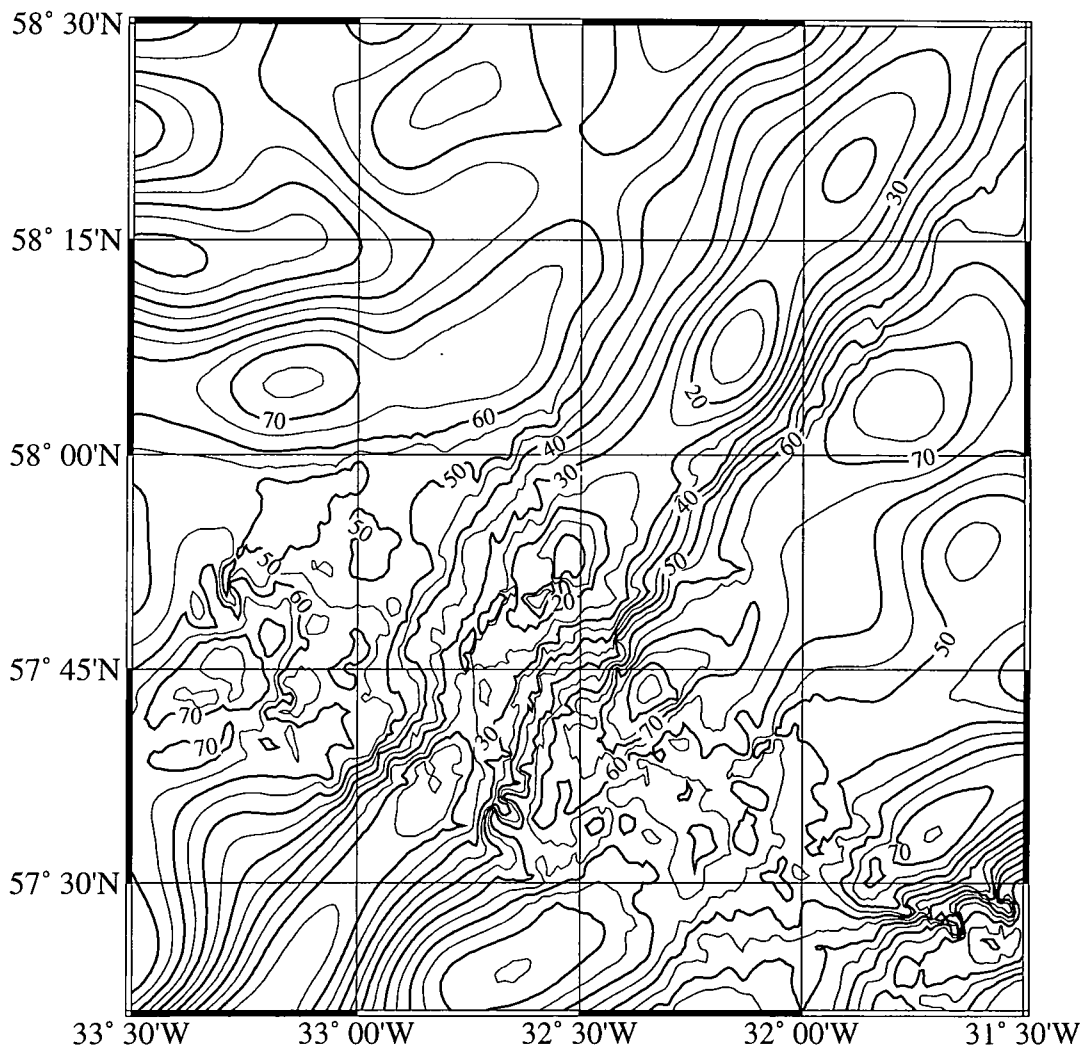


Figure 5.8: Regional free-air gravity anomaly map obtained from combination of the Sandwell and Smith (1986) 2'x2' and shipboard free-air gravity data. The main long-wavelength features of the map remain unchanged from figure 5.6 but short wavelength features observed in the study area have been added to improve resolution. Contour interval is 5 mGal.

boundary using fast Fourier transforms (Kuo and Forsyth, 1988; and see figure 5.9). This method requires a *rectangular* grid of regularly spaced seabed topography data points. As the upward continuation of the gravity field to sea level reduces the wavelength of the gravitational effect of the seafloor bathymetry to the order of the water depth, provided the grid spacing is less than the water depth aliasing is avoided. As the Reykjanes Ridge dataset is not rectangular, the bathymetry data were rotated using GMT version 3.1 (Wessel and Smith, 1995) until the across-axis wide-angle seismic line was horizontal ("east-west" on the resampled grid). The entire dataset was then resampled so that individual data points were located along lines running parallel to

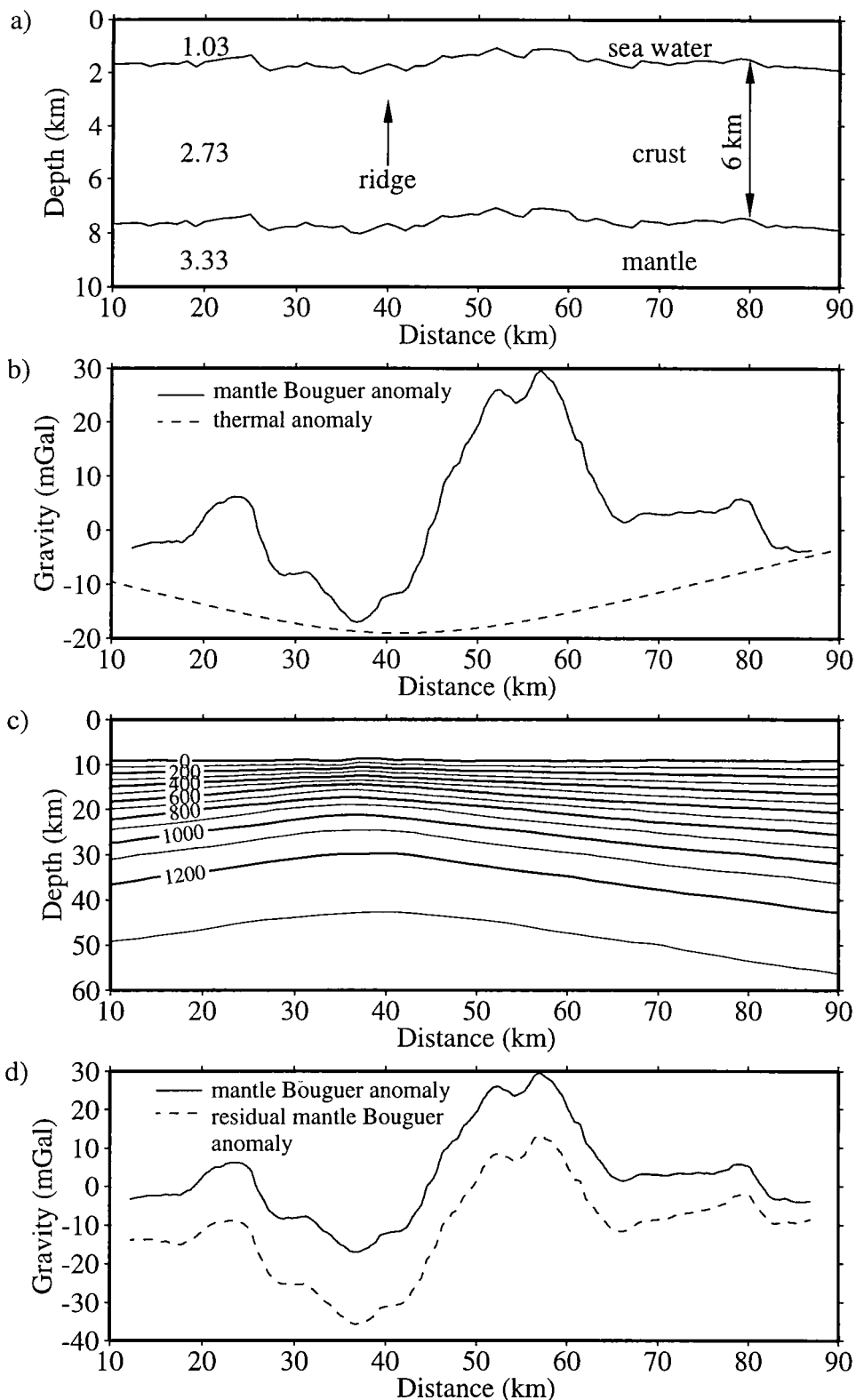


Figure 5.9: Schematic diagrams showing the calculation of the residual mantle Bouguer anomaly at a mid-ocean ridge.

a) Model used to calculate the gravitational attraction due to topography on the sea water–crust and crust–mantle boundaries assuming a constant crustal thickness and density.

b) Mantle Bouguer gravity profile calculated using the model shown in a). This is subtracted from the free-air gravity anomaly to yield the mantle Bouguer gravity anomaly. The dashed line shows the gravity anomaly associated with passive upwelling (c).

c) Thermal effect of passive upwelling at a ridge centred at 40 km offset and spreading at 10 mm yr^{-1} . Contour interval is 100°C and the Moho lies at $\sim 9.25 \text{ km}$ depth.

d) Solid curve – calculated mantle Bouguer gravity as in b). Dashed curve – combined effect of thermal upwelling and the crustal structure shown in a). This combined effect is removed from the free-air anomaly to calculate the residual mantle Bouguer anomaly.

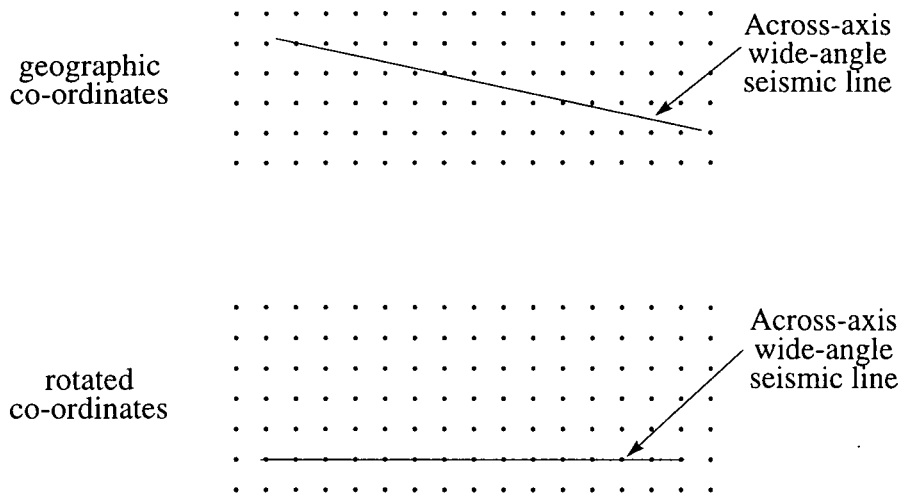


Figure 5.10: Sketch showing the rotation of the bathymetry data from geographic co-ordinates so that the across-axis wide-angle seismic line runs horizontal and coincident with grid nodes parallel to this direction.

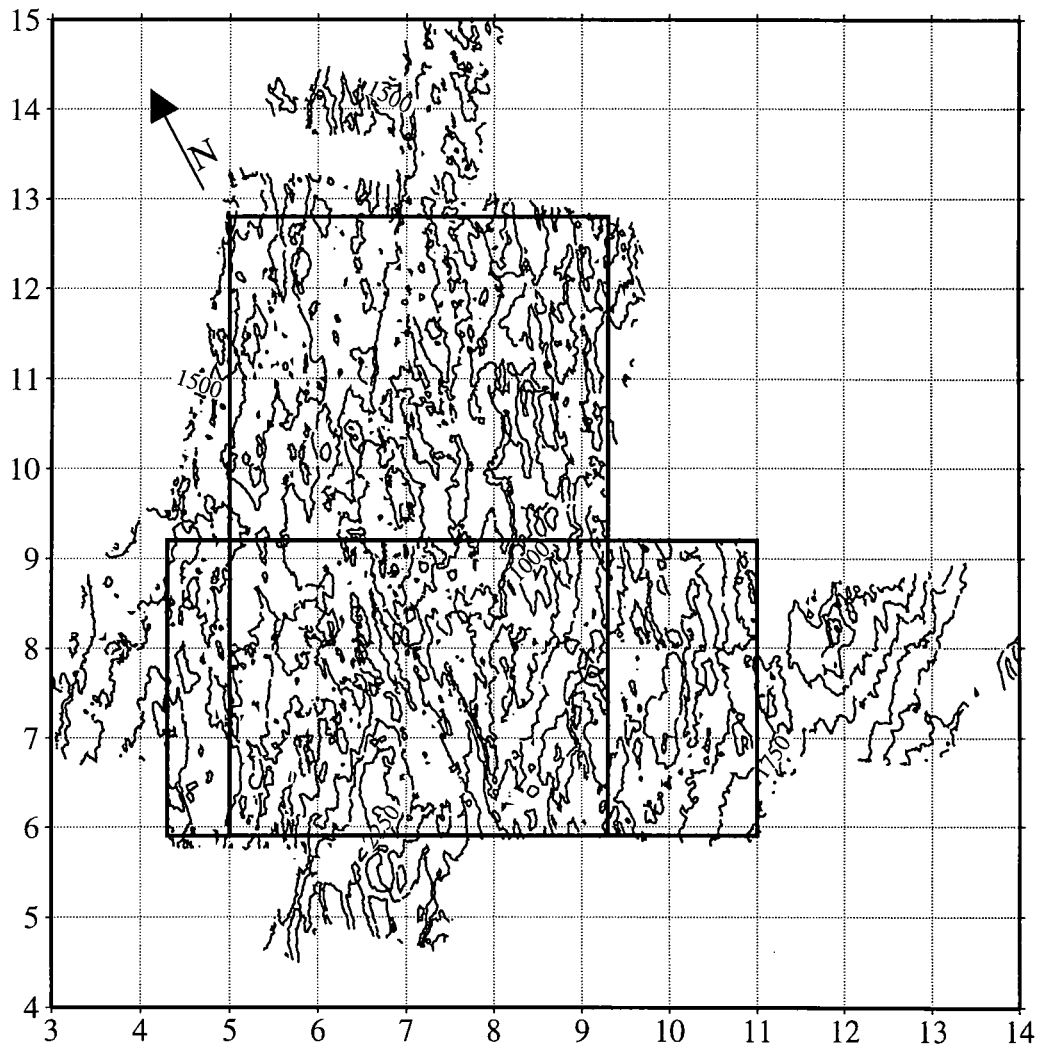


Figure 5.11: Bathymetry data from CD81/93 and Area C of EW9008 (Parson *et al.*, 1993) rotated so that the across-axis wide-angle seismic line is horizontal. The two rectangles outline the subset of bathymetry data used to calculate the mantle Bouguer anomaly. Contour interval is 1000 m. Both axes are annotated in rotated co-ordinates.

this "east-west" direction (see figure 5.10). This process enabled two rectangular sub-grids to be selected so that as much of the bathymetric data as possible could be included under the constraints of the *grav2* program (figure 5.11). These grids were 256 samples square with a node spacing varying from 150 m to 300 m. The densities of the sea water, crust and mantle were assumed to be 1.03 g cm^{-3} , 2.73 g cm^{-3} and 3.33 g cm^{-3} respectively (e.g. Kuo and Forsyth, 1988). Although as seen from 2-D modelling (see figure 5.4) the crustal density generally varies from 2.4 to 2.9 g cm^{-3} , the assumption of a constant 2.73 g cm^{-3} crust results in a difference in the gravity anomaly of less than 1 mGal (Kuo and Forsyth, 1988), which is less than the error in each gravity data point. Also by assuming a constant density crust it may be possible to examine the areal extent of the anomalous features observed in the crust as modelled in 2-D. The crust was assumed to have a constant thickness of 6 km (Kuo and Forsyth, 1988) even though the wide-angle seismic model indicates that a crustal thickness of 7.5 km is more realistic. Investigation of the effect of the difference between the two crustal thicknesses on the gravity signal showed that it results in an offset of the order of the error bounds and therefore could be ignored (Field, 1993). The calculated gravitational attractions of the seafloor and associated mantle relief for each rectangular grid are combined and the anomalies from the combined grids are shown in figure 5.12. All three contour maps show slight lateral offsets in the contours where the two individual rectangular grids meet at approximately 9.3 on the y-axis. These offsets are caused by the edge effects of the fast Fourier transforms used during calculation. However they are of small amplitude and have little effect on the general location and trend of the resulting MBA. The seafloor contribution to the total anomaly (figure 5.12a) has a peak-to-peak amplitude of 60 mGal and its shape, as is to be expected, is approximately equivalent to the bathymetry with a short wavelength filter applied (cf. figure 4.6). The mantle relief contribution to the total predicted gravity field (figure 5.12b) has a peak-to-peak amplitude of approximately 6 mGal and, also as expected, reflects only the long wavelength features of the bathymetry (cf. figure 4.6). The total predicted gravity field due to the sea water and crustal layers has a peak-to peak amplitude of 65 mGal and is shown in figure 5.12c. The shallower sub-sea level depth of the sea water-crust

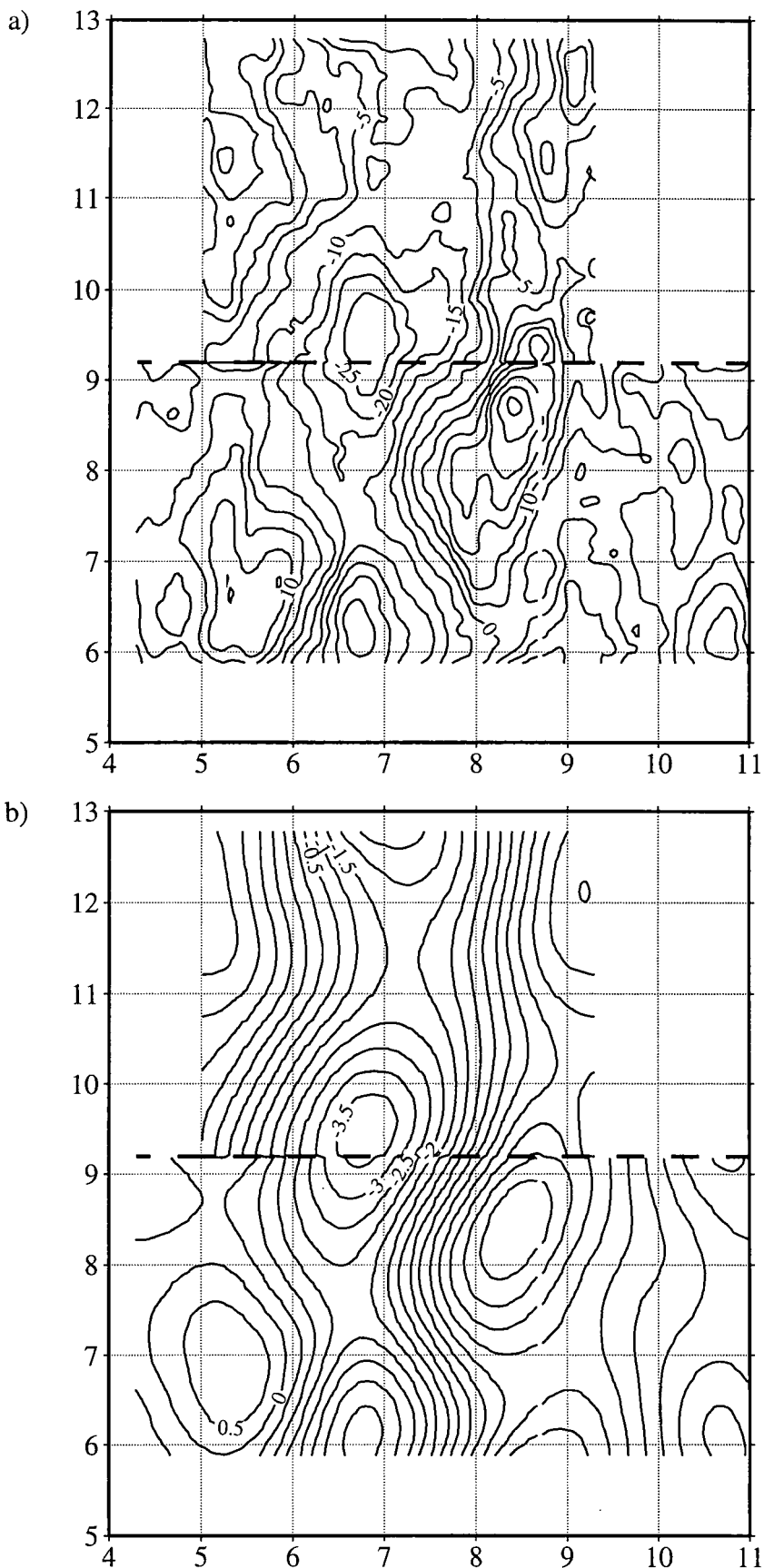


Figure 5.12: Calculated gravitational attraction due to relief on the sea water–crust and crust–mantle boundaries combined for the two rectangular grids shown in figure 5.11. Plotted in rotated co-ordinates. The dashed line marks the intersection of the two grids. The contours on each plot have a slight horizontal offset at this intersection.

- a) Gravitational attraction due to the sea water–crust interface. Contour interval is 5 mGal.*
 b) Gravitational attraction due to the crust–mantle boundary. Contour interval is 0.5 mGal.

* mean seafloor depth is assumed to be 1500m, equivalent to a 0mGal gravity anomaly.

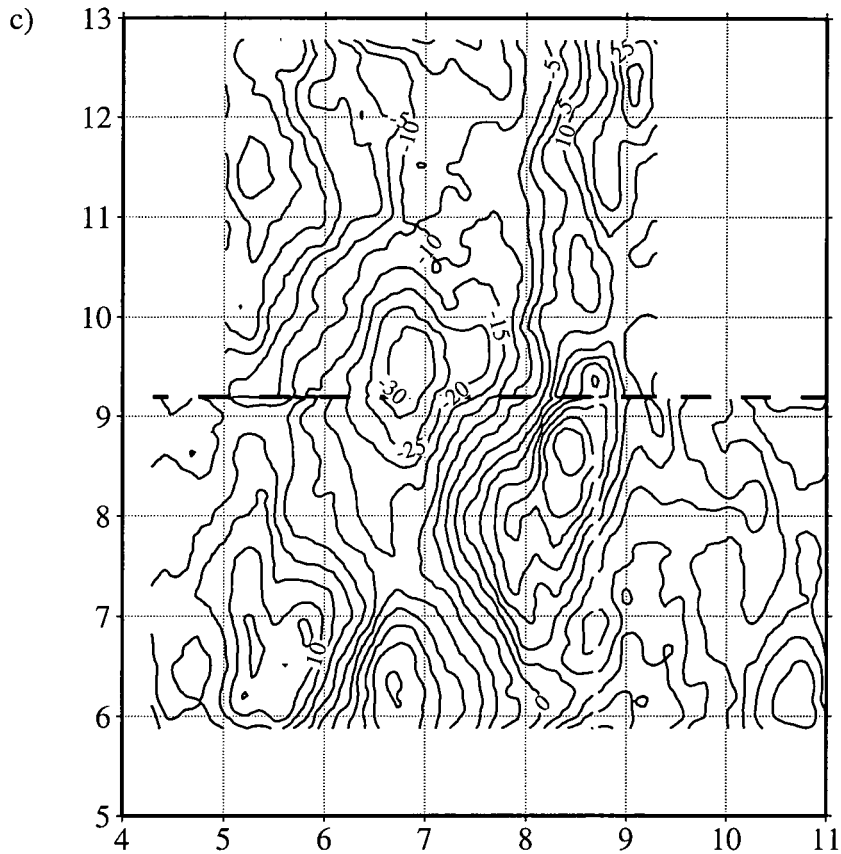


Figure 5.12: cont.. Calculated gravitational attraction due to relief on the sea water–crust and crust–mantle boundaries combined for the two rectangular grids shown in figure 5.11. Plotted in rotated co-ordinates. The dashed line marks the intersection of the two grids. The contours on each plot have a slight horizontal offset at this intersection.

c) Combined gravitational attraction due to relief on the sea water–crust and crust–mantle boundaries. Contour interval is 5 mGal. Note the dominant effect of the sea water–crust interface in this combined dataset.

interface creates a much larger amplitude gravity anomaly than that due to the crust–mantle boundary and hence the combined anomaly (figure 5.12c) is dominated by the gravitational effects of the seabed (figure 5.12a).

The predicted total gravity anomaly for the sea water–crust interface and a constant density crust was then rotated back into geographic co-ordinates and subtracted from the free-air gravity anomaly to give the MBA (figure 5.13). The peak-to-peak amplitude of this MBA is ~38 mGal which is 52 mGal lower than that of the free-air anomaly. Therefore over 60% of the free-air anomaly can be explained by the geometry and density contrasts at the sea water–crust interface and the Moho. The resulting MBA still shows gravity lows on-axis and highs off-axis. In general, away from the ridge axis

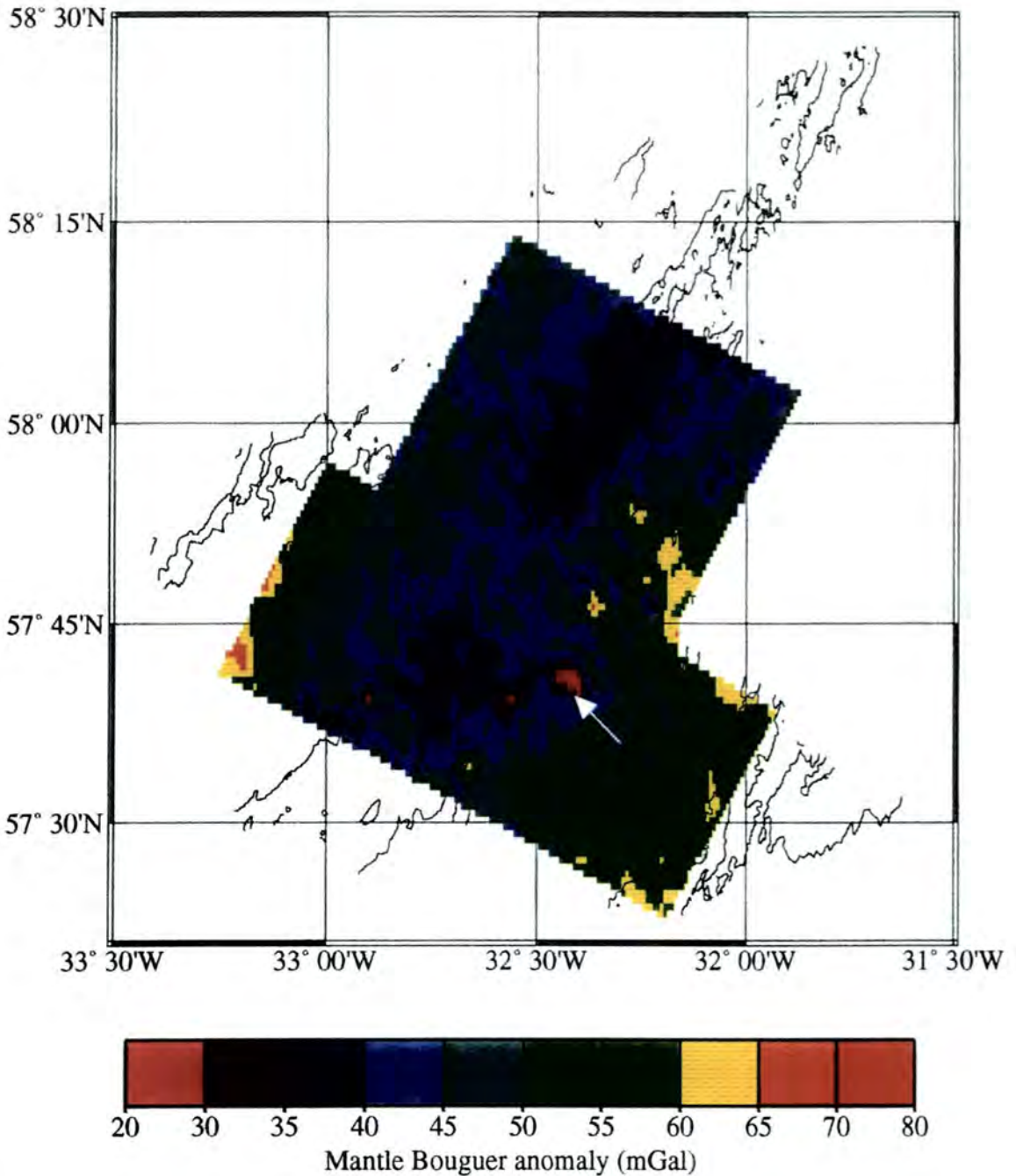


Figure 5.13: Mantle Bouguer anomaly calculated by subtracting from the free-air gravity anomaly shown in figure 5.8 the combined attraction of the sea water–crust and crust–mantle boundaries shown in figure 5.12c. The 1 800 m contour is also plotted to enable a comparison of the MBA the bathymetry. The two main lows are associated with the AVR studied and with those located to the north. A low is also observed (L) over the median valley wall to the east of the AVR centred on 57° 45'N (see text).

the MBA remains approximately constant at 50 mGal even over the median valley walls. However a low of 20 mGal over the median valley wall to the east of the 57°45'N AVR suggests that in this region the walls are isostatically compensated. The remaining lows in the MBA are ~15 mGal below the background level and are centred over the AVRs. The topography of these AVRs is no higher than encountered off-axis suggesting these lows are caused by lower axial densities rather than isostatic compensation of the ridges. Therefore to attempt to account for these lower densities on-axis the gravitational effect of the thermal regime at the axis of spreading was calculated and removed to yield the RMBA (see figure 5.9c and d).

Calculation of the residual mantle Bouguer anomaly

A series of programs written by Forsyth (Forsyth and Wilson, 1984) calculate the thermal effect of a north–south trending ridge–transform–ridge system, assuming passive upwelling in the mantle with vertical motion in a triangular region centred on the ridge and horizontal motion outside this region (Forsyth and Wilson, 1984; Kuo and Forsyth, 1988; Prince and Forsyth, 1988; and see figure 5.14). The Reykjanes Ridge is not a simple ridge–transform–ridge system so to be able to approximate the AVR system of spreading to this pattern, the bathymetry was rotated to orient the AVRs north–south and five ridges, separated by small transforms were used to represent this region of the Reykjanes Ridge (figure 5.15). The ridges were located on a 256 by 256 grid, with a 1 km grid spacing, such that the ridges lay at least 100 km from the perimeter of the grid in an attempt to reduce edge effects due to the periodicity of the Fourier transforms used in the calculation of the thermal anomaly (Kuo and Forsyth, 1988). The thermal effect of this ridge system was calculated on 15 depth slices assuming a constant temperature of 0°C at the Moho and 1350°C at 100 km depth (Kuo and Forsyth, 1988; and see figure 5.14) and that the ridges were spreading at a constant rate of 10 mm yr⁻¹ symmetrically either side of the ridge (Searle *et al.*, 1994). Figure 5.16 shows the temperature for a layer at a depth of 11 km. Note how the highest temperatures are centred on the longer ridge segments as would be expected. These thermal anomalies were then converted to gravity by multiplying by an estimate of the

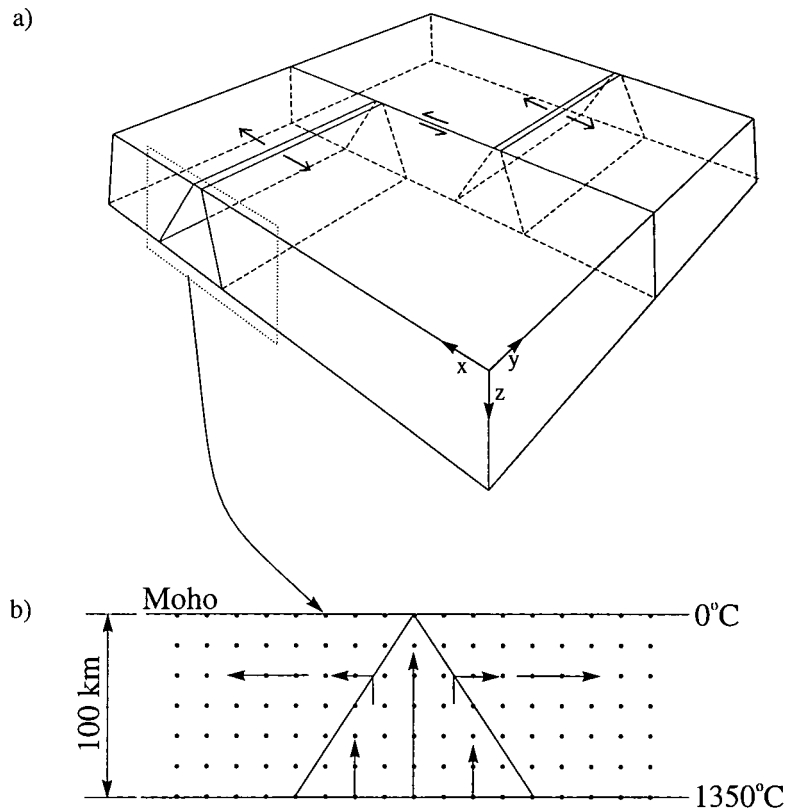


Figure 5.14: Sketch of the ridge–transform–ridge system and passive upwelling assumed in calculating the thermal contribution to the gravity anomaly in the method of Forsyth and Wilson (1984).

a) Ridge–transform–ridge system with ridges and transforms perpendicular and symmetrical spreading about the ridge axis (after Forsyth and Wilson, 1984).

b) Vertical upwelling within a triangular region beneath the ridge axis and horizontal motion outside of this region. The temperature is assumed to be 0°C at the Moho and 1350°C at 100 km depth (Prince and Forsyth, 1988) and the model is divided into 15 layers between these boundaries (after Forsyth and Wilson, 1984).

thermal expansion coefficient of the mantle (Forsyth and Wilson, 1984), and upward continuing the gravity anomaly to the sea surface from the Moho. The gravitational attraction of each layer was summed to provide the total gravity effect due to passive upwelling (figure 5.17). This thermal gravity anomaly was then subtracted from the MBA to give the RMBA (see figure 5.9 and 5.18). The remaining gravity anomaly should represent any anomalous densities due to inhomogeneity in the crust and mantle or crust thickness variations. The RMBA shown in figure 5.18 has been filtered using a 2 km wide cosine filter which removes short wavelength features but leaves the main features of the data intact, enabling easier interpretation of the main trends in the gravity data. The background level of the RMBA is between 60 and 65 mGal. In the axial region the anomaly is generally below 60 mGal and over the centre of the AVRs the anomaly drops to under 55 mGal, reflecting the lower axial densities observed on the 2-D across-axis

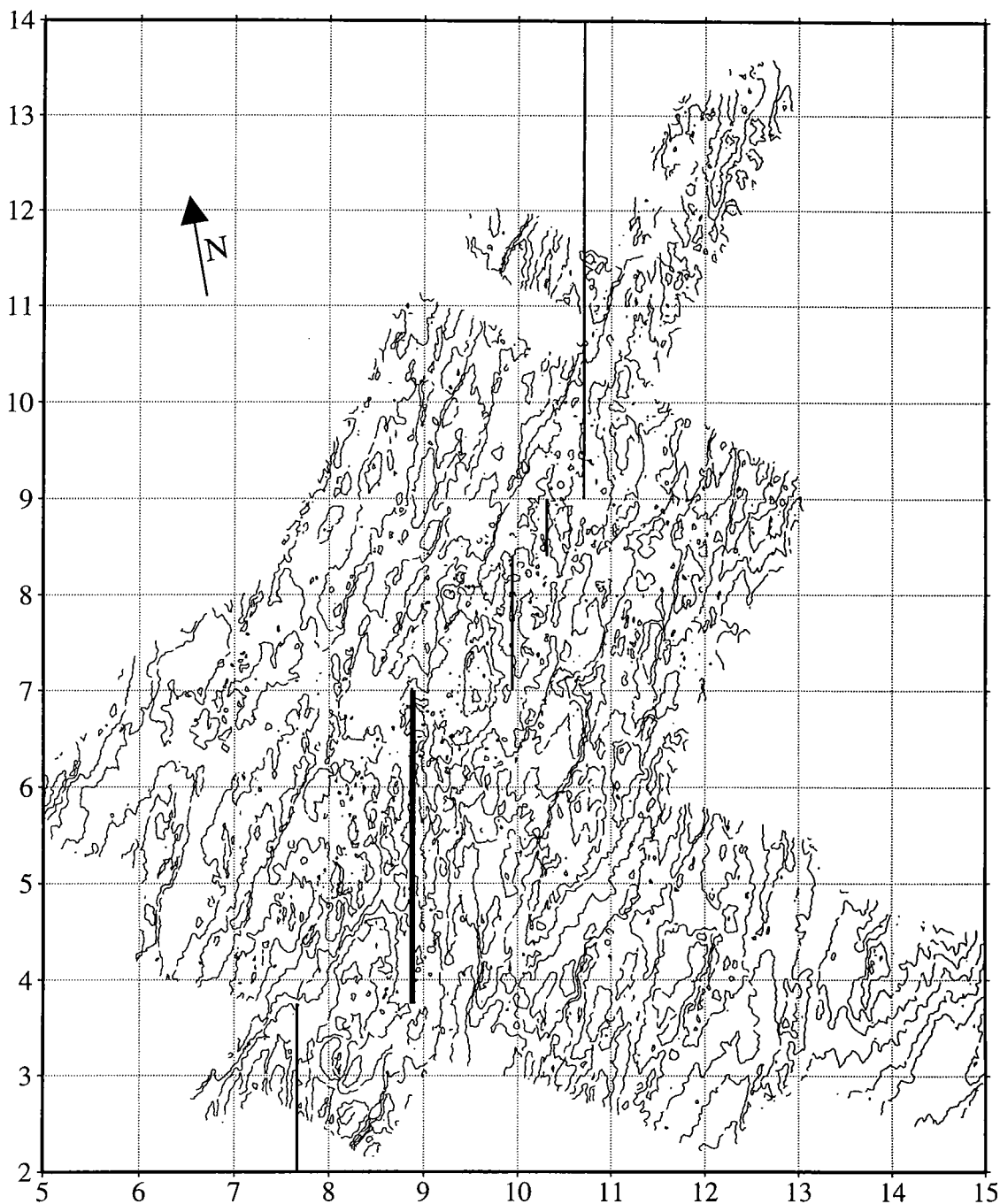


Figure 5.15: Bathymetry data from CD81/93 and EW9008 (Parson *et al.*, 1993) rotated to orient the AVR north-south. The solid lines mark the five ridges used to approximate the en echelon AVR in this region to the ridge–transform–ridge geometry required to calculate the effects of passive upwelling. The thicker line represents the AVR of this study. Contour interval is 1000 m. Both axes are annotated in rotated co-ordinates.

gravity model (see section 5.2.1). As the gravity anomaly amplitude reduces towards the ends of the AVR this indicates that densities increase, or crustal thickness decreases, towards the ends of the along-axis line. This trend is also indicated on the 2-D along-axis gravity model (see section 5.2.1). Two further gravity lows of below 50 mGal are observed 10-20 km to the east of the AVR studied during CD81/93. These lows coincide with two ridges which mark the median valley wall on the eastern side of the

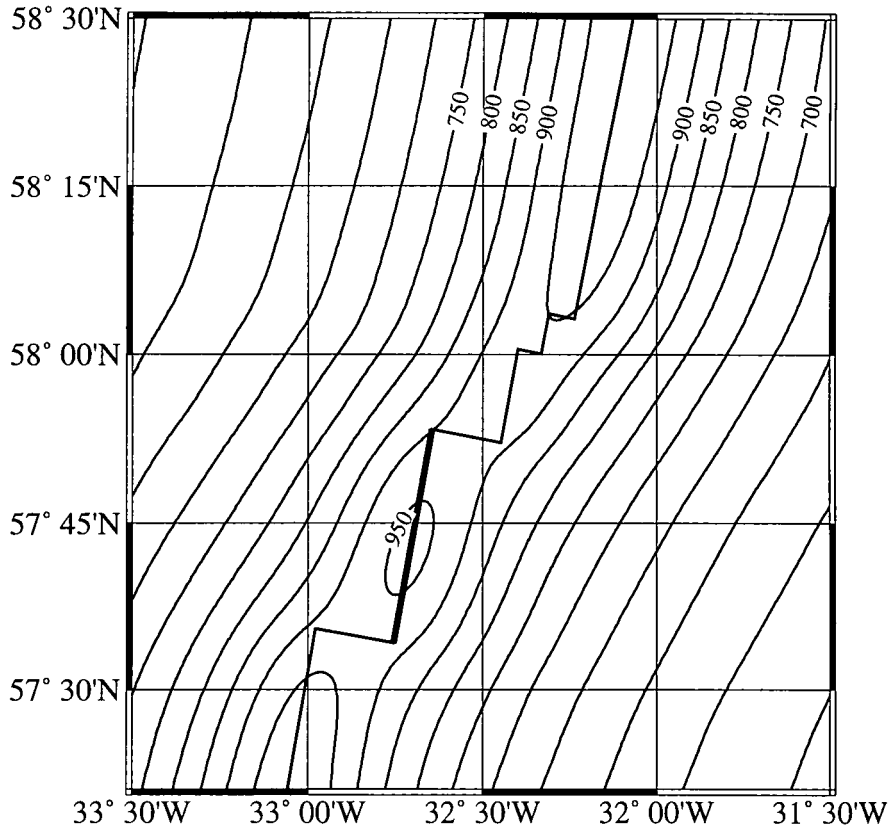


Figure 5.16: Thermal effect of passive upwelling at the ridges due to a layer located 11 km beneath the Moho. The ridge–transform–ridge system used in the calculation is shown, with the AVR of this study shown as a thicker line. Contour interval is 50°C.

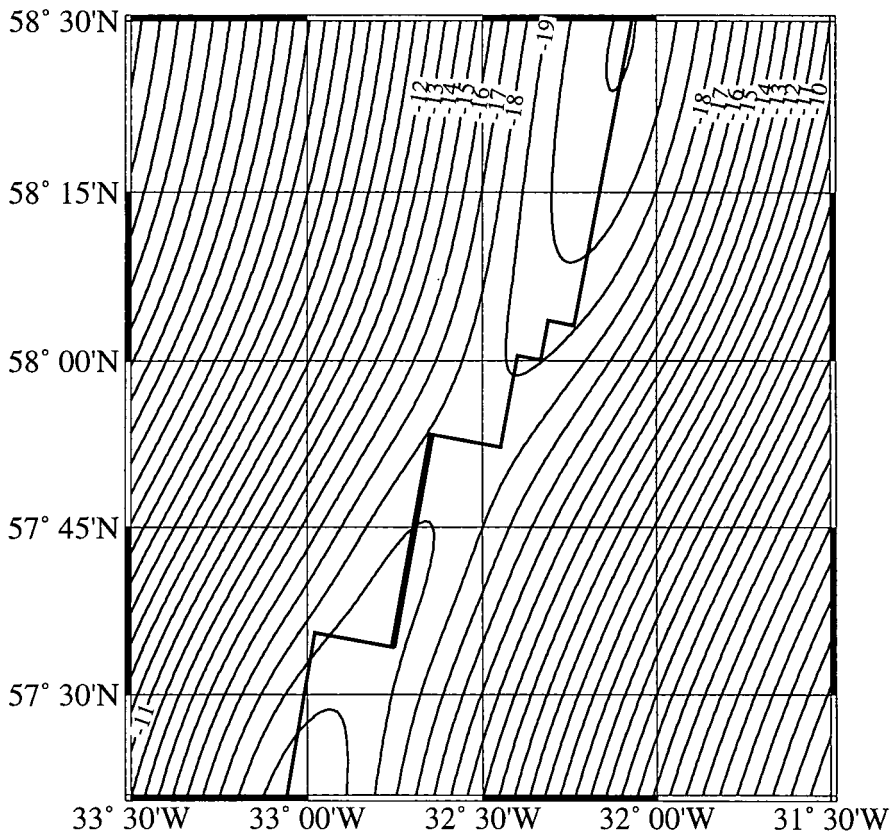


Figure 5.17: Total gravitational effect of passive upwelling at the ridge–transform–ridge system shown as solid lines. The AVR of this study is shown as a thicker line. Contour interval is 1 mGal.

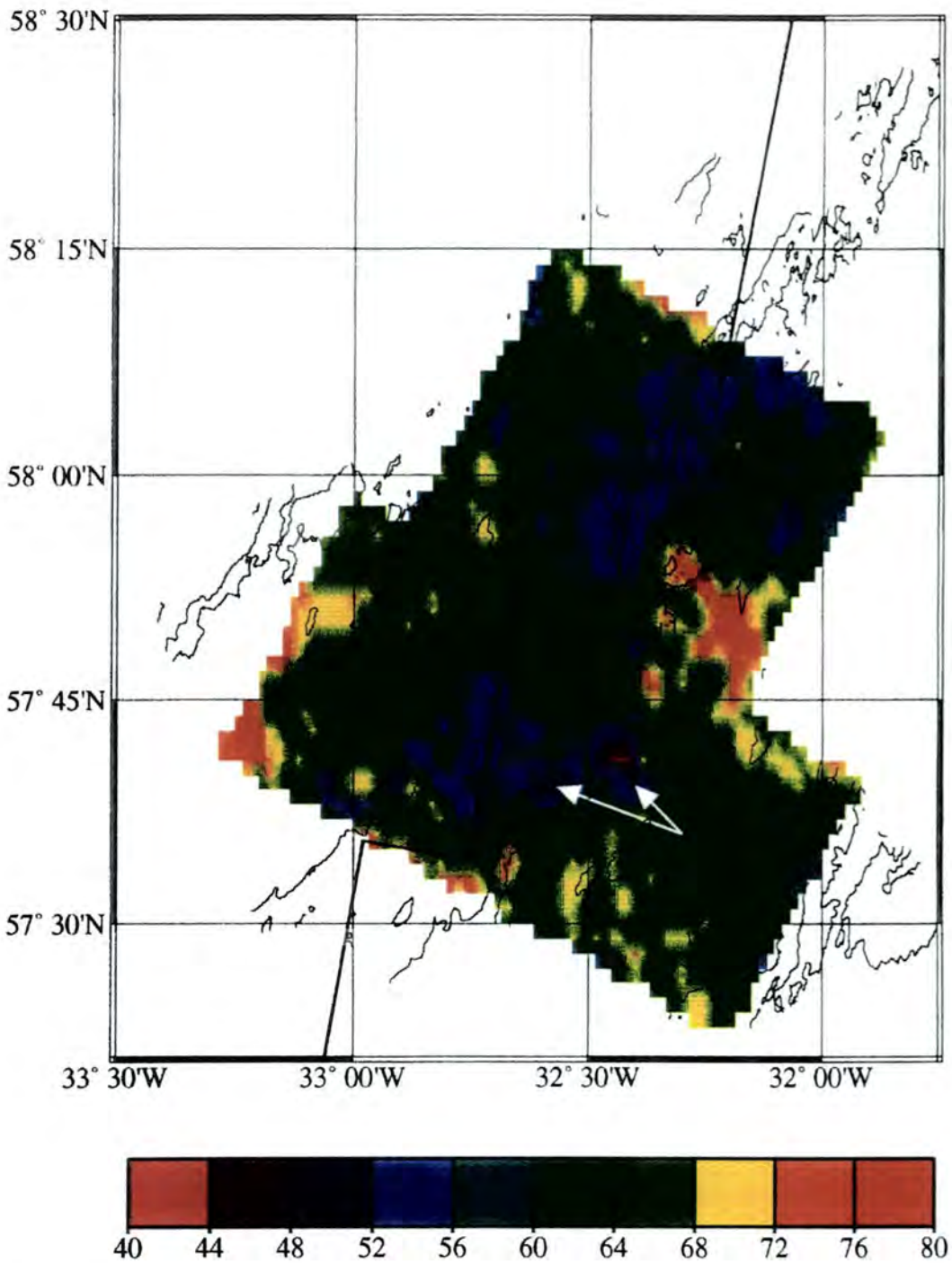


Figure 5.18: Residual mantle Bouguer anomaly obtained by removing the effect of passive upwelling (figure 5.17) from the mantle Bouguer anomaly (figure 5.13). The gravity field is only plotted where values for the MBA exist. The ridge–transform–ridge system is also plotted with the AVR of this study shown as a thicker line. The 1800 m bathymetric contour is overlain for reference. Note the two lows (L) which occur over the median valley wall to the east of the AVR studied (cf. figure 4.10) which are interpreted as indicating that the seabed topographic high is isostatically compensated in this area (see figure 5.19).

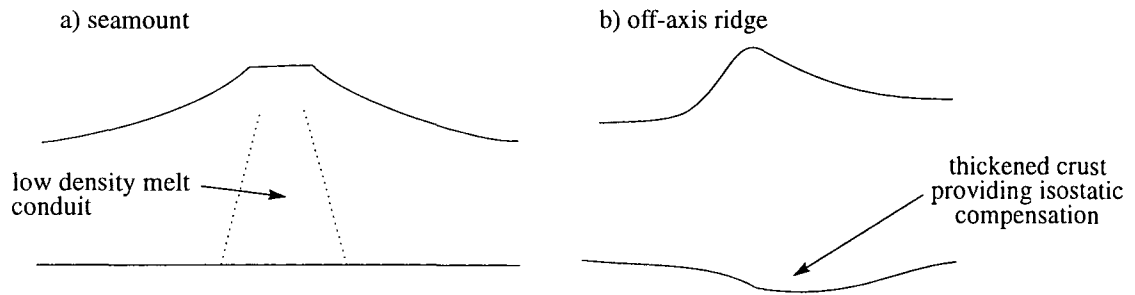


Figure 5.19: Sketch showing the possible causes of the low observed in the RMBA over off-axis ridges.

- a) low density magma conduit beneath a seamount.
 b) thickened crust providing isostatic compensation of the ridge.

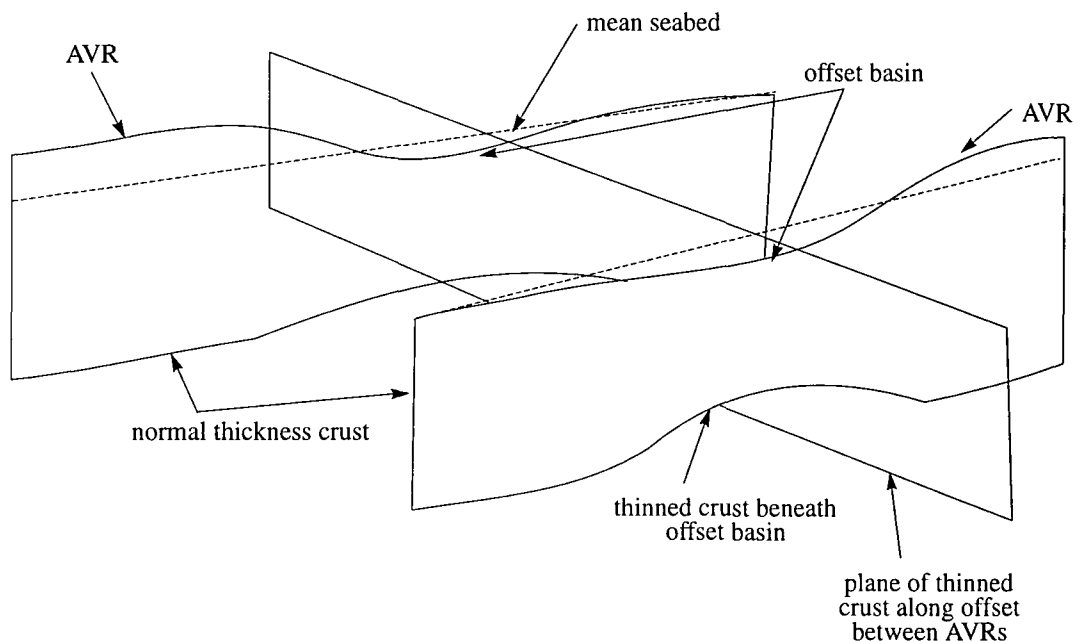


Figure 5.20: Sketch showing thinned crust beneath the offset basin located between an echelon AVR at 57° 55'N.

ridge. It is unlikely that there is a lower density in the crust at this range from the spreading centre unless associated with low density melt routes to seamounts, of which there is no evidence in the bathymetry. Therefore it appears that the crust is thicker in this region, possibly isostatically supporting the change in seabed topography (see figure 5.19). The only gravity high observed is of over 75 mGal and located at 57° 50'N 32° 10'W. This high is located directly along a flow line from the offset basin between the AVR centred on 57° 45'N and that to the north (centred on 57° 55'N), and seems to indicate thinned crust in this region between AVRs (see figure 5.20). This agrees with

the observations made by Field (1993) and Searle *et al.* (1994) for the southern extremity of Parson *et al.* (1993)'s Area C.

5.3 The Reykjanes Ridge normal incidence seismic data

The normal incidence seismic data collected during CD81/93 consists of two 4-fold profiles coincident with the along and across-axis wide-angle seismic profiles and two 8-fold profiles across-axis to the south of the across-axis wide-angle seismic line (see figure 2.17). The acquisition and processing of this dataset are described in Chapter 2, sections 2.8 and 2.9. The rough seabed in the area causes considerable scattering of energy incident on the seafloor. Consequently the seafloor reflector on the recorded normal incidence seismic sections is observed as a low amplitude event (see figures 5.21 and 5.22). This scattering has the effect of reducing the amplitude of the coherent signal propagating into the crust. On the across-axis normal incidence seismic lines the faulted topography of the seafloor also causes diffraction events which interfere with any reflections that may occur in the crust (figure 5.21). The gradational nature of the majority of boundaries in the crust, as modelled from the wide-angle seismic data, also reduces the possibility of observing any intra-crustal reflections.

As the along-axis normal incidence line is parallel to the dominant faulting direction this dataset is not as badly obscured by diffractions. Within the along-axis data two arrivals other than the seafloor reflection and sea bottom multiple are observed between 3.0 and 3.5 s and between 4.0 and 4.5 s TWTT respectively (see figure 5.22). It is possible that arrivals similar to these could be generated by side-swipe from axis-parallel faulted ridges. However examination of the bathymetric dataset shows that no ridges of a continuous enough nature can be identified at distances from the axis corresponding to these TWTTs in sea water (figure 5.23). This lack of causal topography indicates that the observed reflection events must be caused by reflectors within the crust. The only boundary observed on the along-axis wide-angle seismic model that could cause such a reflection event is the low velocity block located at ~2.5 km below the seabed. Therefore to compare these features the wide-angle seismic model was input into a normal incidence forward modelling package (figure 5.24), GXII

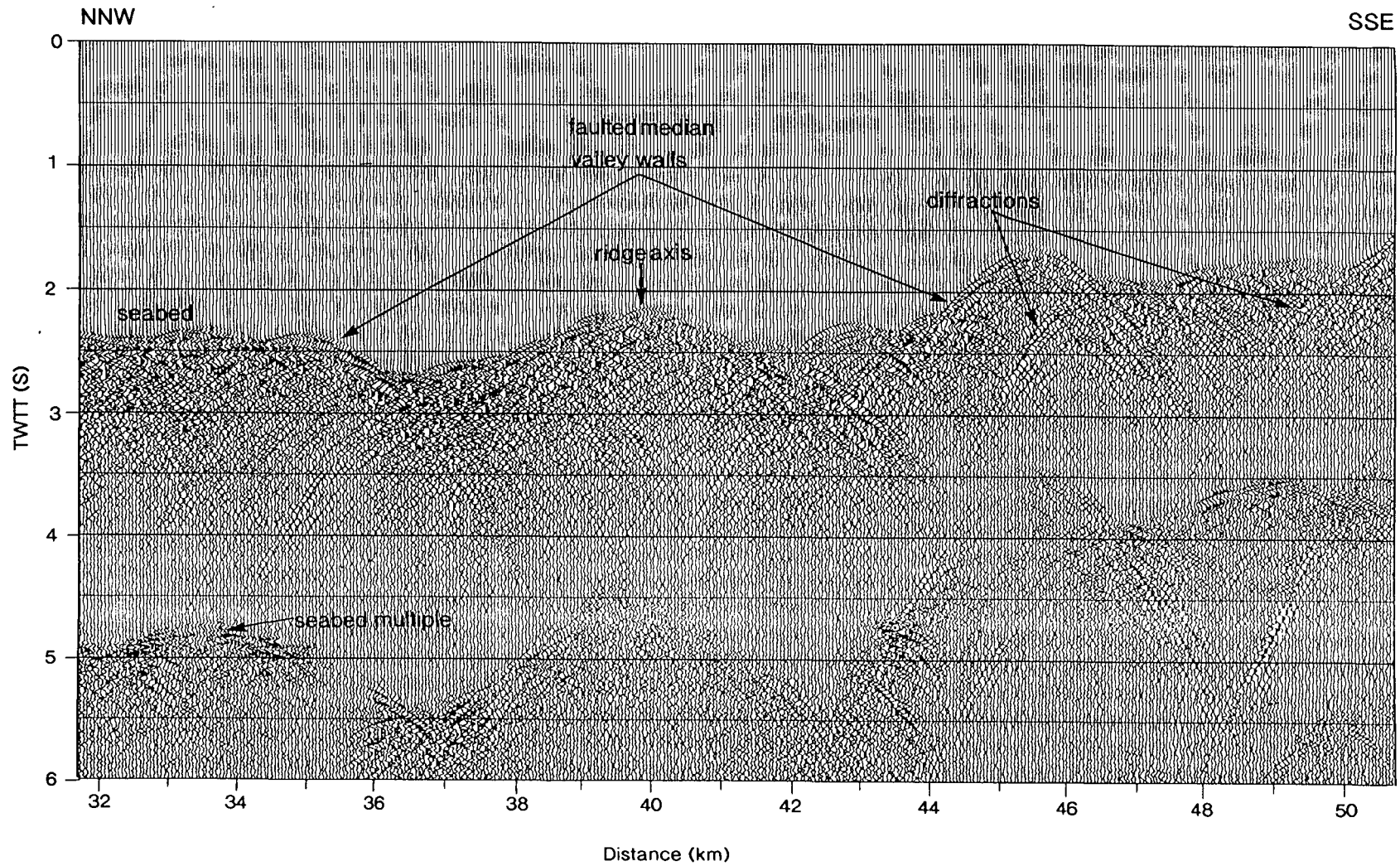


Figure 5.21: Across-axis normal incidence seismic data. Plotted on this section are unmigrated, stacked, 4-fold data (for processing information see section 2.9). Note the dominant diffractions from the faulted seafloor and the lack of coherent intra-crustal reflectors.

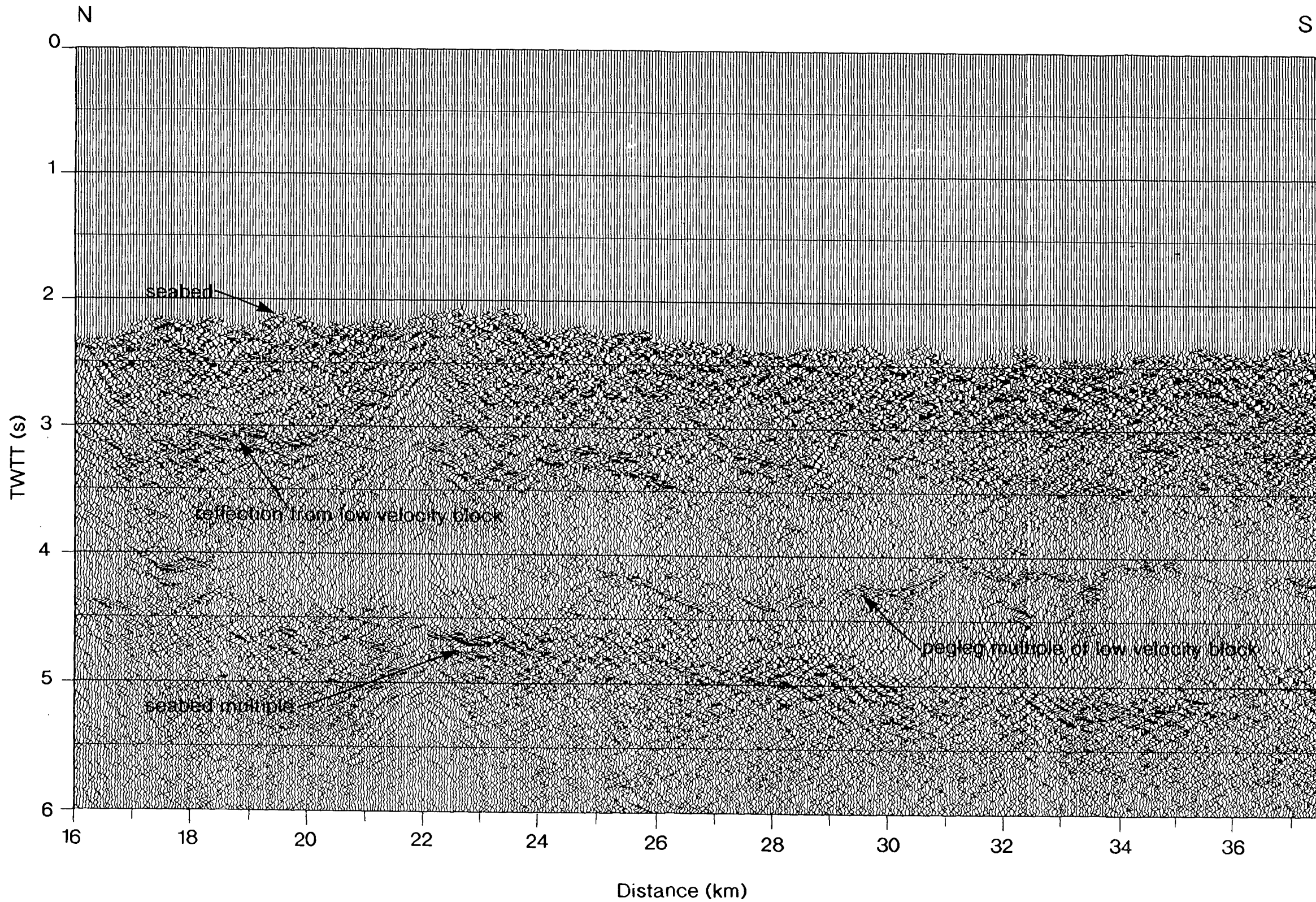


Figure 5.22

Figure 5.22: Along-axis normal incidence seismic data. Plotted on this section are migrated, stacked, 4-fold data (for processing information see section 2.9). Note the reflectors between 3 and 3.5 s TWTT and between 4 and 4.5 s TWTT believed to be from the low velocity block identified in the wide-angle seismic model.

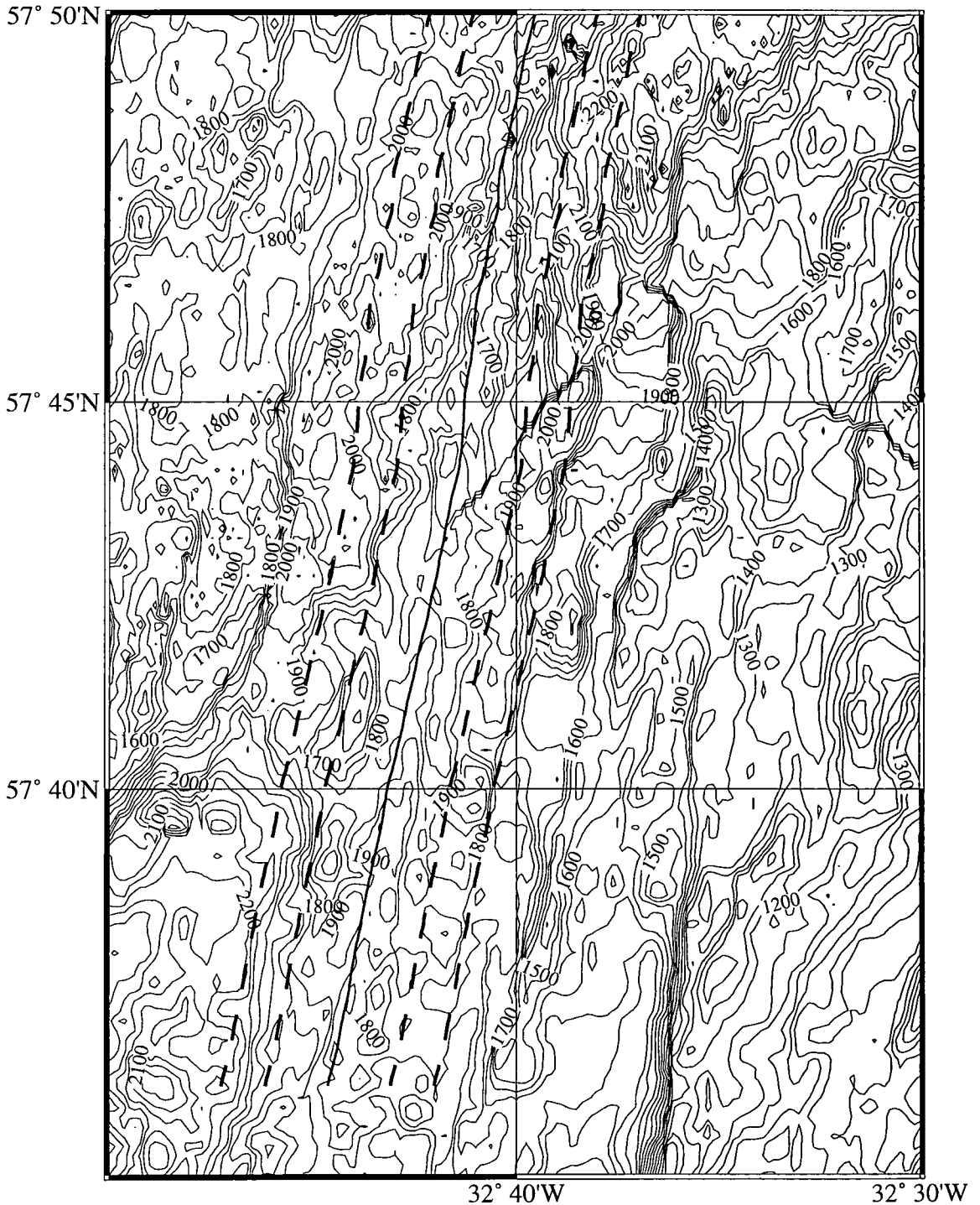


Figure 5.23: Bathymetry in the region of the along-axis seismic line (solid line), where the arrivals between 3.0 and 3.5 s TWTT and 4.0 and 4.5 s TWTT are observed. Contour interval is 50 m. The dashed lines represent ranges at which side-swipe could originate in order to generate these arrivals. Note that although in some localities ridges do coincide with these ranges none of these are of a continuous enough nature to generate the observed arrivals.

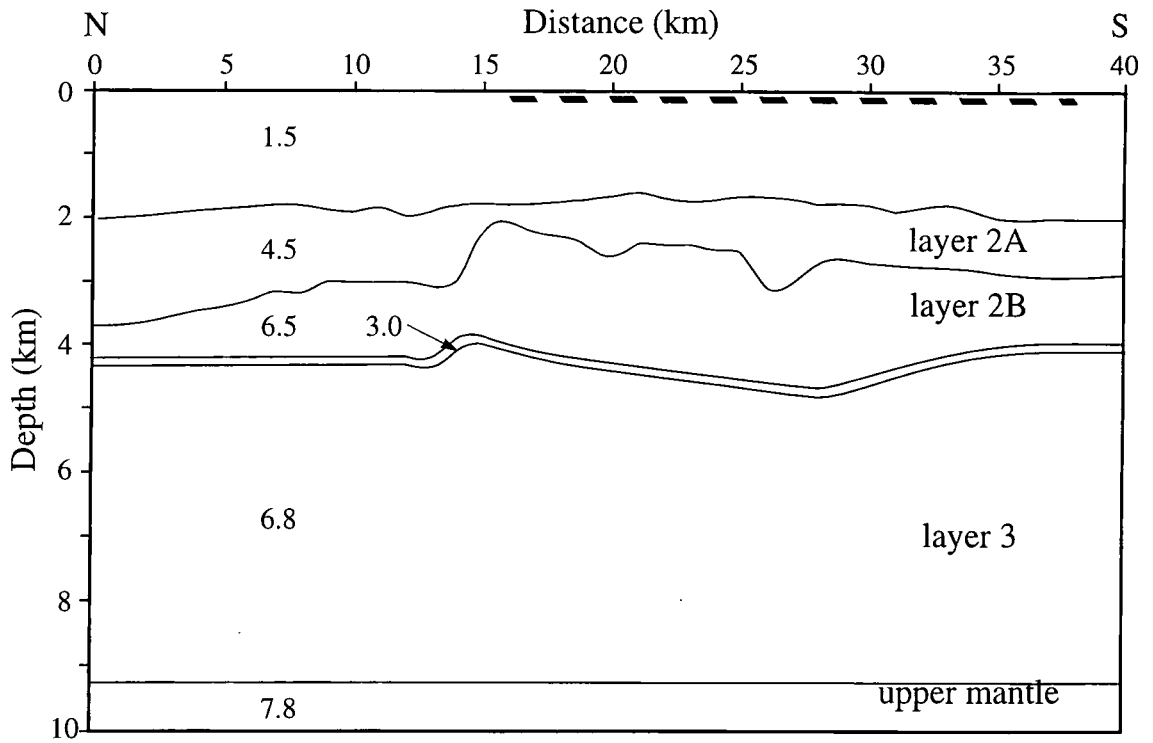


Figure 5.24: Along-axis model used with GXII. Layer geometries are identical to those of the along-axis wide-angle seismic model and velocities are labelled in km s^{-1} . The dashed line shows the region for which normal incidence data are available and over which synthetic data were calculated.

version 2.1 (GXII Technology Corporation, USA), and ray-traced to produce synthetic data between 16 and 38 km model ranges (figure 5.25) where the two recorded seismic datasets are coincident. The geometry of the upper reflector (3.0 to 3.5 s TWTT) in the normal incidence data is well matched by the synthetics generated by a reflection from the top and base of the wide-angle seismic low velocity zone. However, the velocities required to match the TWTT of the reflector were slightly higher for the normal incidence model than for the wide-angle seismic model. Layer 2A is modelled with a constant velocity of 4.5 km s^{-1} and layer 2B with a constant velocity of 6.5 km s^{-1} assuming that the depth to the low velocity block from the wide-angle seismic model, which is constrained to $\pm 200 \text{ m}$ (see section 4.4), is correct (figure 5.25). The later arrival between 4.0 and 4.5 s TWTT is easily reproduced from this model as a seabed pegleg multiple of the low velocity zone (figure 5.25). As either the primary or multiple reflection is observed at all ranges along the entire length of the along-axis normal incidence line this indicates that, where normal incidence seismic data exists from the centre of the AVR to its southern extremity, the low velocity block is continuous

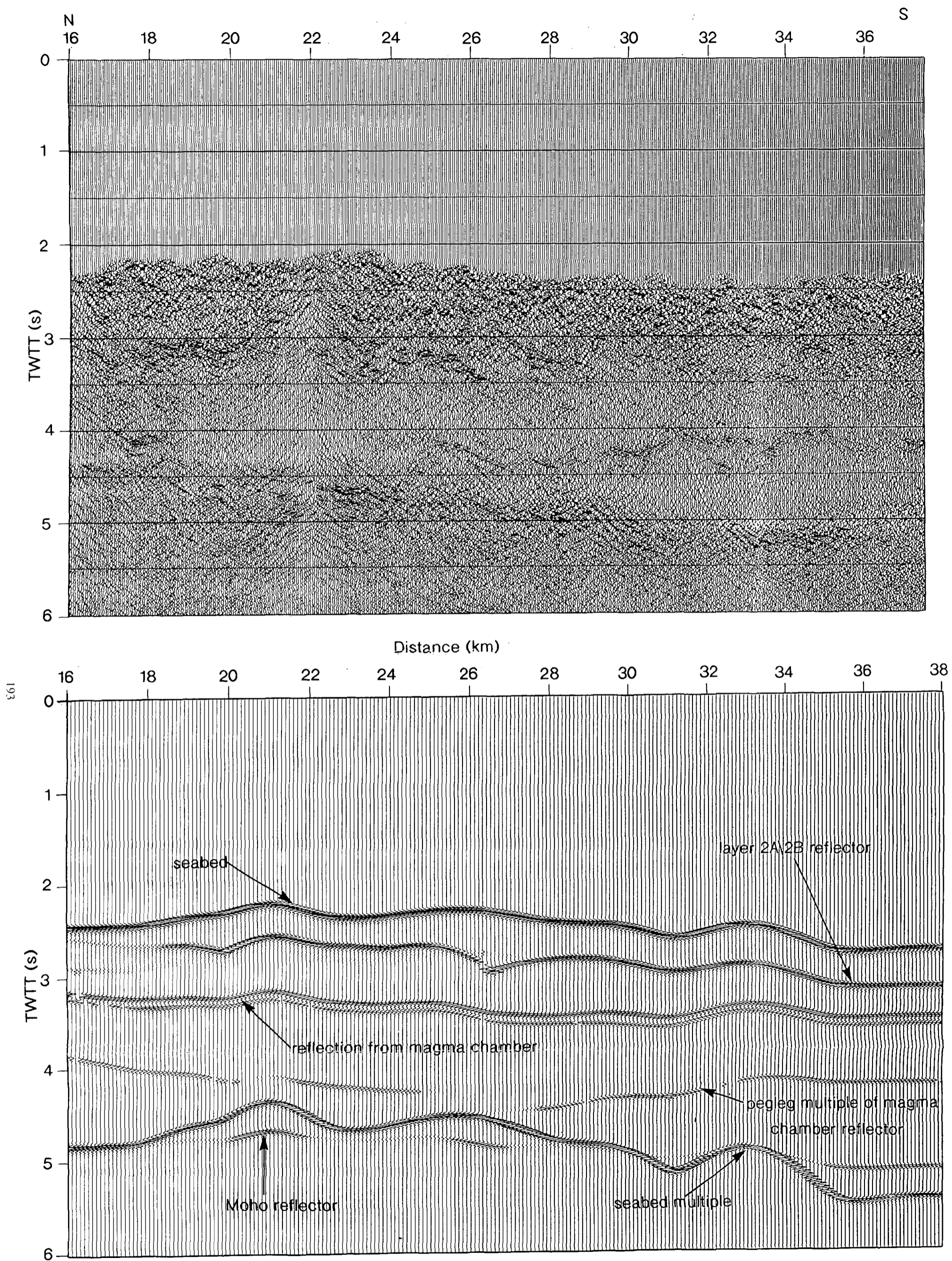


Figure 5.25: Along-axis normal incidence synthetic and observed data between model offsets of 16 and 28 km. The upper diagram shows the observed data, with an overlay of the synthetic data travel times and the lower diagram shows the synthetics generated from the GXII model shown in figure 5.24. The main reflectors are labelled. The layer 2A/2B reflector in the synthetic data is not seen on the observed data. This reflector is generated as layers 2A and 2B are modelled with constant velocities within the constraints of the modelling process and the dataset itself. However the wide-angle model suggest this should be a gradational boundary which should not generate a reflection (see text). The areas where the overlay does not match the seafloor are either due to side-swipe or the limited number of nodes used to define the model.

beneath the axis. To investigate the nature of the boundaries of the low velocity block they were also modelled as being gradational. This type of boundary had the effect of reducing the amplitude of the modelled reflection event. To resolve between the two types of boundary a relative amplitude study would be required. Unfortunately the low quality of the reflection data collected during CD81/93 prevents this kind of analysis. Therefore, based on the results of modelling the gravity and wide-angle seismic datasets a low velocity block with boundaries sharp on the scale of the seismic wavelength was considered to be the best model to match all observed data within their resolving limits.

A Moho reflection is not observed on the along-axis normal incidence seismic section. The high relative amplitude of the reflection from the low velocity layer combined with the degree of seabed scattering suggests that little energy would penetrate down to the Moho which, combined with the possibly gradational nature of the boundary (see section 5.5), would suggest that any Moho reflections would be of a relatively low amplitude if they were observed at all. Also modelling of this phase indicates that it would occur between 4.8 s and 5.2 s TWTT (figure 5.25) which approximately coincides with the seafloor multiple in the data. Therefore should a reflection occur it would probably be obscured by the higher amplitude multiple.

The geometry and amplitude of the prominent reflection events in the synthetic normal incidence data, generated from the wide-angle seismic model, match the observed reflections in the normal incidence data well (see figure 5.25). The upper crustal velocities required in the normal incidence model to match the travel time of the reflections from this low velocity block are $\sim 1 \text{ km s}^{-1}$ higher than those from the wide-angle seismic models. This mismatch between the two models cannot be resolved with this dataset as the exact velocities of reflections in the normal incidence data cannot be easily obtained as the moveout of the data is too low.

In summary a continuous reflection is observed in the normal incidence seismic data corresponding to a low velocity block beneath the ridge axis, which extends at least from the centre of the AVR to its southern extremity. This reflection event is not observed on the across-axis normal incidence seismic dataset, possibly due to the narrow width of the low velocity block (as modelled with the wide-angle seismic data)

and distortion by seafloor diffractions and scattering. The continuous nature of this reflection along-axis and its correspondence with the low velocity block observed on the wide-angle seismic model indicate that it is a reflection from the top of a magma chamber similar to those observed at fast and intermediate spreading ridges, e.g. the East Pacific Rise (Detrick *et al.*, 1987; Harding *et al.*, 1989; Kent *et al.*, 1994; Mutter *et al.*, 1995) and the Valu Fa Ridge (Morton and Sleep, 1985; Collier and Sinha, 1992). However such a bright, continuous reflection event has not previously been observed beneath any other slow spreading ridge (see section 5.5).

5.4 Comparison with the results of modelling the controlled source electromagnetic data

The controlled source electromagnetic (CSEM) technique is described by Chave and Cox (1982), Webb *et al.* (1985) and Cox *et al.* (1986) and the instrumentation used during the Reykjanes Ridge CSEM experiment is described in Sinha *et al.* (1990). The details of this experiment and the modelling of the collected CSEM dataset, together with the geological significance of the final model are the subject of a Ph.D. dissertation by L.M. MacGregor (University of Cambridge). The final CSEM model will be described here in relation to the final across-axis wide-angle seismic model. The CSEM data were modelled using a 2-D forward method (Unsworth *et al.*, 1993) with the initial model based on the final across-axis wide-angle seismic model. The final CSEM model is shown in figure 5.26 and its main features are as follows:-

- 1) The upper layer on-axis is approximately 6 km wide (centred on the ridge axis) and ~0.25 km in thickness. The resistivity in this layer of 1 Ω m indicates a sea water saturated porosity of approximately 30%. This is underlain by a layer of the same width but of 1 km in thickness, with a resistivity of 10 Ω m corresponding to 2% sea water saturated porosity (L.M. MacGregor, pers. com.). The layer 2A/2B boundary of the wide-angle seismic model lies within this lower layer and the low resistivities correlate well with low P-wave and extremely low S-wave velocities, the latter also indicating high porosity. The upper layer is not resolved by the

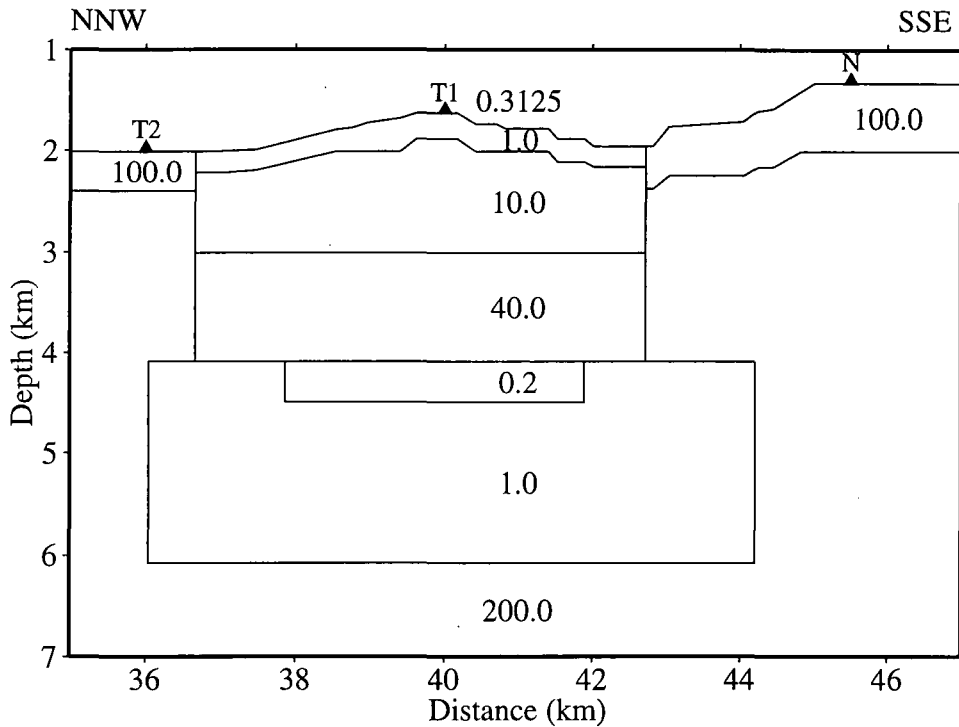


Figure 5.26: The final controlled source electromagnetic model (L.M. MacGregor, pers. com.). Resistivities are labelled in Ω m and the position of the three instruments constraining this dataset are marked by triangles. The ridge axis lies at 40 km model offset with instrument T1 located on the crest of the AVR. Note how the low resistivities are centred on the axis.

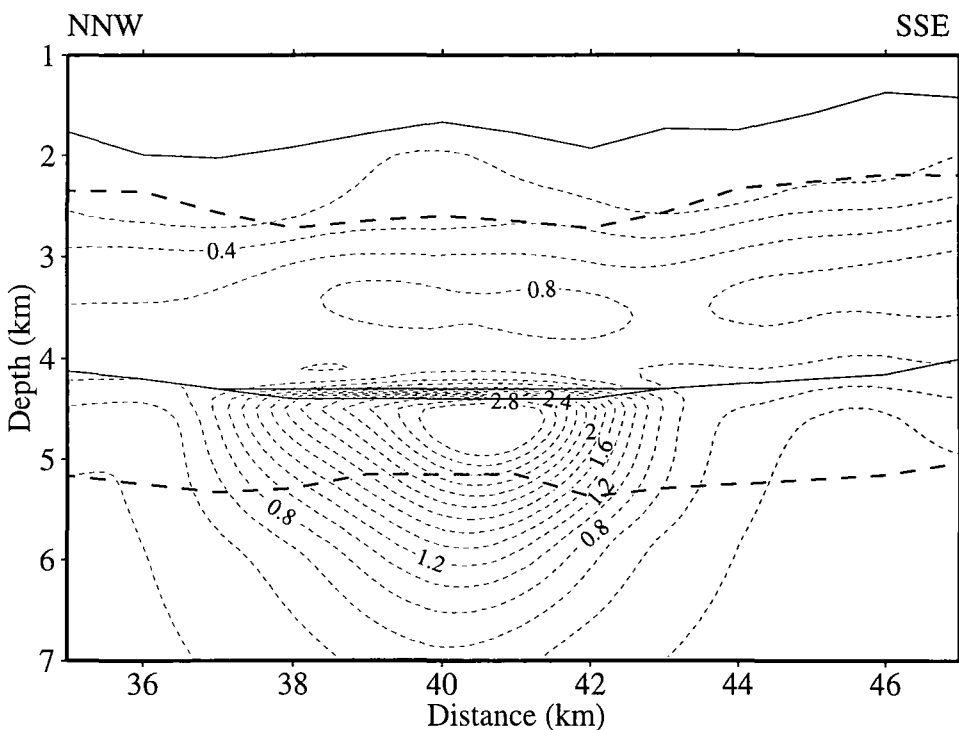


Figure 5.27: Seismic P-wave velocity anomaly (cf. figure 4.10) plotted at the same scale as the CSEM model for comparison. Velocities below those at equivalent depths off-axis are labelled in km s^{-1} . The dashed lines show the locations of the seismic model's second order boundaries. Note the correspondence of the 0.8 km s^{-1} "below-normal" velocity contour in layer 2B with the $40 \Omega\text{m}$ low resistivity block in the CSEM model and the similarity in the horizontal extent of the low resistivity/low velocity zone in layer 3.

seismic data modelling and this mismatch can be partly explained if the transition is gradational (rather than sharp as indicated in the CSEM model) and also because few arrivals are actually observed on the wide-angle seismic model that have turned in the upper 0.25 km of the crust and which do not interfere with the direct water waves (e.g. Christenson *et al.*, 1996). A further source of mismatch between the two datasets is the fact that they resolve different properties, i.e. the resistivity detected by the CSEM technique responds to an interconnected melt fraction whereas the P-wave velocity is affected by disconnection of solid phases.

- 2) Off-axis the upper layer of the CSEM model is approximately 0.5 km in thickness and the base of this layer coincides with the seismic layer 2A/2B boundary. The 100 Ω m resistivity of this layer is not well constrained but modelling indicates that it must increase from the axial values of 1-10 Ω m, implying a decrease in porosity with age. Velocities in layer 2A also increase off-axis although this is far more gradational than is apparent from the CSEM model. It should be noted that the CSEM model is poorly constrained off-axis (see 6 below).
- 3) In oceanic layer 2B resistivities on-axis are 40 Ω m in a 6 km wide, 1.25 km thick block. This resistivity is lower than that off-axis (200 Ω m) at the same level. This axial low resistivity region coincides with the 0.8 km s⁻¹ "below-normal" P-wave velocity region observed in layer 2B and is ~4 km wide (figures 5.26 and 5.27). These low velocities and resistivities on-axis may relate to higher porosity due to fracturing.
- 4) On-axis between layers 2 and 3 there is a 4 km wide low resistivity zone. The resistivity of 0.2 Ω m in this zone corresponds to pure basaltic melt. In CSEM modelling there is a trade off between resistivity and layer thickness. With a resistivity of 0.2 Ω m the layer could be as little as 150-200 m in thickness. By increasing the resistivity and thickness of the layer an equally good agreement between the forward model and the data can be achieved (L.M. MacGregor, pers. com.). The depth (2.5 ± 0.3 km) and width of this low resistivity zone are well constrained by observed data and its geometry and extent match the axial low velocity block in the seismic model well – the latter being ~4 km in width and 100

m in thickness. The thickness and low velocity ($\sim 3.0 \text{ km s}^{-1}$) of this seismic layer acts as a constraint on the CSEM modelling and indicates that the thin, low resistivity layer shown in figure 5.26 is most appropriate for this dataset as seismic modelling of a thicker sub-axis layer does not match the observed data.

- 5) The deepest low resistivity block is not well constrained in depth but the observed data is best matched if the base of this layer lies at least 3 km beneath the seafloor. The low resistivities in this layer ($\sim 1 \text{ } \Omega \text{ m}$) indicate that this region contains approximately 20% melt (L.M. MacGregor, pers. com.). Again a higher resistivity is possible if the layer is thicker. If this is compared to the across-axis wide-angle seismic velocity anomaly plot (figure 5.27) its 9 km width compares well with the low velocity zone in layer 3. Although low velocities seem to extend further down into layer 3 than low resistivities, this could be due to the trade off between layer thickness and resistivity in the CSEM model.
- 6) Due to the failure of a CSEM instrument programmed to record the short range off-axis data, the off-axis resistivity is poorly constrained. However resistivities of greater than $200 \text{ } \Omega \text{ m}$ are required below $\sim 0.5 \text{ km}$ to match the observed data in any way. This value reflects a resistivity typical of young oceanic crust (Chave and Cox, 1982) and the result agrees with the normal crustal velocity structure encountered within 10 km of the ridge axis.

Therefore in general there is good agreement between the across-axis wide-angle seismic and the CSEM models. Although the seismic model indicates that the variations in physical properties are more gradational than in the CSEM model, this could be explained by the geometrical restrictions in the CSEM modelling program. The seismic modelling method provides a much greater constraint on the geometries due to the nature of the ray-tracing technique and the observed dataset itself. The wide-angle seismic and CSEM models both indicate an increase in velocity and resistivity respectively off-axis. These increases correspond in turn to a decrease in porosity in the upper crust and the degree of partial melt in the mid to lower crust. The models also indicate a low velocity/low resistivity block, $\sim 4 \text{ km}$ in width and 100 m in thickness, located 2.5 km beneath the seafloor on-axis which, from the physical properties

(velocity, density and resistivity) must be predominantly molten.

5.5 Relationship with previous studies of mid-ocean ridges

In this section the geophysical evidence for the crustal structure of the Reykjanes Ridge is compared with that found elsewhere on the mid-ocean ridge system and interpreted in terms of the similarities and contrasts in the processes of crustal accretion occurring. In section 5.5.1 the seismic data from this study are interpreted and compared with those from other investigations and in section 5.5.2 the gravity data are considered.

5.5.1 Seismic models

Velocity–depth profiles constructed at 10 km (~1 Ma) intervals along the final across-axis wide-angle seismic model are shown in figures 5.28a and b. Velocity–depth envelopes for young Mid-Atlantic Ridge and East Pacific Rise oceanic crust obtained from the compilation of White *et al.* (1992), and located away from anomalous features such as hot spots and fracture zones, are overlain for comparison. The majority of the Reykjanes Ridge profiles lie within these "standard" envelopes. As mature oceanic crust (≥ 1 Ma) produced at the Reykjanes Ridge has similar layer thicknesses and velocities to that observed elsewhere on the mid-ocean ridge system the processes of accretion should, by implication, also be similar. The axial profile constructed at 0 Ma has velocities below those of the "standard" velocity envelopes for layers 2B and 3, and also for the low velocity block. This deviation is also observed when comparing a "standard" EPR velocity envelope with a zero-age profile from the EPR at 9° 30'N (Vera *et al.*, 1990; and see figure 5.28c). An interpretation of the main layers of the Reykjanes Ridge final across-axis model in terms of previous studies of mid-ocean ridges follows.

Layer 2A

Layer 2A of the EPR profile has an upper layer of approximately 100 m in thickness with an extremely low velocity (~ 2.4 km s⁻¹) which is in turn underlain by a strong velocity gradient with a velocity of greater than 5.0 km s⁻¹ achieved 200 m

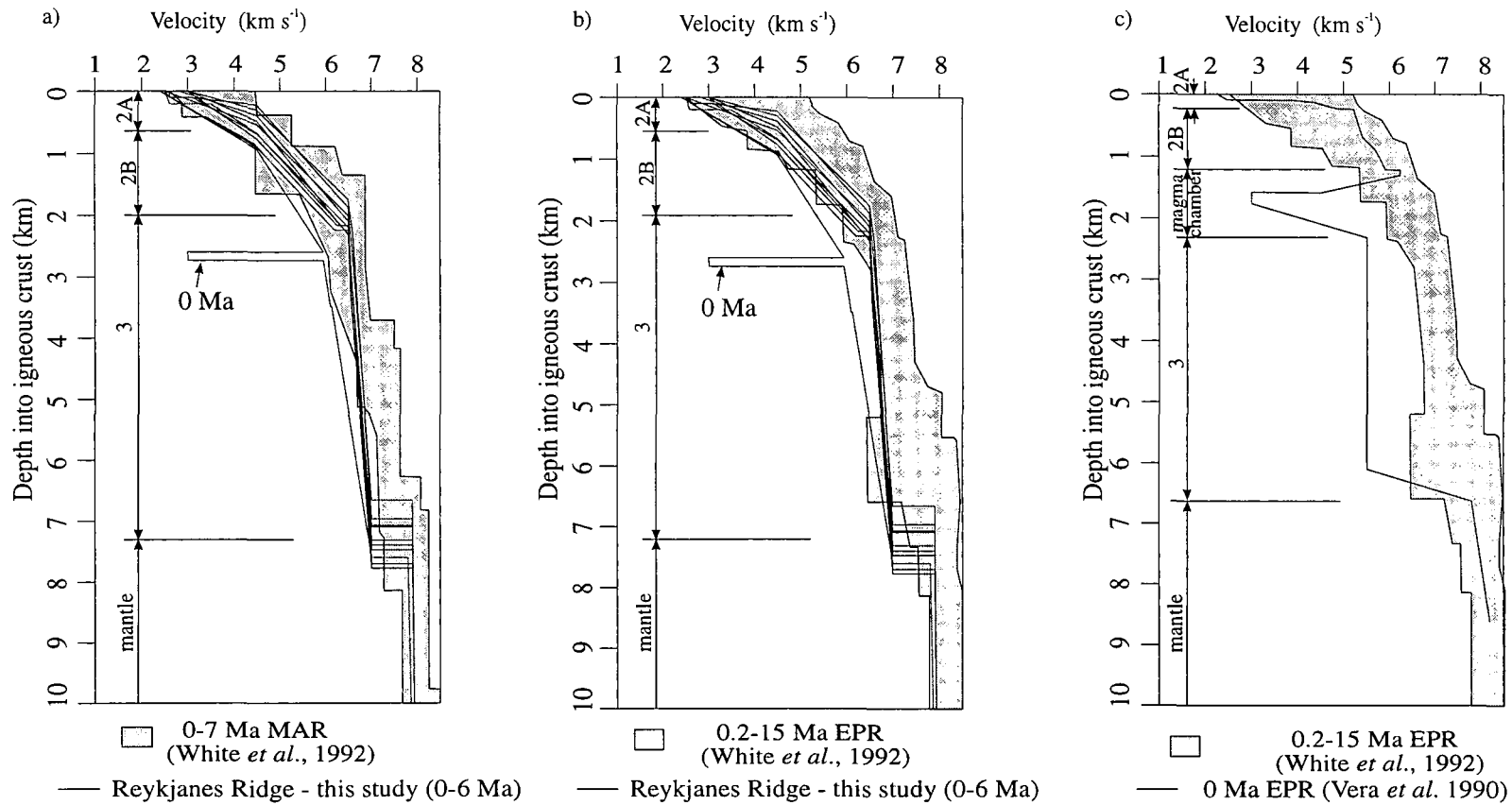


Figure 5.28: Velocity–depth profiles compared with "standard" velocity envelopes for oceanic crust.

a) Velocity–depth profiles constructed at 1 Ma intervals on the Reykjanes Ridge overlain with the "standard" velocity–depth relationships for MAR crust (0-7 Ma; White *et al.*, 1992). Note that the majority of the profiles lie within this velocity–depth envelope with the exception that located at 0 Ma. The crustal layers labelled do not apply to the 0 Ma profile.

b) The same velocity–depth profiles as in a) overlain with the "standard" velocity–depth envelopes for the EPR. Again the only velocity–depth profile lying outside this envelope is that constructed at 0 Ma.

c) A 0 Ma profile from 9° 30'N on the EPR (Vera *et al.*, 1990) which also lies outside of the "standard" EPR profile.

beneath the seafloor. The upper layer in the Reykjanes Ridge profile is represented by a single, fairly steep velocity gradient from 2.5 km s^{-1} at the seafloor to 4.5 km s^{-1} at 800 m depth. The Vera *et al.* (1990) experiment was conducted using the expanding spread technique which can detect rays turning in the upper crust. This method therefore provides more details of the structure in the upper 1 km of the crust than is possible using conventional refraction surveys, where the arrival of rays turning in the upper crust is masked by interference with larger amplitude direct water waves. An on-bottom refraction experiment at 23°N on the MAR (Purdy, 1987) also shows higher gradients in the upper few hundred metres of the crust. Hence the single gradient modelled on the Reykjanes Ridge is probably averaging a more complex structure that is not readily resolvable with the conventional refraction technique used during CD81/93.

From a comparison of this model with previous studies that have related crustal velocities to drill and ophiolite investigations of the oceanic crust (e.g. Spudich and Orcutt, 1980b; Bratt and Purdy, 1984), layer 2A has been identified as highly fractured pillow basalts and lava flows. The P-wave velocities obtained from laboratory studies of mid-ocean ridge basalts lie in the range $5\text{-}6 \text{ km s}^{-1}$ (Christensen and Salisbury, 1975). These values are considerably higher than those observed in layer 2A both on the Reykjanes Ridge and elsewhere in the oceanic crust. This apparent discrepancy in velocities observed by large-scale refraction studies and small-scale sampling of velocities is believed to be due to the presence of large-scale porosity in the upper oceanic crust (Christensen and Salisbury, 1975). The low P and S-wave velocities observed on the Reykjanes Ridge can therefore be explained by the presence of large-scale fracture porosity.

Numerous recent studies of the EPR indicate that layer 2A doubles in thickness within 1-2 km of the ridge axis (Harding *et al.*, 1993; Christenson *et al.*, 1994; Kent *et al.*, 1994; Vera and Diebold, 1994; Christenson *et al.*, 1996). However both this study and that of Smallwood *et al.* (1995) at $61^\circ 40'\text{N}$, indicate that layer 2A thins off-axis. An experiment at 37°N on the MAR also indicates an upper layer of velocity 2.8 km s^{-1} that thins off-axis (Fowler, 1976).

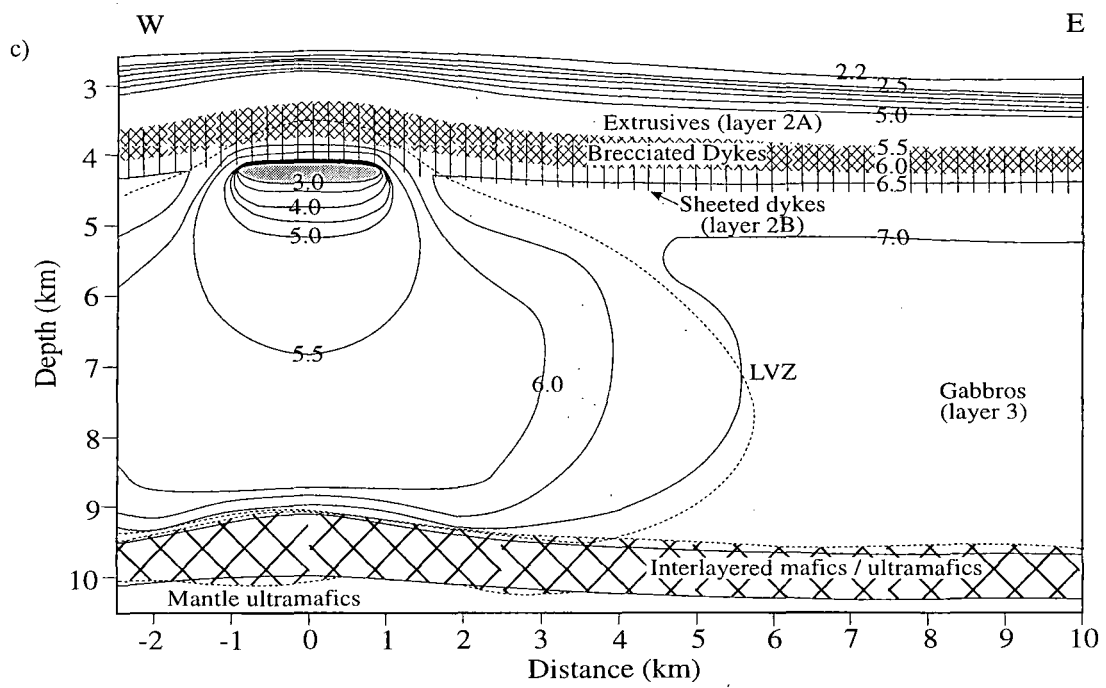
The layer 2A/2B boundary is either caused by a transition from the pillow

basalts of layer 2A into the sheeted dykes of layer 2B or may be a porosity boundary due to increased confining pressure closing the pore space and fractures at depth. The former is believed to be the case at the EPR where there is evidence from the dating of basalts that lavas are emplaced off-axis (Goldstein *et al.*, 1994), hence causing the observed off-axis thickening of layer 2A. However the thinning of this layer off-axis at the Reykjanes Ridge implies that the base of the layer may be marked by a porosity boundary, which shallows off-axis as porosity is reduced due to the infilling of pore space by mineral precipitation by hydrothermal circulation in the cooler off-axis crust. This off-axis thinning also implies that there is no off-axis lava emplacement at the MAR and that the maximum thickness of this layer is achieved on-axis.

Layer 2B

Layer 2B on the EPR axial profile (Vera *et al.*, 1990) consists of a series of velocity gradients such that the velocity increases from 5.1 km s^{-1} at 200 m depth to 6.0 km s^{-1} some 1.3 km beneath the seafloor. The Reykjanes Ridge axial profile shows a single velocity gradient increasing the velocity by 1.45 km s^{-1} to 5.95 km s^{-1} some 2.5 km beneath the seafloor. This layer consists of sheeted dykes with much lower fracture porosity than in layer 2A (e.g. Bratt and Purdy, 1984) as the velocities lie well within the range of values found from laboratory studies of ophiolites and drill samples (e.g. Spudich and Orcutt, 1980b).

A broad region, ~20 km in width and centred on the ridge axis with velocities up to 0.8 km s^{-1} below those at equivalent depths off-axis, is observed on the Reykjanes Ridge across-axis model (figure 5.29a). A similar feature is not observed on the EPR model (figure 5.29b). The low velocities in this region, together with the low resistivities observed in this layer (see section 5.4), indicate that there is a small percentage of porosity not preserved beyond 10 km offset from the axis. If the porosity is caused by tectonic fracturing in the upper crust, this would not occur on the fast spreading EPR due to the higher crustal temperature and would therefore explain why a similar low velocity zone is not observed in layer 2B of EPR models (e.g. Toomey *et al.*, 1990; Vera *et al.*, 1990).



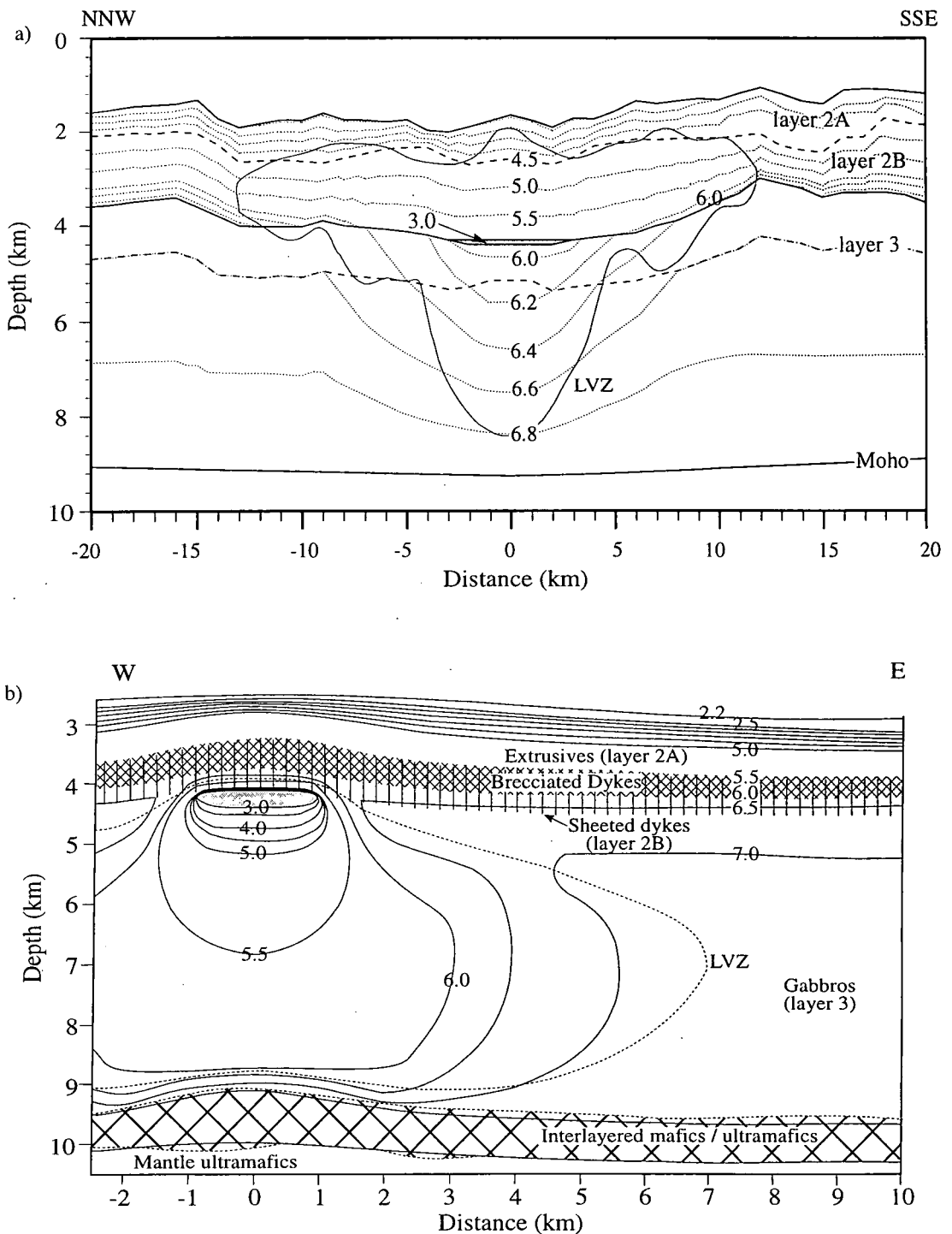


Figure 5.29: Comparison of across-axis crustal structure at the Reykjanes Ridge at $57^{\circ} 45'N$ and the EPR at $9^{\circ} 30'N$ (Vera *et al.*, 1990).

a) Crustal structure of the Reykjanes Ridge. Isovelocity contours are labelled in km s^{-1} with the 0.2 km s^{-1} "below-normal" contour (see figure 4.10) overlain as the boundary of the low velocity zone.

b) Vera *et al.* (1990)'s model of the crustal structure at $9^{\circ} 30'N$ on the EPR. Isovelocity contours are labelled in km s^{-1} and the low velocity zone is marked by the dotted line.

The spreading axis in both cases is located at 0 km.

c) Vera *et al.* (1990)'s model of the crustal structure at $9^{\circ} 30'N$ on the EPR. Isovelocity contours are labelled in km s^{-1} . The low velocity zone shown here by the dotted line is calculated at the 0.2 km s^{-1} "below-normal" contour as in a). Note that the recalculation of this low velocity zone does not significantly alter the main features of b) as described in the text.

Axial low velocity block

At the EPR beneath layer 2B there is a high velocity layer of ~100 m in thickness with a velocity of 6.2 km s^{-1} . Below this layer a negative velocity gradient reduces the velocity from 6.2 km s^{-1} at the base of the high velocity layer to 4.5 km s^{-1} over a zone some 300 m in thickness. The base of this gradient zone is marked by a sharp boundary at the top of a low velocity block 200 m in thickness, located at 1.6 km beneath the seafloor with a velocity of 3.0 km s^{-1} . The base of this low velocity block has a positive gradient with the velocity increasing to 5.5 km s^{-1} over a distance of 500 m. The low velocity block on the Reykjanes Ridge model lies 2.5 km beneath the seafloor, has a thickness of 100 m and a velocity of 3.0 km s^{-1} . There is no evidence for a high velocity lid to this block, although the wavelength of the seismic energy at this depth would make it impossible to observe such a thin feature if it had a relatively small velocity contrast similar to that observed on the EPR.

Laboratory investigations of P-wave velocities in basalts indicate that velocities of the order of 3 km s^{-1} , as observed at the Reykjanes Ridge, only occur when they are completely molten (Murase and McBirney, 1973) – a molten layer is also indicated by the $0.2 \text{ } \Omega\text{m}$ resistivities observed with the CSEM data. Further evidence indicating that low velocity blocks at mid-ocean ridges are in fact molten basalt is the negative polarity of reflections from the top of this zone observed at both fast and intermediate spreading ridges (Collier and Sinha, 1992; Detrick *et al.*, 1993; Kent *et al.*, 1994) and the zero S-wave velocities observed at some localities on the EPR (Vera *et al.*, 1990). The high velocity lid observed at the EPR (Vera *et al.*, 1990) is interpreted as the solidified cap of the axial magma chamber, with this cap having a low porosity. Although the velocity and thickness of the low velocity blocks on the EPR and Reykjanes Ridge are similar there is no evidence for gradational boundaries to this zone on the Reykjanes Ridge. These sharp boundaries may have been caused by the cooler environment (Sleep, 1975) at the slow spreading Reykjanes Ridge with deeper, more efficient hydrothermal cooling in layer 2, facilitated by the high porosity, allowing sharp boundaries to the magma chamber to develop.

Reflections observed from the top of magma chambers vary in amplitude, with

very bright reflections of reversed polarity indicating a high proportion of partial melt (Vera *et al.*, 1990; Collier and Sinha, 1992; Detrick *et al.*, 1993; Kent *et al.*, 1994). However in some regions, e.g. at 13°N on the EPR (Harding *et al.*, 1989), the amplitude of the reflection is lower and the S-wave velocity is non-zero indicating that at specific sections of the fast spreading EPR the axial magma chamber is only partially molten.

The depth to the top of this body obtained from normal incidence surveys at the EPR and the intermediate spreading Valu Fa Ridge (Lau Basin) have been combined with refraction surveys at the intermediate spreading Juan de Fuca Ridge (Christenson *et al.*, 1993) and slow spreading Mid-Atlantic Ridge (Kong *et al.*, 1992) which show velocity inversions, and used to identify an apparent inverse relationship between the depth (below seabed) to the top of the magma chamber and the spreading rate of the ridge itself (Purdy *et al.*, 1992; and see figure 5.30). With this model travel times of magma chamber reflections at the EPR, which are associated with half spreading rates of 55-75 mm yr⁻¹, have indicated average depths to the top of the magma chamber of ~1.4 km (Detrick, 1991; Detrick *et al.*, 1991). The intermediate spreading Valu Fa Ridge has a magma chamber reflector at 3.0 km (Morton and Sleep, 1985; Collier and Sinha, 1990) and the Juan de Fuca Ridge has provided observations of both a low velocity zone 3.2 km beneath the seafloor (Christenson *et al.*, 1993) and a possible magma chamber reflector 2.3 to 2.5 km beneath the seafloor (Morton *et al.*, 1987). These ridges both have half spreading rates of 30-35 mm yr⁻¹ (Morton and Sleep, 1985; Collier and Sinha, 1990; Christenson *et al.*, 1993). Evidence from the slow spreading MAR (half spreading rate ~12 mm yr⁻¹) has shown a low velocity zone exists at 26°N at a depth of 3 km beneath the seafloor (Kong *et al.*, 1992) and at 60°N a small velocity inversion exists between 3.7 and 4.3 km beneath the seafloor (Bunch and Kennett, 1980). This study has indicated a depth to the top of the magma chamber at 57° 45'N on the Reykjanes Ridge of 2.5 km, which is much shallower than would be predicted from the model of Purdy *et al.* (1992) (see figure 5.30). A shallow depth of 1.2 km for an axial magma chamber reflector on the MAR has also been observed by Calvert (1995) (see figure 5.30). The range of depths to the top of magma chambers observed at the EPR (Detrick *et al.*, 1991), from 1.2 to 2.4 km beneath the seafloor also suggests a

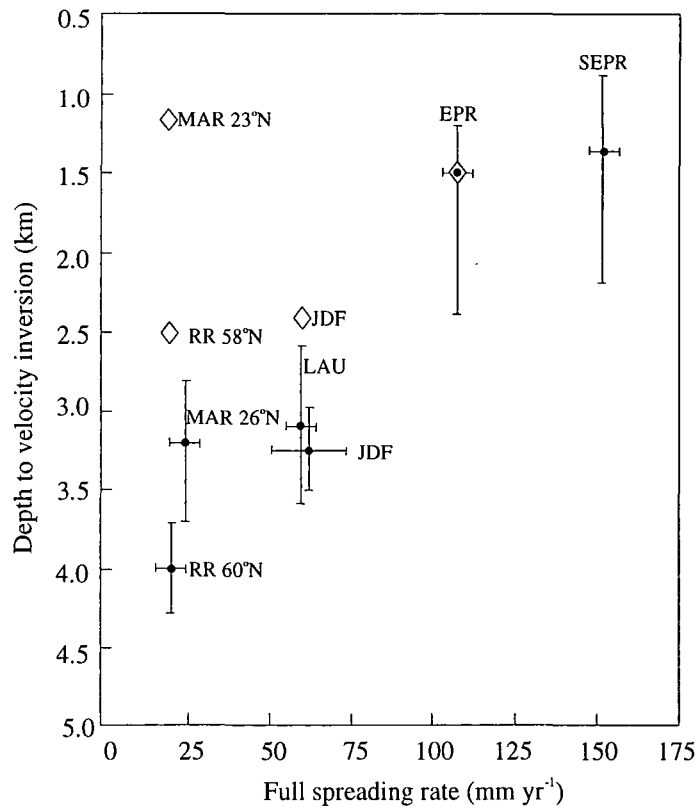


Figure 5.30: Spreading rate dependence of the depth to the top of low velocity zones, after Purdy *et al.* (1992). The dots and their corresponding variance are taken from data compiled by Purdy *et al.* (1992) and indicate an increase in the depth to low velocity zones as spreading rate decreases. The diamonds represent:-

- 1) depth to the top of a partially solidified magma chamber at 13°N on the EPR (Harding *et al.*, 1989) which lies at the mean depth for this section of the EPR;
- 2) depth to the top of a possible magma chamber reflector beneath the intermediate spreading Juan de Fuca Ridge (JDF) (Morton *et al.*, 1987);
- 3) depth to the short reflector identified as a magma chamber reflector at 23°N on the MAR (Calvert, 1995); and
- 4) depth to the top of the magma chamber imaged in this study at 57° 45'N on the Reykjanes Ridge (RR).

These latter three points seem to refute the evidence for a strong spreading rate dependence on the depth to the top of magma chambers.

SEPR – superfast spreading southern East Pacific Rise, LAU – intermediate spreading Valu Fa Ridge, Lau Basin.

dependence of magma chamber depth purely on spreading rate is unlikely. The observations on which the relationship of spreading rate and magma chamber depths are based, are of low velocity zones at the MAR and intermediate spreading Juan de Fuca Ridge which represent regions with a low proportion of partial melt rather than a discrete axial magma chamber. Also the depth estimates from the Valu Fa Ridge are

from a back-arc spreading environment where the mantle is likely to be colder, due to the subduction of a cold slab, and is therefore not typical of a mid-ocean ridge environment. These deep values to low velocity zones probably represent remnant partial melt in the lower crust in periods between active magmatism, with the shallower observations of this study and those of Calvert (1995) and Morton *et al.* (1987) representing periods of current magmatic activity. This episodicity of active magmatism is rarely observed on fast spreading ridges as the axial magma chambers associated with these ridges are active for longer relative periods of time. However a study by Harding *et al.* (1989) at the EPR shows a lower percentage of partial melt in the axial magma chamber. As this study shows a depth to the top of the magma chamber of 1.5 km, which plots on the mean value for the half spreading rate of $\sim 55 \text{ mm yr}^{-1}$ (see figure 5.30), this suggests it could be an observation of a magma chamber towards the end of its life cycle rather than a lower crustal low velocity zone.

The along-axis continuity of low velocity zones around axial magma chambers on the EPR is also greater than that of the magma chamber reflections themselves (Sinton and Detrick, 1992; and see figure 5.31), possibly indicating that regions which are currently magmatically inactive retain a proportion of partial melt in the lower crust. In general along the EPR magma chambers show a great degree of continuity along strike. Detrick *et al.* (1993) observed a magma chamber reflector beneath more than 60% of the length of the ridge between 9° and 13°N and Kent *et al.* (1994) and Mutter *et al.* (1995) have observed a continuous reflector beneath smaller discontinuities in the ridge with the depth to the top of the magma chamber reflector increasing towards the ends of ridge segments, and the reflector only disappearing beneath major discontinuities between segments. The magma chamber reflector observed at the Reykjanes Ridge (see section 5.3) also shows great along-axis continuity, being observed to the southern extreme of the surface expression of the AVR. The size and shape of magma chambers observed at all spreading rates appears to be similar, with a narrow (<1-4 km – Detrick *et al.*, 1987), thin, sill-like body observed at the East Pacific Rise, Valu Fa Ridge and Reykjanes Ridge (Collier and Sinha, 1992; Detrick *et al.*, 1993; Kent *et al.*, 1994) which is in turn underlain by a low velocity zone.

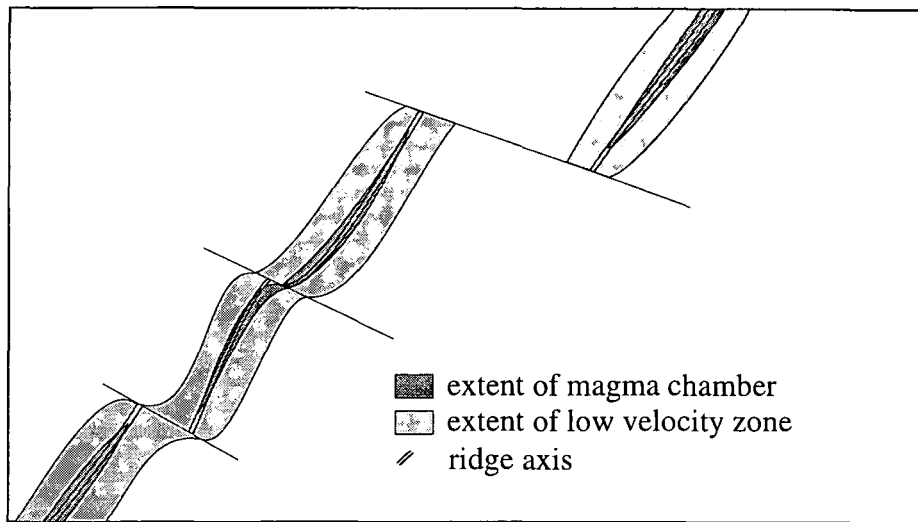


Figure 5.31: Sketch showing the greater continuity of low velocity zones than axial magma chambers. Although magma chambers can be continuous beneath smaller discontinuities, at slightly larger offsets the magma chamber reflections are discontinuous but the low velocity zone is continuous, whilst at larger offsets both features are discontinuous.

The similarities between magma chamber shape, size, along-axis continuity and depth imply processes of accretion are similar at all spreading rates. However, the dissimilarities observed indicate that the process of melt injection is episodic in nature with there being longer periods between active magmatism at slow spreading ridges. This explains one of the reasons why magma chambers are not readily observed at slow spreading ridges, not only does the correct locality have to be chosen, but also the right time frame.

Layer 3

The zero-age EPR profile of Vera *et al.* (1990) indicates that this layer has a thickness of 4.3 km and an approximately constant velocity of 5.5 km s^{-1} , which is poorly constrained but compares well with other studies of the EPR (Orcutt *et al.*, 1975; McClain *et al.*, 1985). A tomographic study of the EPR at the same locality ($9^{\circ} 30' \text{N}$) by Toomey *et al.* (1990) indicates there is a positive velocity gradient in the mid to lower crust on-axis. The Reykjanes Ridge axial profile shows that layer 3 has a thickness of 4.8 km and a constant velocity gradient, with the velocity increasing from 5.95 km s^{-1} at the top of the layer to 7.0 km s^{-1} above the Moho. Within this layer models from both the

Reykjanes Ridge and EPR indicate that there is a zone, less than 20 km in width with P-wave velocities $\sim 1.0 \text{ km s}^{-1}$ below those at equivalent depths off-axis. However the shape of this zone differs between the two regions. The EPR low velocity zone is narrowest ($\sim 2 \text{ km}$ in width) at the axial magma chamber then swells to a maximum width of $\sim 14 \text{ km}$ at the centre of layer 3 and truncates immediately above the Moho (see figure 5.29b). The equivalent zone on the Reykjanes Ridge model is approximately 20 km in width at the layer 2/3 boundary and narrows towards the Moho before truncating $\sim 0.75 \text{ km}$ above the Moho (figure 5.29a). Except at the axial magma chamber both low velocity zones are bounded by gradational boundaries.

Gravity data at the EPR preclude the existence of a large molten body in the crust (Madge *et al.*, 1995). Bratt and Solomon (1984) also found no evidence for a large region of anomalously low S-wave velocities at mid-crustal depths at a segment with a bright axial magma chamber reflector, indicating that there is not a significant proportion of melt beneath the axis unless present as thin sills and unresolvable by seismic methods. The anomalously low P-wave velocities beneath the axis in layer 3 also do not require significant proportions of partial melt to account for them, only an elevated temperature regime (Harding *et al.*, 1989; Toomey *et al.*, 1990). The resistivity data for the Reykjanes Ridge indicate that this low velocity/resistivity zone has $\sim 20\%$ partial melt. This degree of partial melt can be reconciled with the seismic and gravity observations if it is distributed in a solid matrix, where it would therefore have little effect on the density or seismic velocity. Therefore this low velocity zone in layer 3 consists of high temperature basic rock with approximately 20% partial melt distributed in a solid matrix below the axis. This melt crystallises within 10 km offset from the ridge axis to form the gabbros of oceanic layer 3.

Moho and upper mantle

Moho reflections (P_mP) are observed beneath the axial magma chamber at both the EPR (Vera *et al.*, 1990) and Reykjanes Ridge by wide-angle seismic studies but not by normal incidence surveys, indicating that in the latter sufficient seismic energy does not penetrate through the axial magma chamber to produce arrivals with detectable

amplitudes. At the EPR the amplitude of these arrivals indicates that the Moho is a gradational boundary with velocities increasing from 7 km s^{-1} at the base of the crust to 8 km s^{-1} in the top of the upper mantle over a distance of $\sim 1 \text{ km}$ (Vera *et al.*, 1990). For the purpose of this study the Moho was modelled as a distinct boundary with the velocity increasing from 7.0 km s^{-1} above the Moho along the entire length of the across-axis seismic line to 7.8 km s^{-1} beneath the axis and 7.9 km s^{-1} off-axis in the upper mantle. However, modelled reflections from this boundary are of too high an amplitude compared to the observed data, suggesting the reflection coefficient may be too large at this boundary (see section 4.3.2) and/or a gradient zone may be more appropriate. However this gradient must be less than the seismic wavelength at this depth ($\sim 1 \text{ km}$) in order to generate the observed $P_m P$ arrivals. Hence this contradiction between the EPR and Reykjanes Ridge models is unresolvable with this dataset. Therefore beneath the axial magma chamber both at the Reykjanes Ridge and the EPR a Moho exists which is capable of generating wide-angle reflections, implying that it is less than 1 km in thickness (the resolution of the technique at the Moho) and that this boundary is formed on-axis.

At the Reykjanes Ridge the crust has an almost constant thickness of $\sim 7.5 \text{ km}$ possibly with slight thinning off-axis ($\sim 750 \text{ m}$), indicating that the full crustal thickness is generated primarily at the axis, and possible extensional thinning occurs off-axis in the form of faulting which generates the median valley walls. The lack of observed $P_m S$ arrivals implies that magma is not emplaced at the base of the crust off-axis and therefore also indicates that the crust is completely formed on-axis. EPR crust is slightly thinner ($\sim 6.6 \text{ km}$) than that of the Reykjanes Ridge, with the thinnest crust on-axis. This thinner axial crust corresponds to the thinner layer 2A on-axis. Layers 2B and 3 are of a constant thickness implying that they are almost entirely formed at the ridge axis but layer 2A continues to be thickened by off-axis magmatism at the EPR.

The velocities immediately above the Moho at the Reykjanes Ridge and EPR are normal compared with values above the Moho off-axis. Within the upper mantle at the Reykjanes Ridge velocities appear to be slightly lower than in normal off-axis oceanic upper mantle. There is little evidence for similar anomalous upper mantle

velocities on-axis at the EPR, possibly because most recent studies have concentrated on the upper crustal structure. An attenuation study (Wilcock *et al.*, 1995) near 9° 30'N on the EPR which indicates that there is a high degree of attenuation coinciding with the low velocity zone in layer 3, also identifies a second high attenuation zone beginning in the vicinity of the Moho. This second high attenuation zone at the EPR probably also correlates with slightly lower velocities in the mantle as observed at the Reykjanes Ridge and may be caused by mantle upwelling.

5.5.2 Gravity data

Variations in crustal thickness, and therefore in the residual mantle Bouguer anomaly, are lower at fast (Cormier *et al.*, 1995; Madge *et al.*, 1995) and intermediate spreading ridges (Sinha, 1995) than at slow spreading ridges (Kuo and Forsyth, 1988; Detrick *et al.*, 1995). This variation is believed to be predominantly due to 2-D upwelling at fast and 3-D upwelling at slow spreading ridges giving rise to the characteristic "bull's-eye" gravity lows observed on the MAR (Detrick *et al.*, 1995; and see figure 1.6). However recent studies of the superfast spreading segment of the EPR between 18°S and 21° 30'S show evidence of enhanced upwelling towards the centre of segments (Cormier *et al.*, 1995). This evidence implies that upwelling is a 3-D process even at fast spreading ridges. However at fast spreading ridges segments truncate against hotter lithosphere resulting in less cooling at the ends of the segment than at slow spreading ridges for equivalent offsets. This reduced cooling at segment ends at fast spreading ridges results in lower crustal thickness variations than at slow spreading ridges where thin crust is formed at major transforms.

Although the RMBA of the Reykjanes Ridge does show some evidence of this "bull's-eye" structure, with gravity lows centred over the AVRs and a gravity high associated with the basin between AVRs to the north of the 57° 45'N AVR, the peak-to-peak amplitude of these is much lower than elsewhere on the MAR. This observation implies that variations in crustal thickness and density are also lower at this locality. Bell and Buck (1992) suggested that this low amplitude anomaly is due to thicker crust being produced at the Reykjanes Ridge (under the influence of the Iceland hot spot) with

a hotter, weaker lower crust than elsewhere on the MAR, unable to dynamically support large variations in crustal structure. However the crust at the 57° 45'N AVR is not significantly thicker than elsewhere on the MAR, therefore this explanation seems unlikely. The most obvious differences between this AVR and other slow spreading ridges are the low amplitude of along-axis variations in the RMBA and the presence of an axial magma chamber, implying that this area is currently magmatically active. Therefore a possible cause of variations in the RMBA along-axis is that when a ridge segment is undergoing current magmatic activity, mantle upwelling is more vigorous and extends further along ridge segments than in periods between magmatism, where upwelling is limited to the centre of the ridge segment (see figure 5.32). This would explain why the fast spreading EPR, with greater longevity of magmatism predominantly shows low amplitude along-axis variations in the RMBA and hence little variation in the crustal thickness, while the MAR with long periods of magmatic starvation shows large variations in crustal thickness.

5.6 Summary

The different geophysical techniques used during CD81/93 complement each other well with low velocities in the wide-angle seismic model coinciding with low densities and resistivities in the 2-D gravity and CSEM models respectively. However this study has shown that the wide-angle seismic models provide greater constraints on the geometry of crustal structures. The reflections observed in the normal incidence seismic data are interpreted as reflections from the low velocity block incorporated into the final wide-angle seismic models which, in turn, has been interpreted as indicating the presence of an axial magma chamber. The combined models from these techniques have been interpreted in terms of crustal structure and this interpretation can be summarised as follows:-

- Layer 2A consists of porous pillow basalts and lava flows while layer 2B consists of sheeted dykes. Each of these layers have lower velocities, resistivities and densities on-axis which are all indicative of a high degree of fracture porosity.
- Layer 3 is gabbroic in composition and also has low velocities, resistivities and

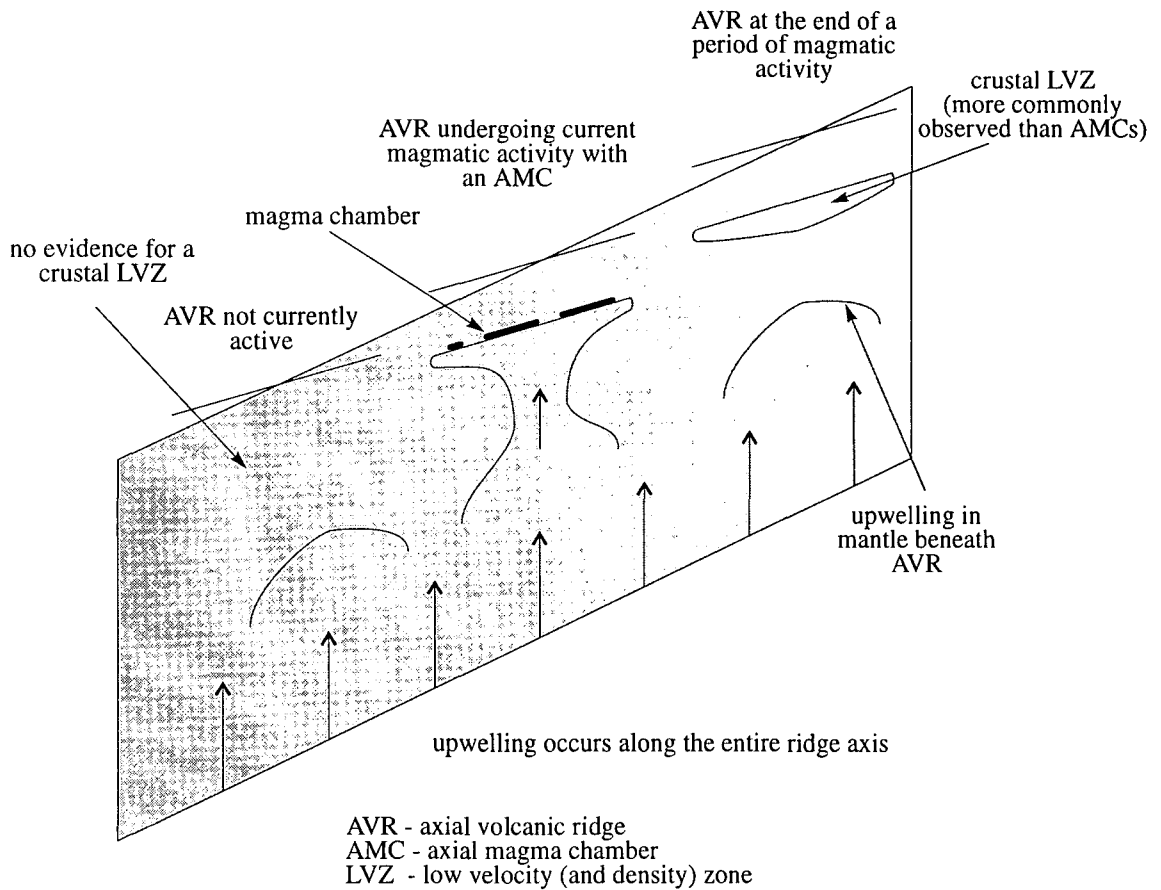


Figure 5.32: Sketch illustrating a possible cause for the lack of strong segmentation seen at the Reykjanes Ridge. Upwelling occurs at a deeper level beneath the full length of the AVR, this upwelling periodically reaches crustal levels along zones of weakness coinciding with the AVRs.

densities on-axis which, in this layer, are due to anomalously high temperatures and ~20% partial melt distributed beneath the axis.

- The crustal thickness at the Reykjanes Ridge is not significantly thicker than elsewhere on the mid-ocean ridge system and the Moho is marked by a sharp (on the scale of the seismic wavelength – i.e. ~1 km) boundary with normal crustal velocities above the Moho and slightly lower than normal velocities below the Moho.
- An axial magma chamber is observed beneath at least 22 km of the axis of the AVR examined in this study, and it has similar dimensions to those observed at the EPR and Valu Fa Ridge.
- Low velocity zones are apparently longer-lived features than actual melt filled

axial magma chambers which only develop periodically with the interval between active magmatism decreasing as spreading rate increases. This results in almost steady-state magma chambers being observed at fast spreading ridges and a low probability of observing axial magma chambers at slow spreading ridges. This observation explains the apparent contradiction between the shallow depth to the top of the magma chamber observed at the Reykjanes Ridge and the models developed for the depth dependence on spreading rate, i.e. different features are imaged at different types of spreading ridges with actual magma chambers being observed at fast spreading ridges while at slow ridges generally low velocity zones are observed.

- The variations in layer thickness observed at the Reykjanes Ridge when compared with those at the EPR, indicate that at slow spreading ridges the total crustal thickness is achieved at the axis, possibly with some extensional thinning occurring off-axis. Whereas at fast spreading ridges the crust is thickened off-axis due to off-axis emplacement of part of layer 2A.
- The "bull's-eye" gravity lows observed at mid-ocean ridges indicate that upwelling is three dimensional at all spreading rates, but the low amplitude of the variation in RMBA at ridges undergoing current magmatic construction, such as the Reykjanes Ridge, implies that mantle upwelling also varies with time.

In the following chapter the main conclusions from the investigation are described together with further studies which could be conducted in order to resolve the uncertainties remaining in the models presented.

Chapter 6

Conclusions and further work

6.1 Introduction

In this chapter our current knowledge of mid-ocean ridges and the processes of crustal accretion operating at these features are summarised. The conclusions on the nature of crustal accretion at the Reykjanes Ridge drawn from this study are related to slow spreading ridges in general and from this the contribution of this study to our knowledge of mid-ocean ridges is considered. Suggestions for further areas of research which could be conducted to better constrain the prominent features of the models and those features not controlled by the dataset analysed in this study are also outlined.

6.2 Processes of crustal accretion at mid-ocean ridges

Seismic studies of fast and intermediate spreading ridges have provided evidence for a crustal magma chamber lying between layers 2 and 3 of the oceanic crust, overlying a region of partial melt in layer 3 (e.g. Detrick *et al.*, 1987; Harding *et al.*, 1989; Vera *et al.*, 1990; Caress *et al.*, 1992; Collier and Sinha, 1992; Kent *et al.*, 1994; Toomey *et al.*, 1994; Mutter *et al.*, 1995). In these studies the axial magma chamber is identified as a thin (10-100 m), narrow (1-2 km) melt lens which is continuous between major ridge discontinuities. The underlying zone of partial melt is ~10 km in width and has a seismic P-wave velocity up to 1 km s⁻¹ below that at equivalent depths off-axis. Eruptions from the melt lens form the extrusives and sheeted dykes of layer 2, while the solidifying partial melt produces layer 3 as the newly formed crust moves off-axis. The narrow axial magma chamber also gives rise to the 1-2 km wide neovolcanic zone observed at mid-ocean ridges (Ballard *et al.*, 1981). This model of ridge structure and crustal generation derived from seismic studies is similar to that obtained from thermal studies (Sleep, 1975). However these thermal studies indicate that a magma chamber

cannot exist in a steady-state at a slow spreading ridge (Sleep, 1975; Kuszniir and Bott, 1976).

Observations of magma chamber reflectors at fast and intermediate spreading ridges (Morton and Sleep, 1985; Collier and Sinha, 1990; Detrick *et al.*, 1991) have been combined with observations of low velocity zones at intermediate and slow spreading ridges (Bunch and Kennett, 1980; Kong *et al.*, 1992; Christenson *et al.*, 1993) and used to identify an inverse relationship between the depth to the top of a magma chamber and the spreading rate of the ridge itself (Purdy *et al.*, 1992).

Numerous studies of slow spreading ridges have failed to find evidence for a magma chamber (Detrick *et al.*, 1990). The only study to date to suggest that a magma chamber exists beneath a slow spreading ridge is that of Calvert (1995) in which a short, indistinct along-axis reflector was identified (in a dataset which was previously used to refute such a suggestion) as a magma chamber reflector at a similar depth to those observed beneath fast spreading ridges. This lack of direct observations of magma chambers beneath slow spreading ridges suggests that the process of crustal accretion at these ridges is different from that operating at fast and intermediate ridges, e.g. the "infinite leak" model (see section 1.3; and Nisbet and Fowler, 1978), although the resulting crustal structure produced at all spreading ridges is identical.

Seismic studies are the main method used to investigate the structure of mid-ocean ridges in situ. At slow spreading ridges the rougher topography (Macdonald, 1982) which causes severe scattering of seismic energy, the long interval between periods of magmatic activity (Bryan and Moore, 1977) and the discontinuous nature of volcanic constructions (Macdonald, 1982) combine to reduce the chances of observing a magma chamber, should one exist, compared to fast and intermediate spreading ridges. Therefore the aim of this study was to attempt to address the apparent discrepancy between geophysical observations at fast, intermediate and slow spreading ridges.

6.3 Results and conclusions from this study

The oceanic crustal structure observed at 57° 45'N on the Reykjanes Ridge is essentially normal, with velocity–depth profiles constructed for crust older than 1 Ma lying within the "standard" velocity envelopes of White *et al.* (1992), implying that the processes of crustal accretion operating at this ridge are similar to those operating elsewhere on the mid-ocean ridge system. However the variation of layer 2 thickness with age appears to differ between fast and slow spreading ridges. Numerous studies of the shallow crustal structure of the EPR have indicated that layer 2A thickens with age due to off-axis volcanism (Harding *et al.*, 1993; Kent *et al.*, 1994; Vera and Diebold, 1994; Christenson *et al.*, 1996). Whereas this study shows that layer 2A thins off-axis, as do some other studies on the Reykjanes Ridge and MAR (Fowler, 1976; Smallwood *et al.*, 1995), indicating that this layer is completely formed on-axis.

This apparent difference between processes of accretion at fast and slow spreading ridges may simply be the effect of eruption of less viscous lavas, which are able to flow up to 4 km off-axis, at fast spreading ridges (see section 1.1.1) giving rise to individually thin lava flows which build up to double the layer 2A thickness within 1-2 km of the ridge axis (e.g. Christenson *et al.*, 1994). The more viscous lavas produced at intermediate and slow spreading ridges tend to form volcanic mounds at the ridge axis. These mounds are then faulted and moved off-axis, giving rise to the greater variability of layer 2A thicknesses observed at these ridges (McDonald *et al.*, 1994). The crust beneath layer 2A appears to be formed on-axis at all spreading rates, with crustal thickening with age occurring at fast spreading ridges only due to the off-axis emplacement of layer 2A and extensional thinning occurring off-axis at the Reykjanes Ridge.

Wide-angle reflections from the Moho beneath the ridge axis are observed on both the across and along-axis Reykjanes Ridge data, indicating that this boundary is formed at an early stage. This early formation of the Moho as a distinct boundary is also observed at the EPR (Vera *et al.*, 1990), however amplitude modelling of the EPR data indicates that the Moho consists of a gradient zone ~1 km in thickness (Vera *et al.*, 1990). The Moho at the Reykjanes Ridge is modelled with a sharp boundary although

the amplitude of the modelled phase generated by this interface is larger than that of the observed phase, indicating that the velocity contrast across the boundary is too large and that a gradational boundary may be more appropriate. However a feature of a similar scale to the gradient zone observed at the EPR is not resolvable with the dataset available as the wavelength of the seismic source used for the Reykjanes Ridge survey is ~ 1 km at Moho depths. In addition the low amplitude of the observed Moho reflections in the Reykjanes Ridge wide-angle seismic dataset, combined with their interference with secondary arriving phases, makes amplitude modelling of this phase to define the exact nature of the boundary (i.e. whether it is sharp or gradational) difficult.

This study has provided the first unequivocal observation of a magma chamber beneath *any* slow spreading ridge using refraction techniques. The attenuation of wide-angle arrivals caused by this magma chamber on both the along and across-axis profiles provides a constraint on its size and depth, lying ~ 2.5 km beneath the seafloor and having a thickness of ~ 100 m and width of ~ 4 km. The location of this magma chamber, as modelled with wide-angle seismic techniques, coincides with a low resistivity block in the CSEM model, and the low seismic P-wave velocity (3 km s^{-1}) and resistivity ($\sim 0.2 \text{ } \Omega \text{ m}$) indicate that it is a completely molten basalt body. Therefore this is also the first multicomponent geophysical experiment to provide coincident observations of a magma chamber using unrelated techniques. The magma chamber is underlain by a region, ~ 8 km in width, with lower than average P-wave velocity, resistivity and density for this depth. This region is believed to contain up to 20% partial melt (L.M. MacGregor, pers. com.). The depth and dimensions of this magma chamber and underlying low velocity zone at the Reykjanes Ridge are similar to those observed beneath the EPR at numerous locations (Harding *et al.*, 1989; Vera *et al.*, 1990; Detrick *et al.*, 1993; Kent *et al.*, 1994), which also indicates that the processes of crustal accretion at the Reykjanes Ridge are similar to those operating at the EPR.

This study has also provided the first observation of clear normal incidence reflections from a magma chamber at a slow spreading ridge. Although it is not possible from the poor quality normal incidence data collected, to identify the polarity of the reflector (which would normally be used to identify whether it was generated at a

boundary with a negative reflection coefficient), forward modelling of the normal incidence data indicates that the reflection occurs at the top of the low velocity block in the wide-angle seismic model and thus is caused by the magma chamber. The continuity of the reflector along-axis indicates that the magma chamber is continuous beneath the entire length of the AVR, a characteristic which could not be resolved with the widely spaced shots and the broadly spaced instruments on the along-axis wide-angle seismic line. This bright continuous reflector is similar to those observed beneath the EPR (Detrick *et al.*, 1987; Harding *et al.*, 1989; Kent *et al.*, 1994; Mutter *et al.*, 1995) and the Valu Fa Ridge (Morton and Sleep, 1985; Collier and Sinha, 1992), and is far more continuous than the only previous observation on the MAR of an ambiguous reflection event extending less than 2 km along-axis (Calvert, 1995).

The EPR has been the target of many detailed studies of crustal structure and has provided models of the axial magma chamber indicating that it has gradational boundaries and is overlain by a high velocity solidified lid (Vera *et al.*, 1990). The conventional wide-angle seismic techniques employed in this study were not designed to identify the structure of the magma chamber boundaries and the normal incidence data were not of a sufficiently high quality to allow detailed amplitude modelling of the magma chamber reflector itself (the latter having been collected in an opportunistic manner). Therefore the magma chamber at the Reykjanes Ridge is modelled with boundaries which are sharp on the scale of the seismic wavelength (~100 m). More efficient cooling by hydrothermal circulation in the highly fractured upper crust may generate sharper boundaries to the magma chamber at the Reykjanes Ridge than encountered at fast spreading ridges which, in turn, may account for this discrepancy. However the axial magma chamber may have gradational boundaries which are simply not resolvable with the available data.

As this is the first observation of a magma chamber beneath a slow spreading ridge an important question is the applicability of these observations to slow spreading ridges in general. The northerly end of the Reykjanes Ridge is profoundly influenced by the Iceland hot spot with an axial high morphology more typically associated with that of fast spreading ridges. However, south of 59°N median valley topography begins to

develop with a true median valley first observed at 58°N (Ritzert and Jacoby, 1985). The depth to the ridge crest also varies with distance from the hot spot, deepening from sea level at the Reykjanes Peninsula to 2 600 m below sea level at the Bight transform (Applegate and Shor, 1994). This shallowing towards Iceland is not smooth. A shallow gradient and smooth topography mark the bathymetric variation to the north of 59°N with the crust buoyantly supported by elevated mantle temperatures and/or thicker crust due to the influence of the mantle plume, while a much steeper gradient and rougher topography south of 59°N mark the decaying influence of the plume with distance (see figure 1.9; and Applegate and Shor, 1994). The distribution of earthquakes along the Reykjanes Ridge also shows a distinct change at ~59°N with fewer earthquakes to the north of this point than to the south (see figure 1.11). These observations indicate that a transition occurs at this latitude from ductile crust to the north to the brittle crust more typical of slow spreading ridges, to the south. This transition from ductile to brittle crust also accounts for the transition from axial high to median valley topography.

Geochemical studies indicate that the Icelandic mantle plume influences the entire length of the Reykjanes Ridge. However this effect only linearly increases towards Iceland from 57°N (Schilling, 1973; Taylor *et al.*, 1995). The geochemical trends which coincide with intermediate length bathymetric anomalies (see section 1.6) are difficult to trace south of 56°N (R.N. Taylor, pers. com.).

The AVR selected for this study is centred at 57° 45'N, over 1 000 km from the Icelandic mantle plume (Smallwood *et al.*, 1995). Although the geochemical evidence indicates the hot spot influence extends beyond the AVR of this study, the effect is rapidly diminishing at this latitude. The brittle nature of the crust and rapid decay of the long wavelength bathymetric swell also indicate that this AVR is beyond the profound influence of the hot spot. More importantly the "normal" crustal structure and thickness also indicate that the hot spot has little influence at this locality and therefore it appears that the results of this survey can be extended to slow spreading ridges in general.

The similarity of crustal structure and magma chambers at fast, intermediate and slow spreading ridges indicates similar processes of crustal accretion occur at all spreading rates. At fast spreading ridges episodes of magmatic inactivity are short,

giving rise to a continuous axial rise, little evidence of three dimensional upwelling in the gravity field and the common observations of long-lived magma chambers. At slow spreading ridges episodes of magmatic activity are widely separated both in space and time, causing discrete AVR's, clear three dimensional upwelling (evident as "bull's-eye" mantle Bouguer gravity lows) and few observations of axial magma chambers. The more common observations of low velocity zones at intermediate and slow spreading ridges, and their greater continuity at fast spreading ridges implies that these are considerably longer-lived features than magma chambers.

Models of the dependence on spreading rate of depth to the top of magma chambers (Purdy *et al.*, 1992; and see figure 5.30) have been biased by the inclusion of these low velocity zones for intermediate and slow spreading ridges. The results of this study, combined with those of Calvert (1995) at the slow spreading MAR, Morton *et al.* (1987) at the intermediate spreading Juan de Fuca Ridge and the actual observations of magma chambers included in Purdy *et al.* (1992)'s compilation, indicate that magma chambers lie between 1 and 3 km beneath the seafloor (see figure 6.1). Although, even with inclusion of these results, there does seem to be a slight increase in magma chamber depth with decreasing spreading rate, this increase is of the order of ~ 1 km over a change in spreading rate of 130 mm yr^{-1} (full rate) as opposed to the ~ 4 km change in depth over the same range of spreading rates implied by Purdy *et al.* (1992)'s study. Also the range of values observed on the EPR indicate that magma chambers are observed at up to 2.4 km depth which is towards the lower end of depth observations for all spreading rates. The observation of an axial magma chamber ~ 3.2 km beneath the Valu Fa Ridge (Lau Basin) clearly lies outside of this trend and may be a function of the relatively recent onset of spreading or alternatively may be anomalous due to its back-arc spreading environment. The MAR magma chamber of Calvert (1995) also seems slightly anomalous, being shallower than the mean depth for the superfast spreading southern EPR ($\sim 155 \text{ mm yr}^{-1}$, full rate). This shallow depth may simply be an upper bound for magma chamber depth at a slow spreading ridge, although the discontinuous nature of this reflection along-axis is also anomalous compared to all other observations of axial magma chambers and therefore these data should be treated with caution. The

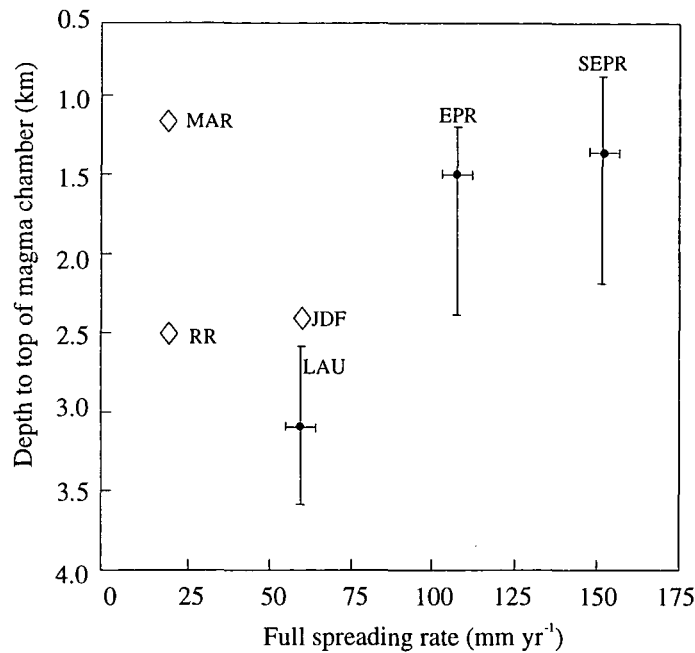


Figure 6.1: Depth to the top of magma chambers plotted as a function of spreading rate. Data points included are from this study – RR, those of Calvert (1995) – MAR and Morton *et al.* (1987) – JDF and those of magma chambers included by Purdy *et al.* (1992) – LAU, EPR and SEPR. SEPR – Southern East Pacific Rise, EPR – East Pacific Rise, JDF – Juan de Fuca Ridge, LAU – Valu Fa Ridge, Lau Basin (back-arc spreading centre), RR – Reykjanes Ridge and MAR – Mid-Atlantic Ridge at 23°N. Where a variety of magma chamber depths are observed along the ridge this variation is indicated by the vertical bar, the horizontal bar indicating the range of spreading rates for which magma chambers were observed. Where a magma chamber was only imaged at one location the data is plotted with a diamond.

Note the relatively narrow range of magma chamber depths, from 1 to 2.5 km, with the exception of the back-arc ridge (LAU).

uniformity of layer 2 thicknesses generated at all spreading rates (see figure 5.28; and White *et al.*, 1992) also indicates little spreading rate dependence on magma chamber depth, although a slightly shallower magma chamber at fast spreading ridges, combined with off-axis emplacement of lavas, would also account for similar crustal structures and a slight increase in magma chamber depth as spreading rate decreases. Whereas a magma chamber near the base of layer 3, as proposed by Purdy *et al.* (1992)'s model for a slow spreading ridge would produce a dramatically different crustal structure at these ridges, e.g. at the Valu Fa Ridge, with a magma chamber depth of ~3.2 km (Collier and Sinha, 1992) layer 2 thickness is greater than for "normal" oceanic crustal structure (I.M. Turner, pers. com.). A more important control on magma chamber depth appears to be

the proximity to major axial discontinuities, with observations at the EPR indicating that magma chambers deepen towards major discontinuities (Mutter *et al.*, 1995) and hence when considering the depth dependence on spreading rate, the proximity of the observation to a major discontinuity should also be considered. The amount of variation in the observations made thus far indicates that perhaps the dataset is still too sparse and the observed features too variable (i.e. measurements to tops of magma chambers at fast spreading ridges and the tops of low velocity zones at slow spreading ridges) for this relationship to be considered irrefutable.

One of the most important results of this study is that the use of a combination of geophysical techniques in a geologically complex and experimentally challenging region has provided improved constraint on the models of crustal structure and accretion processes generated than would be possible using a single method. All four techniques employed on CD81/93 (wide-angle seismic, normal incidence seismic, gravity and CSEM) have been used to produce models which complement and extend each other, providing a well constrained and largely irrefutable model of crustal structure in this region.

6.4 Further work

In this section a consideration of how the remaining ambiguities in the models of crustal structure at the Reykjanes Ridge can be resolved will be discussed and further areas of study or exploration suggested. The remaining questions unanswered by this study are as follows:-

- What is the extent of the magma chamber beyond the ends of the AVR and is it continuous between AVRs?
- How does the crustal thickness and density vary along-axis to generate the gravity anomalies observed?
- Are the boundaries to the axial magma chamber gradational or sharp?
- What is the nature of the Moho transition?

6.4.1 Further work on the existing CD81/93 dataset

Interpretation of the dataset described in this dissertation was limited to two dimensions and hence modelling was conducted in a 2-D manner. However the wide-angle seismic data were collected with a wide areal distribution of shots and receivers and the gravity data were collected along a grid of numerous intersecting lines and hence both datasets could be modelled in three dimensions (see figures 2.8 and 2.20). The final along and across-axis models described here could be used as starting models for a 3-D tomographic study of the wide-angle seismic dataset. This 3-D modelling could provide further constraints on the lateral extent and along-axis continuity of the magma chamber from analysis of the along-axis shots travelling to the across-axis instruments and the across-axis shots recorded by the along-axis instruments. The area which could be constrained by such a study is shown in figure 2.8.

A 3-D or 2.5-D gravity modelling package could be used to model the short wavelength gravity signal to investigate the extent of the axial low density (and low velocity) zone.

The polarity reversals recorded in the magnetic dataset, combined with magnetostratigraphic analysis could be used to study variations in spreading rate at the AVR. Also the short wavelength components of this dataset could be combined with the models of crustal structure to investigate variations in upper crustal thickness and magnetic susceptibility.

6.4.2 Collection of additional data

Resolution of the main ambiguities in the Reykjanes Ridge models requires the collection of additional, more areally comprehensive datasets. These additional surveys are described below and their purpose discussed (cf. Peirce *et al.*, 1996).

3-D grid of seismic and gravity data

A grid of seismic and gravity lines as outlined in figure 6.2 should be collected in order to constrain the along and across-axis extent and variability of the axial magma chamber and low velocity zone. This survey consists of a grid of closely spaced seismic

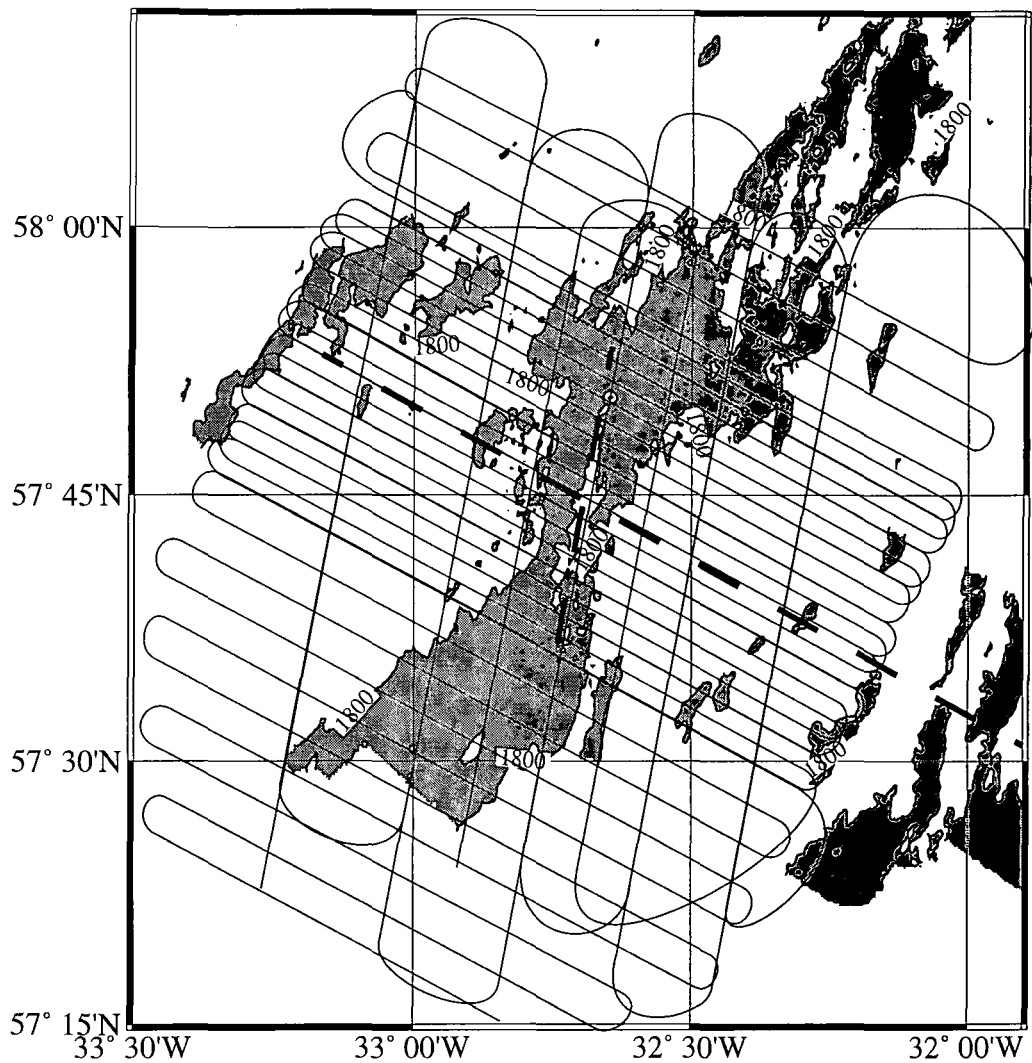


Figure 6.2: Proposed seismic and gravity survey of the Reykjanes Ridge centred on the AVR at $57^{\circ} 45'N$, consisting of seven axis-parallel lines of airgun shots (three of which pass through adjacent AVRs) and 27 across-axis lines perpendicular to the overall trend of the Reykjanes Ridge. These shots would be recorded by a long-offset multichannel streamer. The dashed lines mark the locations of the wide-angle seismic lines collected during CD81/93.

lines with airgun shots fired using a large capacity airgun array. This grid extends from the tip of the AVR to the south of that centred on $57^{\circ} 45'N$ to the tip of that to the north, running across the two offset basins between adjacent AVRs (see figure 6.2). The grid consists of 31 lines perpendicular to the overall trend of the Reykjanes Ridge at a 2 km spacing over the AVR centred on $57^{\circ} 45'N$ and a 4 km spacing beyond this AVR, and seven axis-parallel lines three of which lie along the three AVRs, two lie inbetween these at an ~ 7.1 km spacing to the west of the central AVR and ~ 6.1 km to the east, and the remaining two lie ~ 30 km off-axis from the central AVR.

The shots would preferably be recorded using a long multichannel streamer (e.g. the 6 km Lamont-Doherty Geological Observatory streamer or the NERC 2.4 km streamer on a long tow) to provide a maximum offset of greater than 2.4 km. This dataset would provide a detailed picture of the extent and continuity of the magma chamber beneath the central AVR and identify the presence or absence of such a feature beneath the two adjacent AVRs and their overlapping region, and how these features are effected by the offset basins. This conventional multichannel survey would hopefully also provide images of the Moho and any intra-crustal reflectors occurring at this locality and not previously recognised. The improved quality of data recordable with a truly multichannel (i.e. more than 4-fold) streamer would also enable estimations of layer velocity and allow amplitude modelling of the main reflectors to identify the nature of boundaries (i.e. gradational or sharp). Long-offset streamer data would allow amplitude-versus-offset studies to image the upper crustal structure, particularly the character of the 2A/2B boundary and the magma chamber reflector (see figure 6.3).

However in addition to collecting multichannel seismic data it is suggested that these airgun shots are also recorded using the six Durham' and the four identical SOC DOBSs deployed twice to provide further details of the crustal velocity structure off and on-axis for multichannel seismic data processing and to collect a detailed 3-D wide-angle seismic dataset (see figure 6.4 and 6.5).

On the first deployment of the ten DOBSs, five should be deployed on each of the AVRs to the north and south of the central AVR at node points of the seismic lines to provide velocity information and a tomographic dataset over these AVRs and the offset basins. These DOBSs should be located with one instrument on the axis of each AVR and four in a rectangular grid, with sides approximately 15 km in length, centred on the axial instrument (see figure 6.4). The three seismic lines running through the AVRs, the two axis-parallel lines located ~30 km off-axis and the across-axis lines across the entire area with a 4 km spacing should be shot during this first deployment (see figure 6.4).

The DOBS should then be recovered and their data downloaded prior to a second deployment centred on the 57° 45'N AVR, the main target of this study. The

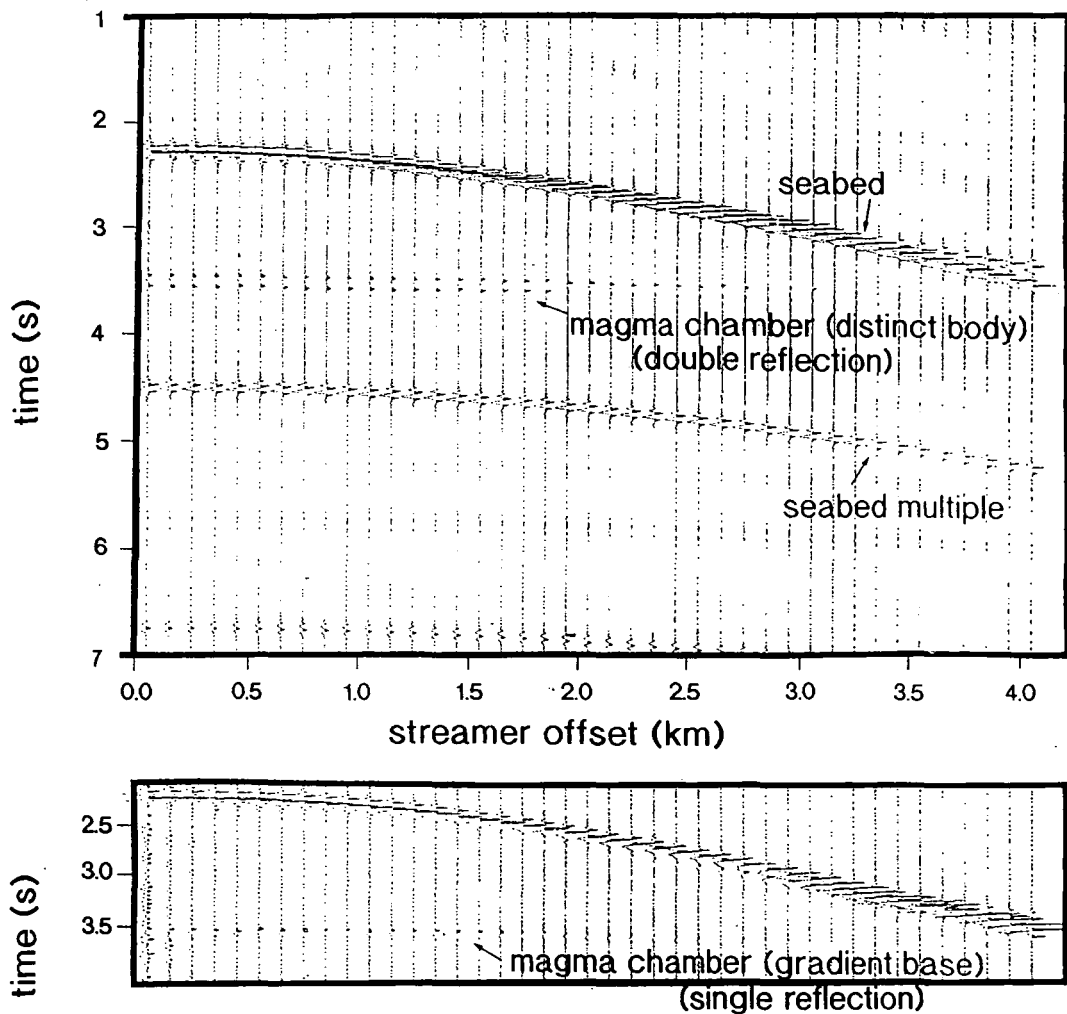


Figure 6.3: Modelled amplitude variation versus offset for a magma chamber 2.5 km beneath the seafloor with sharp boundaries (top) and a gradational base (bottom) (after Peirce *et al.*, 1996).

Note that at an offset of 2.0 km a significantly different character of arrival is seen from the two models. Hence a streamer of at least 2.4 km length (i.e. the NERC streamer) would be sufficient to differentiate between these two magma chamber models. Note also that the character of the upper and lower boundaries can also be distinguished by the "double wiggle" nature of the reflection event. Hence modelling the arrival will enable determination of magma chamber thickness and acoustic impedance contrast.

DOBSs should again be located at node points of the seismic grid with two ~30 km off-axis on either side of the highest point of the AVR; four located ~6-8 km apart centred on the AVR; and the remaining four ~15-20 km apart again centred on the mid-point of the 57° 45'N AVR (see figure 6.5). The multichannel seismic lines of this second group of lines which coincide with those collected during the first DOBS deployment should be shot in the opposite direction. This would enable processing of the coincident multichannel seismic lines to reduce the effects of seafloor scattering.

The 3-D tomographic modelling of the entire dataset would provide

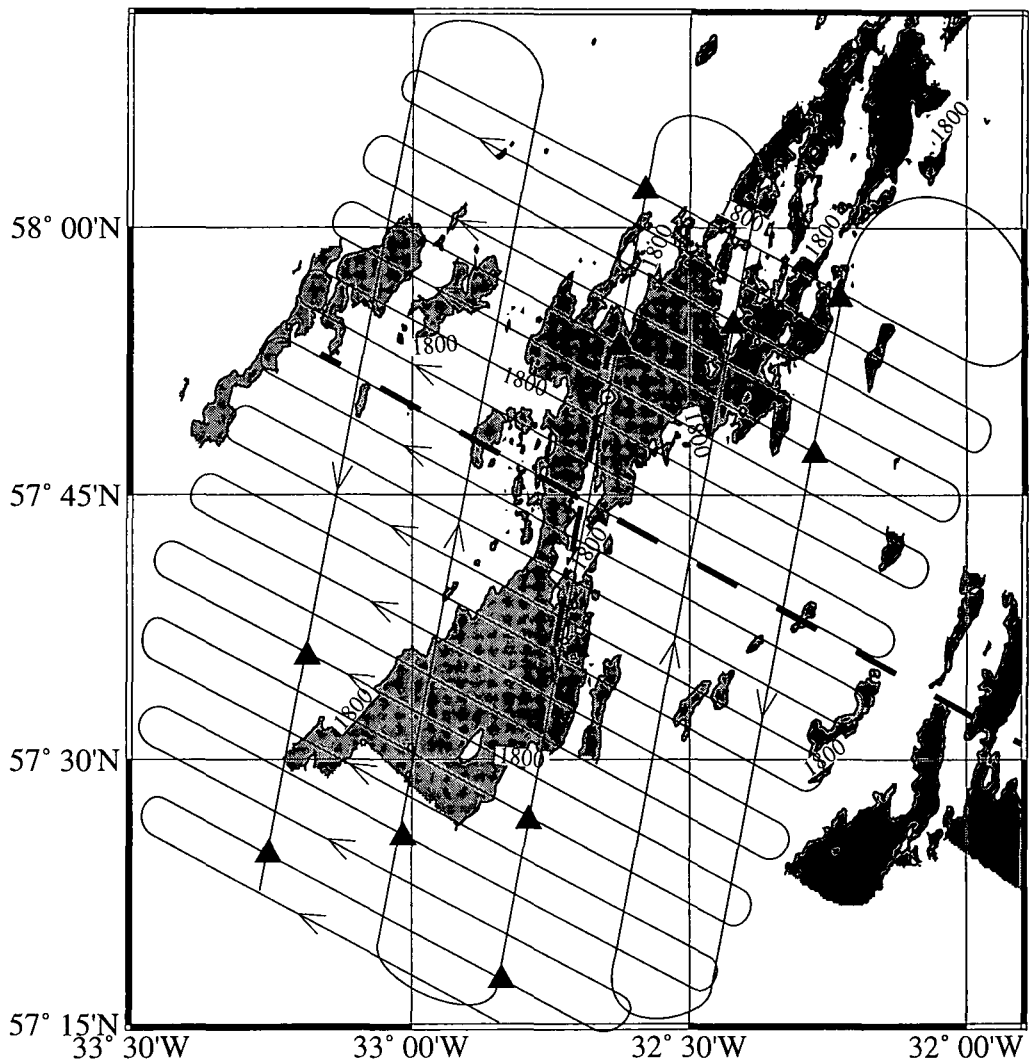


Figure 6.4: Proposed seismic lines to be shot during the first deployment of DOBSs (triangles) to collect multichannel seismic data over the entire region and a detailed grid of wide-angle seismic data over the northern and southern AVRs for tomographic modelling. The dashed lines mark the locations of the wide-angle seismic lines collected during CD81/93.

information on the nature of the Moho, variations in crustal thickness and the extent and location of any magma chambers and low velocity zones.

It is also suggested that during shooting of the seismic lines gravity data is collected to provide a detailed grid which could be combined with the crustal velocity models obtained from the seismic data to model variations in crustal density in 3-D.

This seismic and gravity dataset should provide answers to the questions posed at the beginning of this section, i.e. the extent of the axial magma chamber beyond the ends of the AVR, the nature of the boundaries of the magma chamber and at the Moho. The seismic models would also provide a constraint on the crustal thickness variations

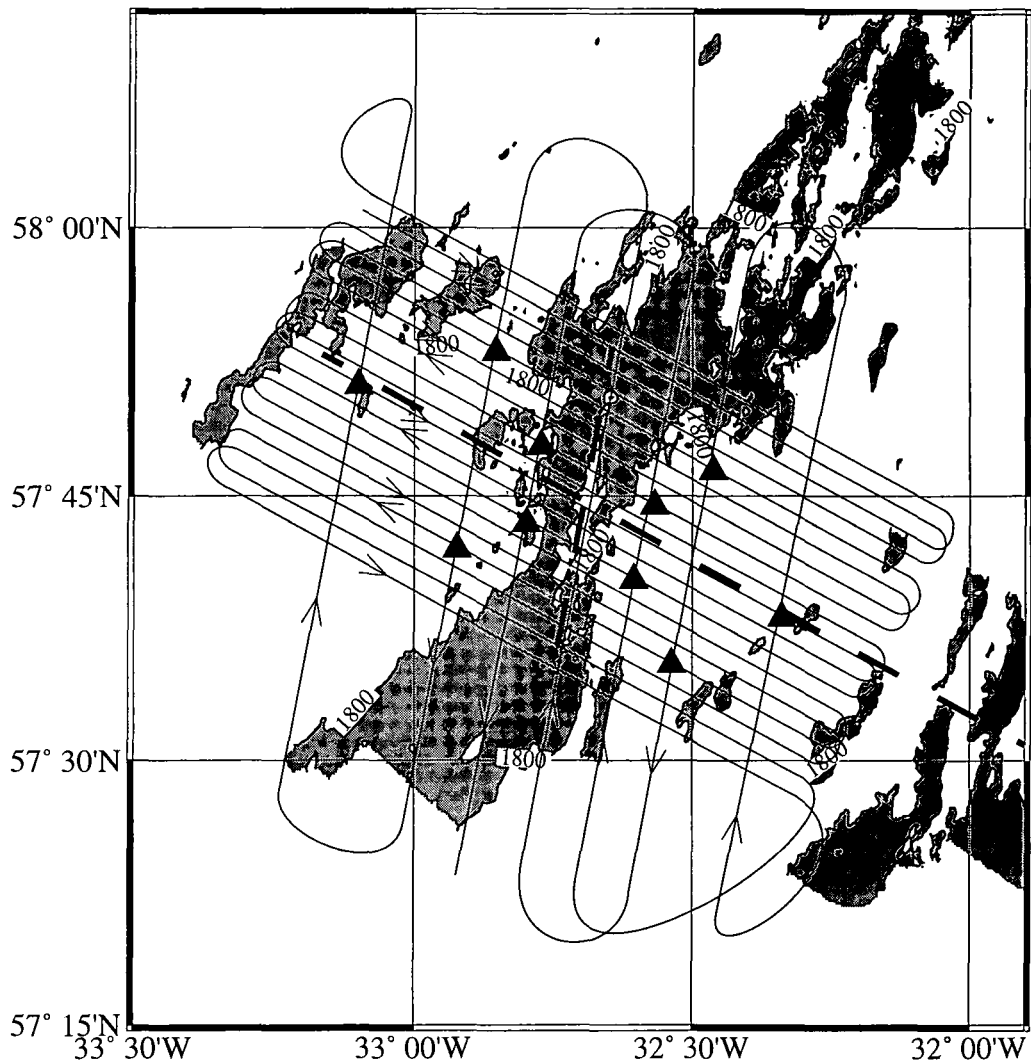


Figure 6.5: Proposed seismic lines to be shot during the second deployment of DOBSs (triangles) to collect a detailed grid of multichannel and wide-angle seismic data over the central AVR. The dashed lines mark the locations of the wide-angle seismic lines collected during CD81/93.

beneath the length of the AVRs and offset basins which could then be combined with gravity models to identify any density variations in the crust and the form of mantle upwelling beneath the Reykjanes Ridge. However, the collection of TOBI (Towed Ocean Bottom Instrument) side-scan sonar, swath bathymetry and three component magnetic data, and water column geochemical data using BRIDGET (BRIDGE Tow) coincident with the seismic and gravity lines could address many other questions about the development of the Reykjanes Ridge.

TOBI data

TOBI side-scan sonar data over the northern AVR and the northerly tip of the AVR centred at 57° 45'N were collected during a research cruise aboard the *R/V Maurice Ewing* in 1990 (EW9008 – Searle *et al.*, 1994). Therefore to complete this coverage of the experiment location TOBI side-scan sonar, and associated three component magnetic and swath bathymetry data should be collected over the entire central AVR and the northerly tip of the southernmost AVR. The proposed survey consists of 12 across-axis lines ~5 km apart which extend up to 20 km off-axis and two along-axis lines, one along the central AVR and one along the southern AVR (see figure 6.6).

The side-scan sonar data collected could be used to:-

- 1) Relate the surface characteristics of the seafloor to the sub-surface features obtained from seismic and gravity modelling. In particular this data could be used to identify surface features which are directly correlatable with sub-axis active magma chambers so that, in future, TOBI surveys could be used to prospect for suitable locations for more major seismic experiments.
- 2) Features identified in the 100% TOBI coverage of the central AVR could be used to investigate along-axis variation in morphology and hence to identify processes of crustal accretion.
- 3) The seafloor characteristics observed at the young central AVR can be compared with the proposed models of the evolution of AVR morphology with age (Parson *et al.*, 1993).
- 4) The off-axis side-scan sonar data could be used to investigate the transition from AVR-parallel to axis-parallel faulting with age as observed by Searle and Laughton (1981).

The three component TOBI magnetic data could be used to:-

- 1) Measure the transition width of the Bruhnes/Matuyama and Matuyama/Gauss magnetic reversals and estimate the width of the volcanic emplacement zone (Searle *et al.*, 1994).
- 2) Variations in the off-axis magnetisation could be used to calculate upper crustal

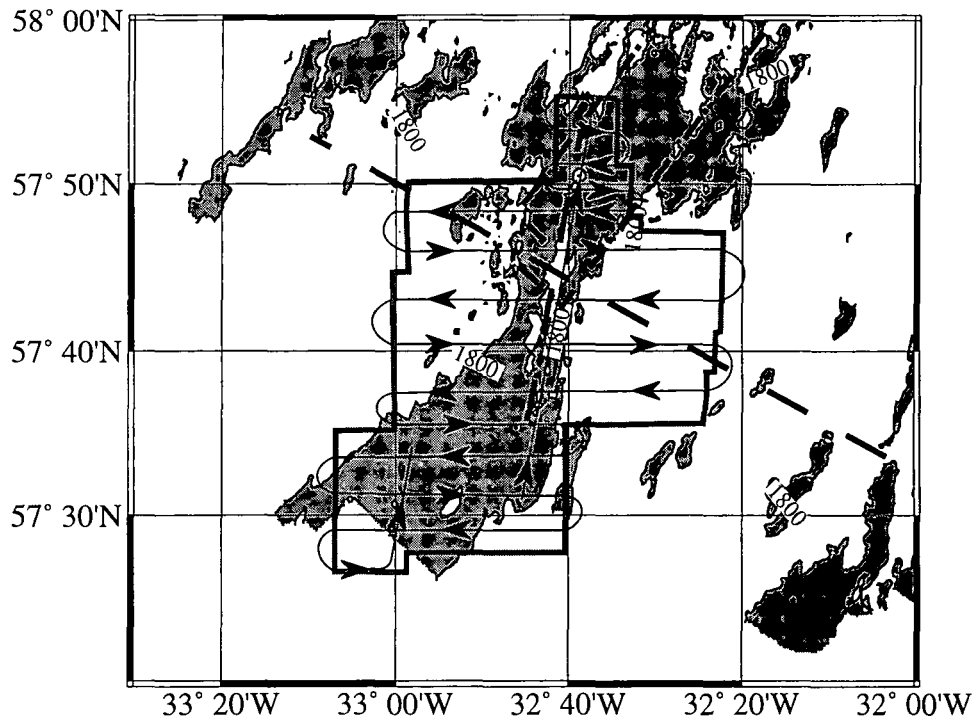


Figure 6.6: Proposed locations of TOBI tow lines designed to collect side-scan sonar, swath bathymetry and three component magnetic data over the AVR centred on 57° 45'N (after Peirce *et al.*, 1996) and that located to the south. The dashed lines mark the positions of the CD81/93 wide-angle seismic lines, the long-short dashed line shows the existing TOBI coverage and the thick outline marks the total TOBI coverage achieved.

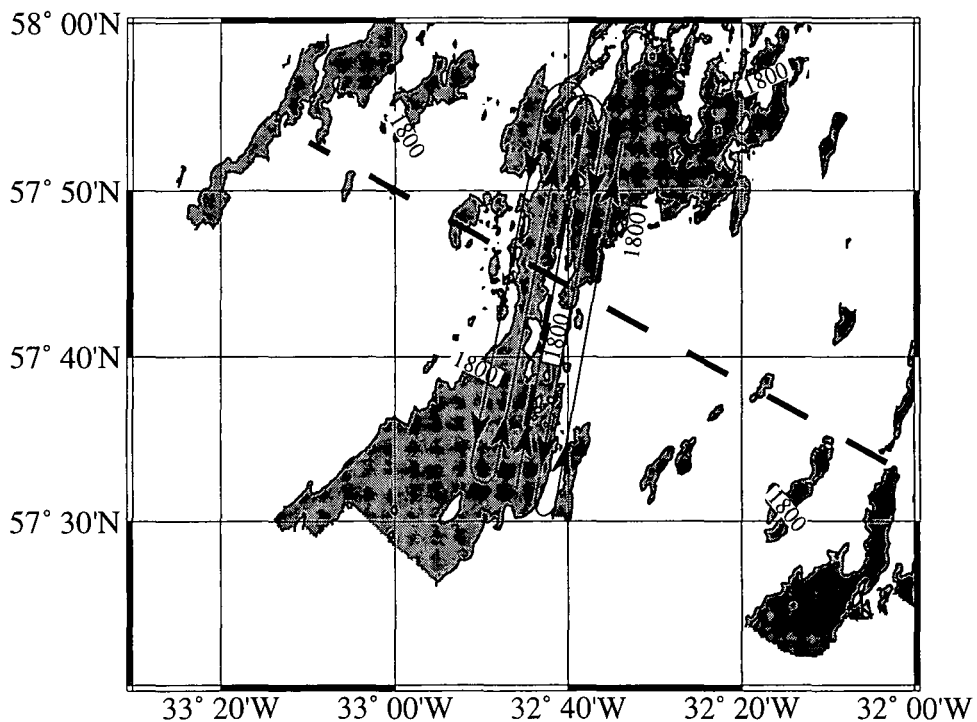


Figure 6.7: Proposed BRIDGET tow lines to explore for hydrothermal activity along the central AVR (after Peirce *et al.*, 1996). The dashed lines mark the location of the CD81/93 wide-angle seismic lines.

thickness variations (Tivey, 1994) and using a direct comparison with the coincident seismic measurements, a methodology for direct application to other slow spreading ridges could be developed.

BRIDGET data

A previous geochemical survey of the Reykjanes Ridge failed to find any evidence of hydrothermal activity between 58°N and Iceland, and this lack of activity was attributed to deep level magma chambers restricting hydrothermal circulation (German *et al.*, 1994a). However the study presented in this dissertation has indicated that a shallow level magma chamber exists beneath the AVR centred on 57° 45'N accompanied by a highly porous upper crust – an apparently ideal situation for the development of hydrothermal activity.

BRIDGET is an instrument designed for collection of underway water column geochemical sampling in deep water (German *et al.*, 1994b; Rudnicki *et al.*, 1995). This instrument has been used to prospect for hydrothermal activity by detecting the enrichment of trace elements in neutrally buoyant plumes overlying high temperature black smokers (Baker *et al.*, 1995). Therefore it is suggested that this instrument is towed along 5 axis-parallel lines on the central AVR with the central tow line coincident with the along-axis seismic and TOBI lines and the remaining 4 lines offset from this by 2.5 and 5 km (i.e. largely within the median valley walls – see figure 6.7) to identify any hydrothermal activity on this AVR. Should any activity be found its relationship to the location and extent of magma bodies could be investigated. A detailed survey of the site of any hydrothermal activity could then provide information on the nature of the upper crustal porosity and the processes of fluid flow and heat exchange.

6.5 Conclusions

This study has provided the first observation of a magma chamber beneath a slow spreading ridge and a detailed model of crustal structure and its formation at the Reykjanes Ridge. Previously the lack of observations of a magma chamber at slow spreading ridges resulted in the development of different models of crustal accretion at

these ridges compared to those at fast and intermediate spreading ridges, even though mature crust produced at all ridges is similar. The results of this study, apart from being a unique observation of a crustal melt body beneath a slow spreading ridge, indicate that similar processes of accretion operate at all spreading rates, and that the main difference between ridge types is that of longevity and periodicity of magmatic activity.

References

- Applegate**, B. and A.N. Shor, 1994, The northern Mid-Atlantic and Reykjanes Ridges: Spreading centre morphology between 55° 50'N and 63° 00'N. *J. geophys. Res.*, vol. 99, no. B9, p.17935-17956.
- Baker**, E.T., C. German and H. Elderfield, 1995, Hydrothermal plumes: global distributions. *Geophysical Monograph, Am. Geophysics Union*, vol. 91, p.47-71.
- Ballard**, R.D., J. Francheteau, T. Juteau, C. Rangin and W. Normark, 1981, East Pacific Rise at 21°N: The volcanic, tectonic and hydrothermal processes of the central axis. *Earth Planet. Sci. Lett.*, vol. 55, p.1-10.
- Barry**, K.M., D.A. Cavers and C.W. Kneale, 1975, Recommended standards for digital tape formats. *Geophysics*, vol. 40, no. 2, p.344-352.
- Barton**, P.J., 1986, The relationship between seismic velocity and density in the continental-crust – A useful constraint. *Geophys. J. R. astr. Soc.*, vol. 87, no. 1, p.195-208.
- Bell**, R.E. and W.R. Buck, 1992, Crustal control of ridge segmentation inferred from observations of the Reykjanes Ridge. *Nature*, vol. 357, p.583-586.
- Ben-Menahem**, A. and W.B. Beydoun, 1985, Range of validity of seismic ray and beam methods in general inhomogeneous media - I. General theory. *Geophys. J. R. astr. Soc.*, vol. 82, p.207-234.
- Beydoun**, W.B. and A. Ben-Menahem, 1985, Range of validity of seismic ray and beam methods in general inhomogeneous media - II. A canonical problem. *Geophys. J. R. astr. Soc.*, vol. 82, p.235-262.
- Blondel**, P. and L. Parson, 1994, Sonar Processing in the UK. *BRIDGE sp. pub.*, pp.27.
- Bram**, K., 1980, New heat flow observations on the Reykjanes Ridge. *J. geophys.*, vol. 47, p.86-90.
- Bratt**, S.R. and G.M. Purdy, 1984, Structure and variability of oceanic crust on the flanks of the East Pacific Rise between 11° and 13°N. *J. geophys. Res.*, vol. 89, no. B7, p.6111-6125.
- Bratt**, S.R. and S.C. Solomon, 1984, Compressional and shear wave structure of the East Pacific Rise at 11° 20'N: Constraints from three-component ocean bottom seismometer data. *J. geophys. Res.*, vol. 89, no. B7, p.6095-6110.
- Brown**, G.C. and A.E. Musset, 1981, The inaccessible earth. George Allen and Unwin Ltd., pp.235.
- Bryan**, W.B. and J.G. Moore, 1977, Compositional variations of young basalts in the Mid-Atlantic Ridge valley near latitude 36° 49'N. *Geol. Soc. Am. Bull.*, vol. 88, p.556-570.
- Bunch**, A.W.H., 1980, Crustal development of the Reykjanes Ridge from seismic refraction. *J. geophys.*, vol. 47, p.261-264.
- Bunch**, A.W.H. and B.L.N. Kennett, 1980, The crustal structure of the Reykjanes Ridge at 59° 30'N. *Geophys. J. R. astr. Soc.*, vol. 61, p.141-166.

- Calvert, A.J.**, 1995, Seismic evidence for a magma chamber beneath the slow-spreading Mid-Atlantic Ridge. *Nature*, vol. 377, p.410-414.
- Cann, J.R.**, 1974, A model for oceanic crustal structure developed. *Geophys. J. R. astr. Soc.*, vol. 39, p.169-187.
- Carbotte, S.M. and K.C. Macdonald**, 1994a, The axial topographic high at intermediate and fast spreading ridges. *Earth Planet. Sci. Lett.*, vol. 128, no. 3-4, p.85-97.
- Carbotte, S.M. and K.C. Macdonald**, 1994b, Comparison of seafloor tectonic fabric at intermediate, fast and super fast spreading ridges: Influence of spreading rate, plate motions and ridge segmentation on fault patterns. *J. geophys. Res.*, vol. 99, no. B7, p.13609-13631.
- Caress, D.W., M.S. Burnett and J.A. Orcutt**, 1992, Tomographic image of the axial low velocity zone at 12° 50'N on the East Pacific Rise. *J. geophys. Res.*, vol. 97, p.9243-9264.
- Carlson, R.L. and G.S. Raskin**, 1984, Density of the oceanic crust. *Nature*, vol. 311, p.555-558.
- Cary, P.W.**, 1987, Waveform inversion of marine refraction data. unpublished Ph.D. thesis, University of Cambridge, pp.175.
- Cervený, V.**, 1985a, Ray synthetic seismograms for complex two-dimensional and three-dimensional structures. *J. geophys.*, vol. 58, p.2-26.
- Cervený, V.**, 1985b, Gaussian beam synthetic seismograms. *J. geophys.*, vol. 58, p.44-72.
- Chapman, C.H. and R. Drummond**, 1982, Body-wave seismograms in inhomogeneous media using Maslov asymptotic theory. *Bull. seism. Soc. Am.*, vol. 72, no. 6, p.5277-5317.
- Chapman, C.H. and J.A. Orcutt**, 1985, The computation of body wave synthetic seismograms on laterally homogeneous media. *Rev. of Geophysics*, vol. 23, no. 2, p.105-163.
- Chave, A.D. and C.S. Cox**, 1982, Controlled EM sources for measuring electrical conductivity beneath the oceans: 1. Forward problem and modelling study. *J. geophys. Res.*, vol. 87, p.5327-5338.
- Chen, Y.J.**, 1992, Oceanic crustal thickness versus spreading rate. *Geophys. Res. Lett.*, vol. 19, no. 8, p.753-756.
- Christensen, N.I. and M.H. Salisbury**, 1973, Velocities, elastic moduli and weathering-age relations for layer 2 basalts. *Earth Planet. Sci. Lett.*, vol. 19, p.461-471.
- Christensen, N.I. and M.H. Salisbury**, 1975, Structure and constitution of the lower oceanic crust. *Rev. Geophys. Space Phys.*, vol. 13, p.57-86.
- Christenson, G.L., G.M. Purdy and K.M.M. Rhor**, 1993, Structure of the northern symmetrical segment of the Juan de Fuca Ridge. *Marine geophys. Res.*, vol. 15, p.219-240.
- Christenson, G.L., G.M. Purdy and G.J. Fryer**, 1994, Seismic constraints on shallow crustal emplacement processes at the fast spreading East Pacific Rise. *J. geophys. Res.*, vol. 99, no. B9, p.17957-17973.

- Christenson, G.L., G.M. Kent, G.M. Purdy and R.S. Detrick, 1996,** Extrusive thickness variability at the East Pacific Rise, 9°-10°N: Constraints from seismic techniques. *J. geophys. Res.*, vol. 101, no. B2, p.2859-2873.
- Collier, J.S. and M.C. Sinha, 1990,** Seismic images of a magma chamber beneath the Lau Basin back-arc spreading centre. *Nature*, vol. 346, p.646-648.
- Collier, J.S. and M.C. Sinha, 1992,** Seismic mapping of a magma chamber beneath the Valu Fa Ridge, Lau Basin. *J. geophys. Res.*, vol. 97, p.14 031-14053.
- Cormier, M.-H., K.C. Macdonald and D.S. Wilson, 1995,** A three-dimensional gravity analysis of the East Pacific Rise from 18° to 21°30'S. *J. geophys. Res.*, vol. 100, no. B5, p.8063-8082.
- Cox, C.S., S.C. Constable, A.D. Chave and S.C. Webb, 1986,** Controlled source electromagnetic sounding of the oceanic lithosphere. *Nature*, vol. 320, p.52-54.
- Cudrack, C.F. and R.M. Clowes, 1993,** Crustal structure of Endeavour Ridge segment, Juan de Fuca Ridge, from a detailed seismic refraction survey. *J. geophys. Res.*, vol. 98, no. B4, p.6 329-6349.
- Detrick, R.S., 1991,** Ridge crest magma chambers: A review of results from recent marine seismic experiments. in *T. Peters, A. Nicolas and R. Coleman (eds.), Ophiolite genesis and evolution of the oceanic lithosphere*, Kluwer Academic, Boston, Mass., p.7-20.
- Detrick, R.S., P. Buhl, E.E. Vera, J.A. Mutter, J.A. Orcutt, J. Madsen and T. Brocher, 1987,** Multichannel seismic imaging of a crustal magma chamber along the East Pacific Rise. *Nature*, vol. 326, p.35-41.
- Detrick, R.S., J.C. Mutter, P. Buhl and I.I. Kim, 1990,** No evidence from multichannel reflection data for a crustal magma chamber in the MARK area on the Mid-Atlantic Ridge. *Nature*, vol. 347, p.61-64.
- Detrick, R.S., P. Buhl, J.C. Mutter, E.E. Vera, A.J. Harding, G.M. Kent and J.A. Orcutt, 1991,** Crustal magma chambers along the southern East Pacific Rise (EPR) – a two-ship multichannel seismic/OBS experiment on the EPR south of the Garrett Fracture Zone. *EOS, Trans. Am. geophys. Un.*, vol. 72, p.506.
- Detrick, R.S., A.J. Harding, G.M. Kent, J.A. Orcutt, J.C. Mutter and P. Buhl, 1993,** Seismic structure of the southern East Pacific Rise. *Science*, vol. 259, p.499-503.
- Detrick, R.S., J. Collins, R. Stephen and S. Swift, 1994,** In situ evidence of the nature of the seismic layer 2/3 boundary in oceanic crust. *Nature*, vol. 370, p.288-290.
- Detrick, R.S., H.D. Needham and V. Renard, 1995,** Gravity anomalies and crustal thickness variations along the Mid-Atlantic Ridge between 33°N and 40°N. *J. geophys. Res.*, vol. 100, no. B3, p.3767-3787.
- Dziewonski, A.M. and J.H. Woodhouse, 1983,** An experiment in systematic study of global seismicity – centroid-moment tensor solutions for 201 moderate and large earthquakes of 1981. *J. geophys. Res.*, vol. 88, no. B4, p.3247-3271.

- Escartin, J.** and J. Lin, 1995, Ridge offsets, normal faulting, and gravity anomalies of slow spreading ridges. *J. geophys. Res.*, vol. 100, no. B4, p.6163-6177.
- Fertig, J.**, 1984, Shear waves by an explosive point-source: The earth's surface as a generator of converted P-S waves. *Geophys. Prospecting*, vol. 32, p.1-17.
- Field, P.R.**, 1993, Crustal structure of the spreading plate boundary in Iceland and the North Atlantic from gravity data., unpublished Ph.D. thesis, University of Durham, pp.225.
- Fleischer, U.**, 1974, The Reykjanes Ridge - A summary of geophysical data. In: *Kristjansson (ed.) Geodynamics of Iceland and the North Atlantic Area*, D. Reidel Publishing Company, Dordrecht-Holland, p.17-31.
- Forsyth, D.W.** and B. Wilson, 1984, Three dimensional temperature structure of a ridge-transform-ridge system, *Earth Planet. Sci. Lett.*, vol. 70, p.355-362.
- Fowler, C.M.R.**, 1976, Crustal structure of the Mid-Atlantic Ridge crest at 37°N. *Geophys. J. R. astr. Soc.*, vol. 47, p.459-491.
- Fowler, C.M.R.**, 1978, The Mid-Atlantic Ridge: Structure at 45°N. *Geophys. J. R. astr. Soc.*, vol. 54, p.167-186.
- Fowler, C.M.R.**, 1990, The solid earth: An introduction to global geophysics. Cambridge University Press, pp.472.
- Francis, T.J.G.**, 1973, The seismicity of the Reykjanes Ridge. *Earth Planet. Sci. Lett.*, vol. 18, p.119-123.
- Fuchs, K.** and G. Müller, 1971, Computation of synthetic seismograms with the reflectivity method and comparison of observations. *Geophys. J. R. astr. Soc.*, vol. 23, p.417-433.
- Garmany, T.**, 1989, Accumulations of melt at the base of young oceanic crust. *Nature*, vol. 340, p.628-623.
- Géli, L.**, V. Renard and C. Rommeuau, 1994, Ocean crust formation processes at very slow spreading centres: A model for the Mohns Ridge near 72°N based on magnetic, gravity and seismic data. *J. geophys. Res.*, vol. 99, p.2995-3013.
- German, C.R.**, J. Briem, C. Chin, M. Danielsen, S. Holland, R. James, A. Jónsdóttir, E. Ludford, C. Moser, J. Ólafsson, M.R. Palmer and M.D. Rudnicki, 1994a, Hydrothermal activity on the Reykjanes Ridge: the Steinhóll vent-field at 63° 06'N. *Earth Planet. Sci. Lett.*, vol. 121, p.647-654.
- German, C.R.**, R. Kirk, R. Cave, M.C. Sinha, S. Riches, M. Rudnicki, G. Klinkhammer, P. Stoffregen, C. Peirce, C. Young, E. Ludford, P. Taylor, R. Pearce, R. Lloyd, G. White, D. Booth, C. Day and J. Scott, 1994b, BRIDGET trials .. initial results from cruise CD90. *BRIDGE Newsletter*, no.7, p.45.
- Goldflam, P.**, W. Weigel and B.D. Loncarevic, 1980, Seismic structure along RRISP - profile 1 on the southeast flank of the Reykjanes Ridge. *J. geophys.*, vol. 47, p.250-260.
- Goldstein, S.J.**, M.R. Perfit, R. Batiza, D.J. Fornari and M.T. Murrell, 1994, Off-axis volcanism at the East Pacific Rise detected by uranium series dating of basalts. *Nature*, vol. 367, p.157-159.

- Hall**, J.M., 1976, Major problems regarding the magnetization of oceanic crustal layer 2. *J. geophys. Res.*, vol. 81, p.4223-4230.
- Harding**, A.J., J.A. Orcutt, M.E. Kappus, E.E. Vera, J.C. Mutter, P. Buhl, R.S. Detrick and T.M. Brocher, 1989, Structure of young oceanic crust at 13°N on the East Pacific Rise from expanding spread profiles. *J. geophys. Res.*, vol. 94, p.12163-12196.
- Harding**, A.J., G.M. Kent and J.A. Orcutt, 1993, A multichannel seismic investigation of upper crustal structure at 9°N on the East Pacific Rise: Implications for crustal accretion. *J. geophys. Res.*, vol. 98, p.13925-13944.
- Hess**, H.H., 1962, History of the ocean basins. in *A.E.J. Engel, H.L. James and B.F. Leonard (eds.), Petrological Studies: A volume in honor of A.F. Buddington*, Geol. Soc. Am., Boulder, Colorado, U.S.A., p.599-620.
- Hooft**, E.E.E. and R.S. Detrick, 1995, Relationship between axial morphology, crustal thickness and mantle temperature along the Juan de Fuca and Gorda Ridges. *J. geophys. Res.*, vol. 100, no. B11, p.22499-22508.
- Houtz**, R. and J. Ewing, 1976, Upper crustal structure as a function of plate age. *J. geophys. Res.*, vol. 81, p.2490-2498.
- Huang**, P.Y. and S.C. Solomon, 1988, Centroid depths of mid-ocean ridge earthquakes: Dependence on spreading rate. *J. geophys. Res.*, vol. 93, p.13445-13477.
- Hwang**, C., and B. Parsons, 1995, Gravity anomalies derived from Seasat, Geosat, ERS-1 and TOPEX/POSEIDON altimetry and ship gravity: a case study over the Reykjanes Ridge. *Geophys. J. Int.*, vol. 122, p.551-568.
- Inglis**, M.A., 1995, Processing of problem marine seismic reflection data: The Reykjanes Ridge, North Atlantic. unpublished MSc. thesis, University of Durham, pp.59.
- Johnson**, J.L. and S.P. Jakobsson, 1985, Structure and petrology of the Reykjanes Ridge between 62°55'N and 63°48'N. *J. geophys. Res.*, vol. 90, p.10073-10083.
- Kappus**, M.E., A.J. Harding and J.A. Orcutt, 1995, A baseline for upper crustal velocity variations along the East Pacific Rise at 13°N. *J. geophys. Res.*, vol. 100, no. B4, p.6143-6161.
- Keen**, C.E. and C. Tramontini, 1970, A seismic refraction survey on the Mid-Atlantic Ridge. *Geophys. J. R. astr. Soc.*, vol. 20, p.473-491.
- Keeton**, J.A., R.C. Searle, B. Parsons, R.S. White, B.J. Murton, L.M. Parson, C. Peirce and M.C. Sinha, Bathymetry of the Reykjanes Ridge. *Marine geophys. Res.*, in press.
- Kent**, G.M., A.J. Harding and J.A. Orcutt, 1993, Distribution of magma beneath the East Pacific Rise between the Clipperton transform and the 9° 17'N deval from forward modelling of common depth point data. *J. geophys. Res.*, vol. 98, p.13945-13969.

- Kent**, G.M., A.J. Harding, J.A. Orcutt, R.S. Detrick, J.C. Mutter and P. Buhl, 1994, Uniform accretion of oceanic crust south of the Garrett transform at 14° 15'S on the East Pacific Rise. *J. geophys. Res.*, vol. 99, no. B5, p.9097-9116.
- Kirk**, R.E., R.B. Whitmarsh and J.J. Langford, 1982, A three-component ocean bottom seismograph for controlled source and earthquake seismology. *Marine geophys. Res.*, vol. 5, p.327-341.
- Kong**, L.S., S.C. Solomon and G.M. Purdy, 1992, Microearthquake characteristics of a mid-ocean ridge along-axis high. *J. geophys. Res.*, vol. 97, no. B2, p.1659-1685.
- Kuo**, B.-Y. and D.W. Forsyth, 1988, Gravity anomalies of the ridge-transform system in the south Atlantic between 31° and 34.5°S upwelling centres and variations in crustal thickness. *Marine geophys. Res.*, vol. 10, p.205-232.
- Kusznir**, N.J. and M.H.P. Bott, 1976, A thermal study of the formation of oceanic crust. *Geophys. J. R. astr. Soc.*, vol. 47, p.83-95.
- Langel**, R.A., 1992, International geomagnetic reference field – the 6th generation. *J. geomag. geo. elect.*, vol. 44, no. 9, p.679-707.
- Langmuir**, C.H., J.F. Bender and R. Batiza, 1986, Petrological and tectonic segmentation of the East Pacific Rise 5° 30'N - 14° 30'N. *Nature*, vol. 322, p.422-429.
- Laughton**, A.S. and R.C. Searle, 1979, Tectonic processes on slow spreading ridges. in *M. Talwani, C.H. Harrison and D.E Hayes (eds.), Deep Drilling Results in the Atlantic Ocean: Oceanic Crust Maurice Ewing Ser.*, vol. 2, AGU. Washington, p.15-32.
- Lawson**, N.K., 1996, Crustal accretion near ridge-transform intersections: Kane Fracture Zone, Mid-Atlantic Ridge. unpublished Ph.D. thesis, University of Durham, pp. 487.
- Lin**, J., G.M. Purdy, H. Schouten, J.C. Sempere and C. Zervas, 1990, Evidence from gravity data for focused magmatic accretion along the Mid-Atlantic Ridge. *Nature*, vol. 344, p.627-632.
- Loasdale**, P., 1977, Structural geomorphology at a fast-spreading rise crest: The East Pacific Rise near 3° 35'S. *Marine geophys. Res.*, vol. 3, p.251-293.
- Ludwig**, W.J., J.E. Nafe and C.L. Drake, 1970, Seismic refraction. In: *A.E. Maxwell (ed.), The Sea*, vol. 4, Wiley, New York, p.53-84.
- Macdonald**, K.C., 1982, Mid-ocean ridges: Fine scale tectonic, volcanic and hydrothermal processes within the plate boundary zone. *Ann. Rev. Earth planet. Sci.*, vol. 10, p.155-190.
- Macdonald**, K.C., 1989, Anatomy of the magma reservoir. *Nature*, vol. 339, p.178-179.
- Macdonald**, K.C., P.J. Fox, L.J. Perram, M.F. Eisen, R.M. Hayman, S.P. Miller, S.M. Carbotte, M.-H. Cormier and A.N. Shor, 1988, A new view of the mid-ocean ridge from the behaviour of ridge-axis discontinuities. *Nature*, vol. 335, p.217-225.
- Macdonald**, K.C., D.S. Scheirer and S.M. Carbotte, 1991, Mid-ocean ridges: Discontinuities, segments and giant cracks. *Science*, vol. 253, p.986-994.

- Madge**, L.S., R.S. Detrick and the TERA group, 1995, Crustal and upper mantle contribution to the axial gravity anomaly at the southern East Pacific Rise. *J. geophys. Res.*, vol. 100, no. B3, p.3747-3766.
- Matthews**, P.A., 1993, Crustal structure of the Baltic Shield beneath the Sea of Bothnia: BABEL line 6. unpublished Ph.D. thesis, University of Durham, pp.268.
- McClain**, J.S. and B.T.R. Lewis, 1980, A seismic experiment at the axis of the East Pacific Rise. *Marine Geol.*, vol. 35, p.147-169.
- McClain**, J.S., J.A. Orcutt and M. Burnett, 1985, The East Pacific Rise in cross-section: A seismic model. *J. geophys. Res.*, vol. 90, p.8627-8639.
- McDonald**, M.A., S.C. Webb, J.A. Hildebrand, B.D. Cornuelle and C.G. Fox, 1994, Seismic structure and anisotropy of the Juan de Fuca Ridge at 45°N. *J. geophys. Res.*, vol. 99, no. B3, p.4857-4873.
- Minshall**, T.A., R.S. White, J.C. Mutter, P. Buhl, R.S. Detrick, C.A. Williams and E. Morris, 1991, Crustal structure at the Blake Spur Fracture zone from expanding spread profiles. *J. geophys. Res.*, vol. 96, no. B6, p.9955-9984.
- Morgan**, J.V., 1988, Seismic studies over continental margins. unpublished Ph.D. thesis, University of Cambridge, pp.138.
- Morton**, J.L. and N.H. Sleep, 1985, Seismic reflections from a Lau Basin magma chamber. In: *D.W. Scholl and T.L. Vallier (eds.), Geology and offshore resources of Pacific Island Arcs – Tonga region, Earth Sci. Ser.*, vol. 2, Circum-Pacific Council for energy and mineral resources, Houston, Texas, p.441-453.
- Morton**, J.L., N.H. Sleep, W.R. Normark and D.H. Tompkins, 1987, Structure of the southern Juan de Fuca Ridge from seismic reflection records. *J. geophys. Res.*, vol. 92, no. B11, p.11315-11326.
- Murase**, T. and A.R. McBirney, 1973, Properties of some common igneous rocks and their melts at high temperatures. *Geol. Soc. Am. Bull.*, vol. 84, p.3563-3592.
- Murton**, B.J. and L.M. Parson, 1993, Segmentation, volcanism and deformation of oblique spreading centres: a qualitative study of the Reykjanes Ridge. *Tectonophysics*, vol. 222, p.237-257.
- Murton**, B.J., L. Parson, J. Evans, R. Owens, N. Satur, L. Redbourn, D. Sauter, R. Taylor, C. Walker, J. Forster, H. Anderson, A. Fern, J. Jones, C. Paulson, R. Phipps and J. Wyner, 1995, RRS Charles Darwin cruise CD80 1 Sept – 1 Oct 1993. The PERTROS program (PETROgenesis of Oblique Spreading). Cruise Report, no. 241, pp.77.
- Mutter**, J.C., S.M. Carbotte, W.S. Su, L.Q. Xu, P. Buhl, R.S. Detrick, G.M. Kent, J.A. Orcutt and A.J. Harding, 1995, Seismic images of active magma systems beneath the East Pacific Rise between 17° 05' and 17° 35'S. *Science*, vol. 268, no. 5209, p.391-395.
- Nafe**, J.E. and C.L. Drake, 1957, Variation with depth in shallow and deep water marine sediment of porosity, density and the velocities of compressional and shear waves. *Geophysics*, vol. 22, p.523-553.

- Nafe, J.E.** and C.L. Drake, 1962, Physical properties of marine sediments. In: *M.N. Hill (ed.), The Sea*, vol. 3, Wiley, New York, p.794-815.
- Nisbet, E.G.** and C.M.R. Fowler, 1978, The Mid-Atlantic Ridge at 37 and 45°N: some geophysical and petrological constraints. *Geophys. J. R. astr. Soc.*, vol. 54, p.631-660.
- Orcutt, J.A., B.L.N. Kennett, L. Dorman and W. Prothero**, 1975, Evidence for a low velocity zone underlying a fast spreading ridge crest. *Nature*, vol. 256, p.475-476.
- Orcutt, J.A., J.S. McClain and M. Burnett**, 1984, Evolution of the oceanic crust: Results from recent seismic experiments. In: *I.C. Glass, S.J. Lippard and A.W. Shelton, Ophiolites and oceanic lithosphere*, Sp. Pub. Geol. Soc. Lond., no. 13, p.7-16.
- Owen, T.R.E.** and P.J. Barton, 1990, The Cambridge digital seismic recorder for land and marine use. *Tectonophysics*, vol. 173, p.145-154.
- Owen, T.R.E.** and M.C. Sinha, 1990, A PC based seismic acquisition system. *First Break*, vol. 8, no. 2, p.57-62.
- Pallister J.S.** and C.A. Hopson, 1981, Semail ophiolite plutonic suite: Field relations, phase variation, cryptic variation and layering, and a model of a spreading ridge magma chamber. *J. geophys. Res.*, vol. 86, p.2593-2644.
- Parker, R.L.**, 1972, The rapid calculation of potential anomalies. *Geophys. J. R. astr. Soc.*, vol. 31, p.447-455.
- Parson, L.M., B.J. Murton, R.C. Searle, D. Booth, J. Evans, P. Field, J. Keeton, A. Laughton, E. McAllister, N. Millard, L. Redbourne, I. Rouse, A. Shor, D. Smith, S. Spencer, C. Sumerhages, C. Walker**, 1993, En echelon axial volcanic ridges at the Reykjanes Ridge: a life cycle of volcanism and tectonics. *Earth Planet. Sci. Lett.*, vol. 117, p.73-87.
- Parsons, B.** and J.G. Sclater, 1977, An analysis of the variation of ocean floor bathymetry and heat flow with age. *J. geophys. Res.*, vol. 82, p.803-827.
- Peirce, C.**, 1990a, Crustal structure of the Africa - Eurasian plate boundary. unpublished Ph.D. thesis, University of Cambridge, pp.248.
- Peirce, C.**, 1990b, Processing wide-angle refraction data using SKS - a manual. Internal report, University of Cambridge, pp.57.
- Peirce, C., M.C. Sinha and R.C. Searle**, 1996, Detailed investigation of accretionary processes occurring at the slow spreading Reykjanes Ridge at 57° 45'N. Grant proposal submitted to NERC (BRIDGE), pp.33.
- Peirce, C.** and R.E. Kirk, A multichannel ocean bottom seismometer and its application in controlled and explosive source seismology. *in prep.*.
- Phipps Morgan J.** and Y.J. Chen, 1993, Dependence of ridge axis morphology on magma supply and spreading rate. *Nature*, vol. 346, p.706-708.

- Prince**, R.A. and D.W. Forsyth, 1988, Horizontal extent of anomalously thin crust near the Vema fracture zone from the 3-D analysis of gravity anomalies. *J. geophys. Res.*, vol. 93, no. B7, p.8051-8063.
- Purdy**, G.M., 1987, New observations of the shallow seismic structure of young oceanic crust. *J. geophys. Res.*, vol. 92, p.9351-9362.
- Purdy**, G.M. and R.S. Detrick, 1986, Crustal structure of the Mid-Atlantic Ridge at 23°N from seismic refraction studies. *J. geophys. Res.*, vol. 91, p.3739-3762.
- Purdy**, E.M., L.S.L. Kong, G.L. Christenson and S.C. Solomon, 1992, Relationship between spreading rate and the seismic structure of mid-ocean ridges. *Nature*, vol. 355, p.815-817.
- Raitt**, R.W., 1963, The crustal rocks. In: *M.N. Hill (ed.), The Sea*, vol. 3, Wiley (Interscience), New York, p.85-102.
- Ritzert**, M. and W.R. Jacoby, 1985, On the lithospheric seismic structure of the Reykjanes Ridge at 62.5°N. *J. geophys. Res.*, vol. 90, p.10117-10128.
- Rudnicki**, M.D., C.R. German, R.E. Kirk, M.C. Sinha, H. Elderfield and S. Riches, 1995, New instrument platform tested at the Mid-Atlantic Ridge. *EOS, Trans. Am. geophys. Un.*, vol. 76, no. 33, p.329-330.
- Sandwell**, D.T., 1986, Thermal stress and the spacings of transform faults. *J. geophys. Res.*, vol. 91, p.6402-6417.
- Sandwell**, D.T. and W.H.F. Smith, 1996, Marine gravity anomaly from Geosat and ERS-1 satellite Altimetry. *J. geophys. Res.*, in press.
- Schilling**, J.-G., 1973, The Iceland mantle plume, geochemical evidence along the Reykjanes Ridge. *Nature*, vol. 242, p.565-578.
- Searle**, R.C. and A.S. Laughton, 1981, Fine scale sonar study of tectonics and volcanism on the Reykjanes Ridge. *Oceanological Acta*, vol. 4, p.5-13.
- Searle**, R.C., P.R. Field and R.B. Owens, 1994, Segmentation and a non-transform ridge offset on the Reykjanes Ridge near 58°N. *J. geophys. Res.*, vol. 99, p.24159-24172.
- Shipboard Scientific Party** with a special contribution by D. Mann, 1979, Site reports. *Initial reports of the Deep Sea Drilling Project*, vol. XLXII, p.233-236.
- Simrad** multibeam echosounder systems, 1992, Product specification: EM12S. pp. 4.
- Sinha**, M.C., 1995, Segmentation and rift propagation at the Valu Fa Ridge, Lau Basin: Evidence from gravity data. *J. geophys. Res.*, vol. 100, no. B8, p.15025-15043.
- Sinha**, M.C., P.D. Patel, M.J. Unsworth, T.R.E. Owen and M.R.G. MacCormack, 1990, An active source electromagnetic sounding system for marine use. *Marine geophys. Res.*, vol. 12, p.59-68.
- Sinha**, M.C., C. Peirce and S. Constable, 1994, An integrated geophysical investigation of the axial volcanic region of the Reykjanes Ridge at 57°45'N. RRS Charles Darwin 81 Cruise report (unpublished), pp.73.

- Sinton, J.M.** and R.S. Detrick, 1992, Mid-ocean ridge magma chambers. *J. geophys. Res.*, vol. 97, no. B1, p.197-216.
- Sleep, N.H.**, 1975, Formation of oceanic crust: some thermal constraints. *J. geophys. Res.*, vol. 80, p.4 037-4042.
- Small, C.** and D.T. Sandwell, 1994, Imaging mid-ocean ridge transitions with satellite gravity. *Geology*, vol. 22, p.123-126.
- Smallwood, J.R., R.S. White** and T.A. Minshull, 1995, Sea-floor spreading in the presence of the Iceland plume: the structure of the Reykjanes Ridge at 61° 40'N. *J. of Geol. Soc. Lond.*, vol. 152, p.1 023-1 029.
- Solomon, S.C.** and D.R. Toomey, 1992, The structure of mid-ocean ridges. *Earth Planet. Sci. Lett.*, vol. 20, p.329-364.
- Speiss, F.N., K.C. Macdonald, T. Atwater, R. Ballard, A. Carraza, D. Cordoba, C. Cox, V.M. Diaz Garcia, J. Francheteau, J. Guerrero, J. Hawkins, R. Hayman, R. Hessier, T. Juteau, M. Kastner, R. Larson, B. Lugendgk, J.D. MacDougall, S. Miller, W. Normark, J.A. Orcutt and C. Rangin**, 1980, East Pacific Rise: Hot springs and geophysical experiments. *Science*, vol. 207, p.1421-1433.
- Spudich, P.** and J.A. Orcutt, 1980a, Petrology and porosity of an oceanic crustal site: results from wave form modelling of seismic refraction data. *J. geophys. Res.*, vol. 85, p.1409-1433.
- Spudich, P.** and J.A. Orcutt, 1980b, A new look at the seismic velocity structure of the oceanic crust. *Rev. Geophys. Space Phys.*, vol. 18, no. 3, p.627-645.
- Talwani, M., J.C. Worzel** and M. Landisman, 1959, Rapid gravity calculations for two-dimensional bodies with application to the Mendocino submarine fracture zone. *J. geophys. Res.*, vol. 64, p.49-59.
- Taylor, R.N., B.J. Murton** and M.F. Thirwall, 1995, Petrographic and geochemical variation along the Reykjanes Ridge, 57°N-59°N. *J. of Geol. Soc. Lond.*, vol. 152, p.1031- 1037.
- Teledyne Geotech**, 1988, PDAS users guide. pp.193.
- Télez, J.** and D. Córdoba, 1996, Observations of converted Moho reflections in the north-west of the Iberian Peninsula. *Geophys. J. Int.*, vol. 124, p.7-17.
- Tivey, M.A.**, 1994, Fine scale magnetic anomaly field over the southern Juan de Fuca Ridge: Axial magnetization low and implications for crustal structure. *J. geophys. Res.*, vol. 99, p.4833-4855
- Thomson, C.J.** and C.H. Chapman, 1986, End-point contributions to synthetic seismograms. *Geophys. J. R. astr. Soc.*, vol. 87, p.285-294.
- Tolstoy, M., A.J. Harding** and J.A. Orcutt, 1993, Crustal thickness on the Mid-Atlantic Ridge: Bull's-eye gravity anomalies and focused accretion. *Science*, vol. 263, p.726-729.
- Toomey, D.R., G.M. Purdy, S.C. Solomon** and W.S. Wilcock, 1990, The three-dimensional seismic velocity structure of the East Pacific Rise near latitude 9° 30'N. *Nature*, vol. 347, p.639-645.

- Toomey**, D.R., S.C. Solomon and G.M. Purdy, 1994, Tomographic imaging of the shallow crustal structure of the East Pacific Rise at 9° 30'N. *J. geophys. Res.*, vol. 99, no. B12, p.24 135-24 157.
- Unsworth**, M.J., B.D. Travis and A.D. Chave, 1993, Electromagnetic induction by a finite electric dipole over a 2-D earth. *Geophysics*, vol. 58, p.198-214.
- Vera**, E.E. and J.B. Diebold, 1994, Seismic imaging of oceanic layer 2A between 9° 30'N and 10°N on the East Pacific Rise from two-ship wide aperture profiles. *J. geophys. Res.*, vol. 99, no. B2, p.3031-3041.
- Vera**, E.E., J.C. Mutter, P. Buhl, J.A. Orcutt, A.J. Harding, M.E. Kappus, R.S. Detrick and T.M. Brocher, 1990, The structure of 0 to 0.2 Ma. old oceanic crust at 9°N on the East Pacific Rise from expanded spread profiles. *J. geophys. Res.*, vol. 95, p.15529-15556.
- Vine**, F.J., 1966, Spreading of the oceanic floor: New evidence. *Science*, vol. 154, p.1405-1415.
- Vine**, F.J. and D.H. Matthews, 1963, Magnetic anomalies over oceanic ridges. *Nature*, vol. 199, p.947-949.
- Walker**, G.P.L., F. Aumento, B.D. Clarke, J.R. Cann, P.J.C Ryall and the Shipboard Scientific Party, 1970, Site 115. *Initial reports of the Deep Sea Drilling Project*, vol. XII, p.361-393.
- Webb**, S.C., S.C. Constable, C.S. Cox and T.K. Deaton, 1985, A seafloor field instrument. *J. geomag. geo. elect.*, vol. 37, p.1115-1129.
- Weber**, M., 1988, Computation of body wave seismograms in absorbing 2-D media using the Gaussian Beam method: comparison with exact methods. *Geophysical J.*, vol. 92, p.9-24.
- Wessel**, P. and W.H.F. Smith, 1995, New version of the Generic Mapping Tools released. *EOS Trans. AGU*, vol. 76, p.329.
- White**, J.E. and R.L. Sengbush, 1963, Shear waves from explosive sources. *Geophysics*, vol. 28, no. 6, p.1001-1019.
- White**, R.S., 1979, Oceanic upper crustal structure from variable angle seismic reflection-refraction profiles. *Geophys. J. R. astr. Soc.*, vol. 57, p.683-726.
- White**, R.S. and A.W.H. Bunch, 1976, Explosive sink rates. *Geophys. J. R. astr. Soc.*, vol. 56, p.473-476.
- White**, R.S. and R.A. Stephen, 1980, Compressional to shear wave conversion in oceanic crust. *Geophys. J. R. astr. Soc.*, vol. 63, p.547-565.
- White**, R.S. and R.M. Clowes, 1994, Seismic attenuation structure beneath the Juan de Fuca Ridge from tomographic inversion. *J. geophys. Res.*, vol. 99, p.3043-3056.
- White**, R.S., D.P. McKenzie and R.K. O'Nions, 1992, Oceanic crustal thickness from seismic measurements and rare earth element inversions. *J. geophys. Res.*, vol. 97, p.19683-19715.
- White**, R.S., J.W. Bown and J.R. Smallwood, 1995, The temperature of the Iceland plume and origin of outward propagating V-shaped ridges. *J. of Geol. Soc. Lond.*, vol. 152, p.1039-1045.

- Whit marsh**, R.B., 1975, Axial intrusion zone beneath the median valley of the Mid-Atlantic Ridge at 37°N detected by explosion seismology. *Geophys. J. R. astr. Soc.*, vol. 52, p.189-215.
- Wilcock**, W.S.D., S.C. Solomon, G.M. Purdy and D.R. Toomey, 1995, Seismic attenuation structure of the East Pacific Rise near 9° 30'N. *J. geophys. Res.*, vol. 100, no. B12, p.24 147-24 165.
- Wolfe**, C.J., G.M. Purdy, D.R. Toomey and S.C. Solomon, 1995, Microearthquake characteristics and velocity structure at 29°N on the Mid-Atlantic Ridge: the architecture of a slow spreading segment. *J. geophys. Res.*, vol. 100, p.24449-24472.
- Zelt**, C.A. and R.B. Smith, 1992, Seismic travel-time inversion for 2-D crustal velocity structure. *Geophys. J. Int.*, vol. 108, p.16-34.

Appendix A

Instrument deployment and shot point locations

This appendix contains listings of the shot and instrument positions for the wide-angle and normal incidence seismic experiments.

Table A1: DOBS deployment positions

DOBS	latitude (N)	longitude (W)	depth (m)
DDOBS 1	57° 52.10'	33° 07.25'	1690
DDOBS 2	57° 47.30'	32° 50.80'	1722
DDOBS 3	57° 50.22'	32° 39.30'	1775
DDOBS 4	57° 38.80'	32° 43.52'	1799
DDOBS 5	57° 42.03'	32° 32.57'	1290
DDOBS 6	57° 36.80'	32° 14.75'	1613
CDOBS 11	57° 49.32'	32° 57.60'	1477
CDOBS 12	57° 45.60'	32° 44.88'	1991
CDOBS 13	57° 44.63'	32° 42.00'	1477
CDOBS 14	57° 43.67'	32° 39.00'	1743
CDOBS 15	57° 40.80'	32° 28.00'	1500

Table A2: Sonobuoy deployment positions

sonobuoy	latitude (N)	longitude (W)	length of profile (km)	duration (minutes)
1	57° 31.97'	32° 19.00'	0 (failed on deployment)	0
2	57° 34.32'	32° 27.00'	0 (failed on deployment)	0
3	57° 50.10'	33° 11.00'	12.45	83
4	57° 46.68'	32° 58.73'	7.2	48

Table A3: Airgun lines

line number	start point		end point	
	latitude (N)	longitude (W)	latitude (N)	longitude (W)
1	57° 52.53'	33° 09.92'	57° 27.18'	31° 42.00'
2	57° 53.33'	32° 39.00'	57° 35.73'	32° 45.00'
3	57° 24.03'	31° 52.28'	57° 47.60'	33° 13.00'
4	57° 50.08'	33° 11.00'	57° 40.20'	32° 37.00'

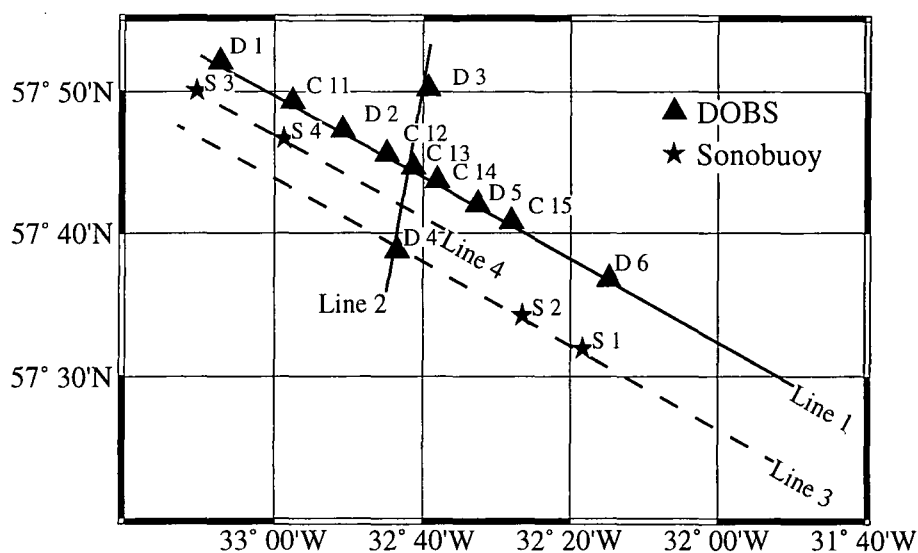
Figure A1: Sketch of the DOBS deployment and shot point locations as listed in tables A1-3.

Table A4: Explosive shot instants and locations

shot no.	shot instant	latitude (N)	longitude (W)	detonation depth (m)	flight time (s)	shot size (kg)
1	08:00:05.127	57° 52.46'	33° 08.79'	204.5	156.0	25
2	08:04:12.227	57° 52.18'	33° 07.80'	227.3	162.7	25
3	08:08:01.699	57° 51.88'	33° 06.90'	225.8	149.0	25
4	08:12:05.402	57° 51.62'	33° 05.99'	223.6	151.8	25
5	08:15:59.690	57° 51.34'	33° 05.01'	221.0	145.8	25
6	08:19:57.321	57° 51.08'	33° 04.06'	217.9	142.4	25
7	08:24:08.167	57° 50.84'	33° 03.18'	233.8	152.0	25
8	08:28:13.007	57° 50.59'	33° 02.29'	234.9	159.0	25
9	08:32:12.790	57° 50.34'	33° 01.45'	227.2	156.7	25
10	08:36:08.722	57° 50.06'	33° 00.50'	230.8	152.6	25
11	08:40:04.813	57° 49.74'	32° 59.64'	223.5	151.6	25
12	08:44:12.339	57° 49.57'	32° 58.75'	232.8	156.6	25
13	08:48:00.000	57° 49.30'	32° 57.83'	misfire	–	25
14	08:52:02.105	57° 49.04'	32° 56.88'	217.7	145.0	25
15	08:55:58.117	57° 48.78'	32° 55.91'	217.4	144.4	25
16	08:59:55.717	57° 48.50'	32° 55.03'	206.7	140.6	25
17	09:03:55.311	57° 48.27'	32° 54.18'	199.5	139.9	25
18	09:08:03.684	57° 48.00'	32° 53.29'	207.5	150.6	25
19	09:12:00.429	57° 47.74'	32° 52.39'	211.9	145.0	25
20	09:13:33.000	57° 47.47'	32° 51.48'	misfire	–	25
21	09:20:04.243	57° 47.22'	32° 50.57'	214.0	150.5	25
22	09:24:08.142	57° 47.00'	32° 49.72'	225.8	154.8	25
23	09:28:05.013	57° 46.73'	32° 48.72'	219.0	153.3	25
24	09:32:14.487	57° 46.47'	32° 47.77'	239.0	162.5	25
25	09:36:04.003	57° 46.20'	32° 46.87'	215.0	149.6	25
26	09:40:07.165	57° 45.90'	32° 45.98'	223.1	153.5	25
27	09:44:03.463	57° 45.67'	32° 45.09'	218.4	150.0	25
28	09:48:07.921	57° 45.43'	32° 44.21'	225.0	153.8	25
29	09:52:02.111	57° 45.16'	32° 43.31'	224.4	147.6	25
30	09:55:57.012	57° 44.91'	32° 42.40'	216.9	143.4	25
31	10:00:06.374	57° 44.64'	32° 41.53'	221.8	150.8	25
32	10:03:53.482	57° 44.34'	32° 40.68'	202.2	140.4	25
33	10:07:58.985	57° 44.04'	32° 39.73'	214.9	144.4	25
34	10:12:06.708	57° 43.80'	32° 38.80'	223.2	151.1	25
35	10:15:54.879	57° 43.55'	32° 37.92'	207.9	141.8	25
36	10:19:50.886	57° 43.34'	32° 37.05'	218.8	136.6	25
37	10:23:56.917	57° 43.05'	32° 36.15'	215.8	144.0	25

Appendix A Instrument deployment and shot point locations

38	10:27:18.051	57° 42.80'	32° 35.27'	132.1	96.1	25
39	10:35:56.376	57° 42.27'	32° 33.47'	220.9	144.8	25
40	10:40:04.263	57° 42.02'	32° 32.52'	213.3	146.8	25
41	10:44:09.504	57° 41.74'	32° 31.61'	221.8	150.0	25
42	10:48:01.125	57° 41.48'	32° 30.71'	219.9	146.4	25
43	10:52:06.615	57° 41.22'	32° 29.82'	217.2	150.0	25
44	10:55:58.584	57° 40.97'	32° 28.89'	207.1	144.0	25
45	11:00:08.734	57° 40.70'	32° 27.97'	214.9	153.6	25
46	11:03:53.117	57° 40.43'	32° 27.05'	196.0	137.8	25
47	11:08:07.823	57° 40.16'	32° 26.15'	221.1	153.2	25
48	11:12:08.655	57° 39.91'	32° 25.21'	215.6	153.7	25
49	11:16:04.487	57° 39.66'	32° 24.25'	226.7	149.2	25
50	11:20:07.070	57° 39.39'	32° 23.35'	217.9	148.6	25
51	11:28:01.302	57° 38.85'	32° 21.49'	216.2	148.8	25
52	11:32:02.865	57° 38.58'	32° 20.59'	210.8	148.6	25
53	11:35:56.395	57° 38.31'	32° 19.67'	226.9	142.8	25
54	11:40:06.792	57° 38.03'	32° 18.78'	224.0	151.2	25
55	11:44:03.966	57° 37.77'	32° 17.91'	222.0	151.2	25
56	11:48:07.804	57° 37.51'	32° 17.00'	226.3	153.9	25
57	11:51:56.408	57° 37.29'	32° 16.12'	219.5	144.4	25
58	11:56:04.502	57° 37.04'	32° 15.18'	194.9	153.7	25
59	12:00:03.741	57° 36.73'	32° 14.30'	204.1	151.4	25
60	12:04:59.625	57° 36.43'	32° 13.39'	197.0	134.9	25
61	12:08:12.946	57° 36.17'	32° 12.50'	221.5	157.1	25
62	14:00:15.108	57° 36.23'	32° 12.80'	231.5	162.7	50
63	14:08:17.429	57° 35.78'	32° 11.06'	240.9	not measured	50
64	14:16:14.893	57° 35.31'	32° 09.31'	215.4	162.5	50
65	14:24:12.866	57° 34.76'	32° 07.58'	213.4	159.3	50
66	14:32:11.033	57° 34.28'	32° 05.79'	217.9	157.9	50
67	14:40:09.191	57° 33.72'	32° 04.01'	200.6	156.3	50
68	14:48:17.482	57° 33.24'	32° 02.16'	270.8	162.3	50
69	14:56:22.087	57° 32.74'	32° 00.40'	196.6	167.9	50
70	15:04:15.379	57° 32.23'	31° 58.67'	216.0	160.9	50
71	15:12:09.132	57° 31.74'	31° 56.95'	230.8	155.6	50
72	15:20:08.944	57° 31.28'	31° 55.17'	misfire	–	50
73	15:28:03.789	57° 30.78'	31° 53.38'	182.4	150.4	50
74	15:36:05.457	57° 30.30'	31° 51.66'	207.5	149.7	50
75	15:44:16.580	57° 29.71'	31° 49.93'	224.9	162.7	50
76	15:49:35.000	57° 29.20'	31° 48.26'	misfire	–	50
77	16:00:07.590	57° 28.70'	31° 46.45'	224.7	153.7	50
78	16:08:21.880	57° 28.19'	31° 44.71'	207.0	169.1	50

79	16:16:16.931	57° 27.69'	31° 43.02'	206.8	163.4	50
80	16:24:08.296	57° 27.21'	31° 41.39'	189.0	154.5	50
81	08:00:10.231	57° 37.38'	32° 44.06'	232.5	159.1	25
82	08:04:13.211	57° 37.94'	32° 43.86'	235.2	159.9	25
83	08:08:12.682	57° 38.41'	32° 43.64'	227.4	157.1	25
84	08:12:07.503	57° 38.93'	32° 43.49'	234.4	150.2	25
85	08:16:05.088	57° 39.47'	32° 43.36'	220.6	150.2	25
86	08:20:09.447	57° 39.97'	32° 43.13'	212.7	154.1	25
87	08:24:11.338	57° 40.50'	32° 42.91'	192.5	158.5	25
88	08:28:11.220	57° 41.03'	32° 42.70'	213.8	155.8	25
89	08:32:05.704	57° 41.58'	32° 42.51'	230.5	150.9	25
90	08:36:01.737	57° 42.17'	32° 42.34'	232.4	149.1	25
91	08:40:04.816	57° 42.74'	32° 42.11'	236.3	152.3	25
92	08:44:04.715	57° 43.28'	32° 41.92'	213.4	153.1	25
93	08:48:12.744	57° 43.84'	32° 41.69'	219.9	157.7	25
94	08:52:07.738	57° 44.39'	32° 41.58'	234.7	155.1	25
95	08:56:06.341	57° 44.92'	32° 41.41'	202.0	153.7	25
96	09:00:29.642	57° 45.45'	32° 41.23'	240.4	177.2	25
97	09:04:06.822	57° 45.99'	32° 41.02'	231.8	151.8	25
98	09:08:10.967	57° 46.51'	32° 40.83'	219.3	157.9	25
99	09:12:13.216	57° 47.04'	32° 40.58'	232.9	161.1	25
100	09:16:08.216	57° 47.56'	32° 40.32'	224.7	154.1	25
101	09:20:01.297	57° 48.10'	32° 40.12'	218.4	150.4	25
102	09:24:01.402	57° 48.63'	32° 39.96'	215.3	149.4	25
103	09:28:04.657	57° 49.17'	32° 39.79'	215.6	151.0	25
104	09:32:05.983	57° 49.70'	32° 39.64'	224.4	152.9	25
105	09:36:07.996	57° 50.24'	32° 39.45'	222.5	153.0	25
106	09:40:00.822	57° 50.75'	32° 39.23'	218.9	145.4	25
107	09:44:06.789	57° 51.32'	32° 39.03'	210.5	141.8	25
108	09:48:05.005	57° 51.83'	32° 38.80'	220.6	153.5	25
109	09:51:53.477	57° 52.35'	32° 38.67'	211.5	143.8	25
110	09:56:00.799	57° 52.88'	32° 38.46'	221.8	148.8	25
111	09:59:57.974	57° 53.40'	32° 38.25'	218.5	144.8	25

Appendix B

Sound velocity profiler data

This appendix contains a table and graphs of the AML sound velocity profiler data collected at $57^{\circ} 47.2'N$ $32^{\circ} 50.45'W$ on the Reykjanes Ridge.

Table B1: AML Sound velocity profile

Date: 3:10:93 Julian day: 276

Lat.: 57° 47.2'N Long.: 32° 50.45'W

Depth (m)	Velocity (ms ⁻¹)	Temperature (°C)
1.91	1487.09	8.82
32.49	1487.09	8.83
37.54	1487.51	8.83
53.42	1487.09	8.70
60.00	1485.57	8.26
63.72	1485.01	8.00
65.66	1484.18	7.77
69.80	1483.08	7.50
75.34	1482.66	7.31
85.64	1482.11	7.15
86.82	1481.97	7.11
96.65	1481.56	6.93
107.31	1480.60	6.70
155.09	1479.63	6.23
159.38	1479.22	6.15
171.51	1479.08	6.08
176.76	1479.63	6.09
181.91	1479.63	6.09
187.15	1479.08	6.01
198.64	1479.22	5.98
203.97	1479.63	5.98
246.00	1479.08	5.72
295.04	1479.22	5.51
300.10	1478.67	5.37
332.65	1478.81	5.30
338.41	1479.22	5.28
343.52	1479.08	5.26
348.96	1478.81	5.22
354.42	1478.67	5.20
359.53	1479.08	5.19
417.62	1479.22	5.05
422.95	1479.63	5.06

460.65	1479.77	4.98
465.85	1480.18	4.98
526.52	1480.73	4.86
543.11	1480.60	4.78
575.80	1480.05	4.62
596.56	1480.60	4.57
602.21	1480.05	4.52
644.25	1480.18	4.35
649.54	1480.46	4.35
654.84	1480.73	4.34
692.33	1480.87	4.29
697.82	1481.15	4.27
731.38	1481.15	4.24
733.69	1481.42	4.23
736.42	1481.56	4.23
784.36	1481.97	4.15
789.82	1482.11	4.15
795.31	1481.70	4.08
816.70	1481.97	4.02
822.07	1482.11	4.02
848.58	1482.11	3.99
852.14	1482.53	4.00
887.24	1482.66	3.95
892.55	1483.08	3.96
908.49	1483.08	3.93
914.24	1483.22	3.93
967.51	1484.18	3.89
1009.44	1484.05	3.82
1014.59	1484.74	3.82
1126.74	1485.71	3.61
1157.31	1485.57	3.57
1162.73	1486.12	3.57
1200.19	1486.54	3.53
1237.26	1486.96	3.50
1264.35	1487.09	3.50
1298.01	1487.79	3.48
1300.51	1488.07	3.48
1329.37	1488.35	3.47

1356.67	1488.62	3.47
1361.86	1489.04	3.46
1393.87	1489.60	3.47
1420.27	1490.02	3.46
1447.97	1490.30	3.45
1473.88	1490.71	3.46
1500.91	1491.13	3.45
1511.74	1491.55	3.45
1527.85	1491.69	3.45
1564.21	1492.11	3.45
1591.06	1492.67	3.45
1646.83	1493.65	3.45
1652.24	1493.93	3.45
1705.06	1494.77	3.45
1731.97	1495.19	3.45
1770.21	1495.90	3.45
1776.01	1496.18	3.45

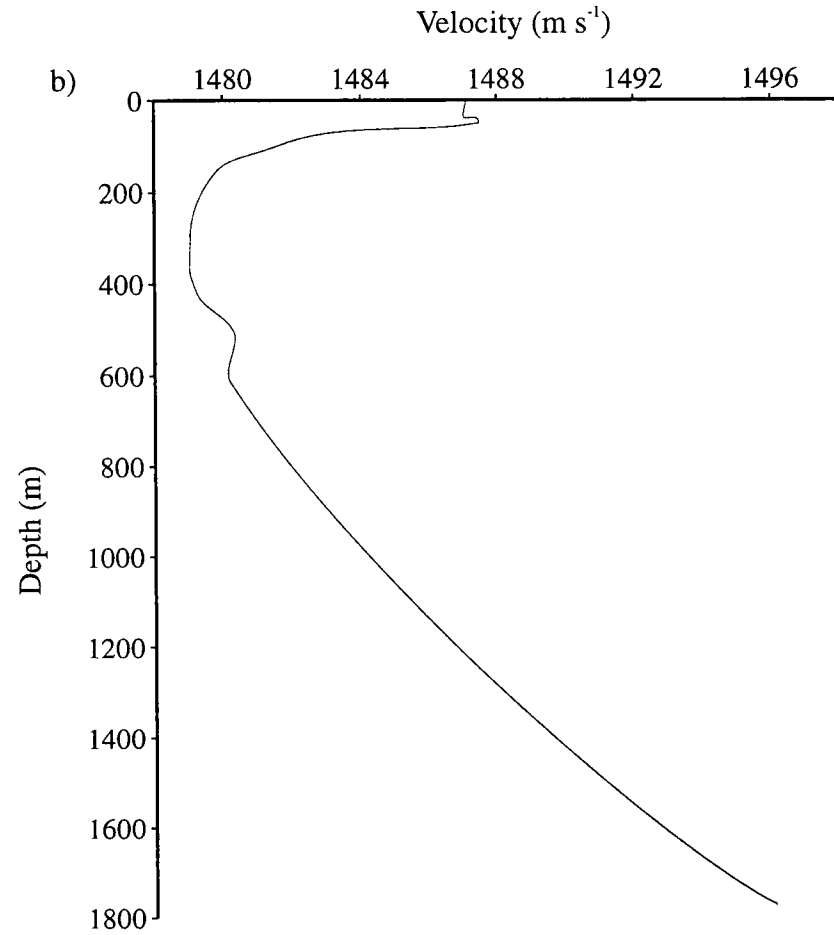
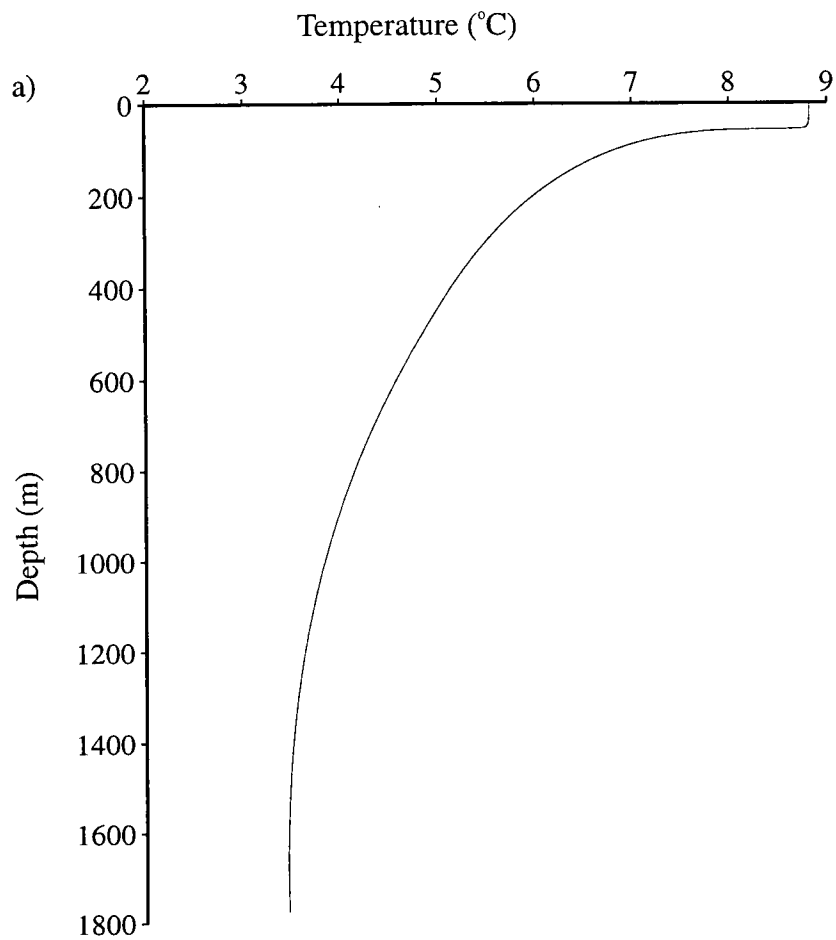


Figure B1: Variation in temperature (a) and velocity (b) with depth in the water column at 57° 47.2'N 32° 50.45'W at the Reykjanes Ridge, measured using the RVS' AML sound velocity profiler.

Appendix C

Definition of SEG-Y_{WA}

This appendix contains the specifications of the in-house seismic data formats used at Cambridge and Durham and the differences between these standards.

Table C1: Byte location information contained in the SEG-Y_{WA} binary trace headers (for a full description see Peirce, 1990b).

The SEG-Y standard was developed for multichannel seismic data storage (Barry *et al.*, 1975) in which each trace header must not only identify the shot number and related values, but also the receiver number, trace order CDP number, etc.. For wide-angle data these latter values are not applicable, i.e. there is only one shot per trace, therefore some of the inapplicable headers from the "standard" SEG-Y are replaced with values required for wide-angle seismic data. However there is no agreed standard for SEG-Y_{WA} and therefore some of these definitions differ between Durham and Cambridge.

The variable names referred to in the second column of this table are based on the terminology used in Merlin Geophysical's SKS seismic processing package which was first designed as a normal incidence data processing program adapted for use with wide-angle seismic data (Peirce, 1990b)

byte no.	variable	Durham definition	Cambridge definition
1-4	ushot	trace sequence no. in line	trace order in line
5-8	utrc	trace sequence no. in reel	trace order on reel
9-12	uflfn	original field record number	shot order (in terms of time)
13-16	ufltn	original field trace number equated to uflfn in SEG-Y _{WA}	trace no. in first gathered record
17-20	usrcpn	energy source point number	shot no.
21-24	ucdp	CDP ensemble no.	not used
25-28	utrace	trace no. in CDP ensemble	not used
29-30	utrtyp	trace type code	trace type code
31-32	unsum	no. summed traces contributing	no. vertically summed traces
33-34	unstk	no. stacked traces contributing	no. horizontally summed traces
35-36	uduse	data use code	production (1) or test (2)
37-40	wrange	source to receiver range	shot receiver range
41-44	wrcvge	receiver group elevation	receiver elevation
45-48	wsrcse	surface elevation at source	not used
49-52	wsrcdp	source depth	shot depth
53-56	wsrcde	datum elevation at source	not used
57-60	wrcvde	datum elevation at receiver group	not used
61-64	wsrcwd	water depth at source	water depth at shot
65-68	wrcvwd	water depth at receiver	water depth at receiver
69-70	wscall	scalar applied to elevation and depth	scalar for bytes 41-68

71-72	wscal2	scalar	scalar for bytes 73-88
73-76	wsrcx	source location x long. (E +ve)	source longitude
77-80	wsrcy	source location y lat. (sec of arc)	source latitude
81-84	wrcvx	receiver group location long.	receiver longitude
85-88	wrcvy	receiver group location lat.	receiver latitude
89-90	ucunit	co-ordinate units (1=length 2=sec)	co-ordinate units (1=length 2=sec)
91-92	wvelw	weathering velocity	water velocity
93-94	wvelsw	sub-weathering velocity	phase velocity
95-96	usrcut	uphole time at source	not used
97-98	urcvut	uphole time at receiver group	not used
99-100	usrcst	source static correction	not used
101-102	urcvst	receiver static	not used
103-104	utotst	total static applied	not used
105-106	ulaga	lag time A (msec)	not used
107-108	ulagb	lag time B (msec)	not used
109-110	udelt	delay recording time	delay from shot inst. to trace start
111-112	umutst	mute start	not used
113-114	umutfn	mute finish	not used
115-116	unsamp	no. samples in trace	no. samples in trace
117-118	wsr	sample interval in μ s	sample interval in μ s
119-120	ugntyp	gain type	gain type (1=fixed, 2=binary, 3=floating pt.)
121-122	wgain	gain constant	instrument gain constant
123-124	wgnst	initial gain (dB)	gain or initial gain
125-126	ucorr	correlation code	correlation code (1=no, 2=yes)
127-128	ufrqst	sweep start frequency	not used
129-130	ufrqfn	sweep end frequency	not used
131-132	uslen	sweep length	not used
133-134	ustype	sweep type	not used
135-136	ustlen	start taper length	not used
137-138	uetlen	end taper length	not used
139-140	utptyp	taper type	not used
141-142	ualfrq	anti-alias frequency	anti-alias frequency
143-144	ualslp	anti-alias slope	anti-alias slope
145-146	unofrq	notch frequency	not used
147-148	unoslp	notch slope	not used
149-150	ulofrq	low cut	not used

151-152	uhifrq	high cut	not used
153-154	uloslp	low cut slope	not used
155-156	uhislp	high cut slope	not used
157-158	uyear	year (start trace)	year (start trace)
159-160	uday	day of year	day of year
161-162	uhour	hour	hour
163-164	umin	minute	minute
165-166	usec	second	second
167-168	utctyp	time bias code	time zone 1=local 2=GMT
169-170		not used	not used
171-172		not used	not used
173-174		not used	receiver no.
175-176		not used	total no. receivers
177-178		not used	no. receivers missing shot
179-180		not used	not used
181-182		not used	hour (shot inst.)
183-184		not used	minute
185-186		not used	second
187-188		not used	millisecond
189-190		not used	cassette recorder no.
191-192		not used	month (instrument time at start of trace)
193-194		not used	day
195-196		not used	hour
197-198		not used	minute
199-200		not used	second
201-202		not used	millisecond
203-204		not used	instrument identity
205-206		not used	shot size
209-210		not used	additional delay from shot inst. and trace start

Appendix D

DOBS data processing programs and example input files

This appendix contains an outline of the processing programs used in processing digital ocean bottom seismometer data from both Durham and Cambridge.

Table D1: DOBS data processing programs

<i>program</i>	application	author
<i>shotinst</i>	calculates shot instants and detonation depths using the bubble pulse periods and arrival times of seabed reflections	originated by A. Bunch in 1978 and subsequently modified by several Cambridge Ph.D. students
<i>psection</i>	plots raw PDAS data as seismic sections for quality control	C. Peirce
<i>convert</i>	converts raw PDAS data into SEG-Y _{WA} files	originated by P.A. Matthews modified for DOBS data by C. Peirce
<i>332COMM</i>	replays raw CDOBS data from C90 cassette to PC	T.R.E. Owen
<i>DB_SHOW</i>	checks raw replayed CDOBS data for unexpected bit streams	T.R.E. Owen
<i>DEPOT</i>	copies the raw replayed CDOBS data onto ½" 9-track tape	T.R.E. Owen
<i>NTR2_94</i>	calculates skeleton SEG-Y headers from event and instrument files	originated by P.J. Barton modified by several Ph.D. students
<i>DB_SEGY</i>	converts raw replayed CDOBS data into files which constitute SEG-Y _{WA}	T.R.E. Owen
<i>SEGSRT4</i>	sorts output from <i>DB_SEGY</i> into consecutive trace order	T.R.E. Owen
<i>TXLCOPY</i>	combines files constituting SEG-Y _{WA} and writes them to ½" 9-track tape	T.R.E. Owen
<i>segy</i>	reads a SEG-Y file from ½" 9-track tape and writes to disk in SEG-Y _i form OR reads SEG-Y _i disk files and writes to ½" 9-track tape as a SEG-Y file	D.L. Stevenson
<i>thead</i>	extracts header information from SEG-Y _i files and writes this information into file	C. Peirce
<i>trtodis</i>	extracts shot number-range pairs from a <i>thead</i> output file and writes these to a file for editing	C. Peirce
<i>dishead</i>	overwrites the headers in the original SEG-Y _i disk file with the edited shot number-range values	C. Peirce
<i>ctrhead</i>	modified version of <i>thead</i> to deal with CDOBS data	C. Peirce modified for CDOBS data by D.A. Navin

<i>ctrshot</i>	extracts trace number and field record number from the <i>ctrhead</i> output file then equates the trace number to the field record number (section 2.6.4)	C.Peirce modified for CDOBS data by D.A. Navin
<i>ctrtostat</i>	extracts shot number and lag time from the <i>ctrhead</i> output file to allow statics to be written into trace headers.	C.Peirce modified for CDOBS data by D.A. Navin
<i>cdisshot and cdisstat</i>	overwrite headers in the original SEG-Y; disk file with new trace numbers and statics respectively	C. Peirce modified for CDOBS data by D.A. Navin
<i>range</i>	ray-traces possible rays paths through the water column for direct water waves and multiples to calculate the shot range	C. Peirce
<i>adjust</i>	calculates airgun ranges assuming constant shot separation	C. Peirce
<i>fspectra</i>	calculates frequency spectra of SEG-Y; disk files	originated by D. Graham modified by C. Peirce
<i>bpfilt</i>	creates a new SEG-Y; disk file with a user specified band-pass filter applied	originated by D. Graham modified by C. Peirce
<i>tget</i>	reads a SEG-Y file from 1/2" 9-track tape, exabyte or disk and creates a disk image SEG-Y file (tput performs the reverse process)	D.L. Stevenson

Table D2: Example input files**Options file for DDOBS data processing using *convert***

(after Matthews, 1993)

PROJECT_NAME:REYKJ RIDGE	title to be put into SEG-Y _i header
STATION_NAME:D108	instrument number
REEL:1	reel number
SEISMIC:1	number of seismic traces
NONSEIS:0	number of non-seismic traces
OUT_FORMAT:1	output format
MEASUREMENT:1	distance units
COORD_UNITS:2	coordinates units
COMBINE:Y	combine trace data and headers?
DEL_PFILE:N	delete used PDAS files?
TIMEBASIS:2	time base
VR:0000	reduction velocity
PRE_RUN:0000	reduced time at start of trace (ms)
LENGTH:18	trace length (s)
COMMENTS:*** This should be the last line of the options file *****	

Station file for DDOBS data processing using *convert*

D108 2Z 0 0 1799.0 0573848.48N 3271629.20W 1 S 000000

inst	no	sen	el	del	wd	lat	long	gain	P/S	corr												
A4	I2	A4	I3	1X	I4	1X	F6.1	1X	I3	I2	F5.2	A1	1X	I3	I2	F5.2	A1	I6	1X	A2	1X	I6

inst	-	instrument name
no	-	channel number
sen	-	sensor type (Z, X, Y, H)
el	-	elevation (0 for marine DOBS data)
del	-	datum elevation (0 for marine DOBS data)
wd	-	water depth (m)
lat	-	latitude (degrees, minutes, seconds, N/S)
long	-	longitude (degrees, minutes, seconds, E/W)
gain	-	gain
P/S	-	recording window type
corr	-	time correction (ms)

Event file for DDOBS data processing using *convert*

line	time	shot	latitude	longitude	shot	delay	water	day	shot size
no.	hr.min.s.ms	no.	xx°xx'xx"	xxx°xx'xx"	depth (m)		depth (m)		(kg)
2	80010231	81	573723.01	3271556.69	232.5	0	01751.5	284	25

2 80010231 81 573723.013271556.69 232.5 0 01751.5 284 25
2 80413211 82 573756.493271608.33 235.2 0 01781.0 284 25
2 80812682 83 573824.643271621.52 227.4 0 01830.0 284 25
2 81207503 84 573855.643271630.86 234.4 0 01809.0 284 25
2 81605088 85 573928.163271638.22 220.6 0 01909.0 284 25
2 82009447 86 573958.323271651.95 212.7 0 01837.5 284 25
2 82411338 87 574029.713271705.57 192.5 0 01794.5 284 25
2 82811220 88 574102.013271718.10 213.8 0 01823.5 284 25
2 83205704 89 574134.513271729.63 230.5 0 01742.0 284 25
2 83601737 90 574210.013271739.52 232.4 0 01731.0 284 25
2 84004816 91 574244.633271753.14 236.3 0 01690.0 284 25
2 84404715 92 574317.073271805.01 213.4 0 01686.5 284 25
2 84812744 93 574350.443271818.63 219.9 0 01585.0 284 25
2 85207738 94 574423.323271825.33 234.7 0 01570.0 284 25
2 85606341 95 574455.293271835.11 202.0 0 01635.0 284 25
2 90029642 96 574526.963271845.99 240.4 0 01643.5 284 25
2 90406822 97 574559.333271858.95 231.8 0 01587.0 284 25
2 90810967 98 574630.873271910.49 219.3 0 01673.0 284 25
2 91213216 99 574702.253271925.43 232.9 0 01626.0 284 25
2 91608216 100 574733.623271940.70 224.7 0 01729.0 284 25
2 92001297 101 574806.053271953.01 218.4 0 01712.5 284 25
2 92401402 102 574837.803272002.23 215.3 0 01683.5 284 25
2 92804657 103 574910.273272012.78 215.6 0 01847.5 284 25
2 93205983 104 574942.243272021.46 224.4 0 01747.0 284 25
2 93607996 105 575014.213272032.78 222.5 0 01763.5 284 25
2 94000822 106 575045.273272046.29 218.9 0 01784.5 284 25
2 94406789 107 575118.903272058.15 210.5 0 01905.5 284 25
2 94805005 108 575150.043272111.89 220.6 0 01990.5 284 25
2 95153477 109 575221.073272120.02 211.5 0 01943.5 284 25
2 95600799 110 575252.823272132.54 221.8 0 01996.5 284 25
2 95957974 111 575324.293272144.85 218.5 0 02021.5 284 25

Instrument file for CDOBS processing using *NTR2_94*

Instrument name

instrument number latitude (° ') longitude (° ') depth (m)

day hr. min. offset of pre-deployment clock check day hr. min. offset post-deployment

CDOBS11.POS

11 57. 49.320 32. 57.600 1490

281 06 10 -010 287 06 10 256

Event file for CDOBS data processing using *NTR2_94*

shot no.	shot no.	latitude xx°xx'	longitude xxx°xx'	water depth (m)	shot depth (m)	year/month/day	day	time hr.min.s.ms	shot size (kg)
81	81	57 37.356	32 44.052	01751	100	1993 10 11	284	8 00 10 231	25

081 081 57. 37.356 32. 44.052 1751 100 1993 10 11 284 8 00 10 231 25
 082 082 57. 37.914 32. 43.860 1781 100 1993 10 11 284 8 04 13 211 25
 083 083 57. 38.406 32. 43.632 1830 100 1993 10 11 284 8 08 12 682 25
 084 084 57. 38.928 32. 43.470 1809 100 1993 10 11 284 8 12 07 503 25
 085 085 57. 39.468 32. 43.374 1909 100 1993 10 11 284 8 16 05 088 25
 086 086 57. 40.632 32. 43.086 1837 100 1993 10 11 284 8 20 09 447 25
 087 087 57. 40.488 32. 42.900 1794 100 1993 10 11 284 8 24 11 338 25
 088 088 57. 41.034 32. 42.678 1823 100 1993 10 11 284 8 28 11 220 25
 089 089 57. 41.568 32. 42.498 1742 100 1993 10 11 284 8 32 05 704 25
 090 090 57. 42.162 32. 42.348 1731 100 1993 10 11 284 8 36 01 737 25
 091 091 57. 42.738 32. 42.108 1690 100 1993 10 11 284 8 40 04 816 25
 092 092 57. 43.278 32. 41.928 1686 100 1993 10 11 284 8 44 04 715 25
 093 093 57. 43.836 32. 41.664 1585 100 1993 10 11 284 8 48 12 744 25
 094 094 57. 44.388 32. 41.586 1570 100 1993 10 11 284 8 52 07 738 25
 095 095 57. 44.922 32. 41.406 1635 100 1993 10 11 284 8 56 06 341 25
 096 096 57. 45.438 32. 41.238 1643 100 1993 10 11 284 9 00 29 642 25
 097 097 57. 45.996 32. 41.004 1587 100 1993 10 11 284 9 04 06 822 25
 098 098 57. 46.536 32. 40.860 1673 100 1993 10 11 284 9 08 10 967 25
 099 099 57. 47.040 32. 40.572 1626 100 1993 10 11 284 9 12 13 216 25
 100 100 57. 47.556 32. 40.314 1729 100 1993 10 11 284 9 16 08 216 25
 101 101 57. 48.084 32. 40.116 1712 100 1993 10 11 284 9 20 01 297 25
 102 102 57. 48.612 32. 39.966 1683 100 1993 10 11 284 9 24 01 402 25
 103 103 57. 49.176 32. 39.780 1847 100 1993 10 11 284 9 28 04 657 25
 104 104 57. 49.698 32. 39.648 1747 100 1993 10 11 284 9 32 05 983 25
 105 105 57. 50.244 32. 39.456 1763 100 1993 10 11 284 9 36 07 996 25
 106 106 57. 50.748 32. 39.228 1784 100 1993 10 11 284 9 40 00 822 25
 107 107 57. 51.342 32. 39.018 1905 100 1993 10 11 284 9 44 06 789 25
 108 108 57. 51.810 32. 38.784 1990 100 1993 10 11 284 9 48 05 005 25

Appendix E

Complete wide-angle seismic dataset and corresponding ray-traced synthetic seismograms and models

This appendix contains a complete set of wide-angle seismic data sections together with ray-traced models and calculated synthetic and observed seismograms for each instrument.

Figures E1 to E19: These figures show all of the wide-angle seismic data collected during CD81/93. All the data shown in these sections have been filtered (parameters specified in table 3.1) with the exception of the airgun data recorded by the vertical geophone of the DDOBS which is shown unfiltered. All sections are reduced at 6 km s^{-1} , plotted at true amplitude, with NNW to the left for the across-axis and N to the left for the along-axis sections. The sections are ordered by increasing offset along each seismic line.

Figures E20 to E34: These figures show final ray-traced models which fit the Reykjanes Ridge wide-angle seismic data. Observed travel time picks are shown on the synthetic data as dots with a diameter equivalent to the modelling error and the ray-traced travel time solution is shown as a solid line. Synthetic and observed data are plotted at the same scale for comparison and are reduced at 6 km s^{-1} . Again these plots are ordered by offset increasing along each seismic line.

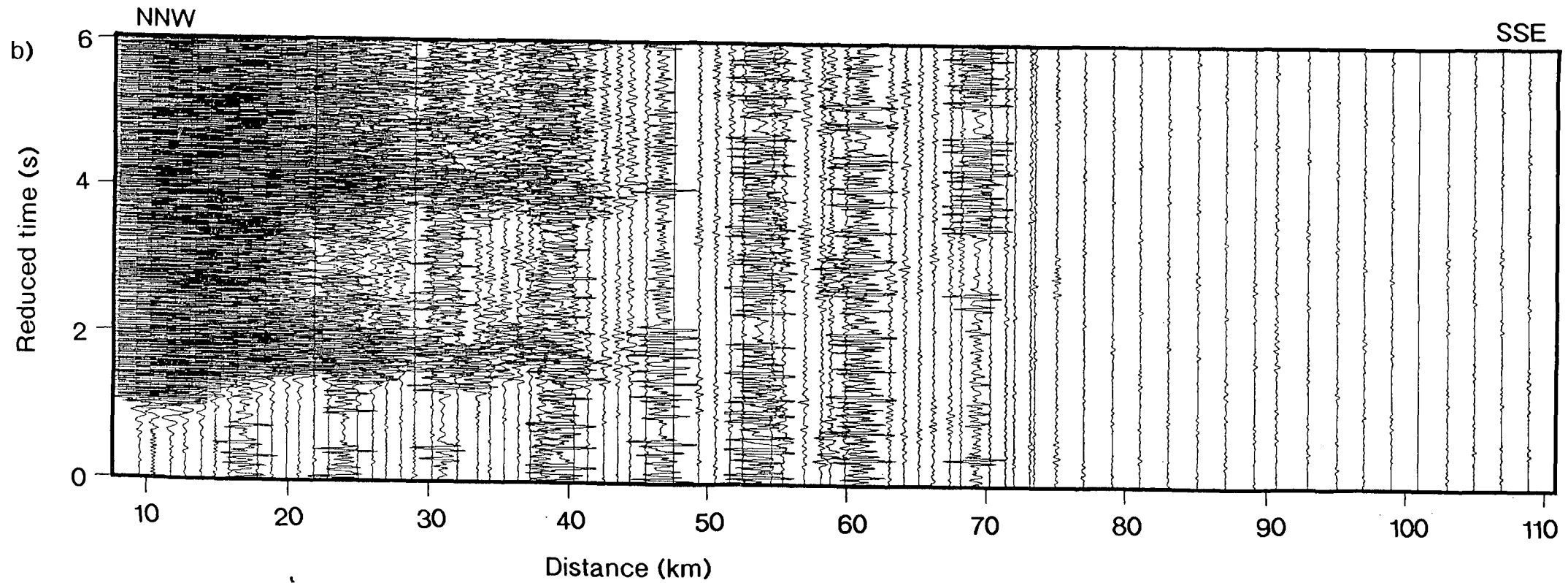
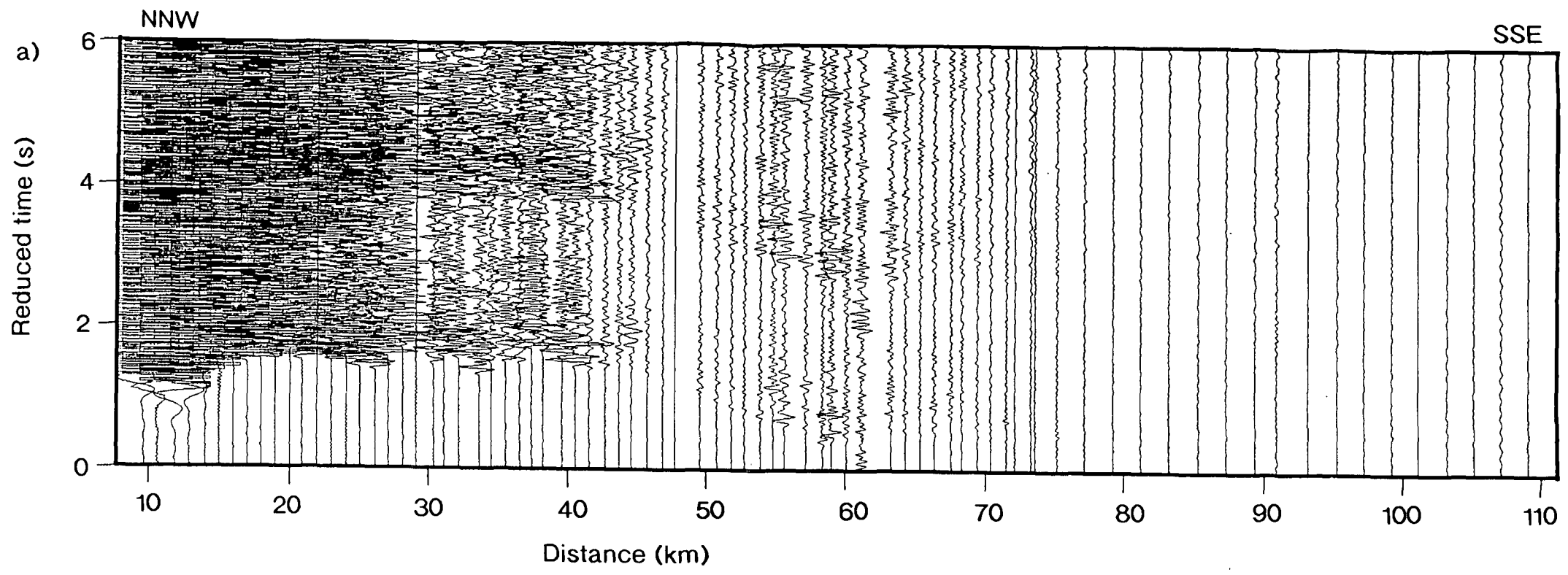


Figure E1: Explosive data recorded by DDOBS 1 at the northwesternmost end of the across-axis line. Sections are plotted at true amplitude and reduced at 6 km s^{-1} . Note the shadow zone between 45 and 50 km.
 a) Vertical geophone component.
 b) Hydrophone component. Prominent noise bursts on this section are caused by disk spin (see section 3.3).

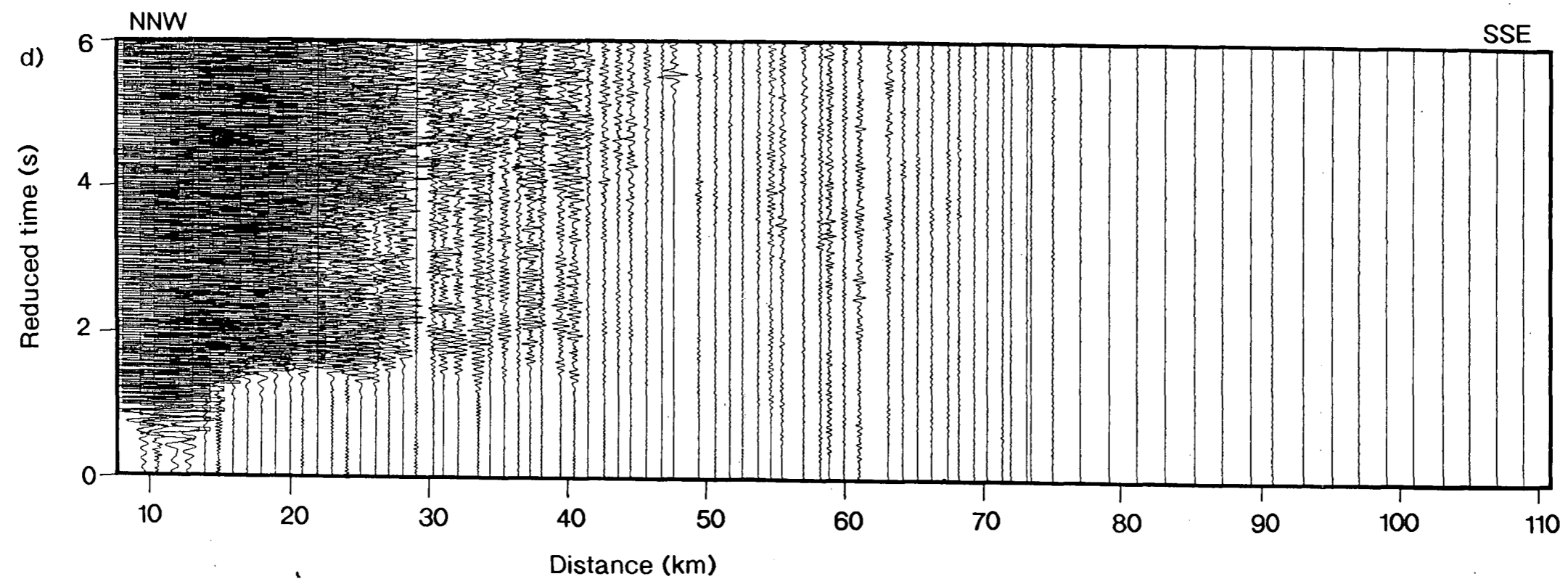
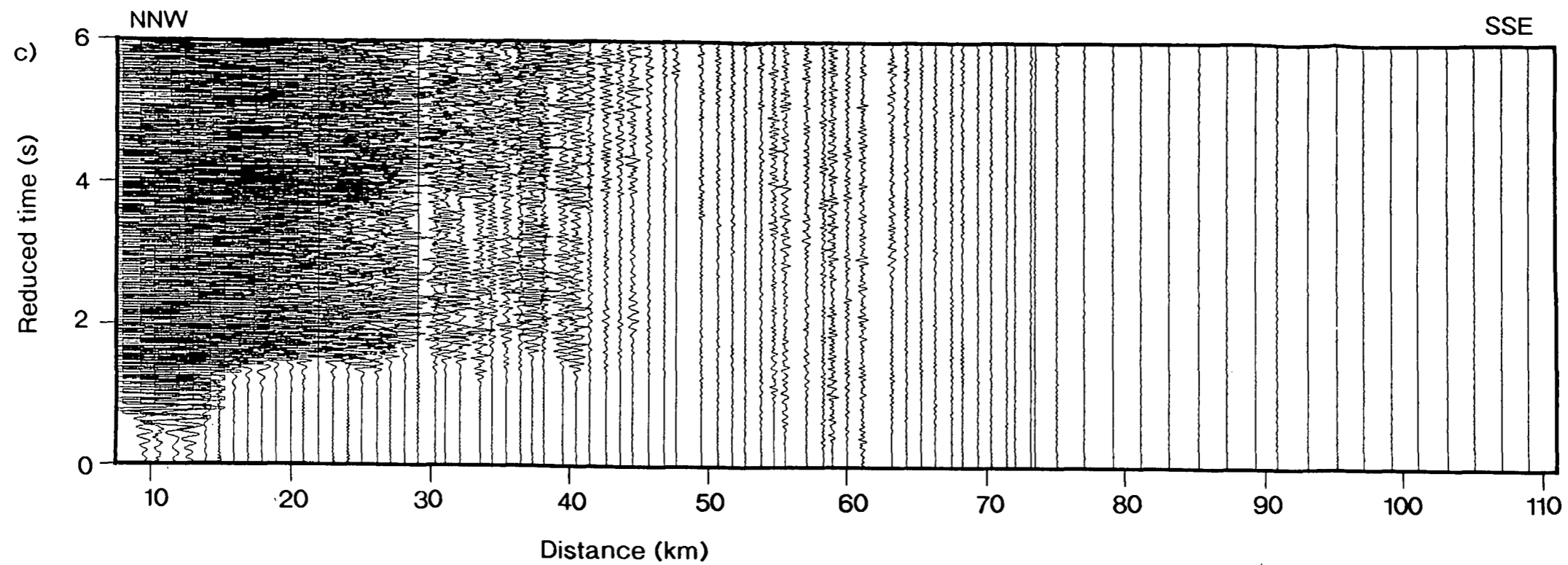


Figure E1: cont.. Explosive data recorded by DDOBS 1 at the northwesternmost end of the across-axis line. Sections are plotted at true amplitude and reduced at 6 km s^{-1} . Note the shadow zone between 45 and 50 km.
 c) Horizontal X-component.
 d) Horizontal Y-component.

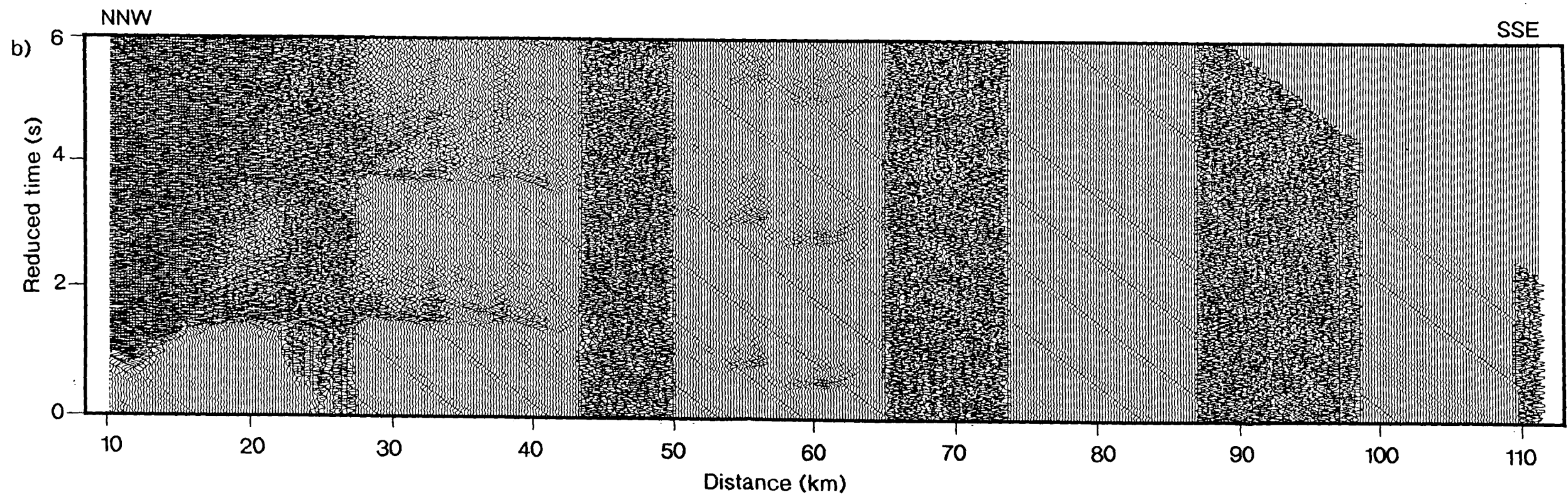
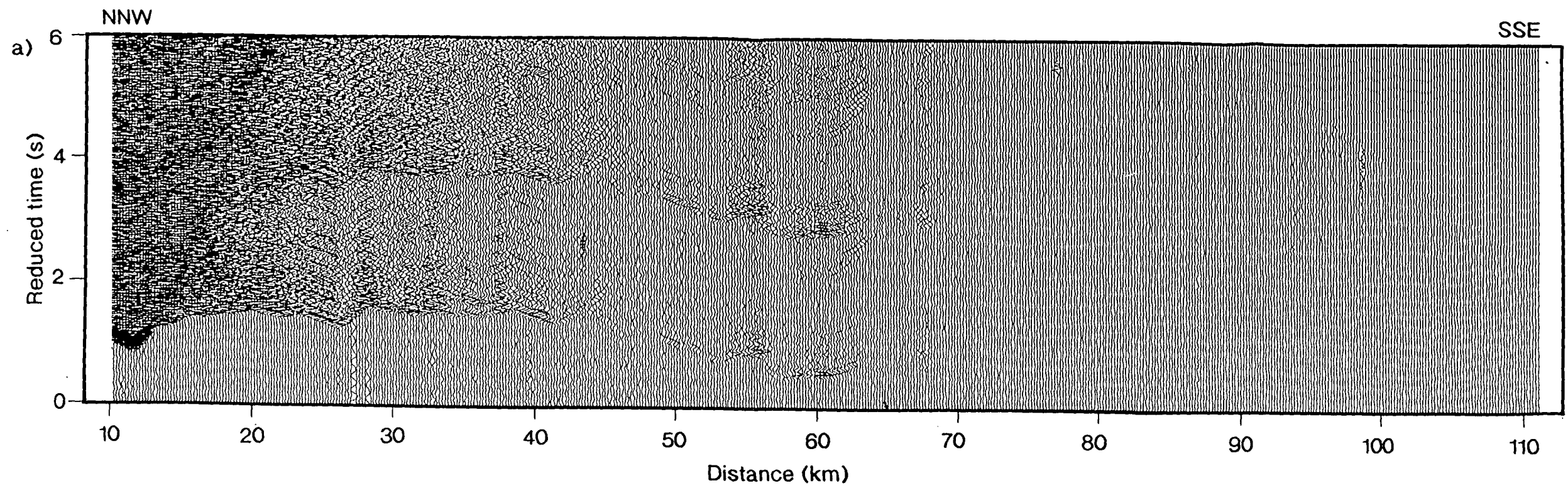


Figure E2: Airgun data recorded by DDOBS 1 at the northwesternmost end of the across-axis line. Sections are plotted at true amplitude and reduced at 6 kms^{-1} . Note the shadow zone between 43 and 49 km.

a) Vertical geophone component.

b) hydrophone component. Prominent noise bursts on this section are caused by disk spin (see section 3.3).

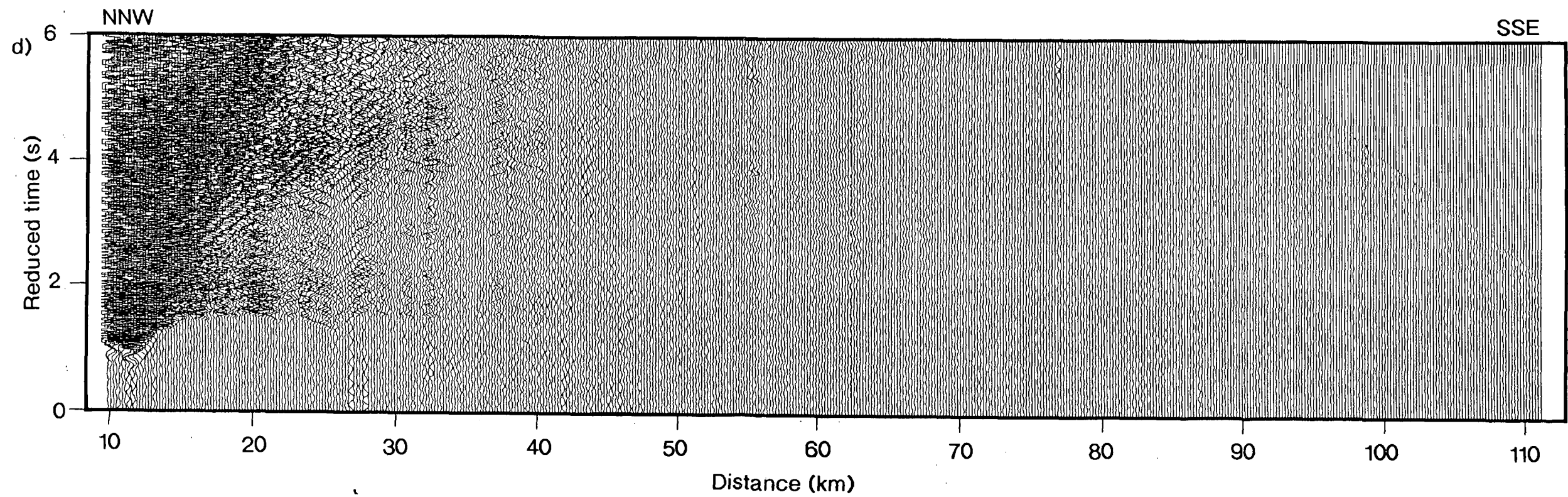
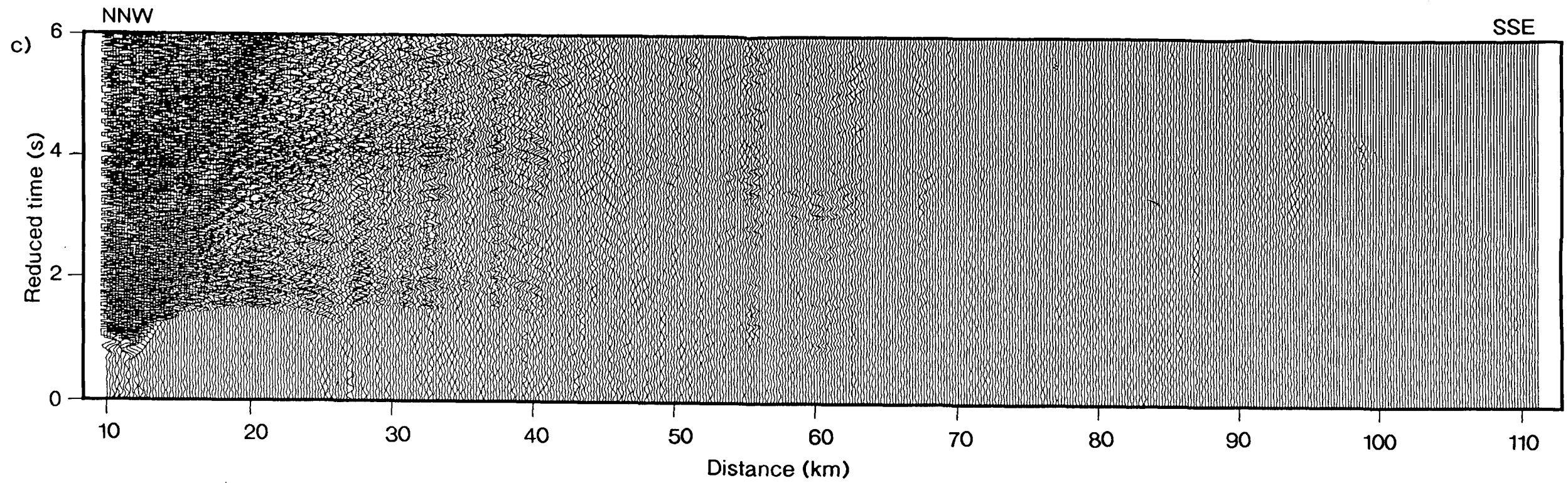


Figure E2: cont.. Airgun data recorded by DDOBS 1 at the northwesternmost end of the across-axis line. Sections are plotted at true amplitude and reduced at 6 km s^{-1} . Note the sharp reduction in the amplitude of arrivals for offsets greater than 41 km.
 c) Horizontal X-component.
 d) Horizontal Y-component.

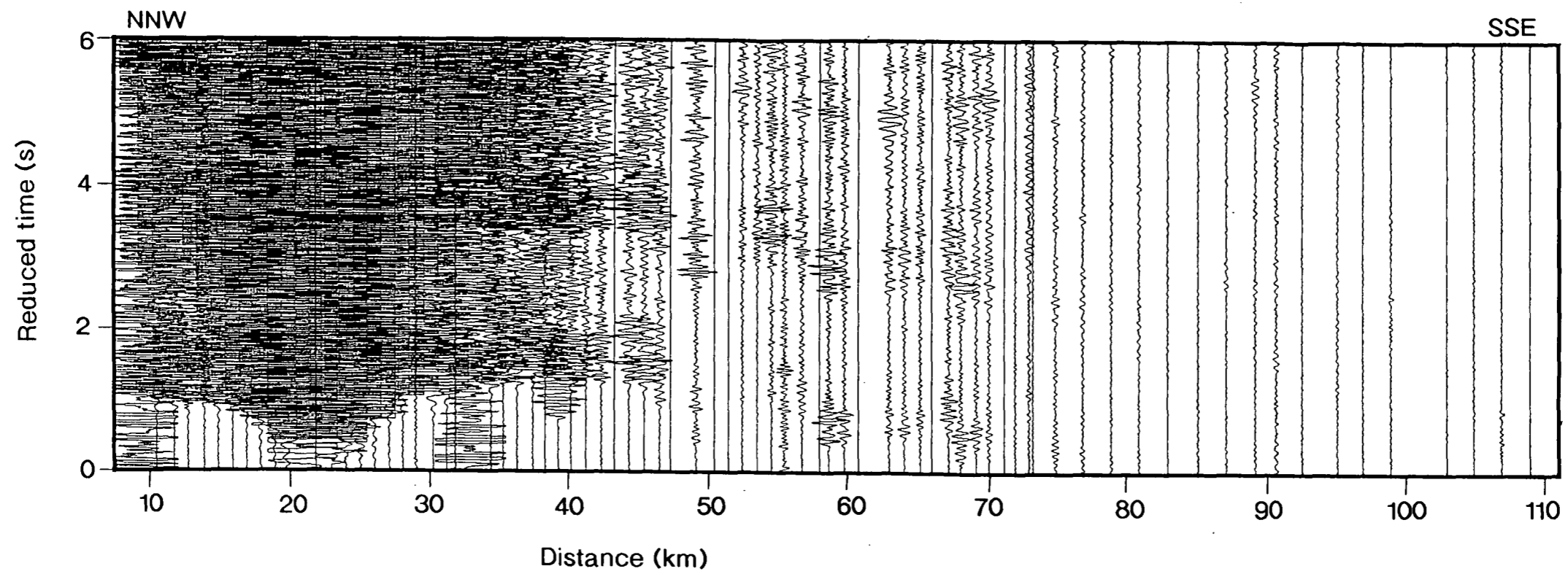


Figure E3: Explosive data recorded by CDOBS 11 along the across-axis line. The section is plotted at true amplitude and reduced at 6 km s^{-1} . Note the shadow zone between 47 and 51 km offset and the noisy traces at 10, 33, 39, 49 and 55 km offset.

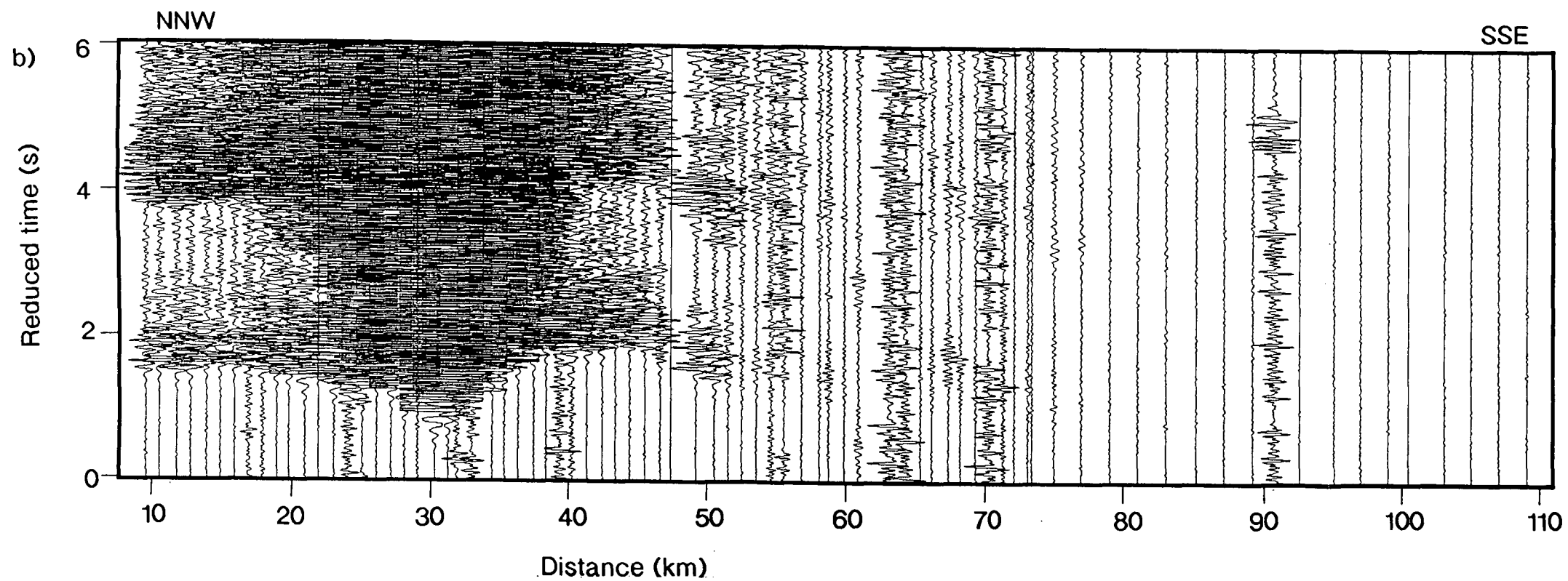
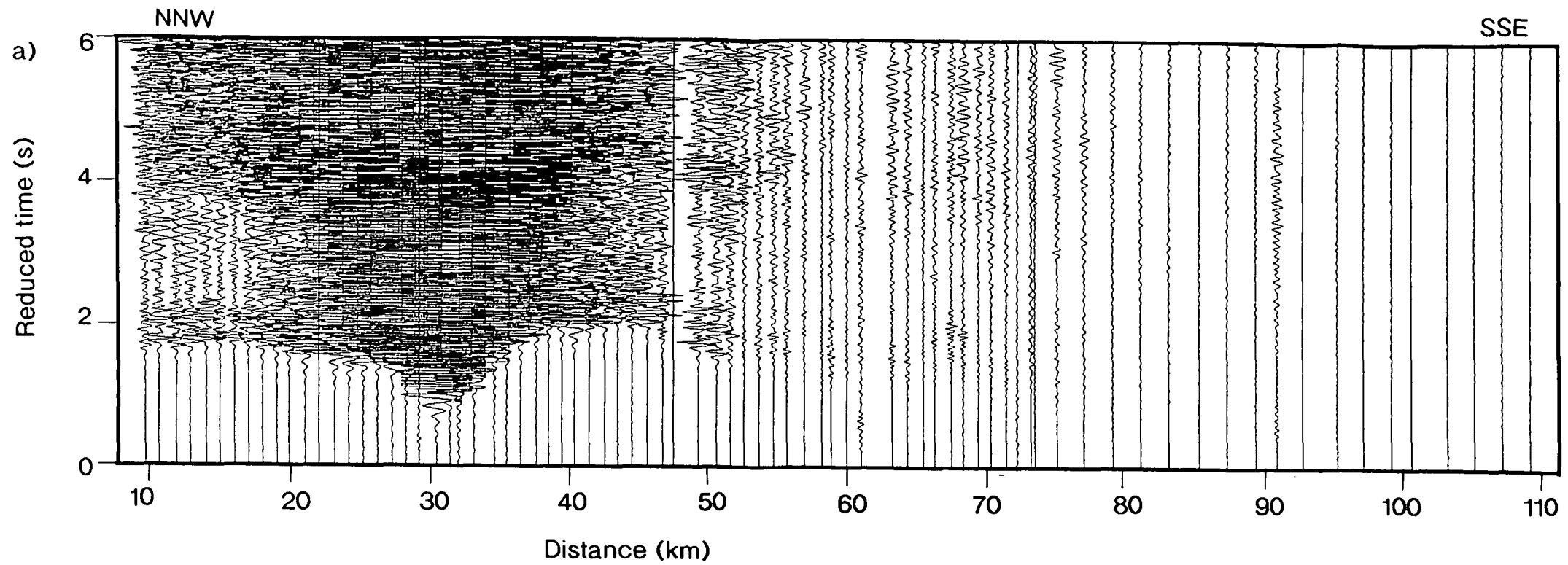


Figure E4: Explosive data recorded by DDOBS 2 along the across-axis line. Sections are plotted at true amplitude and reduced at 6 km s^{-1} . Note the shadow zone at $\sim 47 \text{ km}$ offset.

a) Vertical geophone component.

b) hydrophone component. Prominent noise bursts on this section are caused by disk spin (see section 3.3).

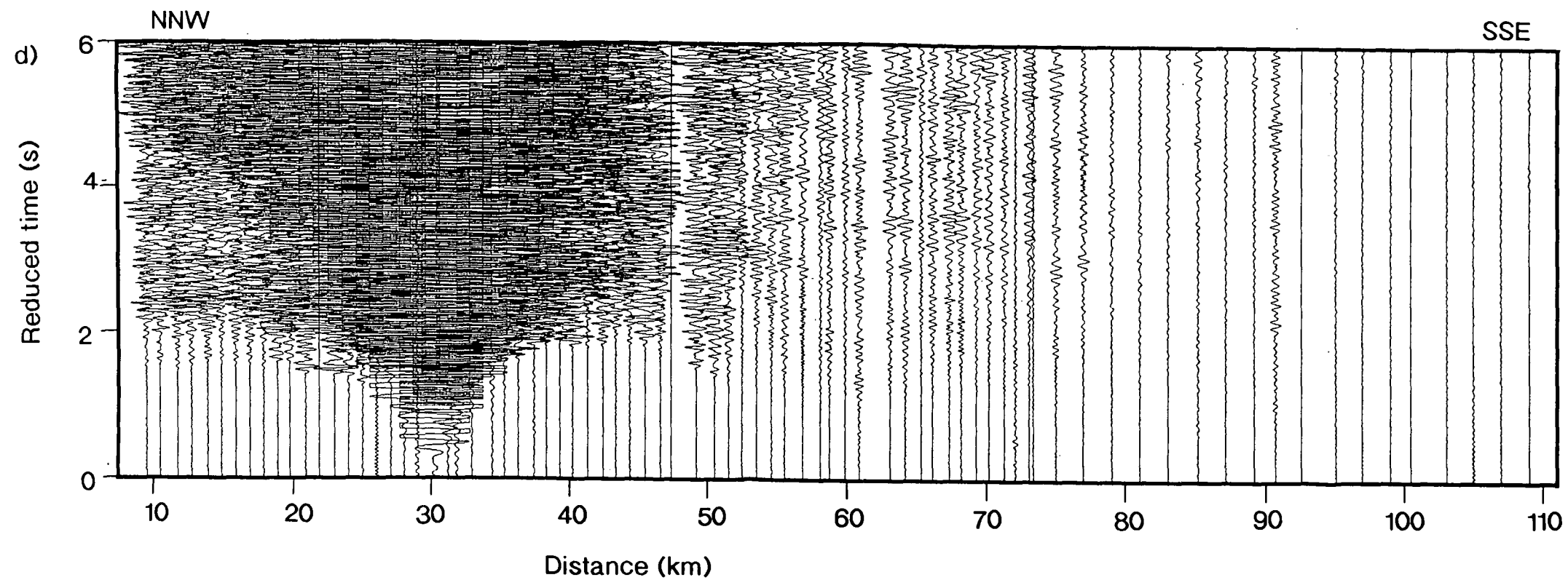
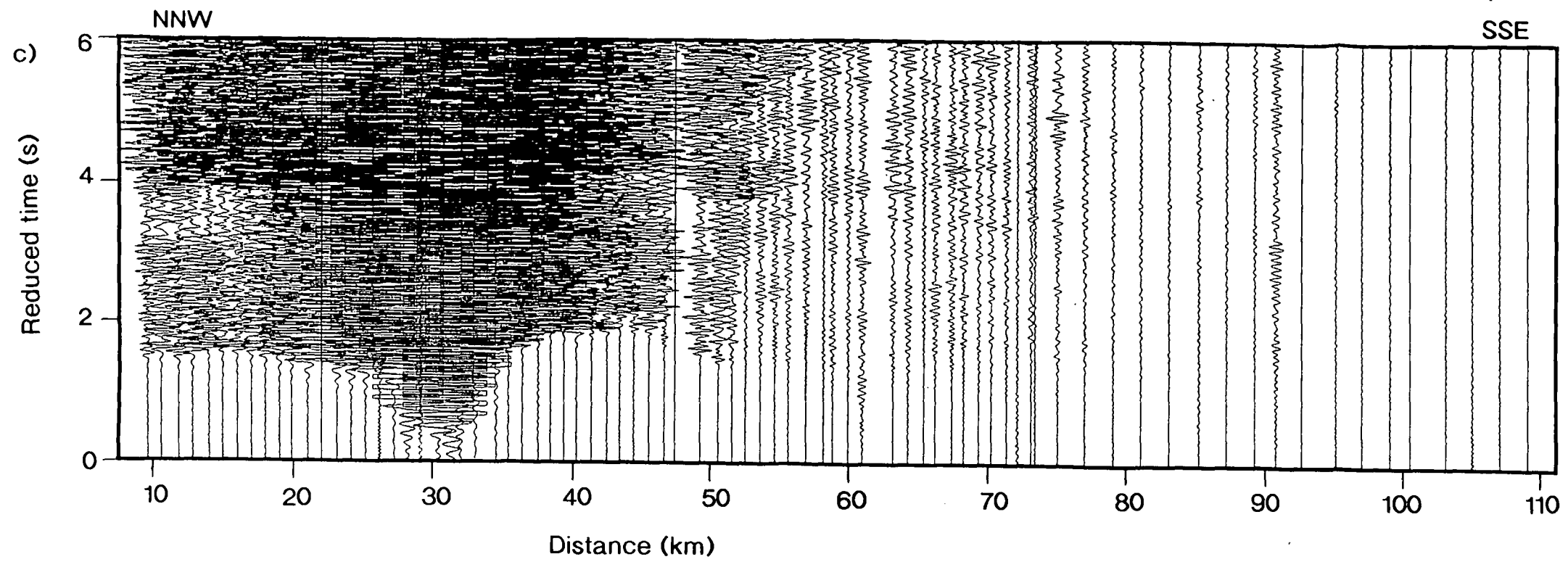


Figure E4: cont.. Explosive data recorded by DDOBS 2 along the across-axis line. Sections are plotted at true amplitude and reduced at 6 km s^{-1} . Note the shadow zone at $\sim 47 \text{ km}$ offset.
 c) Horizontal X-component.
 d) Horizontal Y-component.

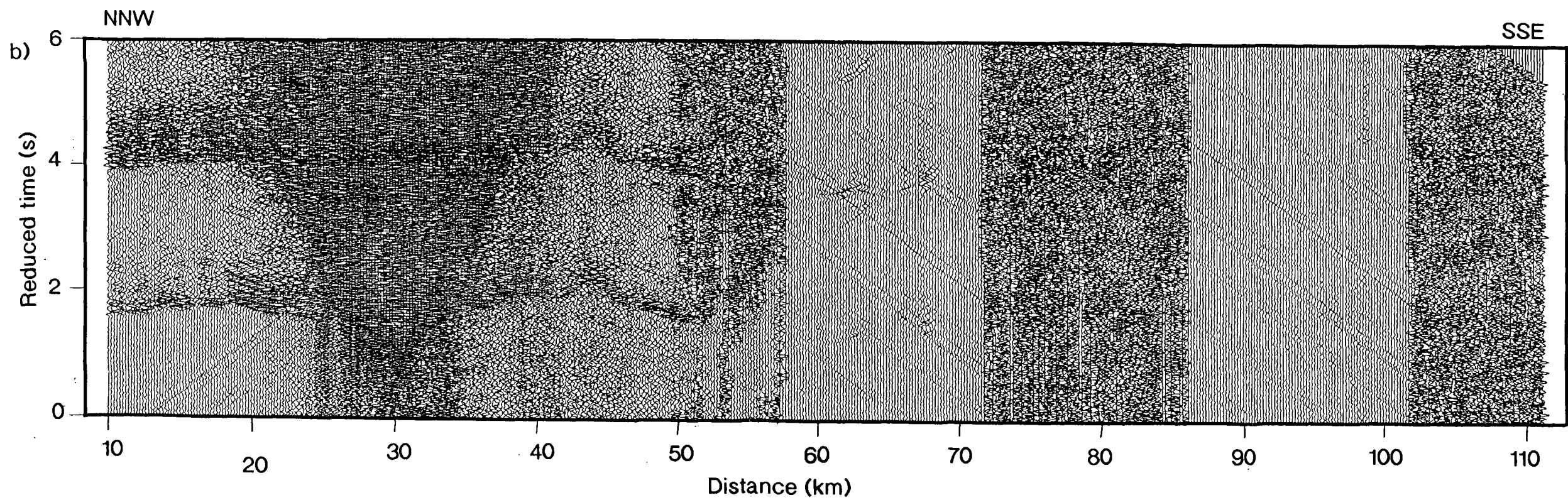
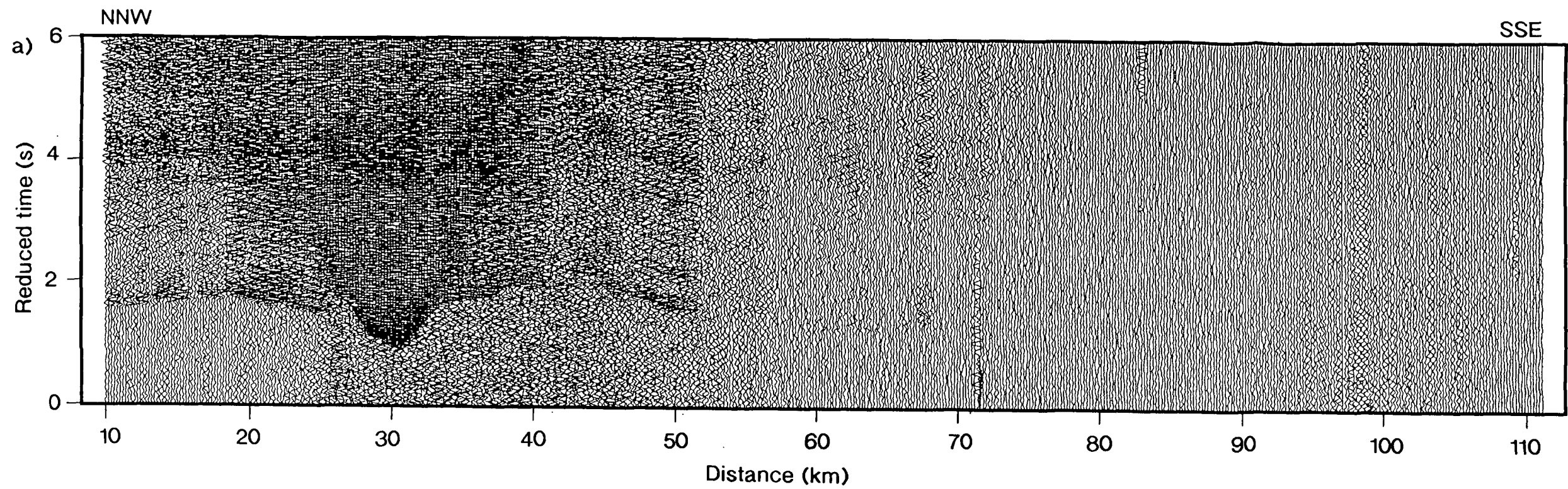


Figure E5: Airgun data recorded by DDOBS 2 along the across-axis line. Sections are plotted at true amplitude and reduced at 6 km s^{-1} . Note the shadow zone between 41 and 47 km offset and the low amplitude of arrivals with offsets of greater than 51 km.

a) Vertical geophone component.

b) hydrophone component. Prominent noise bursts on this section are caused by disk spin (see section 3.3).

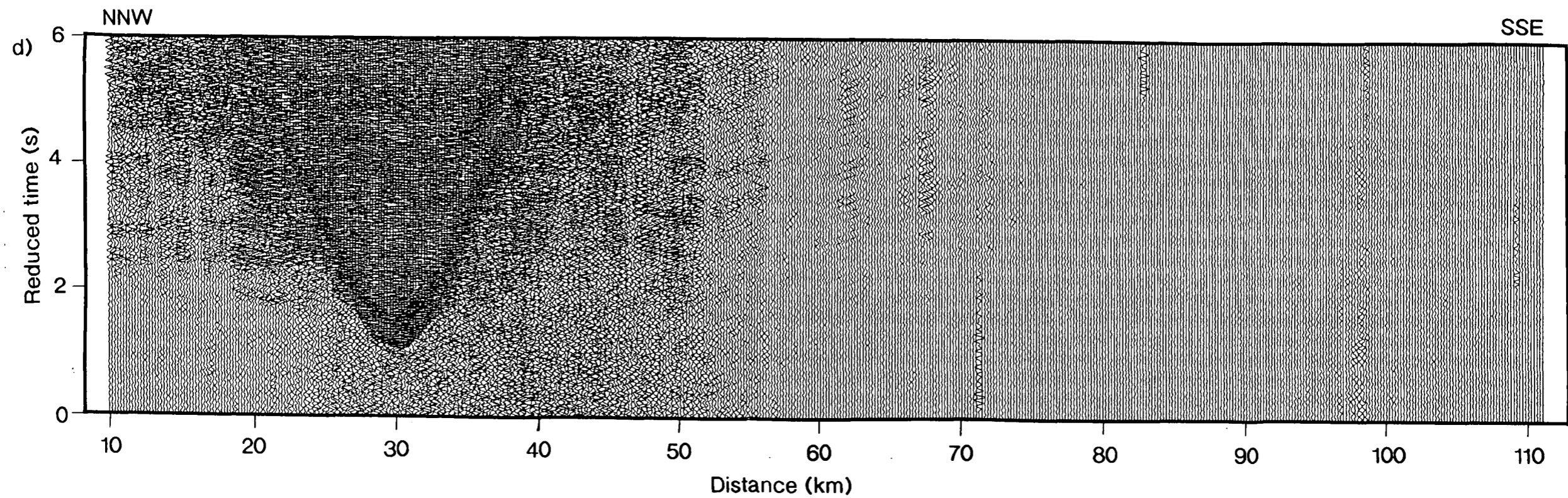
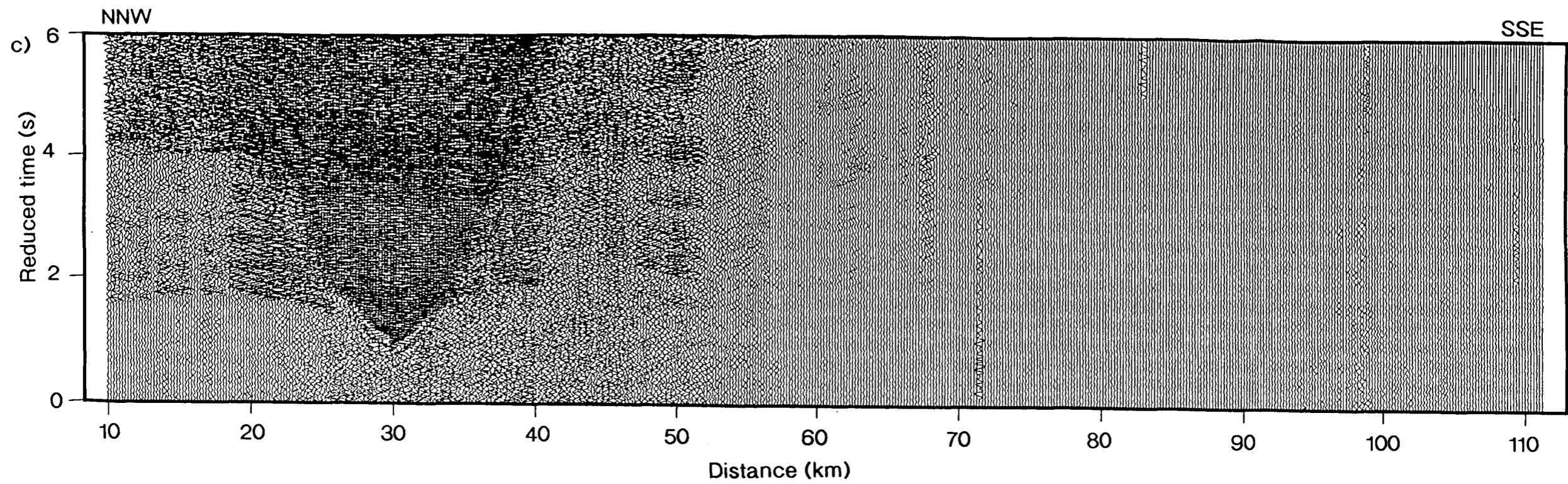


Figure E5: cont.. Airgun data recorded by DDOBS 2 along the across-axis line. Sections are plotted at true amplitude and reduced at 6 km s^{-1} . Note the shadow zone between 41 and 47 km offset and the low amplitude of arrivals with offsets of greater than 51 km.
 c) Horizontal X-component.
 d) Horizontal Y-component.

Figure E5 cont.

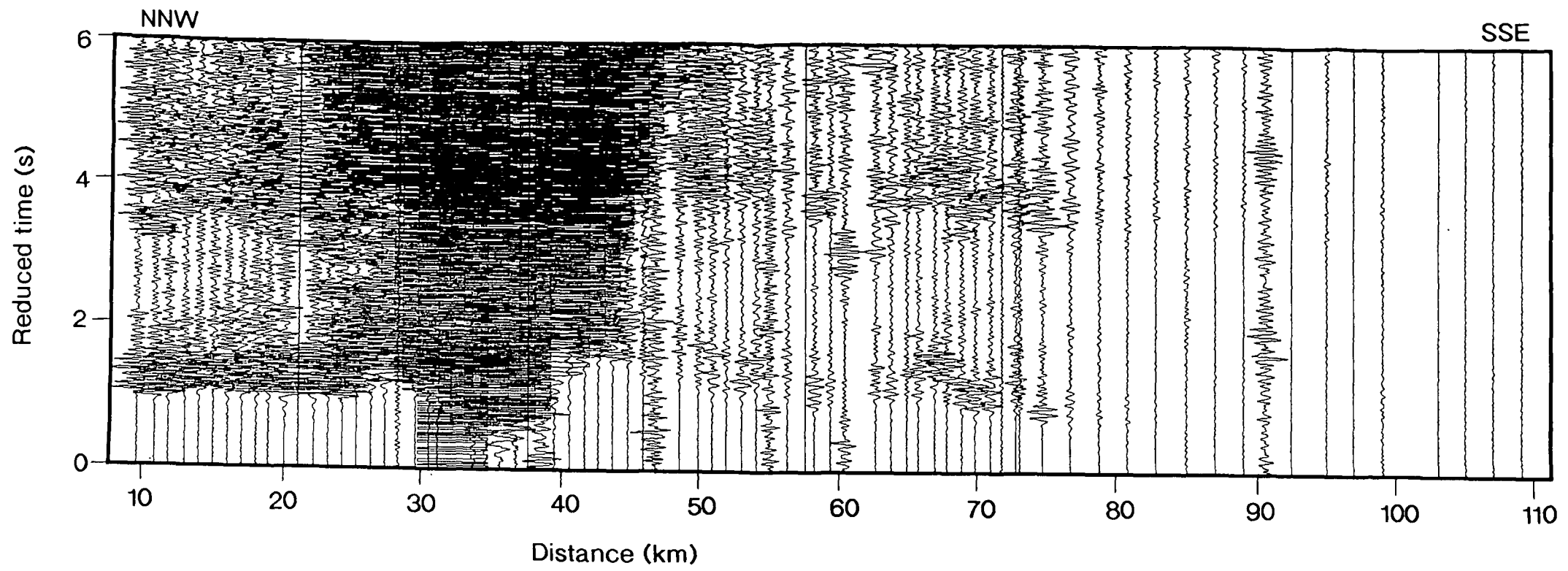


Figure E6: Explosive data recorded by CDOBS 12 along the across-axis line. The section is plotted at true amplitude and reduced at 6 km s⁻¹. Note the shadow zone between 45 and 49 km offset and the noisy traces at ~29, 33, 39, 47, 55, 60 and 90 km offset.

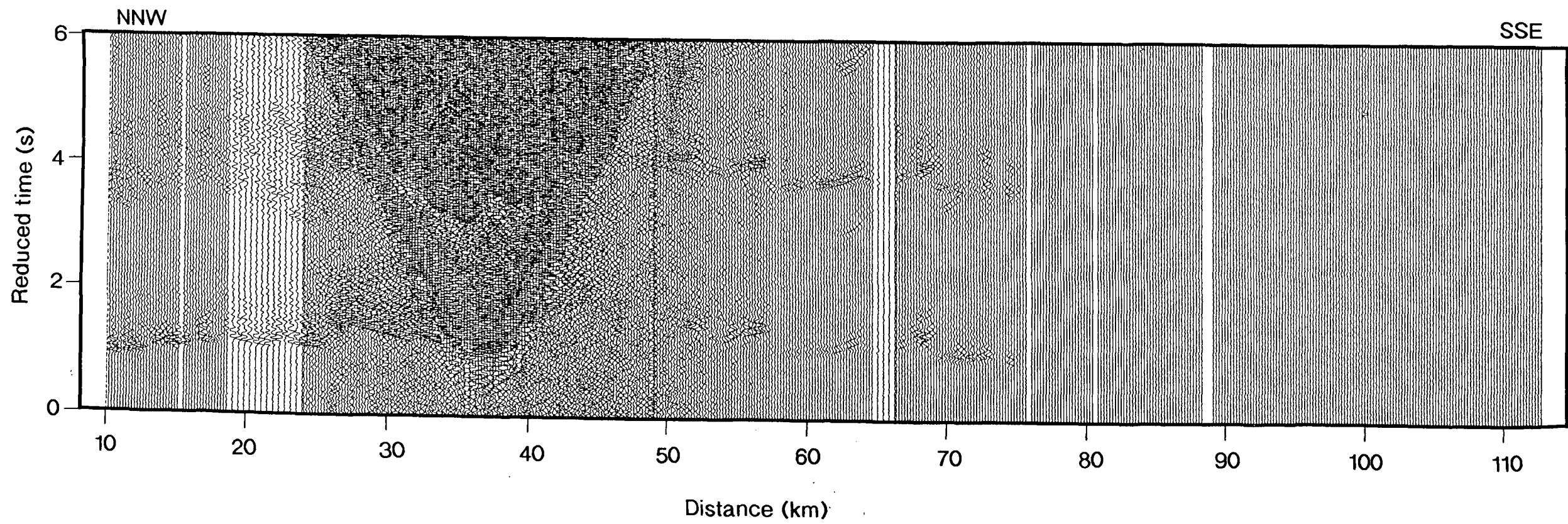


Figure E7: Airgun data recorded by CDOBS 12 along the across-axis line, only alternate shots are plotted for clarity. Section is plotted at true amplitude and reduced at 6 km s⁻¹. Note the shadow zone between ~41 and 50 km offset. Blank traces occur when a trace was corrupted when recorded and therefore not recovered in the replay process.

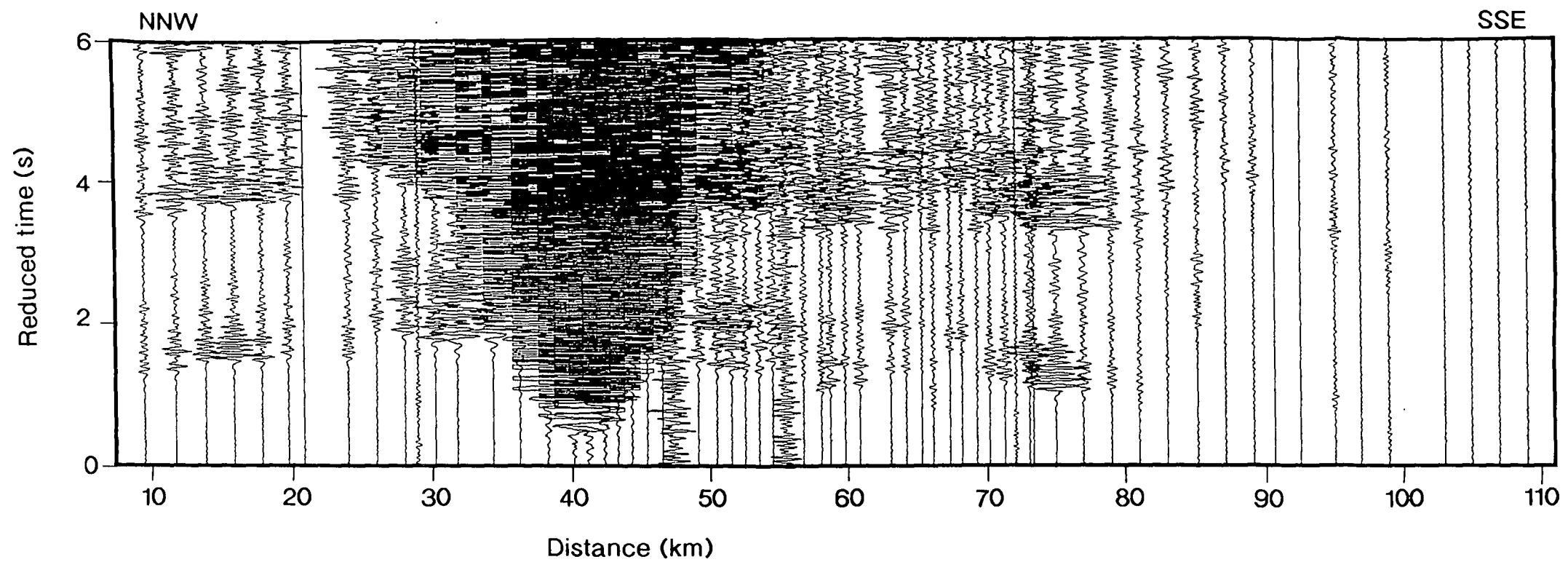


Figure E8: Explosive data recorded by CDOBS 13 along the across-axis line. The section is plotted at true amplitude and reduced at 6 km s^{-1} . Note the noisy traces at 29, 45 and 55 km offset.

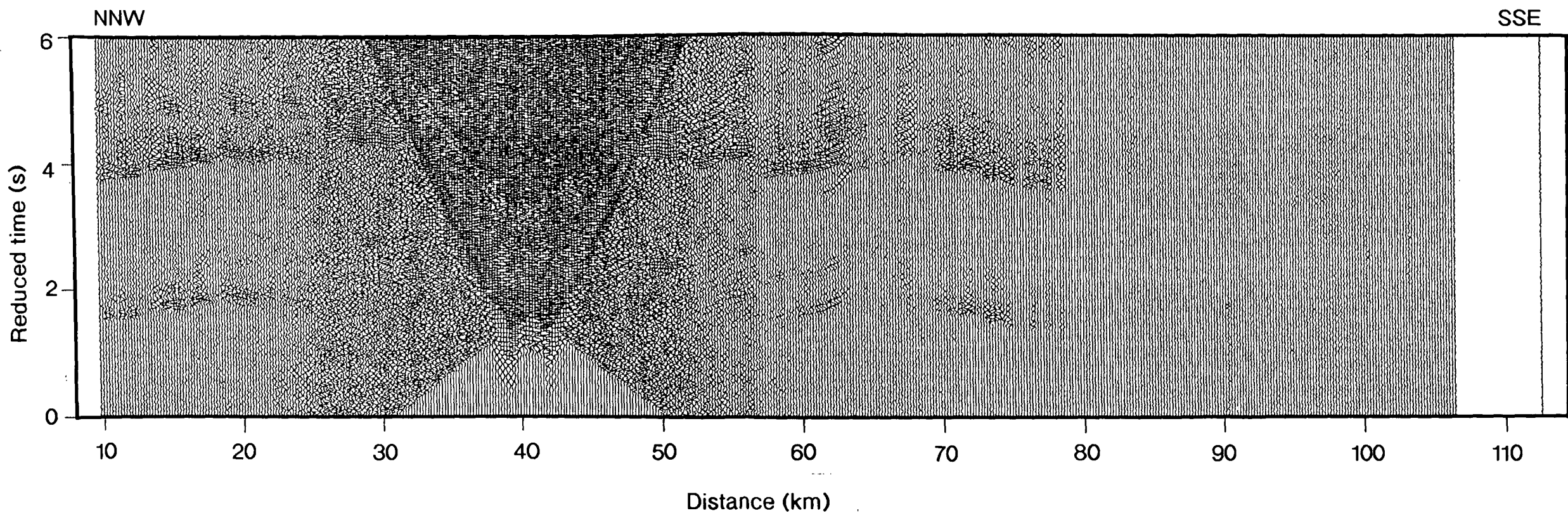


Figure E9: Airgun data recorded by CDOBS 13 along the across-axis line, only alternate shots are plotted for clarity. The section is plotted at true amplitude and reduced at 6 km s^{-1} . The gap in traces between 107 and 112 km offset occurs as a block of traces was corrupted when recorded and therefore were not recoverable in the replay process. Note the blank section of traces near the instrument, this occurs as approximately the first second of data was not recorded by this instrument.

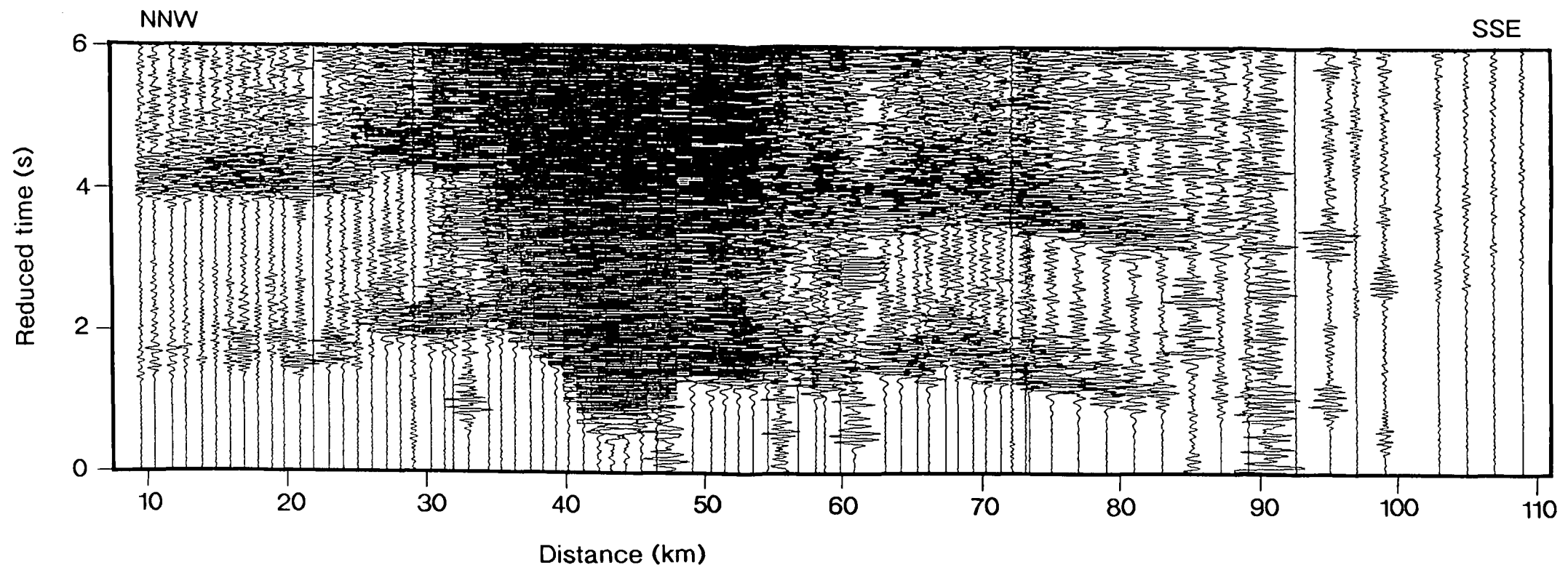


Figure E10: Explosive data recorded by CDOBS 14 along the across-axis line. The section is plotted at true amplitude and reduced at 6 km s^{-1} . Note the noisy traces at 29, 32, 47, 55, 61, 86 and 90 km offset.

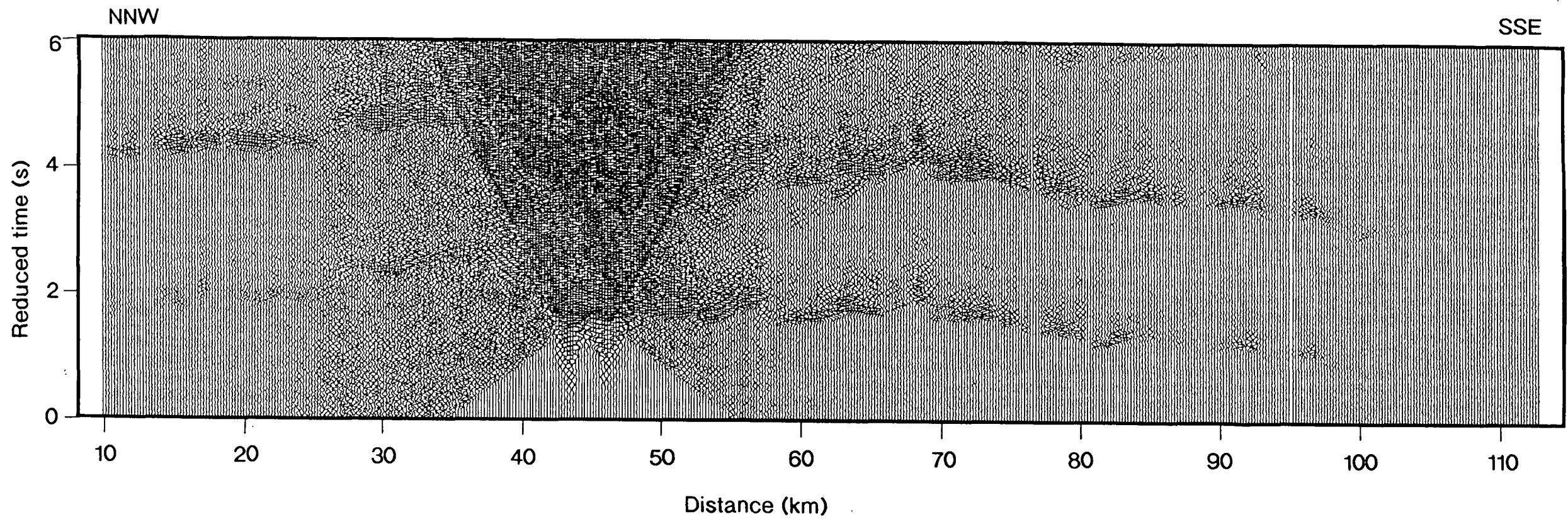


Figure E11: Airgun data recorded by CDOBS 14 along the across-axis line, only alternate shots are plotted for clarity. The section is plotted at true amplitude and reduced at 6 km s^{-1} . Note the blank section of traces near the instrument, this occurs as approximately the first second of data was not recorded by this instrument.

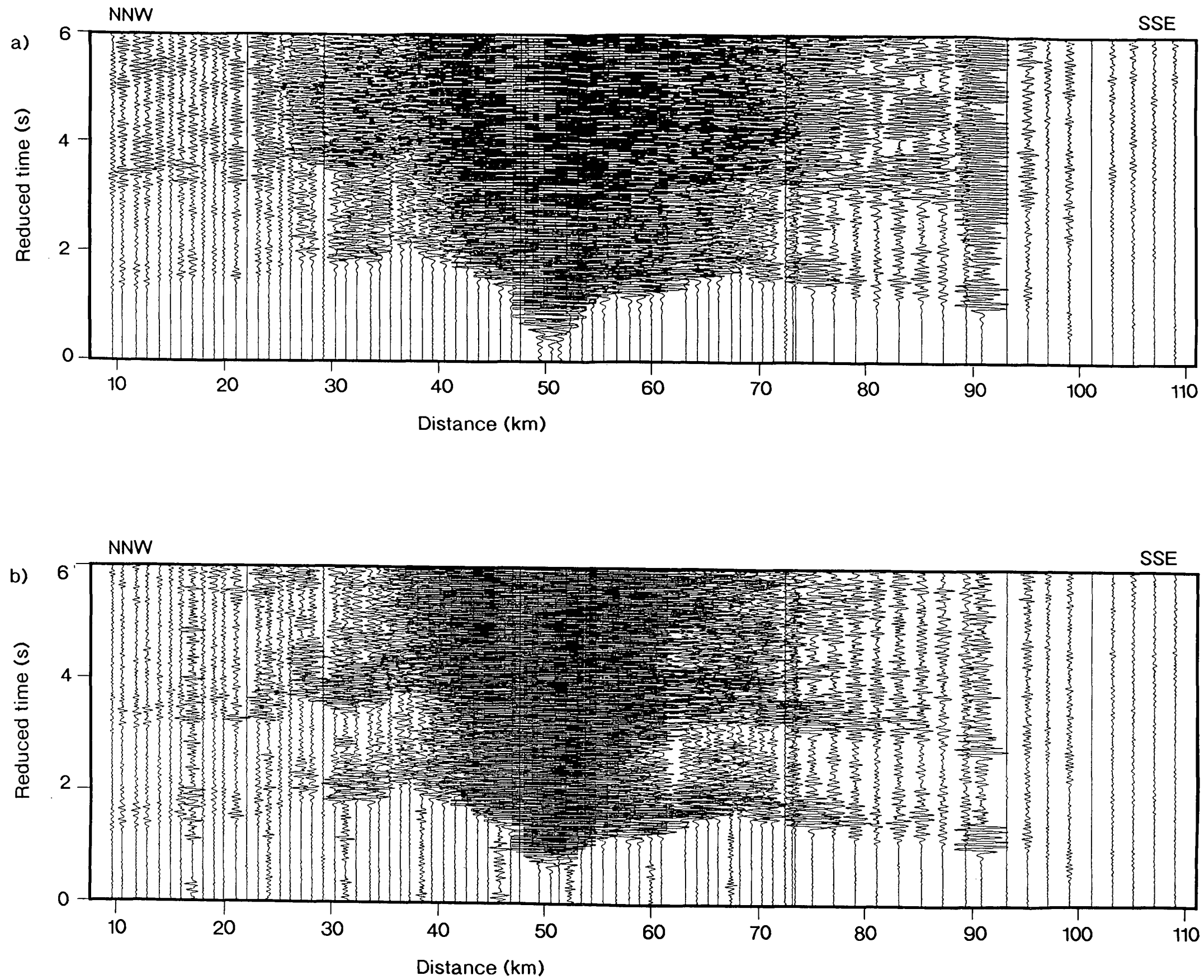


Figure E12: Explosive data recorded by DDOBS 5 along the across-axis line. Sections are plotted at true amplitude and reduced at 6 km s^{-1} .
 a) Vertical geophone component.
 b) hydrophone component. Prominent noise bursts on this section are caused by disk spin (see section 3.3).

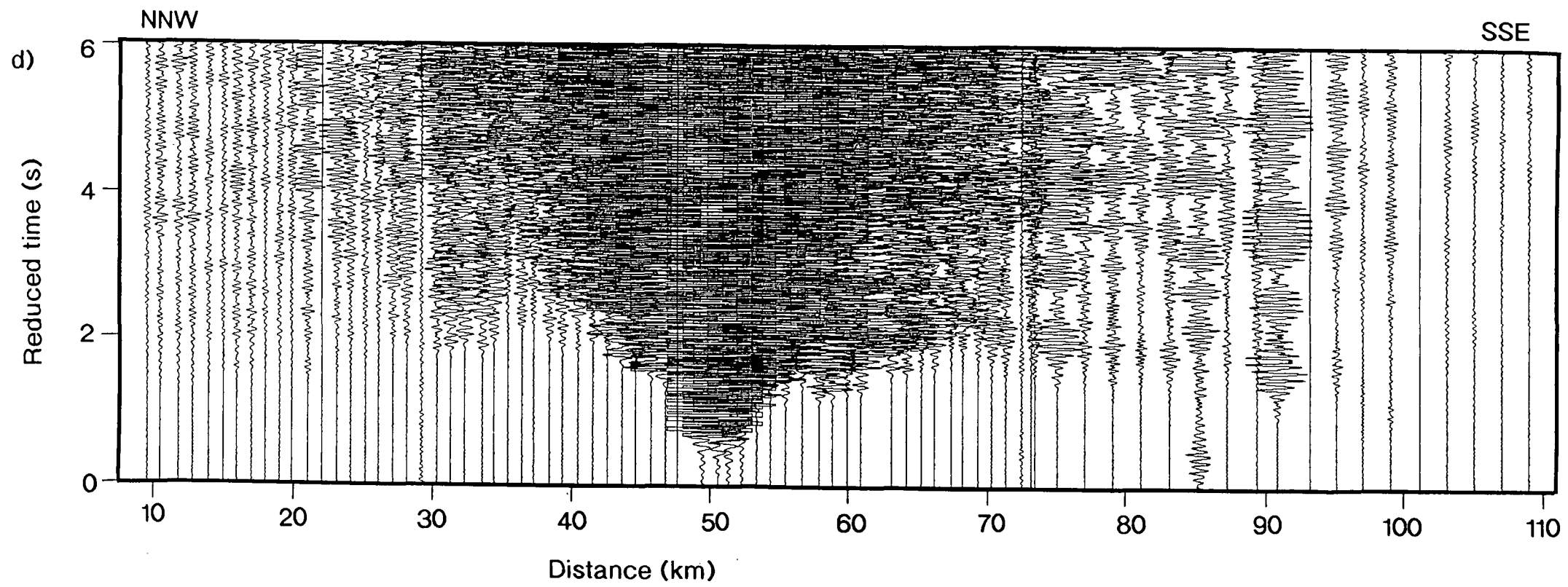
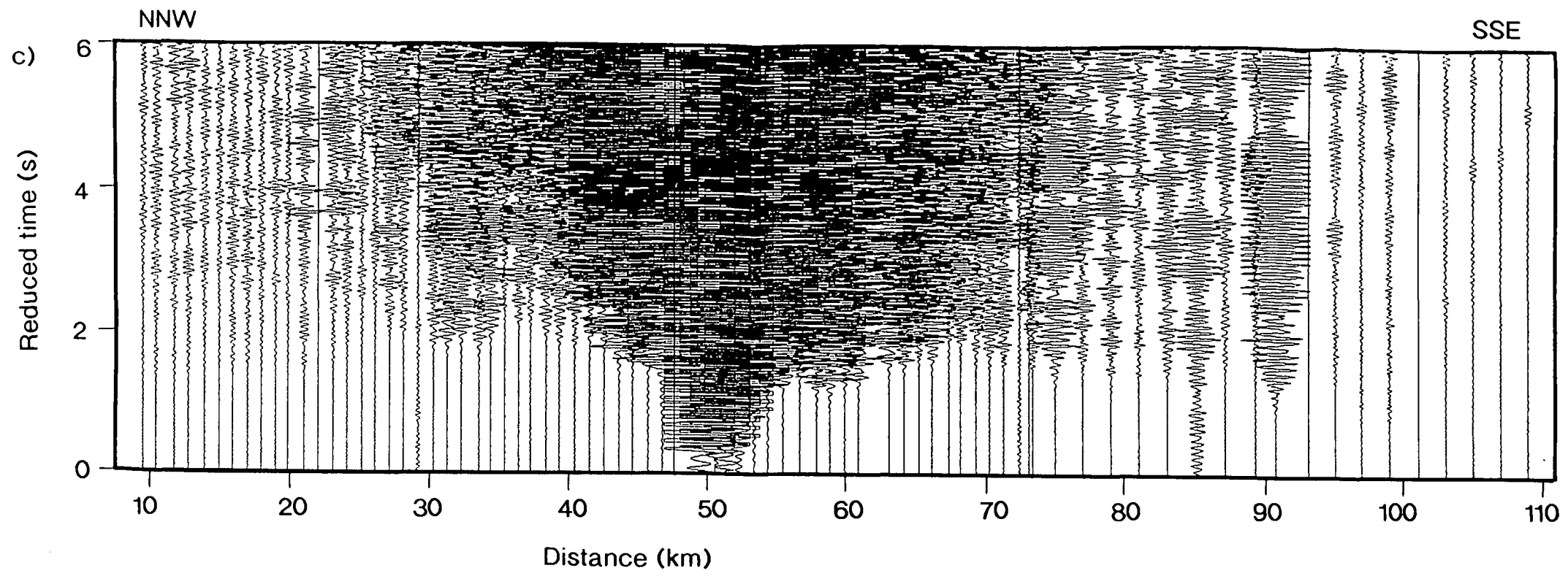


Figure E12: cont.. Explosive data recorded by DDOBS 5 along the across-axis line. Sections are plotted at true amplitude and reduced at 6 km s^{-1} .
 c) Horizontal X-component.
 d) Horizontal Y-component.

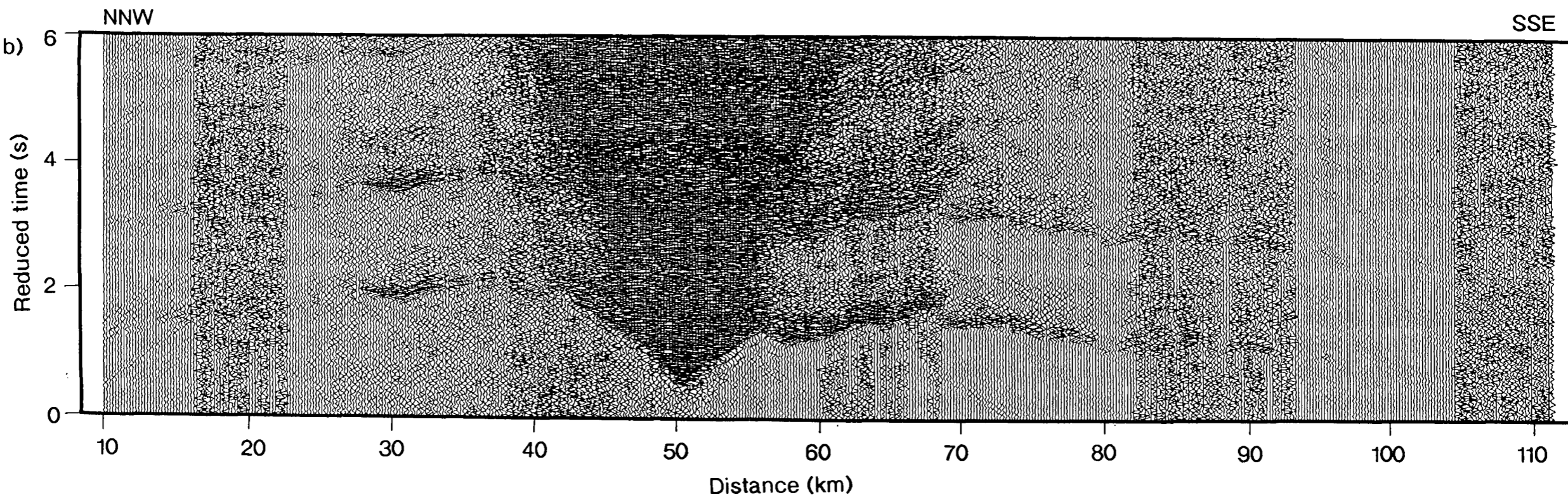
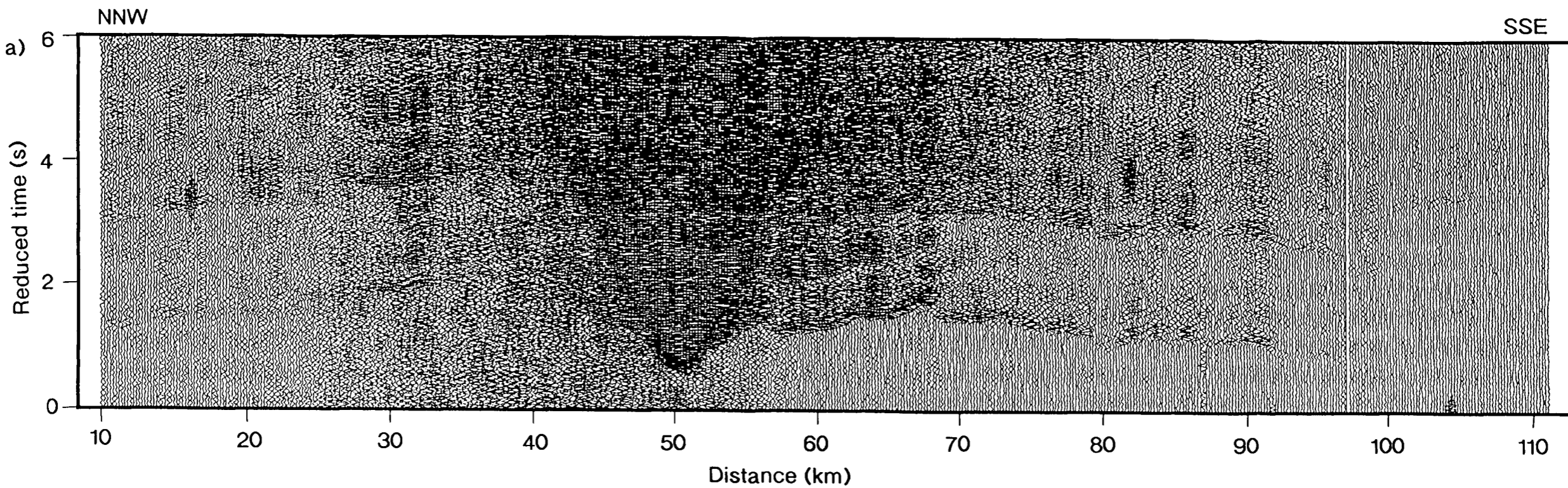


Figure E13: Airgun data recorded by DDOBS 5 along the across-axis line. Sections are plotted at true amplitude and reduced at 6 km s^{-1} . Note the shadow zone between 36 and 38 km offset.

a) Vertical geophone component.

b) hydrophone component. Prominent noise bursts on this section are caused by disk spin (see section 3.3).

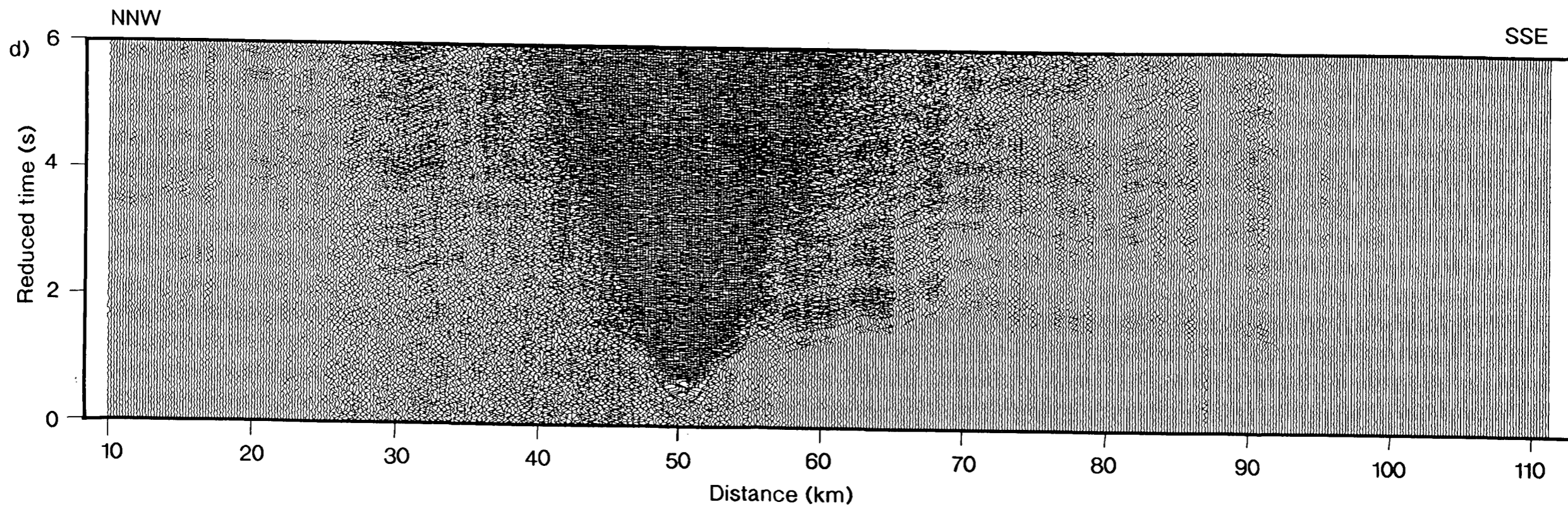
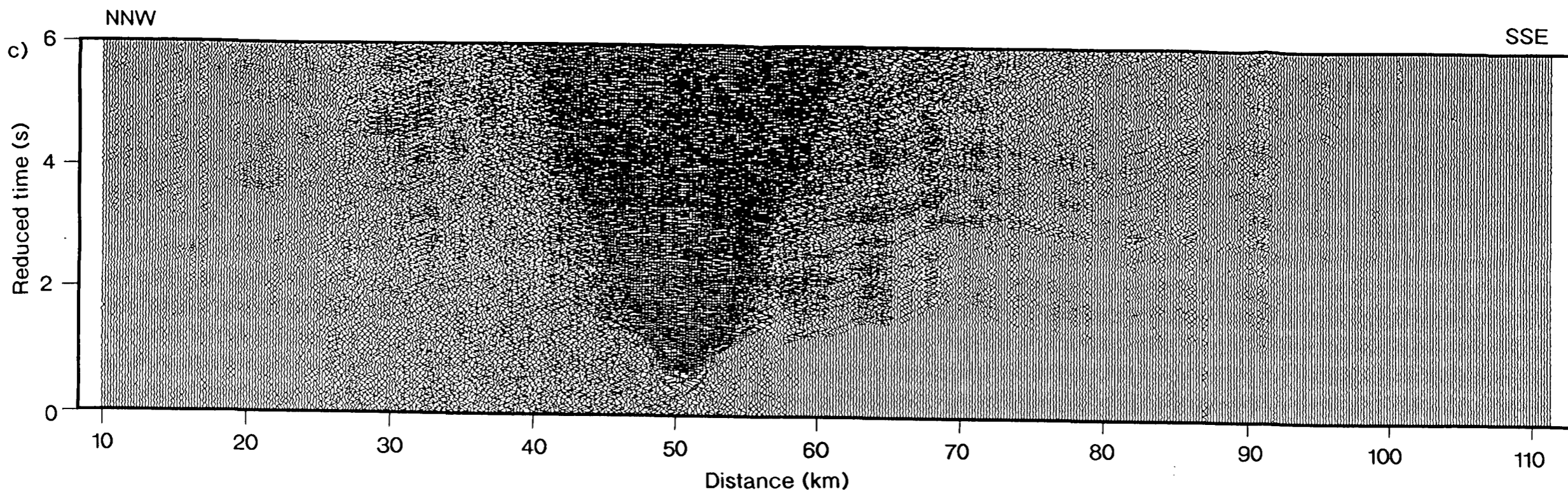


Figure E13: cont.. Airgun data recorded by DDOBS 5 along the across-axis line. Sections are plotted at true amplitude and reduced at 6 km s^{-1} .
 c) Horizontal X-component.
 d) Horizontal Y-component.

Figure E13 cont.

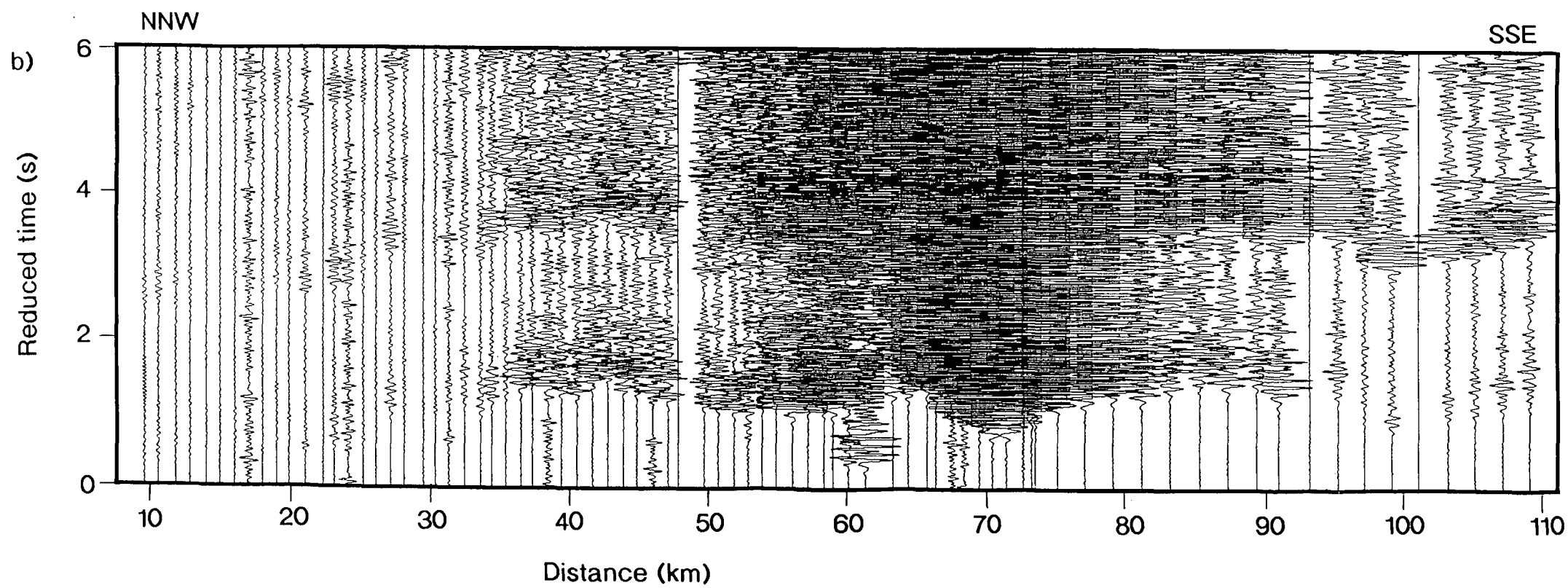
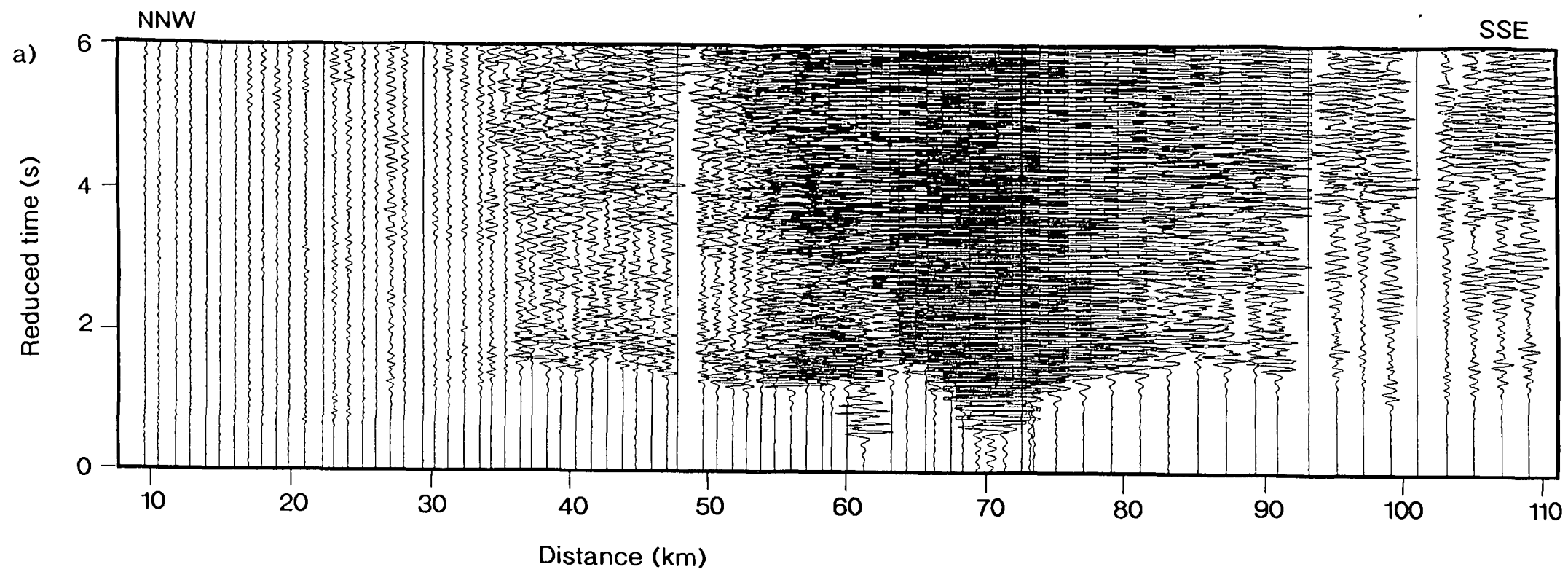


Figure E14: Explosive data recorded by DDOBS 6 at the southeasternmost end the of across-axis line. Sections are plotted at true amplitude and reduced at 6 km s^{-1} .

a) Vertical geophone component.

b) hydrophone component. Prominent noise bursts on this section are caused by disk spin (see section 3.3).

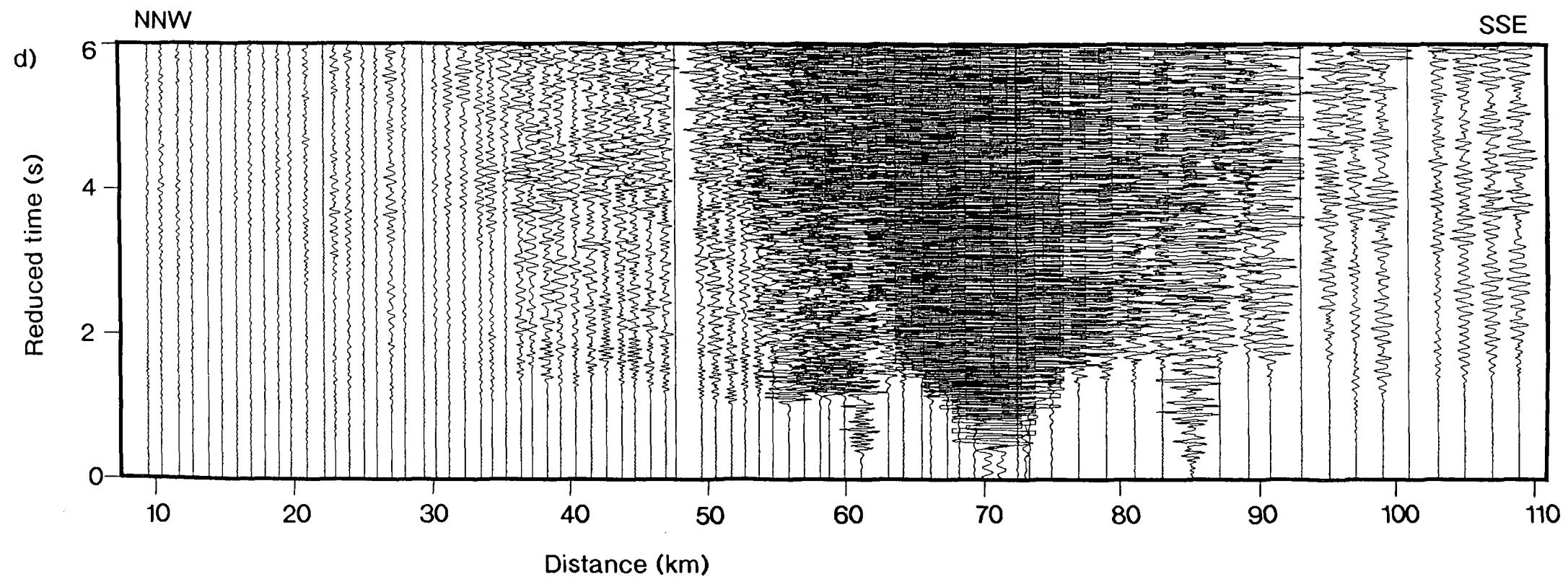
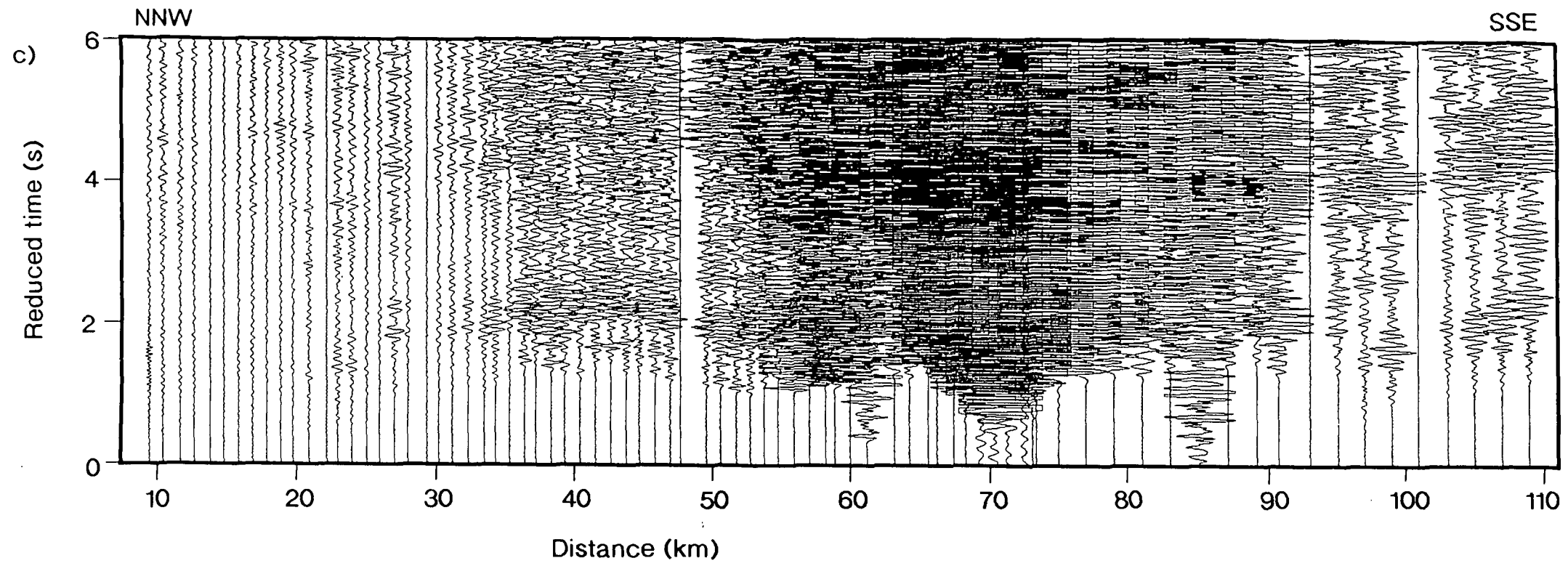


Figure E14: cont.. Explosive data recorded by DDOBS 6 at the southeasternmost end of the across-axis line. Sections are plotted at true amplitude and reduced at 6 km s^{-1} .
 c) Horizontal X-component.
 d) Horizontal Y-component.

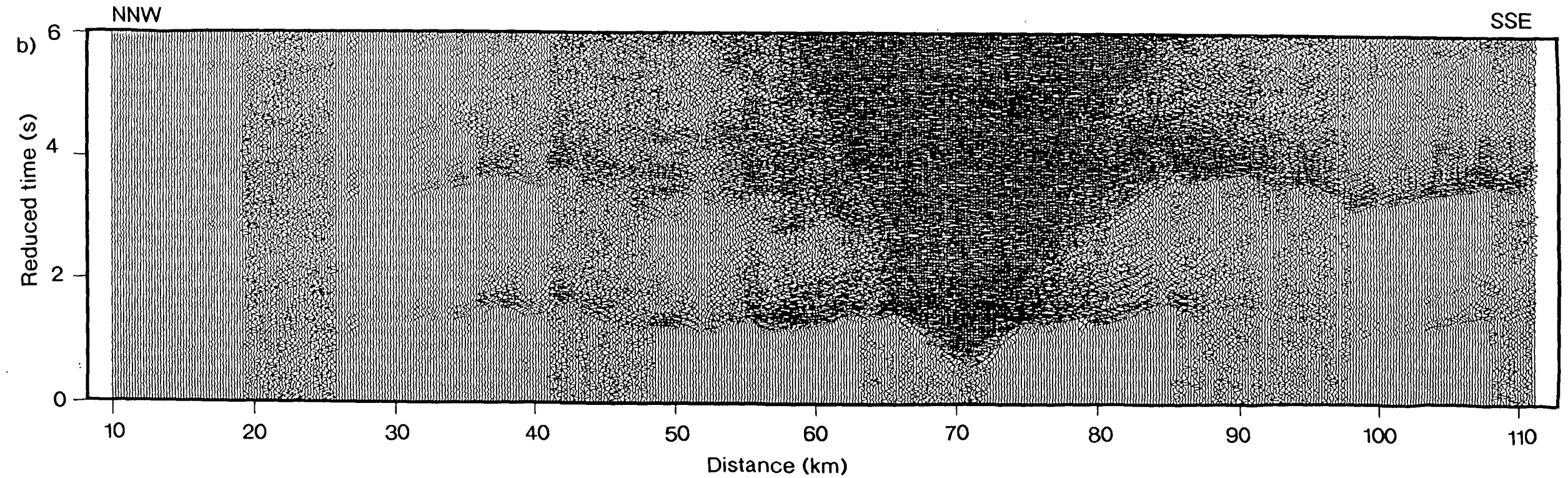
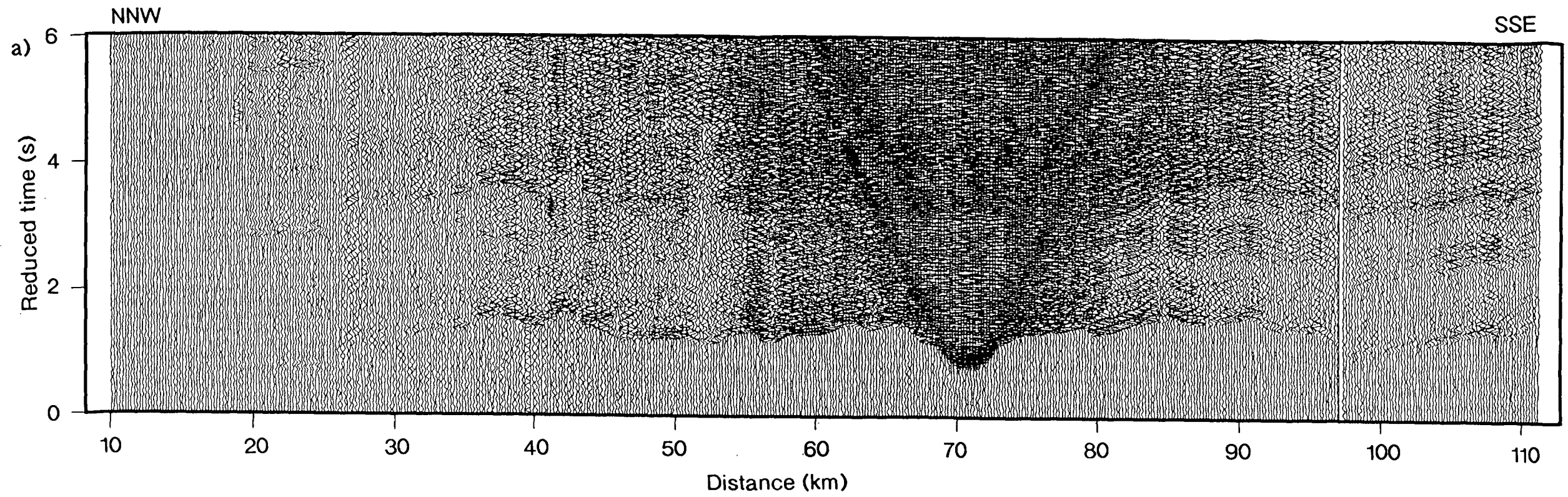


Figure E15: Airgun data recorded by DDOBS 6 at the southeasternmost end of the across-axis line. Sections are plotted at true amplitude and reduced at 6 km s^{-1} .

a) Vertical geophone component.

b) hydrophone component. Prominent noise bursts on this section are caused by disk spin (see section 3.3).

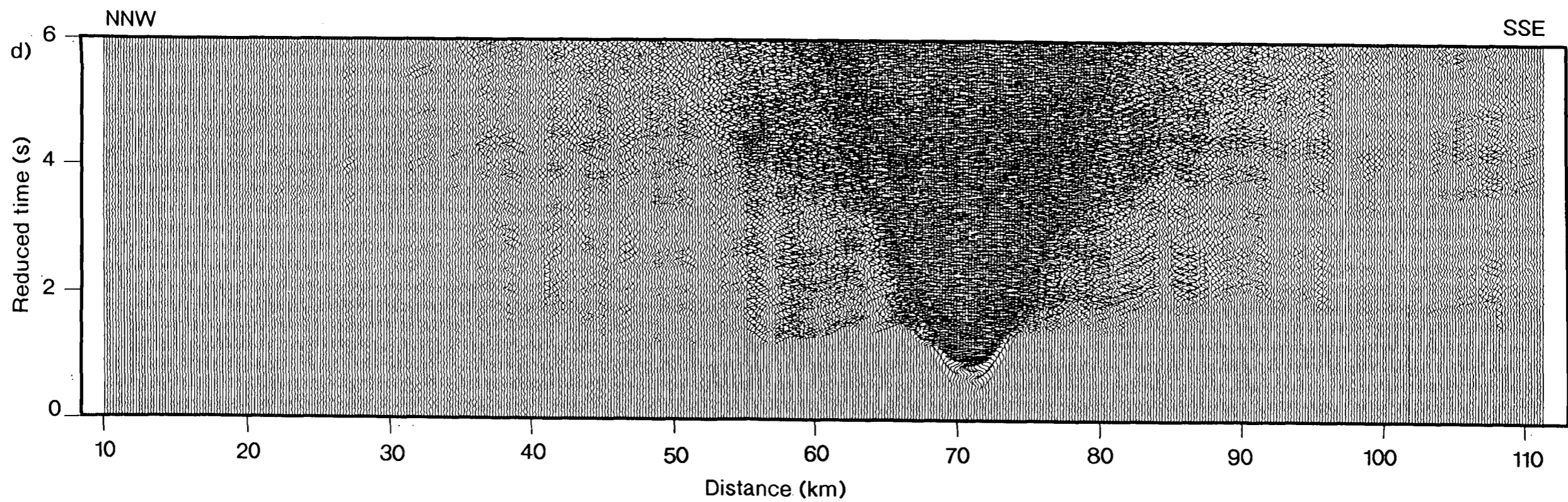
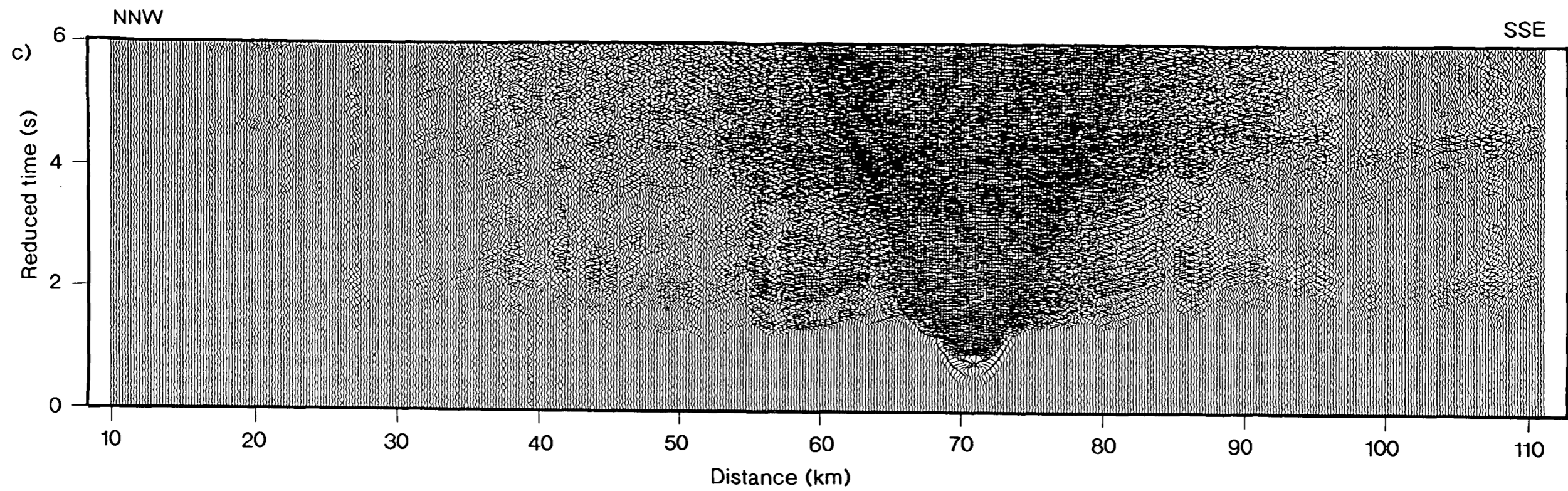


Figure E15: cont.. Airgun data recorded by DDOBS 6 at the southeasternmost end of the across-axis line. Sections are plotted at true amplitude and reduced at 6 km s⁻¹.
 c) Horizontal X-component.
 d) Horizontal Y-component.

Figure E15 cont.

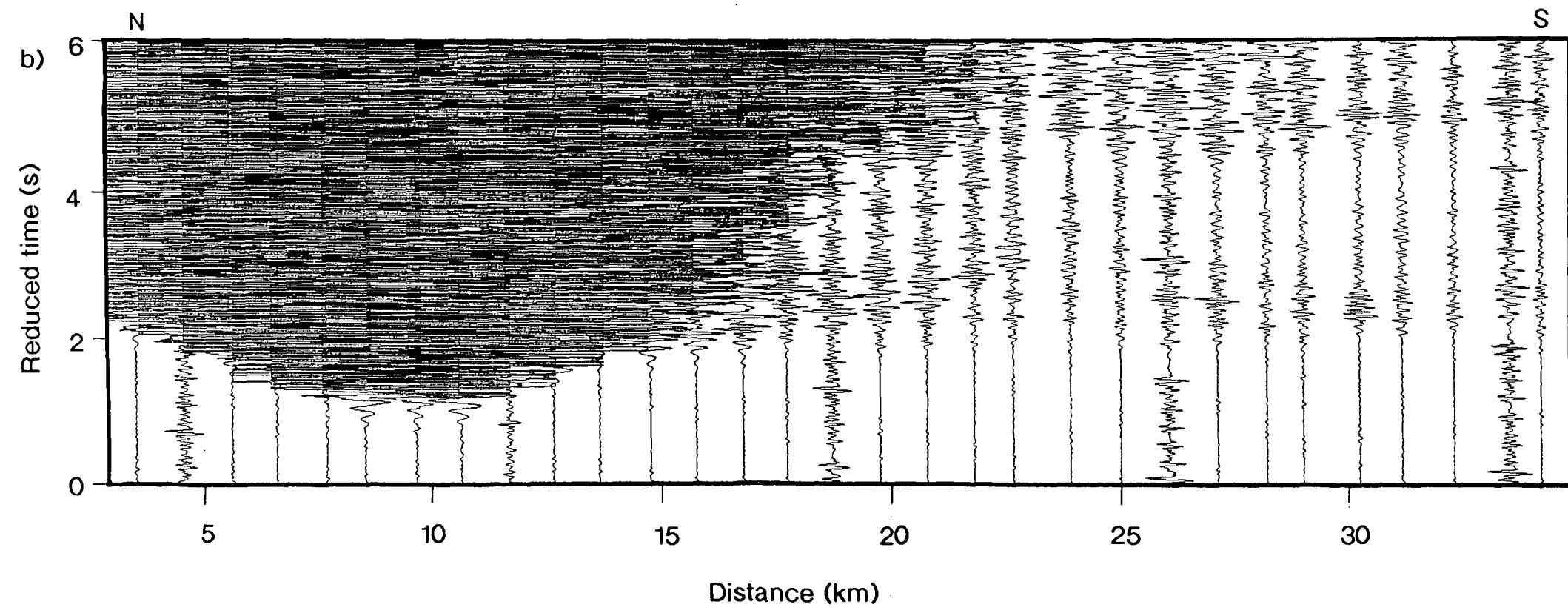
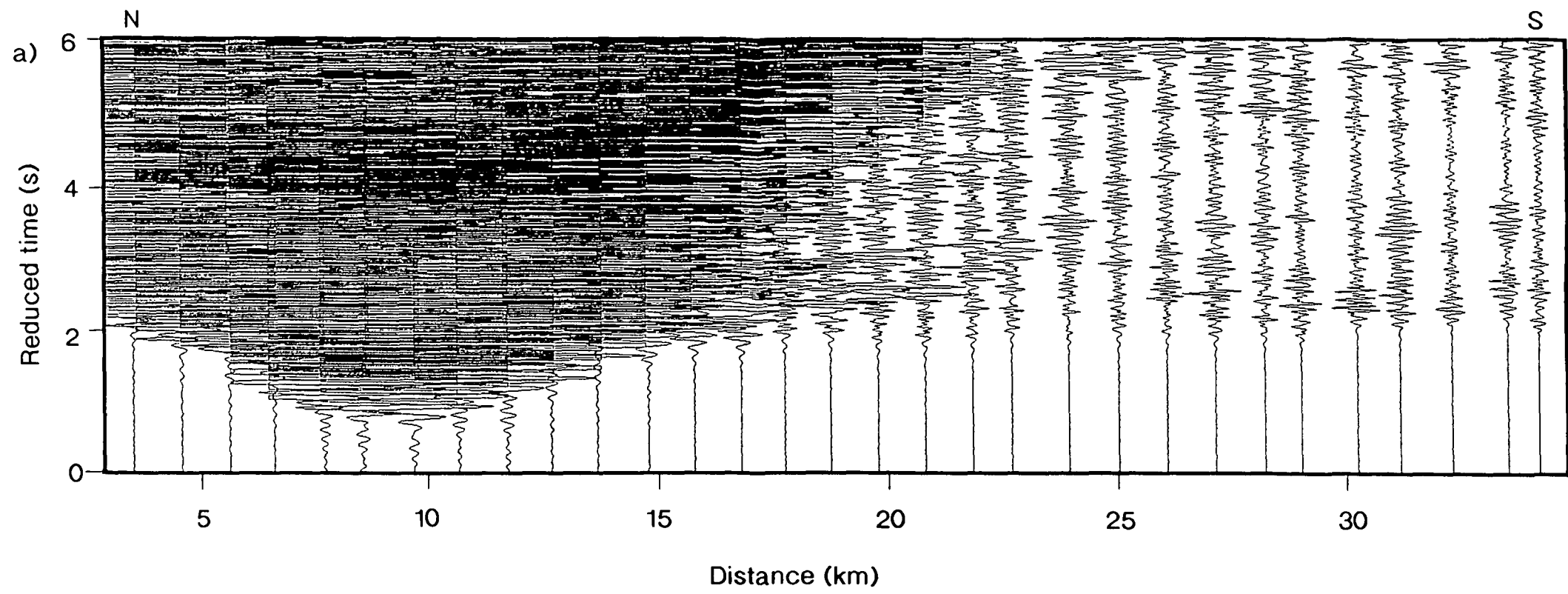


Figure E16: Explosive data recorded by DDOBS 3 at the northern end of the along-axis line. Sections are plotted at true amplitude and reduced at 6 km s^{-1} .
 a) Vertical geophone component.
 b) hydrophone component. Prominent noise bursts on this section are caused by disk spin (see section 3.3).

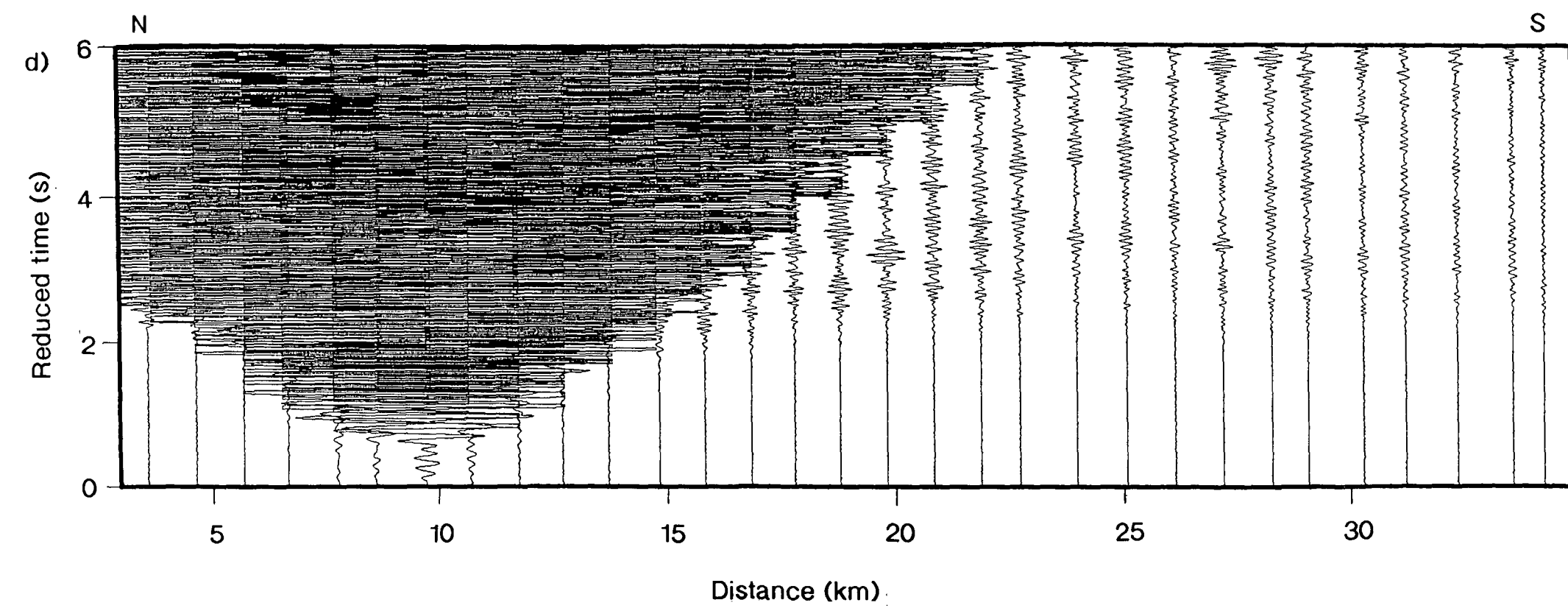
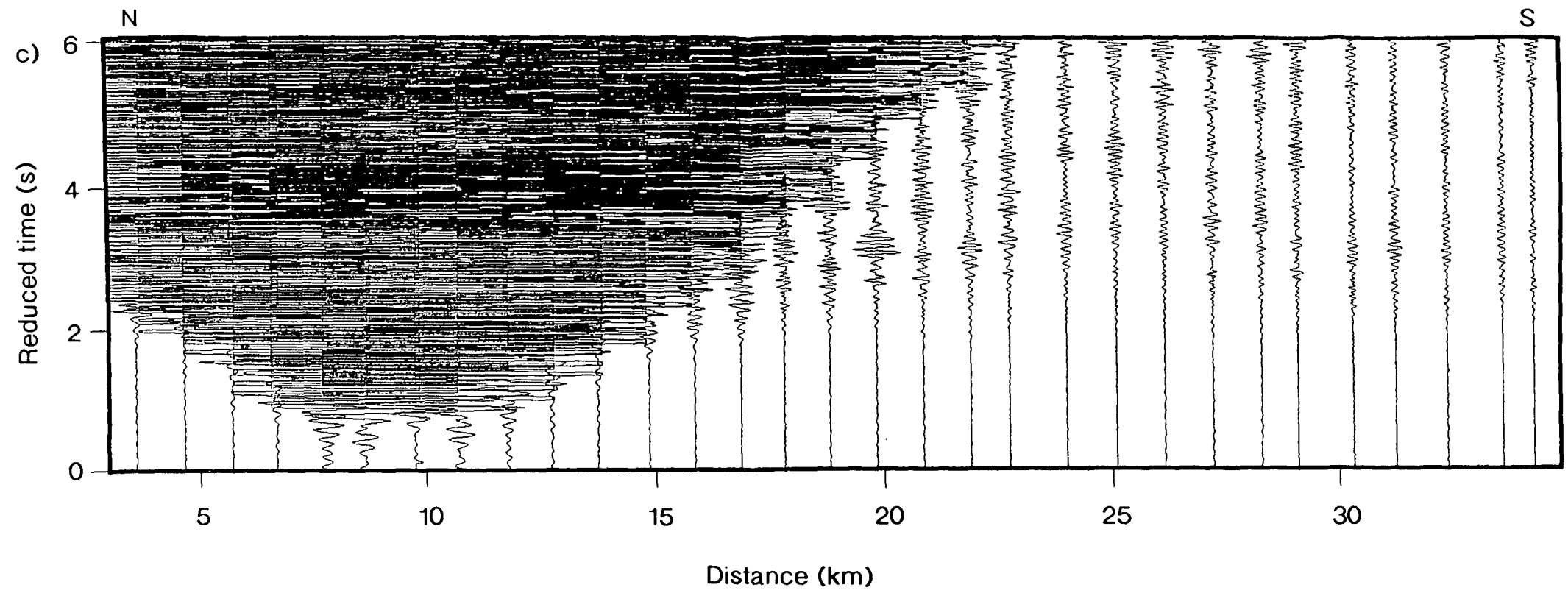


Figure E16: cont.. Explosive data recorded by DDOBS 3 at the northern end of the along-axis line. Sections are plotted at true amplitude and reduced at 6 kms^{-1} .
 c) Horizontal X-component.
 d) Horizontal Y-component.

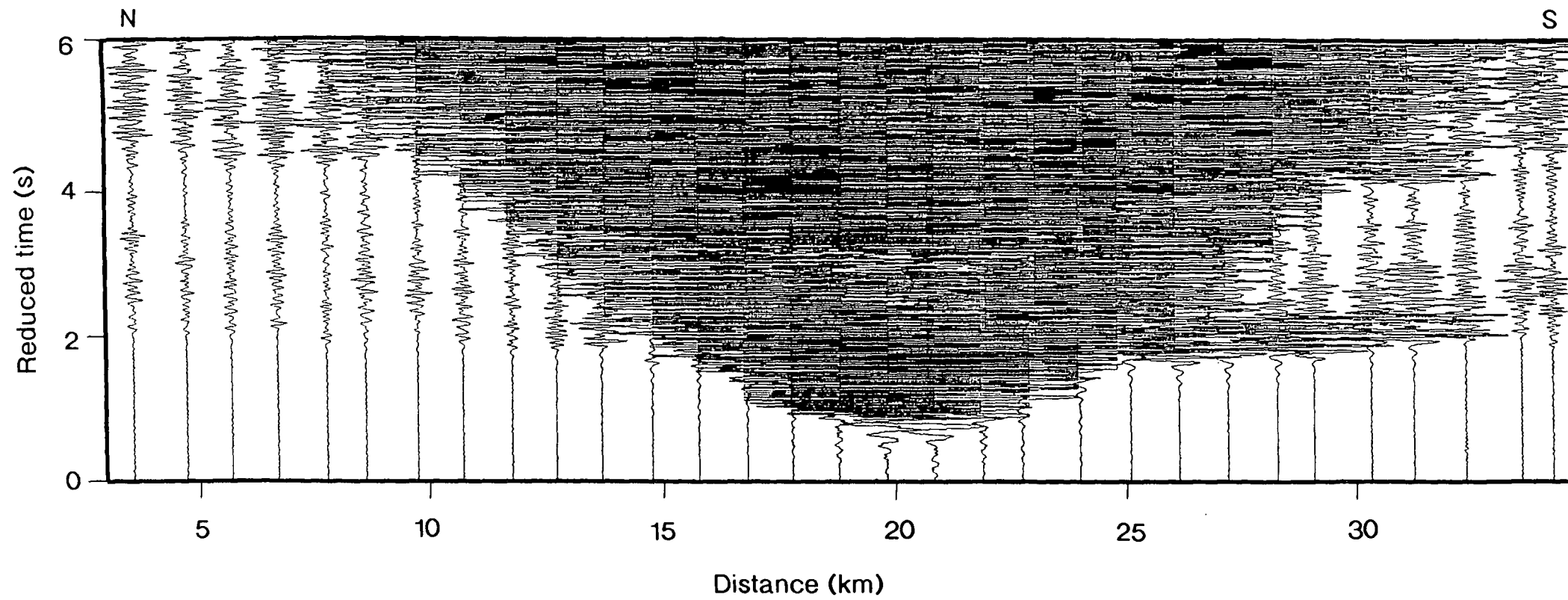


Figure E17: Explosive data recorded by CDOBS 13 at the centre of the along-axis line. The section is plotted at true amplitude and reduced at 6 km s^{-1} .

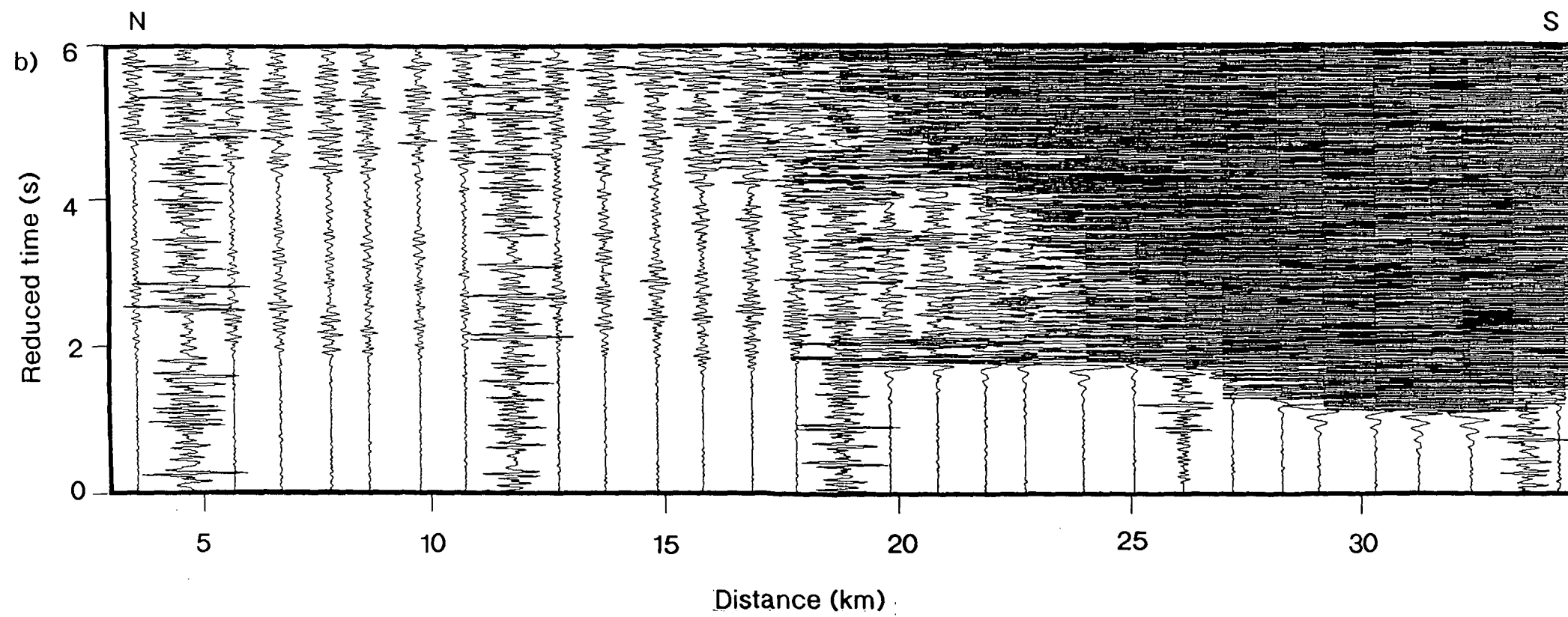
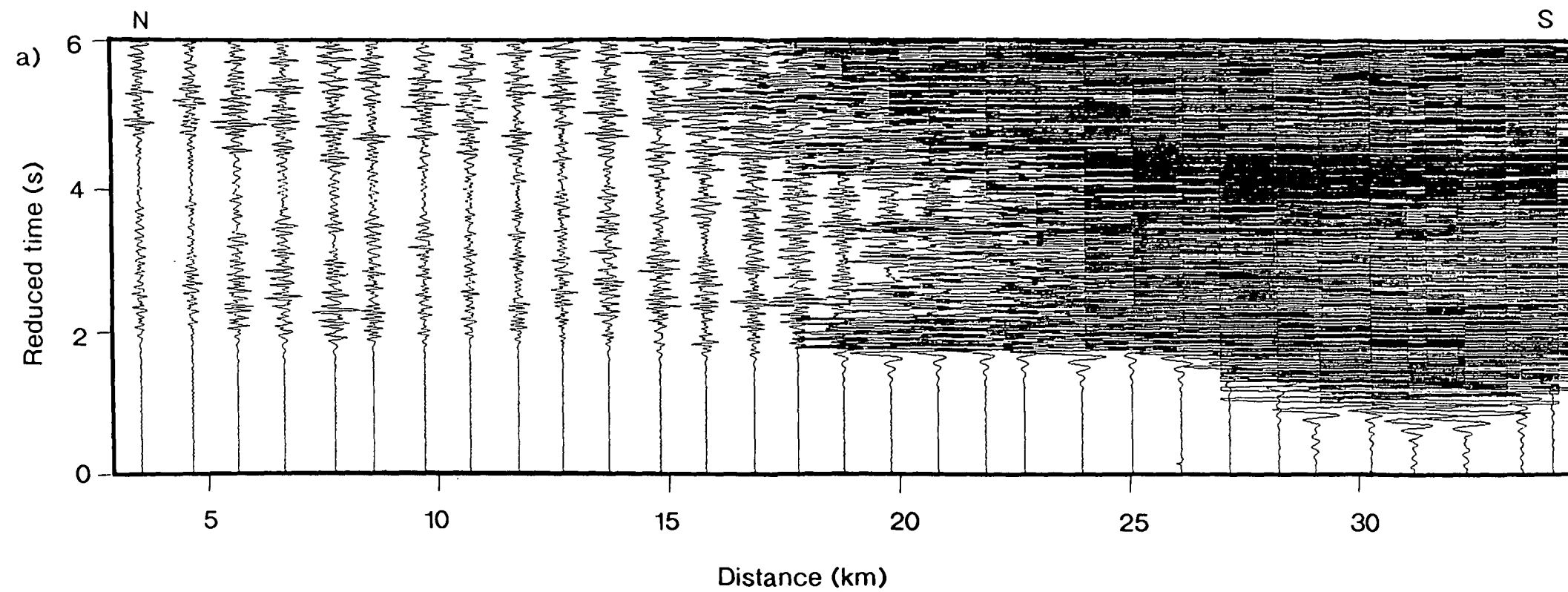


Figure E18: Explosive data recorded by DDOBS 4 at the southern end of the along-axis line. Sections are plotted at true amplitude and reduced at 6 km s^{-1} . Note the low amplitude of arrivals between 9 and 19 km offset.

a) Vertical geophone component.

b) hydrophone component. Prominent noise bursts on this section are caused by disk spin (see section 3.3).

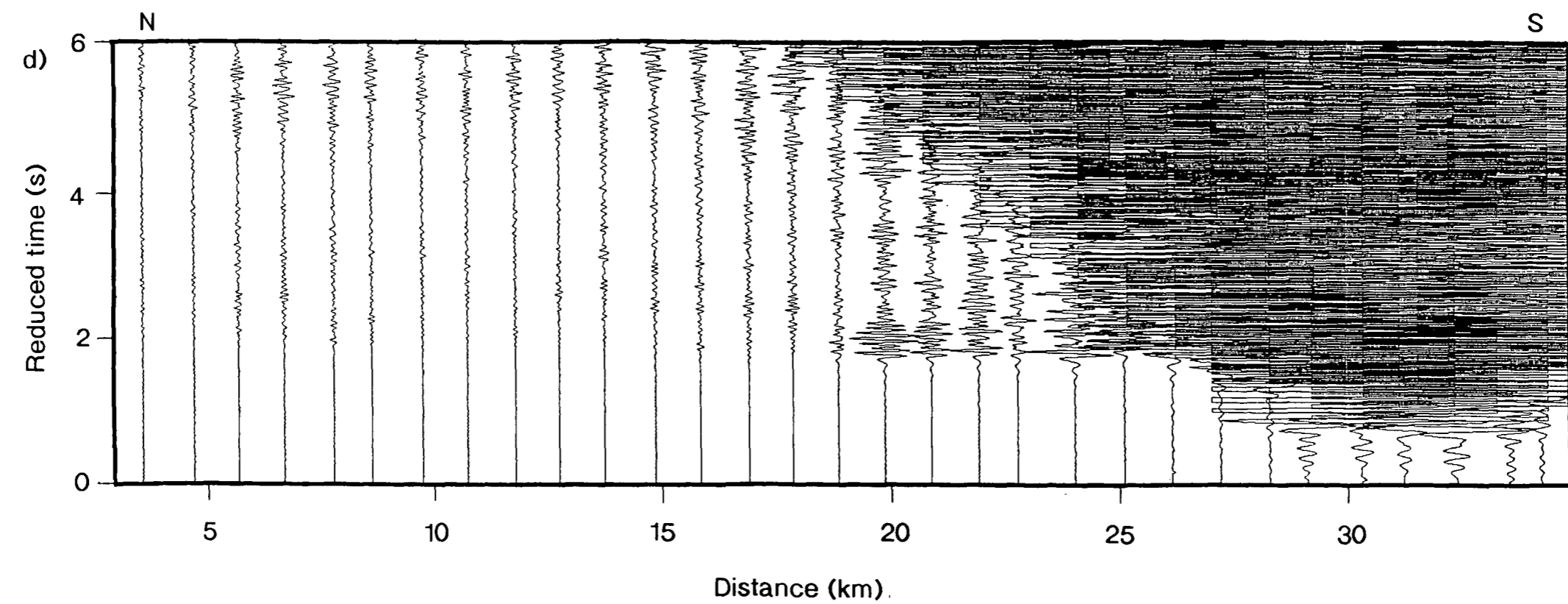
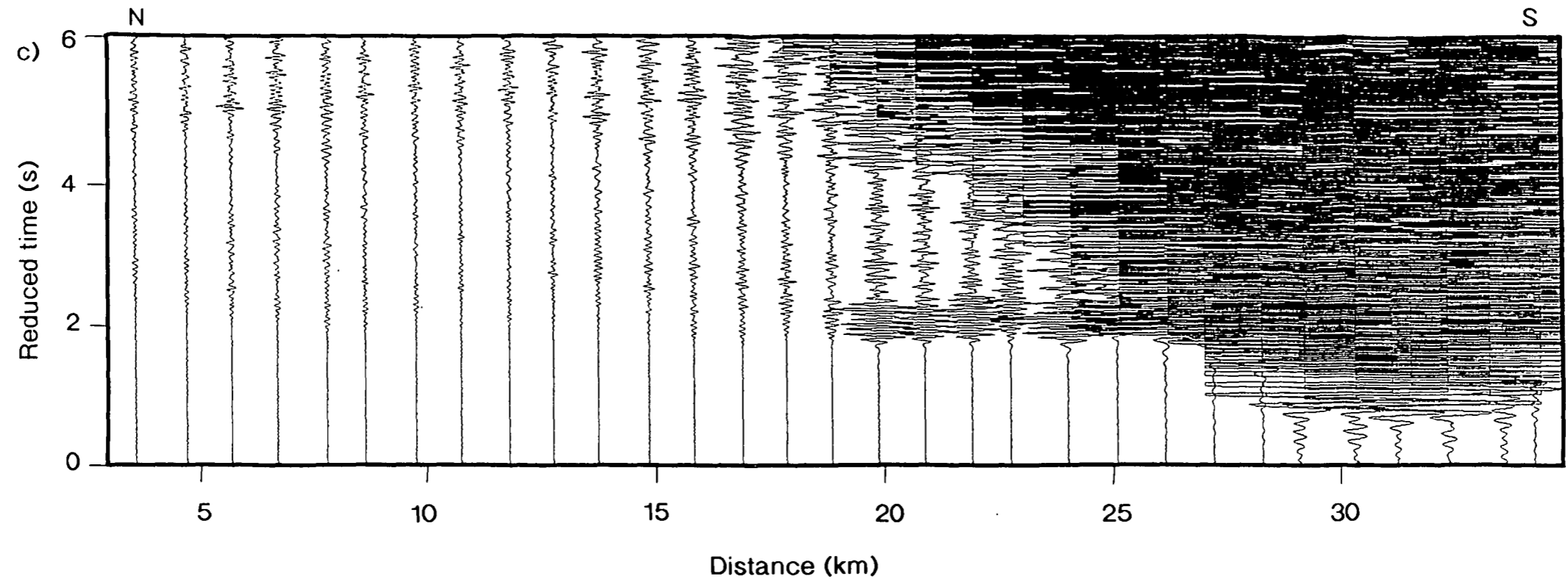


Figure E18: cont.. Explosive data recorded by DDOBS 4 at the southern end of the along-axis line. Sections are plotted at true amplitude and reduced at 6 kms^{-1} . Note the low amplitude of arrivals between 9 and 19 km offset.
 c) Horizontal X-component.
 d) Horizontal Y-component.

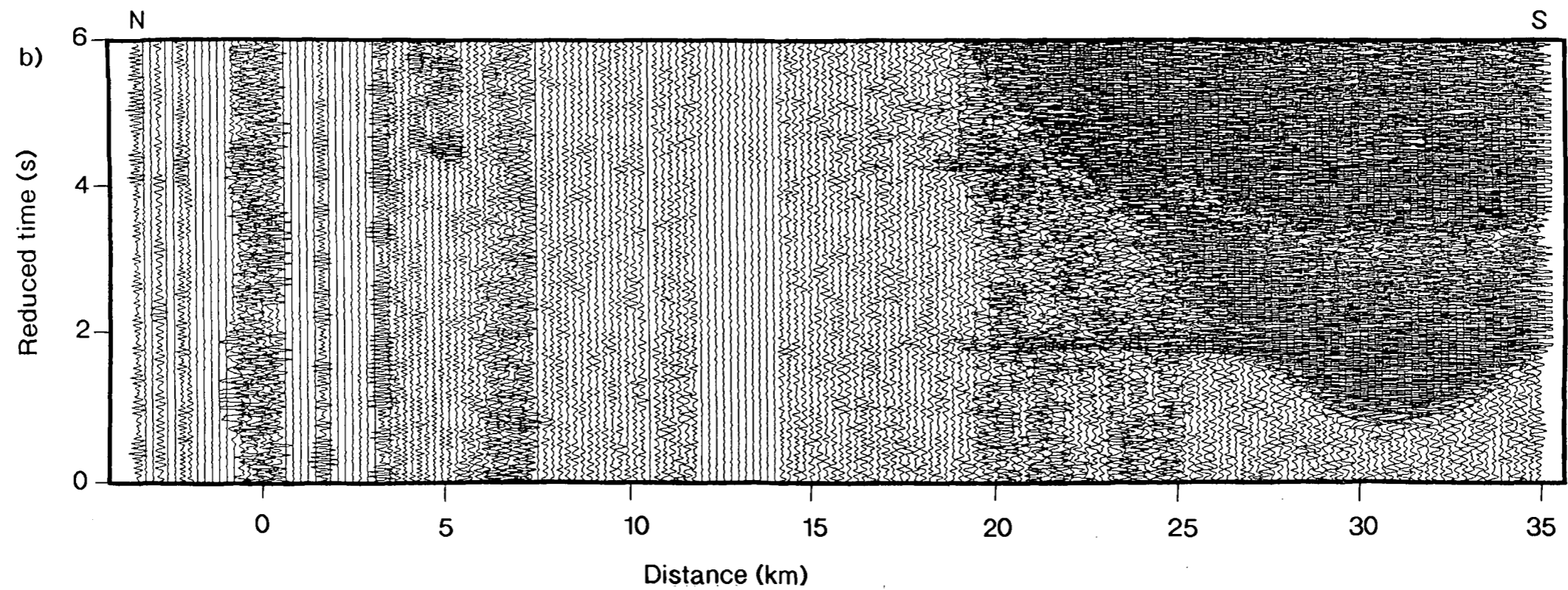
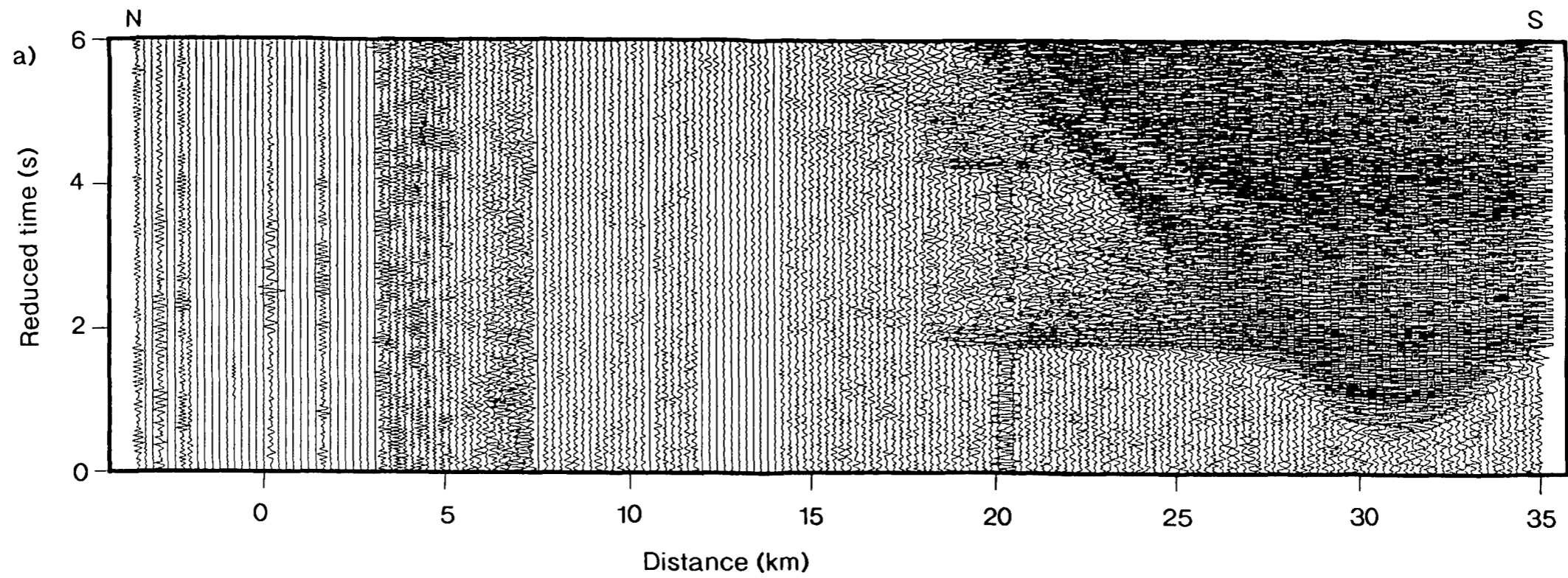


Figure E19: Airgun data recorded by DDOBS 4 at the southern end of the along-axis line. Sections are plotted at true amplitude and reduced at 6 km s^{-1} . Note the low amplitude of arrivals at offsets of less than 18 km. The noisy traces at offsets of less than 7.5 km occurred when the airgun array was not synchronised with the DDOBS recording windows (see section 2.3.2).

a) Vertical geophone component.

b) hydrophone component. Prominent noise bursts on this section are caused by disk spin (see section 3.3).

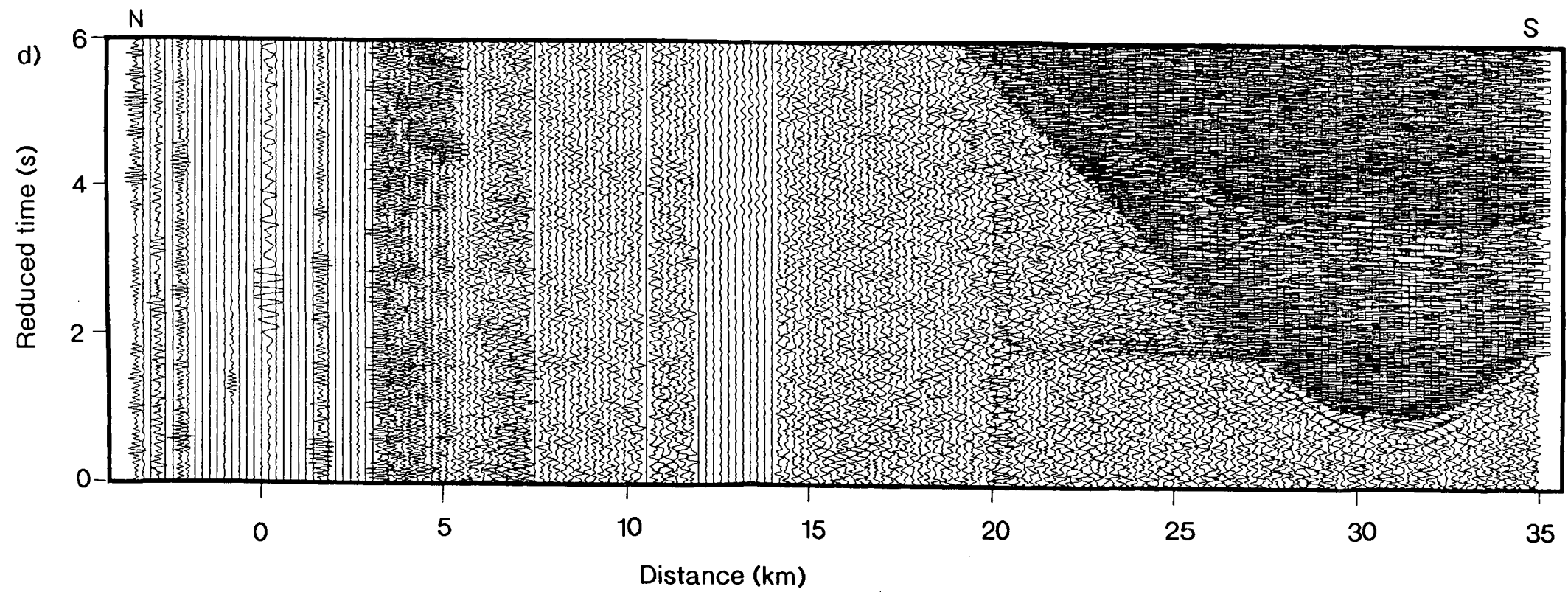
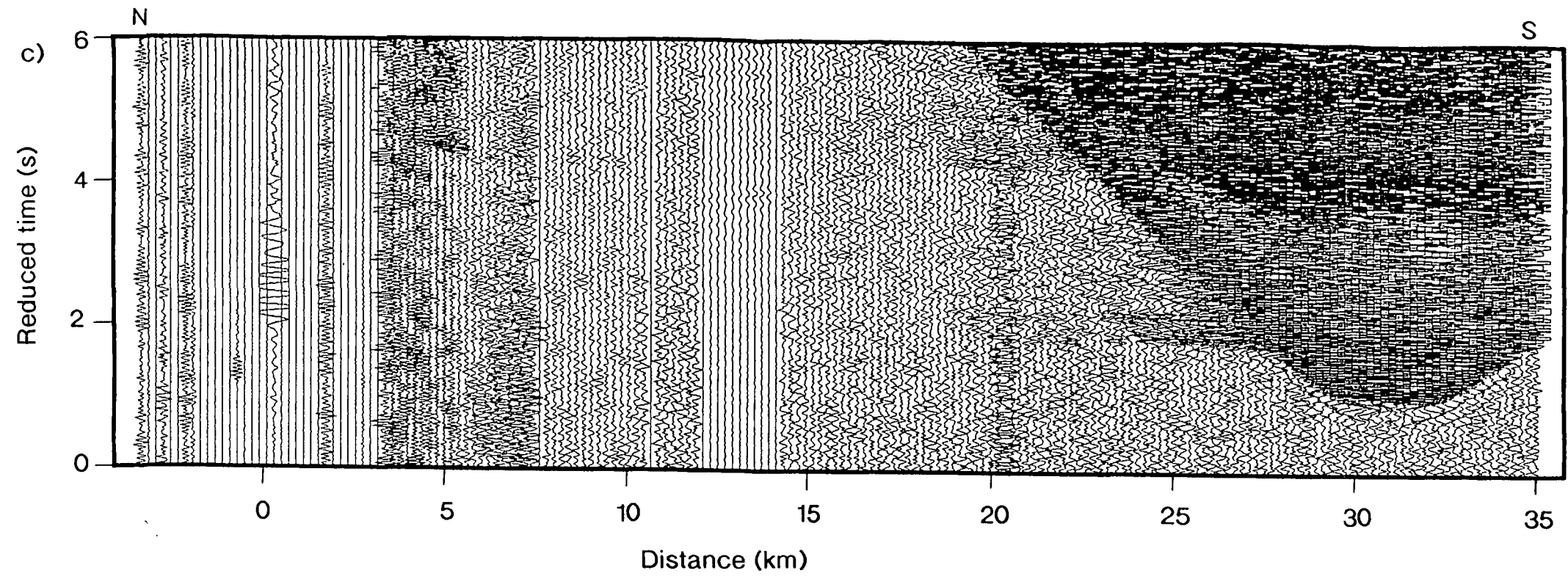


Figure E19: cont.. Airgun data recorded by DDOBS 4 at the southern end of the along-axis line. Sections are plotted at true amplitude and reduced at 6 km s^{-1} . Note the low amplitude of arrivals at offsets of less than 18 km. The noisy traces at offsets of less than 7.5 km occurred when the airgun array was not synchronised with the DDOBS recording windows (see section 2.3.2).
 c) Horizontal X-component.
 d) Horizontal Y-component.

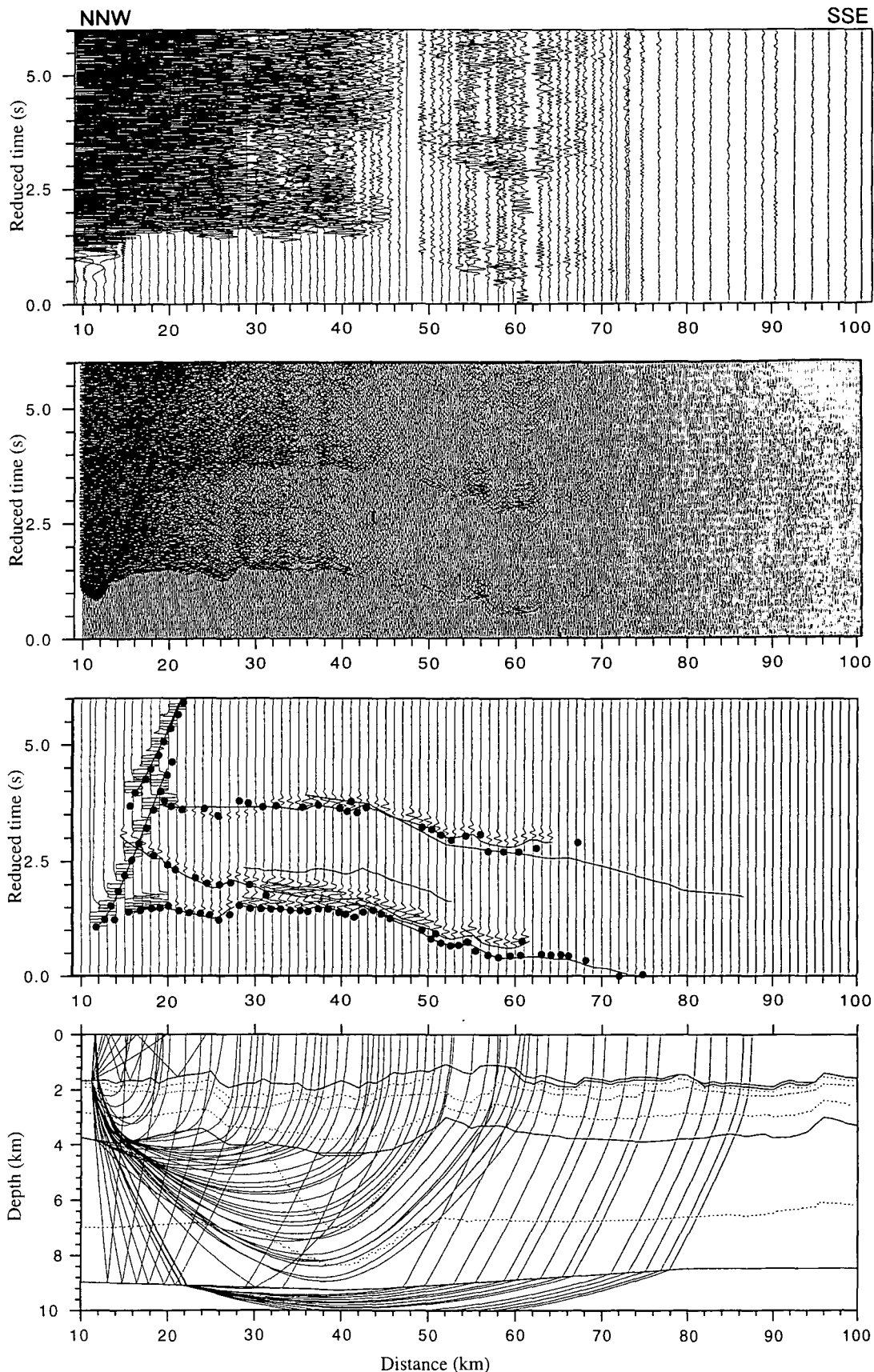


Figure E20: Ray-trace modelling of the Reykjanes Ridge final cross-axis wide-angle seismic model for DDOBS 1. The observed travel time picks are indicated by dots and the geometrical ray-traced solution by a solid line. Dot size gives an indication of the modelling error bounds (see section 2.7). Both the observed explosive and airgun vertical geophone component record sections are shown at the same scale as the calculated synthetic seismograms for comparison. Seismograms are plotted at true amplitude with a reduction velocity of 6 km s^{-1} .

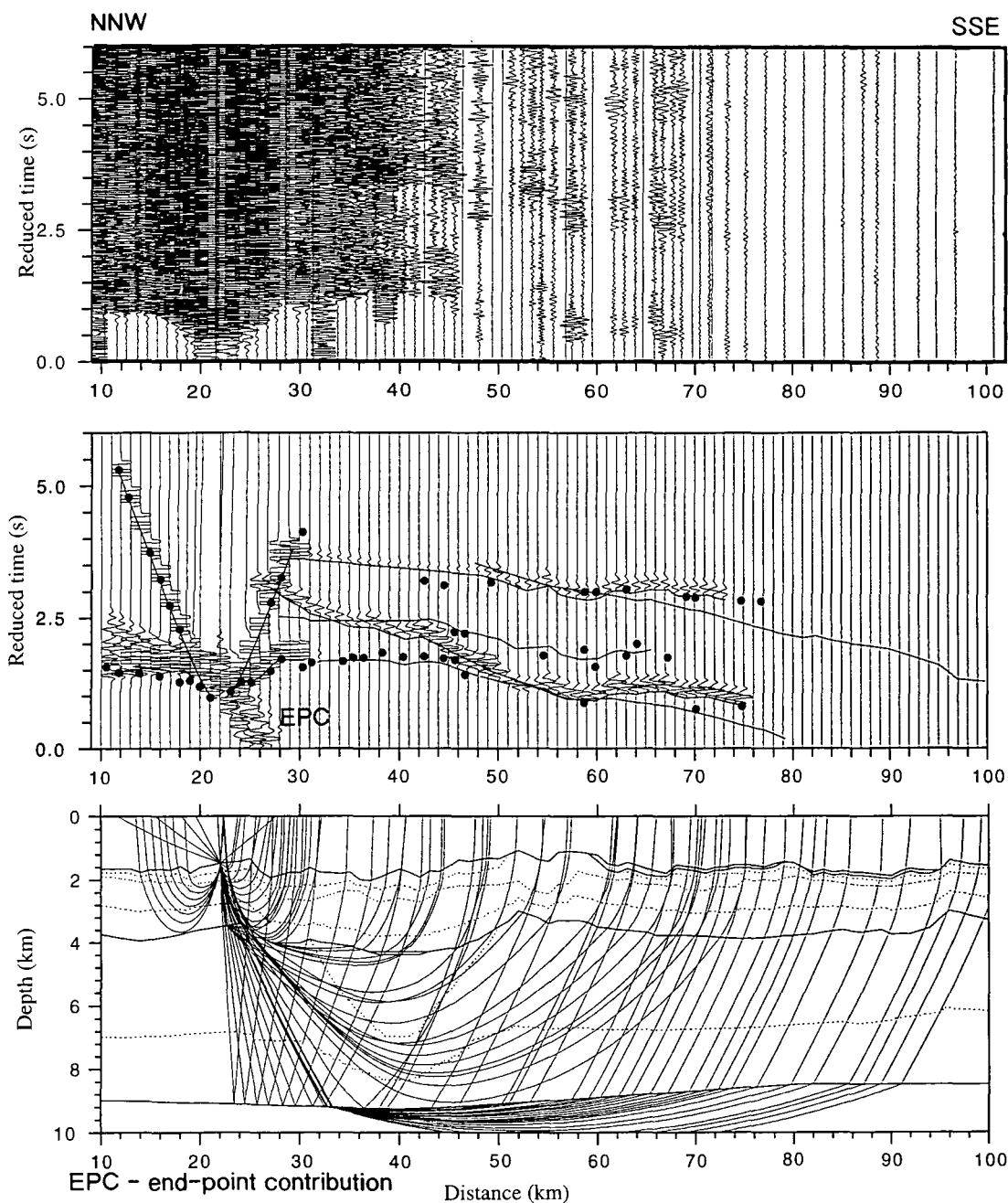


Figure E21: Ray-trace modelling of the Reykjanes Ridge final cross-axis wide-angle seismic model for CDOBS 11. The observed travel time picks are indicated by dots and the geometrical ray-traced solution by a solid line. Dot size gives an indication of the modelling error bounds (see section 2.7). The observed explosive hydrophone component record section is shown at the same scale as the calculated synthetic seismograms for comparison. Seismograms are plotted at true amplitude with a reduction velocity of 6 km s^{-1} .

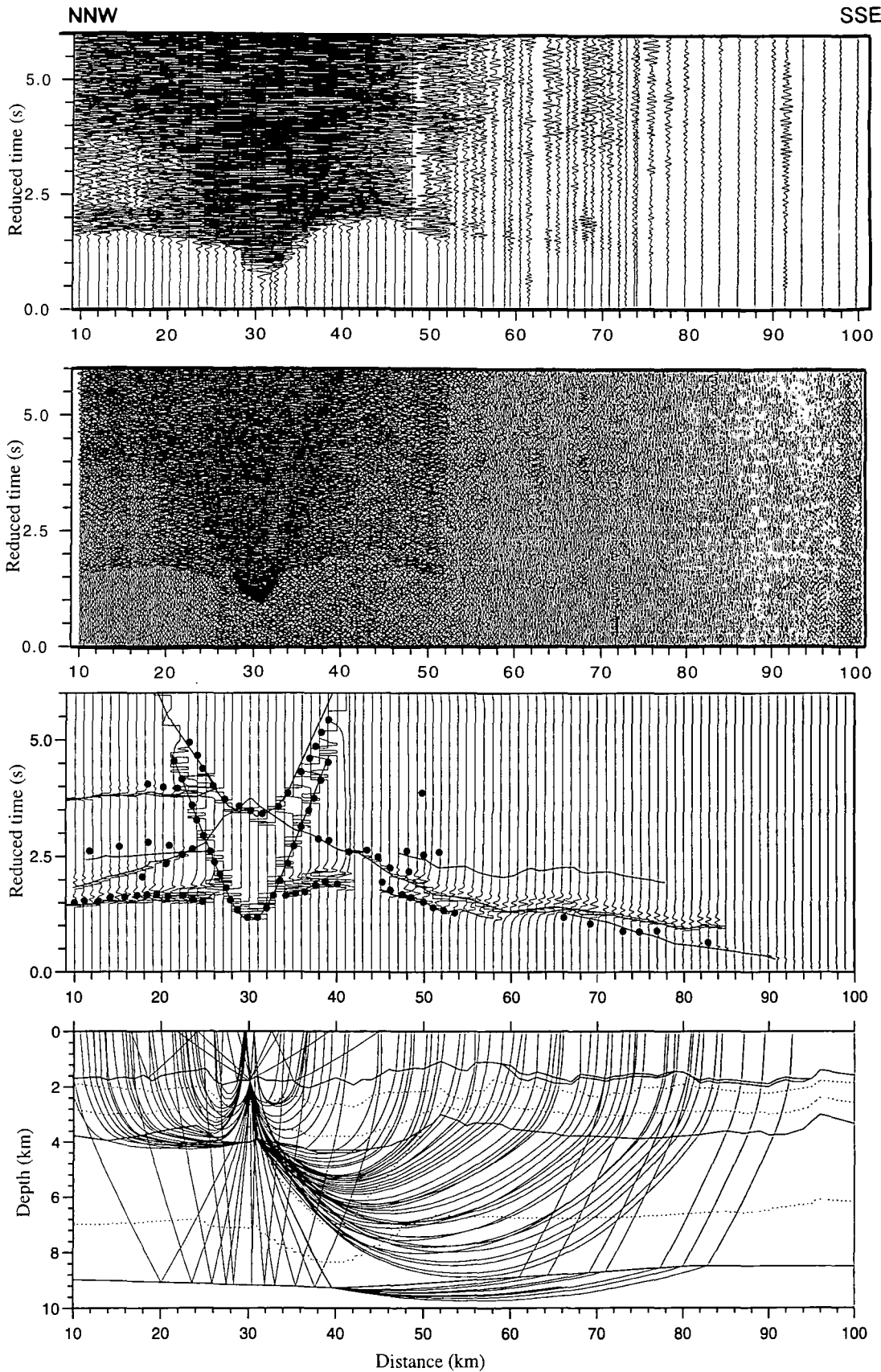


Figure E22: Ray-trace modelling of the Reykjanes Ridge final cross-axis wide-angle seismic model for DDOBS 2. The observed travel time picks are indicated by dots and the geometrical ray-traced solution by a solid line. Dot size gives an indication of the modelling error bounds (see section 2.7). Both the observed explosive and airgun vertical geophone component record sections are shown at the same scale as the calculated synthetic seismograms for comparison. Seismograms are plotted at true amplitude with a reduction velocity of 6 km s^{-1} .

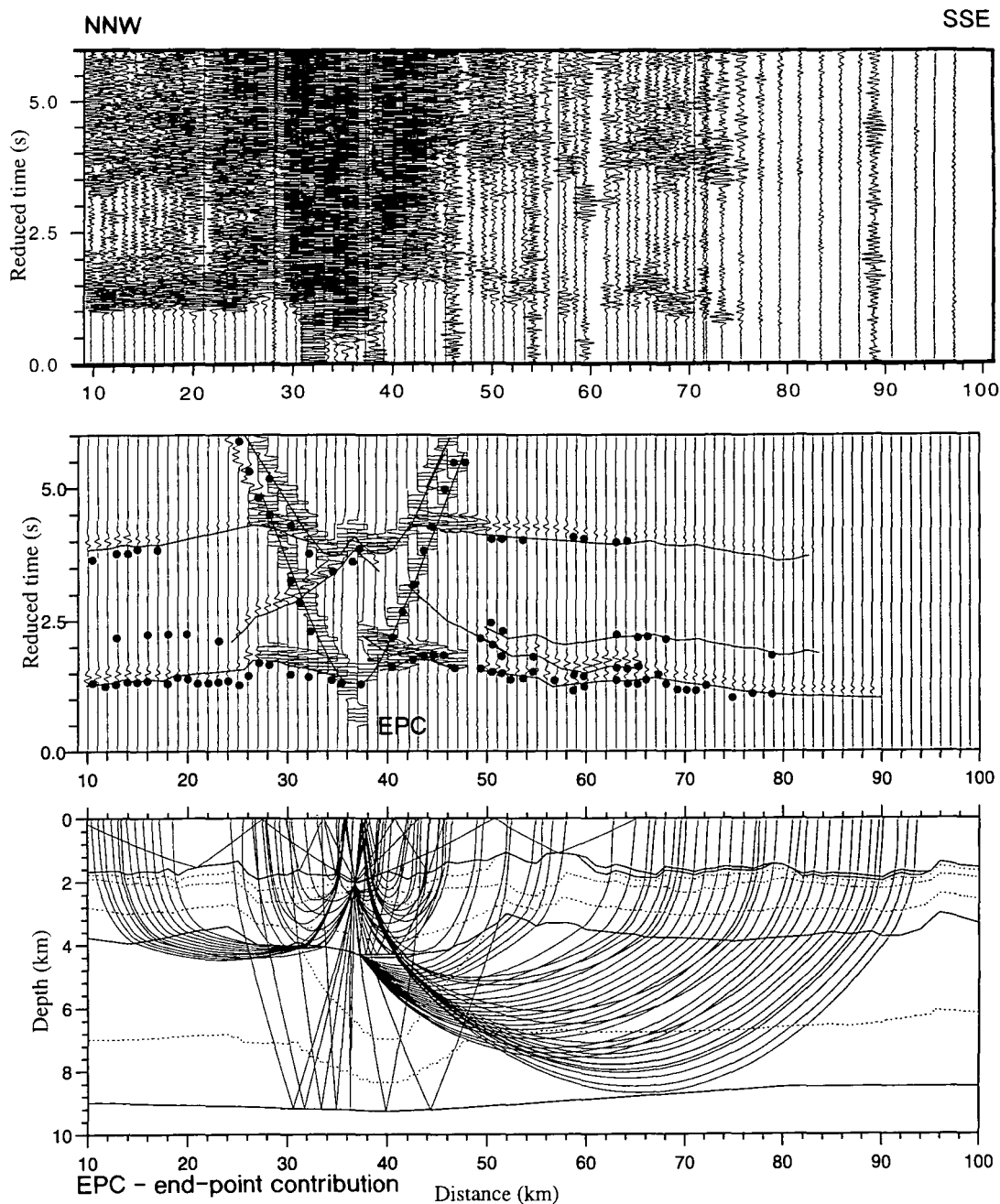


Figure E23: Ray-trace modelling of the Reykjanes Ridge final across-axis wide-angle seismic model for CDOBS 12. The observed travel time picks are indicated by dots and the geometrical ray-traced solution by a solid line. Dot size gives an indication of the modelling error bounds (see section 2.7). The observed explosive hydrophone component record section is shown at the same scale as the calculated synthetic seismograms for comparison. Seismograms are plotted at true amplitude with a reduction velocity of 6 km s^{-1} .

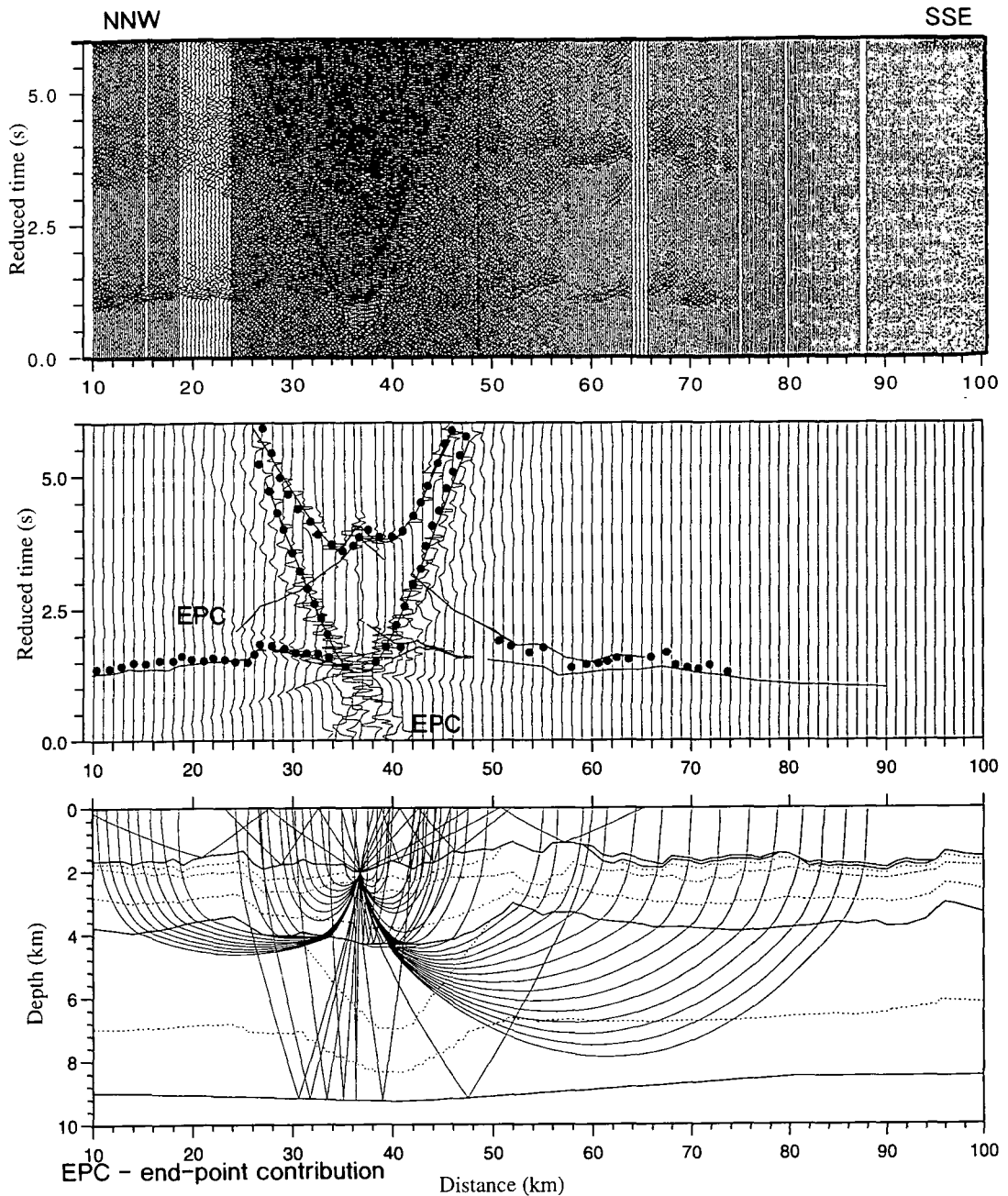


Figure E24: Ray-trace modelling of the Reykjanes Ridge final across-axis wide-angle seismic model for CDOBS 12. The observed travel time picks are indicated by dots and the geometrical ray-traced solution by a solid line. Dot size gives an indication of the modelling error bounds (see section 2.7). The observed airgun hydrophone component record section is shown at the same scale as the calculated synthetic seismograms for comparison. Seismograms are plotted at true amplitude with a reduction velocity of 6 kms^{-1} .

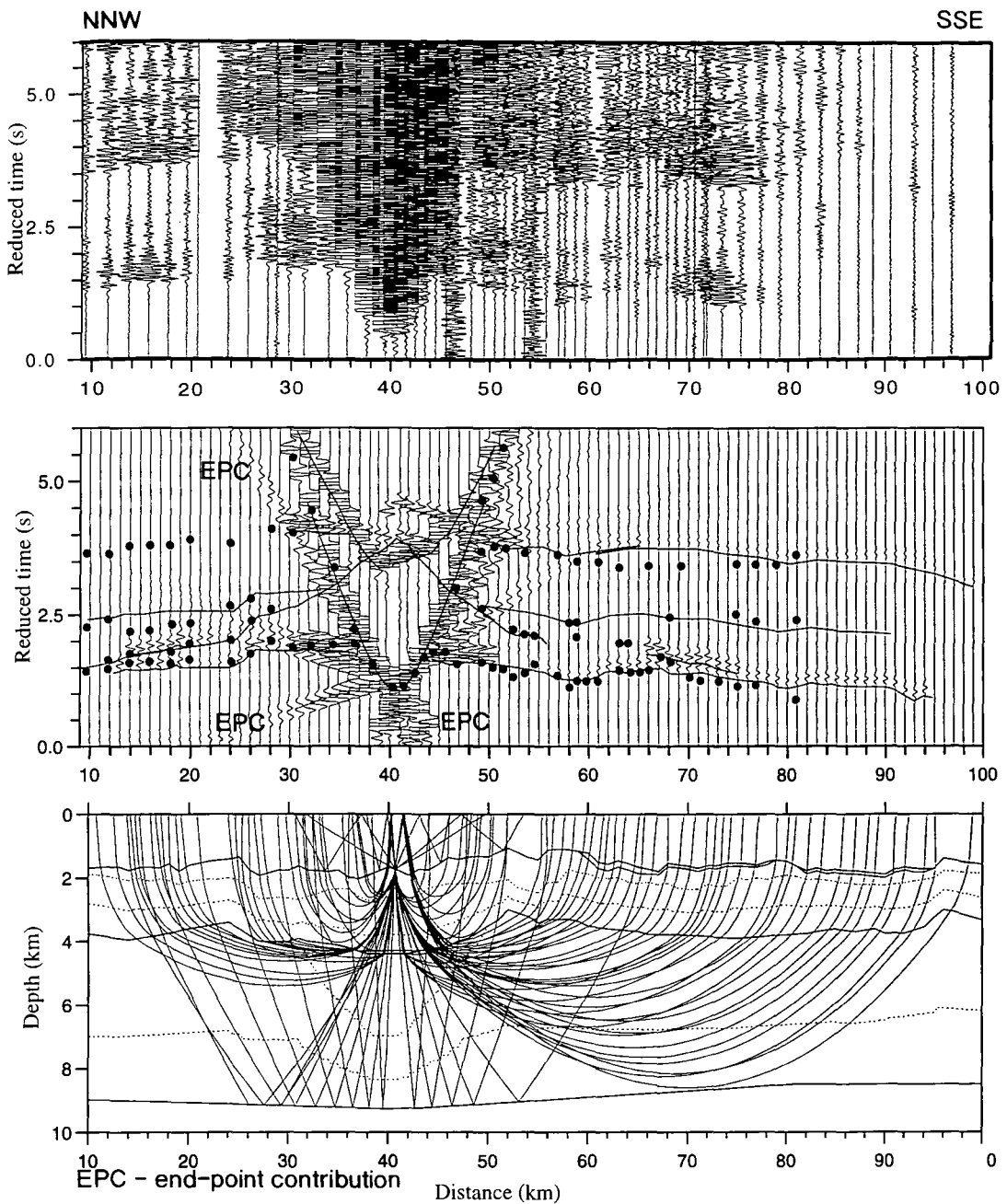


Figure E25: Ray-trace modelling of the Reykjanes Ridge final across-axis wide-angle seismic model for CDOBS 13. The observed travel time picks are indicated by dots and the geometrical ray-traced solution by a solid line. Dot size gives an indication of the modelling error bounds (see section 2.7). The observed explosive hydrophone component record section is shown at the same scale as the calculated synthetic seismograms for comparison. Seismograms are plotted at true amplitude with a reduction velocity of 6 km s^{-1} .

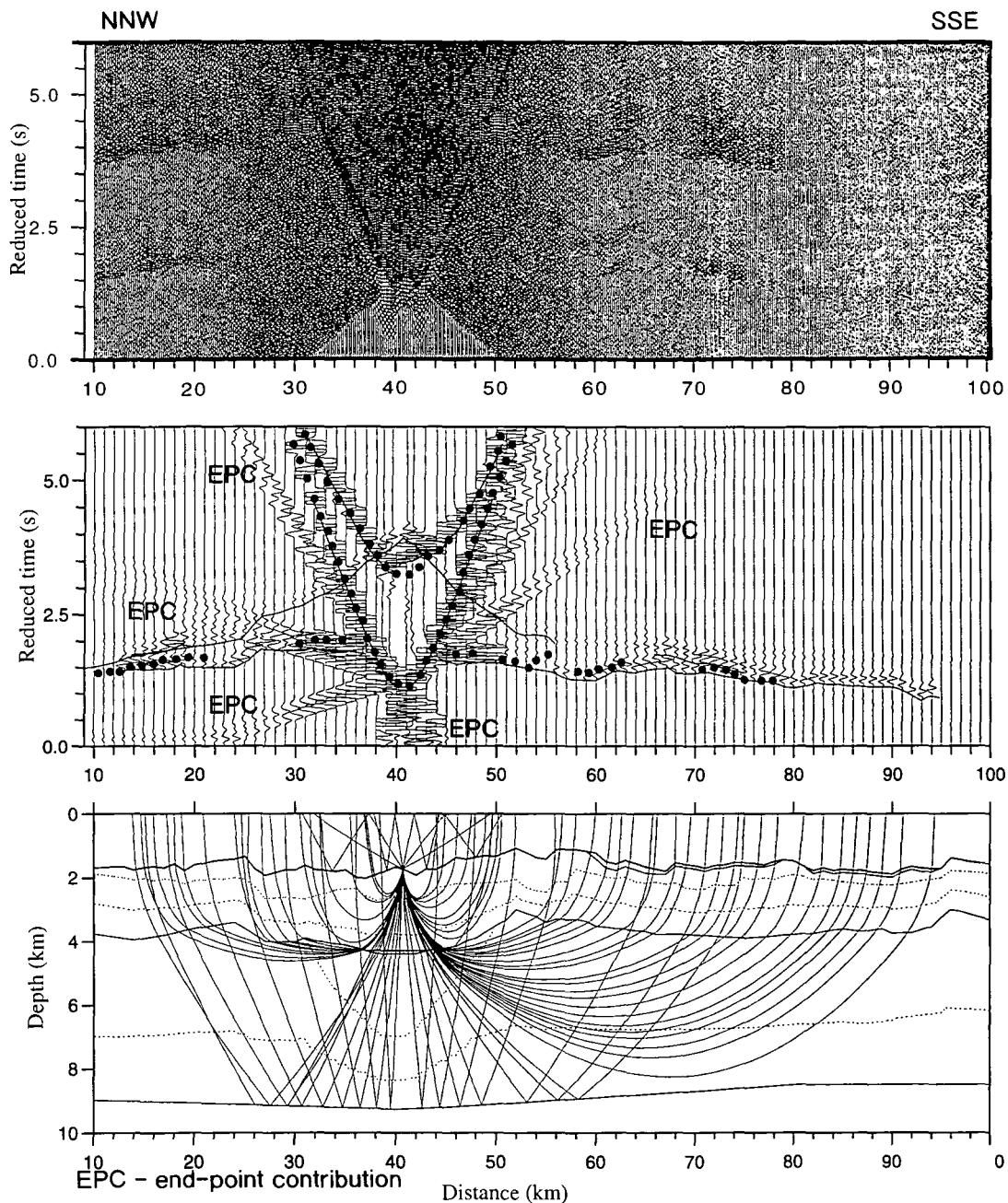


Figure E26: Ray-trace modelling of the Reykjanes Ridge final across-axis wide-angle seismic model for CDOBS 13. The observed travel time picks are indicated by dots and the geometrical ray-traced solution by a solid line. Dot size gives an indication of the modelling error bounds (see section 2.7). The observed airgun hydrophone component record section is shown at the same scale as the calculated synthetic seismograms for comparison. Seismograms are plotted at true amplitude with a reduction velocity of 6 km s^{-1} .

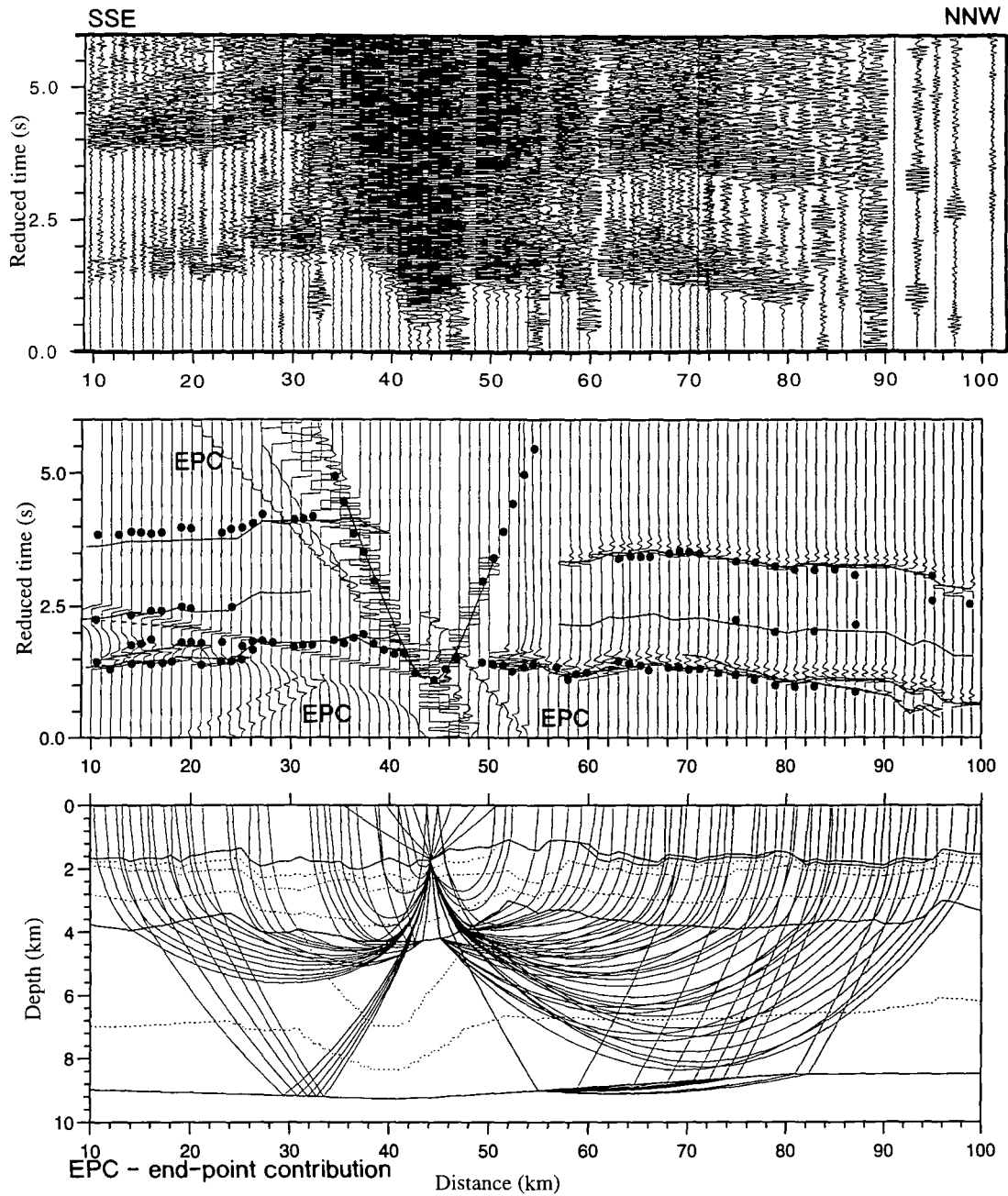


Figure E27: Ray-trace modelling of the Reykjanes Ridge final across-axis wide-angle seismic model for CDOBS 14. The observed travel time picks are indicated by dots and the geometrical ray-traced solution by a solid line. Dot size gives an indication of the modelling error bounds (see section 2.7). The observed explosive hydrophone component record section is shown at the same scale as the calculated synthetic seismograms for comparison. Seismograms are plotted at true amplitude with a reduction velocity of 6 km s^{-1} .

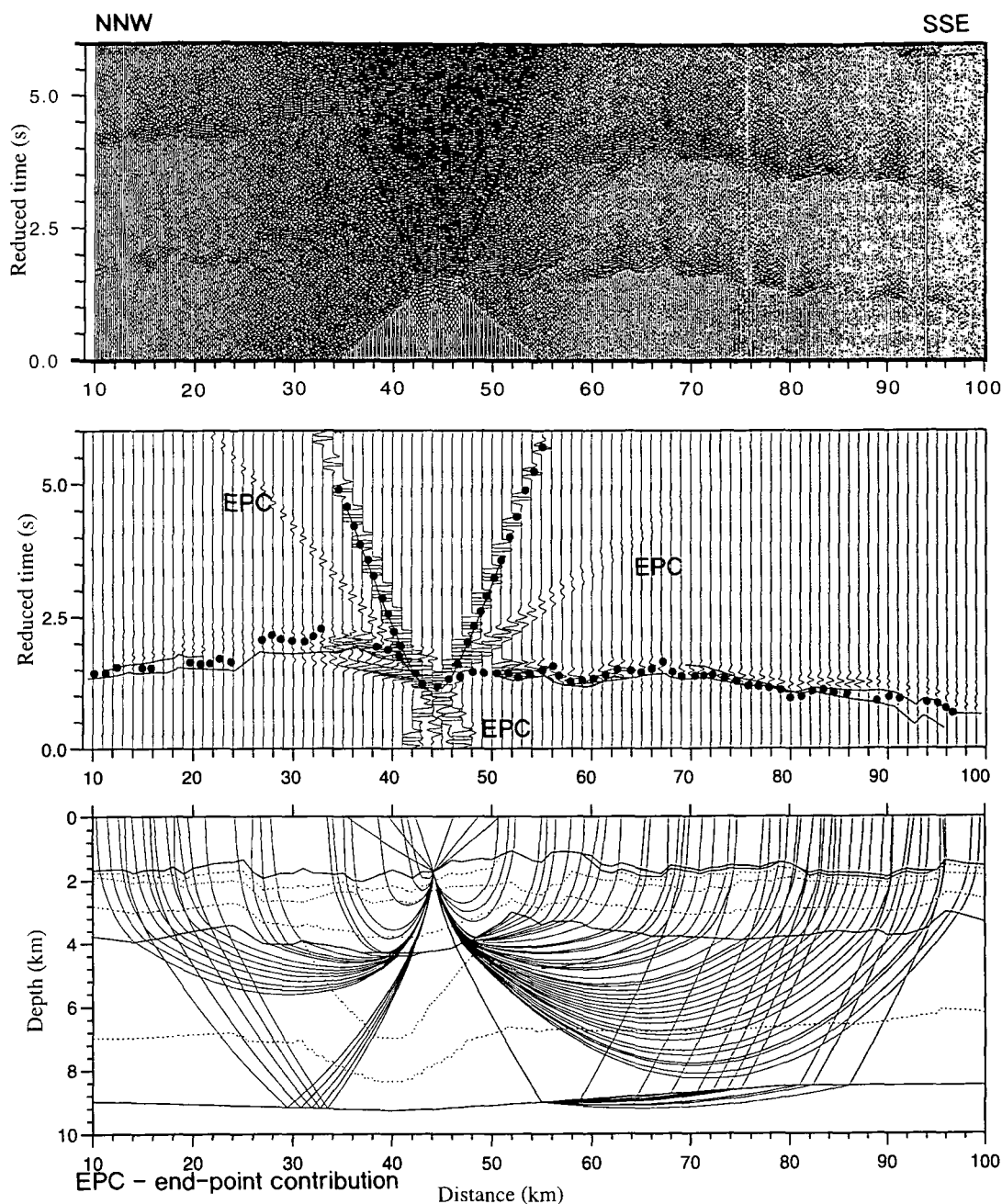


Figure E28: Ray-trace modelling of the Reykjanes Ridge final cross-axis wide-angle seismic model for CDOBS 14. The observed travel time picks are indicated by dots and the geometrical ray-traced solution by a solid line. Dot size gives an indication of the modelling error bounds (see section 2.7). The observed airgun hydrophone component record section is shown at the same scale as the calculated synthetic seismograms for comparison. Seismograms are plotted at true amplitude with a reduction velocity of 6 km^{-1} .

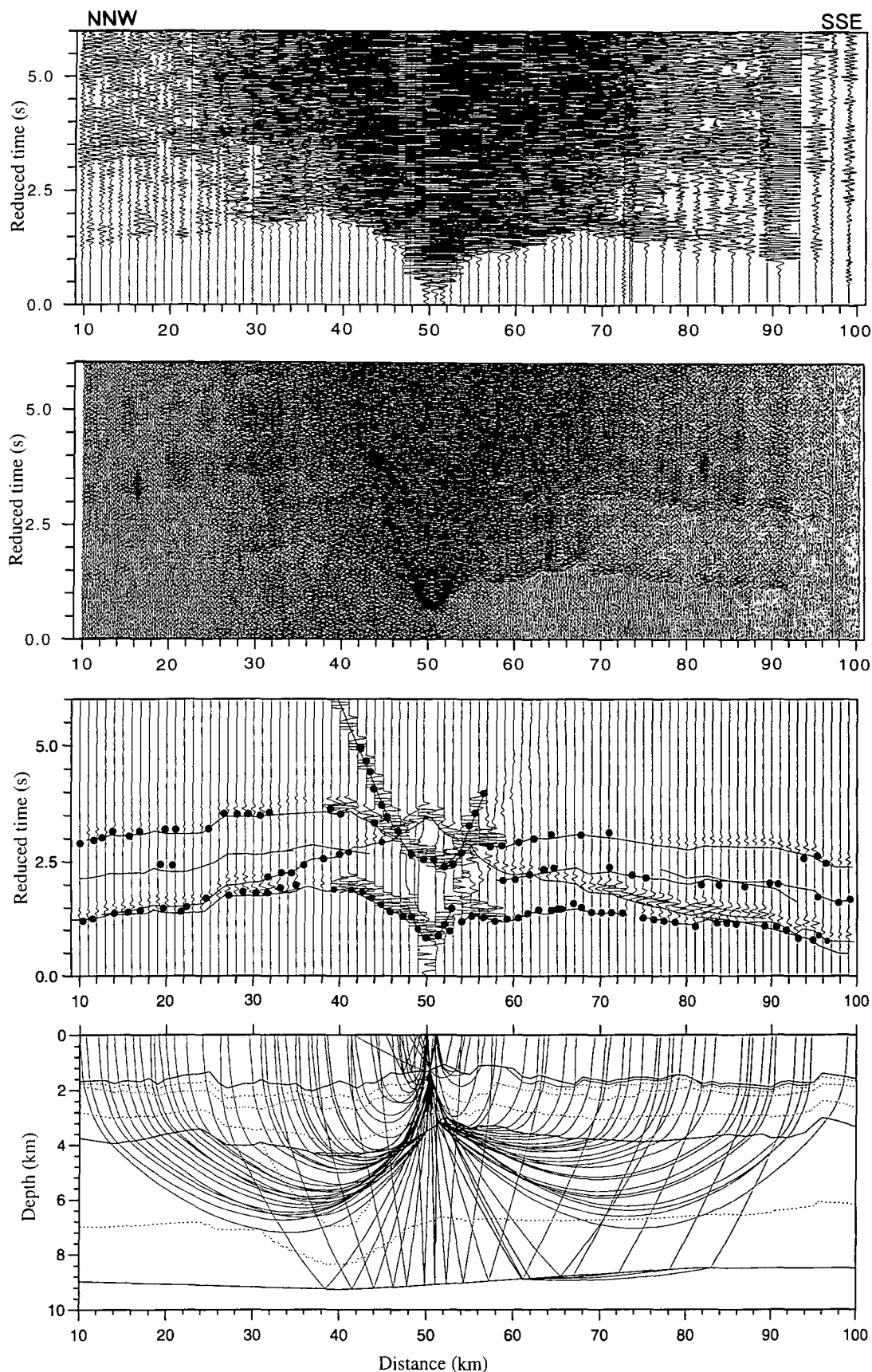


Figure E29: Ray-trace modelling of the Reykjanes Ridge final across-axis wide-angle seismic model for DDOBS 5. The observed travel time picks are indicated by dots and the geometrical ray-traced solution by a solid line. Dot size gives an indication of the modelling error bounds (see section 2.7). Both the observed explosive and airgun vertical geophone component record sections are shown at the same scale as the calculated synthetic seismograms for comparison. Seismograms are plotted at true amplitude with a reduction velocity of 6 km s^{-1} .

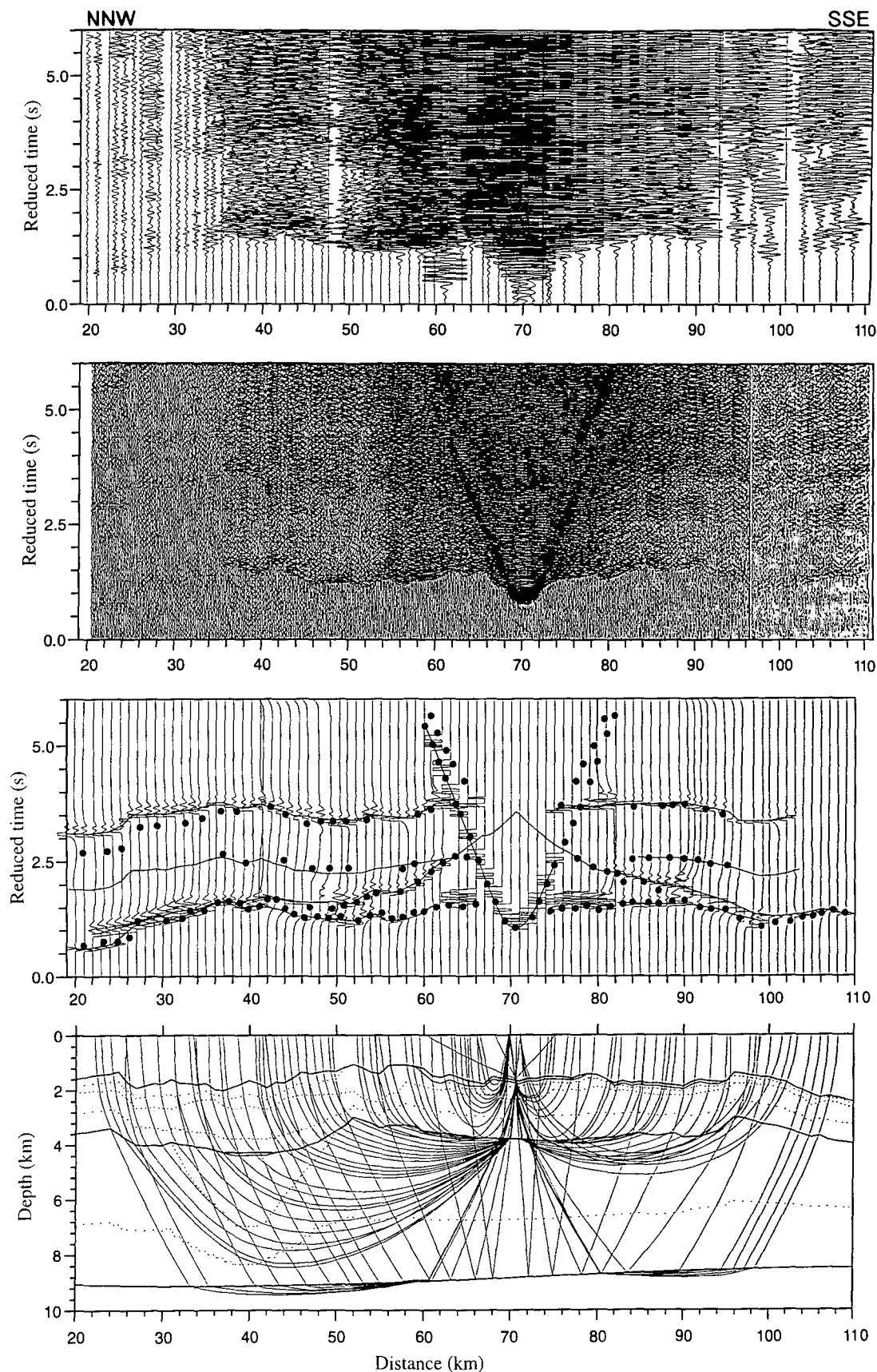


Figure E30: Ray-trace modelling of the Reykjanes Ridge final across-axis wide-angle seismic model for DDOBS 6. The observed travel time picks are indicated by dots and the geometrical ray-traced solution by a solid line. Dot size gives an indication of the modelling error bounds (see section 2.7). Both the observed explosive and airgun vertical geophone component record sections are shown at the same scale as the calculated synthetic seismograms for comparison. Seismograms are plotted at true amplitude with a reduction velocity of 6 km s^{-1} .

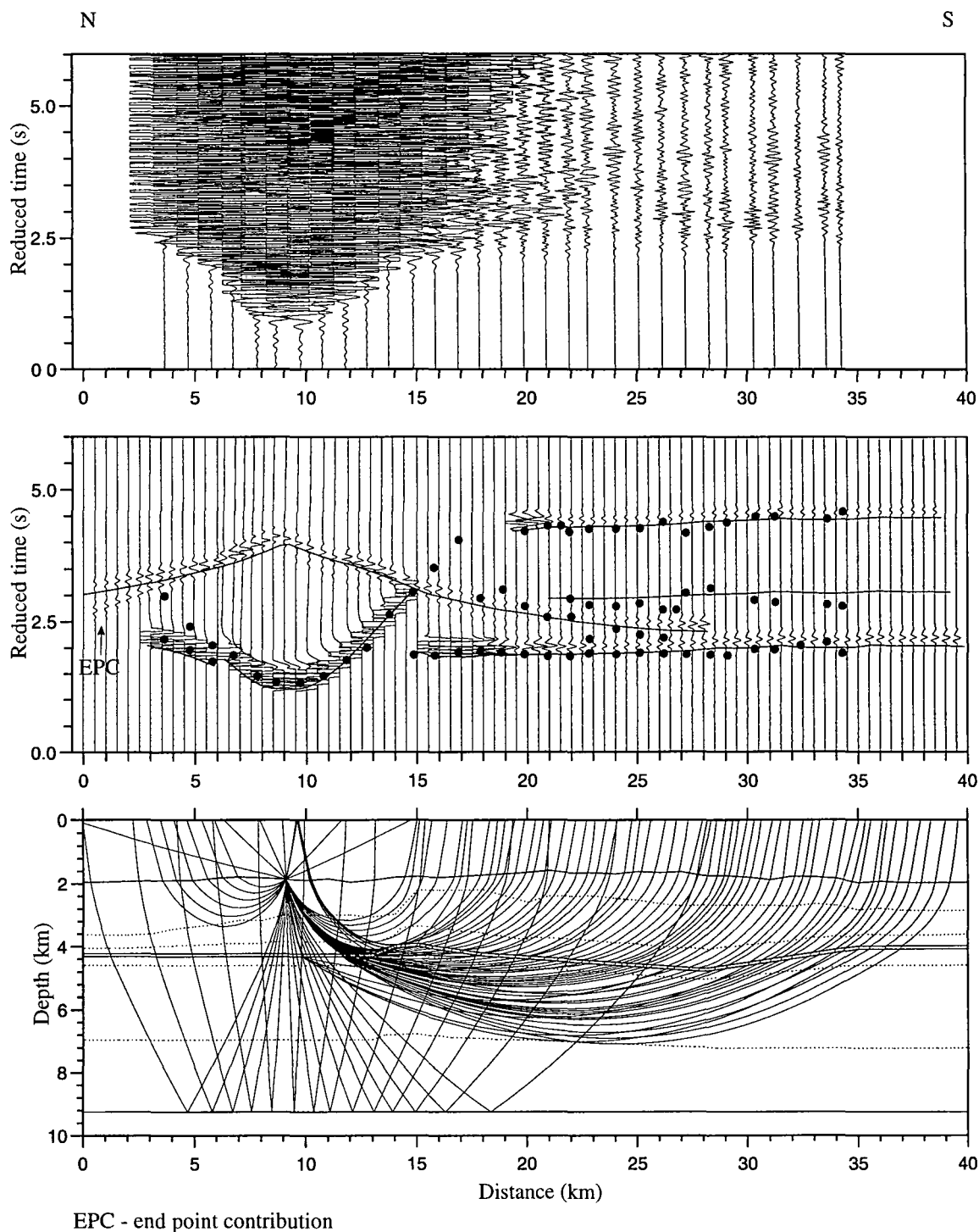


Figure E31: Ray-trace modelling of the Reykjanes Ridge final along-axis wide-angle seismic model for DDOBS 3. The observed travel time picks are indicated by dots and the geometrical ray-traced solution by a solid line. Dot size gives an indication of the modelling error bounds (see section 2.7). The observed explosive vertical geophone component record section is shown at the same scale as the calculated synthetic seismograms for comparison. Seismograms are plotted at true amplitude with a reduction velocity of 6 km s^{-1} .

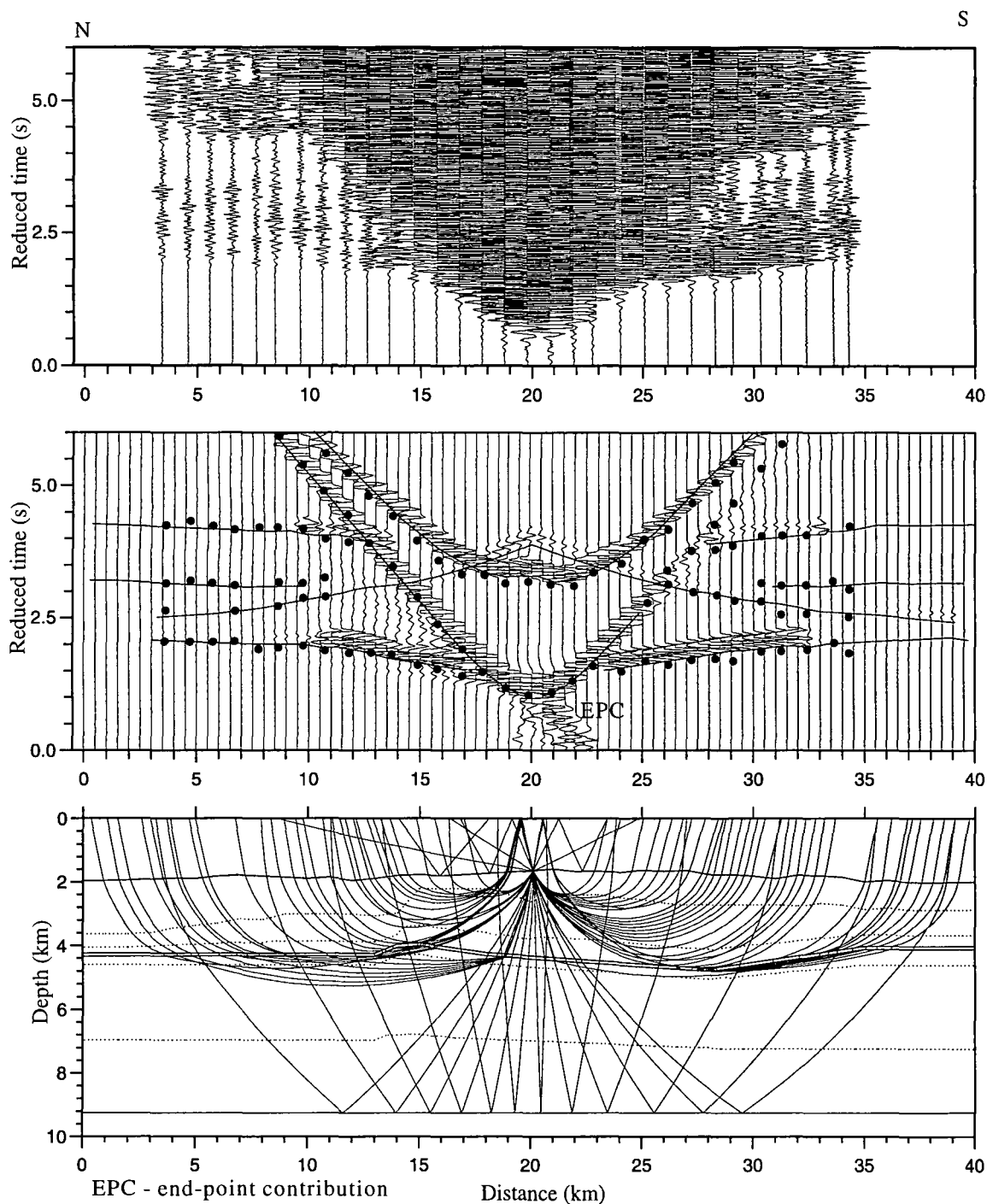


Figure E32: Ray-trace modelling of the Reykjanes Ridge final along-axis wide-angle seismic model for CDOBS 13. The observed travel time picks are indicated by dots and the geometrical ray-traced solution by a solid line. Dot size gives an indication of the modelling error bounds (see section 2.7). The observed explosive hydrophone component record section is shown at the same scale as the calculated synthetic seismograms for comparison. Seismograms are plotted at true amplitude with a reduction velocity of 6 km s^{-1} .

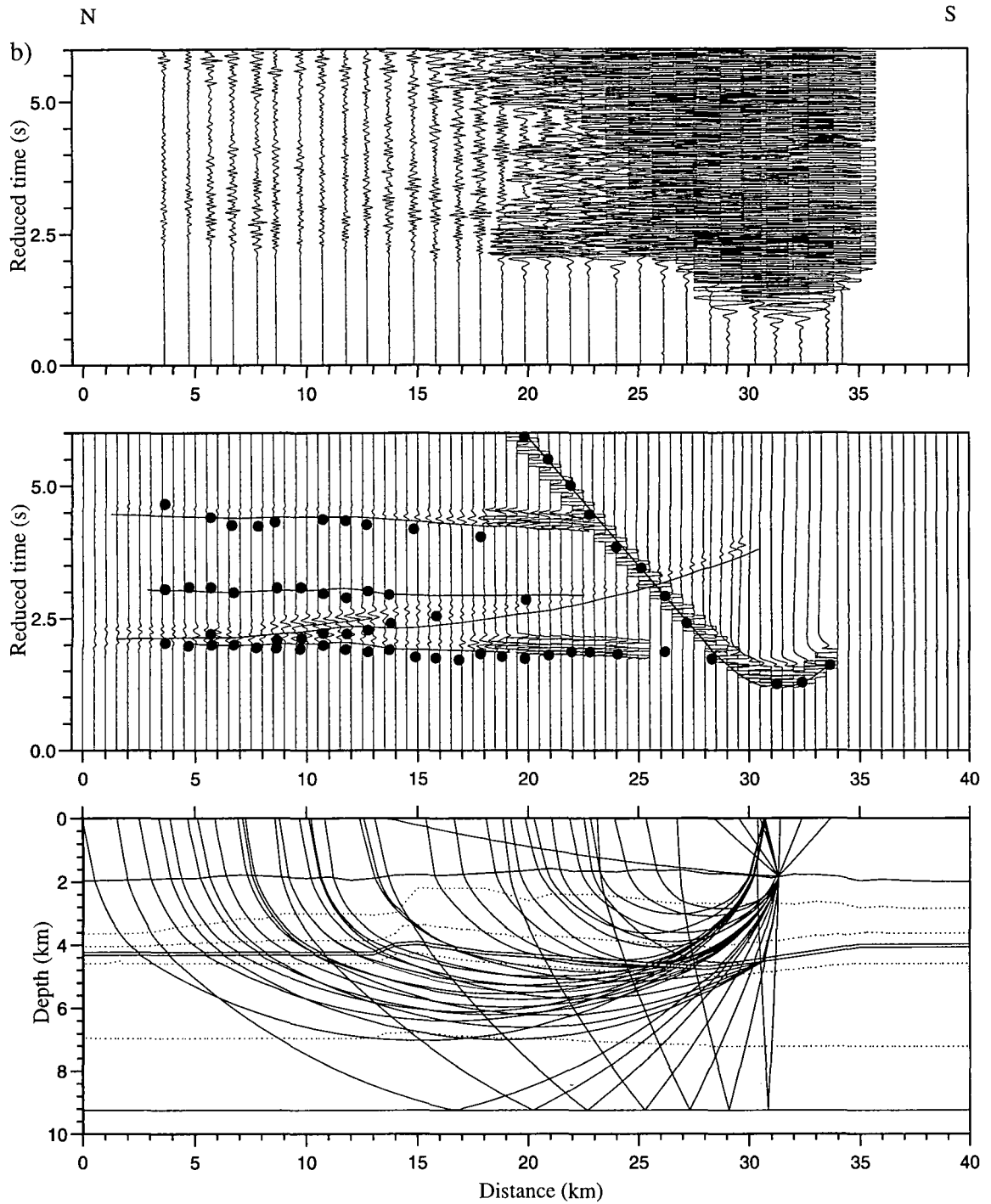


Figure E33: Ray-trace modelling of the Reykjanes Ridge final along-axis wide-angle seismic model for DDOBS 4. The observed travel time picks are indicated by dots and the geometrical ray-traced solution by a solid line. Dot size gives an indication of the modelling error bounds (see section 2.7). The observed explosive vertical geophone component record section is shown at the same scale as the calculated synthetic seismograms for comparison. Seismograms are plotted at true amplitude with a reduction velocity of 6 km s^{-1} .

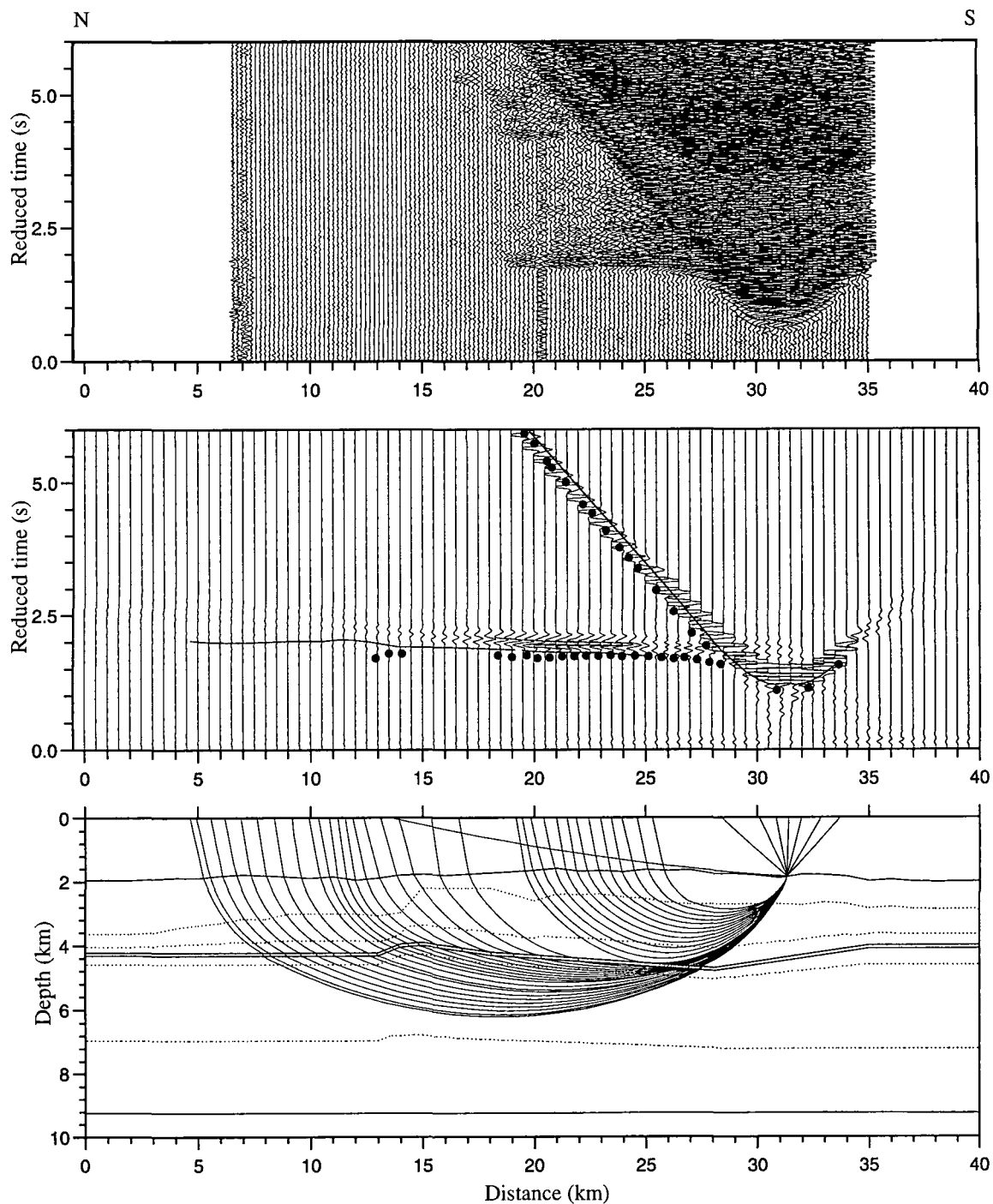


Figure E34: Ray-trace modelling of the Reykjanes Ridge final along-axis wide-angle seismic model for DDOBS 4. The observed travel time picks are indicated by dots and the geometrical ray-traced solution by a solid line. Dot size gives an indication of the modelling error bounds (see section 2.7). The observed airgun vertical geophone component record section is shown at the same scale as the calculated synthetic seismograms for comparison. Seismograms are plotted at true amplitude with a reduction velocity of 6 km s^{-1} .

